VOLUME 77 JANUARY 4, 1973 NUMBER 1

JPCHAx

THE JOURNAL OF PHYSICAL CHEMISTRY

PUBLISHED BIWEEKLY BY THE AMERICAN CHEMICAL SOCIETY

THE JOURNAL OF

PHYSICAL CHEMISTRY

AMERICAN CHEMICAL SOCIETY, *1155 Sixteenth St., N.W., Washington, D. C. 20036*

Books and Journals Division

JOHN K CRUM *Director*
RUTH REYNARD *Assistant to the Director*

CHARLES R. BERTSCH *Head, Editorial Processing Department*
D. H. MICHAEL BOWEN *Head, Journals Department*
BACIL GUILEY *Head, Graphics and Production Department*
JOSEPH H. KUNEY *Head, Business Operations Department*
SELDON W. TERRANT *Head, Research and Development Department*

All manuscripts should be sent to *The Journal of Physical Chemistry*, Department of Chemistry, University of Minnesota, Minneapolis, Minn. 55455.

Additions and Corrections are published once yearly in the final issue. See Volume 76, Number 26 for the proper form.

Extensive or unusual alterations in an article after it has been set in type are made at the author's expense, and it is understood that by requesting such alterations the author agrees to defray the cost thereof.

The American Chemical Society and the Editor of *The Journal of Physical Chemistry* assume no responsibility for the statements and opinions advanced by contributors.

Correspondence regarding accepted copy, proofs, and reprints should be directed to Editorial Processing Department, American Chemical Society, 20th and Northampton Sts., Easton, Pa. 18042. Head: CHARLES R. BERTSCH. Assistant Editor: EDWARD A. BORGER. Editorial Assistant: JOSEPH E. YURVATI.

Advertising Office: Centcom, Ltd., 142 East Avenue, Norwalk, Conn. 06851.

Business and Subscription Information

Remittances and orders for subscriptions and for single copies, notices of changes of address and new professional connections, and claims for missing numbers should be sent to the Subscription Service Department, American Chemical Society, 1155 Sixteenth St., N.W., Washington, D. C. 20036. Allow 4 weeks for change of address. Please include an old address label with the notification.

Claims for missing numbers will not be allowed (1) if received more than sixty days from date of issue, (2) if loss was due to failure of notice of change of address to be received before the date specified in the preceding paragraph, or (3) if the reason for the claim is "missing from files."

Subscription rates (1973): members of the American Chemical Society, $20.00 for 1 year; to nonmembers, $60.00 for 1 year. Those interested in becoming members should write to the Admissions Department, American Chemical Society, 1155 Sixteenth St., N.W., Washington, D. C. 20036. Postage to Canada and countries in the Pan-American Union, $5.00; all other countries, $6.00. Single copies for current year: $3.00. Rates for back issues from Volume 56 to date are available from the Special Issues Sales Department, 1155 Sixteenth St., N.W., Washington, D. C. 20036.

This publication and the other ACS periodical publications are now available on microfilm. For information write to MICROFILM, Special Issues Sales Department, 1155 Sixteenth St., N.W., Washington, D. C. 20036.

Notice to Authors last printed in the issue of November 23, 1972

THE JOURNAL OF

PHYSICAL CHEMISTRY

Volume 77, Number 1 January 4, 1973

JPCHAx 77(1) 1-142 (1973)

COMMUNICATIONS TO THE EDITOR

AUTHOR INDEX

In papers with more than one author the name of the author to whom inquiries about the paper should be addressed is marked with an asterisk in the by-line.

THE JOURNAL OF
PHYSICAL CHEMISTRY

VOLUME 77, NUMBER 1 JANUARY 4, 1973

Solubility Product and Anionic Complexation Constants of Silver Halides, Benzoate, and Acetate in Acetonitrile, *N,N*-Dimethylformamide, and Dimethyl Sulfoxide

M. K. Chantooni, Jr., and I. M. Kolthoff*

School of Chemistry, University of Minnesota, Minneapolis, Minnesota 55455 *(Received June 13, 1972)*

Solubility products, K^{sp}, of silver halides, acetate, and benzoate and formation constants of AgX_2^- have been determined in methanol, acetonitrile (AN), *N,N*-dimethylformamide (DMF), and dimethyl sulfoxide (DMSO). For the halides K^{sp} and $K^f(AgX_2^-)$ were determined from $pa(M^+)$ and $pa(Ag^+)$ measurements in solutions saturated both with respect to AgX and MX ($M^+ = Na^+$ or K^+), $pa(M^+)$ being determined with a calibrated cation-sensitive electrode. Values of K^{sp} and $K^f(AgX_2^-)$ thus obtained were in satisfactory agreement with those in the literature. For benzoate and acetate the above constants were found from potentiometric titration or from $pa(Ag^+)$ and $pa(H)$ measurements in saturated solutions of AgX containing excess parent acid. From the total solubility the dissociation constants of the homoconjugate salts $AgHX_2$ and $Ag(HX)_2X$ were determined. The mobilities in AN of the halide, acetate, and benzoate are approximately the same as those of their respective silver complexes, AgX_2^-, while those of the acetate and benzoate homoconjugates ($(HOAc)_2OAc^-$ and $H(Bz)_2^-$) are much smaller than the corresponding simple ions. An explanation for this behavior is proposed. Medium activity coefficients ($p^W\gamma_i^{AN}$) of the various ions are presented. The difference ($p^W\gamma^{AN}(OAc^-) - p^W\gamma^{AN}(Bz^-)$) $\cong$ ($p^W\gamma^{AN}(HOAc) - p^W\gamma^{AN}(HBz)$) $\cong \frac{1}{2}(p^W\gamma^{AN}(Ag(OAc)_2^-) - p^W\gamma^{AN}(Ag(Bz)_2^-))$, indicating the large effect of the nonelectric part on $p^W\gamma_i^{AN}$. This conclusion is independent of the assumption on the basis of which $p^W\gamma_i^{AN}$ values were calculated.

In previous studies, based on the tetraphenylarsonium tetraphenylborate assumption, the medium activity coefficient ${}^{S(1)}\gamma_i^{S(2)}$, i being a halide ion, benzoate, or acetate, has been reported, S(1), referring to the protic solvent methanol[1,2] and S(2) to the aprotic solvents[1,2] acetonitrile (AN), $D = 36.0$, *N,N*-dimethylformamide (DMF), $D = 36.7$, and dimethyl sulfoxide (DMSO), $D = 46.6$. The solubility products of the corresponding silver salts were determined in S(1) and S(2) and $p\gamma(X^-)$ was calculated from the relation $\Delta pK^{sp}(AgX) = p\gamma(Ag^+) + p\gamma(X^-)$; $p\gamma(Ag^+)$ having been found from the solubility product of silver tetraphenylborate.[2,3] From potentiometric titration of tetraalkylammonium halides with silver nitrate using a silver wire electrode it has been reported that silver ion forms the fairly stable anionic complex AgX_2^- in AN,[4,5] DMF,[4,6] hexamethylphosphoramide,[4] acetone,[5] nitromethane,[7] DMSO,[4,8,9] sulfolane,[10] and propylene carbonate.[11] Similar complexes of silver with azide or thiocyanate have also been found in these aprotic solvents.[4,9] In these solvents additional complexes $Ag_2X_3^-$ and $Ag_3X_4^-$ are formed with iodide and thiocyanate ion.[4,9] From an analysis of the titration curve of X^- with silver ion the values of

$$K^{sp}(AgX) = a(Ag^+)a(X^-) \qquad (1)$$

(1) R. Alexander and A. J. Parker, *J. Amer. Chem. Soc.*, **89**, 5549 (1967).
(2) I. M. Kolthoff and M. K. Chantooni, Jr., *J. Phys. Chem.*, **76**, 2024 (1972), and references therein.
(3) R. Alexander, A. J. Parker, J. Sharp, and W. Waghorne, *J. Amer. Chem. Soc.*, **94**, 1148 (1972).
(4) R. Alexander, E. C. Ko, Y. C. Mac, and A. J. Parker, *J. Amer. Chem. Soc.*, **89**, 3703 (1967).
(5) D. C. Leurs, R. I. Iwamoto, and J. Kleinberg, *Inorg. Chem.*, **5**, 201 (1966).
(6) M. Bréant, C. Buisson, M. Porteix, J. Sue, and J. Terrat, *J. Electroanal. Chem.*, **24**, 409 (1970).
(7) J. C. Bardin, *J. Electroanal. Chem.*, **28**, 157 (1970).
(8) N. Rumbaut and A. Peeters, *Bull. Soc. Chim. Belg.*, **79**, 45 (1970).
(9) M. LeDemézet, C. Madec, and M. L'Her, *Bull. Soc. Chim. Fr.*, 365 (1970).
(10) R. L. Benoit, A. Beauchamp, and M. Deneux, *J. Phys. Chem.*, **73**, 3268 (1969).
(11) J. N. Butler, *Anal. Chem.*, **39**, 1799 (1967).

and

$$K^{f}(AgX_2^-) = [AgX_2^-]/a(Ag^+)[X^-]^2 f(X^-)$$
$$f(AgX_2^-) = f(X^-) \quad (2)$$

have been evaluated.[4-9] It should be realized that such an analysis of the titration curve, which employs a single measured parameter, $a(Ag^+)$, may involve considerable uncertainty, particularly when an appreciable amount of undissociated AgX is present or when the stability of AgX_2^- is small and precipitation of AgX occurs in the early portion of the titration, *e.g.*, in the reaction of acetate with silver ion in AN.[4]

In the present paper values of $K^{sp}(AgX)$ and $K^{f}(AgX_2^-)$ have been estimated from $a(Ag^+)$ and $a(M^+)$ (M^+ = K^+ or Na^+) measurements in AN, DMF, and DMSO solutions saturated *both* with respect to AgX and MX, knowing $K^{sp}(MX)$. In these solutions the following electroneutrality and conservation relations hold, neglecting $Ag_2X_3^-$ and $Ag_3X_4^-$

$$[M^+] + [Ag^+] = [X^-] + [AgX_2^-] \quad (3)$$

$$C(Ag) = [Ag^+] + [AgX_2^-] + [AgX] + 2[AgAgX_2] + [MAgX_2] \quad (4)$$

$$C(X) = [X^-] + 2[AgX_2^-] + [AgX] + 2[AgAgX_2] + [MX] + 2[MAgX_2] \quad (5)$$

$$C(M) = C(X) - C(Ag) = [M^+] + [MX] + [MAgX_2] \quad (6)$$

$$K^{d}(AgX) = a(Ag^+)a(X^-)/[AgX] \quad f(AgX) = 1 \quad (7)$$

In eq 4-6 $C(Ag)$, $C(X)$, and $C(M)$ represent total (analytical) concentrations. The following systems were studied under the above conditions: AN saturated with silver chloride (bromide) and potassium chloride (bromide), DMF with silver chloride and sodium (potassium) chloride, and DMSO with silver chloride and sodium chloride.

Furthermore, when X^- is an anion of a weak acid, whose dissociation constant, $K^{d}(HX)$, is known, $K^{sp}(AgX)$ has been found from $a(H^+)$ and $a(Ag^+)$ measurements in solutions saturated with respect to AgX and containing a known concentration of HX. When the solubility of HX is not too great (<2 *M*) the solution can advantageously be saturated both with respect to HX and AgX. The equilibrium concentration of HX under these conditions can be taken equal to the solubility of HX in absence of AgX. Particularly in AN, a protophobic aprotic solvent, formation constants of homoconjugate species of acetic and benzoic acids, HX_2^- and $(HX)_2X^-$, are large.[12] This homoconjugation combined with the incomplete ionic dissociation of $AgHX_2$ and $Ag(HX)_2X$ results in a marked increase in the solubility of AgX ($C(Ag)$ in eq 9). In solutions saturated with AgX and containing HX the following relations apply

$$[Ag^+] = [X^-] + [HX_2^-] + [(HX)_2X^-] + [AgX_2^-] \quad (8)$$

$$C(Ag) = C(X) = [Ag^+] + [AgX] + 2[AgAgX_2] + [AgX_2^-] + [AgHX_2] + [Ag(HX)_2X] \quad (9)$$

$$C(HX) = [HX] + [AgHX_2] + 2[Ag(HX)_2X] + [HX_2^-] + 2[(HX)_2X^-] \quad (10)$$

$$K^{f}(HX_2^-) = [HX_2^-]/[HX][X^-] \quad f(HX_2^-) = f(X^-) \quad (11)$$

$$K^{f}((HX)_2X^-) = [(HX)_2X^-]/[HX]^2[X^-] \quad f((HX)_2X^-) = f(X^-) \quad (12)$$

$$K^{d}(AgHX_2) = a(Ag^+)[HX_2^-]f(HX_2^-)/[AgHX_2] \quad (13)$$

$$K^{d}(Ag(HX)_2X^-) = a(Ag^+)[(HX)_2X^-]f((HX)_2X^-)/[Ag(HX)_2X] \quad (14)$$

$$K^{d}(HX) = a(H^+)a(X^-)/[HX] \quad (15)$$

In this investigation acetonitrile solutions saturated with silver benzoate and benzoic acid, or saturated with silver acetate and containing 0.5-1 *M* acetic acid, were studied. The latter system was also studied in methanol and DMSO. Also, the total ionic concentration in solutions saturated with AgX and MX or AgX and containing HX (eq 3 and 8, respectively) was estimated from their conductivity, while $a(Ag^+)$ was measured potentiometrically with a silver wire electrode and $a(M^+)$ with a cation-selective electrode. Also $a(M^+)$ was calculated from the difference in total X and silver content, $C(X) - C(Ag)$, in solutions saturated with AgX and MX. Activity coefficients were calculated from the partially extented Debye-Hückel relation $-\log f = A\mu^{1/2}/(1 + Ba\mu^{1/2})$. For simplicity a was taken as 3.5 Å for Ag^+, K^+ and Na^+, a mean of 2.5, 4.5, and 3 Å given for these ions by Kielland[13] in water, while a was taken as 8 Å for $AgCl_2^-$, $AgBr_2^-$, and 12 Å for the homoconjugate ions. For AN and DMF A = 1.5 and B = 0.47, and for DMSO A = 1.1 and B = 0.43.

Experimental Section

Reagents. Acetonitrile,[14] methanol,[15] *N,N*-dimethylformamide,[16] and dimethyl sulfoxide[12] were purified and stored as previously described. Silver acetate was a Baker product, recrystallized from water, while silver benzoate was prepared as described by Kolthoff, *et al.*[17] Silver chloride and bromide were prepared in the conventional way. Sodium chloride, potassium chloride, and bromide were Merck Reagent Grade. Tetraethylammonium acetate, and benzoic and acetic acids were used previously.[12]

Instrumental. The potentiometric cell used in the determination of $a(Ag^+)$ and pa(H) and the 0.01 *M* silver nitrate/Ag reference electrode in the same solvent are those as described for pa(H) measurements in AN.[18] A Beckman No. 39047 cation-selective electrode was used in the above potentiometric assembly for $a(K^+)$ and $a(Na^+)$ determinations in AN, DMF, and DMSO. Prior to use the electrode was soaked for at least 24 hr in a 0.01 *M* solution of sodium or potassium perchlorate in the organic solvent in which $a(M^+)$ measurements were made. It was calibrated in saturated and/or undersaturated solutions of the following salts in the three aprotic solvents: potassium chloride, bromide, perchlorate, and 2,4-dinitrophenolate, and sodium chloride and perchlorate. Solubility products of these salts in AN, DMF, and DMSO and dissociation constants of the various salts in AN have been tabulated elsewhere.[2] Stable electrode potentials reproducible to within ±2 mV were obtained usually after 10 min. Calibration curves in AN, DMF, and DMSO are reproduced in Figure 1. They are linear in the range $a(M^+) = 2 \times 10^{-4}$ to at least 5×10^{-2} *M*, the slopes being practically

(12) I. M. Kolthoff, M. K. Chantooni, Jr., and S. Bhowmik, *J. Amer. Chem. Soc.*, **90**, 23 (1968).
(13) J. Kielland, *J. Amer. Chem. Soc.*, **59**, 1675 (1937).
(14) I. M. Kolthoff, S. Bruckenstein, and M. K. Chantooni, Jr., *J. Amer. Chem. Soc.*, **83**, 3927 (1961).
(15) I. M. Kolthoff and M. K. Chantooni, Jr., *Anal. Chem.*, **44**, 194 (1972).
(16) I. M. Kolthoff, M. K. Chantooni, Jr., and H. Smagowski, *Anal. Chem.*, **42**, 1622 (1970).
(17) I. M. Kolthoff, J. J. Lingane, and W. V. Larson, *J. Amer. Chem. Soc.*, **60**, 2512 (1938).
(18) I. M. Kolthoff and M. K. Chantooni, Jr., *J. Amer. Chem. Soc.*, **87**, 4428 (1965).

Nernstian, 59 ± 2 mV/$\Delta pa(M^+)$ at 25.0°. Measurements of $pa(Na^+)$ were not made in DMF as McClure and Reddy[19] reported that millimolar levels of Na^+ were required for proper electrode response in DMF, possibly because of solvation of this ion by amine impurities in the solvent. Although similar electrode behavior was noted in this study in DMSO (Figure 1) this electrode was satisfactory at the high levels of $a(Na^+)$ encountered. The conductivity cell and bridge have been described previously.[14]

Total Solubility of AgX, MX, and HX. Prior to the operations described below, acetonitrile solutions were taken to dryness and the residues titrated in water. This was not necessary in methanol, DMF, and DMSO solutions, as these solvents do not interfere with the titrations.

In saturated silver and sodium chloride solutions in DMSO, the total silver and chloride contents, $C(Ag)$ and $C(Cl)$, are such to allow their estimation gravimetrically after flooding the sample with 20 volumes of water (yielding $C(Ag)$) or 0.1 M aqueous silver nitrate solution (yielding $C(Cl)$ as AgCl). In AN and DMF solutions saturated with AgX and MX (X = halide) an estimate of the difference $C(X) - C(Ag)$ (eq 4 and 5) was made from potentiometric titration with aqueous silver nitrate of aliquots taken up in 1:10 water–methanol mixtures. In AN or methanol solutions saturated with AgX and containing HX or tetraethylammonium acetate potentiometric titration with sodium iodide (silver wire electrode) yielded $C(Ag)$. Benzoate and acetate do not interfere in the titration. The alkalimetric determination of $C(HA)$ in these solutions was made by flooding an aliquot of the solution with 10 volumes of hot water, cooling, adding 0.5 g of potassium bromide to precipitate the silver and then 2 ml of nitrobenzene to coat the silver bromide, and titrating with aqueous sodium hydroxide using phenolphthalein as indicator. Identical results were obtained by extracting benzoic acid with ethyl ether from the aqueous solution of the residue obtained after evaporation to dryness of the AN solution saturated with benzoic acid and silver benzoate.

Total X (acetate, benzoate) in solutions saturated with AgX and containing HX or tetraethylammonium acetate was estimated by titration in AN with perchloric acid (in acetic acid) using α-naphtholbenzein as indicator.[20] Methanol solutions were taken to dryness and the residue dissolved in 0.5 ml of anhydrous acetic acid and 3 ml of AN and titrated with perchloric acid.

Results

Ionic Mobilities. The following ionic mobilities, λ_0, have been reported in AN: Ag^+ 85;[21] Cl^- 91;[22] Br^- 95;[21] K^+ 86;[23] Et_4N^+ 85;[24] benzoate 62.[25] In DMF[26] $\lambda_0(K^+)$ = 30.8, $\lambda_0(Na^+)$ = 29.9, and $\lambda_0(Cl^-)$ = 55.1. The value of $\lambda_0(OAc^-)$ in AN, equal to 107, was derived from the following conductivity data in solutions of tetraethylammonium acetate: $C(Et_4NOAc)$ = 1.44 × 10^{-3}, 2.88 × 10^{-3}, and 5.75 × 10^{-3} M, Λ = 179, 170, and 165, respectively. From the specific conductivities of saturated silver chloride–potassium chloride and silver bromide–potassium bromide solutions in AN entered in Table I, $\lambda_0(K^+)$, $\lambda_0(Cl^-)$, $\lambda_0(Br^-)$ values and values of $[K^+] = \{C(X) - C(Ag) - [KX]\}$ (see below) and $[X^-]$ from $K^{sp}(KX)$ and $a(Ag^+)$, the latter determined potentiometrically with the silver electrode, values of $\lambda_0(AgCl_2^-)$ and $\lambda_0(AgBr_2^-)$ equal to 96 and 88, respectively, were estimated. At the low ionic strengths in saturated solutions in AN as compared to those in DMF the salts $KAgX_2$ were considered completely dissociated. Incomplete dissociation of $KAgX_2$ would lead to considerably higher values of $\lambda_0(AgX_2^-)$, which are highly improbable. The following conductivity data were obtained in DMF at various dilutions of the saturated silver chloride–sodium chloride solution: $C(NaAgCl_2)$ = 3.19 × 10^{-3}, 5.75 × 10^{-3}, 9.57 × 10^{-3}, 1.23 × 10^{-2}, and 7.18 × 10^{-2} M (saturated), Λ = 91.4, 91.9, 92.5, 92.9, and 74.1, respectively. Fuoss and Kraus and Λ *vs.* $\sqrt{C}$ plots of the above data yield $\lambda_0(AgCl_2^-)$ = 61 and $K^d(NaAgCl_2)$ ~ 0.04 assuming $[AgCl_2^-] \gg [Cl^-]$. Since $\lambda_0(AgCl_2^-) \sim \lambda_0(Cl^-)$, the value of $\lambda_0(AgCl_2^-)$ found in this way would hardly be affected by relatively small amounts of free chloride ion present in the dilute solutions of $NaAgCl_2$. Using the above value of $\lambda_0(AgCl_2^-)$, $K^d(KAgCl_2)$ ~ 0.03 was obtained from the conductivity of a saturated solution of silver chloride–potassium chloride in DMF (Table I).

In similar fashion, ionic mobilities of $Ag(Bz)_2^-$, $Ag(OAc)_2^-$, and $(HOAc)_2OAc^-$ in AN were calculated from the specific conductivities of solutions of saturated silver benzoate in Table II or of saturated silver acetate in presence of tetraethylammonium acetate (Table I) or of acetic acid (Table II) respectively. The concentrations of the various ionic species were calculated as described below. Using the above values of $\lambda_0(Ag^+)$ and $\lambda_0(Bz^-)$ the following mobilities were found in AN at infinite dilution: $Ag(Bz)_2^-$ = 62. $Ag(OAc)_2^-$ = 103, and $(HOAc)_2OAc^-$ = 74.

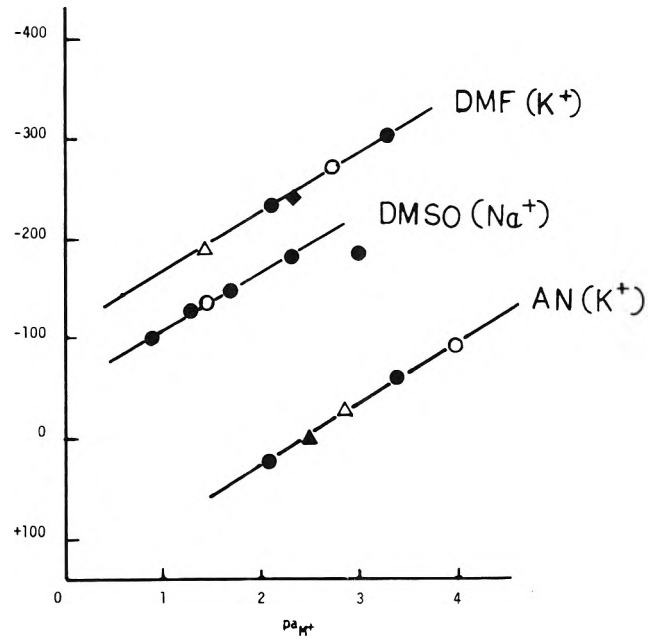

Figure 1. Calibration plots of cation electrode in aprotic solvents: ●, $KClO_4$ or $NaClO_4$; ○, KCl or NaCl; △, KBr, ▲, potassium 2,4-dinitrophenolate, and ♦, potassium *p*-bromobenzoate. Lines drawn with slope of 60 mV/$\Delta pa(M^+)$.

(19) J. E. McClure and T. B. Reddy, *Anal. Chem.*, **40**, 2064 (1968).
(20) I. M. Kolthoff, M. K. Chantooni, Jr., and S. Bhowmik, *Anal. Chem.*, **39**, 1627 (1967).
(21) P. Walden and E. Birr, *Z. Phys. Chem.*, 144 (1929).
(22) A. Popov and H. Humphrey, *J. Amer. Chem. Soc.*, **81**, 2043 (1959).
(23) S. Minc and P. Werblan, *Electrochim. Acta*, 7, 257 (1962).
(24) J. F. Coetzee and G. P. Cunningham, *J. Amer. Chem. Soc.*, **87**, 2529 (1965).
(25) I. M. Kolthoff and M. K. Chantooni, Jr., *J. Phys. Chem.*, **70**, 856 (1966).
(26) J. E. Prue and P. J. Sherrington, *Trans. Faraday Soc.*, **57**, 1795 (1961).

TABLE I: Concentration and Activities of Species in Solutions Saturated with AgX and Containing MX

Solvent	MX	$(C(X) - C(Ag))$	[MX]	pa(M): Cation electrode potential	pa(M): Ag titration from eq 4 and 5	$pa(Ag^+)$	Specific conductance, $ohm^{-1}\ cm^{-1}$	[AgX]	$[AgX_2^-]$	$[MAgX_2]$	$f(M^+)$
AN	KCl (sat.)	2.75×10^{-4}	0.2×10^{-4}	3.6_6	3.6_2	8.6_7	4.46×10^{-5}	~0	2.1×10^{-4}	0	0.95
	KBr (sat.)	2.90×10^{-3}	0.39×1^{-3}	2.7_8	2.6_8	10.6_7	3.97×10^{-4}	~0	1.4×10^{-3}	0	0.84
	Et_4NOAc $(5.75 \times 10^{-3}\ M)$	8.45×10^{-3a}	~0			6.0_5	9.25×10^{-4}	0.23×10^{-3}	2.66×10^{-3b}	~0	0.77
		2.83×10^{-3c}							2.60×10^{-3a}		
	Et_4NOAc $(1.15 \times 10^{-2}\ M)$	1.71×10^{-2a}	~0			6.3_8	1.69×10^{-3}	0.23×10^{-3}	5.00×10^{-3b}	~0	0.70
		5.30×10^{-3c}							5.07×10^{-3a}		
DMF	NaCl (sat.)	7.30×10^{-2}	1.2×10^{-3}		1.5_5	11.2	2.41×10^{-3}	~0	4.8×10^{-2}	2.4×10^{-2}	0.59
	KCl (sat.)	3.86×10^{-2}	~0	1.6_3	1.7_7	11.0	1.37×10^{-3}	~0	2.7×10^{-2}	1.1×10^{-2}	0.63
DMSO	NaCl (sat.)	0.484	3.0×10^{-2}	0.6_0	(0.7_0)	8.1		~0	0.44	~0	(0.45)

[a] $C(OAc^-)$. [b] Calculated from $C(OAc^-)$ using eq 4. [c] $C(Ag)$. [d] Calculated from $C(Ag)$ using eq 5.

Solubility Product of MX. The following values of $pK^{sp}(MX)$ have been reported:[2] potassium chloride and bromide in AN, 8.0 and 5.7, potassium and sodium chlorides in DMF, 5.5 and 5.0, respectively, and sodium chloride in DMSO, 2.9. Values of [MX] in the various saturated solutions were calculated from the dissociation constants of MX in ref 2 and the above values of $pK^{sp}(MX)$ and are listed in Table I.

Dissociation and Homoconjugation Constants of Acids. Values of $pK^d(HA)$ of benzoic and acetic acids equal to 20.7 and 22.3 in AN[12] and $pK^d(HOAc) = 9.6$ in methanol[27] have been reported. The following values of the homoconjugation constant, $K^f(HX_2^-)$, for benzoic and acetic acids have previously been found in AN:[12] 4.0×10^3 and 4.7×10^3, respectively.

Stoichiometry of the $AgCl_n^{(n-1)-}$ Complex in DMSO. From independent gravimetric analysis of a solution saturated with sodium and silver chlorides in DMSO as described in the experimental section, $C(Cl)$, $C(Ag)$, and $C(Cl) - C(Ag)$ were found equal to 0.915, 0.436, and 0.484 M, respectively. The internal agreement between these quantities is good. Substituting the above values of $C(Ag)$ and $C(Cl) - C(Ag)$ in eq 4 and 6, respectively, and [NaCl] = 0.030 (Table I) and neglecting [AgCl], $[AgAgCl_2]$ and $[Ag^+]$, $[Cl^-] \sim 0.01_3$ M. The mole ratio, n, of silver to chloride in the mixture of $AgCl_n^{(n-1)-}$ and $Na_{(n-1)}AgCl_n$ as given by $n = \{C(Cl) - [Cl^-] - [NaCl]\}/C(Ag)$ (eq 4 and 5) turns out to be 2.00, indicating the presence of primarily the 1:1 silver chloride–chloride complex. In eq 4–6 $[Ag^+]$ can be neglected, as $a(Ag^+) \sim 1 \times 10^{-8}$ (Table I). A saturated silver chloride solution in DMSO when flooded with 5 volumes of 0.01 M aqueous silver nitrate remains clear, indicating that $[AgCl] + 2[AgAgCl_2] \leq 10^{-4}$ M. No attempt is made to estimate the dissociation constant of $NaAgCl_2$ in DMSO.

Solutions Saturated with AgX and MX. From eq 3–5 $C(X) - C(Ag) - [MX] - [MAgX_2] \cong [X^-] + [AgX_2^-] \simeq [M^+]$, since $[Ag^+] \ll [AgX_2^-]$ under the experimental conditions. Knowing [MX] (equal to $K^{sp}(MX)/K^d(MX)$) and $[MAgX_2]$ from $K^d(MAgX_2)$, $[M^+]$ is evaluated from the experimental quantity, $C(X) - C(Ag)$. The value of $a(X^-)$ is found from the corresponding value of $a(M^+)$ and $K^{sp}(MX)$; and from this and the experimental value of $a(Ag^+)$, $K^{sp}(AgX)$ is calculated. The formation constant $K^f(AgX_2^-)$ (eq 2) is estimated by substituting the above values of $[X^-]$ and $[M^+]$ into eq 3 and evaluating $[AgX_2^-]$, neglecting $[Ag^+]$.

Solutions Saturated with Silver Acetate and Containing Tetraethylammonium Acetate. From the potentiometric value of $a(Ag^+)$ in these solutions and the value of $pK^{sp}(AgOAc)$ found in saturated solutions of silver acetate containing acetic acid (see below) $a(OAc^-)$ is calculated. Substituting the values of $[OAc^-]$ and [AgOAc] (the latter calculated as described below) in eq 5 yields $[Ag(OAc)_2^-]$, and in turn $K^f(Ag(OAc)_2^-)$ is estimated. Both the salts Et_4NOAc and $Et_4NAg(OAc)_2$ are regarded as completely dissociated. Agreement between the values of $[Ag(OAc)_2^-]$ calculated from $C(OAc)$ and $C(Ag)$ in Table I using eq 5 and 4, respectively, and also agreement between the analytical concentration $[Et_4N^+]$ and the sum $[OAc^-] + [Ag(OAc)_2^-]$ (eq 3) attest to the reliability of the experimental data.

Solutions Saturated with AgX and Containing HX. Ionic Species. The method of estimation of $K^{sp}(AgX)$

(27) T. Shedlowsky and R. L. Kay, *J. Phys. Chem.*, **60**, 151 (1956).

TABLE II: Concentrations and Activities of Species in Solutions Saturated with AgX and Containing HX

Solvent	X	C(HX)	C(Ag)	C(X)	a(Ag$^+$)	pa(H)	Specific conductance
AN	Benzoate	0	7.24×10^{-3}	7.17×10^{-3}	6.5×10^{-4}		1.01×10^{-4}
	Benzoate	1.24[a]	0.269	0.256	3.1×10^{-2}	15.2_5	
	Acetate	0	6.82×10^{-4}	6.80×10^{-4}	(1.6×10^{-4})		(2.8×10^{-5})
	Acetate	0.484	0.031_0	0.030	$1.4_4 \times 10^{-2}$	15.8_2	2.40×10^{-3}
	Acetate	0.902	0.070_3	0.067_5	2.8×10^{-2}	15.3_4	
MeOH	Acetate	0	7.45×10^{-4}	7.49×10^{-4}	4.0×10^{-4}		5.43×10^{-5}
		0.00820	5.86×10^{-4}	6.05×10^{-4}	4.6×10^{-4}	8.19	5.20×10^{-5}
		0.0156	5.83×10^{-4}	6.10×10^{-4}	4.6×10^{-4}	7.87	4.93×10^{-5}
DMSO	Acetate	0	0.012		8.0×10^{-4}		4.03×10^{-5}
	Acetate	0.376	0.0144		3.6×10^{-3}	8.0_3	9.73×10^{-5}
	Acetate	0.900	0.0163		7.0×10^{-3}	7.4_5	1.35×10^{-4}

[a] Solution saturated with respect to HX, [HX] = 0.85 *M*.

and [X$^-$] in solutions saturated with AgX and HX from pa(H) and pa(AgX) measurements is described in the Introduction. In AgX–HX solutions in DMSO the potential of the glass electrode is not affected by Ag$^+$ even at high a(Ag$^+$) and low a(H$^+$). The pa(H) of a solution 5.25×10^{-3} *M* in 2,6-di-*tert*-butyl-4-nitrophenol and 4.54×10^{-3} *M* in its tetraethylammonium salt was 7.4_4 both in presence of 5×10^{-3} *M* silver nitrate and in its absence. The value of a(Ag$^+$) found from the silver electrode was 4.4×10^{-3} in both cases, indicating negligible complexation of Ag$^+$ with the bulky phenolate ion. When the HX–AgX solutions were undersaturated with respect to HX, but saturated with AgX, [HX] was calculated from the relation [HX] = C(HX) − mC(X), m denoting the average number of HX bound to X$^-$ in the homoconjugate species. In solutions saturated with AgX and containing HX, the sum [HX_2^-] + [$(HX)_2X^-$] is found from a(Ag$^+$) and K^{sp}(AgX), using eq 8 and neglecting [AgX_2^-]. When the formation constant, $K^f(HX_2^-)$, (eq 11) of the 1:1 homoconjugate is known from potentiometric pa(H) data in mixtures of the acid (not in large excess) and its tetraalkylammonium salt, $K^f((HX)_2X^-)$ (eq 12) was estimated from [HX], [HX_2^-], and the sum [HX_2^-] + [$(HX)_2X^-$] in the solutions saturated with AgX and containing HX. The value of [HX_2^-] was calculated from [X$^-$] using eq 11. Values of $K^f((HX)_2X^-)$ equal to 1.0×10^4 and 5.6×10^4 were found for benzoic and acetic acid dihomoconjugates, respectively, in AN.

Molecular Species. When the ionic and molecular solubilities of AgX are sufficiently great in absence of HX or MX, *e.g.*, silver benzoate, $[X^-]^0$ and the sum $[AgX]^0 + 2[AgAgX_2]^0$ were calculated from pa^0(Ag$^+$) measurement in saturated AgX solution, knowing K^{sp}(AgX) and using eq 8 and 9, taking [HX_2^-] = [$(HX)_2X^-$] = [$AgHX_2$] = [$Ag(HX)_2X$] = 0. The superscript zero denotes the absence of acid species. In the present study, no attempt was made to take into account possible dimerization of undissociated AgX. Since the total concentration of undissociated silver acetate is small in AN, 2.3×10^{-4} *M*, [$AgAg(OAc)_2$] could be considered negligible. Application of eq 7 yields K^d(AgOAc) of the order of 10^{-5}. The total solubility of the silver halides is too slight in the three aprotic solvents to permit evaluation of K^d(AgX) this way. In solutions saturated with AgX and HX, substituting [Ag$^+$], [AgX_2^-], the sum [AgX] + 2[$AgAgX_2$] and C(Ag) in eq 9 and [HX], [HX_2^-], [$(HX)_2X^-$], and C(HX) in eq 10 and solving eq 9 and 10 simultaneously, [$AgHX_2$] and [$Ag(HX)_2X$] are found from which $K^d(AgHX_2)$ and $K^d(Ag(HX)_2X)$ can be evaluated from eq 13 and 14, respectively.

Experimental values of (C(X) − C(Ag)), pa(Ag$^+$), and pa(M$^+$) in solutions saturated with AgX and MX are entered in Table I. The agreement between a(M$^+$) found from argentimetric titration and cation specific electrode measurements is good. In Table II experimental values of C(HX), C(Ag), C(X), pa(Ag$^+$), and pa(H) in solutions saturated with AgX and containing HX are listed. Values of C(Ag) and C(X) are in agreement. The calculation of the concentrations of the various complexes in the latter solutions is rather involved and the results are summarized in Table a.[28] Values of pK^{sp}(AgX), log $K^f(AgX_2^-)$, pK^d-($AgHX_2$), and p$K^d(Ag(HX)_2X)$ are presented in Table III.

Discussion

In general, values of $K^f(AgX_2^-)$ and pK^{sp}(AgX) found for the silver salts by the two methods described in this paper are in good agreement with the values reported in the literature (Table III) with the exception of silver acetate in AN and DMSO. From the experimental values of log $K^f(AgX_2^-)$ in Tables III and IV and $p^W\gamma^A(Ag^+)$ and $p^W\gamma^S(X^-)$ reported previously[2] values of $p^W\gamma^S(AgX_2^-)$ are calculated and presented in Table IV. From the values of $p^{AN}\gamma^{DMF,DMSO}(Ag^+)$ and $p^{AN}\gamma^{DMF,DMSO}(OAc^-)$ (the latter from sodium acetate) and pK^{sp}(AgOAc) = 8.7 in AN (this work) pK^{sp}(AgOAc) is calculated to be 11.1 in DMF and 7.1 in DMSO as compared with the experimental values of 10.5[4] and 7.4 (this work). The value of pK^{sp}(AgBz) in AN calculated from pK^{sp}(AgBz) in methanol, 6.3,[17] $p^M\gamma^{AN}(H^+)$ = 6.2,[2] $p^M\gamma^{AN}$(HBz) = +0.6 (unpublished data), and pK^d(HBz) = 9.3 in methanol[29] and 20.7 in AN[30] agrees exactly with the experimental value of 7.0 (Table III). In agreement with Parker[4] and Benoit[31] we observe that the medium effect $p^W\gamma^S(Ag(Hal)_2^-)$ (in which Hal = halogen, S = aprotic solvent) generally is small, but $p^W\gamma^S(Hal^-)$ is large and decreases in the order $Cl^- > Br^- > I^-$. We find that $p^{AN}\gamma^{DMF,DMSO}(Hal^-)$ is

(28) A tabulation of calculated concentrations of species in solutions saturated with AgX and containing HX will appear following these pages in the microfilm edition of this volume of the journal. Single copies may be obtained from the Business Operations Office, Books and Journals Division, American Chemical Society, 1155 Sixteenth St., N.W., Washington, D. C. 20036. Remit check or money order for $3.00 for photocopy or $2.00 for microfiche, referring to code number PC-73-1.
(29) J. Juillard, *Bull. Soc. Chim.*, 1727 (1966).
(30) I. M. Kolthoff and M. K. Chantooni, Jr., *J. Amer. Chem. Soc.*, 92, 7025 (1970).
(31) R. L. Benoit, *Inorg. Nucl. Chem. Lett.*, 4, 723 (1968).

TABLE III: Solubility Products and Complexation and Dissociation Constants of Silver Salts at 25° (μ = 0)

Solvent	X^-	$pK^{sp}(AgX)$	$\log K^f(AgX_2^-)$	$pK^d(AgHX_2)$	$pK^d(Ag(HX)_2X)$
AN	Cl^-	13.2,[a] 13.1,[b] 13.0$_5$,[d] 13.0[e]	13.7,[a] 13.3,[b] 13.7[d]		
	Br^-	13.2,[a] 13.9,[b] 13.7,[d] 13.6[e]	14.0,[a] 14.1,[b] 13.8[d]		
	Benzoate	7.0[c]	7.5[c]	2.5[c]	2.2[c]
	Acetate	8.7,[c] 7.9[a]	8.6[c]	*g*	1.4[c]
DMF	Cl^-	14.8,[a] 14.7,[d,f] 14.9[e]	16.6,[a] 16.7[d,f]		
MeOH	Acetate	6.8,[c] 6.6[a]	*g*	*g*	*g*
DMSO	Cl^-	10.6,[a] 10.4,[e] 10.9,[b] 10.9,[i] 10.8[j]	12.0,[a] 12.1,[e,k] 12.5,[b] 12.2,[i] 12.2[j]		
	Acetate	7.4,[c] 4.9,[a] 7.6[i]	8.6,[c] 6.3,[a] 8.9[i]	*h*	*h*

[a] Reference 1, corrected to μ = 0. [b] Reference 3, potentiometric values, corrected to μ = 0. [c] This work. [d] This work, $[M^+]$ in saturated solution from argentimetric titration. [e] This work, $a(M^+)$ in saturated solution from cation specific electrode measurement. [f] Average value from sodium and potassium chlorides. [g] No detectable HX_2^- or AgX_2^-. [h] Salt completely dissociated under experimental conditions. [i] Reference 9. [j] Reference 8. [k] $a(AgCl_2^-)$ assumed equal to $a(Na^+)$ in AgCl–NaCl mixture.

TABLE IV: Medium Activity Coefficient of AgX_2^-

Salt	Solvent	$pK^{sp}(AgX)$	$\log K^f(AgX_2^-)$	$p^W\gamma^S(Ag^+)$[b]	$p^W\gamma^S(X^-)$[b]	$p^W\gamma^S(AgX_2^-)$
AgCl	W	9.7[h]	5.4[h]			
	M	13.2[h]	8.4[c]	+1.3	+2.2	+2.7
	AN	13.2[a]	13.7[b]	−3.8	+7.4	+2.7
	DMF	14.8[a]	16.6[a]	−3.0	+8.1	+2.0
	DMSO	10.4[b]	12.1[b]	−5.9	+6.8	+1.0
AgBr	W	12.2[f]	7.6[h]			
	M	15.5[f]	11.1[c]	+1.3	+2.0	+1.8
	AN	13.7[b]	13.8[b]	−3.8	+5.6	+1.2
	DMF	15.3[a]	16.9[a]	−3.0	+6.1	−0.1
	DMSO	10.6[a]	11.7[a]	−5.9	+4.5	−1.0
AgI	W	16.0[f]	11.2[a]			
	M	18.4[f]	15.3[c]	+1.3	+1.2	−0.4
	AN	14.5[a]	14.0[a]	−3.8	+3.3	0.0
	DMF	16.1[a]	18.1[a]	−3.0	+3.3	−3.3
	DMSO	11.6[a]	12.8[a]	−5.9	+1.6	−4.3
AgOAc	W	2.7[e]	−0.7[e]			
	AN	8.7[b]	8.6[b]	−3.8	9.8	+7.5
	DMF	10.5[a]	11.2[a]	−3.0	11.4	+7.9
	DMSO	7.4[b]	8.6[b]	−5.9	10.3	+5.4
AgBz	W	3.7[g]	0.9[d]			
	AN	7.0[b]	7.5[b]	−3.8	+7.1	+3.8

[a] Reference 4. [b] This work; ref 2. [c] Reference 5. [d] I. Leden, *Acta Chem. Scand.*, **3**, 1318 (1949). [e] F. McDougall and L. Topol, *J. Phys. Chem.*, **56**, 1090 (1952). [f] P. Buckley and H. Hartley, *Phil. Mag.*, **8**, 320 (1929). [g] Reference 17. [h] L. G. Sillen and A. Martell, "Stability Constants of Metal-Ion Complexes," The Chemical Society, London, 1964.

almost independent of the halide and equal to +0.6 to +1.6 as compared to $p^{DMF}\gamma^{DMSO}(Ag^+)$ = −2.9. More drastic even is the difference of 12.0 between $p^W\gamma^{DMSO}(Ag^+)$ = −5.9 and Parker's[3] value of $p^W\gamma^{NM}(Ag^+)$ = 6.1 (NM = nitromethane). The halide ions, in the order $Cl^- > Br^- > I^-$, as well as acetate and benzoate are strongly solvated by hydrogen bonding in water and methanol, but very weakly in the aprotic solvents.[2] In fact, Prue and Sherrington[26] concluded that the halides are unsolvated in DMF and DMSO from comparison of crystallographic and Stokes' radii, the latter obtained from ionic mobilities. Of course, this comparison is insensitive to slight changes in solvation which may be expected by contribution of the nonelectric part on the solvation *(vide infra)*. The mobilities of AgX_2^- and X^- in aprotic solvents are similar, probably because X^- is slightly solvated, while AgX_2^- is essentially not solvated. For example, in AN λ_0 of $AgCl_2^-$ = 96, of Cl^-, 91; in DMF the values are 61 and 55, respectively. Data for other ions are in the Results section. As discussed by Parker,[2] the hydrogen bonding of solvent to $Ag(Hal)_2^-$ appears to be extremely small in water and methanol, and negligible in the aprotic solvents. If we refer the medium effect instead of to water, to methanol, which is close to being isodielectric with AN, DMF, and DMSO, we find, for example, $p^M\gamma^{AN}(AgCl_2^-)$ = 0.0, $p^M\gamma^{DMF}(AgCl_2^-)$ = −0.7, and $p^M\gamma^{DMSO}(AgCl_2^-)$ = −1.7, the differences being mainly determined by nonelectric effects. The nonelectric effect is particularly large for $p^W\gamma^S(OAc^-)$ and $p^W\gamma^S(Bz^-)$. From values of dissociation constants, $p^W\gamma^{AN}(HOAc)$ and $p^W\gamma^{AN}(OAc^-)$, we have calculated $p^W\gamma^{AN}(HOAc)$ = +0.4 and from solubilities $p^W\gamma^{AN}(HBz)$ = −1.5, a difference of −1.9 as compared to $p^W\gamma^{AN}(Bz^-) - p^W\gamma^{AN}(OAc^-)$ = −2.7. It is interesting that $p^W\gamma^{AN}(Ag(Bz)_2^-) - p^W\gamma^{AN}(Ag(OAc)_2^-)$ = −3.7, as compared to 2(−1.9) = −3.8. The hydrogen bonding effects on benzoic and acetic acids are presumed to be equal, as well as the electric effect on their anions. The conclusion of the large contribution of the nonelectric part of the medium effect on the anions is independent of the extrathermodynamic assumption used in the calculation

of $p\gamma_i$.

In contrast to the high mobilities of AgX_2^- and X^- in AN, those of acetate and benzoate homoconjugates are much smaller, λ_0 of $H_2(OAc)_3^-$ = 74 and λ_0 of $H(Bz)_2^-$ = 45 [25] as compared to $\lambda_0(OAc^-)$ = 107 and $\lambda_0(Bz^-)$ = 62.[25] This indicates much stronger solvation of HX_2^- in AN than of X^- or of AgX_2^-. There is an indication from the data in Table a that values of $K^d(Ag(HX)_2X)$ and $K^d(AgHX_2)$ (X^- = acetate, benzoate) are at least 100 times larger than the corresponding values of $K^d(AgX)$ in AN. Unfortunately, values of $K^d(AgX)$ could not be determined accurately as the dimerization constants of AgBz and AgOAc are unknown. For this reason $K^d(AgAgX_2)$ could not be evaluated. However, on grounds that the charge in the HX_2^- ion is more delocalized than in X^- it is reasonable to expect that the silver homoconjugate salts are more dissociated than the simple silver salts.

Acknowledgment. We thank the National Science Foundation for Grant No. GP-20605 in support of this work.

Solvent Structure Dependence of the Optical Excitation Energy of Solvated Electrons[1]

G. R. Freeman

Chemistry Department, University of Alberta, Edmonton, Alberta, Canada, T6G 2G2 *(Received May 19, 1972)*

Publication costs assisted by the University of Alberta

Interpretation of optical excitation energies of solvated electrons in liquids and solids requires consideration of the solvent structure and the polarizabilities of the solvating groups. The importance of solvent structure is illustrated through the use of the Kirkwood correlation factor g_K, which indicates the extent to which molecules align themselves with their neighbors to create short-range order. Values of E_{max}, the energy at the absorption maximum, for e^-_{solv} in water, alcohols, ethers, ammonia, and amines measured over wide ranges of temperature and pressure correlate approximately with $\epsilon d g_K {}^3\alpha_p$ where ϵ and d are the dielectric constant and density of the liquid, respectively, and α_p is the polarizability of the polar group in the molecule. A more detailed treatment would consider the anisotropy of α_p.

Attempts have been made for several decades to interpret the optical absorption spectra of solvated electrons in terms of properties of the solvent.[2] Although most of the early work involved electrons in liquid ammonia, during the past decade experimental and theoretical investigation has been extended to electrons in water and many other solvents.[2-19] In much of the theoretical work the solvent has been considered to be a dielectric continuum, with the electron occupying a cavity in it. The properties of the solvent that have been used in the interpretation of solvated electron spectra have therefore been those of the bulk solvent, mainly the dielectric constant, but also the surface tension and the pressure differential of the dielectric constant (for electrostriction). "Molecular models" of electron solvation[5,7,11,13] have received less attention and are not completely satisfactory.

Most of the models have been able to rationalize a portion of the properties of electrons in a given solvent, but none has explained all of the known optical properties. Neither has any model quantitatively correlated the shift of a given property from solvent to solvent. For example, by comparison with the energy of the absorption maximum E_{max} of electrons in water, E_{max} in ammonia seems too low and that in alcohols seems too high.[6,16]

To facilitate development of the theory, new empirical correlations should be sought to indicate what new factors are needed in the model calculations.

E_{max} has been measured in many polar liquids at 296 ± 3 K (see summary in ref 16), and in several liquids under

(1) Supported by the Defence Research Board of Canada.
(2) J. Jortner, S. A. Rice, and E. G. Wilson, "Metal-Ammonia Solutions," G. Lepoutre and M. J. Sienko, Ed., W. A. Benjamin, New York, N. Y., 1964, p 222. Most of the earlier work is mentioned in this article.
(3) M. J. Blandamer, R. Catterall, L. Shields, and M. C. R. Symons, *J. Chem. Soc.*, 4357 (1964).
(4) M. J. Blandamer, L. Shields, and M. C. R. Symons, *J. Chem. Soc.*, 3759 (1965).
(5) M. Natori and T. Watanabe, *J. Phys. Soc. Jap.*, **4**, 1573 (1966).
(6) G. R. Freeman, Gordon Research Conference on Radiation Chemistry, New Hampton, N. H., Aug 1966.
(7) R. H. Land and D. E. O'Reilly, *J. Chem. Phys.*, **46**, 4496 (1967).
(8) N. F. Mott, *Advan. Phys.*, **16**, 49 (1967).
(9) M. H. Cohen and J. C. Thompson, *Advan. Phys.*, **17**, 857 (1968).
(10) K. Fueki, *J. Chem. Phys.*, **49**, 765 (1968).
(11) K. Iguchi, *J. Chem. Phys.*, **48**, 1735 (1968); *ibid.*, **51**, 3137 (1969).
(12) R. Catterall and N. F. Mott, *Advan. Phys.*, **18**, 665 (1969).
(13) D. A. Copeland, N. R. Kestner, and J. Jortner, *J. Chem. Phys.*, **53**, 1189 (1970).
(14) K. Fueki, D.-F. Feng, and L. Kevan, *J. Phys. Chem.*, **74**, 1976 (1970).
(15) M. Weissmann and N. V. Cohan, *Chem. Phys. Lett.*, **7**, 445 (1970).
(16) L. M. Dorfman, F. Y. Jou, and R. Wageman, *Ber. Bunsenges. Phys. Chem.*, **75**, 681 (1971).
(17) J. Jortner, *Ber. Bunsenges. Phys. Chem.*, **75**, 696 (1971).
(18) S. Ray, *Chem. Phys. Lett.*, **11**, 573 (1971).
(19) R. Catterall, *Nature (London), Phys. Sci.*, **229**, 10 (1971).

TABLE I: Solvated Electron Excitation Energies and Solvent Properties

Solvent	T, K	P, kbar[a]	E_{max}, eV[b]	ϵ	d, g/cm^3	g_K[c]	α, Å^3 [d]	α_p, Å^3 [e]	$\epsilon d g_K^3 \alpha_p$, 10^{-23} g
H_2O	673	0	0.91	~5			1.46	1.46	
	573	0	1.05	19.6	(0.74)	(1.8)			12
	473	0	1.24	34.6	(0.87)	(2.3)			54
	369	0	1.51	56.3	0.961	2.4			112
	345	0	1.57	63.1	0.977	2.5			146
	325	0	1.65	69.3	0.987	2.6			182
	302	0	1.71	77.5	0.996	2.7			217
	298	1.0	1.79	81.2	1.046	2.7			233
	302	2.1	1.84	85.7	1.077	2.6			239
	298	3.8	1.93	91.0	1.127	2.6			266
	302	6.3	2.0	96.9	1.177	2.6			289
CH_3OH	358	0	1.77	23.3	0.729	2.7	3.22	3.22	111
	320	0	1.90	29.0	0.767	2.8			165
	294	0	1.95	33.5	0.792	2.9			219
	298	2.8	2.06	40.1	0.916	2.7			237
	298	4.1	2.14	41.6	0.948	2.7			238
	195	0	2.20	63.8	0.878	3.2			604
	183	0	2.23	69.0	0.888	3.2			672
C_2H_5OH	343	0	1.66	18.4	0.737	2.8	4.92	3.0	92
	296	0	1.80	24.5	0.780	3.0			160
	298	2.1	1.95	28.0	0.894	2.9			176
	298	5.2	2.07	31.5	0.962	2.8			195
	195	0	2.12	48.1	0.870	3.3			428
	173	0	2.22	56.2	0.892	3.4			571
	155	0	2.27	64.5	0.908	3.4			673
NH_3	288	0	0.73	16.3	0.62	1.3	2.16	2.16	5
	240	0	0.80	21.6	0.68	1.2			5
	203	0	0.86	25.3	0.73	1.1			5
$(CH_2OH)_2$	298	0	2.17	37.7	1.109	2.4	5.7	5.7	325
n-C_3H_7OH	298	0	1.67	19.5	0.804	3.1	6.7	3.0	136
$(CH_3)_2CHOH$	298	0	1.51	18.3	0.786	3.1	6.7	2.8	121
THF(C_4H_8O)	298	0	0.59	8.2	0.889	1.3	7.9	3.8	6
$(C_2H_5)_2O$	298	0	0.59	4.3	0.714	1.7	8.7	3.8	6
$(CH_2NH_2)_2$	298	0	0.92	14.2	0.899	1.3	7.3	7.3	19
$(C_2H_5)_2NH$	298	0	0.65	3.6	0.706	1.8	9.5	4.6	7

[a] 0 denotes 1 bar or the vapor pressure, whichever is greater. [b] Data taken from ref 16 and 20–28. [c] Kirkwood correlation parameter; a value > 1.0 is due to the hindered rotation of a molecule relative to its neighbors. [d] Molecular polarizability. [e] Polarizability of the polar group, such as $HOCH_2$–(R).

wide variations of temperature[20-25] and pressure.[24,26-28] A simple plot of E_{max} against the dielectric constant ϵ of the liquid has a positive slope when ϵ is varied in a given compound by changing the temperature or pressure, but the curves for different types of compounds are stratified (Figure 1A). The difference between E_{max} for the alcohols and that for water seemed to be roughly explainable in terms of the differences in molecular polarizabilities α, E_{max} increasing with increasing α, but this argument would have to be reversed to explain the difference between ammonia and water; for a given value of ϵ, E_{max} varies in the order $CH_3OH > H_2O > NH_3$, whereas the α values are in the order $CH_3OH > NH_3 > H_2O$ (Table I).

In alcohols and in water E_{max} increases with decreasing temperature[20,21,23,25] and increasing pressure,[27,28] but the changes in E_{max} do not correlate simply with the changes in ϵ under the two sets of conditions.[25,29] It has recently been shown that E_{max} in a given liquid correlates empirically with the product ϵd, where d is the density, whether ϵd is changed by temperature or by pressure.[25,29] The density presumably represents the r^{-n} factors in the energy equations, where r is the electron–dipole separation; $d \propto r^{-3}$. However, ϵd does not bring the alcohol and water curves together.

One feels intuitively that the liquid structure plays an important role in determining E_{max}.

Kirkwood's interpretation of the dielectric polarization of polar liquids is based upon a molecular model.[30,31] Molecular rotation in some liquids is severely hindered by dipole–dipole interactions, with the result that orientational correlation exists between neighboring molecules. If neighboring dipoles tend to line up in a parallel fashion the contribution of the individual molecular dipoles to the

(20) S. Arai and M. C. Sauer, Jr., *J. Chem. Phys.*, **44**, 2297 (1966).
(21) W. C. Gottschall and E. J. Hart, *J. Phys. Chem.*, **71**, 2102 (1967).
(22) R. K. Quinn and J. J. Lagowski, *J. Phys. Chem.*, **73**, 2326 (1969).
(23) B. D. Michael, E. J. Hart, and K. H. Schmidt, *J. Phys. Chem.*, **75**, 2798 (1971).
(24) R. Vogelsgesang and U. Schindewolf, *Ber. Eunsenges. Phys. Chem.*, **75**, 651 (1971).
(25) K. N. Jha, G. L. Bolton, and G. R. Freeman, *J. Phys. Chem.*, **76**, 3876 (1972).
(26) U. Schindewolf, H. Kohrmann, and G. Lang, *Angew. Chem., Int. Ed. Engl.*, **8**, 512 (1969).
(27) M. G. Robinson, K. N. Jha, and G. R. Freeman, *J. Chem. Phys.*, **55**, 4933 (1971).
(28) R. R. Hentz, Farhataziz, and E. M. Hansen, *J. Chem. Phys.*, **55**, 4974 (1971).
(29) M. G. Robinson, K. N. Jha, G. L. Bolton, and G. R. Freeman, paper presented to the Chemical Institute of Canada Pulse Radiolysis Symposium, Pinawa, Manitoba, Oct 1971.
(30) J. G. Kirkwood, *J. Chem. Phys.*, **7**, 911 (1939).
(31) G. Oster and G. J. Kirkwood, *J. Chem. Phys.*, **11**, 175 (1943).

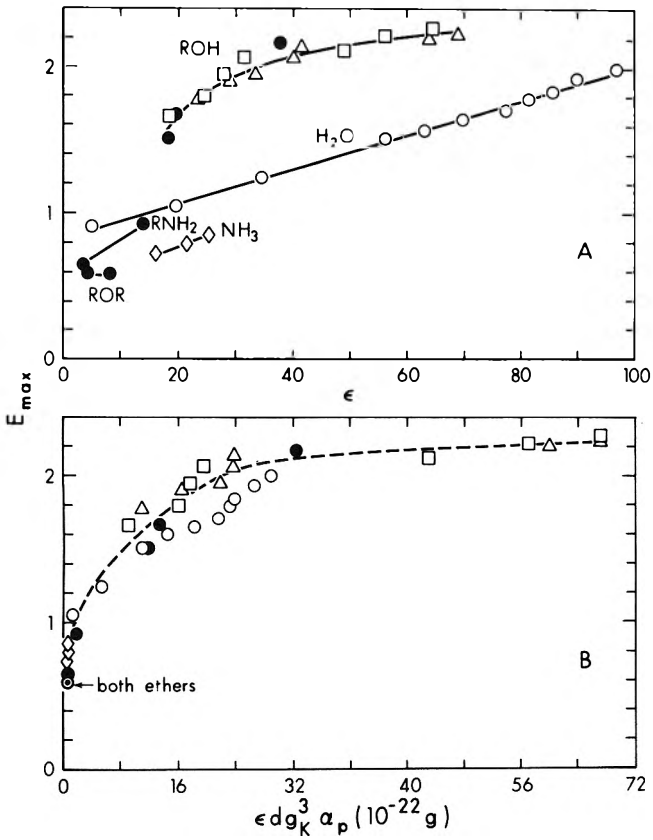

Figure 1. Plots of the energy at the optical absorption peak E_{max} of solvated electrons against properties of the solvent: (A) ϵ is the static dielectric constant; (B) d is the density, g_K is the Kirkwood correlation factor, and α_p the polarizability of the polar group of the molecule: O, water; △, methanol; □, ethanol; ◇, ammonia; ●, other compounds listed in Table I. The open points refer to wide ranges of temperature and pressure: ●, ~296 K and 1 bar. Values of E_{max} were taken from ref 16 and 20-28.

dielectric constant is increased. This behavior is gauged by the correlation parameter g_K in

$$[(\epsilon - 1)(2\epsilon + 1)/9\epsilon](M/d) = (4\pi N/3)[\alpha + (g_K\mu^2/3kT)] \quad (1)$$

where M is the molecular weight, d the density, N Avogadro's number, α the optical polarizability, μ the molecular dipole moment, k Boltzmann's constant, and T the absolute temperature. The correlation parameter g_K accounts for the induction of an electric moment in the environment of a dipole by hindering the rotation of its neighbors relative to itself.[31] Furthermore, the dipole moment μ of a molecule in the liquid phase is greater than its moment μ_0 in the vapor. Liquid-phase values of μ can be estimated in the manner described by Kirkwood.[31] Values of g_K can therefore be calculated from eq 1 (Table I).

It has been suggested that as a basis for classification of liquids according to their thermodynamic behavior, the correlation parameter g_K is more significant than the molecular dipole moment.[31] Liquids possessing values of g_K differing appreciably from unity are associated liquids; those with g_K near unity are normal liquids.

TABLE II: Correlation between E_{max} in Glasses at 77 K and Kirkwood g_K Values for the Liquid at 298 K

Solvent	E_{max}, eV[a]	$g_{K,298}$	ϵ_{298}	d_{298}, g/cm³	α_p, Å³	$(\epsilon dg_K^3\alpha_p)_{298}$, 10^{-23} g
CH_3OH	2.5	2.9	32.8	0.790	3.2	212
C_2H_5OH	2.4	3.0	24.6	0.789	3.0	160
n-C_4H_9OH	2.5	3.2	17.1(?)	0.810	3.0	137(?)
i-C_4H_9OH	2.4	3.4	17.7	0.801	3.0	161
i-C_3H_7OH	2.3	3.1	18.3	0.786	2.8	121
t-C_4H_9OH	<1.8	2.4	15.8	0.789	2.7	45

[a] 77 K. References 32 and 33.

A value of g_K greater than unity indicates a greater local polarity in microscopic regions of the liquid than one would expect from the molecular dipole moment. The enhanced polarity should increase E_{max}. It is not yet known how g_K should be included into the correlation of E_{max} with solvent properties, so a simple empirical factor g_K^x was chosen, where x is some small number. It appears that the polarizability of the polar groups α_p in the molecule should also be included in the E_{max} correlation. The g_K^x factor alone does not bring the alcohol and water curves much closer together because the g_K values are similar for these liquids (Table I). The fact that the optical polarizability affects E_{max} may be related to the fact that the polarizabilities of the polar groups are anisotropic, and the optical transitions are "vertical." Anisotropies are not included in the present work, for the sake of simplicity.

An attempt was therefore made to correlate E_{max} with $\epsilon dg_K^x\alpha_p$. The best value of x was found to be 3, and the resulting plot is shown in Figure 1B. No fundamental significance is given to the value $x = 3$, but it emphasizes the importance of solvent structure in determining E_{max}. Theories that neglect solvent structure will therefore not give satisfactory interpretations of the optical excitation energies of solvated electrons.

The total molecular polarizabilities α are not suitable for use in place of α_p for the larger molecules because they would destroy the correlation among the alcohols and among the amines. This signifies that the electron is mainly associated with the polar ends of the molecules and that the most important interactions have relatively short ranges.

Although g_K values cannot be readily calculated for solids, there is a similar correlation between liquid-phase g_K values and E_{max} in alcohol glasses[32,33] (Table II). In particular, the low value of E_{max} in *tert*-butyl alcohol relative to those in the other butanols is reflected in the g_K values (Table II). The values of E_{max} in liquid butanols have not been reported, but one expects a similar trend of E_{max} in the liquid phase. This is consistent with the belief that electron localization sites are similar in the two phases.

One might speculate from Figure 1B that an upper limit for E_{max} in liquids is ~2.5 eV.

(32) M. J. Blandamer, L. Shields, and M. C. R. Symons, *J. Chem. Soc.*, 1127 (1965).
(33) J. E. Bennett, B. Mile, and A. Thomas, *J. Chem. Soc. A*, 1393 (1967).

Electron Ejection and Electron Capture by Phenolic Compounds

J. Feitelson and E. Hayon*

Pioneering Research Laboratory, U. S. Army Natick Laboratories, Natick, Massachusetts 01760 *(Received August 2, 1972)*

Publication costs assisted by the U. S. Army Natick Laboratories

The flash photolysis of air-free aqueous solutions of *p*-cresol, *p*-hydroxyphenylpropionic acid, tyramine, and tyrosine was studied on illumination of their long-wavelength absorption bands. The photodissociation into phenoxyl radicals, solvated electrons, and hydrogen atoms was examined. Experiments in the presence of 2,4-hexadiene, a typical triplet quencher, showed that the photoelectron ejection of these phenolic compounds in aqueous solution at 25° takes place from a long-lived excited state, probably the *triplet* excited states of these molecules. The transient absorption spectra, extinction coefficients, and decay kinetics of the phenoxyl radicals were determined. The reactivity of all four substances toward hydrated electrons was studied by pulse radiolysis. The reaction rate constants were found to be dependent on the state of protonation of the hydroxyl and the amino groups. The transient absorption spectra due to the reaction of e_{aq}^- and H atoms (produced by photolysis or radiolysis) with these phenolic compounds were observed, with λ_{max} ~350 nm. It is shown that e_{aq}^- and H atoms add predominantly to the phenol ring of the compounds examined.

When phenolic substances are excited by high-intensity light flashes to their first singlet excited state, phenoxyl radicals and solvated electrons (possibly also hydrogen atoms) are produced. Such photodissociations of phenolic substances have been studied in the steady state[1] and by flash photolysis.[2,3] Land and Porter[2] have described the phenoxyl radical with its very characteristic sharp absorption band in the vicinity of 400 nm, and Grossweiner, *et al.*,[3] have found that hydrated electrons (λ_{max} ~710 nm) are formed simultaneously with the phenoxyl radical. The nature of the excited state (singlet or triplet) precursor of the photoionization of phenolic compounds has not been defined as yet. Furthermore, while excited phenol molecules release electrons into aqueous solutions, phenolic substances in their ground state act as electron scavengers (see below). This reactivity with solvated electrons seems to depend to a great extent on the nature of the side chain on the phenol ring.

Because of the importance of tyrosine in the photochemistry and electron transfer processes in some proteins,[4,5] this work was initiated with the object of determining the nature of the precursor leading to the ejection of an electron, as well as electron capture processes by phenol derivatives. This latter process is of particular interest since it has been suggested[5] that in proteins exposed to ionizing radiation part of the reducing equivalent (electrons) primarily absorbed by any group in the protein ultimately finds its way to an aromatic amino acid residue.

Flash photolysis and pulse radiolysis techniques were used and all the compounds examined had a side chain in the para position of the phenol ring (tyrosine, tyramine, *p*-hydroxyphenylpropionic acid, and *p*-cresol, the latter as a model for the chromophore).

Experimental Section

Flash photolysis was carried out with a 2000-J apparatus, which has been described previously.[6] The photoelectric detection system consisted of a Bausch and Lomb monochromator and an EMI 9558Q photomultiplier. The signal was fed into a double beam oscilloscope (Tektronix 565) where the transient trace was simultaneously recorded with a slow and with a fast sweep. Monochromator slit widths were kept narrow (<0.2 mm) in order to improve the spectral resolution, particularly when the absorbance of the narrow 410-nm peak of the phenoxyl radicals was measured. γ-Irradiated and photolyzed triply distilled water was used throughout.

Tyrosine and tyramine were Mann Research Laboratories products. *p*-Cresol was obtained from Baker and Adamson and from Mallinckrodt, and *p*-hydroxyphenylpropionic acid from K & K Laboratories. N_2O was supplied by Matheson & Co., and *tert*-butyl alcohol by Mallinckrodt.

The solutions were illuminated at selected wavelength regions by placing appropriate solution filters in the outer jacket of the optical cell. The following filter solutions were used: acetic acid 90%, cut off at 250 nm; dimethylformamide–water 7:3 by volume, cut off at 265 nm; sodium benzoate 0.01 *N* (pH 10.1), cut off at 280 nm. The last two solutions undergo photochemical changes and therefore could be used for a maximum of six light flashes before being replaced by a fresh solution. Generally, solutions were illuminated in their long-wavelength absorption band only, *i.e.*, above 250 nm at neutral pH and above 265 nm at high pH. In some experiments carried out at very low solute concentrations ($\sim 2 \times 10^{-5}$ *M*) water instead of a cut-off filter solution was placed in the cell jacket.

The pulse radiolysis technique and set-up used has been described elsewhere.[7] The reaction rate constants of e_{aq}^- with phenolic compounds were determined in presence of

(1) J. Jortner, M. Ottolenghi, and G. Stein, *J. Amer. Chem. Soc.*, **85**, 2712 (1963).
(2) E. J. Land and G. Porter, *Trans. Faraday Soc.*, **59**, 2016 (1963).
(3) L. I. Grossweiner, G. W. Swenson, and E. F. Zwicker, *Science*, **141**, 805, 1042 (1963).
(4) G. Stein, "Energetics and Mechanisms in Radiation Biology," G. O. Phillips, Ed., Academic Press, New York, N.Y., 1968, p 467.
(5) R. Shapira and G. Stein, *Science*, **162**, 1489 (1968).
(6) L. Dogliotti and E. Hayon, *J. Phys. Chem.*, **71**, 2511 (1967); M. Langmiur and E. Hayon, *ibid.*, **71**, 3808 (1967).
(7) (a) M. Simic, P. Neta, and E. Hayon, *J. Phys. Chem.*, **73**, 3794 (1969); (b) J. P. Keene, E. D. Black, and E. Hayon, *Rev. Sci. Instrum.*, **40**, 1199 (1969).

~0.1 M *tert*-butyl alcohol (to scavenge the OH radicals produced in the radiolysis of water) by following the pseudo-first-order decay of e_{aq}^- at 690 nm. The extinction coefficients derived in pulse radiolysis work were determined based on $G(e_{aq}^-) = G(OH) = 2.75$, using KCNS as a dosimeter.

Results

In neutral aqueous solution the absorption spectra and the extinction coefficients, ϵ, of *p*-cresol, *p*-hydroxyphenylpropionic acid, tyramine, and tyrosine are almost identical. The spectra have maxima at 276 nm and a shoulder at 282 nm, with ϵ_{max} ~1450 M^{-1} cm^{-1}, and more intense absorptions in the far-ultraviolet. Using appropriate cut-off filters, the long-wavelength absorption bands only were photolyzed. The transient absorption spectra produced on flash photolysis of ~3 × 10^{-4} M air-free aqueous solutions of these phenolic compounds at neutral pH (pH 6.5–7.8) are shown in Figure 1. It is seen that all these compounds show the characteristic optical absorption due to phenoxyl radicals with a maximum at ~410 nm, and a second broader band with a maximum at ~390 nm. For all four substances, these transient absorption bands decay by second-order kinetics.

Another broad absorption band is centered at 350 nm. However, the intensity of this band differs from substance to substance. Moreover, as shown in Figure 1b for tyrosine, its absorbance relative to the 410-nm peak increases with increase in the concentration of tyrosine in solution. The decay of this band follows neither first- nor second-order kinetics. Furthermore, it is not observed in solutions saturated with N_2O.

In alkaline solutions the ground-state absorption spectra of all four phenolic compounds are shifted to longer wavelength. The absorption band at high wavelength lies at 295 nm and has an extinction coefficient of ϵ 2300 M^{-1} cm^{-1}. The transient spectra obtained on flash photolysis at pH ~11.5 are similar to those at neutral pH except that the 410-nm peak is somewhat broadened and the 350-nm band is very weak. However, the decay rate constants for all substances are very similar to those in neutral solutions. We therefore attribute the small spectral changes observed to environmental effects and conclude that the same radical is formed both in neutral and in alkaline solutions. As will be presently explained, the 350-nm band is attributed to an intermediate produced from the reaction of e_{aq}^- with the solutes.

At low solute concentration (~2.5 × 10^{-5} M) another transient with a broad absorption band and a maximum at about 700 nm is observed. This has been attributed to the solvated electron, in agreement with the results of Grossweiner, *et al.*[3] Both in neutral and in alkaline solution it decays with pseudo-first-order kinetics, probably by reaction with the ground-state solute molecules (see more below).

In order to characterize the 350-nm band produced from the reaction of photoejected electrons with phenolic compounds, Figure 1, these compounds were made to react with e_{aq}^- produced from the radiolysis of aqueous solutions. The reaction rate constants of e_{aq}^- with these compounds were determined by pulse radiolysis, and the results are given in Table I and Figure 2. It can be seen that (a) the reactivity of e_{aq}^- is dependent upon the state of protonation of both the $-NH_3^+$ and the -OH groups in tyrosine, with the rate decreasing on deprotonation of these functional groups; (b) the rate of e_{aq}^- with *p*-hydroxyphenylpropionate and *p*-cresol is about a factor of 6 lower than with tyrosine or tyramine, indicating that the presence of an amino group increases significantly the reactivity of these compounds toward attack by e_{aq}^-.

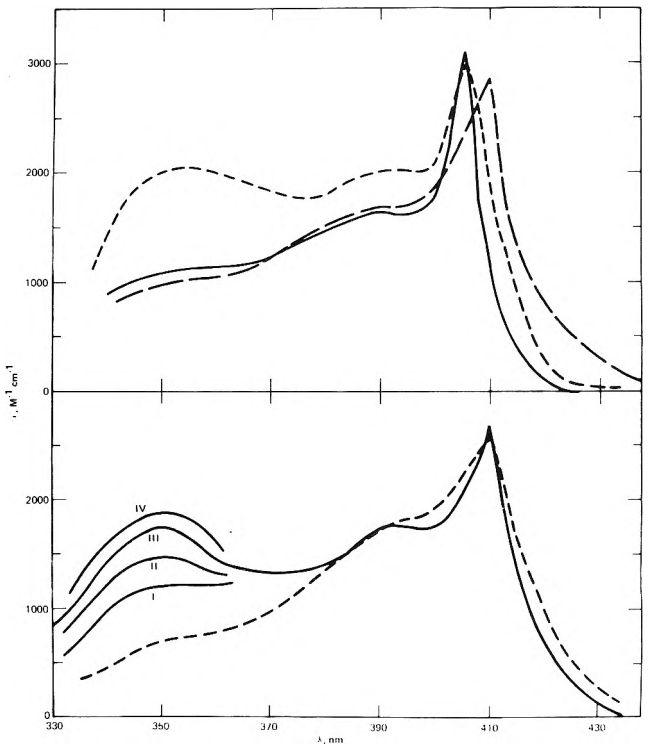

Figure 1. Transient absorption spectra produced in the flash photolysis of oxygen-free aqueous solutions of the following: top, *p*-cresol (——), *p*-hydroxyphenylpropionic acid (– –), and tyramine (- - -) all at pH ~6–7 and ~3 × 10^{-4} M; bottom, tyrosine at pH 7.7 at the following concentrations: 3 × 10^{-5} (I), 1.5 × 10^{-4} (II), 3.0 × 10^{-4} (III), and 7.5 × 10^{-4} M (IV). Dotted spectrum obtained in 7.5 × 10^{-4} M tyrosine at pH 11.5.

Figure 3 shows the transient absorption spectrum produced from the reaction of e_{aq}^- with tyrosine at pH 7.1 (after correction for the absorption due to the H atom adduct to tyrosine, $G(H) = 0.6$ in neutral solution) and the H atom adduct to tyrosine at pH 0.8. Figure 4 shows the e_{aq}^- adduct to tyramine and *p*-hydroxyphenylpropionic acid, and the H atom adduct to tyramine. Figure 5 shows the H atom adducts to *p*-hydroxypropionic acid and *p*-cresol. These H atoms are produced in acid solution by the reaction $e_{aq}^- + H^+ \rightarrow H$, with $k = 2.3 \times 10^{10}$ M^{-1} sec^{-1} (ref 8). The absorption maxima, extinction coefficients, and decay kinetics of the intermediates produced on reaction with e_{aq}^- and H atoms are given in Table II.

The reaction rate constants of H atoms with tyrosine and *p*-hydroxyphenylpropionic acid were determined by pulse radiolysis at pH 9.0 in presence of 1.0 M *t*-BuOH (to scavenge OH radicals) by following the formation of the H atom adduct. Values of 2.0 ± 0.5 × 10^9 and 4.0 ± 1.0 × 10^9 M^{-1} sec^{-1}, respectively, were obtained.

Hydrated electrons have been shown[9] to lead to deamination on reaction with aliphatic amino acids and peptides. The resulting radicals $RCHCOO^-$ absorb[9,10] in the near-uv, and have relatively low extinction coefficients. However, from the similarity in the transient absorption and extinction coefficients of the intermediates produced

(8) M. Anbar and P. Neta, *Int. J. Appl. Radiat. Isotopes*, **18**, 493 (1967).
(9) M. Simic and E. Haycn, *Radiat. Res.*, **48**, 244 (1971).
(10) P. Neta, M. Simic, and E. Hayon, *J. Phys. Chem.*, **73**, 4207 (1969).

TABLE I: Reaction Rate Constants of e_{aq}^- and OH Radicals with Phenolic Compounds in Aqueous Solution

Compound	pK_a	$k(e_{aq}^- + S)$, M^{-1} sec^{-1} [a]	$k(OH + S)$, M^{-1} sec^{-1} [a,b]
Tyrosine	2.2, 9.1, 10.1	$2.8 \pm 0.5 \times 10^8$ (6.6)	$1.4 \pm 0.3 \times 10^{10}$ (5.2)
		$9.6 \pm 1.0 \times 10^7$ (12.5)	$1.3 \times 0.3 \times 10^{10}$ (11.2)
Tyramine	9.5, 10.8	$3.5 \pm 0.2 \times 10^8$ (6.9)	
		$5.8 \pm 0.5 \times 10^7$ (11.2)	$1.5 \pm 0.2 \times 10^{10}$ (11.2)
p-Hydroxyphenylpropionic acid	4.6, 10.1	$4.6 \pm 0.5 \times 10^7$ (7.0)	$1.2 \pm 0.2 \times 10^{10}$ (6.3)
		$2.1 \pm 0.2 \times 10^7$ (12.5)	$1.6 \pm 0.2 \times 10^{10}$ (11.0)
p-Cresol	10.2	$4.2 \pm 0.5 \times 10^7$ (7.9)	$1.2 \pm 0.2 \times 10^{10}$ (5.5)

[a] Values in parentheses are the pH at which rates were determined. [b] Rates determined using KCNS method, and taking $k(OH + CNS^-) = 1.1 \times 10^{10}$ M^{-1} sec^{-1}.

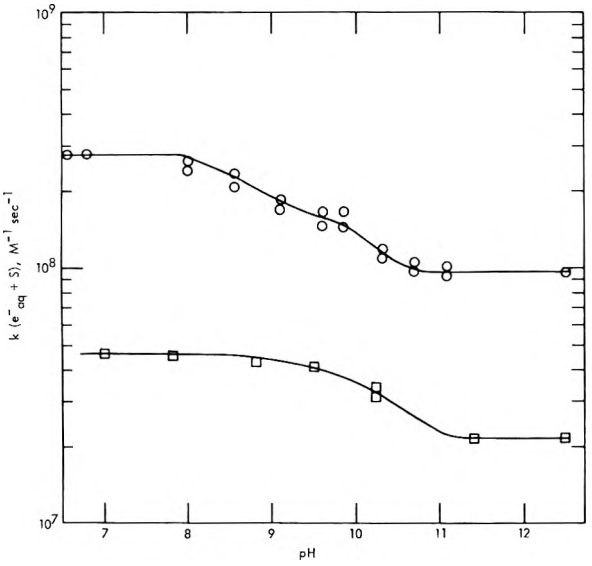

Figure 2. Dependence upon pH of the reaction rate constants of e_{aq}^- with tyrosine (O) and *p*-hydroxyphenylpropionic acid (□).

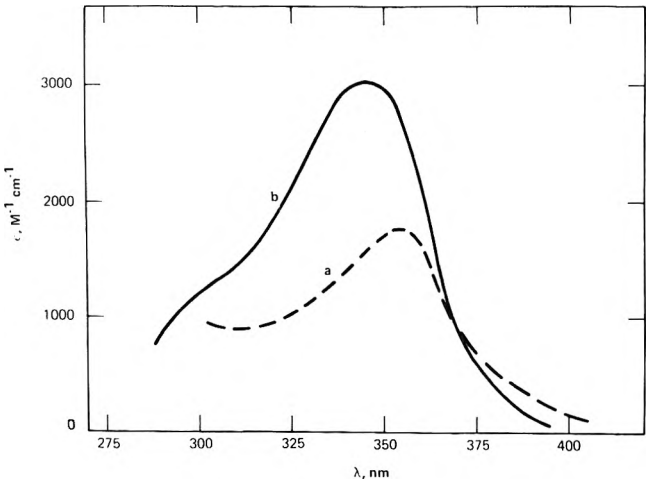

Figure 3. Transient absorption spectra produced in the pulse radiolysis of 10^{-3} *M* tyrosine, 1.0 *M* *tert*-butyl alcohol, and Ar (1 atm) due to the interaction with e_{aq}^- (curve a, pH 7.1) and with H atoms (curve b, pH 0.8).

from the reaction of e_{aq}^- with tyrosine, tyramine, and *p*-hydroxyphenylpropionate (Figures 2-4 and Table II), it is concluded that most of the electrons add to the phenol aromatic ring.

From a comparison of Figures 1b and 3a, it is seen that the 350-nm absorption band produced in the flash photolysis of tyrosine and tyramine resembles the spectrum obtained by pulse radiolysis, both in its wavelength dependence and in its extinction coefficient (see Discussion below). Hidden under the spectrum of this radical in Figure 1 is still some absorbance (ϵ ~3-4 × 10^2 M^{-1} cm^{-1}) of the phenoxyl radical, as found in N_2O-saturated solutions. The low absorbance at 350 nm in alkaline tyrosine and in neutral *p*-cresol and *p*-hydroxyphenylpropionate can be attributed to the lower reactivity (Table I) of these solutes with e_{aq}^- under the experimental conditions used.

The decay rates of the solvated electrons in our flash illuminated solutions yielded, in all cases, larger rate constants than those found by pulse radiolysis (Table I). The discrepancy is probably due to reactions of the solvated electron with impurities, mainly residual oxygen, present in the flashed solutions. If no other electron scavengers were present all solvated electrons would ultimately react with tyrosine even when the latter is present at very low concentration. The fact that the absorbance by the electron adduct is concentration dependent (see Figure 1b) means that a smaller proportion of e_{aq}^- decays *via* reaction with tyrosine, the rest reacting with another scavenger in the solution. Similarly, the absence of the 350-nm absorption band in the transient spectrum produced from *p*-cresol or *p*-hydroxyphenylpropionate reflects only the lower reactivity of these species for solvated electrons relative to other electron scavengers. Withstanding the uncertainty in the actual rate, an extrapolation of the pseudo-first-order decay plots of the solvated electrons formed in flash photolysis to zero time yields nevertheless the initial absorbance of electrons produced in solution. This data, together with the corresponding absorbances of radicals at time zero, allow us to estimate the relative initial quantum yields of the photodissociation products.

Discussion

Various values have been assigned to the molar extinction coefficients of phenoxyl radicals. Values as low as ϵ 1800 M^{-1} cm^{-1} for *tert*-butylphenoxyl,[11] or as high as 11,000 for phenol and 15,000 for *p*-cresol[12] have been obtained by flash photolysis. Data obtained indirectly from pulse radiolysis[13] yielded a value for phenoxyl of ϵ 2200 M^{-1} cm^{-1} from phenol and 2400 for the corresponding radical from *p*-cresol. From measurements of the absorption spectra and the decay rates, it is concluded from this work that the same radical is formed on flash photolysis of both neutral solutions of phenols and alkaline solutions, when the phenolic chromophore in the ground state is in

(11) E. J. Land, G. Porter, and E. Strachan, *Trans. Faraday Soc.*, **57**, 1885 (1961).
(12) G. Dobson and L. I. Grossweiner, *Trans. Faraday Soc.*, **61**, 708 (1965).
(13) E. J. Land and M. Ebert, *Trans. Faraday Soc.*, **63**, 1181 (1967).

TABLE II: Absorption Maxima, Extinction Coefficients, and Decay Kinetics of Intermediates Produced from the Reaction of e_{aq}^- and H Atoms with Phenolic Compounds

Compound	e_{aq}^- adducts[a]			H atom adducts[b]		
	λ_{max}, nm	ϵ, M^{-1} cm^{-1}	$2k$, M^{-1} sec^{-1}	λ_{max}, nm	ϵ, M^{-1} cm^{-1}	$2k$, M^{-1} sec^{-1}
Tyrosine	355	$1.7 \pm 0.3 \times 10^3$	$6.8 \pm 1.6 \times 10^8$	345	$3.1 \pm 0.3 \times 10^3$	$6.2 \pm 1.5 \times 10^8$
Tyramine	350	$1.8 \pm 0.3 \times 10^3$	$7.0 \pm 2.0 \times 10^9$	350	$5.6 \pm 1.0 \times 10^3$	
p-Hydroxyphenylpropionic acid	355	$1.5 \pm 0.3 \times 10^3$	$6.5 \pm 1.5 \times 10^8$	352[a]	$3.3 \pm 0.5 \times 10^3$	
p-Cresol				355	$3.6 \pm 0.5 \times 10^3$	$2.0 \pm 0.4 \times 10^9$

[a] Determined at pH ~6-7. [b] Determined at pH ~1.0.

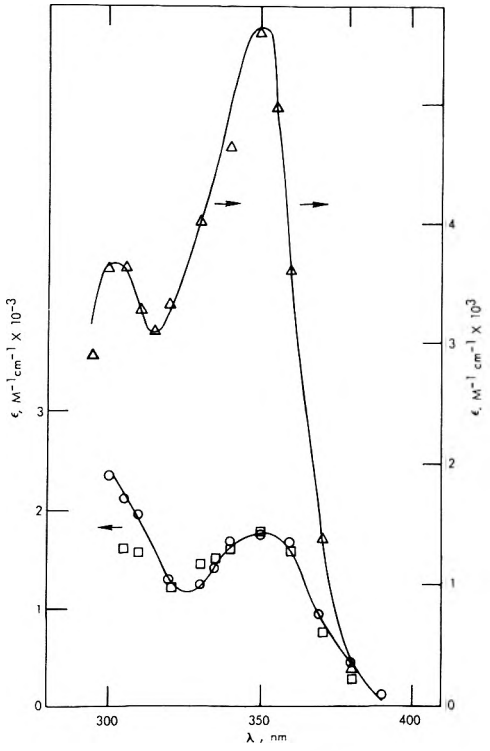

Figure 4. Transient absorption spectra produced from the reaction of e_{aq}^- with tyramine (O, 5×10^{-3} *M*, pH 7.7) and *p*-hydroxyphenylpropionic acid (□, 10^2 *M*, pH 5.2) in 1.5 *M tert*-butyl alcohol, after correction for contribution from H atom adduct. Spectrum of H atom adduct to tyramine (Δ, 5×10^{-3} *M*, pH 0.9, 1.5 *M tert*-butyl alcohol).

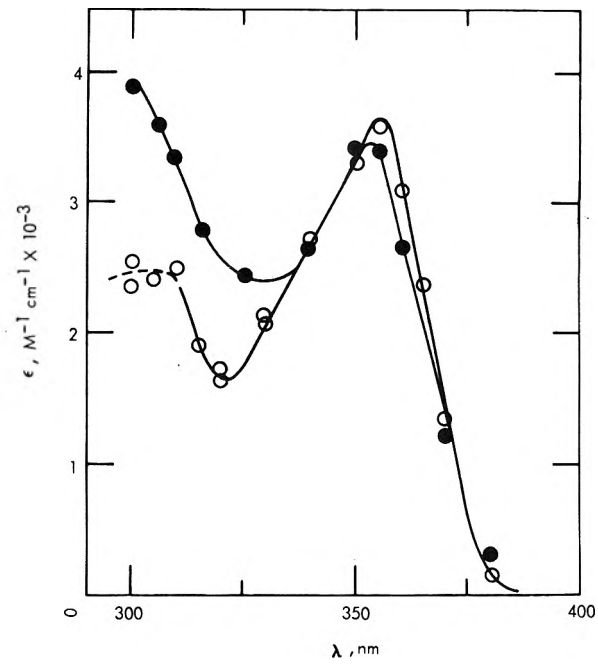

Figure 5. Absorption spectra of the H atom adduct to 2 m*M* *p*-cresol (pH 1.3, Ar, O) and *p*-hydroxyphenylpropionic acid (pH 6.4, N_2O (1 atm), ●) produced from the pulse radiolysis of 1.5 *M* aqueous *tert*-butyl alcohol solutions.

its anionic form. We can assume that in the latter case the solvated electron is formed by direct electron ejection from the excited negative ion

$$RO^{-*} \rightarrow RO\cdot + e_{aq}^- \quad (1)$$

In neutral solution either process 2

$$ROH^* \rightarrow ROH^+ + e_{aq}^- \quad (2)$$

followed by release of a proton takes place, or a hydrogen atom is directly ejected from the excited molecule

$$ROH^* \rightarrow RO\cdot + H \quad (3)$$

We assume, therefore, that at high pH equivalent amounts of phenoxyl radicals and solvated electrons are formed, *i.e.*, $[RO\cdot]_0 = [e_{aq}^-]_0$, where the subscript zero indicates the initial concentrations. From an extrapolation of the pseudo-first-order electron decay plot the initial absorbance of solvated electrons was found. Somewhat arbitrarily we assigned 10 μsec after triggering the flash, *i.e.*, a time close to the midpoint of the flash, as time zero. The extinction coefficient of the solvated electron at 690 nm equals $\epsilon(e_{aq}^-)$ 17,000 M^{-1} cm^{-1} (ref 14). This wavelength was chosen for our measurements as a compromise between the increase in absorbance of the solvated electron and the decrease in sensitivity of the photomultiplier tube. Hence from the absorbancies at 410 (phenoxyl radical) and 690 nm (electron), and from the known value of $\epsilon(e_{aq}^-)$, the extinction coefficient of the phenoxyl radical can be found. The extinction coefficients of the phenoxyl radicals for the various phenolic compounds studied are presented in Table III. These values are fairly consistent but are higher than the $\epsilon(RO\cdot)$ 2200 M^{-1} cm^{-1} obtained[13] from the reaction of OH radicals with phenol by pulse radiolysis.

Similar pulse radiolysis experiments were carried out for the reaction of OH radicals with tyrosine in presence of N_2O (to convert >98% of e_{aq}^- to OH radicals, $e_{aq}^- + N_2O \rightarrow OH + N_2 + OH^-$). At pH 5.3 a transient spectrum due to various isomers of the OH adducts to the phenol ring is observed, Figure 6. At pH 9.0, the OH adducts undergo[13] a base-catalyzed unimolecular elimina-

(14) E. J. Hart and M. Anbar, "The Hydrated Electron," Wiley-Interscience, New York, N.Y., 1970.

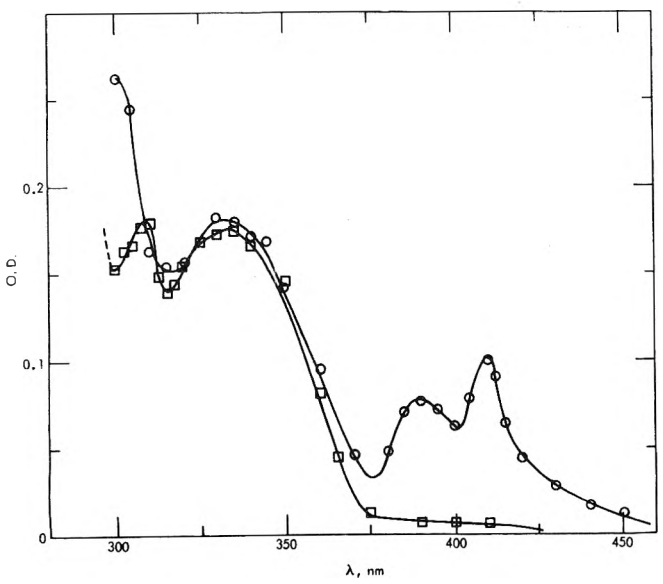

Figure 6. Transient spectra produced from the reaction of OH radicals with ~1.4 m*M* tyrosine, N_2O (1 atm), at pH 5.3 (□) and 9.0 (○). Absorbances extrapolated to ~0.1 μsec after the pulse. Total dose ~4.1 krads/pulse.

TABLE III: Extinction Coefficients of Phenoxyl Radicals and Relative Amounts of e_{aq}^- and H Atoms Produced in the Flash Photolysis of Phenolic Compounds at pH ~7.0

Compound	ϵ(RO·), M^{-1} cm^{-1}	$[e_{aq}^-]/[RO\cdot]$	$[H]/[RO\cdot]$
Tyrosine	2750 ± 200	0.77	0.23
Tyramine	3150 ± 300	0.72	0.28
p-Cresol	3200 ± 300	0.78	0.22
p-Hydroxyphenylpropionic acid	2800 ± 300	1.00	0

tion of water to form the phenoxyl radical RO·, see Figure 6. At pH 9.0 the rate of formation of RO· at 400 nm was found to be 4.2×10^5 sec^{-1} and the rate of decay of the OH adducts at 320–345 nm to be 3.4×10^5 sec^{-1}. Since all the OH adducts do not give rise to phenoxyl radicals (various isomers of the OH adduct are probably formed), an $\epsilon_{410} > 2.3 \times 10^3$ M^{-1} cm^{-1} was calculated. This supports the higher ϵ values derived in Table III from flash photolysis experiments.

By using the above extinction coefficients one can now estimate the relative amounts of e_{aq}^- and H atoms produced at neutral pH, since

$$[e_{aq}^-]/[RO\cdot] = (OD)e_{aq}^-)/OD(RO\cdot))(\epsilon RO\cdot)/\epsilon(e_{aq}^-))$$

in any given optical cell. The relative amounts of H atoms produced are given in Table III.

The amount of electrons produced in neutral solution can also be derived independently from the amount of the electron adduct formed. We have seen that at comparatively high tyrosine concentrations, [Tyr] > 10^{-3} *M*, in a deaerated solution all electrons are scavenged by ground-state tyrosine forming an electron adduct with an absorption peak at 350 nm. On the other hand, in N_2O-saturated solutions containing *t*-BuOH no electron adduct will be formed since all electrons (but not H· atoms) will react under these conditions with N_2O yielding OH radicals, as pointed out before. The latter react with *t*-BuOH according to

$$OH + RH \rightarrow H_2O + R\cdot \quad (4)$$

The *tert*-butyl alcohol radical[7a] formed its relatively unreactive and does not absorb above 280 nm. Therefore the difference in absorbance at 350 nm between solutions saturated with nitrogen and with N_2O will be proportional to the concentration of electrons formed and

$$[OD(N_2) - OD(N_2O)]/\epsilon(\text{electron adduct}) = \text{concentration of adduct} = [e_{aq}^-]_0$$

where $[e_{aq}^-]_0$ is the concentration of solvated electrons formed by flash. The extinction coefficient of the electron adduct of tyrosine was found by pulse radiolysis, as mentioned above. The estimate of the concentration of electrons and hence of the H atoms formed in neutral solutions agrees with that based on the extinction coefficient of the phenoxyl radical and the directly measured absorbance of e_{aq}^-. For tyrosine we find that electrons account for 82% of the phenoxyl radicals as calculated from the electron adduct, while the value in Table III is 77%.

One can see from Table III that, except for *p*-hydroxyphenylpropionate, in all cases the ratio of H atoms to e_{aq}^- formed from the excited phenol ring in neutral solutions is about 1:4.

Nature of Excited State Precursor. The phenoxyl radicals and the electrons formed from the excited phenol derivatives can be produced either from the singlet or from the triplet excited states of the molecule. The lifetime of the singlet ^{1}Tyr is ~5.1 nsec,[15] and the dissociation constants of the singlet and triplet excited states of tyrosine have been estimated,[16] $pK_{S1} \sim 4.5$ and $pK_{T1} \sim 8.5$. In order to determine the origin of the excited state leading to the photoionization of these phenolic compounds, the influence of the typical triplet quencher 2,4-hexadiene[17] on the yield of radicals was tested. Relatively low concentrations of hexadiene were found to reduce the yield of phenoxyl radicals at 410 nm. A Stern–Volmer plot

$$\phi^0/\phi = 1 + k_q[\text{hexadiene}] \quad (5)$$

is shown in Figure 7. The quenching constant of tyrosine by hexadiene is $k_q = 400$ M^{-1}. At the concentrations of hexadiene used it is not possible for it to interact with the short-lived singlet excited state of tyrosine, $\tau \sim 5.1$ nsec, even assuming a quenching rate of 5×10^{10} M^{-1} sec^{-1}.

If one assumes a diffusion-controlled rate constant for the interaction of hexadiene with the excited state precursor of these phenolic compounds one can arrive at a lower limit for the excited state lifetime. From steady-state kinetics $k_q = k\tau$, where k is the bimolecular rate constant for the reaction between hexadiene and the excited tyrosine and τ is the lifetime of the latter. We see that for $k = 10^{10}$ M^{-1} sec^{-1}, τ is at least 2.5×10^{-7} sec, and is in fact probably much longer. We therefore think that the precursor of the electrons and the phenoxyl radicals is the longer lived triplet rather than the singlet excited state of the phenolic chromophore.

This conclusion is also borne out by quenching experiments with compounds containing a disulfide bridge.[18] The most striking finding for us in these experiments is the fact that in *alkaline* solution where the lifetime of the singlet excited phenol derivative is extremely short ($\tau \ll$

(15) J. Feitelson, *Photochem. Photobiol.*, 9, 401 (1969).
(16) E. Yeargers, *Photochem. Photobiol.*, **13**, 165 (1971); E. Van der Donckt, *Progr. React. Kinet.*, **5**, 273 (1970).
(17) A. A. Lamola, *Tech. Org. Chem.*, **12**, (1969).
(18) J. Feitelson and E. Hayon, *Photochem. Photobiol.*, in press.

TABLE IV: Second-Order Decay Kinetics of Phenoxyl Radicals in Aqueous Solution

Compound	$2k/\epsilon$ (pH 7.5)	$2k/\epsilon$ (pH 11.5)	$2k$, M^{-1} sec^{-1} [a]
Tyrosine	4.7×10^5	4.3×10^5	$1.2 \pm 0.2 \times 10^9$ $1.0 \pm 0.2 \times 10^9$ [b]
Tyramine	6.3×10^5	5.8×10^5	$1.9 \pm 0.3 \times 10^9$
p-Hydroxyphenylpropionic acid	2.9×10^5	2.5×10^5	$6.2 \pm 0.2 \times 10^8$
p-Cresol	6.2×10^5	5.6×10^5	$1.9 \pm 0.3 \times 10^9$

[a] Based on extinction coefficients given in Table III. [b] From pulse radiolysis of ~1.4 m*M* tyrosine with N_2O (1 atm) at pH 9.0.

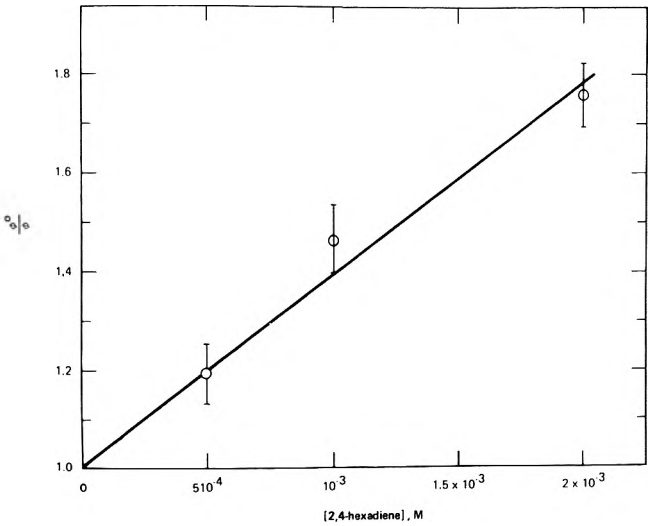

Figure 7. Reciprocal yield plot (Stern–Volmer plot) of the phenoxyl radical produced in the flash photolysis of $\sim 7 \times 10^{-4}$ *M* tyrosine, pH 7.7, as a function of the concentration of 2,4-hexadiene present in solution. Radical monitored at 410 nm using a 280-nm cut-off filter.

10^{10} sec), a reaction between the excited phenolic molecule and a low concentration ($\sim 10^{-3}$ *M*) of disulfide bridges produces the disulfide negative radical ion $RSSR^-$, a reaction which clearly requires a lifetime of more than 1 μsec for the triplet excited species to interact to a measurable extent with the disulfide linkages.

In conclusion, it was found that all four phenol derivatives studied form phenoxyl radicals with very similar spectra and similar decay rates both in neutral and in alkaline solutions, see Table IV. The second-order decay of the resonance-stabilized[19] phenoxyl radicals probably produces o,o′-biphenol derivatives. Astonishingly large differences are found when one compares the rates of reaction between the phenol derivatives in their ground state with solvated electrons or with H atoms. Both *p*-cresol and alanine have rate constants for their reaction with solvated electrons of $\sim 4.2 \times 10^7$ (Table I) and $\sim 5 \times 10^6$ M^{-1} sec^{-1} (ref 9), respectively. However, tyrosine (a β-hydroxylphenylalanine) reacts with a rate constant of 2.8×10^8 M^{-1} sec^{-1} (Table I). With all the phenolic compounds studied, the main reaction with e_{aq}^- appears to be addition to the aromatic ring. For both phenol and phenolate derivatives, the photoejection processes occur from the triplet excited states of these molecules.

Acknowledgment. Partial financial support received from the Army Research Office-Durham is gratefully acknowledged.

(19) H. Musso, "Oxidative Coupling of Phenols," W. I. Taylor and A. R. Battersby, Ed., Marcel Dekker, New York, N.Y., 1967.

Polarographic and Optical Absorption Studies of Radicals Produced in the Pulse Radiolysis of Aqueous Solutions of Ethylene Glycol

K. M. Bansal, M. Grätzel, A. Henglein,* and E. Janata

Hahn-Meitner-Institut für Kernforschung Berlin GmbH, Sektor Strahlenchemie, 1 Berlin 39, West Germany

(Received September 9, 1972)

Publication costs assisted by Hahn-Meitner-Institut für Kernforschung Berlin GmbH

Simultaneous optical absorption and polarographic current measurements were carried out to investigate the free radicals formed in the pulse irradiation of N_2O saturated 10^{-1} M ethylene glycol solutions. In the pH range from 3 to 7, only the 1,2-dihydroxyethyl radical could be observed. It disappears with $2k = 6.7 \times 10^8$ M^{-1} sec^{-1}. Below pH 3, the dehydration of this radical to yield the formylmethyl radical was observed. The equilibrium constant of the protonization of 1,2-dihydroxyethyl and the decay constant of the protonated radical were found to be 1.8×10^{-1} M (or $pK = 0.74$) and 8.6×10^5 sec^{-1}, respectively. The formylmethyl radical disappears with $2k = 9 \times 10^8$ M^{-1} sec^{-1}. In alkaline solutions, a rapid dehydration also occurs. The diffusion-controlled reaction $OH^- + OH\text{-}\dot{C}HCH_2OH \rightarrow H_2O + {}^-O\dot{C}HCH_2OH$ and the rapid decay ${}^-O\dot{C}HCH_2OH \rightarrow OH^- + O\dot{C}HCH_2$ are postulated. The short time polarograms of 1,2-dihydroxyethyl and formylmethyl differ significantly. 1,2-Dihydroxyethyl is oxidized at the mercury electrode at potentials more positive than -1.0 V (*vs.* saturated calomel electrode) and reduced at more negative potentials. Formylmethyl is oxidized beyond -0.1 V and reduced at potentials more negative than -0.3 V. The 1,2-dihydroxyethyl radical therefore is a much stronger reducing agent than the formylmethyl radical.

I. Introduction

The optical absorption spectra and pK values,[1,2] electron spin resonance spectra,[3-5] and the polarographic behavior[6,7] of short-lived free radicals formed by the reaction of OH radicals with aliphatic alcohols have previously been reported by several authors.

From the esr studies of the uv photolyzed aqueous solutions of ethylene glycol containing 1% H_2O_2, Livingston and Zeldes[5] concluded that the 1,2-dihydroxyethyl radical was the primary species obtained by the reaction of the ·OH radical with ethylene glycol. In the presence of H_2SO_4, this radical undergoes dehydration to produce the formylmethyl radical $\cdot CH_2CHO$, the formation of which was explained by a proton-catalyzed dehydration of the 1,2-dihydroxyethyl radical.[5] The existence of this radical was also postulated to explain the yields of various products formed in the photolysis and radiolysis of aqueous ethylene glycol solutions.[8,9]

To understand certain aspects of the mechanism of this dehydration reaction, we investigated the pulse radiolysis of aqueous solutions of ethylene glycol. The optical absorption spectra of the intermediates and the kinetics of their decay at different pH values of the solutions were investigated to find the value of the equilibrium constant of the protonization reaction. Furthermore, polarographic studies of the radicals at different pH values of the solution were undertaken. Previous studies on the polarographic behavior of different types of radicals, a compilation of which will be published elsewhere, clearly pointed out that this technique would provide valuable information on the identity of 1,2-dihydroxyethyl and formylmethyl radicals.

II. Experimental Section

A 12-MeV, 6-A linear accelerator was used for the combined optical and polarographic measurements. The pulse length usually used was 20 nsec. Additional optical measurements were carried out with a Van de Graaff generator (1.5-MeV electrons, 10-μA beam current, 1-μsec pulse length). The aqueous solutions, containing 0.1 M ethylene glycol (Merck Co., analytical grade), were saturated with N_2O (oxygen was removed by bubbling through a column of 0.2 M Cr^{2+} in 1 M $HClO_4$ acid) to scavenge the hydrated electrons according to reaction 1. Such a high ethylene glycol concentration was used to ensure complete scaveng-

$$e_{aq}^- + N_2O \xrightarrow{H_2O} \cdot OH + OH^- + N_2 \qquad (1)$$

ing of ·OH radicals and ·H atoms during the 1-5-μsec pulse. In the polarographic measurements, a capillary with a hanging mercury drop of 0.78 mm diameter (Metrohm Co.) was placed into the optical quartz cell. The solution was slowly flowing through the cell and passing a saturated calomel electrode as reference point for the potential measurements. The light beam for the optical measurements passed through the cell in the vicinity of the hanging mercury drop. Some pertinent details of the technique have been published earlier[7] and other necessary details will be published elsewhere.[10] The solutions

(1) K.-D. Asmus, A. Henglein, A. Wigger, and G. Beck, *Ber. Bunsenges. Phys. Chem.*, **70**, 756 (1966).
(2) M. Simic, P. Neta, and E. Hayon, *J. Phys. Chem.*, **73**, 3794 (1969).
(3) R. Livingston and H. Zeldes, *J. Chem. Phys.*, **44**, 1245 (1966).
(4) A. L. Buley, R. O. C. Norman, and R. J. Pritchett, *J. Chem. Soc. B*, 849 (1966).
(5) R. Livingston and H. Zeldes, *J. Amer. Chem. Soc.*, **88**, 4333 (1966).
(6) J. Lilie, G. Beck, and A. Henglein, *Ber. Bunsenges. Phys. Chem.*, **75**, 458 (1971).
(7) M. Grätzel, A. Henglein, J. Lilie, and M. Scheffler, *Ber. Bunsenges. Phys. Chem.*, **76**, 67 (1972).
(8) C. E. Burchill and K. M. Perron, *Can J. Chem.*, **49**, 2382 (1971).
(9) C. v. Sonntag and E. Thoms, *Z. Naturforsch. B*, **25**, 1405 (1970).
(10) See papers in *Ber. Bunsenges. Phys. Chem.*, in press, by (a) M. Gratzel and A. Henglein; (b) M. Gratzel, A. Henglein, and K. M. Bansal; (c) M. Grätzel, K. M. Bansal, and A. Henglein; (d) A. Henglein and M. Gratzel.

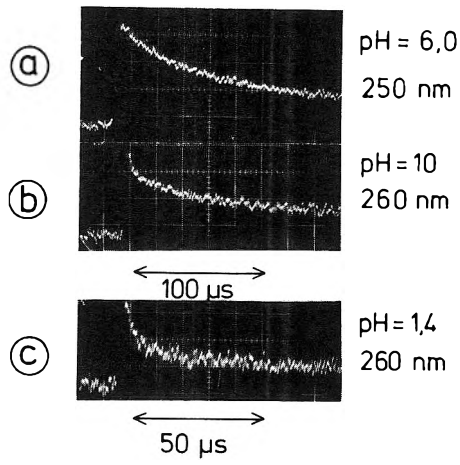

Figure 1. Optical absorption as function of time at different pH values (ethylene glycol concentration, 10^{-1} *M*; $[N_2O]$, 2.5×10^{-2} *M*; pH established with $HClO_4$ and NaOH, pulse dose 2000 rads).

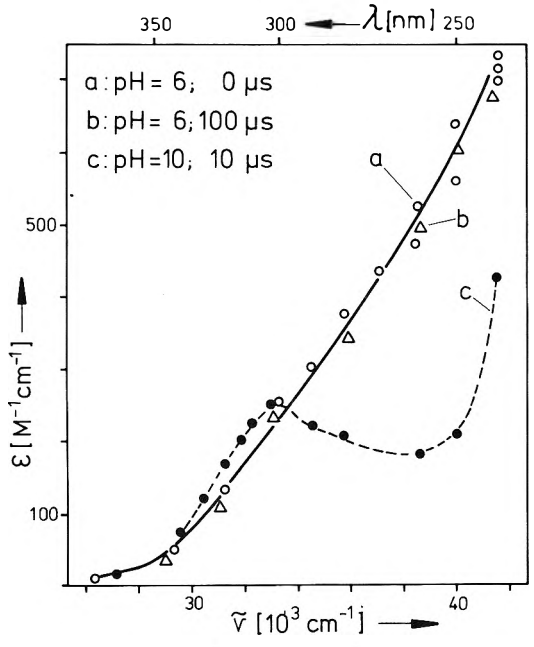

Figure 2. Absorption spectrum of a solution at pH 6.0 immediately after the pulse (a) and after 100 μsec (b) and of a solution at pH 10 after 10 μsec (c).

for the polarographic work contained 0.35 *M* Na_2SO_4 (suprapure from Merck Co.) as an inert electrolyte. The potential of the hanging mercury drop electrode could be varied between 0 and −2.0 V (with respect to the saturated calomel electrode). The current through the polarographic circuit was measured by recording the voltage drop along a working resistor of 20 ohms.

III. Results and Discussion

III. 1. Optical Measurements. Figure 1a shows the optical absorption as function of time at pH 6.0 at 250 nm. The absorption spectra of the intermediates present immediately and 100 μsec after the pulse are reported in Figures 2a and b. The two spectra are identical and furthermore resemble to the spectrum of the $CH_3\dot{C}HOH$ radical.[2] We attribute this spectrum to the 1,2-dihydroxyethyl radical. Absolute extinction coefficients at any particular wavelength were calculated from the extinction immediately after the pulse with $G = G(e_{aq}^-) + G(OH) + G(H) = 6.0$. Spectrum b taken after 100 μsec was normalized to spectrum a immediately after the pulse at 250 nm. The decay of the optical absorption of the radical at 250 nm follows second-order kinetics (this result was obtained from the straight lines that resulted in a plot of the reciprocal optical density *vs.* time after the pulse at different dose rates). A value for $2k/\epsilon = 1.1 \times 10^6$ cm sec^{-1} was obtained. Using a value of ϵ_{250} 610 M^{-1} cm^{-1}, $2k = 6.7 \times 10^8 M^{-1} sec^{-1}$.

A typical oscilloscopic trace tor the decay of the optical absorption with time at pH 10 and 260 nm is reported in Figure 1b. One can easily see that a very fast decay is immediately followed by a much slower decay. The spectrum of the transient present at the end of the first fast decay is presented by curve c in Figure 2. The comparison with curve a of the figure makes it clear that two different intermediates exist at pH 10. It will be pointed out later that spectrum c in Figure 2 is that ot the formylmethyl radical $\cdot CH_2CHO$. It decays by second-order kinetics with $2k/\epsilon = 3.5 \times 10^6$ cm sec^{-1} and using a value of ϵ_{300} 260 M^{-1} cm^{-1}, a value of $2k = 9.1 \times 10^8$ M^{-1} sec^{-1} is obtained.

At pH 1.4, two distinct steps in the decrease in absorption can be recognized (Figure 1c). The absorption spectrum immediately after the pulse was found to be identical with that of 1,2-dihydroxyethyl radical (Figure 2a) and the one at the end of the first decay was found to be identical with that of the formylmethyl radical (Figure 2c). Curve analysis showed that the fast decay immediately after the pulse was of first order provided that the half-life of the fast decay was significantly smaller than the first half-life of the radical at pH 6. We attribute the fast decay in absorption to the dehydration of the 1,2-dihydroxyethyl radical to yield the formylmethyl radical. This subsequently decays by second-order kinetics.

The rate constant of the first-order decay was found to increase with H^+ concentration which can be explained by the mechanism of eq 2. In Figure 3, the half-life is plotted *vs.* the reciprocal H^+ concentration. The straight line obtained intersects the ordinate axis at 8×10^{-7} sec and has a slope of 1.5×10^{-7} M sec^{-1}. If it is assumed that the equilibrium of eq 2 is rapidly attained and no significant radical-radical reaction occurs during the fast dehydration, the following relationship results from the kinetic treatment of the mechanism of eq 2.

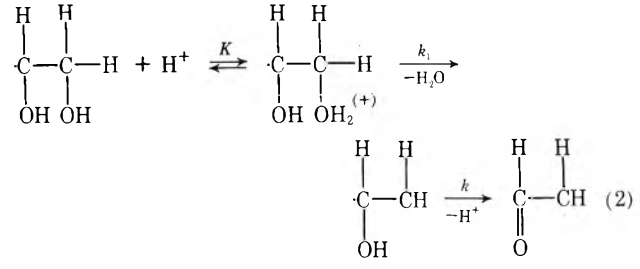

$$\tau_{1/2} = (\ln 2/k_1) + (K \ln 2/k_1)(1/[H^+]) \qquad (3)$$

It is also assumed that the rate constant k in eq 2 is higher than k_1. Using eq 3, a value of $k_1 = 8.6 \times 10^5$ sec^{-1} is calculated from the intersection of the straight line in Figure 3 with the ordinate axis and an equilibrium constant $K = 1.8 \times 10^{-1}$ M is calculated from the slope of the straight line. A pK of 0.74 corresponds to this equilibrium constant.

Below pH 1, the rate of dehydration is so fast that it is practically finished after a 1-5-μsec pulse. The absorption

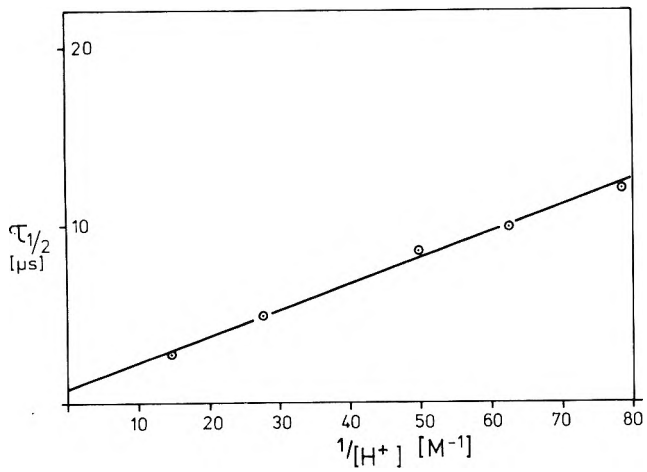

Figure 3. Plot of the half-life of the first-order decay *vs.* the reciprocal H^+ concentration of the solution.

shortly after the pulse is now due to the formylmethyl radical. The absorption decays by second order after the pulse. A rate constant $2k = 9 \times 10^8\ M^{-1}\ \text{sec}^{-1}$ was calculated from this decay which corresponds to the one obtained in the alkaline solutions. The fast formation of the

$$\begin{matrix}\cdot\text{CHOH}\\|\\\text{CH}_2\text{OH}\end{matrix} + \text{OH}^- \xrightarrow{-\text{H}_2\text{O}} \begin{matrix}\cdot\text{CH}-\text{O}^-\\|\\\text{CH}_2\text{OH}\end{matrix} \longrightarrow \begin{matrix}\text{CH}=\text{O}\\|\\\text{CH}_2\end{matrix} + \text{OH}^- \quad (4)$$

formylmethyl radical at pH 10 (see Figure 2b) can be explained by an OH^- catalyzed dehydration of the 1,2-dihydroxyethyl radical (eq 4). The pK values of simple aliphatic alcohol radicals are higher than 10.7.[1] It can hardly be postulated that the pK of the 1,2-dihydroxyethyl radical is significantly lower. However, even at pH 8.5, the decay of the 1,2-dihydroxyethyl radical is very fast. This indicates that no equilibrium on the left-hand side of eq 4 is established between the acid and base form of 1,2-dihydroxyethyl. Apparently, the OH^- ion reacts very fast with the 1,2-dihydroxyethyl radical to yield HOH_2CCHO^- This radical anion has a much higher rate of OH^- loss to form the formylmethyl radical than of its reaction with H_2O to establish the equilibrium with its acid form. Furthermore, the rate of OH^- loss must be higher than that of the reaction between HOH_2CCHOH and OH^-, the rate of the latter being therefore the determining rate of the overall process. This rate could not be measured accurately; however, it can be concluded from the results obtained that the rate of the reaction of OH^- with the 1,2-dihydroxyethyl radical is that of a diffusion-controlled process.

III. 2. Polarographic Measurements. The polarographic measurements are to give additional information about the identity of the radicals. We have shown that "short-time polarograms" of short-lived free radicals can be obtained by recording the polarographic current at the mercury drop electrode as a function of time after formation of the radicals by irradiation of the solution with a short electron pulse.[6,7] Such current *vs.* time curves are taken at different potentials of the mercury drop. The plot of the current at a given time after the pulse *vs.* the electrode potential constitutes a polarogram. Polarograms have been determined for a large number of free radicals. They are typical for certain types of radicals and can therefore be used now for the identification of new species found in pulse experiments. A compilation of such polarograms will be published elsewhere.

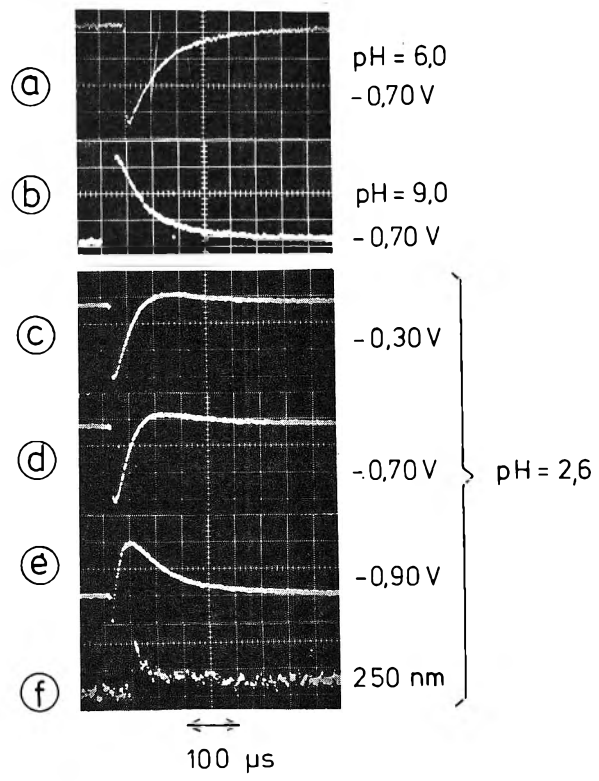

Figure 4. Polarographic current *vs.* time curves at different pH values and potentials (*vs.* saturated calomel electrode) (curves a–e). Curve f shows 2500-Å absorption *vs.* time at pH 2.6.

The current *vs.* time curves are determined (a) by the rate of radical disappearance, (b) by the formation of a concentration gradient at the mercury drop, and (c) by the kinetics of the transfer reaction through the double layer. These curves therefore are not exactly parallel to the curves showing the optical absorption as function of time for the radicals in the bulk of the solution. It is not the purpose of the present paper to describe the details of the current *vs.* time curves, *i.e.*, the kinetics of the electrode processes involved. A description of these phenomena will be given elsewhere.[10] Only those features of the current *vs.* time curves will be discussed which are important for the identification of the radicals.

Figures 4a–e show the oscilloscope traces of the polarographic currents as function of time at different pH values and potentials at the mercury electrode in the pulse-irradiated aqueous N_2O saturated ethylene glycol solutions. On the left side, the zero line before the pulse can always be recognized. Negative signals represent oxidation, and positive signals the reduction of a radical. Figure 4f gives the optical absorption as function of time to complete the polarographic current *vs.* time curves c–e at pH 2.6.

At pH 6.0, oxidation of the radical present after the pulse occurs at −0.70 V. The negative signals decays to zero after about 200 μsec (Figure 4a). In Figure 5, the maximum signal after the pulse is plotted *vs.* the potential of the mercury electrode for pH 5.9, 4.9, and 3.9. It can be seen that a constant negative signal is obtained at potentials between −0.7 and −0.2 V. At more positive potentials weaker negative signals are observed. This effect is due to an adsorption of the sulfate ions at the mercury electrode by which the transfer reaction is hindered. This effect has been observed with other simple aliphatic alcohols and will be described in detail elsewhere.[10c,d] At potentials more negative than −0.7 V, the negative signal be-

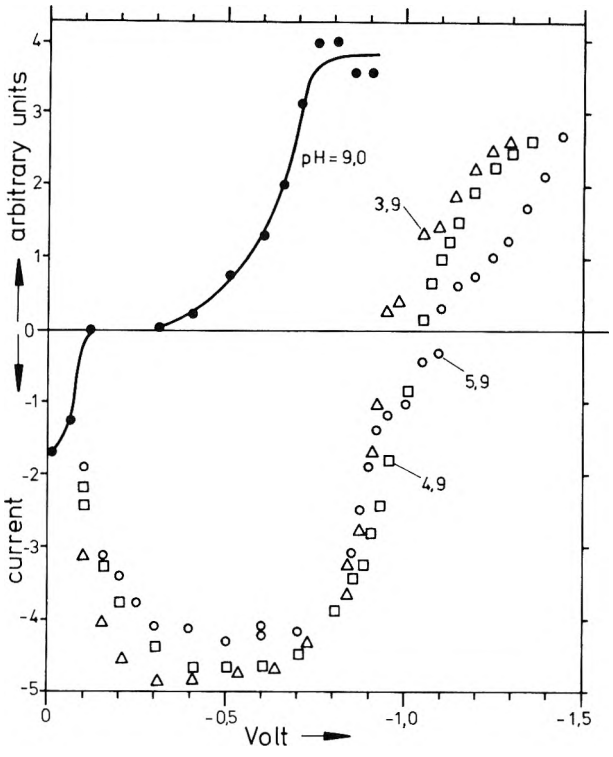

Figure 5. Maximum signal of the polarographic current after the pulse as function of the potential (*vs.* saturated calomel electrode) at different pH values. The polarograms at pH 5.9, 4.9, and 3.9 are attributed to the 1,2-dihydroxyethyl radical, the polarogram at pH 9.0 to the formylmethyl radical.

comes rapidly weaker and at about −1.0 V, a positive signal after the pulse can be observed. This signal rises with increasing the negative potential. The polarogram of Figure 5 corresponds to similar polarograms of α alcohol radicals.[7] Oxidation at the mercury electrode occurs below about −1.0 V independent of the pH in acid solutions. Reduction of the radical occurs at more negative potentials, whereby the polarographic "wave" is shifted to less negative potentials with increasing H^+ concentration. The polarograms of Figure 5 at pH 5.9, 4.9, and 3.9 are attributed to the 1,2-dihydroxyethyl radical. This radical differs from the ethanol radical (CH_3-$\dot{C}H$-OH) in that one H atom of the methyl group is replaced by OH. Comparing the polarograms of both radicals[7] one realizes that the oxidation wave and especially the reduction wave of the CH_2OH-$\dot{C}HOH$ radical are at more positive potentials than the corresponding waves of CH_3-$\dot{C}HOH$.

At pH 9.0, a radical is present after the pulse that is reduced at the potential of −0.70 V, as can be recognized from the positive current signal of Figure 4b. The maximum signal after the pulse is plotted in Figure 5 *vs.* the potential for a solution of pH 9.0. It can be seen that oxidation of the radical occurs only if the potential is more positive than −0.1 V. Reduction becomes noticeable at potentials more negative than −0.30 V. The full height of the polarographic "wave" is reached at −0.75 V. The polarographic behavior of the radical present in alkaline solution is significantly different from that present in neutral or slightly acid solutions. The polarogram at pH 9.0 in Figure 5 is attributed to the formylmethyl radical. This polarogram is similar to that of the $\cdot CH_2COO^-$ radical[7] and to the radical $CH_3\dot{C}HCOCH_3$ formed in the reaction of OH with ethyl methyl ketone. Apparently, the formylmethyl radical is a much weaker reducing species than its precursor, the 1,2-dihydroxyethyl radical.

The curves c–e in Figure 4 show a complex behavior. The solution is now acidic enough to allow the observation of the dehydration according to eq 2. The optical absorption shows the typical fast decay within the first 50 μsec after the pulse (Figure 4f). At both −0.30 and −0.70 V (curves c and d), a negative signal immediately after the pulse is observed which indicates the presence ot the 1,2-dihydroxyethyl radical. After about 80 μsec, the signal is slightly positive since the formylmethyl radical is now present. The low height of this positive signal is due to the fact that after 80 μsec an extended diffusion layer has already been established before the mercury drop and that part of the radicals have already disappeared by mutual interaction. The weakly positive signal finally decays to zero at longer times. At −0.90 V (curve e), still a weak negative signal is seen immediately after the pulse since the 1,2-dihydroxyethyl radical is still oxidized at this potential (Figure 5). However, the signal now rapidly switches to a strong positive signal which finally decays to zero. It has always to be kept in mind that the observed current signal is composed of two components: the oxidation (or negative) signal of the 1,2-dihydroxyethyl radical and the reduction (or positive) signal of the formylethyl radical. During the first 100 μsec after the pulse, both radicals are always present although with a changing ratio in concentrations. If the signal of 1,2-dihydroxyethyl (at −0.90 V) is weak, a small amount of formylmethyl formed is sufficient to switch the signal to a strong positive value (since formylmethyl has already maximum current at −0.90 V according to Figure 5).

Acid–Base Reactions of Condensed Phosphates with Molten Alkali Nitrates. A Kinetic and Stoichiometric Investigation[1]

James L. Copeland* and Leslie Gutierrez

Department of Chemistry, Kansas State University, Manhattan, Kansas 66502 *(Received June 5, 1972)*

Publication costs assisted by the National Science Foundation

Stoichiometries of Lux–Flood acid–base reactions of $(NaPO_3)_x$, $Na_3(PO_3)_3$, $Na_4(PO_3)_4$, $Na_5P_3O_{10}$, and P_4O_{10} with molten $NaNO_3$, and of $Na_3(PO_3)_3$, $Na_4P_2O_7$, and $Na_5P_3O_{10}$ with molten $LiNO_3$ were studied. Kinetics investigations of reactions of $Na_3(PO_3)_3$ and $Na_5P_3O_{10}$ with excess molten $NaNO_3$ were performed by measurement of rate of total gas evolution ($4NO_2 + O_2$) and by ^{31}P nmr analyses of quenched reaction residues. With $NaNO_3$ at 400° and above, all phosphates indicated except P_4O_{10} were degraded to $Na_4P_2O_7$ while P_4O_{10} at 325° was depolymerized only to $Na_3(PO_3)_3$. With $LiNO_3$ a cation effect was observed in that the final phosphate product was PO_4^{3-}, probably due to polarization of -P-O-P- bonds in $P_2O_7^{4-}$. Kinetics studies of the reaction of $Na_3(PO_3)_3$ with excess $NaNO_3$ as solvent revealed two distinct stages. Stage I is the formation of $Na_5P_3O_{10}$ *via* a set of complex unidentified intermediates, among which is an apparently cyclic phosphate anion formed in large amount very early in the reaction with a ^{31}P nmr chemical shift very close to that of the parent $(PO_3)_3^{3-}$ resonance, and a steady-state trace quantity of $(PO_3)_4^{4-}$. Some tentative concepts are advanced to interpret some intermediates of stage I. Stage II is the direct depolymerization: $2P_3O_{10}^{5-} + [O^{2-}] \rightarrow 3P_2O_7^{4-}$ (k_2), with second-order behavior in $P_3O_{10}^{5-}$ and no detectable intermediates. At 400, 411, 425, and 437°, k_2 is 3.63×10^{-2}, 5.14×10^{-2}, 9.58×10^{-2}, and 13.06×10^{-2} (arbitrary units)$^{-1}$ min^{-1}, respectively, giving an activation energy of 34.1 kcal. During stage II, $4NO_2 + O_2$ are evolved with pseudo-first-order behavior in total gas volume at constant pressure. Reaction of $Na_3(PO_3)_3$ with $NaNO_3$ proceeds very slowly, if at all, under vacuum, but proceeds equally vigorously under an ambient of either Ar or O_2. Rate of reaction of $Na_5P_3O_{10}$ with $NaNO_3$ appears unaffected by presence or absence of an ambient atmosphere.

Introduction

High-temperature systems containing oxides and/or oxyanions have been characterized as acid–base systems by Lux[2] and by Flood and Forland.[3] In this concept an oxide ion donor is a base while an oxide ion acceptor is an acid.

It has been known for some time that the NO_3^- ion in molten nitrates is a good Lux-Flood base, decomposing by some as yet incompletely understood mechanism into NO_2 and O_2 gases, in a 4:1 mole ratio, upon donating the O^{2-} ion. Duke, *et al.*,[4] felt that the basic mechanism might be

$$NO_3^- \rightleftharpoons NO_2^+ + O^{2-} \quad (1a)$$

$$NO_2^+ + NO_3^- \rightarrow 2NO_2 + O \quad (1b)$$

$$O + O + M \rightarrow O_2 + M \quad (1c)$$

where M is a third body, and the equilibrium of eq 1a is shifted to the right upon addition of a sufficiently strong oxide ion acceptor (Lux–Flood acid). Topol, *et al.*,[5] have disputed the existence of NO_2^+ in nitrate melts, and have advanced an alternate hypothesis

$$2NO_3^- \rightleftharpoons 2NO_2(g) + (1/2)O_2(g) + O^{2-} \quad (2)$$

These latter investigators[5] have also demonstrated the ability of $NO_2(g)$ itself to act as an acid, as in the reactions

$$2NO_2(g) + O^{2-} \rightarrow NO_3^- + NO_2^- \quad (3a)$$

$$NO_2(g) + NO_2^- \rightarrow NO_3^- + NO(g) \quad (3b)$$

$$2NO_2(g) + 2CrO_4^{2-} \rightarrow NO_3^- + NO_2^- + Cr_2O_7^{2} \quad (3c)$$

Zambonin and Jordan[6] claim that the O^{2-} ion cannot exist at any appreciable concentration at all in equilibrium with nitrate melts. However, the purpose of the present investigation was *not* the nature of this mechanism, but rather the mechanisms of condensed phosphate depolymerizations resulting from treatment with excess nitrate melts acting in their known capacity as bases. Thus, for our purposes a reaction of the type of eq 2 will suffice to illustrate the *net* role of NO_3^- as an oxide ion donor *in reaction*, even though O^{2-} may never exist *per se* as an independent intermediate; *i.e.*, O^{2-} has been effectively transferred to the acid by $2NO_3^-$ ions in excess nitrate melt.

The family of condensed phosphates represents a very interesting series of potential Lux–Flood acids. Schematic structural formulas for the phosphates studied in the present work, and also orthophosphate, are as given (I–VII). (The letter symbols OP, PP, TMP, TTMP, and TPP

(1) Presented in part at the 8th Midwest Regional Meeting of the American Chemical Society, Columbia, Mo., Nov 1972.
(2) H. Lux, *Z. Electrochem.*, **45**, 303 (1939).
(3) H. Flood and T. Forland, *Acta Chem. Scand.*, **1**, 781 (1947).
(4) (a) F. R. Duke and M. L. Iverson, *J. Amer. Chem. Soc.*, **80**, 5061 (1958); (b) F. R. Duke and S. Yamamoto, *ibid.*, **81**, 6378 (1959); (c) F. R. Duke and E. A. Shute, *J. Phys. Chem.*, **66**, 2114 (1962); (d) F. R. Duke and J. Schlegel, *ibid.*, **67**, 2487 (1963); (e) F. R. Duke, *J. Chem. Educ.*, **39**, 57 (1962); (f) F. R. Duke in "Fused Salts," B. R. Sundheim, Ed., McGraw-Hill, New York, N. Y., 1964, pp 409–417; (g) R. N. Kust and F. R. Duke, *J. Amer. Chem. Soc.*, **85**, 3328 (1963); (h) F. R. Duke and M. L. Iverson, *Anal. Chem.*, **31**, 1233 (1959).
(5) L. E. Topol, R. A. Osteryoung, and J. H. Christie, *J. Phys. Chem.*, **70**, 2857 (1966).
(6) (a) P. G. Zambonin and J. Jordan, *Anal. Lett.*, **1**, 1 (1967); (b) *J. Amer. Chem. Soc.*, **89**, 6365 (1967); (c) *ibid.*, **91**, 2225 (1969).

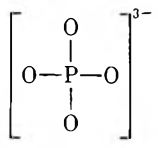

I. orthophosphate
(OP), PO_4^{3-}

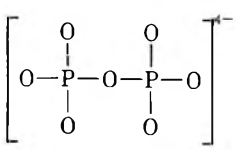

II. pyrophosphate
(PP), $P_2O_7^{4-}$

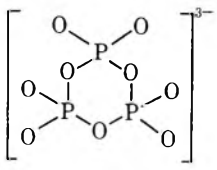

III. trimetaphosphate
(TMP), $(PO_3)_3^{3-}$

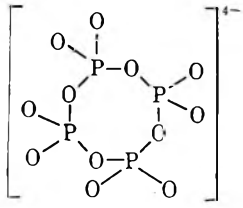

IV. tetrametaphosphate
(TTMP), $(PO_3)_4^{4-}$

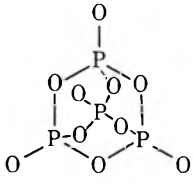

V. phosphorus "pentoxide"
P_4O_{10}

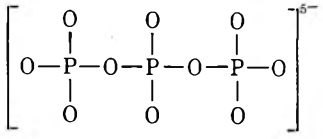

VI. tripolyphosphate
(TPP), $P_3O_{10}^{5-}$

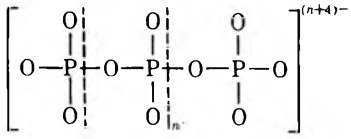

VII. a polyphosphate
(classical "metaphosphate"),

$$P_xO_{3x+1}^{(x+2)-} \longrightarrow P_xO_{3x}^{x-} = xPO_3^- \text{ as } x = n+2 \longrightarrow \infty$$

will be used occasionally for brevity.) With the exception of P_4O_{10}, all these species are stable almost indefinitely in aqueous solution near pH 7 and room temperature. Inspection of the structures reveals the existence of four basic types of phosphate groups:[7] (a) the isolated PO_4^{3-} group (structure I), (b) the end group (as in structure II), (c) the middle group (as in structures III and IV), and (d) the branching point group (structure V). Species VI and VII are seen to be constructed from both middle and end groups. In many chemical respects the relative stabilities of such groups appear to be ordered as isolated PO_4^{3-} group > end group > middle group > branching point group, apparently as a result of decreasing resonance stabilization as more and more isolated oxygen atoms become involved in bridging bonds between phosphorus atoms.[8] One also observes that, stoichiometrically speaking, the only differences among these types of groups are the relative lack or excess of O^{2-} ions. Thus, $P_2O_7^{4-}$ becomes $2PO_4^{3-}$ upon addition of O^{2-}; $(PO_3)_3^{3-}$ becomes $P_3O_{10}^{5-}$ upon addition of O^{2-}, or becomes $P_2O_7^{4-}$ + PO_4^{3-} upon addition of $2O^{2-}$, etc. In each case a P-O-P bridge would be ruptured in some way by an attacking O^{2-} ion in some form. Based upon the relative ordering of chemical stability of the groups just given, then, one would expect a Lux-Flood acid strength arrangement to be ordered in the reverse sequence. Thus, for the phosphates discussed here, acid strength in the presence of a given base (NO_3^- in the present work) should be P_4O_{10} > $(PO_3)_3^{3-}$ > $P_2O_7^{4-}$ > PO_4^{3-} with $(PO_3)_4^{4-}$ being about the same as $(PO_3)_3^{3-}$, and $P_3O_{10}^{5-}$ being somewhere between $(PO_3)_3^{3-}$ and $P_2O_7^{4-}$.

Shams El Din, *et al.*,[9] have performed the more noted experiments concerning the degradations of various condensed phosphates and P_4O_{10} in molten salts. These workers have reported studies of the degradations of P_4O_{10}, $Na_4P_2O_7$, and $NaPO_3$ [apparently $Na_3(PO_3)_3$, but reported only as $NaPO_3$ by these authors] in various molten salts. Of particular interest to the present work were their potentiometric acid–base titrations of $NaPO_3$. The degradation was found to depend on both the base used and the molten salt solvent. Thus, when $NaPO_3$ was dissolved in a LiCl-KCl eutectic and titrated with Na_2O_2 at 400°, the acid–base reaction was represented as

$$2PO_3^- + O^{2-} \rightleftharpoons P_2O_7^{4-} \quad (4)$$

with no further degradation to PO_4^{3-}. In molten KNO_3, however, titration of $NaPO_3$ with Na_2O_2 apparently resulted in eq 4 followed by

$$P_2O_7^{4-} + O^{2-} \rightleftharpoons 2PO_4^{3-} \quad (5)$$

Finally, when $NaPO_3$ was dissolved in KNO_3 at 350° and titrated with any one of the bases CO_3^{2-}, HCO_3^-, $HCOO^-$, $(COO)_2^{2-}$, or CH_3COO^-, the apparent reaction sequence was

$$3PO_3^- + O^{2-} \rightleftharpoons P_3O_{10}^{5-} \quad (6)$$

$$2P_3O_{10}^{5-} + O^{2-} \rightleftharpoons 3P_2O_7^{4-} \quad (7)$$

followed by eq 5. The extent of depolymerization of the condensed phosphates was also found to depend on the associated cation. Titration of P_4O_{10} in fused KNO_3 at 350° was complicated by rapid initial degradation of P_4O_{10} by NO_3^-, so that only the degradation product could be titrated by any of the previously mentioned bases. This initial reaction was suggested as being

$$P_4O_{10} + 4NO_3^- \rightarrow 4PO_3^- + 2N_2O_5(g) \quad (8)$$

Markowitz, *et al.*,[10] have also studied acid–base degradations of some alkali pyrophosphates and metaphosphates with ClO_4^- as the base. $LiPO_3$ and KPO_3 were of the long-chain form of "metaphosphate" (structure VII) while $Na_3(PO_3)_3$ was the trimetaphosphate (structure III). Degradation depended on the associated cation. $LiPO_3$ was degraded completely to Li_3PO_4, whereas $Na_3(PO_3)_3$ and KPO_3 were depolymerized only to the pyrophosphates. These studies apparently indicated the following reaction sequence

$$2MPO_3 + 2MClO_4 \rightarrow M_4P_2O_7 + Cl_2(g) + (7/2)O_2(g) \quad (9)$$

and further, in the case of M = Li

$$M_4P_2O_7 + 2MClO_4 \rightarrow 2M_3PO_4 + Cl_2(g) + (7/2)O_2(g) \quad (10)$$

Traces of $Li_5P_3O_{10}$ were found, but its existence was at-

(7) J. R. Van Wazer, "Phosphorus and Its Compounds," Vol. 1, Interscience, New York, N. Y., 1958, pp 390–393.
(8) Reference 7, pp 437–441.
(9) (a) A. M. Shams El Din, *Electrochim. Acta*, 7, 285 (1962); (b) A. M. Shams El Din, A. A. El Hosary, and A. A. A. Gerges, *J. Electroanal. Chem.*, 6, 131 (1963); (c) *ibid.*, 8, 312 (1964); (d) A. M. Shams El Din and A. A. A. Gerges, *Electrochim. Acta*, 9, 123 (1964); (e) A. M. Shams El Din and A. A. El Hosary, *ibid.*, 13, 135 (1968); (f) A. A. El Hosary and A. M. Shams El Din, *ibid.*, 16, 143 (1971); (g) A. M. Shams El Din, H. D. Taki El Din, and A. A. El Hosary, *ibid.*, 13, 407 (1968).
(10) M. M. Markowitz, H. Stewart, Jr., and D. A. Boryta, *Inorg. Chem.*, 2, 768 (1963).

tributed to

$$2MPO_3 + M_3PO_4 \rightarrow M_5P_3O_{10} \quad (11)$$

On the basis of their study, Markowitz, *et al.*, assigned the relative acidity of the alkali pyrophosphates and metaphosphates as decreasing according to $Li^+ >>> Na^+, K^+ = 0$ for $P_2O_7^{4-}$, and $Li^+ >>> Na^+ > K^+$ for PO_3^-, and finally meta ≫ pyro.

In view of the observed spontaneous reactions of many condensed phosphates with molten $NaNO_3$, and the foregoing background, the objectives of the present work were formulated as follow. Overall stoichiometries of the reactions of $Na_3(PO_3)_3$, $Na_4(PO_3)_4$, $Na_5P_3O_{10}$ (form II of structure VI),[11] $(NaPO_3)_x$ (insoluble and glass forms of structure VII),[11] and P_4O_{10} with $NaNO_3$ were determined, as well as the reactions of $Na_3(PO_3)_3$, $Na_5P_3O_{10}$, and $Na_4P_2O_7$ with $LiNO_3$. These studies were performed using weight loss techniques with careful analyses of evolved gases and crystalline residues. Kinetics of the reactions of $Na_3(PO_3)_3$ and $Na_5P_3O_{10}$ with excess molten $NaNO_3$ solvent were studied by measurements of the rate of total gas ($NO_2 + O_2$) evolution, and by ^{31}P nmr analyses of aqueous solutions of quenched reaction residues. The results shed some interesting light on the mechanism of an overall reaction of the type of eq 6 and 7, although much still remains to be done.

Experimental Section

Materials. Reagent grade P_4O_{10} and the insoluble form of $(NaPO_3)_x$ were obtained from the Baker and Adamson Co. Purified grade $Na_5P_3O_{10}$ (form II) was obtained from the Fisher Scientific Co. and reagent grade $NaNO_3$ and $LiNO_3$ were from the Mallinckrodt Co. These chemicals were used without further purification other than oven drying at *ca.* 125° for at least 24 hr and storage in a Drierite charged dessicator just prior to use.

$Na_3(PO_3)_3$ was prepared by thermal treatment of $NaH_2PO_4.H_2O$, and was purified by dissolving in distilled water, filtering off any insoluble "metaphosphate," and recrystallization from ethanol.[12] $Na_4(PO_3)_4$ was prepared by the low-temperature hydrolysis of P_4O_{10}.[13] Purities of these prepared cyclic metaphosphates were established as at least 95% from crystalline infrared spectra and from the occurrence of a single ^{31}P nmr peak for an aqueous solution at *ca.* +21 ppm from 85% H_3PO_4 for $Na_3(PO_3)_3$, and at *ca.* +23.2 ppm from 85% H_3PO_4 for $Na_4(PO_3)_4$.[14] The glass form of $(NaPO_3)_x$ was prepared by fusion of the insoluble form in a platinum test tube followed by quenching with cold water.

Oxygen and argon gases, used as ambients in gas evolution studies, were from the National Cylinder Gas Co., and were specified as being of better purity than 99.9%. These were used without further purification except for being passed through a $Mg(ClO_4)_2$ charged drying tower at the time of use.

Apparatus and Instrumentation. Rate of total gas evolution studies for $Na_3(PO_3)_3$ and $Na_5P_3O_{10}$ with $NaNO_3$ were performed by measuring the total volume of gases evolved as a function of time at fixed room temperature, and under a constant 1-atm total pressure. The apparatus was constructed in our laboratory, and was very similar to that employed by Freeman[15] in his investigations of thermal decompositions of $NaNO_2$ and $NaNO_3$. Our apparatus was provided with accessory traps and fittings which permitted sampling of the evolved gases for analysis at the end of a run. Each run was performed with the apparatus filled with an Ar atmosphere (or with O_2 in one special case), initially at 1-atm pressure. This apparatus is described in detail elsewhere.[16]

Infrared spectra of crystalline samples in KBr pellets, and of evolved gas samples, were performed with a Perkin-Elmer Model 337 grating infrared spectrophotometer.

Gas chromatography runs were performed using a locally fabricated gas chromatograph with He carrier gas. Mass spectra of evolved gas samples were obtained from an Electronics Associates Inc. Model 250 quadrupole mass spectrometer.

All nmr analyses were performed using a Varian Associates Model XL-100 nmr spectrometer provided with a ^{31}P probe and deuteron lock, necessitating use of D_2O as sample solvent (a proton lock had not yet been received for our instrument). The nmr spectra were accumulated with a Varian Associates Model C-1024 time average computer. Samples were contained in Wilmad Glass Co. 12-mm o.d. nmr sample tubes with plastic caps. The chemical shift reference signal, at 0.0 ppm, was provided by 85% H_3PO_4 in a small capillary tube placed in the unknown sample tube. This reference sample was preserved and was the same one used for every nmr determination.

A constant high-temperature bath, for quenched reaction studies, was constructed in the form of a thermostated, stirred bath of molten $NaNO_3$.[16]

All temperature measurements were performed using a Leeds and Northrup Co. No. 8691 millivolt potentiometer with chromel–alumel thermocouples. An ice-bath reference junction was employed.

A Vacuum Atmosphere Corporation Model He-43-2 Dri-Lab drybox, provided with a dry Ar atmosphere, was used for all experimentation with P_4O_{10}, and for handling of $LiNO_3$.

Reaction Stoichiometry Procedure. On the assumption (subsequently confirmed) that NO_3^- decomposes in acid–base reactions according to an overall reaction scheme of the type of eq 2, stoichiometries of the reactions of $Na_3(PO_3)_3$, $Na_4(PO_3)_4$, $Na_5P_3O_{10}$ (form II), $(NaPO_3)_x$ (insoluble and glass forms), and P_4O_{10} with $NaNO_3$ were determined by a method based on weight loss due to evolved NO_2 and O_2, and analyses of the final solid residues. In addition, similar investigations were performed for $Na_3(PO_3)_3$, $Na_5P_3O_{10}$, and $Na_4P_2O_7$ with $LiNO_3$.

In the cases of $Na_3(PO_3)_3$ and $(NaPO_3)_x$, intimate mixtures of a phosphate with $NaNO_3$, of varying weight ratios, were prepared and weighed in Coors No. 00 porcelain crucibles. The crucibles were placed in a crucible furnace of fixed temperature, and the samples were allowed to react until no further weight losses were observed when the crucibles were withdrawn, cooled in a dessicator, and reweighed. A similar procedure was followed for $Na_5P_3O_{10}$ and $Na_4(PO_3)_4$ except that 13 × 100 mm Pyrex test tubes placed inside 23 × 230 mm Vycor test tubes served as reaction vessels. These were placed in the constant high-temperature bath rather than a crucible furnace. No observable attack occurred to either the crucibles or the Pyrex test tubes.

(11) Reference 7, pp 605–606.
(12) R. N. Bell, *Inorg. Syn.*, **3**, 103 (1950).
(13) R. N. Bell, L. F. Audrieth, and O. F. Hill, *Ind. Eng. Chem.*, **44**, 568 (1952).
(14) M. M. Crutchfield, C. H. Dungan, J. H. Letcher, V. Mark, and J. R. Van Wazer, "^{31}P Nuclear Magnetic Resonance," Interscience, New York, N. Y., 1967.
(15) E. S. Freeman, *J. Phys. Chem.*, **60**, 1487 (1956).
(16) L. Gutierrez, Ph.D. Thesis, Kansas State University, 1972.

For P_4O_{10} with $NaNO_3$ in the drybox, mixtures of varying weight ratios were prepared in the test tube vessels, which were then stoppered. These assemblies were placed in the constant high-temperature bath, and the stoppers were removed about 15 sec later. After reaction, each tube was flushed with dry Ar while still in the bath, stoppered, removed to the drybox, and reweighed. Again, no attack on the test tubes was noted.

Reactions of phosphates with $LiNO_3$ were performed using the test tube assemblies, however, the $LiNO_3$ was handled in the drybox. No attack on the test tubes was noted.

Solid residues remaining after each run were analyzed by infrared spectroscopy utilizing KBr pellets, and by ^{31}P nmr analyses of aqueous solutions. Evolved gas analyses were performed with the aid of the constructed gas line in conjunction with the rate of total gas evolution studies, to be discussed later.

For each reaction series of a phosphate with $NaNO_3$ or $LiNO_3$, a plot of weight loss per gram of nitrate *vs.* initial weight ratio of phosphate to nitrate gave a straight line of positive slope from the origin for weight ratios less than the stoichiometric equivalence point, and a horizontal straight line for weight ratios greater than this point. The intersection of these lines gave the stoichiometric equivalence point in terms of weight ratio, which was then converted to a molar ratio. The $(NaPO_3)_x$, $Na_3(PO_3)_3$, and $Na_5P_3O_{10}$ reactions were run at 450°, the $Na_4(PO_3)_4$ reaction was at 400°, and the P_4O_{10} reaction was at 325°. 400° was chosen for $Na_4(PO_3)_4$ to preclude any possible conversion of $(PO_3)_4^{4-}$ to $(PO_3)_3^{3-}$, known to occur slowly at *ca.* 450°.[17] 325° was used for P_4O_{10} since this substance sublimes at 360°.[18]

Gas Evolution Rate Procedure. The gas evolution apparatus was employed for this study.[16] In the case of the $Na_3(PO_3)_3$ + $NaNO_3$ reaction, 1.7000 g of $NaNO_3$ was placed in the outer portion of the reaction vessel, and 0.1109 g of $Na_3(PO_3)_3$ was held suspended in the inner portion of this vessel, just above the nitrate.[16] The entire system was evacuated for *ca.* 1 hr, and was then filled with dry Ar (or dry O_2 in one special case) at 1-atm pressure. An electrical cylindrical furnace was raised to encircle the reaction chamber, causing fusion of the $NaNO_3$, and it and the phosphate to attain a common, specified temperature. The $Na_3(PO_3)_3$ sample was then made to fall into the excess molten $NaNO_3$ (phosphate:nitrate mol ratio of *ca.* 1:55), and timing commenced. At various times total gas volume (Ar + NO_2 + O_2), at constant 1-atm total pressure and room temperature, was observed on the gas buret. The total gas volumes so obtained were corrected to STP and plotted *vs.* time. At room temperature the $2NO_2 = N_2O_4$ equilibrium was decidedly complicating and was unable to be corrected for in these studies, as well as in the similar ones using $Na_5P_3O_{10}$. This definitely limits the value of the gas evolution results to semiquantitative purposes. Reaction runs were performed at 400, 411, 425, 437, and 448°. In each case the $Na_3(PO_3)_3$ was totally soluble in the excess fused $NaNO_3$, resulting in completely homogeneous reactions.

In the case of the $Na_5P_3O_{10}$ + $NaNO_3$ reaction, the procedure was the same except that 0.4000 g of this phosphate was reacted with 5.0000 g of molten $NaNO_3$ (still a 1:55 mol ratio) in each run, and two sets of runs were performed: one using *ca.* 250-μ particle size of $Na_5P_3O_{10}$, and the other using *ca.* 125-μ particle size. The particle size of this phosphate had an effect on the reaction rate since solubility in $NaNO_3$ was not complete, resulting in some degree of heterogeneous reaction. This fact obviously renders the results somewhat less valuable than those obtained for the trimetaphosphate. Runs were performed at 401, 411, 418, 424, 435, and 442° for the *ca.* 250-μ particles, and at 400, 411, 425, and 437° for the *ca.* 125-μ particles.

In both phosphate cases, the amount of excess $NaNO_3$ was made purposely large so as to be treated as a solvent of approximately constant concentration. The use of 0.1109 g of $Na_3(PO_3)_3$ and of 0.4000 g of $Na_5P_3O_{10}$ was intentional, since these quantities depolymerize to $Na_4P_2O_7$ with evolution of equal amounts of gaseous products.

The same apparatus was employed for completely reacting all the phosphates studied with $NaNO_3$ and collecting the total gases evolved for analyses. These gaseous products were analyzed by infrared spectrometry, mass spectrometry, gas chromatography, and quantitatively for $NO_2(N_2O_4)$ by the technique of Whitnack, *et al.*,[19] using standard solutions prepared according to the methods of Skoog and West.[20]

Quenched Reaction Rate Procedure. Reaction vessels consisted basically of 23 × 230 mm Vycor test tubes. Each such tube contained 1.7000 g of $NaNO_3$ for the reaction with $Na_3(PO_3)_3$, or 1.6400 g of $NaNO_3$ for the reaction with $Na_5P_3O_{10}$. These tubes were thermostated in the constant high-temperature bath at appropriate temperatures. A dropping device, similar to that employed in the gas evolution rate studies,[16] containing either 0.1109 g of $Na_3(PO_3)_3$ or 0.1333 g of $Na_5P_3O_{10}$, was positioned in each tube, and dry Ar was swept through each such assembly for *ca.* 3 hr. The Ar flow was terminated, and reaction was commenced by dropping the phosphate charge suspended above the molten $NaNO_3$ into the latter in each tube, as in the gas evolution work. A swirling motion was imparted to each tube for *ca.* 1 min to ensure rapid dissolution and mixing of the reactants. At various times reaction vessels were withdrawn and immediately thrust into cold water, thereby quenching the reactions. The solid residue in each tube was dissolved in 5 ml of D_2O, and the ^{31}P nmr spectrum was obtained using 85% H_3PO_4 in a capillary as a standard. Twenty scans of a 1000-Hz sweep width spectrum were accumulated on the time average computer (CAT). Sweep rate was at 4 Hz sec^{-1}. To increase the area of each resonance signal in the accumulated spectrum, the read out of the CAT was at 4 Hz sec^{-1} and the spectrum was recorded at 10 Hz sec^{-1}. This had the effect of multiplying each of the accumulated peak areas by a factor of 2.5. A reference spectrum from 0.1109 g of $Na_3(PO_3)_3$ and 1.7000 g of $NaNO_3$ in D_2O, or from 0.1333 g of $Na_5P_3O_{10}$ and 1.6400 g of $NaNO_3$ in D_2O was also obtained for the zero reaction time point. No observable attack occurred to the Vycor reaction vessels.

Since ^{31}P nmr resonance signals are nicely identifiable by chemical shift,[14] end groups occurring at *ca.* 4–7 ppm upfield from H_3PO_4, and middle groups at *ca.* 18–24 ppm upfield from H_3PO_4, it was a simple matter to obtain the phosphorus content due to each such general type of group by peak area integrations. These areas were normalized by dividing each by the reference peak area due to

(17) D. E. C. Corbridge, M. S. Pearson, and C. Walling, *Top. Phosphorus Chem.*, 3, 265 (1966).
(18) Reference 7, p 274.
(19) G. C. Whitnack, C. J. Halford, E. S. Gantz, and G. B. L. Smith, *Anal. Chem.*, 23, 464 (1951).
(20) D. A. Skoog and D. M. West, "Analytical Chemistry, An Introduction," Holt, Rinehart and Winston, New York, N. Y., 1965.

the constant amount of H_3PO_4. In each case all phosphorus initially present in a reaction as either $(PO_3)_3^{3-}$ or $P_3O_{10}^{5-}$ was accounted for, within experimental error, as end and/or middle group form with no PO_4^{3-} other than that present in the standard H_3PO_4. Not all *specific* phosphate species could be unambiguously identified by chemical shift and spin–spin splitting patterns. However, it was generally possible in the $Na_3(PO_3)_3$ case to trace the decay of $(PO_3)_3^{3-}$, growth and subsequent decay of $P_3O_{10}^{5-}$, and growth of final $P_2O_7^{4-}$ product throughout the course of a run. In addition, some $(PO_3)_4^{4-}$ was found. An unidentified species consisting of all equivalent middle groups, close to $(PO_3)_3^{3-}$, and some complex splitting patterns due to one or more unidentifiable transients were found during early times in a run. In the case of the $Na_5P_3O_{10}$ reaction, all phosphorus was accounted for as $P_3O_{10}^{5-}$ and/or $P_2O_7^{4-}$ during the course of a run. The latter reaction was not quite so clean, kinetically speaking, being complicated by the solubility problem of $Na_5P_3O_{10}$ in $NaNO_3$ as mentioned before.

A given run consisted of 15 to 20 quenched reactions at various times, and runs were performed at 389, 400, 411, 425, and 437° for $Na_3(PO_3)_3$, and at 389, 400, 406, and 411° for $Na_5P_3O_{10}$. 0.1333 g of $Na_5P_3O_{10}$ was chosen for reaction with 1.6400 g of $NaNO_3$ since these amounts represent the quantities of these substances that would remain if 0.1109 g of $Na_3(PO_3)_3$ reacted with 1.7000 g of $NaNO_3$ to produce only $Na_5P_3O_{10}$. As in the gas evolution studies, the mole ratio of $Na_3(PO_3)_3$ to $NaNO_3$ was 1:55; however, the mole ratio of $Na_5P_3O_{10}$ to $NaNO_3$ was only about 1:53 for the reasons just cited.

Results and Discussion

A. Reaction Stoichiometries. To within experimental error (*ca.* ±5%) weight loss experiments, with analyses of solid and gaseous products, indicate that the reactions of the various phosphates with $NaNO_3$ are

$$(NaPO_3)_x + xNaNO_3 \xrightarrow{450^\circ} (x/2)Na_4P_2O_7 + xNO_2(g) + (x/4)O_2(g) \quad (12a)$$

$$2Na_3(PO_3)_3 + 6NaNO_3 \xrightarrow{450^\circ} 3Na_4P_2O_7 + 6NO_2(g) + 1.5O_2(g) \quad (12b)$$

$$2Na_5P_3O_{10} + 2NaNO_3 \xrightarrow{450^\circ} 3Na_4P_2O_7 + 2NO_2(g) + 0.5O_2(g) \quad (12c)$$

$$Na_4(PO_3)_4 + 4NaNO_3 \xrightarrow{400^\circ} 2Na_4P_2O_7 + 4NO_2(g) + O_2(g) \quad (12d)$$

$$P_4O_{10} + 4NaNO_3 \xrightarrow{325^\circ} (4/3)Na_3(PO_3)_3 + 4NO_2(g) + O_2(g) \quad (12e)$$

where $(NaPO_3)_x$ denotes both glass and insoluble forms of polyphosphates. The reasons for the use of 400 and 325° for the $Na_4(PO_3)_4$ and P_4O_{10} reactions, respectively, have already been explained. It is apparent that the $Na_3(PO_3)_3$ formed from P_4O_{10} must be reasonably stable to further depolymerization at 325°, since no additional detectable reaction occurred within a reasonable time period. Treatment of this trimetaphosphate residue with additional $NaNO_3$ at higher temperatures yielded $Na_4P_2O_7$ in accordance with eq 12b. Reactions of $Na_4P_2O_7$, $Na_3(PO_3)_3$, and $Na_5P_3O_{10}$ with $LiNO_3$ occur as

$$P_2O_7^{4-} + 2NO_3^- \xrightarrow[Li^+]{420^\circ} 2PO_4^{3-} + 2NO_2(g) + 0.5O_2(g) \quad (13a)$$

$$(PO_3)_3^{3-} + 6NO_3^- \xrightarrow[Li^+]{420^\circ} 3PO_4^{3-} + 6NO_2(g) + 1.5O_2(g) \quad (13b)$$

$$P_3O_{10}^{5-} + 4NO_3^- \xrightarrow[Li^+]{420^\circ} 3PO_4^{3-} + 4NO_2(g) + O_2(g) \quad (13c)$$

where the mixed Na^+ and Li^+ cations are omitted for clarity. Complete details of the data and plots leading to these results are found elsewhere.[16]

A strong cation effect is apparent. A reasonable interpretation of the results using $LiNO_3$ is that the small Li^+ ion, with its high ionic potential, is capable of weakening P–O–P bridge bonds, *via* induced polarization, in any $P_2O_7^{4-}$ that may form as an intermediate. Such weakened bonds would be more susceptible to basic attack by O^{2-} in whatever form it may exist. Further details of the reactions in Li^+-containing molten media were not studied at this time.

B. Gas Evolution Rate Studies. Figure 1 contains plots of total volume of evolved gases, $NO_2(N_2O_4) + O_2$, corrected to STP, *vs.* time for the reaction of $Na_3(PO_3)_3$ with molten $NaNO_3$ at 400, 411, and 425°. Curves for 437 and 448° are similar in shape, but cannot be shown because of crowding. An expanded time scale plot would show their like profiles. Data for these plots, and similar ones for the $Na_5P_3O_{10} + NaNO_3$ reaction, are tabulated elsewhere.[16] From the form of the curves it is apparent that the rate of total gas evolution is characterized by two stages. In stage I initially rapid production of total gas is followed by a deceleration in this evolution. At the onset of stage II the evolution rate is accelerated once again, followed by relaxation as the reaction approaches completion (conversion to $Na_4P_2O_7$). Reaction times at the inflections between stages I and II, obtained from intersections made by extrapolating upper and lower portions of stages I and II for each curve, are 29.0, 19.0, 11.5, 5.5, and 2.5 min for the 400, 411, 425, 437, and 448° plots, respectively. These times will later be seen to correlate significantly with the times of occurrence of maximum $P_3O_{10}^{5-}$ intermediate concentration in the reacting systems, as determined by the nmr quenched reaction studies. Indeed, from the nmr studies it will be seen that the reactions occurring just after these inflection point times, and proceeding on to completion (stage II), are essentially simple second-order breakdowns of $P_3O_{10}^{5-}$ to $P_2O_7^{4-}$, with no other phosphate species being detectable in the systems. Thus, the gas evolution curves during most of stage II are in reality the curves for the reaction of $Na_5P_3O_{10}$ with excess $NaNO_3$. Based on this latter observation, if one sets an adjusted time scale with $t = 0$ just after the inflection points on curves of the type of Figure 1, one has total gas evolution *vs.* time plots for the $Na_5P_3O_{10}$ reaction with $NaNO_3$ without the complication of the dissolution problem of solid tripolyphosphate in the molten nitrate, which occurred when these reagents were mixed directly. It is of empirical interest that the corrected total volume of evolved gas, V_t, at time t, during this stage II reaction of $Na_5P_3O_{10}$ with $NaNO_3$ obeys the equation

$$V_t = V_\infty(1 - e^{-kt}) \quad (14)$$

where V_∞ is the final total volume at infinite time and k is a constant. Plots of $\ln(1 - V_t/V_\infty)$ *vs.* t permit calculations of the constant k as 4.59×10^{-2}, 7.74×10^{-2}, 10.8×10^{-2}, 15.2×10^{-2}, and 20.2×10^{-2} min^{-1} at 400, 411, 425, 437, and 448°, respectively. A plot of $\ln k$ *vs.* $1/T$ (T

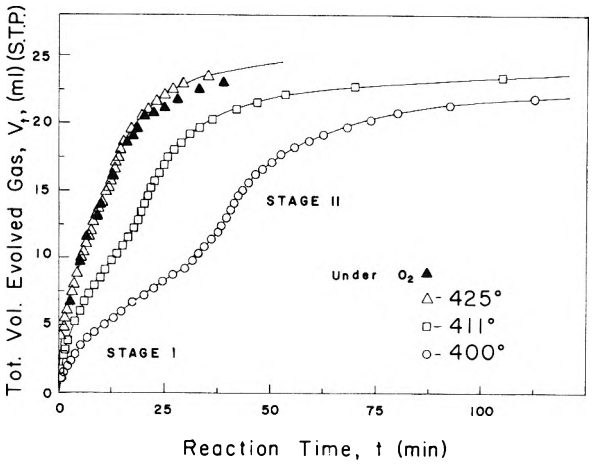

Figure 1. Total volume of gas evolved at constant pressure, corrected to STP, V_t, *vs.* reaction time, *t*, for the $Na_3(PO_3)_3$ + $NaNO_3$ reaction at 400, 411, and 425°. All open points are for runs under an Ar ambient, while the solid points at 425° are for an O_2 ambient.

in °K) is fairly linear[16] with a slope of -6.33×10^3 deg, yielding a pseudo "activation energy" of 28.9 kcal mol^{-1}. Direct reactions of $Na_5P_3O_{10}$ with $NaNO_3$ are roughly approximated by eq 14 also. At a given temperature *k* for *ca.* 125-μ $Na_5P_3O_{10}$ particles is distinctly smaller than that for stage II of the $Na_3(PO_3)_3$ reaction, and *k* for 250-μ particles is still smaller. As temperature is increased, *k* for both particle sizes approaches *k* for the stage II process, reflecting the decreasing rate determining role of the dissolution process which complicates the direct reaction of $Na_5P_3O_{10}$ in $NaNO_3$, as mentioned before. Equation 14 and its derived properties are of empirical observational interest only for both stage II of the $Na_3(PO_3)_3$ reaction and the direct reaction of $Na_5P_3O_{10}$, since this equation is based on the rate of production of total gaseous *products* (further complicated by the $2NO_2 = N_2O_4$ equilibrium) rather than on amounts of remaining reactants. In view of this, it is not deemed worthwhile to devote additional time or space to further discussion of this aspect of the study which cannot lead to any substantive conclusions or interpretations at this time. Complete data and plots for the foregoing are, therefore, available elsewhere.[16]

It was discovered that the reaction of $Na_3(PO_3)_3$ with $NaNO_3$ *in vacuo* proceeded to an imperceptible extent, if at all. When stoichiometric amounts of these reagents [*ca.* 0.2400 g of $Na_3(PO_3)_3$ and 0.2000 g of $NaNO_3$] were thoroughly mixed and reacted at *ca.* 412° for 90 min under vacuum, no noticeable gaseous products were formed, and the ^{31}P nmr spectrum of the residue showed that little of the trimetaphosphate had been degraded. When $Na_3(PO_3)_3$ was caused to react with excess $NaNO_3$ (1:55 mole ratio) under vacuum at 412° for 60 min, examination of the ^{31}P nmr spectrum of the residue showed that very little $P_2O_7^{4-}$ had formed, and that most of the phosphorus was in the form of $P_3O_{10}^{5-}$. When the same starting reaction mixture at 412° was under an Ar atmosphere, the conversion to $P_2O_7^{4-}$ was nearly complete after 60 min. Since the presence or absence of an ambient atmosphere had such marked effects on the rate of the $Na_3(PO_3)_3$ + $NaNO_3$ reaction, an attempt was made to ascertain if the nature of the ambient was critical. A gas evolution rate study was performed for the reaction at 425° under a pure O_2 atmosphere. Some points for this run appear as solid points on the 425° isotherm in Figure 1, and it is seen that there is negligible difference between the effect of using Ar or O_2 as an ambient for the reaction. No attempt was made to study the effect of ambient pressure (both Ar and O_2 were at *ca.* 1 atm), nor was the effect of a possibly more reactive gas, such as NO_2, investigated at this time. Thus, the presence of an ambient atmosphere is essential for the reaction to proceed at a reasonable rate, but the nature of this ambient would seem to be of little importance, assuming no direct chemical reaction of the gas of course. It is unlikely that any trace of moisture in the gas could have assisted the reaction, since in all cases gases were passed through a magnesium perchlorate drying tower prior to entry into the system, as discussed earlier. There appeared to be no effect at all on the rate of the $Na_5P_3O_{10}$ + $NaNO_3$ reaction if it was run under vacuum or an ambient gas. Thus, one must conclude that there is a fundamental difference between the initiating mechanism for the degradation of $(PO_3)_3^{3-}$ by NO_3^- and that for $P_3O_{10}^{5-}$ by NO_3^-. This will be made more apparent in the quenched reaction studies.

Gas evolution rate data and plots for the direct reaction of $Na_5P_3O_{10}$ with $NaNO_3$ are not recorded here, but are available elsewhere.[16] Because of the complication of incomplete solubility already discussed, these results are inconclusive. However, as mentioned, plots of corrected total evolved gas volume *vs.* time do follow eq 14. Fortunately stage II of the $Na_3(PO_3)_3$ + $NaNO_3$ reaction corresponds, as discussed, to the simple reaction of $NaNO_3$ with $Na_5P_3O_{10}$ produced as an intermediate. Thus, uncomplicated runs of this reaction are already available as parts of the trimetaphosphate reactions. This will be more apparent from the quenched reaction results.

Quenched Reaction Studies. Figures 2–4 consist of a series of time-averaged ^{31}P nmr spectra of the residues of quenched reactions of $Na_3(PO_3)_3$ with excess $NaNO_3$ at 400° at various times. The actual run consisted of 23 such samples at times from 0 to 105.00 min. However, for brevity here only representative highlight spectra are shown for 0, 1.00, 5.00, 8.00, 18.00, 27.00, 32.00, 41.00, 52.00, and 105.00 min. The series of spectra for runs at all other temperatures are similar to that for the 400° experiment. On each spectrum the common 85% H_3PO_4 reference peak occurs at 0.0 ppm and is labeled OP.

At time zero, the blank residue consists of the single peak at *ca.* 20.6 ppm due to the three equivalent phosphorus atoms in the cyclic trimetaphosphate anion (TMP). At 1.00 min, the unreacted TMP peak is, of course, still present, a trace of cyclic tetrametaphosphate (TTMP) has arisen at *ca.* 22.9 ppm, and a pronounced, unidentifiable middle group peak at *ca.* 21.2 ppm has appeared, which is labeled CP for "complex" phosphate. Since virtually no end groups have yet formed, this CP peak must be due to a new, apparently cyclic phosphate structure consisting of all equivalent middle group phosphorus atoms and very similar to TMP. Indeed, in other runs at shorter times there is not even a trace of end groups present, only TMP, CP, and a trace of TTMP accounting for the total phosphorus content. (The TMP and TTMP peaks were identified as being such by later adding pure TMP and TTMP to the residue solutions and observing that the peaks so labeled grew appropriately in areas.) As time progresses, the TMP peak diminishes while CP grows, TTMP not changing significantly. In addition, unidentifiable end groups begin to appear between 4 and 5 ppm, as seen, for example, at 5 min. By the time 8 min have elapsed, the doubly split end groups of tripolyphosphate (TPP) are definitely showing at *ca.* 5.4 and 5.9 ppm, and the single

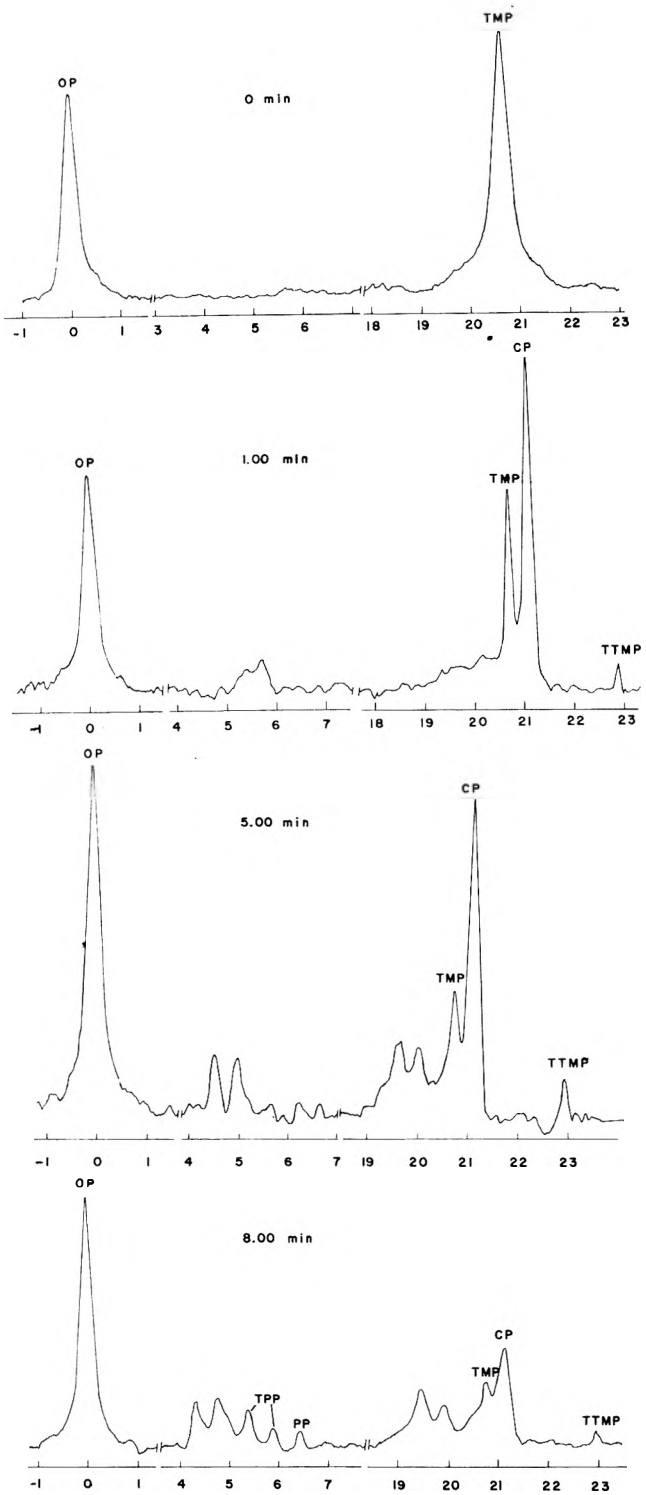

Figure 2. Series of time-averaged ^{31}P nmr spectra of residues of quenched reactions of the $Na_3(PO_3)_3$ + $NaNO_3$ reaction at 400° at 0, 1.00, 5.00, and 8.00 min. 85% H_3PO_4 is reference (OP) peak; chemical shift is recorded in ppm.

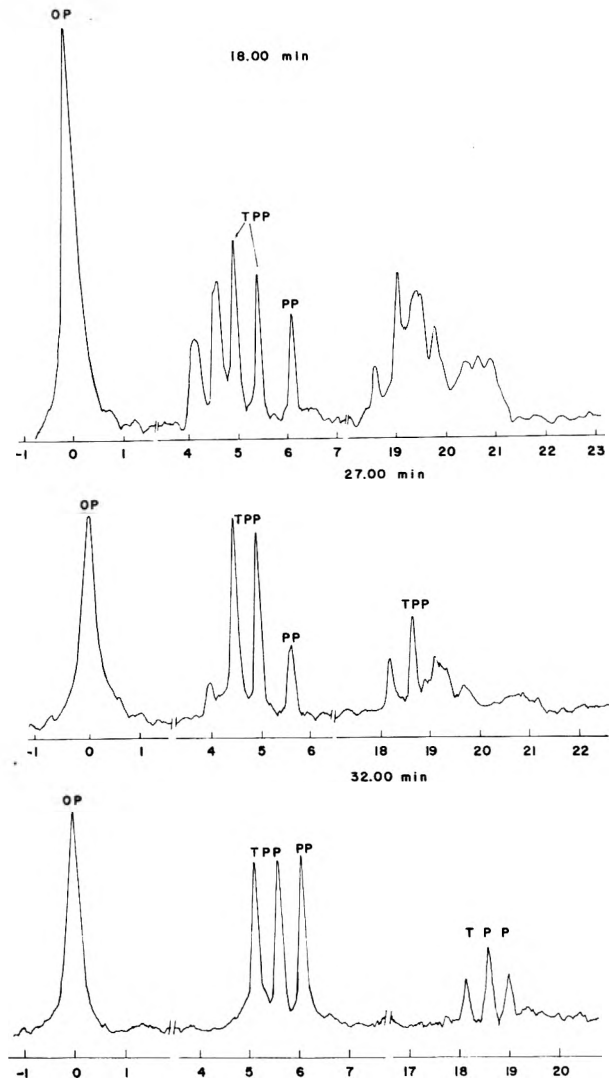

Figure 3. Series of time-averaged ^{31}P nmr spectra of residues of quenched reactions at 18.00, 27.00, and 32.00 min. See caption to Figure 2.

peak from the equivalent end groups of pyrophosphate (PP) is appearing at *ca.* 6.4 ppm. These latter peaks continue to grow while TMP, CP, and TTMP diminish. All the while unidentifiable end and middle group peaks are growing in and/or diminishing, giving fairly complex spectra as, for example, at 18 min. By the time 27 min are attained, TPP has essentially reached a maximum value, much of the unidentifiable phosphates have vanished, and the triplet peak of the middle group of TPP becomes more visible. From this time on to the end the reaction is essentially TPP going to PP, as can be seen from the representative spectra at 32, 41, 52, and 105 min. During this latter time period no phosphates other than TPP and PP are detectable in the residue solutions, and the total phosphorus from these species accounts for all the phosphorus content originally present in the system.

Although some of the phosphates are specifically unidentifiable during the early parts of a reaction of TMP with $NaNO_3$, they can certainly be categorized into end and middle groups. Figure 5 features plots of total middle groups, total end groups, TPP, and PP *vs.* time for the 400° reaction. Similar graphs hold for the other temperatures. The total middle group and end group curves are mirror images, and the constancy of phosphorus content resulting from totalling these curves demonstrates that all phosphorus is accounted for. The maximum in TPP content at *ca.* 27 min is easily visible, and corresponds roughly with the maximum slope in build-up of PP at *ca.* 30 min. As mentioned earlier, the time from 27 to 30 min corresponds approximately to the occurrence of the inflection in the gas evolution curve at *ca.* 29.0 min at 400°. These aspects are true for all temperatures.

In the present method, the earliest convenient time at

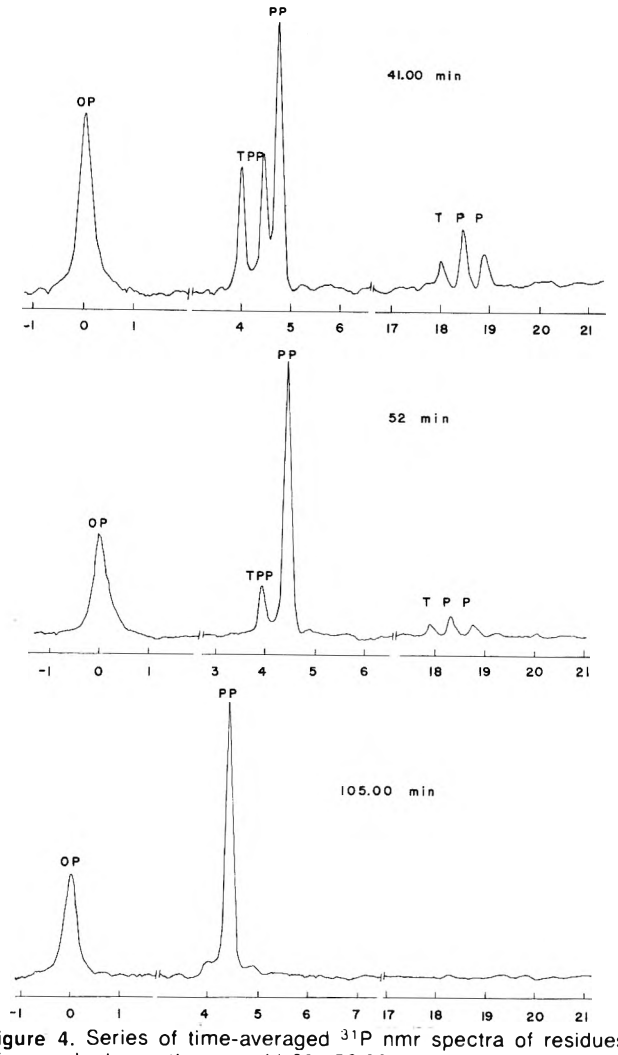

Figure 4. Series of time-averaged ^{31}P nmr spectra of residues of quenched reactions at 41.00, 52.00, and 105.00 min. See caption to Figure 2.

which a reaction can be quenched for its residue analysis is about 1 min. At such a time the concentration of CP, denoted (CP), is already at or past its maximum, and its subsequent decay with $t \gtrsim 1$ min follows simple first-order kinetics

$$(CP) = ce^{-k_1 t} \tag{15}$$

where c = constant and $t \gtrsim 1$ min, in that plots of ln (CP) *vs.* t are nicely linear for the 400 and 411° reactions (reactions at higher temperatures are too rapid to permit accurate data acquisition for (CP) alone. The rate constant $k_1 = (12.35 \pm 0.75) \times 10^{-2}$ min^{-1} at 400°, and $k_1 = (17.91 \pm 0.81) \times 10^{-2}$ min^{-1} at 411°, yielding an activation energy, E_{a1}, of 30.9 ± 8.9 kcal (errors are probable errors). Furthermore, the sum of the TMP concentration, (TMP), and (CP), after $t \gtrsim 1$ min, also decays with first-order kinetics

$$[(TMP) + (CP)] = c'e^{-k_1' t} \tag{16}$$

where c' = constant and $t \gtrsim 1$ min, yielding $k_1' = (10.87 \pm 0.36) \times 10^{-2}$ min^{-1} at 400°, $k_1' = (16.89 \pm 0.75) \times 10^{-2}$ min^{-1} at 411°, and $E_{a1}' = 38.6 \pm 4.5$ kcal. It is thus apparent that (TMP) itself cannot decay with simple first-order properties, and this is evident from the lack of any reasonably linear behavior of ln (TMP) *vs.* t plots. The data leading to eq 15 and 16 are found in Table I.

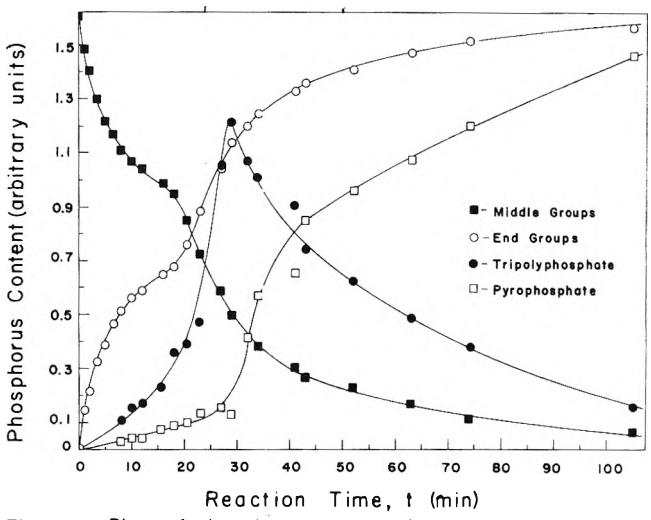

Figure 5. Plots of phosphate content of various kinds, in arbitrary units, *vs.* time for the 400° reaction of $Na_3(PO_3)_3$ + $NaNO_3$ as determined from ^{31}P nmr analyses of quenched reaction residues.

Attempts were made to elucidate the structure of the unknown intermediate arising in the early stages of a TMP reaction in terms of the numbers of end and middle groups. Ratios were taken of phosphorus content in the form of unidentified end groups to phosphorus content in the form of unidentified middle groups for various times in a reaction. In all cases consistent ratio values were *not* obtained, indicating the likely existence of more than one unknown intermediate phosphate.

As mentioned, at a time shortly after (TPP) has achieved its maximum, as in Figure 5, the reaction is essentially a simple degradation of TPP to PP.

$$2P_3O_{10}^{5-} + [O^{2-}] \xrightarrow{k_2} 3P_2O_7^{4-} \tag{17}$$

Table II summarizes the data for this process for 400, 411, 425, and 437°, and also shows adjusted reaction times from whose new zero points the kinetics can be deduced. These kinetics clearly result as second order in (TPP) in the presence of excess (approximately constant concentration) $NaNO_3$ solvent. Plots of [1/(TPP)] *vs.* adjusted time, t', yield linear curves from whose slopes second-order rate constants result as $k_2 = (3.63 \pm 0.17) \times 10^{-2}$ (au)$^{-1}$ min^{-1} at 400°, $k_2 = (5.14 \pm 0.58) \times 10^{-2}$ (au)$^{-1}$ min^{-1} at 411°, $k_2 = (9.58 \pm 0.62) \times 10^{-2}$ (au)$^{-1}$ min^{-1} at 425°, and $k_2 = (13.08 \pm 0.62) \times 10^{-2}$ (au)$^{-1}$ min^{-1} at 437°. These values yield an activation energy $E_{a2} = 34.1 \pm 2.6$ kcal.

As for the gas evolution work, rate data and plots for the direct reactions of $Na_5P_3O_{10}$ with $NaNO_3$ are not recorded here but are available elsewhere.[16] This is again because of the complications of the solubility problem, and the fact that sufficient data are already available for this reaction in terms of the adjusted reaction times, t', of the latter part of the $Na_3(PO_3)_3$ + $NaNO_3$ reaction, as tabulated in Table II and subsequently analyzed.

D. General Discussion. The salient features of this work may be summarized as follow. $(NaPO_3)_x$, $Na_3(PO_3)_3$, $Na_4(PO_3)_4$, and $Na_5P_3O_{10}$ all react with excess molten $NaNO_3$ to yield $Na_4P_2O_7$, and NO_2 and O_2 in 4:1 molar ratio at temperatures of *ca.* 400° and above, and P_4O_{10} reacts with $NaNO_3$ at 325° to yield $Na_3(PO_3)_3$, all in accordance with eq 12. $Na_4P_2O_7$, $Na_3(PO_3)_3$, and $Na_5P_3O_{10}$ react with excess molten $LiNO_3$ at *ca.* 420° and above to degrade completely to PO_4^{3-} (eq 13), indicating a strong

TABLE I: Summary of Degradation Data for the Apparent Trimetaphosphate "Complex," (CP), and Sum of This Complex and Trimetaphosphate, [(CP) + (TMP)], at 400 and 411° for $t \geq 1$ min

Reaction time, t, min	(CP), arbitrary units (au)	−Log(CP)	[(CP) + (TMP)], arbitrary units (au)	−Log[(CP) + (TMP)]
		400°		
1.00	0.770	0.11351	1.160	−0.06446
2.00	0.722	0.14146	0.968	0.01412
3.50	0.570	0.24413	0.800	0.09691
5.00	0.545	0.26360	0.736	0.13312
6.50	0.423	0.37366	0.573	0.24185
8.00	0.298	0.52176	0.486	0.31336
10.00	0.256	0.59176	0.444	0.35262
12.00	0.215	0.66756	0.331	0.48017
	$[k_1 = (12.35 \pm 0.75) \times 10^{-2}$ min$^{-1}]$		$[k_1' = (10.87 \pm 0.36) \times 10^{-2}$ min$^{-1}]$	
		411°		
1.00	0.760	0.11919	0.982	0.00789
2.00	0.569	0.24489	0.771	0.11295
3.00	0.483	0.31605	0.661	0.17980
4.00	0.443	0.35360	0.621	0.20691
5.00	0.363	0.44009	0.495	0.30539
6.00	0.313	0.50446	0.417	0.37986
7.00	0.221	0.63078	0.324	0.48945
	$[k_1 = (17.91 \pm 0.81) \times 10^{-2}$ min$^{-1}]$		$[k_1' = (16.89 \pm 0.75) \times 10^{-2}$ min$^{-1}]$	
	$(E_{a1} = 30.9 \pm 8.9$ kcal)		$(E_{a1}' = 38.6 \pm 4.5$ kcal)	

cation effect probably in the form of -P-O-P- bond weakening by induction.

Kinetic studies of the $Na_3(PO_3)_3$ + excess $NaNO_3$ reaction by measurement of the rate of total gas evolution indicate that such a reaction proceeds in two stages (Figure 1) with an inflection point occurring at essentially the same time that the $P_3O_{10}^{5-}$ ion has reached a maximum concentration (Figure 5), as shown by nmr studies of the quenched reaction samples. At or shortly after this inflection point (the adjusted time scale, t', of Table II), the process consists solely of a second-order reaction in $P_3O_{10}^{5-}$ going to $P_2O_7^{4-}$ by reaction with $NaNO_3$ solvent, with no intermediates being detectable by this nmr technique (Figures 2-5). This latter reaction essentially constitutes stage II on the gas evolution curve, during which the total volume of gases is generated in a pseudo-first-order manner in accordance with eq 14. At time less than 1 min, a "complex" phosphate, CP, consisting wholly of nmr-equivalent middle groups, has attained a maximum concentration greater than that of the remaining $(PO_3)_3^{3-}$ itself, and subsequently decays during stage I of the reaction with first-order behavior (Table I). In addition, the sum of $(PO_3)_3^{3-}$ and CP concentrations decays during stage I with essentially first-order behavior as well (Table I). During stage I an essentially steady-state trace amount of $(PO_3)_4^{4-}$ persists (Figures 2-4), having also been formed during the first minute of reaction. The decay of CP, TMP, and TTMP progresses to TPP *via* more than one complicated, unidentifiable intermediate consisting of various numbers of end and middle groups (Figures 2-4). Stage I of the reaction of $(PO_3)_3^{3-}$ with NO_3^- proceeds much more slowly, if at all, under vacuum than it does under an ambient atmosphere. At present it is not yet possible to elucidate further any detailed mechanism for stage I. One may summarize at best for now that

Stage I

$$(PO_3)_3^{3-} \xrightarrow[NaNO_3]{?} P_3O_{10}^{5-} + 2NO_2 + 0.5O_2 \qquad (18a)$$

Stage II

$$2P_3O_{10}^{5-} \xrightarrow[NaNO_3]{k_2} 3P_2O_7^{4-} + 2NO_2 + 0.5O_2 \qquad (18b)$$

in which stage I progresses *via* CP, $(PO_3)_3^{3-}$ itself, and a trace of $(PO_3)_4^{4-}$ through further unidentifiable intermediates, to $P_3O_{10}^{5-}$. In addition, from separate studies with $P_3O_{10}^{5-}$ itself, it is known that reaction 18b proceeds equally well under vacuum or an atmosphere, in contrast to 18a. In view of the work of Zambonin and Jordan,[6] stage II is probably preferably written as eq 18b rather than eq 17, although the latter implies the *net* addition of O^{2-} from excess NO_3^- ions not necessarily as the free oxide ion.

Tentative suggestions concerning the nature of CP may be advanced. Crutchfield, *et al.*,[14] observed a relatively weak resonance at *ca.* 21.2 ppm in the ^{31}P nmr spectrum of an aqueous solution containing a variety of polyphosphate ions, and tentatively assigned this resonance to the $(PO_3)_5^{5-}$ ion. This is essentially the chemical shift of our CP resonance. However, it is difficult to visualize the rapid production of a significant amount of such a species from $(PO_3)_3^{3-}$ in the present work without a noticeable quantity of end groups appearing as well. Scale molecular models show that it is possible to envision a structure of the type

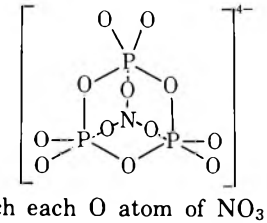

or $[(PO_3)_3 \cdot NO_3]^{4-}$

in which each O atom of NO_3^- is coordinated to one of the P atoms of the $(PO_3)_3^{3-}$ ring. Such fivefold coordination is not unknown for phosphorus (*e.g.*, PCl_5), which is even known to exhibit sixfold coordination (*e.g.*, PCl_6). This increase in covalency can be achieved by phosphorus accepting electron pairs into its empty d orbitals. In view

TABLE II: Summary of the Production of $Na_4P_2O_7$ End Product from the Reaction of Molten $NaNO_3$ with $Na_5P_3O_{10}$ Produced from the $Na_3(PO_3)_3 + NaNO_3$ Reaction at 400, 411, 425, and 437°

Reaction time,[a] t, min	Adjusted reaction time,[b] t', min	(TPP), arbitrary units (au)	$[1/(TPP)]$, $(au)^{-1}$
	400°		
29.0	0.0	1.213	0.824
32.0	3.0	1.073	0.932
34.0	5.0	1.011	0.989
41.0	12.0	0.914	1.094
43.0	14.0	0.744	1.344
52.0	23.0	0.623	1.605
63.0	34.0	0.485	2.062
	$[k_2 = (3.63 \pm 0.17) \times 10^{-2}\ (au)^{-1}\ min^{-1}]$		
	411°		
22.0	0.0	1.077	0.929
25.0	3.0	0.823	1.215
28.0	6.0	0.780	1.282
35.0	13.0	0.610	1.577
	$[k_2 = (5.14 \pm 0.58) \times 10^{-2}\ (au)^{-1}\ min^{-1}]$		
	425°		
9.0	0.0	1.088	0.919
10.5	1.5	0.969	1.031
12.0	3.0	0.900	1.111
14.0	5.0	0.716	1.397
16.0	7.0	0.638	1.567
	$(k_2 = (9.58 \pm 0.62) \times 10^{-2}\ (au)^{-1}\ min^{-1}]$		
	437°		
6.0	0.0	0.976	1.025
7.0	1.0	0.905	1.105
8.0	2.0	0.821	1.218
9.5	3.5	0.696	1.437
11.0	5.0	0.600	1.667
	$[k_2 = (13.08 \pm 0.62) \times 10^{-2}\ (au)^{-1}\ min^{-1}]$		
	$E_{a2} = 34.1 \pm 2.6$ kcal		

[a] Total elapsed time from start of $Na_3(PO_3)_3 + NaNO_3$ reaction. [b] From new zero time taken at about maximum experimental value of (TPP).

of the ability of phosphorus to increase its coordination number through dative bonding, a structure for CP similar to the above does not seem unreasonable. Perhaps a conceivable next step in the stage I mechanism, involving CP, *could* then be

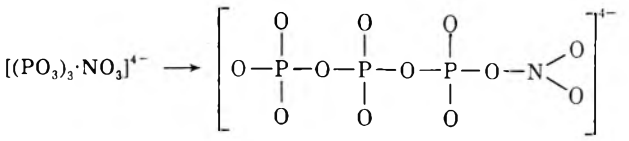

(19)

followed by

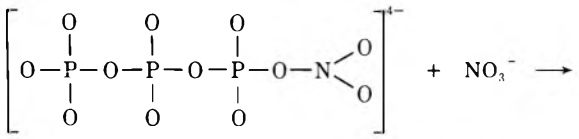

(20)

after which N_2O_5 decomposes in its usual way to $2NO_2 + 0.5O_2$, *etc.* Thus, the nitrophosphate could be one of the unidentifiable intermediates. Whatever the nature of CP it forms very rapidly from TMP, yet there must exist an equilibrium with TMP, or other controlling mechanism, since TMP continues to coexist with CP during all of stage I, presumably itself decaying to TPP through still another process. Of course, processes of the type of eq 19 and 20 do not account for the inhibition of stage I under vacuum, and for the role of the small amount of $(PO_3)_4^{4-}$. In addition, one must admit the possibility of one or more relatively unstable phosphate intermediates being changed in form by hydrolysis upon dissolution in water for the nmr analyses.

In conclusion, further work needs to be done to try to isolate and identify CP, as well as the other unknown intermediates. It would also be highly desirable to be able to obtain nmr spectra of the reacting system itself, without quenching and dissolution in water. It would also be worthwhile to employ a different solvent with which to take up the reaction residues. However, in view of the difficulties already encountered in completely dissolving sufficient amounts of these sparingly soluble samples in minimum water, to yield reasonably intense nmr spectra, the search for good alternate solvents is pessimistic at present.

Acknowledgments. The authors gratefully acknowledge the support of the National Science Foundation, Grant No. GP-12002, A1. Deep appreciation is also extended to Dr. Joseph V. Paukstelis of this department for his extensive aid and assistance in obtaining and interpreting the nmr spectra, and to Mr. Philip R. Zillinger for help in some of the experimental work. This work is based in part of the Ph.D. Thesis of Leslie Gutierrez, accepted by the Graduate School of Kansas State University.

Ion–Molecule Reactions in Monogermane[1]

J. K. Northrop and F. W. Lampe*

Whitmore Laboratory, Department of Chemistry, The Pennsylvania State University, University Park, Pennsylvania 16802
(Received July 14, 1972)

Publication costs assisted by the U.S. Atomic Energy Commission

Ion–molecule reactions occurring in ionized monogermane have been studied by high-pressure mass spectrometry at pressures up to 200 μ and rate constants for second- and third-order reactions of all primary ions have been measured. As expected the reactions observed and the specific reaction rates are much more similar to those occurring in monosilane than to those occurring in methane.

Recent interest in the ion–molecule reactions occurring in ionized monosilane[2-4] has developed in an effort to elucidate possible ionic mechanisms in the radiolysis[5-7] and other high-energy reactions[8-10] of monosilane, in view of the fact that ionic mechanisms are well established in methane systems.[11,12] Since ion–molecule reactions in monosilane differ significantly from those in methane,[13] it is of interest to determine those in monogermane to uncover any correlations of the germane system with its lighter group IV analogs and for their possible importance in high-energy systems where ions are present.

Experimental Section

Appearance potential measurements and low-pressure (2–10 μ) kinetic studies were carried out on a Bendix Model 14-101 time-of-flight mass spectrometer, the basic design of which has been described previously.[2,14] The ionizing electron beam was pulsed at 10 kc/sec with pulse width 1.4 μsec during appearance potential measurements and 0.25 μsec during the kinetic studies at 75-eV electron energy. A 280-V ion drawout pulse of 2.5 μsec was imposed after a variable delay time of 0.00 to 1.00 μsec. Source pressures were measured with a calibrated McLeod gauge. Higher pressure (10-200 μ) kinetic studies were carried out on a Nuclide 12-90-G magnetic spectrometer which also has been described elsewhere.[15] The electron beam energy was 70 eV, the repeller potential was 6.25 V/cm leading to an ion-exit energy of 2.1 eV, and the accelerating voltage was 2500 V. Source pressure, as a function of the measured reservoir pressure, was determined using the rate constant for the disappearance of GeH_2^+ obtained from the low-pressure studies.

Mono- and digermane were prepared by reduction of GeO_2 by KBH_4 in acid solution under 100 Torr of N_2 according to the method of Jolly and Drake.[16] A cold trap at $-108°$ and successive traps of ascarite and anhydrous magnesium perchlorate removed the solvent and higher germanes. Digermane was separated from monogermane by two cold traps at $-117°$.

Thermal drift effects[17] in the time-of-flight spectrometer were determined by measuring the dependence of $^{132}Xe^+$ and $^{84}Kr^+$ intensities on time delay. As expected, for heavy ions the effect was negligible in the range 0.00–0.60 μsec; thus only this range was used to determine rate constants and no correction factors were employed.

All experimental ion currents as a function of m/e were converted to monoisotopic ion currents using the natural abundances of germanium (^{70}Ge, 20.5; ^{72}Ge, 27.43%; ^{73}Ge, 7.76%; ^{74}Ge, 36.5; ^{76}Ge, 7.76%) in a system of simultaneous equations. The matrix of coefficients involved was inverted by the Gauss–Jordan method.

Results and Discussion

A. Low-Pressure Studies. The variation of monogermane ions with time delay at two source pressures is shown in Figure 1. Ge^+ and GeH^+ are essentially independent of pressure and time delay and would *appear* to be neither significant reactants nor products in secondary reactions; however, high-pressure studies, to be discussed later, show both to be reactants. GeH_3^+ increases both with pressure and time delay, while the only primary ion which shows a marked decrease in ion fraction is GeH_2^+. Thus, GeH_2^+ is the major, if not the only, reactant ion and GeH_3^+ is a secondary as well as a major primary ion. The variation of digermanium ions with time delay, shown in Figure 2, indicates they are all products of secondary reactions.

Appearance potentials of the monogermanium ions and those digermanium ions which are accessible with a minimum of isotopic interference are given in Table I. Of these digermanium ions it appears all result from reaction of GeH_2^+ with GeH_4. Formation of $Ge_2H_6^+$ from bimolecular reaction of GeH_3^+ can be eliminated, since this process would require an absurdly low ionization potential of digermane. While $Ge_2H_6^+$ formation from reaction of

(1) United States Atomic Energy Commission Document No. COO-3416-4.
(2) G. G. Hess and F. W. Lampe, *J. Chem. Phys.*, **44**, 2257 (1966).
(3) J. M. S. Henis, G. W. Stewart, M. K. Tripodi, and P. P. Gaspar, *J. Chem. Phys.*, in press.
(4) Tung-Yang Yu, T. M. H. Cheng, V. Kempter, and F. W. Lampe, *J. Phys. Chem.* **76**, 3321 (1972).
(5) W. Ando and S. Oae, *Bull. Chem. Soc. Jap.*, **35**, 1540 (1962).
(6) G. J. Mains and T. Tiernan, USAEC Rept. No. NYO—2007-8 (1965).
(7) J. F. Schmidt and F. W. Lampe, *J. Phys. Chem.*, **73**, 2706 (1969).
(8) P. P. Gaspar, B. D. Pate, and W. Eckelman, *J. Amer. Chem. Soc.*, **88**, 3878 (1966).
(9) P. P. Gaspar, S. A. Boch, and W. L. Eckelman, *J. Amer. Chem. Soc.*, **90**, 6914 (1968).
(10) D. K. Snediker and W. W. Miller, *Radiochim. Acta*, **10**, 30 (1968).
(11) F. W. Lampe, *J. Amer. Chem. Soc.*, 79, 1055 (1957).
(12) G. G. Meisels, W. H. Hamill, and R. R. Williams, *J. Phys. Chem.*, **61**, 1456 (1957).
(13) F. P. Abramson and J. H. Futrell, *J. Chem. Phys.*, **45**, 1925 (1966), and references cited therein.
(14) W. C. Wiley and I. H. McLaren, *Rev. Sci. Instrum.*, **26**, 1150 (1955).
(15) P. Potzinger and F. W. Lampe, *J. Phys. Chem.* **74**, 587 (1970).
(16) W. J. Jolly and J. E. Drake, USAEC Rept. No. UCRL 9615, University of California, Los Angeles, Calif. (1961).
(17) P. M. Becker and F. W. Lampe, *J. Chem. Phys.*, **42**, 3857 (1965).

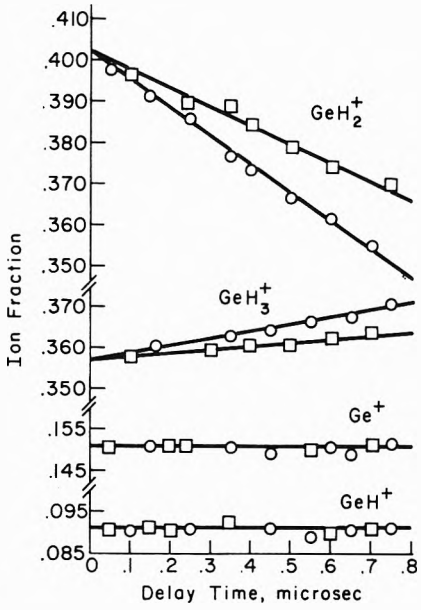

Figure 1. Ion fractions of primary ions as a function of delay time: □, 4.9 μ; ○, 8.7 μ.

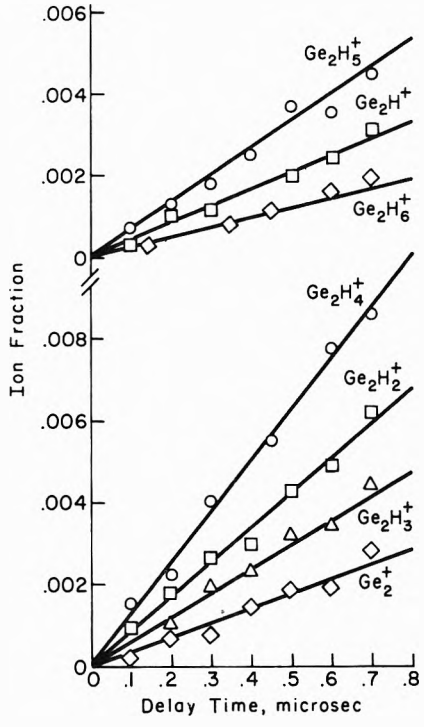

Figure 2. Ion fractions of secondary ions as a function of delay time.

GeH_2^+ is energetically feasible, it is unlikely that the lifetime of the excited $Ge_2H_6^+$ so formed is sufficiently long for its detection in a bimolecular process. As will be discussed later the high-pressure studies indicate the formation of $Ge_2H_6^+$ to be a termolecular process and also that $Ge_2H_5^+$ arises from reaction of GeH_3^+. Thus, we conclude that the important bimolecular reactions in monogermane are

$$GeH_2^+ + GeH_4 \xrightarrow{k_1} GeH_3^+ + GeH_3 \quad (1)$$

$$GeH_2^+ + GeH_4 \xrightarrow{k_2} Ge_2^+ + 3H_2 \quad (2)$$

$$GeH_2^+ + GeH_4 \xrightarrow{k_3} Ge_2H^+ + 2H_2 + H \quad (3)$$

TABLE I: Appearance Potentials of Monogermanium and Some Digermanium Ions from GeH_4[a]

Ion	Ap, eV	Ion	AP, eV
$^{70}Ge^+$	10.4 ± 0.2	$^{70}Ge_2^+$	12.0 ± 0.2
$^{70}GeH^+$	11.2 ± 0.2	$^{70}Ge_2H^+$	11.9 ± 0.2
$^{76}GeH_2^+$	11.9 ± 0.2	$^{70}Ge_2H_2^+$	11.9 ± 0.3
$^{76}GeH_3^+$	10.9 = 0.2	$^{70}Ge_2H_3^+$	12.0 ± 0.3
		$^{70}Ge_2H_4^+$	11.9 ± 0.3

[a] Argon used as internal standard.

$$GeH_2^+ + GeH_4 \xrightarrow{k_4} Ge_2H_2^+ + 2H_2 \quad (4)$$

$$GeH_2^+ + GeH_4 \xrightarrow{k_5} Ge_2H_3^+ + H_2 + H \quad (5)$$

$$GeH_2^+ + GeH_4 \rightarrow Ge_2H_4^+ + H_2 \quad (6)$$

$$GeH_3^+ + GeH_4 \rightarrow Ge_2H_5^+ + H_2 \quad (7)$$

The rate of change of $[GeH_2^+]$ can be written as

$$-d[GeH_2^+]/dt = \Sigma_i k_i[GeH_2^+][GeH_4] \quad (8)$$

where i indexes all reactions involving disappearance of GeH_2^+. Assuming $[Ge_2H_4]$ is constant, integrating and replacing ion concentration by ion fraction, X, leads to

$$X(GeH_2^+) = X^0(GeH_2^+)\exp(-\Sigma_i k_i[GeH_4]t) \quad (9)$$

where X^0 is the initial fraction formed in the electron beam. Expanding the exponential in (9) with retention of only the linear term introduces a maximum error of 1%. To the same order of approximation the rate equations of the other ions give

$$X(GeH_3^+) = X^0(GeH_3^+) + (k_1X^0(GeH_2^+) - k_7X^0(GeH_3^+)[GeH_4]t \quad (10)$$

$$X(Ge_2H_y^+) = k_{y-2}X^0(GeH_2^+)[GeH_4]t; \quad y = 0, \ldots, 4 \quad (11)$$

$$X(Ge_2H_5^+) = k_7X^0(GeH_3^+)[GeH_4]t + \vartheta([GeH_4]^2t^2) \quad (12)$$

where the higher order terms in (12) denoted by ϑ can be neglected on the basis of the linearity of the plots in Figure 2. Thus, $\Sigma_i k_i$ and the individual k_i are easily determined by appropriate combination of the slopes and intercepts of Figures 1 and 2.

B. High-Pressure Studies. The variation of mono- and digermanium ions with source pressure is shown in Figures 3 and 4. $Ge_2H_3^+$ was also observed but the intensity is constant beyond 50 μ and is not shown. It is clear from Figure 3 that Ge^+ and GeH^+ also react with GeH_4; also, a material balance indicates that reaction of GeH_2^+ does not account for the formation of all product ions. Since the trigermanium ions do not contribute significantly to the sum of ion fraction increases until after 120 μ, Ge^+ and GeH^+ must be involved in digermanium ion formation. Inasmuch as these reactions could not be identified by appearance potential correspondence, an attempt was made to eliminate reactions on energetic grounds. The ionization and appearance potentials and corresponding $\Delta H_f°$ of primary ions from mono- and digermane measured by Saalfeld and Svec[18] are given in Table II with the upper limits to $\Delta H_f°$ obtained in this study. The latter were calculated from calorimetric data,[19] the exother-

(18) F. E. Saalfeld and H. J. Svec, *Inorg. Chem.*, **2**, 46, 50 (1963).
(19) S. R. Gunn and L. G. Green, *J. Phys. Chem.*, **65**, 779 (1961).

TABLE II: Ionic Heats of Formation

Ion	AP from GeH_4, eV[a]	ΔH_f, kcal/mol	Ion	AP from Ge_2H_6, eV[a]	ΔH_f, kcal/mol: From AP	ΔH_f, kcal/mol: This work
Ge^+	10.7 ± 0.2	269	Ge_2^+	13.1 ± 0.3	341	≤314
GeH^+	11.3 ± 0.3	253	Ge_2H^+	13.0 ± 0.3	286	≤262
GeH_2^+	11.8 ± 0.2	294	$Ge_2H_2^+$	12.9 ± 0.3	336	≤314
GeH_3^+	10.8 ± 0.3	219	$Ge_2H_3^+$	12.8 ± 0.3	282	≤262
			$Ge_2H_4^+$	12.7 ± 0.3	332	≤314
			$Ge_2H_5^+$	12.6 ± 0.3	277	≤239
			$Ge_2H_6^+$	12.5 ± 0.3	327	

[a] Reference 18.

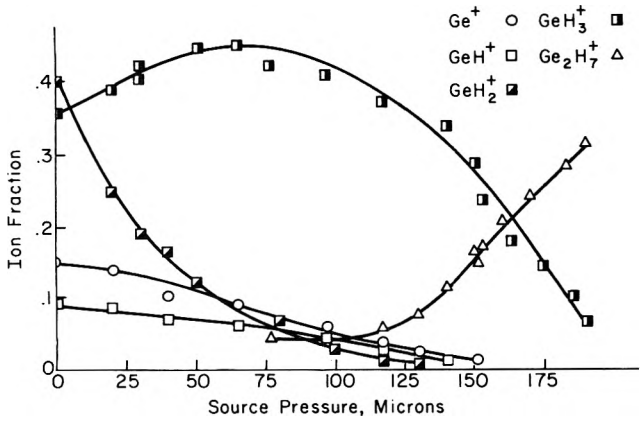

Figure 3. Ion fractions of primary ions and $Ge_2H_7^+$ as a function of source pressure.

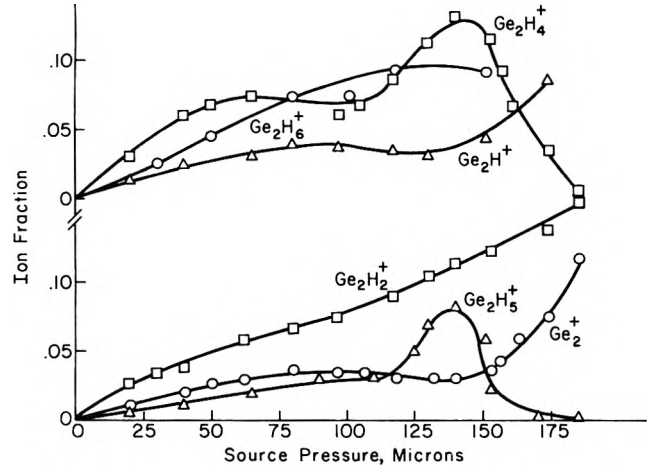

Figure 4. Ion fractions of digermanium ions as a function of source pressure.

micity requirement, and the observed reactions at low pressure. We may first observe that the appearance potentials measured in our work for monogermanium ions (Table I) are in good agreement with those of Saalfield and Svec.[18]

The heats of formation of ions from monogermane shown in Table II are probably the most accurate values available, since extreme care was taken to eliminate excess kinetic energy from fragments and monoisotopic monogermane was used.[18] For ions from digermane it was not possible to eliminate this excess kinetic energy and, as Saalfeld and Svec point out,[18] the appearance potentials may be high. Comparison with the upper limits obtained in this study indicates this to be the case since the heats of formation of digermanium ions indicate no ion-molecule reactions to be possible. In the absence of accurate thermodynamic data, indirect energetic considerations and material balances were used to eliminate the following reactions.

$$Ge^+ + GeH_4 \rightarrow Ge_2^+ + 2H_2 \quad (13)$$

$$Ge^+ + GeH_4 \rightarrow Ge_2H^+ + H_2 + H \quad (14)$$

$$GeH^+ + GeH_4 \rightarrow Ge_2^+ + 2H_2 + H \quad (15)$$

$$GeH^+ + GeH_4 \rightarrow Ge_2H^+ + 2H_2 \quad (16)$$

$$GeH^+ + GeH_4 \rightarrow Ge_2H_2^+ + H_2 + H \quad (17)$$

$$GeH^+ + GeH_4 \rightarrow Ge_2H_4^+ + H \quad (18)$$

Using the known heats of formation of GeH^+ and GeH_4 and the exothermicity condition, the upper limits to the heats of formation of digermanium ions were calculated assuming they were formed by reaction of GeH^+. For (15), (17), and (18) to be energetically possible the appearance potentials of the digermanium ions from Ge_2H_6 would be necessarily ≤7.9 eV, which is absurdly low. The initial slopes of the ion fraction curves of Ge_2^+ and Ge_2H^+ in Figure 4 in the range 0–80 μ are identical with those predicted, assuming that these ions come only from reactions of GeH_2^+ having rate constants determined in the low-pressure study. This observation eliminates (13), (14), and (16). At pressures beyond 25 μ termolecular reactions are sufficiently probable for detection and possible reactions of Ge^+ and GeH^+ can be described by

$$I^+ + GeH_4 \xrightarrow{k_{19}} Ge_2H_x^+ + F \quad (19)$$

$$I^+ + 2GeH_4 \xrightarrow{k_{20}} Ge_yH_z^+ + F \quad (20)$$

where I^+ is either primary ion and F is a neutral fragment. These reactions lead to an ion fraction pressure dependence of

$$\ln [X^0(I^+)/X(I^+)] = k_{19}[GeH_4]t + k_{20}[GeH_4]^2t \quad (21)$$

Experimental $X(Ge^+)$ and $X(GeH^+)$ were fitted to (21) and in both cases k_{19} is very small, accounting for the fact that neither ion is an observed reactant at low pressure. This is shown in Figure 5a in which (21) is plotted for $[I^+] = [GeH^+]$, neglecting the linear term. The analogous curve for Ge^+ is nearly identical. The second- and third-order rate constants determined from the fitting procedure in conjunction with the low-pressure rate constants allow the prediction of digermanium ion fraction curves. The digermanium ions whose experimental pressure dependences agree most closely with these predicted curves are taken to be the product ions. By this method the loss of Ge^+ and GeH^+ in the pressure range 0–110 μ can best be

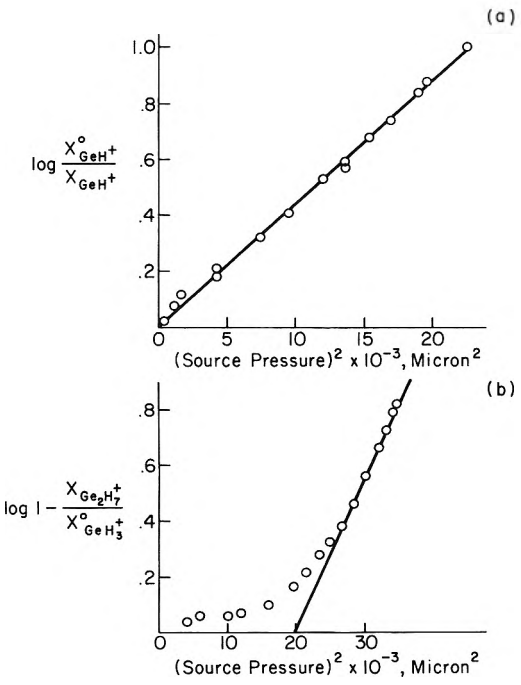

Figure 5. Third-order kinetic plots: (a) reaction of GeH^+; (b) formation of $Ge_2H_7^+$ from GeH_3^+.

accounted for by the following reactions.

$$Ge^+ + GeH_4 \xrightarrow{k_{22}} Ge_2H_2^+ + H_2 \quad (22)$$

$$Ge^+ + 2GeH_4 \xrightarrow{k_{23}} Ge_2H_4^+ + GeH_4 \quad (23)$$

$$GeH^+ + GeH_4 \xrightarrow{k_{24}} Ge_2H_3^+ + H_2 \quad (24)$$

$$GeH^+ + 2GeH_4 \xrightarrow{k_{25}} Ge_2H_5^+ + GeH_4 \quad (25)$$

Beyond this pressure several competing reactions make it impossible to fit experimental ion fraction curves with a unique set of rate constants.

Figure 3 shows that at higher pressures GeH_3^+ becomes an important reactant ion. A material balance indicates the major reaction depleting GeH_3^+ to be

$$GeH_3^+ + 2GeH_4 \xrightarrow{k_{26}} Ge_2H_7^+ + GeH_4 \quad (26)$$

since, in the pressure region where $X(Ge_2H_7^+)$ increases, GeH_3^+ is the only ion present in sufficient abundance to account for $Ge_2H_7^+$ formation. In addition, the form of the $X(Ge_2H_7^+)$ curve suggests GeH_3^+ as the precursor to $Ge_2H_5^+$. The basis for this is as follows. If $Ge_2H_7^+$ were the only ion produced by reaction of GeH_3^+ as in (26), the rate of change of $[Ge_2H_7^+]$ would be described by

$$d[Ge_2H_7^+]/dt = k_{26}[GeH_4]^2\{[GeH_3^+]_0 - [Ge_2H_7^+]\} \quad (27)$$

in the pressure region where GeH_2^+ makes negligible contribution to GeH_3^+ formation by (1). From Figure 3, (27) and its integrated form, namely

$$\ln\{1 - [X(Ge_2H_7^+)/X^0(GeH_3^+)]\} = -k_{26}[GeH_4]^2t \quad (28)$$

should be valid beyond $\sim$100 μ. The left-hand side of (28) is plotted *vs.* the square of the pressure in Figure 5b where the predicted linear relationship may be recognized but only at much higher pressure ($\lesssim$165 μ) than expected if there were no competing reaction of GeH_3^+ of lower order. The most probable competing second-order reaction, analogous to (6), (22), and (24), and to the methane[13] and silane[4] systems as well, is (7).

As mentioned above, it is the high-pressure dependence of $X(Ge_2H_6^+)$ in Figure 4 which suggests its formation by a termolecular rather than a second-order process as Figure 2 would seem to indicate. If one assumes the second-order process

$$GeH_2^+ + GeH_4 \xrightarrow{k_{29}} Ge_2H_6^+ \quad (29)$$

and determines k_{29} from Figure 2 and an equation analogous to (11), the resulting rate constant predicts a high-pressure curve inconsistent with that obtained experimentally both in general shape and in the value of X at the plateau. If instead one assumes that k_{29}, determined from Figure 2, is actually $k_{30}/[GeH_4]$ where k_{30} is the third-order rate constant corresponding to

$$GeH_2^+ + 2GeH_4 \xrightarrow{k_{30}} Ge_2H_6^+ + GeH_4 \quad (30)$$

one obtains a functional dependence consistent within experimental error with the experimental curves at all pressures.

It should be pointed out that the appropriate value of t in the pressure region corresponding to termolecular processes is not the collision-free residence time but depends on the pressure. Using the E/P value at 150 μ, our source dimensions, and the drift velocity results of Warneck[20] adjusted to the average monogermanium ion mass, the average residence time over the pressure range was calculated to be 1.2×10^{-5} sec.

The rate constants obtained as described above are summarized in Table III with the rate constants for analogous reactions in monosilane.

Figure 6 shows the intensities of the trigermanium ions observed as a function of source pressure cubed, with the exception of $Ge_3H_4^+$ whose curve is nearly identical with that of $Ge_3H_2^+$. In the region of significant trigermanium ion intensity increase, the primary ions are essentially depleted (Figure 3) and thus the precursors must be digermanium ions. Of the trigermanium ions only Ge_3^+ and $Ge_3H_3^+$ are cubic in the pressure over a large range (0–165 μ). Contrasted with this cubic pressure dependence from zero pressure, $Ge_3H_2^+$, $Ge_3H_4^+$, and $Ge_3H_5^+$ appear at a much higher pressure ($\sim$135 μ) and increase with at least a fourth-order pressure dependence. The intensities of the remaining trigermanium ions, $Ge_3H_6^+$, $Ge_3H_7^+$, $Ge_3H_8^+$, and $Ge_3H_9^+$, have essentially the same pressure dependence, the order of which increases gradually as the pressure is increased, indicating that these ions or their precursors are formed by more than one process depending on the pressure region. Since $Ge_2H_4^+$ and $Ge_2H_5^+$, which are formed in two processes, are the only digermanium ions whose intensity decreases in the pressure region corresponding to significant trigermanium ion intensity increase, it is reasonable that these are the reactant ions involved. The similarity of both reactant ion curves as well as that of product ions, coupled with a lack of accurate thermodynamic data for both di- and trigermane, preclude further reaction identification.

From Table III four reactions can be placed into the following form at low pressure

$$]GeH_x^+ + GeH_4 \underset{k_{-a}}{\overset{k_a}{\rightleftharpoons}} GeH_x{\cdot}GeH_4^+ \xrightarrow{k_d} Ge_2H_{x+2}^+ + H_2 \quad (31)$$

(20) P. Warneck, *J. Chem. Phys.*, **46**, 502 (1967).

TABLE III: Comparison of Reactions in Monogermane and Monosilane

Eq no.	Reactant ion	Product ion	$k \times 10^{10}$, cm³/molecule sec: M = Si[a]	$k \times 10^{10}$, cm³/molecule sec: M = Ge
		Bimolecular Reactions		
22	M^+	$M_2H_2^+$	4.8 ± 0.6; 3.2 ± 0.3	1.0 ± 0.2
	MH^+	M_2H^+	0.7 ± 0.2;	Not observed
24		$M_2H_3^+$	2.8 ± 0.07; 2.0 ± 0.3	<0.25
1	MH_2^+	MH_3^+	10.7 ± 0.2; 2.5 ± 0.3	2.8 ± 0.3
2		M_2^+	Not observed;	0.48 ± 0.05
3		M_2H^+	Not observed; not observed	0.53 ± 0.05
4		$M_2H_2^+$	0.55 ± 0.075; 0.31 ± 0.06	1.1 ± 0.1
5		$M_2H_3^+$	Not observed; not observed	0.79 ± 0.08
6		$M_2H_4^+$	2.5; 1.1 ± 0.1	1.6 ± 0.1
		$M_2H_5^+$	Not observed; 0.08 ± 0.02	
7	MH_3^+	$M_2H_5^+$	0.24 ± 0.04; 0.07 ± 0.02	0.98 ± 0.1
			$k \times 10^{26}$, cm⁶/molecule² sec: M = Si[b]	M = Ge
		Termolecular Reactions		
23	M^+	$M_2H_4^+$	1.4 ± 0.6	1.0 ± 0.5
25	MH^+	$M_2H_5^+$	1.3 ± 0.5	1.1 ± 0.5
30	MH_2^+	$M_2H_6^+$	Not observed	7 ± 3
26	MH_3^+	$M_2H_7^+$	1.8 ± 0.7	1.44 ± 0.6

[a] References 3 and 4. [b] Reference 4.

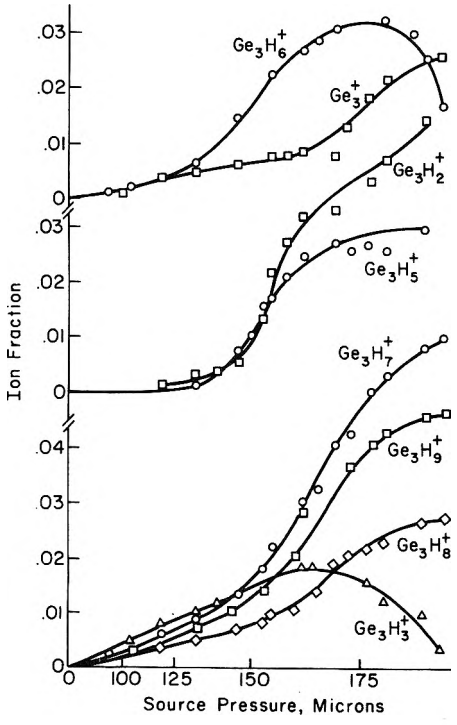

Figure 6. Ion fractions of trigermanium ions as a function of source pressure.

while at high pressure, the collisional stabilization of the intermediate must be added, *viz.*

$$GeH_x{\cdot}GeH_4^+ + GeH_4 \xrightarrow{k_8} Ge_2H_{x+4}^+ + GeH_4 \quad (x = 0, \ldots, 3) \quad (32)$$

where the experimental rate constants for each form are nearly the same regardless of the value of x. This is also the case in methane[13] and silane which suggests similar intermediates which are not symmetrical but are such as to encourage elimination of H_2. The only primary ion which undergoes other bimolecular reactions in addition to that of (31) is GeH_2^+. Here the nonsymmetrical nature of the intermediate is suggested further by the large discrepancy in the distribution of ions resulting from decomposition of the intermediate and that resulting from primary ionization of digermane shown in Table IV. However, as was pointed out for the silane system,[2] the considerable excess energy of $GeH_2{\cdot}GeH_4^+$ [18,19] relative to $Ge_2H_6^+$ may result in the absence of $Ge_2H_6^+$ from the secondary spectrum, as well as alter the probability of formation of other ions. The distinguishing feature among the six reactions of GeH_2^+ at thermal energies is the consistent inverse relationship between the probability of the intermediate decomposing to a given product ion and the amount of molecular rearrangement necessary. This indicates that if the intermediate is the same for all reactions and energy transfer is efficient, increasing ion impact energies would reverse this trend. This effect is well established in methane[13] and there is some evidence it occurs in silane[3] as well. By comparison with the lighter

TABLE IV: Relative Abundance of Digermanium Ions from Primary Ionization of Digermane and Secondary Spectra of $GeH_2^+ + GeH_4$

Ion	Primary[a]	Secondary
Ge_2^+	67.6	28.2
Ge_2H^+	62.4	30.4
$Ge_2H_2^+$	100.0	65.8
$Ge_2H_3^+$	33.5	49.3
$Ge_2H_4^+$	72.7	100.0
$Ge_2H_5^+$	28.8	0
$Ge_2H_6^+$	42.6	0

[a] Electron energy, 70 eV.

group IV hydrides the reactions in germane are more similar to those in silane as expected. The main differences are the formation of a small amount of Ge_2^+ and the precursors to M_2H^+ and $M_2H_3^+$. While C_2 type ions are certainly formed in methane,[13] the preference for condensation in the silane and germane systems is replaced by a preference for atomic ion transfer. Furthermore, there is no evidence for product ions in methane larger than the C_3 type,[13] while in silane and germane very large polymers have been observed. This difference can be accounted for partly on the basis of relative size and by the difference in the primary ion spectra, *i.e.*, the distribution of potential reactants.[21]

From the collisional stabilization model, (31) and (32), it is easily shown that the measured second- and third-order rate constants are respectively

$$k^{(2)} = k_a k_d/(k_{-a} + k_d)$$

$$k^{(3)} = k_a k_s/(k_{-a} + k_d)$$

Thus for the case $x = 3$, the ratio k_s/k_d is equivalent to $k_{26}/k_7 = 1.4 \times 10^{-16}$. The analogous ratios are the same, within experimental error, for all x in both the germane and silane systems, with the exception of that for the reactions involving $Si_2H_7^+$ in silane for which $k_s/k_d = 3 \times 10^{-15}$. In terms of the model, this order of magnitude difference results from a difference in the probability of the two paths open to dissociation of the intermediate. For the exceptional case in silane, dissociation to original reactants is favored over dissociation to products ($k_{-a} \gg k_d$) while for the others both paths are equally likely, and by the same considerations the lifetime of the intermediates for the latter cases is an order of magnitude longer.

Acknowledgment. This work was supported by the United States Atomic Energy Commission under Contract No. At(11-1)-3416. We also wish to thank the National Science Foundation for providing funds to assist in the original purchases of the mass spectrometers.

(21) D. P. Beggs and F. W. Lampe, *J. Chem. Phys.*, **49**, 4230 (1968).

A High-Pressure Investigation of the Rhodium/Palladium/Hydrogen System

B. Baranowski, S. Majchrzak, and Ted B. Flanagan*[1]

Institute of Physical Chemistry, Polish Academy of Sciences, Warsaw, Poland *(Received May 3, 1972).*

An investigation of the absorption of hydrogen at high pressures by a series of Rh/Pd alloys up to 80% (atom) rhodium is reported. These alloys absorb large quantities of hydrogen, *e.g.*, the Rh(30%)/Pd alloy attains an H-to-Pd atomic ratio of 1.44 (H-to-metal atomic ratio of 1.00 ± 0.02 at 5100 atm). This demonstrates that rhodium can act as an absorber of hydrogen when situated in the palladium matrix. Data are extrapolated to the experimental conditions necessary to form the β phase in the Rh/H_2 system.

Introduction

The absorption of hydrogen by palladium has been the subject of many investigations[2] and the extension to absorption studies of alloys of palladium has been a natural one. The absorption of hydrogen by silver/palladium alloys has evoked great interest[3-6] because of both practical and theoretical reasons. Silver is adjacent to palladium in the periodic table and evidence is available that it donates electrons to the partially empty d band of palladium.[7] Although the rigid band model is no longer believed to be fully valid,[8] silver atoms are still believed to act as electron donors to the empty palladium d bands.[9] Models of absorption for the silver/palladium/hydrogen system have been proposed in which both the hydrogen and silver atoms act as electron donators to the d band of palladium.[5] Other alloying elements which have filled d bands have been tested similarly.[10,11] By way of contrast, there is no simple picture available for the interpretation of hydrogen absorption data where the alloying elements also have holes in the d band, *e.g.*, platinum and rhodium. The rhodium/palladium/hydrogen system is of particular interest because of rhodium's adjacent position to palladium in the periodic table.

Tammann and Rocha[12] studied this system by electrolytic charging but their data are of limited usefulness. The first detailed study was performed by Tverdovskii and Stetsenko[13] who investigated this system by removing

(1) Chemistry Department, University of Vermont, Burlington, Vt.
(2) F. A. Lewis, "The Palladium/Hydrogen System," Academic Press New York, N. Y., 1967.
(3) (a) A. Sieverts and H. Hagen, *Z. Phys. Chem., Abt. A*, **174**, 359 (1935); (b) G. Rosenhall, *Ann. Phys. (Leipzig)*, **24**, 297 (1935).
(4) A. C. Makrides, *J. Phys. Chem.*, **68**, 2160 (1964).
(5) H. Brodowsky and E. Poeschel, *Z. Phys. Chem. (Frankfurt am Main)*, **44**, 143 (1965).
(6) A. Carson and F. A. Lewis, *Trans. Faraday Soc.*, **63**, 1453 (1967).
(7) N. F. Mott and H. Jones, "The Theory of Metals and Alloys," Clarendon Press, Oxford, 1936.
(8) *E.g.*, F. M. Mueller, A. J. Freeman, J. Dimmock, and A. M. Furdyna, *Phys. Rev. B*, **1**, 4617 (1970).
(9) J. S. Dugdale and A. M. Guenault, *Phil. Mag.*, **13**, 503 (1966).
(10) H. Brodowsky and A. Husemann, *Ber. Bunsenges. Phys. Chem.*, **70**, 626 (1966).
(11) K. Allard, A. Maeland, J. Simons, and T. B. Flanagan, *J. Phys. Chem.*, **72**, 136 (1968).
(12) G. Tammann and H. Rocha, *Festchr. Siebertsch. Platinschmelze*, **3**, 213 (1931).
(13) I. P. Tverdovskii and A. I. Stetsenko, *Dokl. Akad. Nauk SSSR*, **84**, 997 (1952).

TABLE I: Lattice Parameters of H-Free Rh/Pd Alloys (−190°)

% Rh	a, Å	% Rh	a, Å
0	3.884	30	3.857
5	3.881	40	3.851
10	3.876	60	3.833
15	3.871	80	3.816
20	3.866		

hydrogen anodically from fully charged, dispersed alloys. Absorption isotherms were constructed from electrode potential–current passed relationships. Lewis and coworkers[14,15] also investigated this system electrochemically. Both absorption and desorption isotherms were derived up to hydrogen pressures of about 5 atm. The only gas phase study available has been that of Brodowsky and Husemann[10] which was limited to the (Rh) 5%/Pd alloy. They found that $\Delta\bar{H}_H°$, *i.e.*, the relative partial molar enthalpy at infinite dilution, was less exothermic than that for pure palladium. In keeping with predictions of the "lattice strain–electron donation" model[10,16] this suggests that the H–H interaction is greater in this alloy than in pure palladium and this is borne out by the data[10] and is consistent with the smaller lattice spacings of these alloys compared to pure palladium.[17] These earlier studies, which were limited to pressures ≤5 atm,[10,13-15] found no evidence of any unusual behavior in this system save the fact that the 1-atm hydrogen solubility was somewhat greater in alloys of about 5% rhodium content than in pure palladium (25°).

Quite recently the authors noted that several rhodium/palladium alloys absorb hydrogen rather dramatically at high pressures of gaseous hydrogen.[18] For example, at 5100 atm (25°) a value of H-to-Pd atomic ratio = 1.44 ± 0.02 (H-to-metal ratio of n = 1.00 ± 0.02) was found for a Rh(30%)/Pd alloy. This proves that rhodium can function as an absorber of hydrogen, at least, when it is situated within the palladium matrix. The observation of values of n, H-to-metal ratios, = 1.00 ± 0.02 is noteworthy because such a ratio has not been directly observed in high-pressure studies of the Pd/H_2 system, *i.e.*, direct analysis has not yielded such a nearly stoichiometric ratio but, of course, a stoichiometric ratio may have been formed within the high-pressure vessel prior to analysis,[19] however, the estimated pressure at which PdH would be formed is greater than that needed for the 20 and 30% rhodium alloys. Oates and Flanagan[20] have, by a different technique, recently prepared PdH (n = 0.99 ± 0.01) using direct reaction of H atoms with palladium.

The motive of the present research was to extend the previous high-pressure study[18] to alloys of larger rhodium content in order to be able to predict the pressure at which pure rhodium may absorb hydrogen. Another motive was to attempt to understand why such large hydrogen contents were found in certain of the Rh/Pd alloys at relatively low pressures.

Experimental Section

The reaction vessel and the arrangement suitable for high pressures of gaseous hydrogen have been described elsewhere.[21] The course of absorption was followed *in situ* by changes of electrical resistance of the sample as a function of hydrogen pressure. The pressure was determined by the electrical resistance of a manganin wire within the reaction vessel.

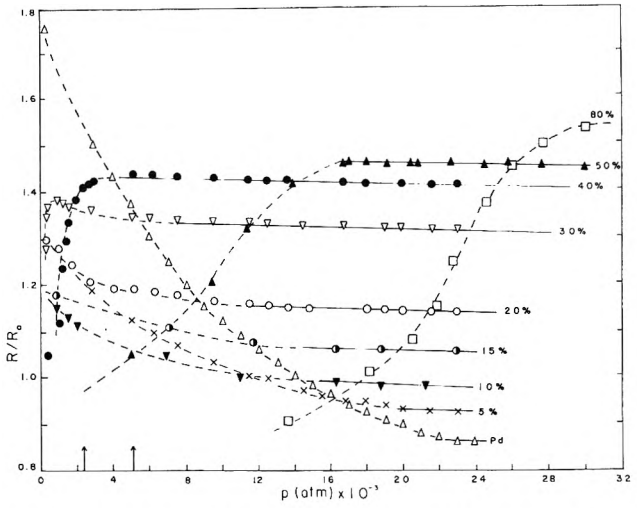

Figure 1. Values of R/R_0 as a function of pressure (25°) for a series of Rh/Pd alloys. The linear solid lines drawn through the data all have the same slope. The region where stoichiometric hydrides are formed for the 20 and 30% alloys are indicated along the p axis by arrows. The straight-line segments all have the same slope.

The samples were in the form of thin foil, ~10 μ, which weighed ~10 mg.

The hydrogen contents of the samples were determined by cooling the high-pressure vessel (~−50°), reducing the pressure, and analyzing the content mass spectrometrically. X-Ray diffraction patterns of the hydrogen-containing samples were determined generally at −190° in order to avoid loss of hydrogen. The alloys were all face-centered cubic and showed no evidence of any ordering (Table I).

Results

Since hydrogen contents cannot be measured directly in the high-pressure vessel, electrical resistance measurements were employed to monitor the course of hydrogen absorption. In the special case of rhodium/palladium alloys, it appears that rather definite conclusions can be drawn about the hydrogen content from the behavior of the electrical resistance–pressure relationships.

Figure 1 shows the values of R/R_0, the electrical resistance at any hydrogen content to the hydrogen-free resistance, as a function of the hydrogen pressure. The relationships all exhibit an initial region where R/R_0 is nearly unchanged with pressure (not shown) and absorption does not occur; this is followed by a rapid increase of R/R_0 with pressure and thereafter values of R/R_0 decline slowly with pressure. The noteworthy feature of this system is that after cooling the vessel (−50°) and analyzing the hydrogen contents of the sample, stoichiometric H-to-metal ratios of 1 were found for the 20 and 30% Rh/Pd alloys in the pressure range between 2335 and 5060 atm which is indicated on Figure 1 (Table II).

Since it is known that nearly stoichiometric ratios were formed in the indicated region for the 20 and 30% alloys, it

(14) J. Green and F. A. Lewis, *Trans. Faraday Soc.*, **62**, 971 (1966).
(15) J. Barton, J. Green, and F. A. Lewis, *Trans. Faraday Soc.*, **62**, 960 (1966).
(16) H. Brodowsky, *Z. Phys. Chem. (Frankfurt am Main)*, **44**, 129 (1965).
(17) E. Raub, H. Beeskow, and D. Menzel, *Z. Metallk.*, **50**, 428 (1959).
(18) T. B. Flanagan, B. Baranowski, and S. Majchrzak, *J. Phys. Chem.*, **74**, 4299 (1970).
(19) *E.g.*, B. Baranowski, *Platinum Metals Rev.*, **16**, 10 (1972).
(20) W. A. Oates and T. B. Flanagan, *Nature (London)*, **231**, 19 (1971).
(21) B. Baranowski and W. Bujnowski, *Rocz. Chem.*, **44**, 2271 (1970).

TABLE II: Hydrogen Contents and Lattice Parameters Observed in Rh/Pd Alloys after Removal from High-Pressure Vessel

Alloy, % Rh	H-to-Pd atom ratio	H-to-metal atom ratio	Maximum H_2 pressure (atm) attained before cooling	a_0, Å. after removal from pressure vessel (−190°)
5	0.90 ± 0.02	0.86 ± 0.02	2,300	
5	0.86	0.82	5,100	4.07_3
5	0.95	0.91	23,200	4.06_5
10	0.99	0.89	2,300	
10	1.02	0.92	21,300	4.07_9
15	1.07	0.91	21,300	4.07_7
20	1.15	0.91	2,300	
20	1.26	1.01	5,100	4.08_3
20	1.22	0.97	23,200	4.07_4
30	1.34	0.93	2,300	
30	1.44	1.00	5,100	4.07_0
30	1.46	1.01	23,200	4.06_8
40	1.52	0.90	2,300	
40	1.61	0.96	5,100	4.06_5
40	1.52	0.90	23,200	4.07_2

can be reasonably assumed that comparable behavior in the relationships for other alloys implies that a stoichiometric hydride has also been formed for that alloy. Thus, for the 40% alloy, which gave upon analysis values of n = 0.90 and 0.95 (Table II) and a further value of 0.90 after reaching 22,900 atm, it can be assumed that a stoichiometric ratio was attained, ~4000 atm, but hydrogen was lost prior to analysis. It should be added that for this alloy H-to-Pd atom ratios of 1.52 and 1.61 were found at 2300 and 5100 atm, respectively. The small decrease in the values of R/R_0 with pressure after attainment of stoichiometry can be attributed to the effect of pressure upon the electrical resistance of the hydride. For a pressure change from 10,000 to 20,000 atm Bridgman[22] noted a decrease in R/R_0 of 2% (Pd) and 1.6% (Rh).

The observed changes are in the right direction to be attributed to a purely hydrostatic pressure effect but are somewhat smaller, ~1%. This is not unreasonable because the hydride would be expected to behave differently from the pure metals or alloys. Thus, the presence of hydrogen in palladium decreases Young's modulus[23] and increases its hardness.[24] The slopes of the region in the R/R_0 against pressure relationships corresponding to purely pressure effects are comparable for the 20 and 30% alloys which suggests that similar slopes for the other Rh/Pd alloys can be attributed to purely pressure effects and therefore a stoichiometric hydride has been formed.

Ratios of n = 1 were noted by analysis to correspond to ratios of R/R_0 slightly before the onset of the linear region in the R/R_0 against p relationship. Of course, the term stoichiometric hydride refers to the analysis and undoubtedly unfilled interstitial sites exist when n = 1 ± 0.02 and these unfilled sites, which introduce disorder into the system, would be expected to contribute significantly to the electrical resistance. For example, in the pure palladium/H_2 system at n = 0.015, R/R_0 = 1.05 (25°).[25] If a comparable effect occurs in these alloy systems, the small difference observed in values of R/R_0 at the "stoichiometry" ratio and at the onset of the linear region would correspond to Δn = 0.006. It is suggested that stoichiometry may, in fact, only occur where the R/R_0 against p relationships become linear. On this basis, the pressures at

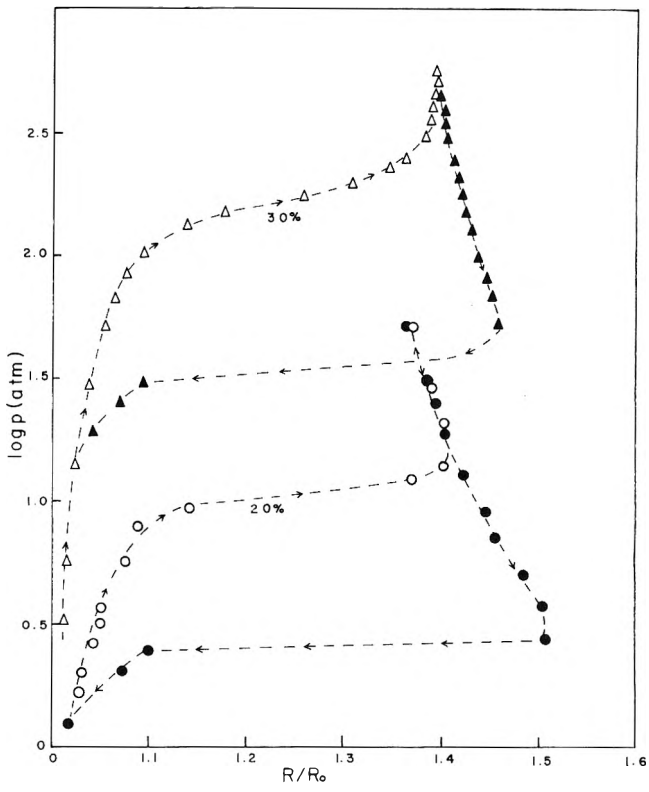

Figure 2. Absorption and desorption relationships observed for the 20 and 30% Rh/Pd alloys (25°).

TABLE III: Estimated Pressures where Stoichiometric Hydrides Are Formed (25°)

% Rh	Pressure, atm	% Rh	Pressure, atm
0	>24,000	30	7,000
5	22,000 ± 2,000	40	4,000
10	19,000	60	18,000
15	16,000	80	>30,000
20	10,000		

which stoichiometric hydrides are formed can be estimated from Figure 1 and are given in Table III. It is of interest that the pressure at which a stoichiometric hydride forms exhibits a minimum at about the Rh(40%)/Pd alloy.

Figures 2 and 3 show values of R/R_0 recorded against log p during absorption and desorption of hydrogen for several alloys. A marked hysteresis can be noted indicating the presence of a two-phase α-β region in analogy with the behavior of the Pd/H_2 system.[2] The hysteresis extends over many thousands of atmospheres of pressure in the alloys of higher rhodium content. The two-phase nature of these systems was confirmed in some cases by the X-ray diffraction patterns of the hydrogen-containing alloys.

The fortunate combination of the relatively low-pressure range needed for the formation of the β phase and the large hysteresis helps to retain the hydrogen in the 20 and 30% Rh/Pd alloys prior to their analysis. By contrast, the Rh(40%)/Pd alloy appeared to lose some of its hydrogen and the 60 and 80% Rh/Pd alloys lost all of their hydrogen prior to analysis.

(22) P. W. Bridgman, *Daedalus*, **77**, 187 (1949).
(23) F. Kruger and H. Jungnitz, *Z. Tech. Phys.*, **17**, 302 (1936).
(24) T. Sugero and H. Kowaka, *Mem. Inst. Sci. Ind. Res., Osaka Univ.*, **11**, 119 (1954).
(25) T. B. Flanagan and F. A. Lewis, *Z. Phys. Chem. (Frankfurt am Main)*, **27**, 104 (1960).

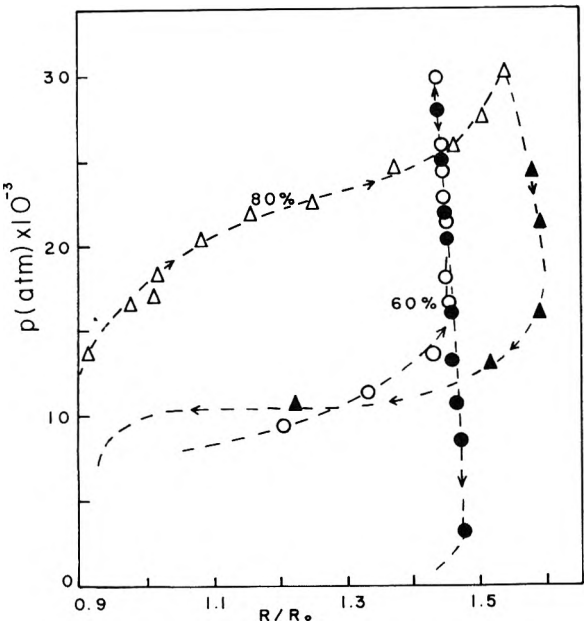

Figure 3. Absorption and desorption relationships observed for the 60 and 80% Rh/Pd alloys (25°).

A ternary phase diagram is shown in Figure 4. Again the marked contrast with previously examined binary palladium alloy/H_2 systems can be noted. The hydrogen contents have been estimated from the lattice parameters corresponding to the α and β phases and these estimations should be accurate to $n = \pm 0.05$.[26] From the behavior shown in Figure 4 there is no reason to suspect the pure rhodium will not absorb hydrogen to form a hydrogen-rich β phase, although attempts made in this laboratory to date have failed.

Discussion

In marked contrast to the behavior of the other Pd binary alloy/H_2 systems which have been studied,[2] the lattice parameter of the β phase hydrides of the Rh/Pd alloys increase with Rh content at least for those with Rh contents below 50%. This is consistent with the large hydrogen contents observed in these alloys.

Values of $\Delta G_{\alpha\rightarrow\beta}^{\circ}$, *i.e.*, the Gibbs' free energy change for the reaction H_2(1atm) + $(Rh/Pd/H_2)_\alpha \rightarrow (Rh/Pd/H_2)_\beta$ can be estimated from the fugacity at which the relative resistance rises steeply with pressure (Figure 2). Although data are available for the fugacity–pressure relationship only to about 3000 atm,[27] the relationship can be extrapolated further[28] if the constants determining the relationship are assumed to be independent of pressure. It is of interest that on this basis a pressure of 21,000 atm equals 10^9 atm in fugacity.[19] A plot of $\Delta G_{\alpha\rightarrow\beta}^{\circ}$ against percentage of rhodium in the alloy is shown in Figure 5 together with the data of Green and Lewis for the 2.7, 7.1, and 10.0% Rh/Pd alloys. The data of the two studies are in good agreement.

It may be anticipated from Figure 5 that pure rhodium will form a second nonstoichiometric β phase at log f = 12(25°) or p = 35,000 atm (25°). Since this pressure exceeds the range of the present high-pressure equipment, it is desirable to find alternative experimental conditions for the synthesis of β phase Rh/H_2. A value of $\Delta H_{\alpha\rightarrow\beta}^{\circ}$ can be estimated from the extrapolated value of f, 10^{12} atm, at 298°K and the observation that the average value of $\Delta S_{\alpha\rightarrow\beta}^{\circ}$ for various face-centered-cubic metals and alloys

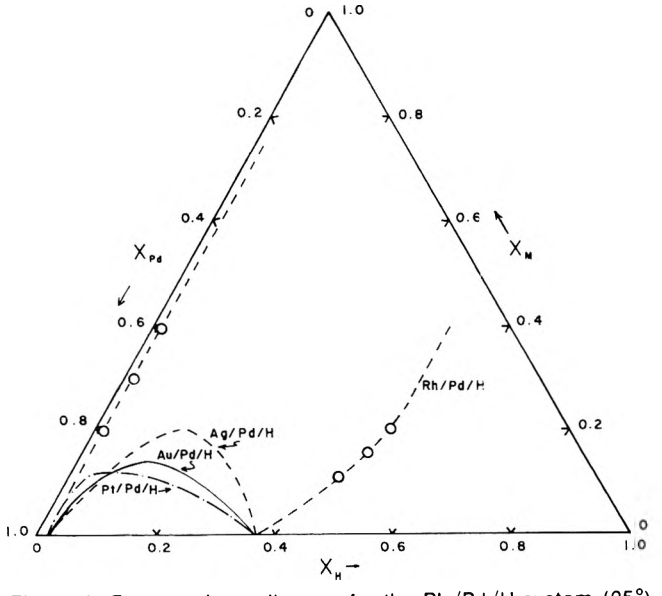

Figure 4. Ternary phase diagram for the Rh/Pd/H system (25°) as compared to several others systems: Ag/Pd/H (ref 5); Pt/Pd/H (A. Maeland and T. B. Flanagan, *J. Phys. Chem.*, **68**, 1419 (1964)); Au/Pd/H (A. Maeland and T. B. Flanagan, *ibid.*, **69**, 3575 (1965)). Since the 60 and 80% Rh/Pd alloys form β phases, the immiscibility gap can be extended as shown by the dotted lines. The concentration variables X_H, X_{Pd}, and X_M are atomic fractions of hydrogen, palladium, and added metal, respectively.

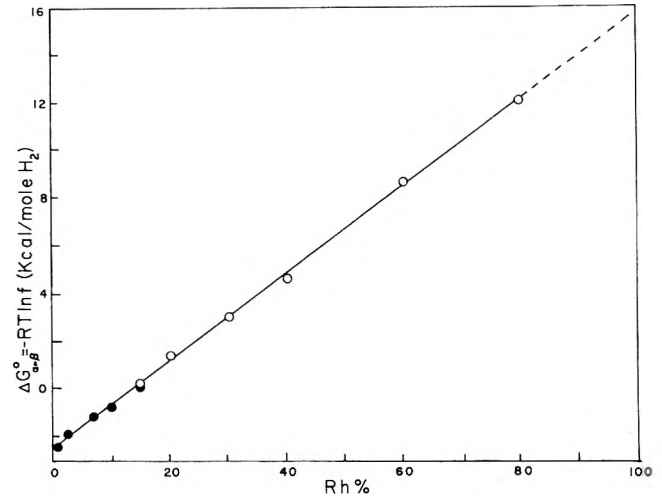

Figure 5. Relationship between $\Delta G_{\alpha\ \beta}^{\circ}$ and percentage Rh as determined from the fugacity at which the values of R/R_0 increase rapidly during absorption: ●, ref 14: O, present data.

is −25 + 5 cal/deg mol H_2.[2] On this basis, a value of $\Delta H_{\alpha\rightarrow\beta}^{\circ}$ of 8800 ± 1500 cal/mol H_2 can be estimated. A pressure of 30,000 atm ($f = 10^{11}$ atm) can be obtained in the present apparatus and at this pressure the temperature at which absorption corresponding to the $\alpha \rightarrow \beta$ transformation should occur is 83 ± 12°. An attempt is being made to prepare β phase Rh/H_2 under these conditions. One problem connected with the attempted synthesis of this hydride is that the diffusion coefficient of hydrogen in rhodium is probably very small. One of the au-

(26) B. Baranowski, S. Majchrzak, and T. B. Flanagan, *J. Phys. F*, 1, 258 (1971).
(27) W. DeGraaff, Thesis, University of Amsterdam, 1960.
(28) B. Baranowski, unpublished results.

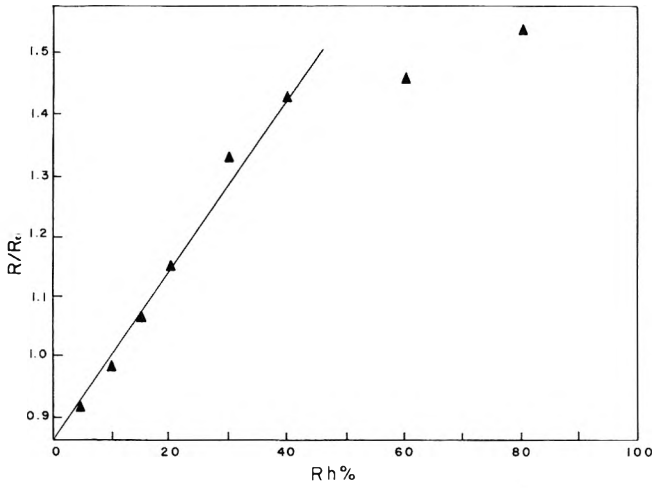

Figure 6. Relationship between the value of R/R_0 observed when further absorption of hydrogen has apparently ceased (25°) and % Rh in alloy.

thors and his coworker[29] have measured the diffusion coefficients in Rh/Pd alloys and it was observed that in passing from pure palladium to Rh(40%)/Pd the diffusion coefficient declines by a factor of 1000. Oates and McLellan[30] have recently found a value of 12.8 kcal/mol of H_2 for the relative partial molar enthalpy of absorption of hydrogen by rhodium at high temperatures and small hydrogen contents. The difference in this value and that observed, for example, in the Ni/H_2 system[30] is only about 4 kcal and therefore it is not unlikely that rhodium will absorb hydrogen. The difference in the value at infinite dilution and that estimated for the $\alpha \rightarrow \beta$ transition is 4.0 ± 1.5 kcal/mol of H_2. The increase in the exothermicity in passing from a vanishing small concentration to the $\alpha \rightarrow \beta$ transition is due mainly to the H/H attractive interaction in the Pd/H_2 system. It can be assumed that a similar effect operates in the Rh/H_2 system.

Andersen[31] has recently calculated a value of 1.27 holes in the d band for rhodium in contrast to the value of 0.37 for palladium.[32] If rhodium does indeed absorb hydrogen, it can be assumed that this large number of holes in the d band is a factor. Switendick and coworkers[33] have recently reported that some of the electrons from hydrogen in β Pd/H_2 occupy sp states below the d bands of palladium. It will be of extreme interest to ascertain what such band calculations will give for the β Rh/H_2 system.

The electrical resistance–pressure relationships (25°) observed here require some comment because of the formation of stoichiometric hydrides in several of the alloys. It is surprising that the values of R/R_0 (Figure 1) did not decline to very small values when stoichiometry was obtained. In the Pd/H_2 system, values of R/R° fall to values below 1 at very high pressures (Figure 1). Such behavior is not unexpected because complete order exists when stoichiometry is attained. The residual resistivity due to scattering by impurities should vanish at this point. The fact that the metallic alloy matrix has itself disorder should not alter this argument because values of R/R_0 are measured and both R and R_0 contain the disorder inherent in the alloy. The values of R/R_0 in the pressure range where the resistance changes are apparently caused only by pressure increases, and not by absorption of hydrogen, increase steadily in passing from pure palladium to Rh(80%)/Pd (Figure 6). In fact, the relationship is closely linear between alloy content and the limiting value of R/R_0 up to Rh(40%)/Pd.

The changes of R/R_0 with pressure during the desorption of hydrogen (Figure 1) is similar to the trends noted by Lewis and coworkers for low content Rh/Pd and Ni/Pd alloys,[14,15] *i.e.*, the values of R/R_0 increase to greater values during the desorption cycle than were observed during absorption.

Acknowledgments. The authors wish to thank Dr. H. T. Weaver of Sandia Laboratory for kindly supplying us with the 60 and 80% Rh/Pd alloys. We also wish to thank Professor Dr. E. Wicke for the Rh(15%)/Pd alloy. We are grateful for experimental assistance by Mr. S. Filipek and Mr. M. Krukowski. One of the authors (T. B. F.) is grateful for his appointment as a participant in the exchange program between the National (U. S.) and Polish Academies of Sciences and for the hospitality of the Polish Academy of Sciences (Warsaw). We are grateful to Dr. A. C. Switendick of Sandia Laboratory for informative discussions of the band structure of rhodium.

(29) D. Artman and T. B. Flanagan, research to be submitted for publication.
(30) W. A. Oates and R. McLellan, results to be submitted for publication.
(31) O. K. Andersen, *Phys. Rev. B*, **2**, 883 (1970).
(32) J. J. Vuillemin and M. G. Priestley, *Phys. Rev. Lett.*, **14**, 307 (1965).
(33) D. E. Eastman, J. Cashion, and A. C. Switendick, *Phys. Rev. Lett.*, **27**, 35 (1971).

Mechanism of Decay of Alkyl Radicals in Irradiated Polyethylene on Exposure to Air as Studied by Electron Spin Resonance

Tadao Seguchi* and Naoyuki Tamura

Takasaki Research Establishment, Japan Atomic Energy Research Institute, Takasaki, Gunma-ken, Japan

(Received June 30, 1972)

Publication costs assisted by the Japan Atomic Energy Research Institute

The mechanism of decay of alkyl radicals in the crystalline region of polyethylene has been investigated. The decay of alkyl radicals is observed with various kinds of polyethylene by electron spin resonance. A close relation is found between the decay rate and the sizes of crystallites. It is suggested that the alkyl radicals trapped in the crystalline region migrate to the surfaces of crystallites through hydrogen abstraction and decay by reaction with oxygen at the surfaces. The kinetics of the radical decay is well explained by the diffusion theory assuming that the decay rate is controlled by the rate of radical migration in the crystallites. The diffusion constant of alkyl radicals is estimated to be 3.0×10^{-18} cm^2/sec at 20°. It is shown that the migration of alkyl radicals occur intermolecularly rather than intramolecularly and the activation energy of migration is 18 kcal/mol.

Introduction

The free radicals produced in irradiated polyethylene have been investigated by many workers using electron spin resonance (esr). The identification of free radicals has been established. The irradiation of polyethylene at 77°K causes the formation of alkyl radicals, $-CH_2-\dot{C}HCH_2-$. When the irradiated sample is warmed up to room temperature or the sample is irradiated at room temperature, the allyl radicals, $-CH_2\dot{C}HCH{=}CH-$, are observed. These radicals are more stable than the alkyl radicals under vacuum but decay more rapidly in reactive gases such as oxygen. Various interpretations have so far been made concerning the kinetics of alkyl radical decay. It seems that discussion has been concentrated on whether the decay kinetics is first or second order. In the first-order kinetics,[1-4] the decay is presumed to consist of more than two stages with different rate constants. Other workers have suggested that the decay curve of the radicals can be analyzed by the second-order kinetics,[5-8] though the initial and the last stages of the actual decay curve do not coincide with the second-order kinetics. We have also investigated the decay of alkyl radicals under vacuum at room temperature and suggested that part of the alkyl radicals convert to allyl radicals with first-order kinetics and the rest decay with second-order kinetics.[9]

However, the kinetics of radical decay under grafting reactions have not been clearly explained by either first- or second-order kinetics. Though the monomers cannot diffuse into the crystalline regions, they can react with the radicals which come out of the inside of crystallites by migration along or across the chains. Since rate of reaction with monomers at the surface of crystallite is much faster than the rate of radical migration,[10] the decay rate should be controlled by the rate of migration. Waterman and Dole[4] have suggested that the alkyl radicals migrate by hydrogen transfer across the polymer chains. Shimada, Kashiwabara, and Sohma[8] have argued that alkyl radicals migrate along the polymer chains.

Here, we will report that the rate of alkyl radical decay in the atmosphere of reactive gases can be well explained by the diffusion of radicals in the crystallites of polyethylene and the diffusion constant is estimated from the experiment with various crystallite sizes of polyethylene.

Experimental Section

Samples used are high-density polyethylene (Sholex 6050) and radiation-polymerized polyethylene (Takathene). Sholex 6050 samples were prepared in various forms. Powder samples were prepared by boiling the pellet of polyethylene in 3% xylene solution and cooling to room temperature; the xylene was replaced by acetone and the resulting solution was allowed to dry at room temperature. Single crystal samples were prepared in 0.1% xylene solution at 75 and 85° for 48 hr. Annealed samples were prepared by heat treatments of single crystals at 110, 120, and 125° for 24 hr. The thickness of lammelae in single crystal samples was determined by measurement of the long period of X-ray small-angle scattering. Takathene was used in powder form as polymerized in gas phase of 400 kg/cm^2; sample P3 was polymerized at 30°; and sample P12 was polymerized at 70°. The percentages of crystallinity are 83, 77, and 63% for the powder samples of Sholex 6050, Takathene P3, and Takathene P12, respectively. Samples were packed in esr quartz tubes of 10 mm o.d.

The samples were irradiated with electrons of 2 MeV from a resonant transformer type of electron accelerator in

(1) E. J. Lawton, J. S. Balwit, and R. S. Powell, *J. Chem. Phys.*, **33**, 395, 405 (1960).
(2) M. Dole and F. Cracco, *J. Phys. Chem.*, **66**, 193 (1962).
(3) F. Cracco, A. J. Arvia, and M. Dole, *J. Chem. Phys.*, **37**, 2449 (1962).
(4) D. C. Waterman and M. Dole, *J. Phys. Chem.*, **74**, 1913 (1970).
(5) M. G. Ormerod, *Polymer*, **4**, 451 (1963).
(6) A. Charlesby, D. Libby, and M. G. Ormerod, *Proc. Roy. Soc., Ser. A*, **262**, 207 (1961).
(7) S. Nara, S. Shimada, H. Kashiwabara, and J. Sohma, *J. Polym. Sci., Part A-2*, **6**, 1435 (1968).
(8) S. Shimada, H. Kashiwabara, and J. Sohma, *J. Polym. Sci., Part A-2*, **8**, 1291 (1970).
(9) T. Seguchi and N. Tamura, "Large Radiation Sources for Industrial Processes," IAEA, Vienna, 1969, p 353.
(10) Diffusion constant of oxygen in the amorphous region of polyethylene is $D = 1.5 \times 10^{-7}$ cm^2/sec, G. A. Bohm, *J. Polym. Sci., Part A-2*, **5**, 639 (1967).

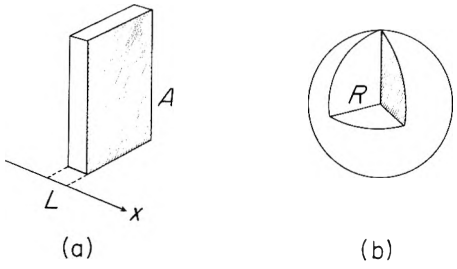

Figure 1. Models of the crystallite form: (a) plate-like and (b) spherical.

air at room temperature up to the dosage of 3 Mrads. The dose rate was 0.1 Mrad/sec. Esr spectra were repeatedly recorded immediately after irradiation with Varian V-4502 X-band spectrometer using 100-kHz field modulation.

Diffusion Equation

A diffusion equation is expressed as

$$\frac{\partial u(x,y,z,t)}{\partial t} = D\left(\frac{\partial^2}{\partial x^2} + \frac{\partial^2}{\partial y^2} + \frac{\partial^2}{\partial z^2}\right) u(x,y,z,t) \quad (1)$$

where D is the diffusion constant of radicals, and $u(x,y,z,t)$ is the concentration of the radicals at point (x,y,z) and a time t. In case (case I) the crystallite form of polyethylene is plate-like as shown in Figure 1a, eq 1 becomes

$$\partial u(x,t)/\partial t = D(\partial^2 u(x,t)/\partial x^2) \quad (2)$$

In case (case II) the crystallite is spherical as shown in Figure 1b, eq 1 is reduced to

$$\frac{\partial u(r,t)}{\partial t} = D\left(\frac{\partial^2 u(r,t)}{\partial r^2} + \frac{2\partial u(r,t)}{r\partial r}\right) \quad (3)$$

where r is radius of the sphere. In case I the direction of radical diffusion is perpendicular to the surface of plate (x direction in eq 1). The equation is solved with the following conditions: (a) the distribution of initial radicals is homogeneous in the crystalline regions, $u(x,t) = u_0$ at $t = 0$; (b) the concentration of radicals at the surface of crystallite is always zero, $u(x,t) = 0$ at $x = 0$ and L, where L is the thickness of the crystallite plate. Equation 2 can be written by Fourier transformation as

$$u(x,t) = \sum_{n=1}^{\infty} \frac{4}{n\pi} \sin\left(\frac{n\pi}{L} x\right) e^{-\lambda n^2 t} \quad (4)$$

where $n = 2k - 1$ (odd number) and $\lambda_n^2 = n^2\pi^2 D/L^2$. Concentration of the total radicals in the crystallite after time t is determined by integration of eq 4 from $x = 0$ to $x = L$ as

$$U(t) = A\int_0^L u(x,t)\mathrm{d}x, \quad (5)$$

where A is the area of the cross section. Substitution of eq 4 into eq 5 yields

$$U(t) = \frac{AL}{\pi^2}\left(e^{-\lambda_1^2 t} + \frac{1}{3^2} e^{-(3\lambda_1)^2 t} + \frac{1}{5^2} e^{-(5\lambda_1)^2 t} + \cdots\right) \quad (6)$$

The relationship between $U(t)$ and t can be calculated when $\lambda_1^2 = \pi^2 D/L^2$ is known. Equation 6 can be also applied when the direction of diffusion is isotropic if the area of cross section is much larger than the thickness.

In case II, the form of crystallite is spherical and the direction of diffusion is isotropic. Equation 3 is solved with the same conditions of plate-like crystallite, $u(r,t) = u_0$ at $t = 0$ and $u(r,t) = 0$ at $r = R$, where R is a distance from center to surface. The solution for eq 3 can be written as

$$u(r,t) = \frac{2R}{r\pi}\sum_{m=1}^{\infty} \frac{(-1)^m}{m\pi} e^{-\lambda m^2 t} \sin\frac{m\pi r}{R} \quad (7)$$

where $\lambda_m^2 = m^2\pi^2 D/R^2$ and $m = 1,2,3,\ldots$. The concentration of the total radicals $U(t)$ in the crystallite after time t is determined by integration eq 7 from $r = 0$ to $r = R$ as

$$U(t) = \int_0^R 4\pi r^2 u(r,t)\mathrm{d}r \quad (8)$$

Equation 8 can be calculated with computer when $\lambda_1^2 = \pi^2 D/R^2$ is given. Figure 2 shows the changes of $U(t)$ with time t in the case of $D/R^2 = 2 \times 10^{-5}$ in eq 8 and $D/L^2 = 10^{-5}$ in eq 6.

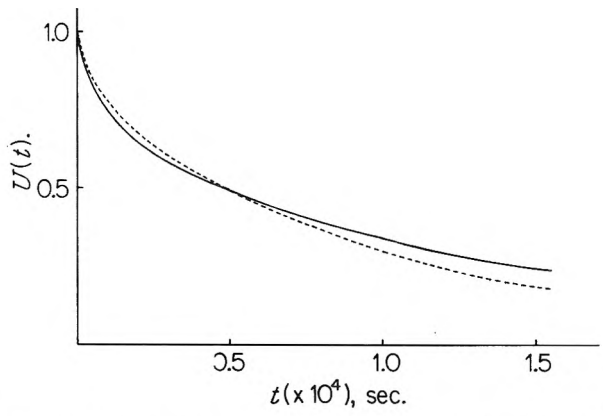

Figure 2. Calculated curves of $U(t)$: (a) from eq 8 for $D/R^2 = 2.0 \times 10^{-5}$ sec^{-1}, (b) from eq 6 for $D/L^2 = 1.0 \times 10^{-5}$ sec^{-1}.

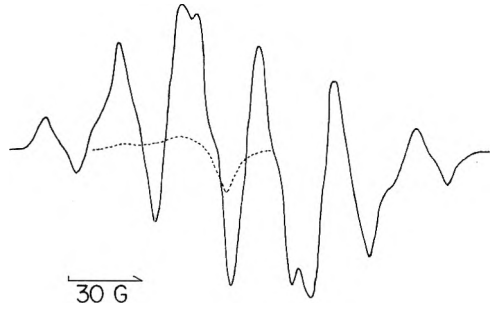

Figure 3. Esr spectrum at 20° for polyethylene (Sholex 6050) immediately after irradiation in air. Broken line shows a component of peroxy radicals.

Results

(1) Radical Species Trapped in Air at Room Temperature. When polyethylene is irradiated in air at room temperature, the esr spectrum obtained immediately after irradiation consists of a six-line component with a slight amount of an asymmetrical component as shown in Figure 3; the six-line spectrum is assigned to alkyl radicals and asymmetric line spectrum to peroxy radicals as is well known. Allyl radicals or dienyl radicals are not observed and are presumed to rapidly react with oxygen. From the experiment with the oriented mat of single crystals, it was found that the radicals trapped immediately after irradiation in air consist mainly of alkyl radicals trapped in crys-

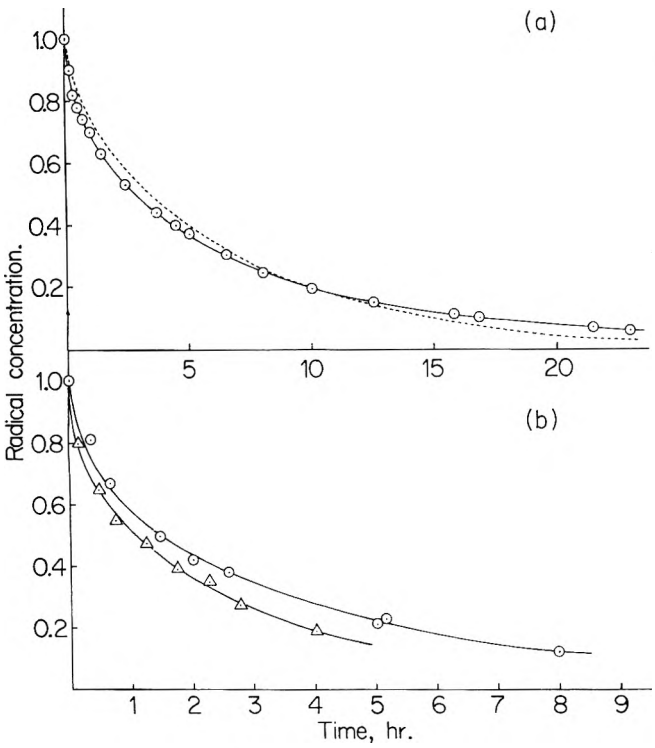

Figure 4. Decay of alkyl radicals in air at 20°: (a) Sholex 6050 (O), observed; (——), calculated from eq 8 for $D/R^2 = 9.6 \times 10^{-6}$ sec^{-1}; (-------), calculated from eq 6 for $D/L^2 = 4.6 \times 10^{-6}$ sec^{-1}: (b) Takathene, (△), P3; (⊙), P12 observed. Solid lines are calculated from eq 8: $D/R^2 = 1.4 \times 10^{-5}$ sec^{-1} and $D/R^2 = 2.5 \times 10^{-5}$ sec^{-1}.

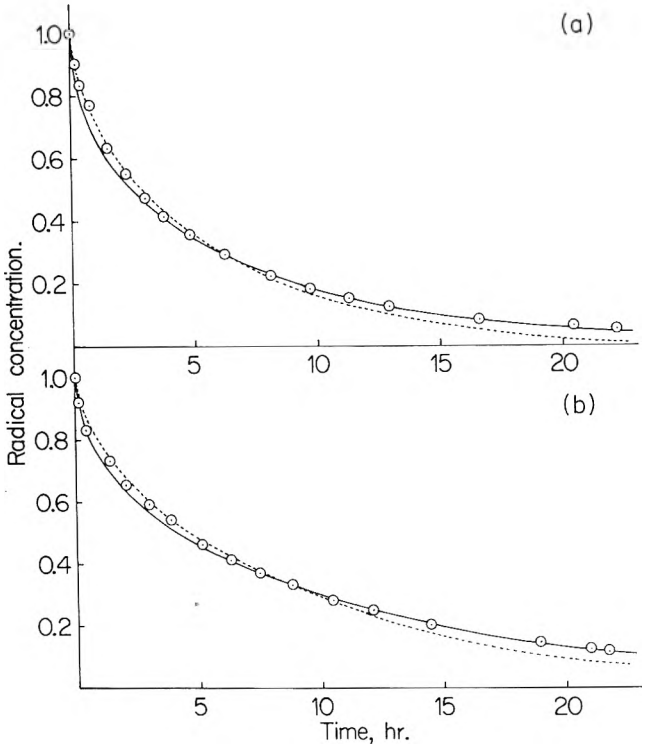

Figure 5. Decay of alkyl radicals in air at 20° in polyethylene crystallized at 75° (a) and 85° (b): (⊙), observed; (——), calculated from eq 8; (-------), calculated from eq 6.

talline regions at room temperature.

(2) Decay of Alkyl Radicals in Air. The decay of alkyl radicals with the powder samples of Sholex 6050 in air at 20° and that with Takathene P3 and P12 is shown in Figure 4. Here the concentration of alkyl radicals is measured from the height of outermost peaks of six-line spectrum, since the outermost peaks do not overlap with the peaks due to radicals such as peroxy or allyl radicals and the shape of the outermost peaks does not change with the radical concentration. The initial concentrations of radicals are 9.8, 2.4, and 5.3 (10^{17} spins/g) for Sholex 6050, Takathene P3, and Takathene P12, respectively. The decay rate in air is much faster than that observed under vacuum; the half-life of the radicals is about 20 hr under vacuum and about 3 hr in air. The behavior of radical decay does not agree with the formula, $dc/dt = kc^n$ (n = 1, 2, 1.5, etc.).

Assuming that the alkyl radicals can migrate in the crystalline regions of polyethylene and rapidly react with oxygen at the surface of crystallites, the rate of decay is controlled by the radical migration. Then the diffusion theory would be applied to the analysis of the decay curve in Figure 4. The migration of alkyl radicals in the crystallites suggests proton transfer either intramolecular

$$-CH_2\dot{C}HCH_2- \rightarrow -CH_2CH_2\dot{C}HCH_2- \qquad (a)$$

or intermolecular

$$\begin{matrix} -CH_2\dot{C}HCH_2- \\ -CH_2CH_2CH_2- \end{matrix} \longrightarrow \begin{matrix} -CH_2CH_2CH_2- \\ -CH_2\dot{C}HCH_2- \end{matrix} \qquad (b)$$

Two assumptions are made, namely, that the distribution of alkyl radicals immediately after irradiation is homogeneous and that there are no radicals at the surface of crystallites. The first assumption is reasonable because a first measurement immediately after irradiation (relative intensity 1.0 at time zero) was carried out within 10 min after irradiation, which is much shorter compared with the decay rate. The second assumption is based on the fact that molecules of oxygen can penetrate into amorphous region to reach the surface of crystallite and react with alkyl radicals.

Although the actual form of crystallite is thought to be complex, two simplified forms can be treated: plate-like and spherical crystallites. Equation 6 is applied to the case of plate-like crystallites and eq 8 to the case of spherical crystallites. Calculated decay curves thus obtained are shown in Figure 4. The solid line and the broken line are for the cases $D/R^2 = 9.6 \times 10^{-6}$ sec^{-1} in eq 8 and $D/L^2 = 4.6 \times 10^{-6}$ sec^{-1} in eq 6, respectively (Figure 4a). The upper line and the lower line in Figure 4b are for the cases $D/R^2 = 1.4 \times 10^{-5}$ sec^{-1} and $D/R^2 = 2.5 \times 10^{-5}$ sec^{-1} in eq 8, respectively. These results show that the curve from eq 8 agrees well with the observed plots.

When the single crystal samples that crystallized at 75 and 85° are irradiated, the decays of alkyl radicals are similar to the powder samples as shown in Figure 5. The solid line and the broken line in Figure 5 are calculated using eq 8 and 6, respectively. The solid line shows good agreement with the observed points except the slight deviation at the initial stage. On the other hand, the broken line agrees with the observed points at the initial stage, but then greatly deviates.

The decay curves obtained with annealed single crystals are shown in Figures 6a and 6b for the samples crystallized at 75 and 85°, respectively; the solid line is calculated from eq 8 and the broken line is calculated from eq 6. It is well known that single crystal sample consists of lamellae crystals and the thickening of lamellae is induced by

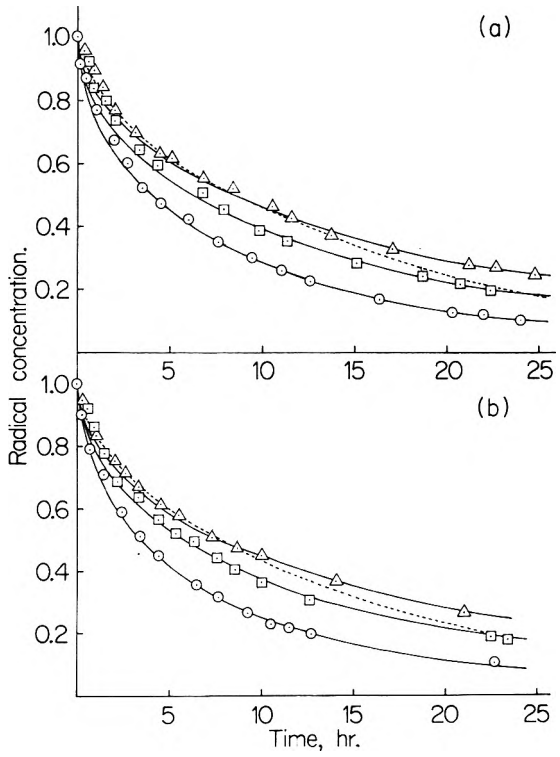

Figure 6. Decay of alkyl radicals in air at 20° in polyethylene crystallized at 75 (a) and at 85° (b), and annealed at 110 (⊙), 120 (⊡), and 125° (△). Solid line calculated from eq 8. Broken line calculated from eq 6 for annealing temperature of 125°.

annealing of the sample. With thickening of lamellae the decay rate decreases, *i.e.*, D/R^2 in eq 8 or D/L^2 in eq 6 decreases. The relationship between annealing temperature and the calculated values of D/R^2 and D/L^2 are presented in Table I; these values are derived from eq 8 and 6 best fitted with the observed points. Changes of lamellae thickness with annealing temperature, measured by X-ray small-angle scattering, are also shown in Table I.

If the diffusion constants D does not change with samples, the values of D/R^2 or D/L^2 depend only on crystallite size. In such cases the values $2R$ and L can be calculated using the data in Table I. These data are presented in Table II for the cases $D = 4.0 \times 10^{-18}$, 3.0×10^{-18}, and 2.5×10^{-18} cm²/sec.

(3) Temperature Dependence of Decay Rate. The radical decay in air was investigated at different temperatures above 20° with single crystal samples. As shown in Figure 7, it also obeys eq 8 and the decay rate depends on temperature. Since the size of crystallite does not change, the

TABLE I: D/R^2 and D/L^2 for Annealed Samples and the Long Period from X-Ray Small-Angle Scattering

Crystallization temp, °C	Annealing temp, °C	D/R^2, 10^{-6} sec^{-1}	D/L^2, 10^{-6} sec^{-1}	Long period, Å
75		11.1	4.68	113
	110	6.95	3.04	123
	120	4.33	2.01	189
	125	3.18	1.61	265
85		8.96	3.76	123
	110	7.93	3.50	128
	120	4.65	2.16	171
	125	3.45	1.76	221

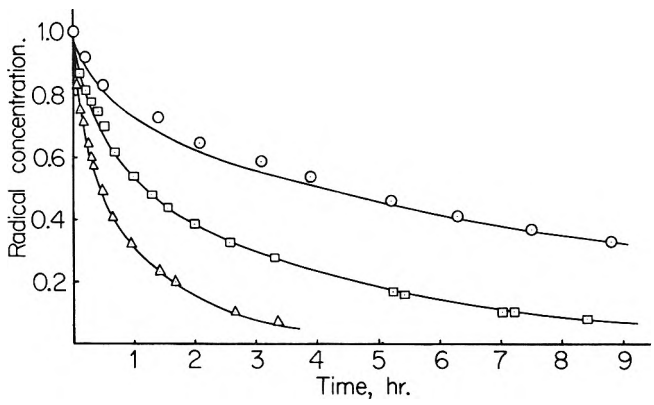

Figure 7. Decay of alky radicals in polyethylene crystallized at 85°. Stored in air at 22 (⊙), 30 (⊡), and 40° (△) after irradiation. Solid line calculated from eq 8.

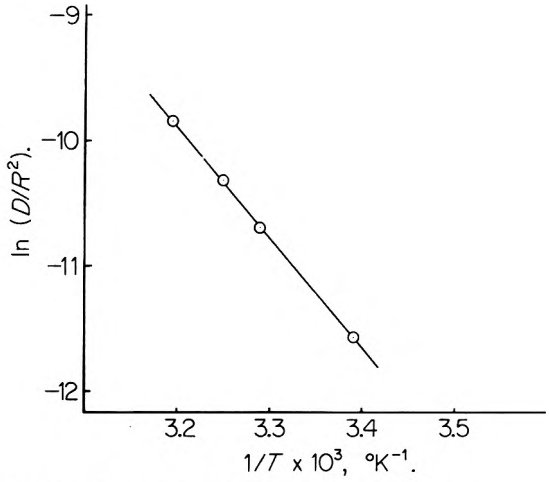

Figure 8. Plots of ln D *vs.* $1/T$ derived from Figure 7.

D/R^2 depends only on D. The relation between ln D and $1/T$ is linear as shown in Figure 8, from the slope of which activation energy of radical diffusion is calculated to be 17.9 and 17.5 kcal/mol for the samples crystallized at 75 and 85°, respectively.

Discussion

It was found that the decay of alkyl radicals in air is well explained by the diffusion of radicals in the crystalline regions. Although a part of alkyl radicals would decay by recombination or be converted to allyl radicals through the reaction with double bond in the crystalline region, the relative amount of radicals decaying through such processes is very small in air. Since the decay curve obtained with powder samples obeys eq 8 well, it is suggested that the presumed initial conditions to solve diffusion equations are reasonable.

It should be noted that in the single crystal samples, the decay curve is explained well by using eq 8 rather than eq 6. Since the single crystals of polyethylene consist of lamellae-like crystals, which have thickness of about 100 Å and width of a few microns, and the molecular chains are oriented perpendicular to the surface of lamellae, the decay curve should obey eq 6 assuming the alkyl radicals migrate only along the molecular chains or the lamellae consist of perfect crystals even if the migration is random. Therefore, the alkyl radicals must migrate intermolecularly rather than intramolecularly and the lamellae

TABLE II: Crystallite Sizes L(Å) and $2R$(Å) of Annealed Samples for Three Cases of Diffusion Constant D[a]

Crystallization temp, °C	Annealing temp, °C	Crystallite size, Å					
		a		b		c	
		L	$2R$	L	$2R$	L	$2R$
75		93	120	80	104	73	95
	110	115	152	100	131	91	120
	120	140	182	122	167	111	152
	125	157	224	137	194	125	177
85		103	134	89	115	82	106
	110	107	142	94	123	85	112
	120	136	186	118	161	108	146
	125	151	214	131	187	119	170

[a] (a) 4.0×10^{-18}, (b) 3.0×10^{-18}, and (c) 2.5×10^{-18} cm²/sec.

crystal must have many defects which behave like surfaces of crystals for the reaction with reactive gases such as oxygen.

The form of crystallites can be adequately approximated by sphere rather than plate. The slight deviation of the calculated curve from the observed plots at the initial stage of the radical decay may be due to rough approximation of crystallite form. Supposedly the actual form of single crystals is rectangular rather than spherical forms.

The decay rate of the radicals in the annealed single crystals is slower than that observed in the original samples. Though the same results have been reported by Ormerod[11] and Takamatsu and Kaibara,[12] they have not given clear explanation for such phenomena. As shown in Table I, $\lambda^2/\pi^2 = D/R^2$ in eq 8 or $\lambda^2/\pi^2 = D/L^2$ in eq 6 decreases with thickening of lamellae. When the migration rate of alkyl radicals or the diffusion constant D does not change by the annealing of sample, λ^2/π^2 should be proportional to $1/R^2$ or $1/L^2$. Since R or especially L of annealed single crystals can be measured by X-ray small-angle scattering, we can estimate D. The values L and $2R$ are compared with long periods measured by X-ray small-angle scattering in Table I. It is found that the values of the long periods agree well with $2R$. This result also supports the model of intermolecular migration of radicals in the crystalline regions. To fit these values of long periods with L, diffusion constant D must greatly increase with annealing temperature, such phenomena are unlikely to occur.

Crystallite sizes of Takεthene are estimated, as shown in Table III, assuming that the diffusion constant in Takathene are the same as in Sholex 6050. The relative values of crystallite size derived by this method are in good agreement with the relative values obtained by X-ray diffraction.[13] This result supports the fact that the decay rate of alkyl radicals depends on the crystallite size of polyethylene. The most probable value of diffusion constant is estimated to be $D = 3 \times 10^{-18}$ cm²/sec at 20° assuming $2R$ corresponds to long period.

Since the decay rate at a certain temperature depends only on diffusion constants, the linear relation between ln D and $1/T$ is obtained as shown in Figure 8. The activation energy of radical diffusion derived from Arrhenius plot is about 18 kcal/mol. This value is in good agreement with the value 17 kcal/mol obtained by Waterman and Dole[4] and the value 18 kcal/mol obtained by Shimada, *et al.*,[8] although they obtained these values of activation energy using the first-order kinetics. The activation energy for radical migration would be divided into two components, that is, the energy a neighboring proton approaching the radical (E_{ph}) and the energy the radical extracting a proton (E_{ch}). In vapor-phase reactions of low molecular weight compounds the activation energy for alkyl radicals to extract protons is 12–13 kcal/mol.[14,15] Waterman and Dole have reported that the activation energy of alkyl radical decay of polyethylene in hydrogen gas is 13 kcal/mol.[4] In our experiment E_{ph} becomes 5 kcal/mol, when E_{ch} is taken to be 13 kcal/mol.

TABLE III: D/R^2 and $2R$ for Various Samples in the Case $D = 3.0 \times 10^{-18}$ cm²/sec

Sample	D/R^2, 10^{-5} sec^{-1}	$2R$, Å	Crystal size,[a] Å
Sholex 6050	1.07	106	207
Takathene P3	2.5	63	120
Takathene P12	1.4	92	180

[a] The value was measured from a width of the (110) peak of X-ray diffraction.[13]

Although the diffusion constant D of radicals is presumably dependent upon the molecular motions in the crystallite region of polyethylene, the values of E_{ph} thus obtained are much smaller than the activation energy of the molecular motions such as α or β process to which nmr or dynamic mechanical studies refer.[16,17] Activation energies of these processes are reported as 40–50 and 14–17 kcal/mol[16] for α and β processes, respectively. The value of E_{ph} is rather near to the value of γ process. Since the γ process is assigned to the local molecular motions of noncrystalline regions of polyethylene it seems that no correlation exists between the radical migration and the molecular motions. However, the molecular motions of radical sites are supposed to differ with the motions of parent molecules, since the radical sites in the crystalline regions form a kind of defects. Molecular motion must have some role in the radical migration in the crystalline regions of polyethylene.

Acknowledgments. We wish to acknowledge Dr. Waichiro Kawakami for the calculation of diffusion equation using a computer.

(11) M. G. Ormerod, *Phil. Mag.*, **111**, 681 (1965).
(12) T. Takamatsu and M. Kaibara, *Rep. Inst. Phys. Chem. Res., Tokyo*, **42**, 231 (1966).
(13) N. Tamura, N. Hayakawa, and T. Fujimura, *Reo. Progr. Polym. Phys. Jap.*, **13**, 339 (1970).
(14) M. H. J. Wijnen and E. W. R. Steacie, *J. Chem. Phys.*, **20**, 205 (1952).
(15) G. H. Miller and E. W. R. Steacie, *J. Amer. Chem. Soc.*, **80**, 6486 (1958).
(16) N. Saito, K. Okano, S. Iwayanagi, and T. Hideshima, *Advan. Solid State Phys.*, **14**, 462, 343 (1963).
(17) M. Takayanagi and T. Matsuo, *J. Macromol. Sci., Phys.*, **1**, 407 (1967).

Yields of Excited States in the Pulse Radiolysis of Cyclohexane Solutions

Sir Frederick Dainton, M. B. Ledger, R. May, and G. A. Salmon*

The University of Leeds, Cookridge High Energy Radiation Research Centre, Cookridge Hospital, Leeds LS16 6QB
(Received July 13, 1972)

Publication costs assisted by The University of Leeds

The yields of excited singlet states formed on the electron irradiation of cyclohexane solution of a series of naphthalene and anthracene derivatives and also of a number of miscellaneous scintillators have been determined by a method which involves a comparison of the yields of radiation and light stimulated fluorescence from the solutions. Determinations have also been made of the triplet–triplet extinction coefficient of the naphthalene derivatives and also for anthracene and 9-bromoanthracene. Estimates are thus obtained for the ratios of the yield of initial triplet excited states formed to the yield of excited singlet states for these compounds, *i.e.*, $G(T)_i:G(S)$. For the naphthalene derivatives $G(T)_i:G(S) \simeq 1.0$ and for anthracene and 9-bromoanthracene $G(T)_i:G(S) \simeq 1.5$. The effect of excimer formation on $G(S)$ has been illustrated for PPO and anthracene and the rate constants for excimer formation for these solutes have been estimated to be $5.6 \pm 1.4 \times 10^9$ and $7.4 \pm 2.0 \times 10^9$ M^{-1} sec^{-1}, respectively.

Introduction

The radiolysis of cyclohexane solutions of aromatic hydrocarbons is known to give rise to singlet and triplet excited states of the solute. While it is generally agreed that some, if not all, of these excited states are formed in ion recombination reactions following initial charge scavenging by the solute,[1-5] there is some doubt as to the proportion of singlet and triplet states produced. Some workers have claimed that the singlet yield is small relative to the triplet yield,[6,7] while others have presented evidence in favor of comparable yields of both excited states.[5,8,9]

Baxendale and Wardman[5] have reported determinations of the absolute yields of singlet and triplet states for solutions of biphenyl, naphthalene, and anthracene in cyclohexane. In the case of naphthalene, they find that the singlet yield, $G(S)$, and the *initial* triplet yield, $G(T)_i$, *i.e.*, that yield of triplet excited states not formed by intersystem crossing from the singlet excited state, are very similar (*i.e.*, $G(T)_i/G(S) \simeq 1.0$), in agreement with our earlier results.[8,9] However, for both biphenyl and anthracene, they find $G(T)_i/G(S) \simeq 2.0$.

From their examination by pulse radiolysis of a series of anthracene derivatives, Kemp and Roberts[6] concluded that the singlet yield was negligible in comparison with the triplet yield. This conclusion was based on the observation that the *total* triplet yield, $G(T)$, appeared to be independent of ϕ_F, the fluorescence quantum yield of the anthracene (*i.e.*, the yield of singlets which do *not* intersystem cross to give triplets). However, if substituents do not significantly affect the radiation chemistry, then one would expect to find a higher $G(T)$ for a nonfluorescent anthracene, such as the 9-bromo derivative, than for a highly fluorescent anthracene, such as the 9,10-dimethyl derivative. One would in fact predict an increase of *ca.* 50%.

As part of a program aimed at resolving these discrepancies and ascertaining what factors determine scintillation efficiencies, we have measured the absolute singlet yields for a variety of aromatic solutes in cyclohexane using a technique referred to in an earlier communication.[8,9] In a few cases we have also determined the absolute triplet yields for comparison.

Experimental Section

The pulse radiolysis facility and sample preparation techniques have been fully described elsewhere.[10,11] However in the present study an EMI 9781 photomultiplier was used throughout. The sample cell was as previously described[11] except that the wall opposite that through which the electron beam entered was also of optical quality.

Determination of Singlet Yields. The method used to measure singlet yields relies upon the assumption that the fate of singlet excited molecules is independent of their mode of formation. The fluorescence from solutions irradiated with pulses of electrons is measured using the pulse radiolysis detection system (see above) and the efficiency of the light collection and detection system is then calibrated by observing the fluorescence from the solution when stimulated by uv light.

Pulse radiolysis of a solution of a fluorescent aromatic compound in cyclohexane produced a burst of fluorescence which usually followed closely the shape of the electron pulse (rectangular and 600 nsec wide for most of this work). For compounds with relatively long fluorescence lifetimes, the shape of the light pulse was modified to the

(1) E. J. Land and A. J. Swallow, *Trans. Faraday Soc.*, **64**, 1247 (1968).
(2) J. K. Thomas, K. Johnson, T. Klippert, and R. Lowers, *J. Chem. Phys.*, **48**, 1608 (1968).
(3) R. R. Hentz and R. J. Knight, *J. Phys. Chem.*, **72**, 1783 (1968).
(4) E. L. Frankevich, G. A. Salmon, and T. Morrow, *Nature (London)*, **219**, 481 (1968).
(5) J. H. Baxendale and P. Wardman, *Trans. Faraday Soc.*, **67**, 2997 (1971).
(6) T. J. Kemp and J. P. Roberts, *Trans. Faraday Soc.*, **65**, 725 (1969).
(7) J. W. Hunt and J. K. Thomas, *J. Chem. Phys.*, **46**, 2954 (1967).
(8) F. S. Dainton, G. A. Salmon, T. Morrow, and G. F. Thompson, *J. Chem. Soc. D*, 326 (1968).
(9) F. S. Dainton, R. May, T. Morrow, G. A. Salmon, and G. F. Thompson, *Proc. Roy. Soc., Sec. A*, **328**, 457 (1972).
(10) T. J. Kemp, J. P. Roberts, G. A. Salmon, and G. F. Thompson, *J. Phys. Chem.*, **72**, 1464 (1968).
(11) E. L. Frankevich, T. Morrow, and G. A. Salmon, *Proc. Roy. Soc., Sec. A*, **328**, 445 (1972).

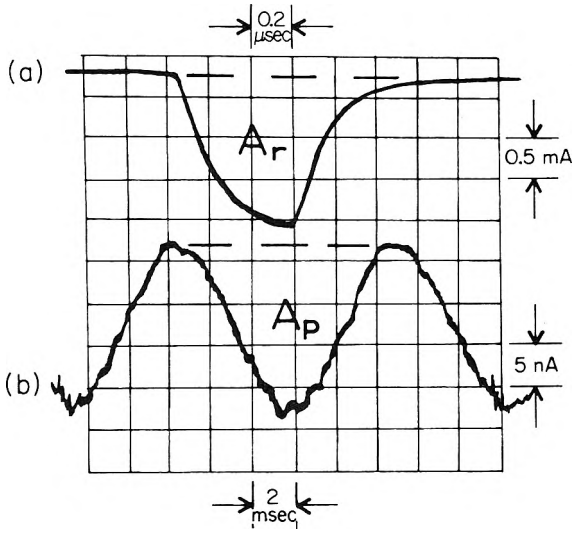

Figure 1. Fluorescence emission at 340 nm from solutions of naphthalene in cyclohexane: (a) 10^{-2} *M* solution subjected to a 500 rad, 600 nsec electron pulse; (b) 2×20^{-3} *M* solution subjected to photoexcitation by the ac light source (313 nm, 10^{15} quanta sec^{-1}).

expected dorsal, as shown in Figure 1a for the case of naphthalene. The calibration procedure was carried out by illuminating the solution with a suitable mercury line from a Hanovia 550-W medium-pressure lamp with an appropriate combination of glass and solution filters. The exciting light was focussed through the cell window opposite to that through which the electron beam entered. The solution thus emitted a train of fluorescence pulses, following the power output waveform of the ac light source (see Figure 1b).

Photographs of the radiation and photoinduced light pulses were taken under identical conditions of photomultiplier gain, though it was necessary to employ a much greater output load resistance in order to observe the relatively weak photoinduced signal. The time profiles so obtained were then enlarged and traced onto graph paper so that the area under each light pulse could be measured by the cut-out-and-weigh procedure. Having carried out dosimetry and actinometry of the electron and light pulses, respectively, it was then possible to calculate the radiation chemical yield of excited singlet states using

$$G(S) = (A_r/A_p)(a_\lambda I_p/I_r)C \text{ mol } (100 \text{ eV})^{-1} \qquad (1)$$

where A_r and A_p are the areas under the radiation induced and photoinduced light pulses, respectively, a_λ is the percentage of the exciting light absorbed by the solution at the exciting wavelength λ, I_p is the intensity of the light source (in photons per 10-msec pulse), I_r is the intensity of the radiation source (in eV per pulse), and C is a constant which incorporates the output loads and sweep speeds for the two sets of photographs. In our work, dosimetry and actinometry were carried out using aqueous solutions of potassium ferrocyanide[12] and potassium ferrioxalate,[13] respectively. In employing eq 1 we make the assumption that delayed fluoresence is insignificant in comparison with normal fluorescence. In the pulse radiolysis experiments the time scales are such that this is so and in the case of photoexcitation of the solutes the experiments of Parker and Hatchard[14] and Parker, Hatchard, and Joyce[15] indicate that at the rates of light absorption used in this work-delayed fluorescence is again insignificant in comparison with normal fluorescence.

In practice, it was usually necessary to employ a more dilute solution for the photoexcitation measurements than for the pulse radiolysis in order to avoid any reduction in the yield of fluorescence across the 7-mm cell due to the inner filter effect. To this end, the optical density of the solution used for these photographs was adjusted to be ≤ 0.2 at the exciting wavelength. Thus it is necessary to make the further assumption that the ratio a_λ/A_p is independent of concentration, an assumption which is valid except when excimer formation is significant (see below) since the observed fluorescence signal was shown to be a linear function of the per cent absorption. This same observation was taken as evidence that the collection efficiency of the optical system was insensitive to variations across the cell of the concentration of fluorescing excited singlet states.

In the present work, this method was used to measure $G(S)$ at some chosen concentration of solute, where excimer effects were unimportant, and G values at other concentrations were calculated by direct proportion from a knowledge of the relative fluorescence intensities.

Determination of Triplet Yields. The products $G(T)\epsilon_T$, where ϵ_T is the maximum extinction coefficient of the triplet-triplet absorption, were measured using 600-nsec pulses of about 5 krads and a monochromator bandwidth of 2 nm. Corrections for decay of the triplet during the electron pulse were made, but seldom amounted to more than 5%.

Two methods were used to estimate extinction coefficient, ϵ_T. For the naphthalenes studied, we employed the energy transfer method described by Bensasson and Land.[16] The triplet extinction coefficients of anthrancene and 9-bromoanthracene were determined using a flash photolysis technique which compares the absorption due to the triplet with the transient depletion of the ground-state absorption.[17]

Results and Discussion

Singlet Yields. In Figure 2 we have plotted $G(S)$ against log([solute] *M*) for a variety of naphthalene derivatives in cyclohexane. It is clear that, within experimental error, there is very little difference between one derivative and another, though 1-chloronaphthalene may be slightly anomalous. Figure 3 shows a similar plot for several anthracene derivatives. Deviations from the smooth curve are apparent at higher concentrations for some anthracenes because of self-quenching of the singlet state. Nevertheless, in the region where this is unimportant ($<10^{-3}$ *M*) the anthracenes behave very similarly, with the notable exception of 9-bromoanthracene which has a lower $G(S)$ at all concentrations.

Finally, in Table I we have collected $G(S)$ values for a variety of solutes at various concentrations so that comparisons may be made. These figures reveal little in the way of a general pattern, though it may be that there is a trend for the physically larger molecules to have somewhat higher singlet yields than the smaller ones *at the*

(12) G. E. Adams, J. W. Boag, and B. D. Michael, *Trans. Faraday Soc.*, **61**, 492 (1965).
(13) C. G. Hatchard and C. A. Parker, *Proc. Roy. Soc., Sec. A.* **235**, 518 (1956).
(14) C. A. Parker and C. G. Hatchard, *Proc. Roy. Soc., Sec. A.* **269**, 574 (1962).
(15) C. A. Parker, C. G. Hatchard, and T. A. Joyce, *J. Mol. Spectrosc.*, **14**, 311 (1964).
(16) R. Bensasson and E. J. Land, *Trans. Faraday Soc.*, **67**, 1904 (1971).
(17) S. G. Hadley and R. A. Keller, *J. Phys. Chem.*, **73**, 4351 (1969).

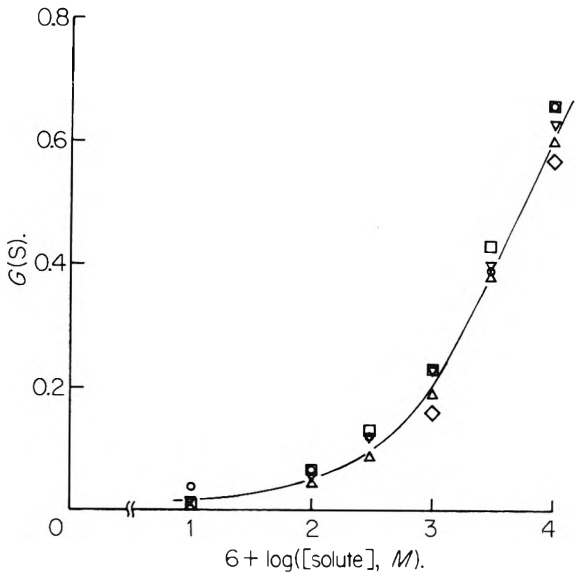

Figure 2. Variation of $G(S)$ with solute concentration for a variety of naphthalene derivatives in cyclohexane; O, naphthalene; △, 2,3-dimethylnaphthalene; ▽, 2,6-dimethylnaphthalene; □, acenaphthene, ◇, 1-chloronaphthalene.

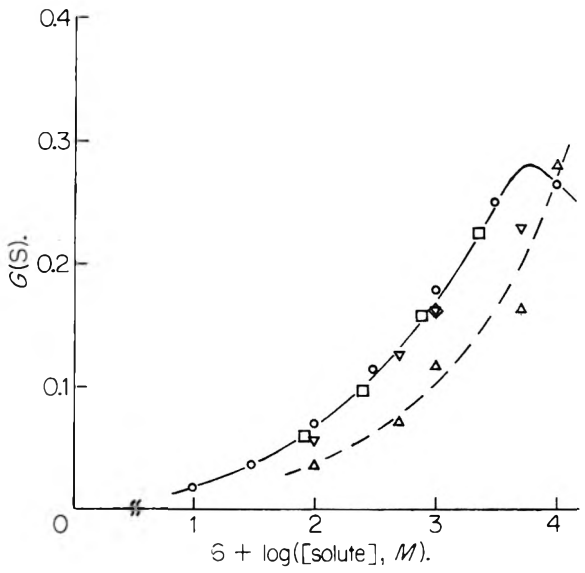

Figure 3. Variation of $G(S)$ with solute concentration for a variety of anthracene derivatives in cyclohexane: O, anthracene; △, 9-bromoanthracene; ▽, 9,10-dichloroanthracene; □, 9,10-dimethylanthracene; ◇, 9,10-diphenylanthracene.

TABLE I

Solute	Concentration, M	$G(S)^a$
Benzene	10^{-2}	0.25 ± 0.05
Toluene	10^{-2}	0.40
p-Xylene	10^{-2}	0.40
Naphthalene	10^{-2}	0.66
Naphthalene	10^{-3}	0.23
Anthracene	10^{-3}	0.18
Biphenyl	10^{-3}	0.38
p-Terphenyl	10^{-3}	0.27
Perylene	5×10^{-4} (sat)	0.25
TPB[b]	10^{-3}	0.31
PPO[c]	10^{-3}	0.25
PPD[d]	10^{-3}	0.25
α-NPO[e]	10^{-3}	0.26
α-NPO	5×10^{-5}	0.068
POPOP[f]	5×10^{-5}	0.112
p-Quaterphenyl	6×10^{-5} (sat)	0.077

[a] $G(S)$ to ±10%, except where otherwise indicated. [b] Tetraphenylbutadiene, [c] 2,5-Diphenyloxazole. [d] 2,5-Diphenyl-1,3,4-oxadiazole. [e] 2-(1-Naphthyl)-5-phenyloxazole. [f] *p*-Bis[2-(5-phenyloxazolyl)]benzene.

same concentration, perhaps indicating a dependence of electron-capturing ability on molecular size. The rather low $G(S)$ for benzene as compared with toluene and *p*-xylene may reflect a breakdown of the assumption that the behavior of the singlet excited states is independent of their origin. In the case of benzene there may be, for example, more isomerization of the excited state(s) formed radiation chemically than of that formed by excitation with 253.7-nm light, so that $G(S)$ is underestimated by our method.

Similar reasoning may explain the rather high result obtained for biphenyl (which we were able to reproduce in a second experiment). However, this result does not agree with the figures reported by Baxendale and Wardman[5] who found very similar $G(S)$ values for biphenyl, naphthalene, and anthracene. Since our results for naphthalene and anthracene agree fairly well with those of Baxendale and Wardman, we can offer no explanation at present for this discrepancy.

TABLE II: Triplet Absorption Spectra and Total Triplet Yields, $G(T)$, for Pulse-Irradiated 10^{-2} M Solutions of Various Naphthalenes in Cyclohexane

Solute	ϵ_T, $M^{-1}cm^{-1}$	λ_{max}, nm	$G(T)\epsilon_T$	$G(T)^a$
Naphthalene	23,400	412.5	22,600	0.96
2,3-Dimethylnaphthalene	22,000	420	18,800	0.86
2,6-Dimethylnaphthalene	20,700	425	19,900	0.96
Acenaphthene	15,000	432.5	13,000	0.87
1-Chloronaphthalene	20,700	417.5	18,100	0.87

[a] $G(T)$ to ± ~10%.

Triplet Yields. In order that comparisons may be made with singlet yields, we have determined the total triplet yields, $G(T)$, for a limited number of aromatic solutes in cyclohexane. Unfortunately, while it is relatively simple to measure the product of $G(T)$ and ϵ_T, the independent determination of $G(T)$ and ϵ_T is more difficult.

Using the method described by Bensasson and Land,[16] we have measured ϵ_T for the naphthalene derivatives represented in Figure 2. These values, together with corresponding estimates of λ_{max}, $G(T)\epsilon_T$, and hence $G(T)$, are given in Table II for 10^{-2} M solutions. In each case, the variation of $G(T)\epsilon_T$ with concentration was found to be closely similar to that of $G(S)$, so that normalized plots of $G(T)\epsilon_T$ or $G(S)$ *vs.* log [solute] are superimposable.

Using values of ϕ_F obtained from the literature and assuming that $\phi_F = 1 - \phi_F$, one may calculate what fraction of the total triplet yield arises *via* intersystem crossing from the excited singlet state. Table III gives the values of $G(T)_i$ which we deduce.

For each derivative, $G(T)_i : G(S)$ is close to 1:1, but $G(T)$ does not reveal the expected dependence on ϕ_T. This is perhaps due to the solutes having efficiencies of scavenging electrons and positive charge which fortuitously obscure the dependence on ϕ_T.

Using the flash photolytic technique described by Hadley and Keller,[17] we have also determined the maximum extinction coefficients for the triplet–triplet absorptions of

TABLE III: Relative Yields of Singlet and Triplet States in the Radiolysis of 10^{-2} *M* Solutions of Various Naphthalenes in Cyclohexane

Solute	$G(S)$	ϕ_F	$G(T)_i$	$G(T)_i/G(S)$
Naphthalene	0.66	0.29[a]	0.50	0.76 ± 0.15
2,3-Dimethylnaphthalene	0.60	0.38[b]	0.48	0.80 ± 0.16
2,6-Dimethylnaphthalene	0.63	0.43[b]	0.60	0.95 ± 0.19
Acenaphthene	0.66	0.55[a]	0.57	0.86 ± 0.17
1-Chloronaphthalene	0.57 ± 0.10	0.04[c]	0.33	0.58 ± 0.16

[a] C. A. Parker and T. A. Joyce, *Trans. Faraday Soc.*, **62**, 2785 (1966). [b] I. B. Berlman, "Handbook of Fluorescence Spectra of Aromatic Molecules," Academic Press, New York, N. Y., 1965. [c] J. G. Calvert and J. N. Pitts, Jr., "Photochemistry," Wiley, New York, N. Y., 1966.

anthracene and 9-bromoanthracene to be 73,700 (λ_{max} 425 nm, bandwidth 2 nm) and 67,600 M^{-1} cm^{-1} (λ_{max} 427.5 nm, bandwidth 2 nm). Table IV summarizes the results for the anthracenes. The total triplet yield for 9-bromoanthracene is rather similar to that for anthracene, despite the difference in ϕ_T. This appears to be due primarily to the smaller $G(S)$ of the bromo derivative, though $G(T)_i$ may also be somewhat reduced. The lower total excited state yield found for 9-bromoanthracene (and perhaps 1-chloronaphthalene) may indicate that, in the case of the halogenated aromatics, some dissociation of the anion formed on electron capture (reaction I) may occur before neutralization takes place

$$(A\text{-}Br) + e \rightarrow (A\text{-}Br)\cdot^- \rightarrow A\cdot + Br^- \qquad (I)$$

thereby reducing the yield of excited states obtained in reaction II.

$$(A\text{-}Br)\cdot^- + (A\text{-}Br)\cdot^+ \rightarrow {}^{1,3}(A\text{-}Br)^* \qquad (II)$$

Our results for anthracene and 9-bromoanthracene suggest that for both compounds $G(T)_i:G(S) \simeq 3:2$. These results are to be compared with those of Baxendale and Wardman[5] who found $G(T)_i:G(S) \simeq 2:1$ for anthracene although this difference is primarily due to these authors using the value of ϵ_T determined by Bensasson and Land.[15]

The earlier experiments of Kemp and Roberts were apparently too insensitive to detect differences in the overall triplet yield, $G(T)$, from one anthracene to another.

Concentration Dependence of Excited State Yields. It is generally a rather difficult matter to fit exactly the dependence of $G(S)$ and $G(T)$ on solute concentration to a well-defined mathematical expression. Elsewhere,[9] it has been shown that the data for naphthalene in cyclohexane can be fitted to an equation of the type

$$G(^1naph^*) = b_s'G_{fi} + b_sG_{gi} \times \{\alpha_-^{1/2}[naph]^{1/2}/(1 + \alpha_-^{1/2}[naph]^{1/2})\} \times \{\alpha_+^{1/2}[naph]^{1/2}/(1 + \alpha_+^{1/2}[naph]^{1/2})\} \qquad (2)$$

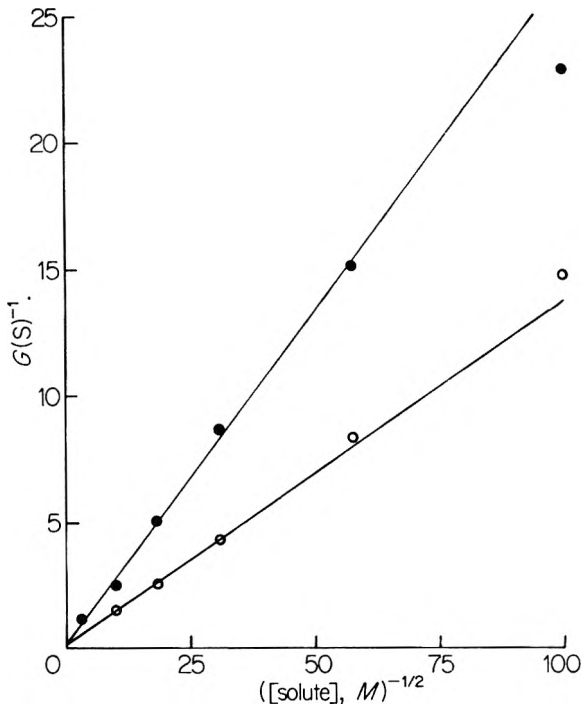

Figure 4. Demonstration of the approximate validity of eq 3: ●, *p*-xylene; O, naphthalene.

where G_{fi} and G_{gi} are the yields of free and geminate ions, respectively, b_s' and b_s are factors which represent the fraction of ion recombinations of the type

$$naph^+ + naph^- \rightarrow {}^{1,3}naph^*$$

which leads to the formation of singlet excited naphthalene (generally different for free and geminate ion recombinations), and α_- and α_+ are parameters related to the efficiency with which naphthalene scavenges the geminate ion pairs ($C_6H_{12}\cdot^+$, e^-) and ($C_6H_{12}\cdot^+$, $naph^-$), respectively. Similar equations may be written to describe the variation of total and initial triplet yields with concentration.

It is readily shown that eq 2 reduces to the approximate form given by

$$G(S)^{-1} \simeq (b_sG_{gi})^{-1}(1 + A[naph]^{-1/2}) \qquad (3)$$

where $A = (\alpha_-^{-1/2} + \alpha_+^{-1/2})$, so that plots of $G(S)^{-1}$ against $[solute]^{-1/2}$ are approximately linear over certain concentration ranges. This is demonstrated in Figures 4 and 5, where such plots are given for *p*-xylene, naphthalene, anthracene, and PPO.

The plots of Figure 5 show the effect of excimer formation on the measured value of $G(S)$. It is possible from these data to make estimates of the rate constants for ex-

TABLE IV: Yields of Excited States in the Radiolysis of 10^{-3} *M* Solutions of Various Anthracenes in Cyclohexane

Solute	$G(S)$	$G(T)\epsilon_T(\lambda_{max}, nm)$	$G(T)$	ϕ_F	$G(T)_i$	$G(T)_i/G(S)$
Anthracene	0.18	27,000 (420)	0.37	0.30[a]	0.24	1.33 ± 0.25
9-Bromoanthracene	0.12 ± 0.02	21,700 (425)	0.32	0.02[b]	0.20	1.67 ± 0.30
9,10-Dichloroanthracene	0.16	21,100 (417.5)		0.56[c]		
9,10-Dimethylanthracene	0.18	14,500 (427.5)		0.89[d]		
9,10-Diphenylanthracene	0.16	6,000 (445)		0.89[d]		

[a] See footnote a, Table III. [b] T. Medinger and F. Wilkinson, *Trans. Faraday Soc.*, **61**, 620 (1965). [c] See footnote *b*, Table III. [d] C. A. Parker and T. A. Joyce, *Chem. Commun.*, 744 (1967).

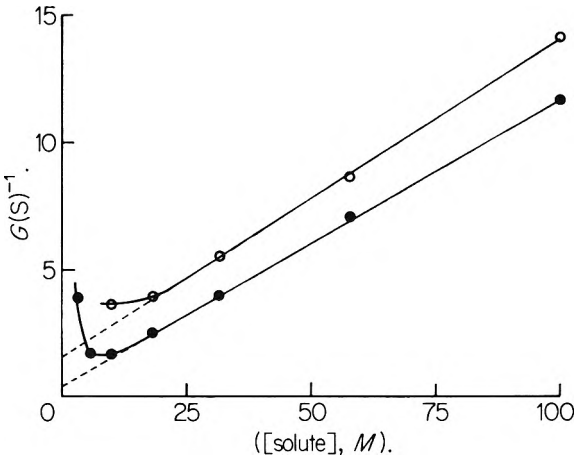

Figure 5. Application of eq 3 to systems where excimer formation is significant: ●, PPO; O, anthracene.

cimer formation, provided it is assumed that eq 3 holds in the concentration range 10^{-2}–10^{-1} M. On this basis we find values of $5.6 \pm 1.4 \times 10^9$ and $7.4 \pm 2.0 \times 10^9$ M^{-1} sec^{-1} (one point only) for the self-quenching rate constants of PPO and anthracene, respectively.

Conclusions

The application of an absolute method for determining the radiation chemical yields of excited singlet states has been demonstrated. The results indicate that in the concentration region 10^{-3}–10^{-2} M there is little difference between the energy-capturing abilities of different aromatic solutes. In most cases the yield of singlet excited states probably constitutes an appreciable fraction of the total excited state yield, indicating that spurs produced in cyclohexane radiolysis are small in size.[18]

The dependence of excited state yield on solute concentration is complicated by several factors including the differential contribution made by free ions[9] and the possibility of excimer formation. However, a knowledge of the b_s, b_t, and α values for the various scintillators would provide an adequate description of the factors affecting the efficiencies of excited state formation and charge scavenging, and should provide a basis for correlating these with structural properties of the solute. These parameters can be obtained from detailed studies of the effects of charge scavengers on the yields of excited states.[9]

Assessments of $G(S):G(T)_i$ are critically dependent on the values of ϵ_T used and therefore reflect any uncertainty in this parameter which at the moment shows wide variations depending on the method used for its determination.

Acknowledgments. We wish to thank I.C.I., Ltd., for the award of a Post Doctoral Fellowship to M. B. L. and the S. R. C. for financial assistance and the award of a Research Studentship to R. M.

(18) J. L. Magee, "Comparative Effects of Radiation," M. Burton, J. S. Kirby-Smith, and J. L. Magee, Ed., Wiley, London, 1960, p 130.

Spectra of Matrix Isolated Transition Metal Monoxides. Manganese(II) and Copper(II) Oxides. Evidence for a $^2\Pi$ Ground State for Copper(II) Oxide

Kenneth R. Thompson,* [1] Warren C. Easley, and Lon B. Knight

Department of Chemistry, University of Florida, Gainesville, Florida 32601 *(Received June 29, 1972)*

Publication costs assisted by the National Science Foundation

Following photolysis of oxygen–metal atom mixtures isolated in inert gas matrices at 4°K, the visible absorption spectra of MnO and CuO were observed. Vibrational progressions starting at 5809 and 4829 Å were found for MnO and CuO, respectively. No esr signals attributable to CuO were observed, although the optical spectra indicated concentrations in excess of the minimum detectable concentration. This result is interpreted in terms of a $^2\Pi$ ground state for CuO.

Although there has been a great deal of interest in the spectra of the first-row transition metal monoxides,[2] only the first few members of the series have been extensively studied since the remainder do not exist in the equilibrium vapor in any large concentration.[3] The electronic spectra of the diatomic oxides CrO–ZnO have been reported in emission, and in a few cases in absorption,[2] but in general the nature of the states involved remains unknown.

Many of these molecules exhibit several emission band systems in the visible and ultraviolet regions, and it is of considerable interest to establish which of these systems terminate in the ground state. The recent results of Shirk and Bass[4] indicate that only the blue-green system of CuO involves the ground state, in contrast with earlier

(1) Present address: Experimental Station, E. I. du Pont de Nemours & Co., Wilmington, Delaware 19898.
(2) B. Rosen, "Données Spectroscopigues Relatives aux Molécules Diatomiques," Pergamon Press, Oxford, 1971.
(3) See, for example, R. T. Grimley, R. P. Burns, and M. G. Inghram, *J. Chem. Phys.*, **35**, 551 (1961).
(4) J. S. Shirk and A. M. Bass, *J. Chem. Phys.*, **52**, 1894 (1970).

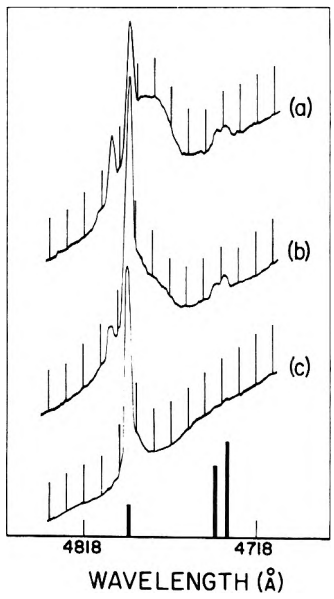

Figure 1. Spectra of the (1,0) band of $Cu^{18}O$ in an argon matrix as recorded (a) following photolysis at 4°K; (b) following warming to ~10°K; and (c) following further warming to ~17°K. The data of Shirk and Bass (ref 4) are shown as bars at the bottom. Wavelength markers are at 10-Å intervals.

work.[5] Their fluorescence measurements on the matrix-isolated molecule indicate that the red system is due to the B-A transition and, on the basis of the fluorescence measurements, they tentatively conclude that the ground state of CuO is $^2\Pi$, as might be expected by analogy with AgO.[6] Although the ground state of MnO has been tentatively assigned as a $^2\Sigma$ by observation of the visible spectrum,[7] virtually nothing is known of the ultraviolet transition reported by Callear and Norrish.[8] We have carefully examined the optical spectra of MnO and CuO isolated in inert gas matrices in order to establish which transitions involve the ground state.

Because of the possibility of a change in the ground state relative to AgO, similar to that observed in the TiO-ZrO and perhaps the VO-NbO pairs,[9] we have searched for esr lines attributable to CuO in order to establish whether the ground state is $^2\Sigma$ or $^2\Pi$.

Experimental Section

The general matrix trapping apparatus has been described.[10,11] CsI and CaF_2 were employed as deposition target materials for the optical experiments and a flat sapphire rod was used for the esr experiments. No differences in the optical spectra were observed with the various targets. The target was cooled to 4°K for all experiments. Oxygen and rare gas (all research grade) were used without further purification and were mixed in approximately a 1:200 ratio. Isotopically enriched $^{18}O_2$ (Oak Ridge National Laboratories) was used in some experiments.

The oxygen–rare gas mixture was cocondensed onto the target with a molecular beam of metal atoms produced by vaporizing the metal from resistively heated graphite or tantalum crucibles. Initial concentrations of O_2 and metal atoms were approximately equal.

In some of the optical experiments, the matrices were annealed using a temperature control device similar to that described by Weltner and McLeod.[10] The temperature of the deposition target was monitored with a chromel–gold (2.1 atomic per cent iron) thermocouple embedded in the copper block housing the target. Several experiments using neon as a matrix gas demonstrated the absence of thermal gradients across the target and the absence of a significant temperature gradient between the copper block and the target.

Following deposition, the matrix was photolyzed using a xenon resonance lamp similar to that described by Warneck.[12] LiF or CaF_2 windows in the cryostat were used to pass the 1470-Å radiation from the lamp, and the gap between the lamp and cryostat was purged with nitrogen.

Ultraviolet and visible spectra were recorded using a Jarrell-Ash 0.5-m Ebert spectrograph equipped with appropriate sources and photomultipliers. Infrared spectra were recorded using a Perkin-Elmer 621. Esr experiments were carried out in a cryostat described previously,[11] and a Varian V4500 X-band superheterodyne spectrometer. The instrument sensitivity at 4°K is approximately 1×10^{13} ΔH spins at S/N = 1, where ΔH is the line width, in gauss, of the esr signal.

Results

CuO. Prior to photolysis, only the Cu atom absorption bands and esr lines were observed. Following photolysis, our visible spectra are in agreement with those of Shirk and Bass,[4] except for a difference in intensities. They observed that each vibrational band was split into three components, two strong and closely spaced and one weak and separated from the others by ~250 cm^{-1}. The weak band and one of the strong bands were considered to be shifted by matrix effects. We observed the same bands, only the intensity was reversed. The (1,0) band of $Cu^{18}O$ is shown in Figure 1, as recorded (a) immediately following photolysis; (b) after warming to ~10°K; and (c) after warming the matrix to ~17°K. The absorption spectrum reported by Shirk and Bass is shown at the bottom of the figure. The fine structure on the strong absorption band at 4794 Å almost completely disappears upon warming to ~10°K and the weak bands to the blue completely disappear upon further warming.

The esr experiments were carried out using matrices that exhibited fairly strong blue-green absorption bands. Approximately 1×10^{17} CuO molecules were produced during the photolysis, as estimated from a knowledge of the initial copper atom concentration and the decrease (~50%) in the copper atom esr signals.[13] Following photolysis, the esr spectrum was carefully scanned from 0–11 kG, with negative results.

MnO. No absorption bands other than those attributable to manganese atoms were found in the unphotolyzed matrices and no perturbations of the atomic bands were observed.[14] Following photolysis of an O_2^- argon matrix containing Mn atoms, a progression of bands starting at 5808 Å appeared. The first three members of the progres-

(5) A. Antic-Jovanovic, D. S. Pesic, and A. G. Gaydon, *Proc. Roy. Soc., Sec. A*, **307**, 399 (1968).
(6) U. Uhler, *Ark. Phys.*, **7**, 125 (1953).
(7) J. G. Kay, private communication, 1969.
(8) A. B. Callear and R. G. W. Norrish, *Proc. Roy. Soc., Sec. A*, **259**, 304 (1960).
(9) C. J. Cheetham and R. F. Barrow, *Advan. High Temp. Chem.*, **1**, 7 (1967).
(10) W. Weltner, Jr., and D. McLeod, Jr., *J. Chem. Phys.*, **45**, 3096 (1966).
(11) P. H. Kasai, E. B. Whipple, and W. Weltner, Jr., *J. Chem. Phys.*, **44**, 2581 (1966).
(12) P. Warneck, *Appl. Opt.*, **1**, 721 (1962).
(13) P. H. Kasai and D. McLeod, Jr., *J. Chem. Phys.*, **55**, 1566 (1971).
(14) D. M. Mann and H. P. Broida, *J. Chem. Phys.*, **55**, 84 (1971).

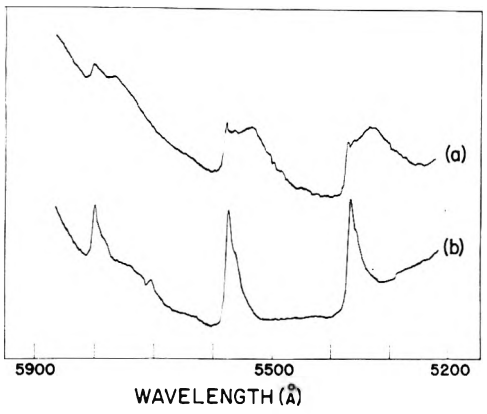

Figure 2. Absorption spectra of $Mn^{16}O$ in argon observed (a) following photolysis at 4°K and (b) following warming the matrix at ~10°K.

sion are shown in Figure 2a. As may be seen, the absorption bands are quite broad (~100 Å) and their center is difficult to determine. If the matrix is allowed to warm to ~10°K and then quenched back to 4°K, spectrum (b) is recorded. All of the bands have sharpened considerably with little or no loss in intensity. Upon warming to higher temperatures, no new effects were observed other than the normal decrease in band intensity following a solid-state diffusion.

Figure 3 illustrates the complete band progressions observed for $Mn^{16}O$ and $Mn^{18}O$, both spectra recorded after warming the matrix to ~10°K. No other absorption bands attributable to MnO were observed in this study despite a careful search of the region 2500–2700 Å.

The observed band positions and vibrational frequencies for both oxygen isotopes of MnO are given in Table I. The ratio ($\nu(^{18}O)/\nu(^{16}O)$) is also given in the table, the theoretical value being 0.9558. Variations in the listed ratio are due primarily to an uncertainty of ±0.5 Å in the determination of the band centers.

A very weak infrared absorption band was observed at 822 cm^{-1}, which may be due to $Mn^{16}O$, but we are unable to make a definite assignment since we were unable to observe the corresponding band for $Mn^{18}O$.

Although absorption bands were obtained after photolyzing a neon matrix, they were much weaker than those obtained in argon matrices. Evidently, photolysis proceeds at a much slower rate in neon; a similar trend from argon to neon was observed in the photolytic production of CN from ICN.[15] The absorption bands in neon were also very broad and quite similar to the unannealed argon bands. Annealing in neon matrices is difficult because it requires more precise temperature control and was not done here. The positions of the bands in neon are listed in Table II along with the vibrational frequencies. $^{18}O_2$ experiments were not attempted.

Discussion

Spin Resonance Experiments. It is well known that $^2\Sigma$ ground state molecules isolated in inert gas matrices in sufficient numbers give strong, narrow esr signals in the region of $g = 2$ (for example, CuF_2 in argon),[11] while resonances due to $^2\Pi$ molecules have not been observed. The resonances of a random distribution of $^2\Pi$ molecules with unquenched orbital degeneracy will be broadened beyond detection due to excessive g tensor anisotropy. Our failure to observe any resonances other than those previously reported for Cu atoms[13] despite the fact that the number of

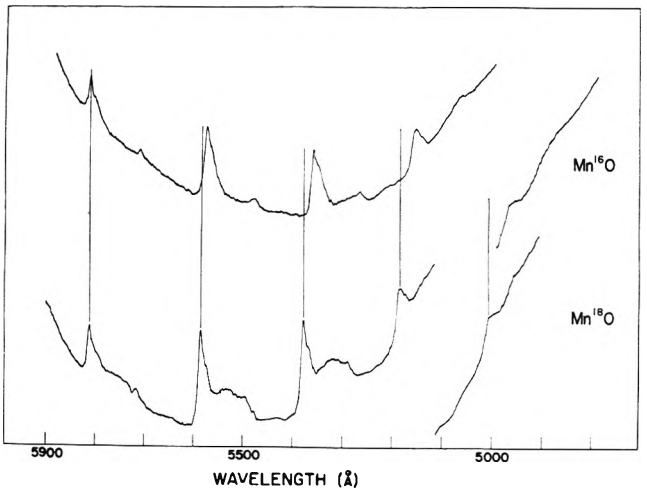

Figure 3. Observed vibrational progressions for $Mn^{16}O$ and $Mn^{18}O$.

TABLE I: Observed Absorption Bands of MnO in an Argon Matrix at 4°K[a]

	$Mn^{16}O$			$Mn^{18}O$			
v'	λ, Å	ν, cm^{-1}	$\Delta G(v' + \frac{1}{2})$	λ, Å	ν, cm^{-1}	$\Delta G(v' + \frac{1}{2})$	$\nu(^{18}O)/\nu(^{16}O)$[b]
0	5809	17,210	732	5806	17,219	700	0.956
1	5572	17,942	727	5579	17,919	691	0.950
2	5355	18,669	725	5372	18,610	693	0.956
3	5155	19,394	729	5179	19,303	691	0.947
4	4968	20,123		5000	19,994		

[a] Bands observed after annealing the matrix at 10°K to remove broadening. [b] Theoretical ratio 0.9558.

TABLE II: Observed Absorption Bands of MnO in a Neon Matrix at 4°K

v'	λ, Å	ν, cm^{-1}	$G(v' + \frac{1}{2})$, cm^{-1}
0	5571	17,945	755
1	5346	18,700	727
2	5146	19,427	

CuO molecules in the matrix exceeded the sensitivity of the instrument by at least two orders of magnitude indicates that the ground state of CuO is $^2\Pi$, similar to that observed for AgO,[6] and in agreement with Shirk and Bass.[4]

Optical Spectra. The carriers of the bands observed here have been established from earlier gas-phase studies.[2,5,7] As expected from earlier results,[16,17] the observed vibrational spacings in argon are slightly lower and in neon slightly higher than those found in the gas phase (746.6 cm^{-1} for $Mn^{16}O$[7] and 615 cm^{-1} for CuO[5]). The position of the (0,0) band of MnO in neon is, within experimental error, the same as that observed in the gas phase (17,941.7 cm^{-1}),[7] while the argon (0,0) band is shifted 730 cm^{-1} to the red. A shift of comparable magnitude was observed by Shirk and Bass and by us for CuO in argon.

(15) W. C. Easley and W. Weltner, Jr., *J. Chem. Phys.*, **52**, 197 (1970).
(16) W. Weltner, Jr., and D. McLeod, Jr., *J. Phys. Chem.*, **69**, 3488 (1965).
(17) W. Weltner, Jr., and D. McLeod, Jr., *J. Chem. Phys.*, **42**, 882 (1965).

The variation in intensities between the CuO spectra obtained here and those of Shirk and Bass[4] may be due to the relatively high concentration of O_2 in our matrices, although some care was taken to reproduce the previous experimental conditions. Dilution experiments could conceivably resolve this question, but our purpose in the CuO work was to provide a large enough concentration of CuO in the matrix so that we would be assured of strong esr signals if the molecule had a $^2\Sigma$ ground state. Since the production of oxide species proceeds slowly at 4°K, requiring extended (4 hr) periods of photolysis even in concentrated matrices, higher dilution was not worthwhile. Another explanation for the band intensity differences is the population of two different matrix sites at different photolysis temperatures, our experiments being carried out at 4°K and those of Shirk and Bass[4] at 14°K. Such an explanation is somewhat speculative, but appears to be the most reasonable if our O_2:Ar ratio is close to that used earlier.

Our failure to observe MnO bands in the region of 2500–2700 Å in the 4°K spectra indicates that the bands reported by Callear and Norrish[8] in absorption probably do not involve the ground state.

Conclusion

MnO and CuO have been prepared in inert matrices by photolysis of oxygen in the presence of metal atoms. Absorption bands corresponding to the visible system of MnO and the blue-green system of CuO were observed. The ultraviolet system of MnO was not observed, indicating that it probably does not involve the ground state.

The failure to observe electron spin resonances attributable to CuO indicates that the ground state of the molecule is $^2\Pi$.

Acknowledgment. The authors wish to thank Professor W. Weltner for the use of the facilities of his laboratory and for many helpful discussions. This research was supported in part by a grant from The National Science Foundation.

Raman and Infrared Spectral Study of Magnesium Nitrate–Water Systems

T. G. Chang and D. E. Irish*

Department of Chemistry, University of Waterloo, Waterloo, Ontario, Canada *(Received August 16, 1972)*

Publication costs assisted by the National Research Council of Canada

Detailed studies of the Raman and infrared line shapes of magnesium nitrate–water systems ranging from dilute solutions to hydrate melts are reported. No evidence of contact ion pairs has been found up to saturation at 25°. Weak perturbations of the spectra of solvated nitrate ion suggest solvent-shared ion pairs in solutions more concentrated than 2.5 *M*. The nitrate ion exists in three environments in hydrate melts. As water content is diminished the free nitrate concentration is reduced and a fraction of the anions are oriented in monodentate fashion in the field of Mg^{2+}. Further reduction of water causes some nitrate ions to assume a bidentate orientation. This labile structure becomes frozen into the crystalline tetrahydrate and dihydrates.

Introduction

Six water molecules bind to the magnesium ion to create an approximately octahedral hexaquomagnesium cation in crystalline hexahydrates.[1,2] The peripheral hydration sphere is probably similar in aqueous solution.[3,4] The stability of this species is consistent with the high charge-to-radius ratio of Mg^{2+}, 3.3, and the high hydration energy.[5] It has been inferred from both conductance[6] and vapor pressure measurements[7] that complex formation between Mg^{2+} and NO_3^- in aqueous solutions is unlikely. In a previous communication we reported that the absence of Raman intensity in the region ~740 cm^{-1} provided strong evidence that no contact ion pairs were formed in aqueous $Mg(NO_3)_2$ solutions up to saturation at 25°.[8] Vollmar[9] also concluded that ion pair formation was unfavorable in this system, from a study of the 1050-cm^{-1} Raman line intensity of the NO_3^- ion.

We now report detailed studies of the magnesium nitrate–water systems ranging from dilute aqueous solutions to hydrate melts. Vibrational spectral studies of the hexa-, tetra-, and dihydrated magnesium nitrate crystals have also been completed and are reported elsewhere.[10] Spec-

(1) A. Braibanti, A. Tiripicchio, A. M. M. Lanfredi, and F. Bigoli, *Acta Crystallogr., Sect.B*, **25**, 354 (1969).
(2) W. H. Baur, *Acta Crystallogr.*, **17**, 1361 (1964).
(3) H. G. Hertz, *Angew. Chem., Int. Ed. Engl.*, **9**, 124 (1970).
(4) S. F. Lincoln, *Coord. Chem. Rev.*, **6**, 309 (1971).
(5) J. S. Muirhead-Gould and K. J. Laidler, "Chemical Physics of Ionic Solutions," B. E. Conway and R. G. Barradas, Ed., Wiley, New York, N. Y., 1966, p 75.
(6) E. C. Righellato and C. W. Davies, *Trans. Faraday Soc.*, **26**, 592 (1930).
(7) R. A. Robinson, J. M. Wilson, and H. S. Ayling, *J. Amer. Chem. Soc.*, **64**, 1469 (1942).
(8) D. E. Irish, T. G. Chang, and D. L. Nelson, *Inorg. Chem.*, **9**, 425 (1970).
(9) P. M. Vollmar, *J. Chem. Phys.*, **39**, 2236 (1963).
(10) T. G. Chang and D. E. Irish, *Can. J. Chem.*, in press.

tral studies have previously been reported by Hester and Krishnan[11,12] and more recently by Peleg.[13]

Experimental Section

Aqueous solutions were prepared from distilled water and $Mg(NO_3)_2 \cdot 6H_2O$ (Fisher certified ACS reagent). They were treated with activated charcoal and filtered through a 0.45-μ Millipore filter. Densities were measured and the molar ratios of water to magnesium nitrate *(R)* were calculated from the known concentration. Raman spectra were excited by the 435.8-nm line of a Toronto arc and recorded with a Cary 81 Raman spectrophotometer. Infrared spectra were recorded on a Beckman IR-9 spectrometer, using either silver chloride windows or a 60° silver chloride prism and the Wilks Model 9 multiple internal reflection (MIR) accessory. Sample temperature was controlled at 25°.

To obtain samples with $R < 6$, $Mg(NO_3)_2 \cdot 6H_2O$ was placed under vacuum at 30–40°. The partially dehydrated magnesium nitrate was melted at 150° in an oven and transferred to a specially designed high-temperature Raman cell. The tube containing the sample was positioned in an unsilvered dewar. Nitrogen gas was passed through a flowmeter and heater and then evenly distributed within the dewar through numerous holes in a gas inlet tube. The temperature in the cell was controlled by regulating the voltage in the heater coil and the flow rate of nitrogen. It was monitored by a chromel-alumel thermocouple in conjunction with a dc differential voltmeter and a Beckman 10 in. recorder. The temperature in the cell could be maintained up to 200° with a fluctuation of less than 3°. The cell is illustrated elsewhere.[14] The water contents of the melts were determined by Karl Fisher titration. Samples with a water to magnesium nitrate ratio greater than 3 were stable as melts, but with ratios less than 3 slight decomposition occurred during a prolonged heating period. Spectra which consisted of closely spaced and overlapping lines were analyzed with a computer facility.[15]

Results and Discussion

Aqueous Solutions. Two Raman bands at *ca.* 240 and 357 cm^{-1} were observed besides the water bands at *ca.* 70 and 170 cm^{-1} in the low-frequency region. The 240-cm^{-1} band is very weak and broad. The 357-cm^{-1} band is polarized and its intensity is directly proportional to the concentration of magnesium ions up to 3.85 *M*. Its frequency is independent of concentration within 1 cm^{-1} and its half-width is 45 ± 2 cm^{-1}. A band at 315 cm^{-1} reported by da Silviera, *et al.*,[16,17] was not found in this study. The 240- and 357-cm^{-1} bands have previously been assigned to the $Mg(H_2O)_6^{2+}$ species;[17-19] a higher frequency is observed for crystals. The properties of the line suggest that, up to saturation, the Mg^{2+} ion is aquated by six water molecules. A solvation number of six has been inferred from pmr experiments.[20,21]

An aquated nitrate ion is known to generate vibrational lines at 718 $\nu_4(E')$, 830 $\nu_2(A_2'')$, 1049 $\nu_1(A_1')$, ~1354 and ~1410 $\nu_3(E')$, and 1660 cm^{-1} $2\nu_2(A_1')$. A weak feature at about 690 cm^{-1} is attributed to water in the environment of nitrate.[22] $Mg(NO_3)_2$ solutions generate a single 718-cm^{-1} Raman band. The position shifts upward by only 1.5 cm^{-1} and the integrated intensity is directly proportional to concentration. In contrast, its line width increases from 21 to 29 cm^{-1} over the composition range. In heavy water a single infrared and Raman line at 721 cm^{-1} was observed. These observations confirm that no contact ion pairs are formed until forced by reduction of water.[8] A single infrared line, 832–830 cm^{-1}, a single overtone $2\nu_2$, 1659–1657 cm^{-1}, and a single, polarized 1049-cm^{-1} line with intensity directly proportional to concentration (frequency change 1048–1050 cm^{-1}; half-width change 15–17 cm^{-1}) support the inference that contact ion pairs are not formed for concentrations below 3.85 *M*.

Cation–anion interactions are revealed in the spectra, however. $\nu_3(E')$ appears as a broad envelope with two maxima in both Raman and MIR spectra. The intensity ratio inverts, as noted for alkali metal nitrates,[22] when Raman and infrared spectra are compared. Computer analysis requires only two component bands. Raman lines shift from 1342 and 1405 cm^{-1} in dilute solution to 1344 and 1415 cm^{-1} in concentrated solution. The infrared components are not coincident. The separation, 63–71 cm^{-1}, can be compared with 56 cm^{-1} observed for 1+ ions and 74 cm^{-1} observed for 3+ cations.[23] The striking properties are the decrease of the depolarization ratio of the 1344-cm^{-1} line when $C > 2.5$ *M* and the downward shift of the infrared line from 1344 to 1325 cm^{-1}. A lower frequency polarized Raman component in this region has been previously observed when ion pairs are present.[23] In the absence of strong indications of contact ion pairs, the presence of a solvent shared ion pair is suggested. It is known that the Raman spectrum does not substantially reveal second nearest neighbor interactions. The broadening of $\nu_4(E')$, Raman activity of $\nu_2(A_2'')$ in concentrated solutions, and its small shift to lower frequencies are consistent with a weak perturbation. The infrared activity of $\nu_1(A_1')$ could also be indicative; although this digression from D_{3h} selection rules is believed to be a feature of the solvated nitrate ion, a significantly higher molar intensity for concentrated solutions is attributable to perturbations by the cation. The high charge density of Mg^{2+} makes the formation and detection of the elusive solvent-shared ion pair a possibility. The perturbation is not sufficient to generate a set of vibrational bands well separated from those of the solvated nitrate ion.

The infrared-active, water bending mode occurs at 1636 cm^{-1} for dilute solutions. It broadens, shifts to higher frequency (1645 cm^{-1}) as the salt concentration increases, and becomes asymmetric indicating the presence of several water environments. It is inferred that a line at 1636 cm^{-1} from bulk water is replaced by a line with greater molar intensity at 1650 cm^{-1} from the water of $Mg(H_2O)_6^{2+}$. The molar intensity increase is attributed to polarization of H_2O by Mg^{2+}. The observed displacement of the OH stretching band of water (*ca.* 3500 cm^{-1}) toward higher frequencies with increasing concentration of salt is

(11) R. E. Hester and K. Krishnan, *J. Chem. Phys.*, **47**, 1747 (1967).
(12) R. E. Hester and K. Krishnan, *J. Chem. Soc. A*, 1955 (1968).
(13) M. Peleg, *J. Phys. Chem.*, **76**, 1019 (1972).
(14) T. G. Chang, Ph.D. Thesis, University of Waterloo, Waterloo, Ontario, Canada, 1972. Details, additional tables of data, and illustrations of spectra can also be found in this source.
(15) A. R. Davis, D. E. Irish, R. B. Roden, and A. J. Weerheim, *Appl. Spectrosc.*, **26**, 384 (1972).
(16) A. da Silveira and E. Bauer, *C. R. Acad. Sci.*, **195**, 416 (1932).
(17) A. da Silveira, M. A. Marques, and N. M. Marques, *Mol. Phys.*, 9, 271 (1965).
(18) R. Lafont, *Ann. Phys. (Paris)*, **4**, 905 (1959).
(19) V. Ananthanarayanan, *J. Chem. Phys.*, **52**, 3844 (1970).
(20) A. Fratiello, R. E. Lee, V. M. Nishida, and R. E. Schuster, *J. Chem. Phys.*, **48**, 3705 (1968).
(21) N. A. Matwiyoff and H. Taube, *J. Amer. Chem. Soc.*, **90**, 2796 (1968).
(22) D. E. Irish and A. R. Davis, *Can. J. Chem.*, **46**, 943 (1968).
(23) D. L. Nelson and D. E. Irish, *J. Chem. Phys.*, **54**, 4479 (1971).

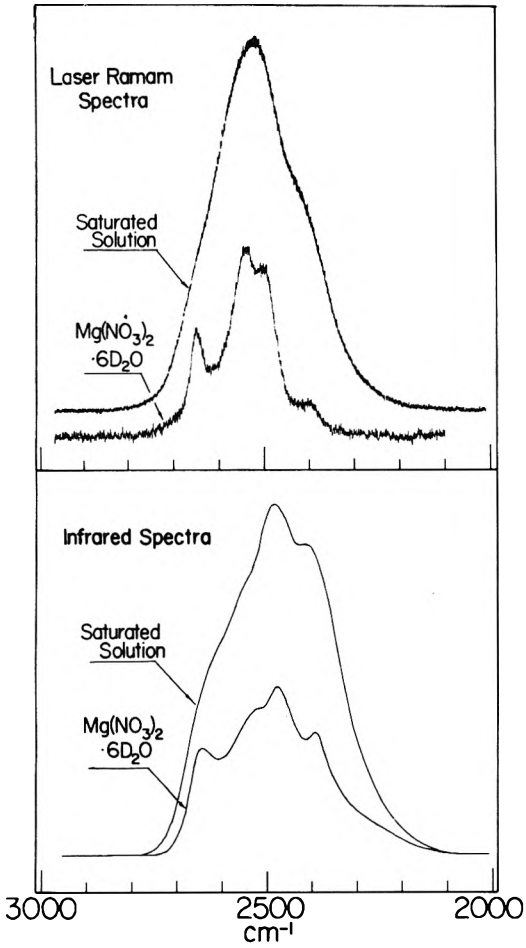

Figure 1. Argon ion laser Raman and infrared spectra in 2000–3000-cm^{-1} region for $Mg(NO_3)_2 \cdot 6D_2O$ crystals and its saturated solution in D_2O.

typical of the perturbation of the water spectrum by large anions and has been attributed to the disruption of water structure and formation of bonds between water and ions.[24] Similarities exist between the spectra of crystals of $Mg(NO_3)_2 \cdot 6H_2O$[10] and $Mg(NO_3)_2 \cdot 6D_2O$ and their respective saturated solutions (Figure 1). If each maximum in the spectrum of the crystal is attributed to a symmetric O–H stretch in a distinct environment it is apparent that there are four different environments for O–H in the crystal.[10] If, on the other hand, some of the maxima result from coupling, the number of distinct sites in the crystal will be less than four. The distinctions become less clear and the lines broaden due to rapid exchange in the liquid phase but the structure of the concentrated solution can be considered to approach that of the hexahydrate.

Intensity comparisons for a series of cations is also instructive. The total relative integrated intensity (718 and ~740 cm^{-1}, if present) in the $\nu_4(E')$ region is plotted against NO_3^- concentration in Figure 2. The intensities exhibit positive departures from the linearity exhibited by Mg^{2+} in the order $Sr^{2+} > Ca^{2+} > Ag^+ \sim Na^+ \sim NH_4^+$. This order does not correlate with that for the refractive indices of the solutions (Figure 3[25]) but parallels the degree of formation of ion pairs in these systems. This is further support for the lack of ion pairs in the magnesium system. Although ion pairs have not been observed by Raman spectroscopy in NH_4NO_3 solutions evidence of them was provided by Wishaw and Stokes.[26a] The perturbation of the nitrate ion by NH_4^+ is not sufficient to generate a set of distinctive lines separable from those of aquated nitrate ion (*cf.* $NaNO_3$[26b]). The intensity data for $\nu_4(E')$ converge to a common slope in dilute solution

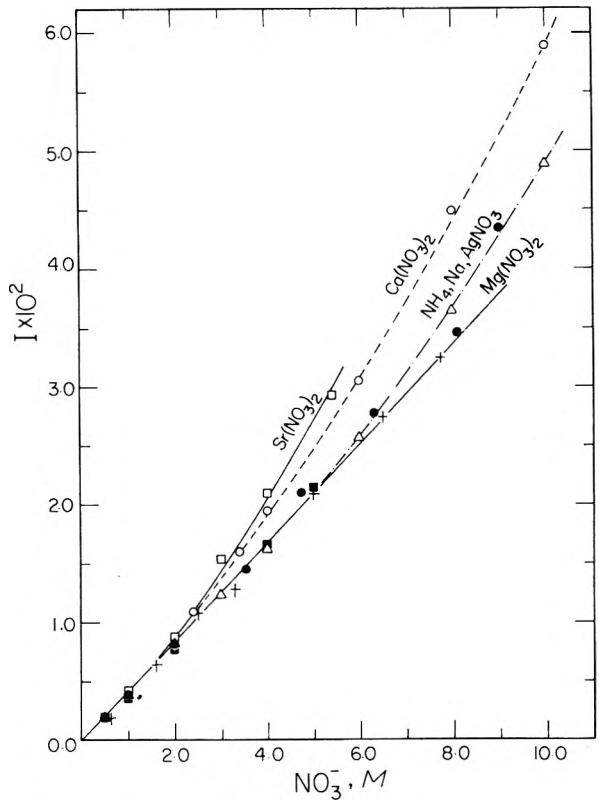

Figure 2. Total intensities (integrated intensity relative to I_{459} of CCl_4) of the $\nu_4(E')$ mode of vibration for the aqueous solutions of various metal nitrates as functions of nitrate ion concentration: □, $Sr(NO_3)_2$; O, $Ca(NO_3)_2$; ●, $AgNO_3$; △, NH_4NO_3; ■, $NaNO_3$; +, $Mg(NO_3)_2$.

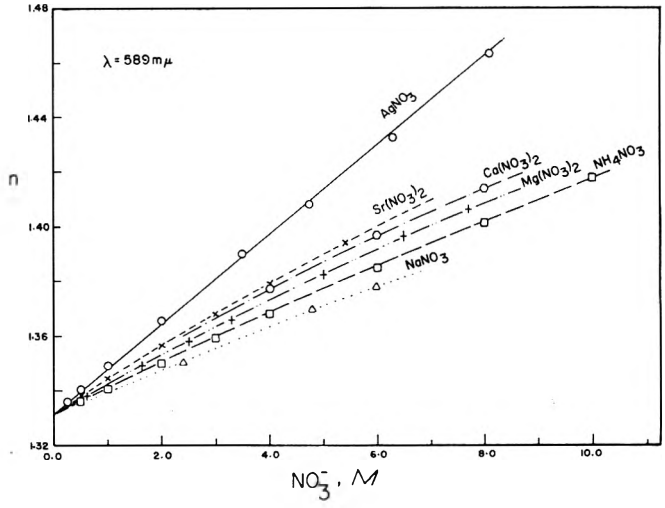

Figure 3. Refractive indices of $NaNO_3$, $AgNO_3$, NH_4NO_3, $Mg(NO_3)_2$, $Ca(NO_3)_2$, and $Sr(NO_3)_2$ in aqueous solutions: O, $AgNO_3$; ×, $Sr(NO_3)_2$; ○, $Ca(NO_3)_2$ (ref 25); +, $Mg(NO_3)_2$; □, NH_4NO_3; △, $NaNO_3$ (ref 25).

(24) G. E. Walrafen, *J. Chem. Phys.*, **36**, 1035 (1962).
(25) Y.-K. Sze, M.Sc. Thesis, University of Waterloo, Waterloo, Ontario, Canada, 1970.
(26) (a) B. F. Wishaw and R. H. Stokes, *Trans. Faraday Soc.*, **49**, 27 (1935); (b) J. D. Riddell, D. J. Lockwood, and D. E. Irish, *Can. J. Chem.*, **50**, 2951 (1972).

TABLE I: Curver Analyzed Results in the 660–800-cm^{-1} Region for $Mg(NO_3)_2 \cdot nH_2O$ Melts

R	Temp, °C	ν, cm^{-1}	$\Delta\nu_{1/2}$, cm^{-1}	I,[a] %	ν, cm^{-1}	$\Delta\nu_{1/2}$, cm^{-1}	I,[a] %	ν, cm^{-1}	$\Delta\nu_{1/2}$, cm^{-1}	I,[a] %	ν, cm^{-1}	$\Delta\nu_{1/2}$, cm^{-1}	I,[a] %
6.03	98	718	30	71.9	739	32	27.0	759	18	1.0	686	26	1.7
5.17	98	718	29	63.6	740	34	33.7	759	19	2.5	690	25	1.4
4.44	98	717	28	56.8	740	34	39.7	758	20	5.6			
4.06	98	718	29	54.8	741	33	33.6	759	22	11.7	690	22	1.4
3.45	99	717	28	45.4	739	36	38.0	759	26	17.0	693	20	1.1
2.90	134	716	29	49.2	740	35	27.4	760	29	25.2			
2.18	137	716	29	43.3	739	37	24.7	763	28	34.6			

[a] Intensity expressed as (I/I_{total}) 100%.

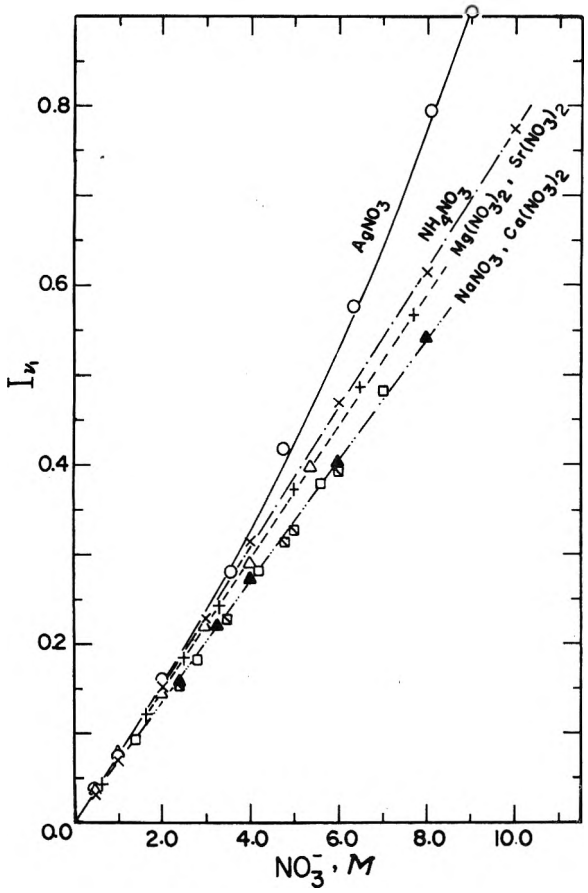

Figure 4. $\nu_1(A_1')$ band intensities of aqueous solutions of various metal nitrates as functions of nitrate ion concentration: O, $AgNO_3$; ×, NH_4NO_3; +, $Mg(NO_3)_2$; Δ, $Sr(NO_3)_2$; ⊠, $NaNO_3$ (ref 25); □, $NaNO_3$ (ref 22); ▲, $Ca(NO_3)_2$ (ref 25).

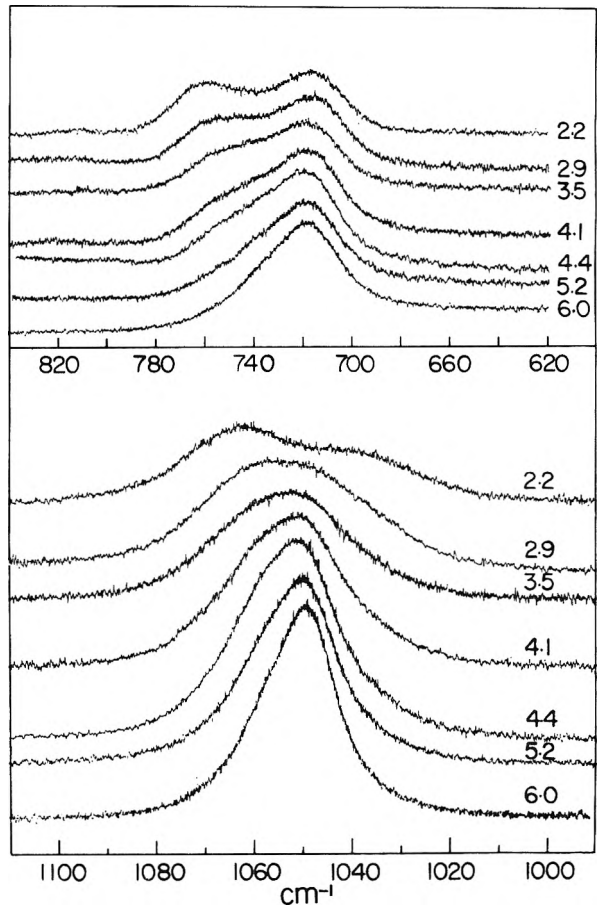

Figure 5. Raman spectra for $Mg(NO_3)_2 \cdot xH_2O$ melts: upper spectrum shows contours in 620–820-cm^{-1} region, 10 cm^{-1} slit width; lower shows 1000–1100-cm^{-1} region, 5 cm^{-1} slit width.

and this slope has been used as the molar intensity of free nitrate ion, J_F, in several studies. The value 4.05 ± 0.02 × 10^{-3} M^{-1} relative to the 459-cm^{-1} intensity of CCl_4 appears to be independent of cation and concentration. The curvatures suggest that J_F is less than the molar intensity of the ion pairs, J_B, although the difference is probably not large for 1+ cations.

The intensities of the $\nu_1(A_1')$ line are presented in Figure 4. It is clear that the rules which describe the relationship between intensity and concentration of a polarized band are different from those for a depolarized band and are not readily apparent. Silver nitrate in particular exhibits a number of unique spectral properties and will be discussed in detail in a subsequent paper. The linearities are not consistent with the data of Vollmar.[9]

Hydrate Melts. At temperatures of 98° and R = 6 three lines were observed in the low-frequency region: 82, 240, and 345 cm^{-1}. On reduction of R the 240-cm^{-1} line disappeared, the 345-cm^{-1} line shifted down to about 340 cm^{-1} and became very weak, the 82 cm^{-1} line shifted upward to 90 cm^{-1}, and a 190-cm^{-1} line was observed when R < 3.0. The 90- and 190-cm^{-1} lines may be attributed to restricted translatory or rotatory motions of nitrate ion. The other features are consistent with aquated magnesium cations.

Nitrate ions exist in three distinct environments in these systems. Raman spectra of the $\nu_4(E')$ region and $\nu_1(A_1')$ region reveal several closely spaced lines (Figure 5). Computer analysis indicates three components in each region: 717, 739, and 759 cm^{-1} (Table I and Figure 6A) and 1052, 1064, and 1039 cm^{-1}. The frequency of ν_2 and $2\nu_2$ drops from 825 to 819 cm^{-1} and from 1648 to 1637

TABLE II: Raman Frequencies[a] of the Three Kinds of Nitrate Ions in Hydrated Magnesium Nitrate Melts

Free nitrate ion	Monodentate nitrate ion	Bidentate nitrate ion
718 dp $\nu_3(A_1)$, $\nu_5(B_1)$	740 dp $\nu_3(A_1)$, $\nu_5(B_1)$	759 dp $\nu_3(A_1)$, $\nu_5(B_1)$
825 dp $\nu_6(B_2)$	821 dp $\nu_6(B_2)$	819 dp $\nu_6(B_2)$
1052 p $\nu_2(A_1)$	1039 p $\nu_2(A_1)$	1064 p $\nu_2(A_1)$
1360 p $\nu_1(A_1)$	1330 p $\nu_1(A_1)$	1377 dp $\nu_4(B_1)$
1430 dp $\nu_4(B_1)$	1466 dp $\nu_4(B_1)$	1515 p $\nu_1(A_1)$
1648 p $2\nu_6(A_1)$	1642 p $2\nu_6(A_1)$	1637 p $2\nu_6(A_1)$

[a] Frequencies of the ν_1 and ν_4 bands are uncertain to about 10 cm^{-1} because of serious overlapping.

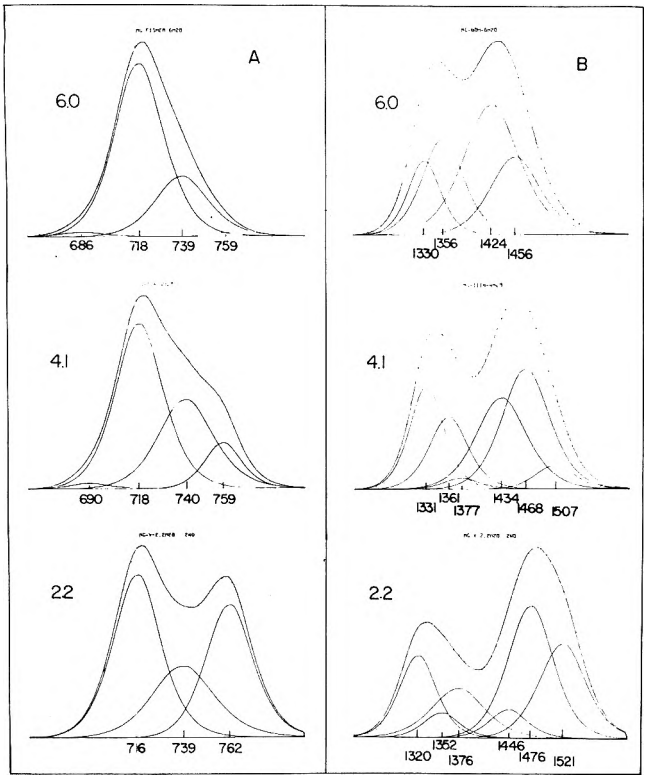

Figure 6. Computer analyzed contours from 660 to 800 cm^{-1} and from 1230 to 1620 cm^{-1} for $Mg(NO_3)_2 \cdot xH_2O$ melts. The molar ratios of water to magnesium nitrate are shown beside the contours.

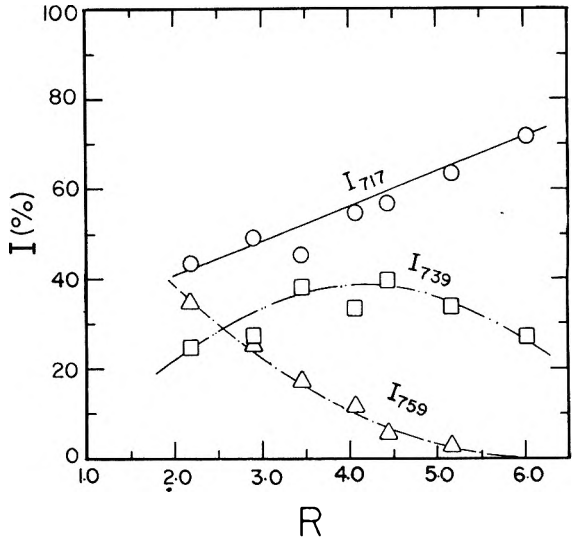

Figure 7. Percentage intensity in the 717-, 739-, and 759-cm^{-1} lines as a function of R.

cm^{-1}, a feature which is also characteristic of cation-anion contact. The envelope in the $\nu_3(E')$ region resolves into three pairs of lines (Figure 6B). For R = 6 two pairs are apparent at 1424 dp, 1356 p and 1456 dp, 1330 p. As R is reduced the intensity of the first pair continuously decreases and the intensity of the second pair rises to a maximum at about R = 3.5. A third pair, 1507-1521 p, 1377 dp increases in intensity as R is reduced below three. These positions are probably within 10 cm^{-1} but the trends are clear and similar to those observed for the ν_4 and ν_1 regions. The intensity changes, illustrated for the ν_4 region in Figure 7, permit division of the lines into three groups as summarized in Table II.

The assignments of the lines (Table II) are based on a C_{2v} perturbation of NO_3^-. The positions differ but the trends parallel those observed for the three different crystalline hydrates.[10] For example, 1052 changing to 1039 for monodentate and 1064 for bidentate types of nitrate is paralleled by 1060 (hexahydrate) changing to 1050 (tetrahydrate) and 1070 cm^{-1} (dihydrate). The orientation to the cation, monodentate or bidentate, is inferred from the polarization of the 1330- and 1515-cm^{-1} lines, respectively, and from their comparative intensities.[27-29] Because the molar intensities of the three types of nitrate are unknown, and the total intensities of the samples have not been calibrated against a standard, the populations in the three environments cannot be deduced. It is possible that bound nitrate also contributes intensity at 717 cm^{-1} (Figure 7) in these melts and thus inferences concerning populations may be unreliable. It appears, however, that as R decreases, outer-sphere nitrate is replaced by nitrate ion contacting Mg^{2+} in monodentate fashion which converts to bidentate fashion on further reduction of water content. It has been shown that this coordination scheme is frozen into the crystalline hydrates.[10]

These conclusions differ from those of Peleg[13] who adopted a model involving nonspecific, increasing perturbation of nitrate ion with decreasing water content. Evidence for contact cation-anion aggregates presented above is strong however at R = 6 and 98° and is interpretable in terms of a distribution of nitrate ions between several environments. The analysis of the ν_4 region differs in that Peleg assumed only one line which continuously shifts from 725 (R = 6) to 755 cm^{-1} (R = 2) in addition to the 717-cm^{-1} band; in our interpretation this shifting contour has been analyzed in terms of two bands from nitrate ions in two different environments which differ in orientation to the cation. Similarly the changing contours in the ν_1 and ν_3 regions have been interpreted in terms of lines

(27) H. Brintzinger and R. E. Hester, *Inorg. Chem.*, **5**, 980 (1966).
(28) R. E. Hester and W. E. Grossman, *Inorg. Chem.*, **5**, 1308 (1966).
(29) D. Smith, D. W. James, and J. P. Devlin, *J. Chem. Phys.*, **54**, 4437 (1971).

from these three types of nitrate ion, which successively become significant as water content decreases, rather than by abrupt changes at particular values of R. The evidence for the monodentate-to-bidentate reorientation has also not been advanced before. It should be noted that aqueous systems at 98° and with $R > 6$ which were studied by Peleg have not been examined in this work. We anticipate that as the water content increases the concentrations of contact ion aggregates smoothly decrease at 98°. The higher temperature may enhance inner-sphere interaction.[30]

No extensive water structure can exist in these melts and all water must be strongly oriented by the ions. The Raman active water bending vibration is weak and obscured by $2\nu_2$ of nitrate ion. The intensity at 3250 cm^{-1} is greatly diminished and the contour maximum shifts from 3425 to 3510 cm^{-1}. Although the lines are still broad, reflecting rapid exchange of water among a number of sites such that computer analysis does not appear fruitful, the positions of maxima are very similar to the sharper features observed for each corresponding crystalline sample.[10]

Conclusions

The constitution of the $Mg(NO_3)_2$–H_2O systems is conveniently summarized in terms of a series of equilibria (Scheme I) sensitive to the water content. Solvent-shared ion pairs are present when $2 < C < 3.9$ (25°) (*i.e.*, $42 < R < 11$). Contact ion aggregates are present when R is 6 (98°) and a monodentate to bidentate conversion occurs as water is further reduced. Although six coordination can be retained about Mg^{2+} when $R < 6$ (*cf.* ref 10) it need not be so.

Scheme I: Equilibria in the $Mg(NO_3)_2$–H_2O System

$$Mg(H_2O)_6^{2+} + NO_3^-(aq) \overset{-H_2O}{\rightleftharpoons} \underset{\text{solvent-shared ion-pair}}{Mg^{2+}(H_2O)_6NO_3^-} \overset{-H_2O}{\rightleftharpoons}$$

$$\underset{\text{monodentate}}{Mg^{2+}(NO_3^-)_x(H_2O)_{6-x}} \overset{-H_2O}{\rightleftharpoons} \underset{\text{bidentate}}{Mg^{2+}(NO_3^-)_x(H_2O)_{6-2x}}$$

Acknowledgments. This work was supported by the National Research Council of Canada. The assistance of Dr. D. J. Lockwood is greatly appreciated. Thanks are also extended to Dr. M. Peleg for providing a preprint of his manuscript and for helpful discussion.

(30) S. A. Al-Baldawi, M. F. Brooker, T. E. Gough, and D. E. Irish, *Can. J. Chem.*, **48**, 1202 (1970).

Infrared Spectrum of the Water–Hydrochloric Acid Complex in Solid Nitrogen

Bruce S. Ault and George C. Pimentel*

Chemistry Department, University of California, Berkeley, California 94720 *(Received September 11, 1972) Publication costs assisted by the Office of Naval Research*

The infrared spectrum was recorded of the 1:1 complex of HCl and H_2O (and the deuterated counterparts) isolated in a nitrogen matrix at 15°K. The H_2O·HCl complex absorbs at 2638, 2540, and 460 cm^{-1}, whereas D_2O·DCl absorbs at 1916, 1849, and 330 cm^{-1}. The spectra of the mixed isotopic species show that the hydrogen atoms are not equivalent. This fact, and a comparison to the spectra of prototype compounds, show that the complex does not involve hydronium ion, but, rather, a simple hydrogen bond, $H_2O\cdots H$–Cl, in which the HCl hydrogen atom remains attached to the chlorine atom. This result can be rationalized with thermodynamic considerations about the stability of an isolated $H_3O^+\cdot Cl^-$ ion pair.

It is well established that an equimolar mixture of HCl and H_2O condenses to an ionic crystal made up of H_3O^+ and Cl^- ions.[1,2] However, it seems likely that this formation of H_3O^+ may depend to a significant extent upon the stabilization furnished by the crystalline environment.[3,4] Whether the proton transfer from HCl to H_2O would occur in absence of this stabilization is not known, a matter whose importance is enhanced by the often presumed presence of H_3O^+ in aqueous solutions of strong acids.

In principle, the dimer formed between a molecule of H_2O and a molecule of HCl could be spectroscopically studied either in the gas phase or in inert solvent solutions. However, such studies of weakly bound complexes are rather difficult, in part because of the diffuse infrared spectra displayed by hydrogen bonded substances, and because solubilities are very low in the weakly interacting infrared transparent solvents. Consequently, we have employed the matrix isolation technique to investigate the nature of the hydrogen bond formed between single molecules of HCl and H_2O and to determine whether the complex can be said to involve H_3O^+.

(1) C. C. Ferriso and D. F. Hornig, *J. Chem. Phys.*, **23**, 1464 (1955).
(2) Y. K. Yoon and G. B. Carpenter, *Acta Crystallogr.*, **12**, 17 (1959).
(3) C. A. Coulson, "Valence," 1st ed, Oxford University Press, New York, N. Y., 1952, p 268.
(4) C. Kittel, "Introduction to Solid-State Physics," Wiley, New York, N. Y., 1971.

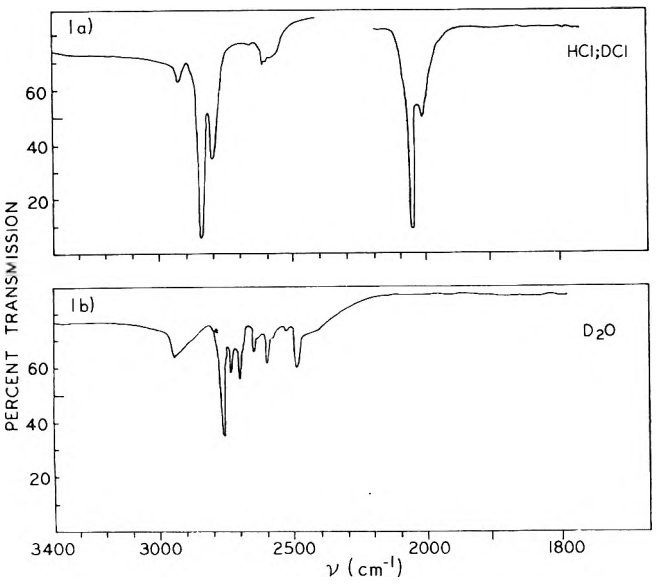

Figure 1. (a) The infrared spectrum of HCl and DCl isolated in a nitrogen matrix at 15°K. (b) The ir spectrum of D_2O isolated in a N_2 matrix under the same conditions.

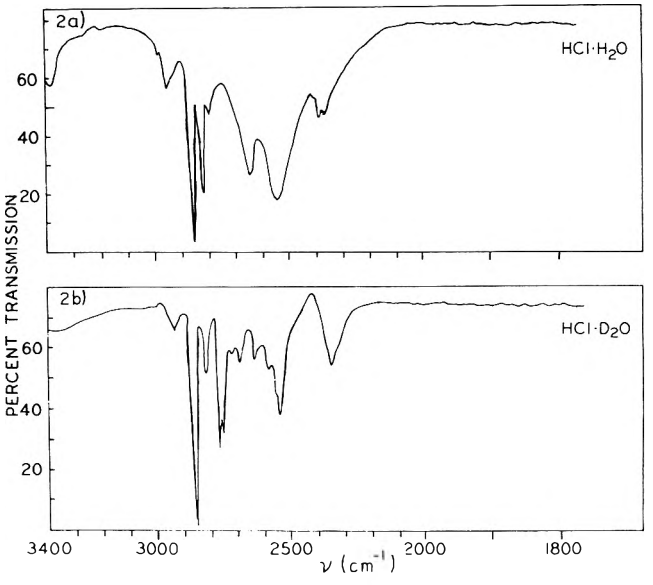

Figure 2. (a) The infrared spectrum of the products of a one-jet deposition of H_2O:HCl:N_2 at 1:1:350, over the spectral region 3400–1800 cm^{-1}. (b) The infrared spectrum of the products of a two-jet codeposition of HCl and D_2O, both 1:175 in N_2.

Experimental Section

We used a conventional double dewar, liquid hydrogen cold cell, equipped with two deposition inlets and a cesium iodide cold window. In each experiment, about 40 mmol of a matrix sample was deposited at 5 mmol/hr. The window temperature was maintained at 15°K and its temperature was monitored during deposition and spectroscopic study with a Au-Co/Cu thermocouple embedded in the window. The infrared spectrum was scanned from 200 to 4000 cm^{-1} with a Perkin-Elmer Model 225 infrared spectrophotometer. Frequency accuracy was ±0.5 cm^{-1} and the spectral slit width was 2.0 cm^{-1} at 3000 cm^{-1}.

Some samples were prepared by placing 2 ± 0.2 Torr pressure of H_2O vapor in a 3-l. bulb, then an equal pressure of HCl was added, followed by 700 Torr of N_2 to give a mixture with approximate composition H_2O:HCl:N_2 = 1:1:350. For two-jet experiments, an H_2O:N_2 = 1:175 mixture was prepared in one bulb and an HCl:N_2 = 1:175 mixture in another and then the two mixtures were simultaneously deposited from separate deposition lines. Both HCl (Matheson, 99%) and DCl (Merke, Ltd., Canada) were purified by double distillation from a Dry Ice–acetone bath into a liquid nitrogen trap. Both liquid H_2O and D_2O (ICN, 99.8%) were used without purification except for degassing by repeated freeze-thaw cycles under vacuum, using a Dry Ice–acetone bath.

Results

For reference, spectra were recorded of the parent substances, HCl, DCl, H_2O, and D_2O, each in turn deposited alone in N_2 in a mole ratio of 1 to 350. Then HCl and H_2O were examined together, both with single- and two-jet depositions. Next, a succession of experiments were conducted using a variety of isotopic mixtures.

Parent Spectra. Figure 1a shows the spectra of HCl:N_2 and DCl:N_2 samples, as recorded between 3400 and 1800 cm^{-1}. At this concentration, HCl absorbs at 2854 (0.85) and 2810 (0.39) cm^{-1} (optical densities are given parenthetically). The DCl bands are found at 2062 (0.89) and 2033 (0.30) cm^{-1}. Figure 1b shows the spectrum of a D_2O:N_2 = 1:350 sample in this same spectral region. Six distinguishable features are observed, at 2761 (0.35), 2722 (0.10), 2704 (0.13), 2645 (0.06), 2590 (0.10), and 2495 (0.08) cm^{-1}. When an H_2O:N_2 = 1:350 sample is deposited, there are no absorptions in the region 3400–1800 cm^{-1}.

None of these parent molecule spectra displayed any absorption in the spectral range 600–250 cm^{-1}. Of course, the water bending modes were observed: H_2O at 1600 cm^{-1}, HDO at 1402 cm^{-1}, and D_2O at 1178 cm^{-1}. Three weak absorptions that seemed related to each other were occasionally observed at 1260, 1070, and 815 cm^{-1}; these features grew after diffusion and they are attributed to H_2O polymeric species.

HCl + H_2O. Figure 2a shows part of the spectrum of an H_2O:HCl:N_2 = 1:1:350 mixture deposited from a single jet. The HCl absorptions shown in Figure 1a are clearly apparent together with two new broad features at 2638 and 2540 cm^{-1}. The latter, more prominent band is about 50 cm^{-1} in breadth at half-height. The apparent absorption near 2330 cm^{-1} is not reproducible (in these and in the spectra of isotopically substituted samples) and is evidently due to instrument drift in the region of atmospheric CO_2 absorption. In the spectra of some samples, there were other quite weak bands at 900, 970, and 1200 cm^{-1}, the last extremely broad, all of which were too weak and irreproducible to be assigned to the absorber responsible for the 2540-cm^{-1} band.

Figure 3a shows the spectral range 600–200 cm^{-1} for the same sample whose spectrum is shown in Figure 2a. There is a broad band centered at 460 cm^{-1} with a shoulder at 520 cm^{-1}. All of these absorptions are listed in Table I together with their optical densities.

No new bands could be detected near 3500 cm^{-1}, but this spectral region is badly obscured by parent H_2O bands.

The sample whose spectrum is shown in Figures 2a and 3a was carefully warmed to 35–40°K and then recooled to 15°K. All of the features listed in the first column of Table I disappeared (though the low-frequency spectrum

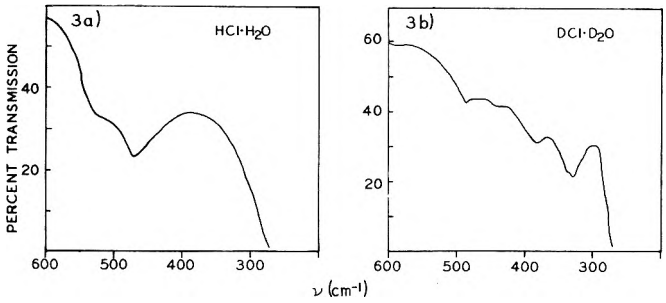

Figure 3. (a) The ir spectrum of the products of a one-jet deposition of HCl and H_2O, in the spectral region 600–200 cm^{-1}. (b) The same spectral region for the products of the one-jet deposition of DCl and D_2O in N_2.

TABLE I: Absorption Frequencies[a] and Optical Densities[b] of Water and Hydrochloric Acid Mixtures (N_2, 15°K)

H_2O:HCl ν, cm^{-1}	D_2O:DCl ν, cm^{-1}	D_2O:HCl ν, cm^{-1}	H_2O:DCl ν, cm^{-1}
2638 (0.57)		2645 (0.12)	
2540 (0.85)		2533 (0.29)	
	1916 (0.34)		1915 (0.38)
	1849 (0.38)		1850 (0.39)
520 (0.14)			
460 (0.31)			
	393 (0.06)		
	330 (0.18)		

[a] Absorptions also observed in the parent molecule matrix spectra are omitted as well as absorptions that grow on diffusion (see text). [b] Optical densities are given parenthetically.

was of poor quality because of scattering) and intense, broad bands centered near 3400, 2800, and 1600 cm^{-1} appeared, all attributable to polymers and higher aggregates of H_2O and HCl.

A two-jet experiment was conducted with H_2O and HCl and the bands at 2638 and 2540 cm^{-1} were reproduced with the same relative intensity to each other, though somewhat weaker relative to parent bands. The feature at 460 cm^{-1} was observed as well, but it was more diffuse.

DCl + D_2O. Figure 4a shows the 3400–1800-cm^{-1} spectral region for a D_2O:DCl:N_2 = 1:1:350 sample. The HCl and DCl features show that exchange in the vacuum line established a D/H ratio near 3–4. The band at 2540 cm^{-1} is present but weak, evidently replaced by the intense, and rather broad bands at 1916 and 1849 cm^{-1}. Figure 3b shows no absorption at 460 cm^{-1} but a weak band appears near 330 cm^{-1} and a shoulder near 393 cm^{-1}. The intensities of these features are listed in Table I.

HCl + D_2O and DCl + H_2O. Figure 2b shows the spectrum obtained in a two-jet deposition involving HCl and D_2O. The freedom from exchange is demonstrated by the complete absence of the DCl parent absorptions at 2062 cm^{-1}. Of course, the region near 2600 cm^{-1} is cluttered by the D_2O bands in this region, but a broad band at 2533 cm^{-1} is observed that is remarkably similar to the 2540-cm^{-1} absorption shown by HCl + H_2O (Figure 2a). No absorption whatsoever is observed near 1800 cm^{-1}.

Figure 4b shows the counterpart two-jet deposition spectrum involving DCl and H_2O. This time, there is HCl parent absorption at 2854 cm^{-1} due to DCl exchange with the vacuum line. Nevertheless, the major spectral features are found at 1915 and 1850 cm^{-1} with only weak absorption in the 2600-cm^{-1} region.

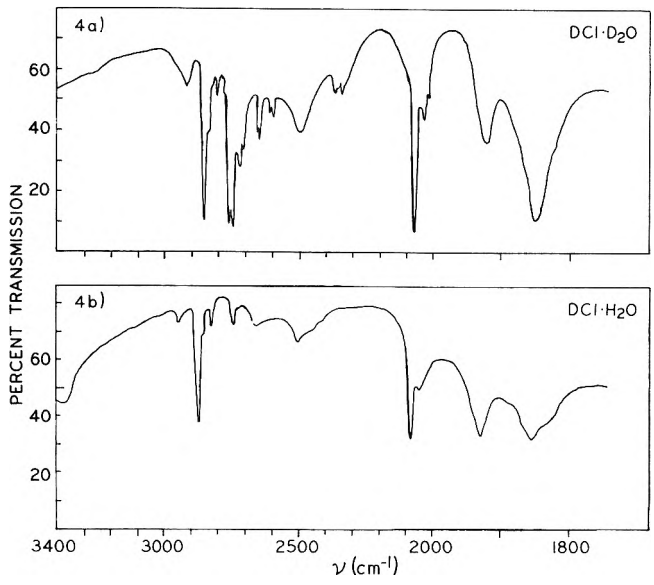

Figure 4. (a) The infrared spectrum of the products of the one-jet deposition of DCl and D_2O in N_2, at 1:1:350, over the region 3400–1800 cm^{-1}. (b) The ir spectrum of the products of the two-jet codeposition of DCl and H_2O, both 1:175 in N_2.

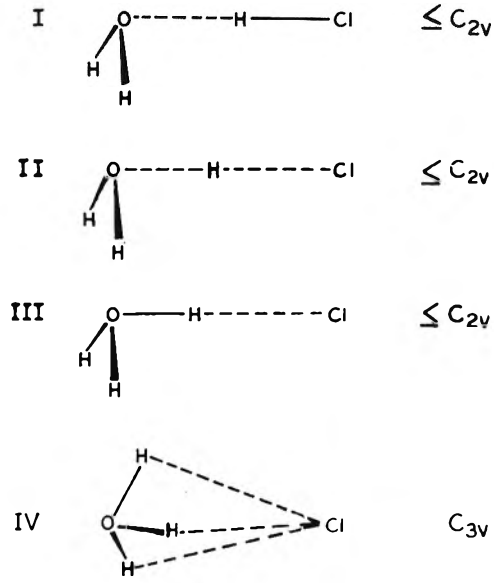

Figure 5. Four possible prototype structures for the isolated H_2O·HCl complex.

In these, as in all two-jet experiments, no definite band identifications could be made in the 600–200-cm^{-1} region.

Discussion

Figure 5 shows four possible distinctive structures of the H_2O·HCl complex. The first structure could be characterized as a "normal" hydrogen bonding interaction in which the proton donor forms a hydrogen bond and weakens, but does not rupture the parent A–H bond. The structure II we will call a "complete sharing" hydrogen bond, one in which the proton is not preferentially attached to either terminal atom. This would be analogous to the situation in $(FHF)^-$, except that the bond would not be centrosymmetric because the terminal atoms are different. Structures III and IV involve hydronium chloride ion pairs in which the proton has been transferred over from HCl to the H_2O molecule to form an identifiable H_3O^+ ion. Such

TABLE II: Prototype Spectra Compared to $H_2O \cdot HCl$ (N_2 Matrix)

	System (ref)			
$H_2O \cdot HCl$ N_2 matrix	$(CH_3)_2O \cdot HCl$ (10)	$(ClHCl)^-$ (13)	$H_3O^+ \cdot Cl^-$ (see text)	$H_3O^+Cl^-$ (1)
	Prototype for Structure			
This work	I	II	III	IV
	Frequencies, cm^{-1}			
			3400–3800[a]	
				3235
			3020[a]	
2638	2690			
2540	2570			2590
		1800–800[a]	1600[a]	1700
		1600–600[a]		1060
520	525			
460	475			
(100)[b]	(120)[b]			
(60)[c]	(50)[c]			

[a] Estimated; see text. [b] Inferred from the difference between 2640 and 2538 cm^{-1} (and between 2690 and 2570 cm^{-1}). [c] Inferred from the difference between 520 and 460 cm^{-1} (and between 525 and 475 cm^{-1}).

an ion pair could have C_{2v} or lower symmetry (structure III) or C_{3v} symmetry (structure IV).

The present work provides a significant basis for choosing among these four possibilities, first through the implications of the mixed isotope spectra and then, further, through comparisons to prototype systems.

Mixed Isotope Spectra. The obvious similarities in Figures 2a and 2b and again in Figures 4a and 4b show unequivocally that the broad absorptions centered at 2540 and at 1849 cm^{-1} are due specifically to the hydrogen atom provided by the hydrochloric acid molecule. Under the conditions of the experiment, there is clearly no exchange between this atom and the two hydrogens of the water molecule. This immediately rules out structure IV, the $H_3O^+ \cdot Cl^-$ complex involving equivalent H atoms in a C_{3v} structure. The behavior is obviously consistent with the hydrogen bond formation implied by structure I, in which the unique hydrogen atom remains closest to and most strongly bound to its parent chlorine atom. The evidence can be reconciled with structures II and III only if it is postulated that there is a significant barrier to interchange among the hydrogen atoms in the complex, even though the unique proton has been substantially "released" by the chlorine atom. This seems a particularly unlikely postulate for structure III, in which relatively small barrier to reorientation would be expected in the ion pair.

Thus the mixed isotope spectra favor structure I, they perhaps are consistent with II, they disfavor III, and they eliminate IV.

Prototype Compounds. Structure I is like that of the dimethyl ether–hydrochloric acid complex, whose spectrum has been thoroughly studied in the gas,[5-7] solution,[8] and solid[9] phases. In the gas-phase spectrum, part of which is reproduced in Table II, the peak of the broad HCl absorption is found at 2570 cm^{-1} (2530 cm^{-1} in the crystal[9]). Coarse structure is observed on both sides of the peak with spacings near 120 cm^{-1}. The bending motion, in which the proton moves perpendicular to the hydrogen bond, is found at 475 cm^{-1} [10] and it shifts to 335 cm^{-1} for DCl.

Structure IV can be likened to crystalline $H_3O^+ \cdot Cl^-$, which has crystal symmetry R_{3m} with a rhombohedral unit cell.[2] In this lattice, the hydronium ion is a flat pyramid occupying a site of C_{3v} symmetry; each O–H forms a hydrogen bond to the nearest Cl^- ion. Hence the three hydrogen atoms are equivalent; the O···Cl distances are each 2.95 Å. The vibrational frequencies[1] and symmetry assignments[11] are 3235 (ν_3,E), 2590 (ν_1,A), 1700 (ν_4,E), and 1060 cm^{-1} (ν_2,A). This set of frequencies furnishes a model spectrum for structure IV, as given in Table II.

An expected spectrum for structure III can be reasonably conjured from the $H_3O^+ \cdot Cl^-$ spectrum. The degeneracy weighted average of the H_3O^+ stretching modes, 3020 cm^{-1}, can be taken to be a frequency characteristic of an O–H bond of H_3O^+ when only that bond is hydrogen bonded to Cl^- at 2.95-Å separation. The other two O–H stretching modes would not be shifted by hydrogen bonding, so they would be found at much higher frequencies, probably between 3400 (the mean frequency for NH_3) and 3800 cm^{-1}.

Though we have no direct prototype for structure II, its spectrum can be guessed with sufficient confidence. "Complete sharing" in hydrogen bonds is well identified in a number of centrosymmetric cases, such as FHF^-, $(H_2O \cdot H \cdot H_2O)^+$, and in a number of O···H···O hydrogen bonds in acid salts. Invariably these "complete sharing" situations are accompanied by extremely large frequency shifts,[12] always exceeding 1000 cm^{-1}, and the bending frequencies are always high. The two types of bichloride ion identified by Evans and Lo[13] are also relevant. These workers conclude that type II crystals involve a centrosymmetric $(ClHCl)^-$ ion with ν_3 near 770 cm^{-1} and the bending mode ν_2 is assigned to be near 1050 cm^{-1}. This ν_3 frequency represents a shift exceeding 2000 cm^{-1}. In contrast, ν_3 is found near 1575 cm^{-1} in type I crystals, where the proton is considered to be asymmetrically placed, hence not completely shared. With these examples in mind, ν_3 of structure II must be below 2000 cm^{-1}, probably in the range 1800–800 cm^{-1} and the bend would fall in the range 1600–600 cm^{-1}.

Table II summarizes these prototype spectra and compares them to the matrix spectrum reported here. The similarity to the $(CH_3)_2O \cdot HCl$ spectrum could hardly be closer and it strongly favors structure I.

Hydrogen Bond Vibrational Potential Function. By analogy to the $(CH_3)_2O \cdot HCl$ complex, our spectrum indicates that the HCl stretching frequency is at 2540 cm^{-1} and one of the Cl–H bending frequencies is at 460 cm^{-1}. Treating each of these as an isolated vibration, we obtain force constants of 3.98 and 0.13 mdyn/Å, respectively.

The assignment of the low-frequency mode at 100 cm^{-1}, inferred from the structure on the 2540-cm^{-1} band, is more doubtful. The spacing in the deuterium compound shows a large isotope shift, which dictates that the vibration be assigned as another hydrogen bending mode with a

(5) J. E. Bertie and D. J. Millen, *J. Chem. Soc.*, **497**, 514 (1965).
(6) J. Arnold and D. J. Millen, *J. Chem. Soc.*, **503**, 510 (1965).
(7) J. Le Calve, P. Grange, and J. Lascombe, *C. R. Acad. Sci.*, **260**, 6065 (1965); **261**, 2075 (1965).
(8) I. M. Aref'ev and V. I. Malyshev, *Opt. Spektrosk.*, **13**, 112 (1962).
(9) R. M. Seel and N. Sheppard, *Spectrochim. Acta, Part A*, **25**, 1287 (1969).
(10) J. E. Bertie and M. V. Falk, "On the Infrared Spectrum of Gaseous $(CH_3)_2O \cdot HCl$," Paper 17, International Conference on Hydrogen Bonding, August 21–25, Ottawa, Canada.
(11) M. Fournier, G. Maskharpa, D. Rousselet, and J. Potier, *C. R. Acad. Sci.*, **269**, 279 (1969).
(12) H. N. Shrivastava and J. C. Speakman, *J. Chem. Soc.*, **1151** (1961).
(13) J. C. Evans and G. Y-S. Lo, *J. Phys. Chem.*, **70**, 11 (1966).

surprisingly low force constant, 0.006 mdyn/Å. The spacing of the shoulder on the band at 460 cm^{-1} suggests another low-frequency mode at 60 cm^{-1}. Since this spacing displays no deuterium shift, this mode might be the O···Cl stretching mode. If so, the hydrogen bond stretching force constant would be 0.023 mdyn/Å.

We have, of course, no evidence about the hydrogen bond energy except that it must be near that of the $(CH_3)_2O \cdot HCl$ complex, which has been measured to be 7.1 kcal/mol.[14]

Comparison to Other Systems. Many acids react with water or ammonia to form ionic crystals but in very few cases is there evidence about the nature of the corresponding bimolecular complex. The $H_3N \cdot NH_3$ complex was the first such system to be investigated using matrix isolation in a search for ion pair formation. Van Thiel and Pimentel[15,16] examined the infrared spectra of codeposited ammonia and hydrazoic acid in a nitrogen matrix. The spectra revealed a 400-cm^{-1} shift of the H–N stretching frequency of HN_3 and a rather intense bending mode at 1220 cm^{-1} but there was no evidence for the characteristic absorptions of ammonium ion. More recently, Jones and Sheppard[17] have recorded the gas-phase spectrum of the $H_3N \cdot HCN$ complex and concluded that the proton does not transfer to form an ammonium cyanide ion pair structure.

Clementi[18,19] has attempted *ab initio* LCAO–SCF calculations on the $H_3N \cdot HCl$ complex. In the later work,[19] minimum energy is shown to occur at an N–Cl distance of 2.86 Å, much shorter than the N–Cl distance in solid NH_4Cl, 3.26 Å (NaCl form). Furthermore, the energy minimum[19] is obtained with the H atom in a position that is best characterized as completely shared, as in structure II. The H···Cl distance is 1.62 Å, 0.21 Å longer than in HCl, and the N···H distance is 1.24 Å, 0.23 Å longer than in NH_3. The complex is calculated to be stable by 19.5 kcal.[18] Thus, this theoretical calculation suggests that the $H_3N \cdot HCl$ complex will be like the structure II, rather than like the structure I that was found here for the $H_2O \cdot HCl$ counterpart. Of course, the omission of configuration interaction in the calculations and, hence, correlation energy, introduces an unknown uncertainty in the theoretical calculations.

Thus, there are relatively few analogous cases with which to compare. All of the experimental results concur in that the proton transfer does not occur.

Thermodynamic Considerations. Since Kebarle, *et al.*,[20] have measured the heat of formation of gaseous H_3O^+, we can calculate ΔH for the gaseous reaction

$$H_2O(g) + HCl(g) \rightarrow H_3O^+(g) + Cl^-(g) \quad \Delta H = +168 \text{ kcal/mol}$$

If ion pair formation is to occur with $\Delta H = -7$ kcal, then the two (point) charges would have to be brought together to a distance of 1.90 Å, far below the observed 2.95 Å O···Cl distance in the $H_3O^+ \cdot Cl^-$ crystal. Plainly, these energetics are quite unfavorable and they provide a gross rationalization of the preference for structure I.

Conclusions

These spectra strongly indicate that the $H_2O \cdot HCl$ complex in solid N_2 involves a hydrogen bond much like that in the $(CH_3)_2O \cdot HCl$ complex in which proton transfer to form H_3O^+ does not occur. This conclusion is consistent with the other cases for which experimental information is available: $H_3N \cdot HN_3$ (matrix) and $H_3N \cdot HCN$ (gas). The ubiquitous formation of ionic crystals between acids and water or ammonia must, then, be attributed to cooperative stabilization of the ionic species by the ionic lattice.

Acknowledgment. We gratefully acknowledge support of this research by the U. S. Office of Naval Research under Grant No. N00014-69-A-0200-102.

(14) G. Govil, A. D. H. Clague, and H. J. Bernstein, *J. Chem. Phys.*, **49**, 2821 (1968).
(15) M. Van Thiel and G. C. Pimentel, *J. Chem. Phys.*, **32**, 133 (1960).
(16) M. Van Thiel, Ph.D. Dissertation, University of California, Berkeley, 1958.
(17) W. J. Jones and N. Sheppard, *Spectrochim. Acta, Part A*, **25**, 385 (1969).
(18) E. Clementi, *J. Chem. Phys.*, **46**, 3851 (1967).
(19) E. Clementi and J. N. Gayles, *J. Chem. Phys.*, **47**, 3837 (1967).
(20) P. Kebarle, S. K. Searles, A. Zolla, J. Scarborough, and M. Arshadi, *J. Amer. Chem. Soc.*, **89**, 6393 (1967).

Gas-Phase Ultraviolet Absorption Spectrum of Nitric Acid Vapor

Harold Johnston* and Richard Graham

Department of Chemistry, University of California and Inorganic Materials Research Division, Lawrence Berkeley Laboratory, Berkeley, California 94720 *(Received July 27, 1972)*

Publication costs assisted by the University of California

The absorption cross section for nitric acid vapor has been determined between 190 and 325 nm at room temperature. The results agree with work by Dalmon over a shorter wavelength interval. The nitric acid spectrum is a continuum, consists of at least two different electronic states, and obeys Beer's law throughout the region. The absorption cross section is above 10^{-17} cm^2 at 190 nm, about 10^{-20} cm^2 between 240 and 290 nm, and less than 10^{-22} cm^2 from 322 to 370 nm, which is the upper wavelength range of this study.

Nitric acid vapor is an important by-product of photochemical smog,[1] and it is an important trace constituent in the lower stratosphere.[2] For photochemical smog, the interesting wavelength region for the absorption coefficient and quantum yields is that above 300 nm. For the stratosphere, the entire wavelength region above 190 nm is interesting. This article gives the absorption spectrum from 190 to 370 nm. Work is in progress concerning the quantum yields and the identity of the primary products of the photolysis processes.

Experimental Section

The observations were made with a McPherson 0.3-m scanning monochromator in conjunction with a multiple reflection long-path gas cell. The 45-l. cell consisted of a 6-ft long quartz tube, 6 in. in diameter, and nickel-plated stainless-steel end caps. External lines were glass or stainless steel. The base path of the cell is 8.6 m, and optical paths of 8.6 to 34.4 m were used. A slit width of 0.5 mm gave 0.7-nm resolution. The source lamp was a Sylvania deuterium arc, and a set of mirrors mounted near the cell entrance and exit windows diverted part of the light as a reference beam. A filter was used above 370 nm to remove light diffracted in second order. The source beam was chopped at 400 cps and detected with a photomultiplier and a lock-in amplifier. Scans were recorded and evaluated by a PDP 8/L computer interfaced with a Fabritek 1074 computer.

Pure nitric acid was prepared from a mixture of dry sodium nitrate and 98.5% sulfuric acid. The distilling bulb was filled at Dry Ice temperature, then evacuated and warmed to 40°; the collecting vessel for the nitric acid was placed in a −40° bath (these temperature limits should not be exceeded, or nitric acid will decompose above 40°). The product was stored as a white solid at Dry Ice temperature. Westef greaseless Teflon and Viton O-ring stopcocks were used. Gas samples were collected in either an 80-cc bulb or a 3-l. bulb, and the pressure was measured with an oil manometer. The gas was then expanded into the evacuated gas cell and scans were made within 10 min.

Nitrogen dioxide gas of 99.5% purity from Matheson Co. was liquified and stored for 48 hr at 0° with 1 atm of oxygen. The NO_2 was then frozen at Dry Ice temperature and the oxygen was pumped off. The solid was transferred twice and pumped on to remove any trapped oxygen. The white product was stored at Dry Ice temperature. Nitrogen dioxide samples were collected in an 80-cc bulb at 25°, and the pressure was measured with an oil manometer. Corrections for N_2O_4 were made using the equilibrium constant of Verhoek and Daniels.[3] The gas samples were then expanded into the evacuated cell. The absroption spectrum is based on ten gas samples which gave cell concentrations between 5×10^{14} and 3×10^{15} molecules cm^3. The maximum amount of N_2O_4 present under these conditions was less than 0.1% of the NO_2 present. Beer's law was obeyed and no pressure dependence was observed between 50 μ and 1 atm total pressure. The absorption spectrum so obtained had a 1% standard deviation above 300 nm. Values of the detailed absorption cross sections of nitrogen dioxide were stored in the computer and used to correct the observed nitric acid spectrum for the nitrogen dioxide impurity. The amount of nitrogen dioxide was determined from its detailed spectrum between 310 and 370 nm, and it was found to be between 0.1 and 0.2% of the HNO_3. The absorption due to this source was subtracted from the HNO_3 spectra.

Fifteen gas samples of nitric acid were used and gave cell concentrations between 8×10^{13} and 6×10^{16} molecules cm^{-3}. The composite spectrum is presented on a semilogarithmic plot in Figure 1. The ordinate is in cm^2 molecule^{-1} and the standard deviation is expressed as per cent at the top of the figure. The absorption is very strong between 190 and 210 nm, falls to much lower values between 230 and 290 nm, and rapidly falls to a vanishingly low value above 325 nm.

Discussion

The absorption spectrum of nitric acid in Figure 1 indicates two or more electronic states. To effect some separation of overlapping absorptions, it was assumed that the long-wavelength absorption was symmetrical in energy, centered at 260 nm. This curve is indicated by a dashed line in Figure 1, and it was subtracted from the total ab-

(1) P. A. Leighton, "Photochemistry of Air Pollution," Academic Press, New York, N. Y., 1961.
(2) (a) D. G. Murcray, T. G. Kyle, F. M. Murcray, and W. J. Williams, *J. Opt. Soc. Amer.*, **59**, 1131 (1969); (b) W. J. Williams, J. N. Brooks, D. G. Murcray, F. M. Murcray, P. M. Fried, and J. A. Weinman, in press.
(3) F. H. Verhoek and F. Daniels, *J. Amer. Chem. Soc.*, **53**, 1250 (1931).

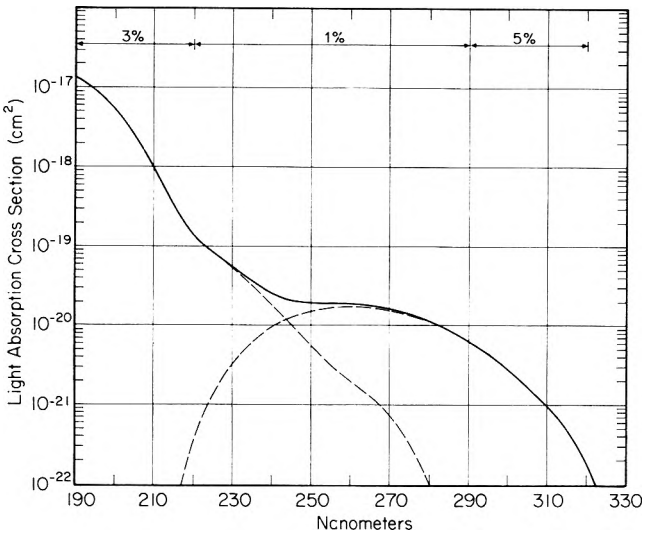

Figure 1. The ultraviolet absorption spectrum of nitric acid vapor; $\ln(I_0/I) = \sigma[HNO_3]L$, where $[HNO_3]$ is in molecules cm^{-3} and L is optical path in cm. The percentages at the top of the figure refer to the standard deviation based on 15 gas samples.

sorption curve to give the other dashed line. According to this analysis the short-wavelength absorption has its origin near 280 nm.

The continuous nature of the absorption spectrum suggests that photodissociation is taking place. Four energetically possible reactions are

$$HNO_3 + h\nu \rightarrow HO + NO_2 \quad \lambda \leq 598\ nm \qquad (A)$$

$$HNO_3 + h\nu \rightarrow HNO_2 + O(^3P) \quad \lambda \leq 401\ nm \qquad (B)$$

$$HNO_3 + h\nu \rightarrow H + NO_3 \quad \lambda \leq 290\ nm \qquad (C)$$

$$HNO_3 + h\nu \rightarrow HNO_2 + O(^1D) \quad \lambda \leq 245\ nm \qquad (D)$$

These wavelength limits are derived from thermodynamic data.[4]

This study agrees rather well with that of Dalmon[5] between 230 and 300 nm. The comparison is given in Table I. The disagreement at 290 and 300 nm could be due to Dalmon's having 1.5% NO_2 in his nitric acid.

For considerations of photochemical air pollution in the troposphere, the important region is that above 300 nm. The observed curve in this region is extremely sensitive to traces of nitrogen dioxide as impurity in the nitric acid and to the completeness with which corrections can be applied for such nitrogen dioxide and for the nitrogen tetroxide in equilibrium with it. In this study the nitrogen dioxide was kept below 0.2% and the nitrogen tetroxide was negligible, about 10^{-10} atm. To provide a firm basis for correcting for the 0.1 to 0.2% NO_2 in our sample, we determined the NO_2 absorption cross section at low pressures and with a long optical path. The absorption cross sections agree with those of Hall and Blacet[6] between 370 and 420 nm and are somewhat lower at shorter wavelengths (as well as the points can be read off of their graph). The cross sections for NO_2 between 200 and 270 nm agreed with those of Nakayama, Kitamura, and Watanabe[7] within their experimental error of 30%. The reproducibility and sensitivity of the apparatus are such that between 330 and 370 nm

$$\sigma(HNO_3) \ll 10^{-22}\ cm^2$$

Furthermore, pure anhydrous nitric acid in the vapor or in the liquid state is clear and colorless, which implies no significant absorptions between 400 and 700 nm. We disagree with the strong absorption indicated for nitric acid vapor between 320 and 440 nm by Schmidt, *et al.*,[8] and we suggest that they have present some major impurity or an instrumental malfunction.

TABLE I: Ultraviolet Absorption Spectrum for Nitric Acid Vapor

λ,nm	σ, cm^2 [a]	σ, cm^2 [b]	Standard deviation, %
190		1.32 (−17)[c]	3
195		9.1 (−18)	3
200		5.5 (−18)	3
205		2.55 (−18)	3
210		9.7 (−19)	3
215		3.28 (−19)	3
220		1.44 (−19)	3
225		8.51 (−20)	1
230	5.35 (−20)[c]	5.63 (−20)	1
235	3.59 (−20)	3.74 (−20)	1
240	2.56 (−20)	2.60 (−20)	1
245	2.10 (−20)	2.10 (−20)	1
250	1.93 (−20)	1.95 (−20)	1
255	1.91 (−20)	1.94 (−20)	1
260	1.93 (−20)	1.90 (−20)	1
265	1.91 (−20)	1.80 (−20)	1
270	1.64 (−20)	1.63 (−20)	1
275	1.34 (−20)	1.40 (−20)	1
280	1.07 (−20)	1.14 (−20)	1
285	8.79 (−21)	8.77 (−21)	1
290	7.26 (−21)	6.34 (−21)	1
295	5.73 (−21)	4.26 (−21)	5
300	4.59 (−21)	2.76 (−21)	5
305		1.68 (−21)	5
310		9.5 (−22)	5
315		4.7 (−22)	5
320		1.8 (−22)	5
325		2 (−23)	>10

[a] Reference 5. [b] This work. [c] 5.35 (−20) means 5.35×10^{-20}; $\ln(I_0/I) = \sigma[HNO_3]L$.

Acknowledgment. This work was supported in part by the Climatic Impact Assessment Program by means of an interagency agreement between the Department of Transportation and the Atomic Energy Commission, and in part by AP-104 Air Pollution Control Office, Environmental Protection Agency.

(4) "JANAF Thermochemical Tables," 2nd ed, Report No. NSRDS-NBS-37, National Bureau of Standards, Washington, D.C.
(5) R. Dalmon, *Mem. Serv. chim. état.* **30**, 141 (1943).
(6) T. C. Hall and F. E. Blacet, *J. Chem. Phys.*, **20**, 1745 (1952).
(7) T. Nakayama, M. Y. Kitamura, and K. Watanabe, *J. Chem. Phys.*, **30**, 1180 (1959).
(8) S. C. Schmidt, R. C. Amme, D. G. Murcray, A. Goldman, and F. S. Bonomo, *Nature (London), Phys. Sci.*, **238**, 109 (1972).

Solvent Effects on the Near-Ultraviolet Spectrum of Phenol and Its Distribution in Micellar Solutions[1a]

George Némethy*[1b] and Ashoka Ray

The Rockefeller University, New York, New York 10021 *(Received August 21, 1972)*

The near-uv absorption spectrum of phenol was studied as a function of solvent concentration in cyclohexane–dioxane, cyclohexane–methanol, water–ethylene glycol, dioxane–ethylene glycol, and dioxane–water mixtures. Besides the changes due to altered solvent refractive index, hydrogen bonding causes alterations in the spectra. Equilibrium constants for hydrogen-bonded phenol–proton acceptor association in cyclohexane solution were determined as 16 ± 1 with dioxane and 10 ± 3 with methanol. It is suggested that a hydrogen bond in which phenol acts as a proton donor is more important than that in which phenol is the proton acceptor, even in hydroxylic solvents. The spectrum of phenol in the presence of nonionic detergents was compared with the spectra in the above solvent pairs. It appears that phenol molecules entering the micelle are located in a polar environment, and are hydrogen bonded in a manner similar to that in aqueous or alcohol solutions.

Introduction

It is well known that near-uv spectra of aromatic compounds are affected both by changes in solvent polarity and by specific interactions causing shifts in the electron distribution of the molecule, such as hydrogen bonding in the case of phenol, aniline and similar derivatives.[2-6] The effect of both factors on π–π^* and n–π^* transitions have been discussed in general terms by several authors.[2,3,7] The hydroxyl group of phenol can act as proton donor toward both hydroxylic compounds and proton acceptors such as ketones or ethers.[8,9] Many studies on such systems have been carried out in an inert solvent, with small amounts of phenol and the proton acceptor present, in order to study the π–π^* transition. On the other hand, interaction with a hydroxylic compound, in which the phenol acts as a proton acceptor, was followed by the changes in the n–π^* transition.[7-10] While such studies on phenol have been carried out in the presence of a variety of polar proton acceptor or donor solvent components in an inert solvent, few investigations were extended to high concentrations of this component;[9] measurements under comparable conditions in diverse polar solvents are scarce, making comparisons of the effects of various polar solvents difficult.

In connection with an investigation of detergent micelle formation, in which phenol was used to detect micelles,[11] we undertook a systematic study of the changes in the near-uv (π–π^*) spectrum of phenol as a function of solvent composition. Solvent pairs were selected to cover various hydrogen-bonding possibilities: an inert solvent (cyclohexane) in combination with a proton acceptor (dioxane) and with a hydroxylic solvent (methanol); dioxane in combination with two hydroxylic solvents (ethylene glycol and water), and ethylene glycol–water mixtures. The results can be used to obtain limited information on the interaction of dissolved phenol with the micelles in detergent solutions.

Experimental Section

Chromatoquality (Matheson Coleman and Bell) organic solvents were used. After testing for the absence of impurities absorbing in the uv range studied, they were used as obtained. Mallinckrodt analytical reagent grade phenol was vacuum dried over anhydrous NaOH to remove water. For the measurements in detergent solution, Tergitol 15-S-9, supplied by the Union Carbide Corp. (sample No. D-21015), was used as received. This is an alkyl (polyethoxy) ethanol, a nonionic detergent of the composition $C_{15}H_{31}(OC_2H_4)_9OH$. Samples were prepared by weight.

The spectra were recorded on a Cary 14 recording spectrophotometer, using 0.5 or 1.0 cm path length quartz cells. The cell holders and compartments were thermostated at 25 ± 0.05°.

Results

Phenol concentrations were maintained between 4 and 6.5×10^{-4} M in all measurements of solvent effects. In this concentration range, self-association is absent, since solutions of phenol in both pure cyclohexane and pure dioxane, tested over the concentration range from 1×10^{-5} to 1.1×10^{-3} M, obey Beer's law. Ito[12] showed that phenol in inert solvents exists in the monomeric form near 5×10^{-4} M.

Figure 1 shows the spectra of phenol in the pure solvents used. Spectra in binary solvent mixtures are shown in Figures 2–6. Figures 2 and 3 indicate the effects of adding a hydrogen-bonding solvent component to solutions in cyclohexane, while Figures 4–6 represent solutions in mixtures of two hydrogen bonding solvents. Due to the

(1) (a) This work was supported by the National Science Foundation under Grants No. GB-8410 and GB-23920. (b) Present address: Laboratoire d'Enzymologie Physico-chimique et Moléculaire, Batiment 433, Université de Paris-Sud, Orsay, France.
(2) N. S. Bayliss and E. G. McRae, *J. Phys. Chem.*, **58**, 1002 (1954).
(3) G. C. Pimentel, *J. Amer. Chem. Soc.*, **79**, 3323 (1957).
(4) E. Lippert, "Hydrogen Bonding," D. Hadži, Ed., Pergamon Press, New York, N.Y., 1959, p 217.
(5) F. A. Bovey and S. S. Yanari, *Nature (London)*, **186**, 1042 (1960).
(6) C. N. R. Rao, "Ultra-Violet and Visible Spectroscopy, Chemical Applications," Plenum Press, New York, N.Y., 1967.
(7) H. McConnell, *J. Chem. Phys.*, **20**, 700 (1952).
(8) S. Nagakura and H. Baba, *J. Amer. Chem. Soc.*, **74**, 5693 (1952).
(9) H. Baba and S. Suzuki, *J. Chem. Phys.*, **35**, 1118 (1961).
(10) G. J. Brealey and M. Kasha, *J. Amer. Chem. Soc.*, **77**, 4462 (1955).
(11) A. Ray and G. Némethy, *J. Phys. Chem.*, **75**, 804 (1971).

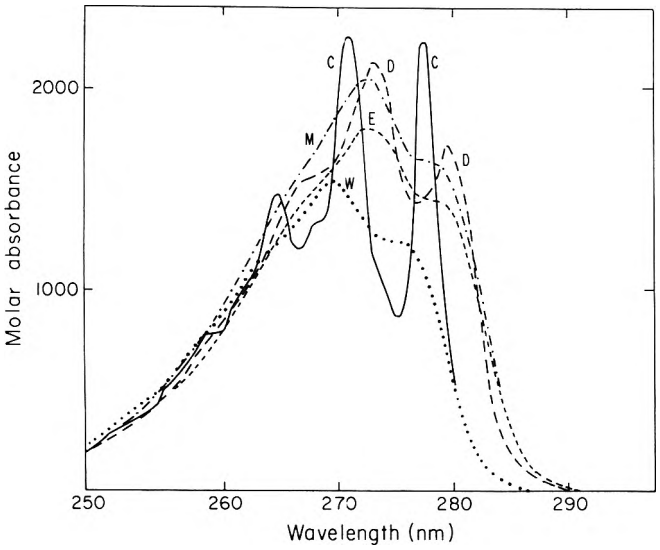

Figure 1. Near-uv spectra of phenol in pure solvents: C(——), cyclohexane; D(---), dioxane; M(-·-·-), methanol; W(· · · ·), water; E(-----), ethylene glycol. The spectra correspond to a phenol concentration of 5.5×10^{-4} *M*, where there is no self-association.

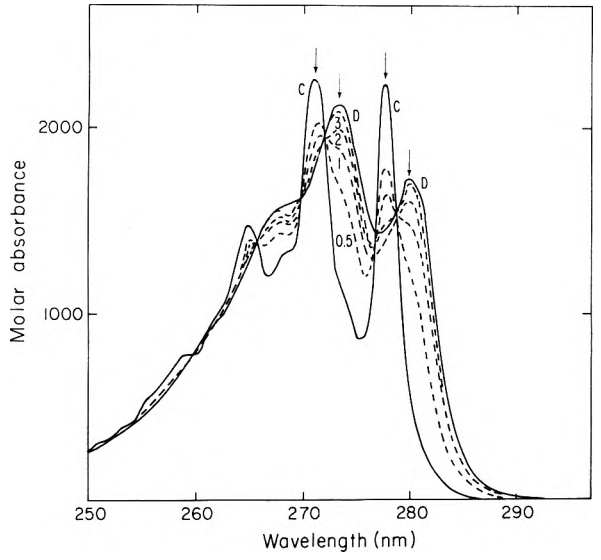

Figure 2. Near-uv spectra of phenol (5.5×10^{-4} *M*) in cyclohexane–dioxane mixtures. Solid curves show spectra in pure solvents (C = cyclohexane and D = dioxane). Dashed curves show spectra in mixtures. The numbers indicate the dioxane concentration in vol %. Absorbance values at each of the wavelengths indicated by arrows were used for double reciprocal plots (see text).

low solubility of ethylene glycol in cyclohexane, methanol had to be used as the hydroxylic solvent component in Figure 3.

Discussion

Changes in the polarity of the solvent medium usually shift the π–π^* transition band of aromatic compounds toward longer wavelengths when the refractive index of the solvent medium is raised (*e.g.*, upon changing from water to a nonpolar organic solvent).[5-12] However, if hydrogen bonding with the solvent changes at the same time, its effects are superimposed on those due to changing polarity. These effects are the main subject of this study.

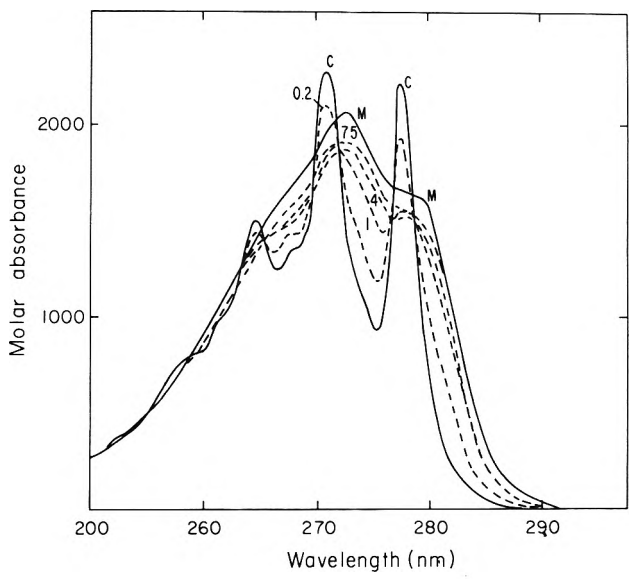

Figure 3. Near-uv spectra of phenol (5.4×10^{-4} *M*) in cyclohexane–methanol mixtures. Solid curves show spectra in pure solvents (C = cyclohexane and M = methanol). Dashed curves show spectra in mixtures. The numbers indicate the methanol concentration in vol %.

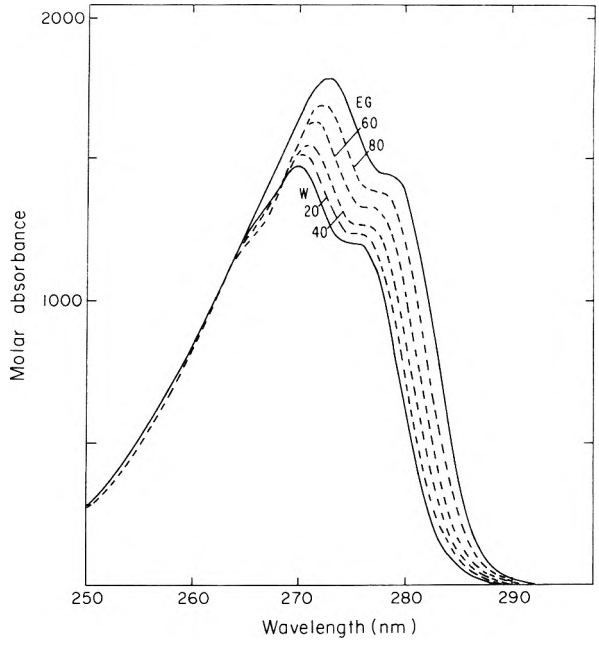

Figure 4. Near-uv spectra of phenol (1.0×10^{-3} *M*) in water–ethylene glycol mixtures. Solid curves show spectra in pure solvents (W = water and EG = ethylene glycol). Dashed curves show spectra in mixtures. The numbers indicate the ethylene glycol concentration in vol %.

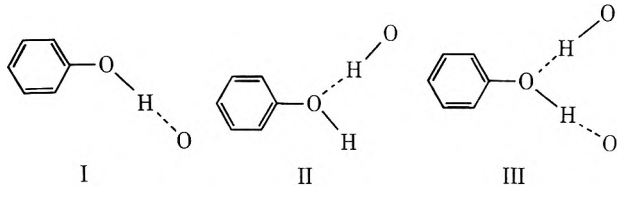

Hydrogen bonding can cause shifts of various directions and magnitudes (*cf.* ref 12). Formation of a hydrogen bond in which the phenolic hydroxyl group is the proton donor (I)

(12) M. Ito, *J. Mol. Spectrosc.*, **4**, 125 (1960).

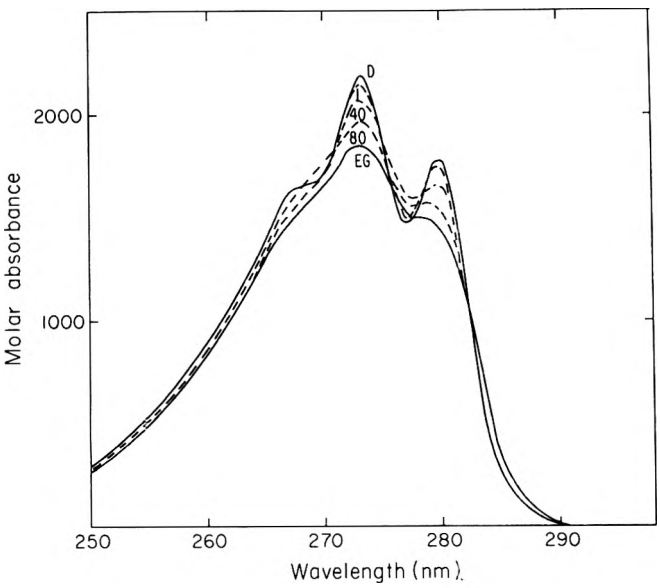

Figure 5. Near-uv spectra of phenol (5.7×10^{-4} *M*) in dioxane–ethylene glycol mixtures. Solid curves show spectra in pure solvents (D = dioxane and EG = ethylene glycol). Dashed curves show spectra in mixtures. The numbers indicate the ethylene glycol concentration in vol %.

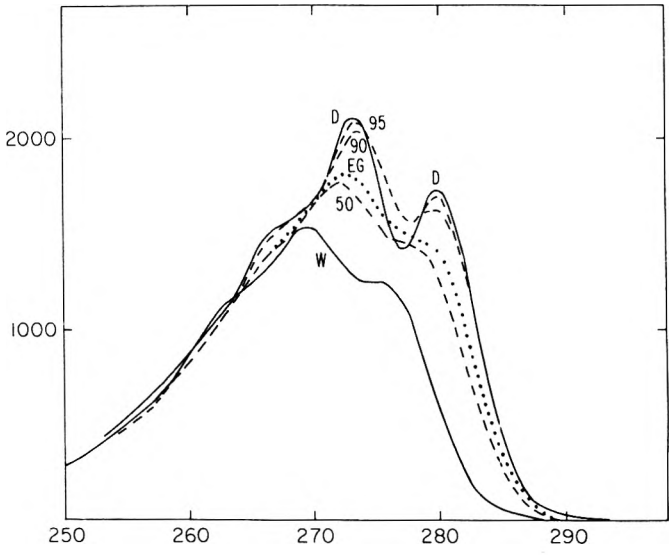

Figure 6. Near-uv spectra of phenol (4.8×10^{-4} *M*) in water–dioxane mixtures. Solid curves show spectra in pure solvents (W = water and D = dioxane). Dashed curves show spectra in mixtures. The numbers indicate the dioxane concentration in vol %. The dotted curve marked EG is the spectrum in pure ethylene glycol, shown here for comparison (*cf.* Discussion in the text).

releases electron density from the O–H bond toward the oxygen and hence, by an inductive effect, toward the aromatic ring. This causes a red shift of the π–π^* transition (Figure 2, *cf.* ref 12 and 13). Conversely, if a hydrogen bond is formed in which the phenolic oxygen is a proton acceptor (II), electrons are withdrawn from the ring, and an opposite shift is to be expected.[12,14] In a hydroxylic solvent, both bonds could possibly form at the same time (III); since their effects on the partial charges of the oxygen are opposite, the change in the net charge on the oxygen[15] and hence on the aromatic ring may be small. If both hydrogen bonds in III were to form with equal ease, the shift, relative to the position of the band in a non-hydrogen-bonding solvent ought to be small.[16] In pure water or in aliphatic alcohols, the two hydrogen bonds corresponding to structures I and II form equally easily. However, for phenol, structures of type I may be favored over those of type II even in hydroxylic solvent media, due to the increased acidity of the oxygen attached to an aromatic ring. In addition, there may be other effects in particular solvent systems, as discussed below.

In the *cyclohexane–dioxane* system, only type I hydrogen bonds can form. Thus there is a simple equilibrium between the hydrogen-bonded complex I and the unbonded phenol molecule, as seen in Figure 2. The results reported here agree well with those of Baba and Suzuki.[9] From a double reciprocal plot $(1/(A - A_0)$ *vs.* $1/c_{\text{dioxane}}$, where A_0 = absorbance of phenol in the unbonded form, *i.e.*, in cyclohexane), using absorbances at several wavelengths, indicated in Figure 2, we obtain a value $K = 16 \pm 1\ M^{-1}$ for the association constant

$$K = c_{(\text{phenol-dioxane complex})}/c_{\text{phenol}}c_{\text{dioxane}}$$

while Baba and Suzuki's data give[9,18] $K = 14$ at 25°. Nagakura and Baba[8] report $K = 15$ at 23° with dioxane and $K = 12$ at 7° with ethyl ether, in a hydrocarbon solvent in both cases. Using the method proposed by Chignell and Gratzer,[13] *i.e.*, plotting $(A - A_0)/c_{\text{dioxane}}$ *vs.* A, we obtained $K = 16.4 \pm 0.5\ M^{-1}$. Thus most of the changes in the spectra occur when the first few per cents of dioxane are added. Similar changes in the spectrum were observed by Mizushima, *et al.*,[19] for phenol in isooctane solution upon the addition of amides.

Since *cyclohexane* and *methanol* are not completely miscible at 25°, measurements in this solvent system were limited to the composition ranges 0–4 and 75–100 vol% methanol. In the former range, the change of the spectrum is similar to that observed in the cyclohexane–dioxane system, *i.e.*, there is a rapid decrease of the non-hydrogen-bonded peaks, and a slight increase in the absorption at higher wavelengths (Figure 3). However, the newly appearing peaks (corresponding to hydrogen-bonded phenol) are not well separated from the former peaks. Reciprocal plots, based on the absorbances at 271.0 and 277.5 nm (non-hydrogen-bonded peaks), give an equilibrium constant, analogous to that defined in eq 1, $K = 11 \pm 1\ M^{-1}$. The plot of $(A - A_0)/c_{\text{methanol}}$ *vs.* A at 277.5 nm yields $K = 8 \pm 2\ M^{-1}$. While the plotted data show some scatter, it appears that the spectral change in this composition range can be described in terms of the formation of a 1:1 complex between phenol and methanol. This would agree with a preference for structure I over III, as discussed above.

(13) D. A. Chignell and W. B. Gratzer, *J. Phys. Chem.*, **72**, 2934 (1968).
(14) H. Grinspan, J. Birnbaum, and J. Feitelson, *Biochim. Biophys. Acta*, **126**, 13 (1966).
(15) *Cf.* calculations for water: J. Del Bene and J. A. Pople, *J. Chem. Phys.*, **52**, 4858 (1970).
(16) Actually, all species probably coexist in a hydroxylic solvent since the extent of hydrogen bonding is less than complete.[17] In addition, distorted (bent or stretched) hydrogen bonds, of less than maximal strength, may be present.[17] The net effect of all this would be a broadening of the bands around the absorption maxima corresponding to structure III and a "smearing" out of the features of the spectrum. This is observed often (*cf.* Figure 1).
(17) For a review of relevant arguments in the case of liquid water, see *e.g.*, (a) G. Nemethy, *Ann. Ist. Super. Sanita*, **6**, 491 (1970); (b) D. Eisenberg and W. Kauzmann, "The Structure and Properties of Water," Oxford University Press, New York, N.Y., 1969.
(18) Based on the value at 20°, $K = 16.4$, reported by them and corrected by using the ΔH value they report.
(19) S. I. Mizushima, M. Tsuboi, T. Shimanouchi, and Y. Tsuda, *Spectrochim. Acta*, **7**, 100 (1954).

The spectra in pure methanol and pure ethylene glycol are very similar; the extinction coefficient is higher in the former. Upon addition of cyclohexane to methanol (in the high methanol region), no shift appears, but merely a decrease in the intensity. Both observations can be ascribed to the change in solvent polarity.

In pure *water*, pure *ethylene glycol*, and their mixtures, only a broad peak and a shoulder are seen (Figure 4). Going from ethylene glycol to water, the wavelength of the peak shifts gradually from 275.0 to 269.8 nm, that of the shoulder from about 278.0 to 275.0 nm. This is accompanied by a fairly uniform intensity decrease of the entire band (*cf.* ref 14). These changes can be attributed to the effect of solvent polarity. Apparently there is no change in the predominant manner of hydrogen bonding of the phenol, as expected.

In *dioxane–ethylene glycol* mixtures, increasing the amount of ethylene glycol causes a decrease in intensity and a loss of the details of the band; the 280.0 nm peak in dioxane becomes a shoulder in ethylene glycol, and the shoulder at 268.0 nm disappears (Figure 5). The intensity of the main peak decreases, but there is only a very slight change in wavelength (from 273.3 to 272.7 nm). The refractive index of the two solvents is very close, so that any changes in the wavelength would be due to changes in hydrogen bonding, as discussed above. Thus, apparently, in spite of the ability of the added EG to form type II hydrogen bonds on the phenol molecules, such bonds are not present extensively, or if they form, they do not affect the spectrum significantly. The former conclusion is consistent with the above discussion of the relative stability of type I and II hydrogen bonds.

In *dioxane–water* mixtures, the changes up to about 40% water are similar to those reported above for dioxane–EG mixtures (over the entire concentration range); the spectrum in 40% water–60% dioxane is very similar to that in pure EG. Further addition of water causes changes similar to those in the EG–water mixtures (Figure 6). Thus it appears that at relatively low water concentrations, the same changes in hydrogen bonding or local medium effect occur as in dioxane–EG mixtures, but between 40 and 100% water, the medium effect, as expressed in the changing refractive index, becomes important. These findings are similar to those seen for tyrosine in these mixtures.[14]

In both solvent systems containing dioxane, the absence of a wavelength change might reflect a lack of hydrogen bonding of type II and III. First, the bond of type II probably is less stable, as discussed above. Second, since the concentration of dioxane is much higher than that of phenol, the first molecules of water or ethylene glycol added bind mostly to dioxane molecules which are better hydrogen acceptors than is phenol.

In aqueous solutions, dioxane alters the spectrum more than ethylene glycol (Figures 4 and 6); the changes caused by about 60% dioxane and 100% EG are very similar. This observation agrees well with the result reported by Grinspan, *et al.*,[14] on the effects of dioxane and ethanol on the spectrum of tyrosine; they found that dioxane appeared about twice as effective in changing the wavelength of the maximum.

In conclusion, the changes of the near-uv spectrum of phenol, in solvent mixtures containing small amounts of polar solvents in a hydrocarbon as the main component, show the rapid onset of hydrogen bonding, with the OH group of the phenol acting as proton donor. At higher concentrations of the polar component, or in mixtures of two polar solvents, the changes in the spectra seem to reflect mostly general solvent effects, and do not furnish information regarding details of the hydrogen-bonding equilibria.

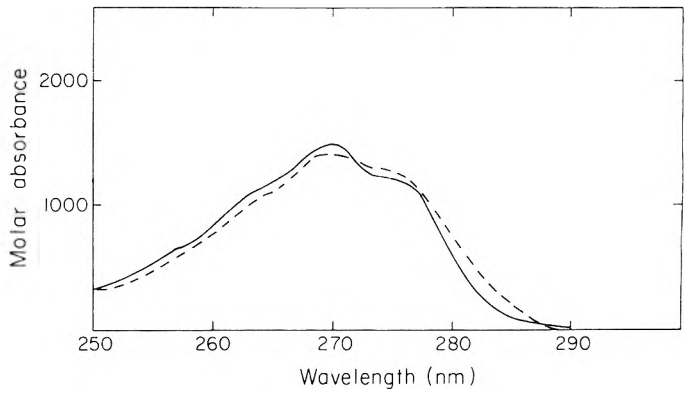

Figure 7. Near-uv spectrum of phenol (6×10^{-4} *M*) in aqueous solution in the presence (-----) and absence (——) of detergent micelles. The detergent is Tergitol 15-S-9 at 2×10^{-2} *M* concentration.

Spectrum of Phenol in Detergent Micelle Solution. In an earlier publication,[11] we showed that the near-uv spectrum of dissolved phenol can be used to detect the formation of micelles in detergent solutions. The technique is similar in principle to that based on solubilization.[20] When micelles are formed, some of the phenol is incorporated into them. The resulting red shift, due to the change in the polarity of the environment of the phenol molecules, can be detected by a difference spectrophotometric technique.[11] It was also expected that a comparison of the absorption spectra under these conditions provides some information on the local environment of the phenol in the micelles. It was shown in several studies that various aromatic derivatives[20-22] can be incorporated into micelles, with concomitant changes in the uv spectrum. It has also been suggested that phenol[23] and other aromatic derivatives containing a hydroxyl group[24] form complexes with polyethylene glycol by means of hydrogen bonding to the ether oxygens.

Mukerjee[22] discussed the effects of solubilization in two different regions of nonionic micelles, *viz.*, the hydrocarbon core and its interface, or the polyoxyethylene mantle, using hydroxy and other derivatives of benzoic acid as examples, and showed that the chemical nature of the solubilizate affects greatly the distribution between these regions.

Figure 7 shows the absorption spectrum of a 6×10^{-4} *M* solution of phenol in a 2×10^{-2} *M* solution of Tergitol 15-S-9, as compared with the same phenol concentration in pure water. This detergent concentration is 24 times higher than the critical micelle concentration (8.3×10^{-4} *M*), so that the concentration of micelles is of the same order of magnitude as that of the phenol. Consequently, many of the phenol molecules can be expected to be dissolved in a micelle. However, the spectrum differs very

(20) Reviewed by T. Nakagawa, "Nonionic Surfactants," M. J. Schick, Ed., Marcel Dekker, New York, N.Y., 1967, p 558.
(21) S. Riegelman, N. A. Allawala, M. K. Hrenoff, and L. A. Strait, *J. Colloid Sci.*, **13**, 208 (1958).
(22) P. Mukerjee, *J. Pharm. Sci.*, **60**, 1528 (1971).
(23) D. Guttman and T. Higuchi, *J. Pharm. Sci.*, **45**, 659 (1956).
(24) B. A. Mulley and A. D. Metcalf, *J. Pharm. Pharmacol.*, **8**, 774 (1956).

little from that in pure water. The main peak is not shifted, but there is a general broadening of the spectrum at the long-wavelength side and a blurring of the distinction between the peak and the shoulder. The spectrum could be interpreted as the superposition of the spectrum in water and of a weaker spectrum corresponding to that found in methanol or ethylene glycol (*cf.* Figure 1). It does not correspond to that in a uniform mixed aqueous solvent medium (*cf.* Figure 4 or 6). Thus it appears that the phenol molecules incorporated in the micelle are hydrogen bonded in the manner found in water or alcohols, and that their environment is polar, *i.e.*, they do not penetrate into the alkyl interior of the micelle. However, the lack of definite features in the spectrum of Figure 7 precludes the drawing of more detailed or specific conclusions.

Acknowledgment. We thank Mr. Gerald Rosenberg and Miss Hilda Malodeczky for their competent technical assistance.

Carbon-13 Magnetic Resonance in Diamonds, Coals, and Graphite

H. L. Retcofsky* and R. A. Friedel

Pittsburgh Energy Research Center, Bureau of Mines, U. S. Department of the Interior, Pittsburgh, Pennsylvania 15213

(Received June 30, 1972)

Publication costs assisted by the U. S. Bureau of Mines

Carbon-13 magnetic resonance (^{13}C nmr) spectra of gem-quality diamonds, powdered natural graphite, and four coals were obtained as part of a comprehensive spectral investigation of the structure of coal and other carbonaceous materials. The chemical shift in diamond was found to agree well with empirical predictions based on prior studies of pure aliphatic and alicyclic hydrocarbons. The spectrum of graphite reflects both a chemical shift anisotropy and the semiconductivity of the material. The results for the coals were compared with those for diamond and graphite and found to be best rationalized in terms of increasing carbon aromaticity with increasing coal rank leading finally to the formation of graphite-like structures.

Introduction

Despite recent advances in experimental techniques,[1-5] applications of carbon-13 magnetic resonance (^{13}C nmr) spectrometry to materials in the solid state are relatively few. Of the studies that have appeared in the literature, most have been concerned with the determination of chemical shift anisotropies,[5-8] although some have been devoted to semiconductors,[9,10] intercalation compounds,[10] and simple paramagnetic systems.[11] It is of interest that one of the earliest observations of dynamic nuclear polarization in a nonmetallic solid was the result of a ^{13}C nmr experiment.[12]

Practically nonexistent in the literature are actual examples of the use of ^{13}C nmr in problems typical of those encountered by the practicing chemist engaged in structure elucidation of solids of complex chemical makeup. The present authors have applied ^{13}C nmr to studies of the chemical structure of coal. After detecting the ^{13}C resonance in an anthracitic coal,[13] the high aromaticity of anthracites was confirmed by comparing a later, more highly resolved spectrum with that of solid adamantane.[14] It should be noted that Pines, Gibby, and Waugh[2] have recently shown that spin-decoupled, *high-resolution* spectra of solids can be obtained by use of a specialized series of pulse sequences followed by a Fourier transformation. These experiments, though quite exciting, are generally beyond the scope of most laboratories; the work described in the present paper was all accomplished using conventional broadline techniques with accompanying signal averaging of spectra. The primary purpose of this investigation is to deduce information about the chemical structure of coal and the changes that occur in chemical structure during the coalification process. Because of the long periods of signal averaging required, the coals studied were limited to four: two bituminous coals, an anthracite, and a meta-anthracite. In addition, spectra of the two allotropes of carbon, diamond and graphite, were also ob-

(1) J. S. Waugh and L. M. Huber, *J. Chem. Phys.*, **47**, 1862 (1967).
(2) A. Pines, M. G. Gibby, and J. S. Waugh, *J. Chem. Phys.*, **56**, 1776 (1972).
(3) M. Schwab and E. L. Hahn, *J. Chem. Phys.*, **52**, 3152 (1970).
(4) H. E. Bleich and A. G. Redfield, *J. Chem. Phys.*, **55**, 5405 (1971).
(5) C. S. Yannoni and H. E. Bleich, *J. Chem. Phys.*, **55**, 5406 (1971).
(6) P. C. Lauterbur, *Phys. Rev. Lett.*, **1**, 343 (1958).
(7) A. Pines, W-K. Rhim, and J. S. Waugh, *J. Chem. Phys.*, **54**, 5438 (1971).
(8) A. Pines, W-K. Rhim, and J. S. Waugh, *J. Magn. Resonance*, **6**, 457 (1972).
(9) M. N. Alexander, *Phys. Rev.*, **172**, 331 (1968).
(10) G. P. Carver, *Phys. Rev. B*, **2**, 2284 (1970).
(11) D. G. Davis, *J. Chem. Phys.*, **46**, 388 (1967).
(12) A. Abragam, A. Landesman, and J. M. Winter, *C. R. Acad. Sci.*, **247**, 1852 (1958).
(13) H. L. Retcofsky and R. A. Friedel, "Spectrometry of Fuels," R. A. Friedel, Ed., Plenum Press, New York, N. Y., 1970, p 99.
(14) H. L. Retcofsky and R. A. Friedel, *Anal. Chem.*, **43**, 485 (1971).

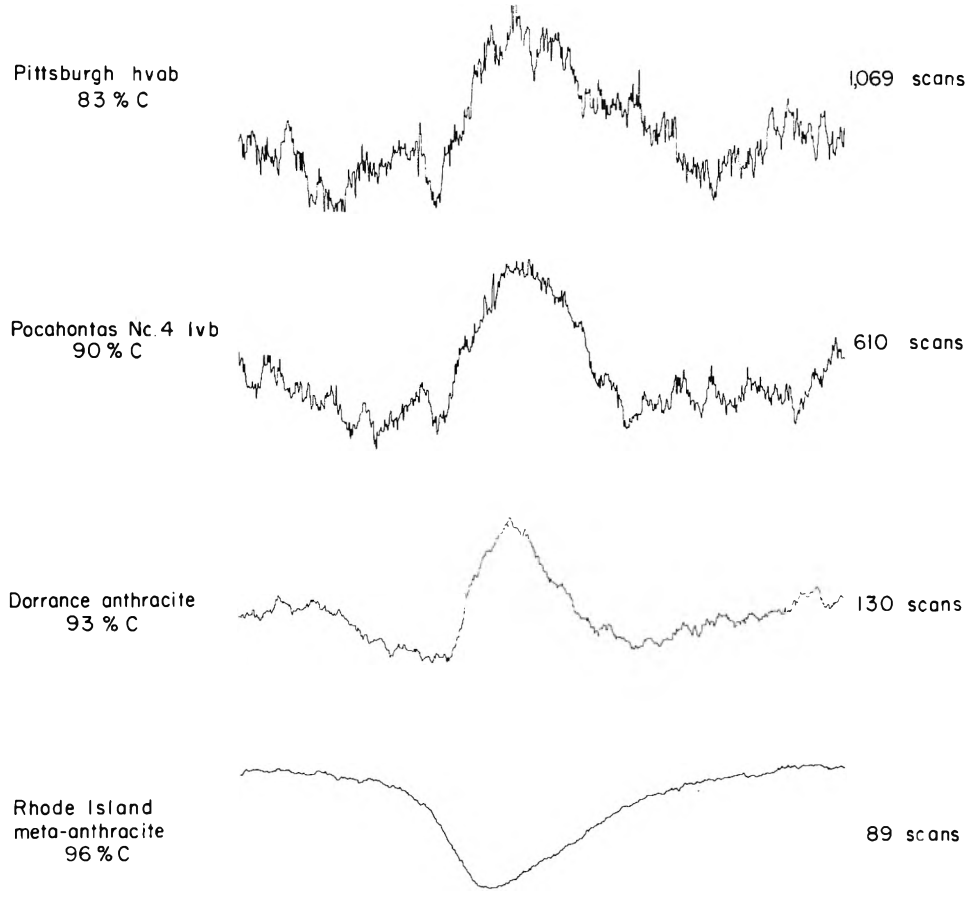

Figure 1. 15.085-MHz ^{13}C nmr spectra of selected coals.

tained since the presence of both graphite-like layers[15] and diamond-like structures[16] in coal has been considered.

Experimental Section

The four coals examined were high-quality vitrains separated petrographically from bulk samples. The graphite was a polycrystalline sample from Madagascar; the diamonds were gem-quality ones believed to be low in paramagnetic impurities. Spectra were obtained essentially as described in a previous publication[14] and are presented as first derivatives of the dispersion mode. All chemical shifts are referred to that of carbon disulfide and are designated δ_C. The semiconductivity of the graphite sample was such that the sample had to be finely ground and dispersed in silica in order to prevent electrical contact between the particles.

Results and Discussion

Representative spectra of the four coals investigated are reproduced in Figure 1; that of diamonds is shown in Figure 2. The spectrum of graphite is not shown but is qualitatively quite similar to that of the meta-anthracite (Figure 1, bottom).

Diamonds. The ^{13}C nmr spectrum of gem-quality diamonds (Figure 2) yields a chemical shift δ_C of 156 ppm with an estimated error of $\sim\pm3$ ppm. The chemical shift is well within the range of values reported for quaternary carbons in paraffins[17,18] and not far removed from the average chemical shift observed for solid adamantane.[2,14] It is concluded that the diamond chemical shift is little different from those of carbon atoms in similar chemical environments.

Diamond crystals being dilute in magnetic nuclei and having a structure which should result in essentially an isotropic chemical shift, would be expected to exhibit a reasonably narrow nuclear resonance even in the tube of randomly oriented stones used in the present determination. The observed line width 0.4 G is due to instrumental broadening and does not represent the natural line width of the resonance. This is readily apparent from Figure 2; the resonance of the external carbon disulfide chemical shift standard ($\delta_C = 0$) exhibits essentially the same line width as the diamonds, although it is well known that the natural line width in liquid carbon disulfide is less than 1 mG.

Graphite. The ^{13}C resonance in graphite was first detected by Abragam, Landesman, and Winter[12] using nuclear Overhauser enhancement. By saturating the electron spin resonance absorption, a nuclear polarization of 3–12% of the maximum theoretical value was observed. Twelve years later, Carver[10] reported the ^{13}C resonance in spectroscopic-grade graphite powder as part of a study of cesium–graphite intercalation compounds. Most of Carver's measurements were made at temperatures near that of liquid helium using a pulse spectrometer. In the present work, room-temperature, broadline ^{13}C nmr spectra of

(15) H. Brusset, J. Devaux, and A. Guinier, *Compt. Rend.*, **216**, 152 (1943).
(16) R. A. Friedel, *Science*, **130**, 220 (1959).
(17) R. A. Friedel and H. L. Retcofsky, *J. Amer. Chem. Soc.*, **85**, 1300 (1963).
(18) L. P. Lindeman and J. Q. Adams, *Anal. Chem.*, **43**, 1245 (1971).

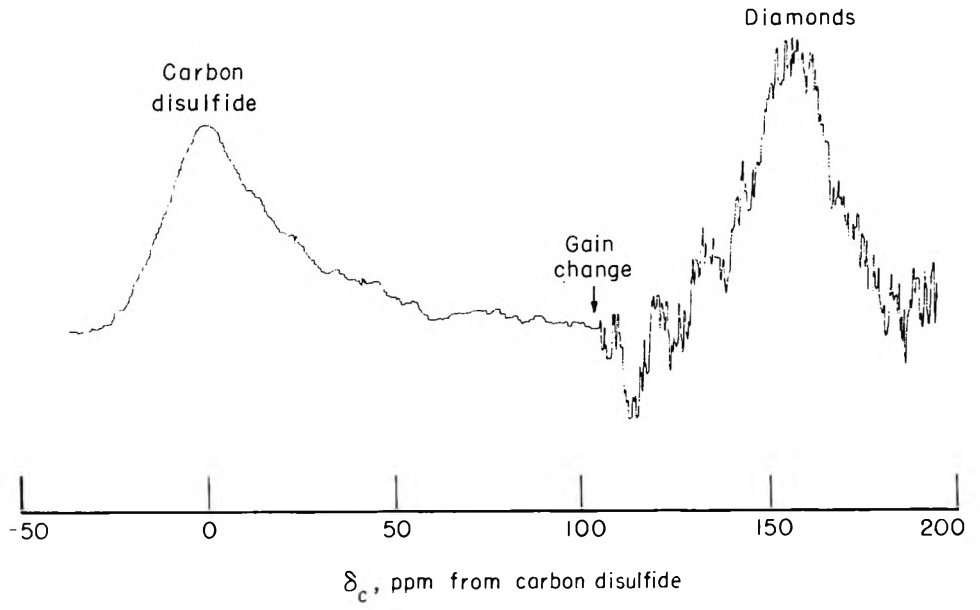

Figure 2. ^{13}C nmr spectrum of diamonds (250 scans).

natural graphite powder were acquired. It should be noted that a room-temperature spin-lattice relaxation time T_1 of 89 ± 10 sec has been reported for spectroscopic graphite.[10]

The nuclear magnetic resonance line shape exhibited by graphite suggests an anisotropic chemical shift. An axially symmetric shielding tensor would be predicted on the basis of the well-known molecular and crystal structure of graphite. Spectra obtained at higher magnetic fields or single crystal studies (in progress) should permit determination of the principal components of the tensor. Other properties of graphite, *e.g.*, the esr g factor,[19] also are anisotropic.

The maximum in the graphite spectrum occurs at δ_C ~35 ppm, a much lower chemical shift than that published for any condensed polynuclear aromatic hydrocarbon.[20-23] ^{13}C spectral data for very large polynuclears such as circumanthracene, ovalene, and circumovalene, which possess two-dimensional networks of hexagonal rings similar to but much fewer in number than those in graphite, are not available for comparison. The observed width of the graphite resonance was measured to be ~1.0 G; the asymmetry of the spectrum precludes extraction of a value for the spin-spin relaxation time T_2.

Probably the most unusual feature of the graphite spectrum is that the resonance is inverted relative to that of diamond. A tentative explanation, based on passage conditions used in the experiments, is proposed for this behavior. Weger,[24] in his comprehensive study of passage effects in paramagnetic resonance experiments, has shown that the *major* effect on first derivative, dispersion mode spectra in going from rapid (adiabatic) passage to slow passage is inversion of the resonance. He further shows that the spectrum obtained in either of the two cases is independent of the direction in which the magnetic field is scanned. In the present investigation, all spectra obtained by scanning from low to high magnetic field were identical with the corresponding ones obtained while scanning from high to low field. Long periods for nuclear relaxation would be expected in the case of diamond since the material is dilute in magnetic nuclei; in the case of graphite, the presence of conduction electrons and charge carriers would probably lead to faster relaxation. Our results suggest, therefore, that the diamond spectra were obtained under conditions of fast passage, whereas essentially slow passage conditions were satisfied in the case of graphite. This argument is admittedly speculative at this time.

Coals. The ^{13}C spectra of the coals examined (Figure 1) are presented in order of increasing rank (degree of coalification); the spectrum of the most highly metamorphosed material appears at the bottom of the figure. The width of the coal resonances decreases with increasing rank for the three lower rank samples; in the case of the meta-anthracite, the signal inverts and broadens. The position of maximum signal intensity appears near δ_C = 65 ppm, the chemical shift value for liquid benzene,[25] in each case except that of the meta-anthracite which exhibits its maximum (inverted!) at considerably lower magnetic field. To account for this behavior, both chemical and physical properties of coals must be considered.

Since all coals exhibit esr signals, it is important to consider the possible effects of the presence of paramagnetic species, presumably free radicals in the case of most coals, upon the line widths of the nuclear resonances. The paramagnetic contribution to the line width can be approximated by the equation[9,26]

$$\Delta H = 3.8\gamma\hbar n$$

where γ is the magnetogyric ratio of the electron, $\hbar$ is the modified Planck constant, and n is the concentration of unpaired spins in the sample. In the case of the coals studied, the esr intensities of which have been previously

(19) G. Wagoner, *Proc. Carbon Conf., 4th*, 197 (1960).
(20) H. L. Retcofsky, J. M. Hoffman, Jr., and R. A. Friedel, *J. Chem. Phys.*, **46**, 4545 (1967).
(21) T. D. Alger, D. M. Grant, and E. G. Paul, *J. Amer. Chem. Soc.*, **88**, 5397 (1966).
(22) R. J. Pugmire, D. M. Grant, M. J. Robins, and R. K. Robins, *J. Amer. Chem. Soc.*, **91**, 6381 (1969).
(23) N. Defay, D. Zimmerman, and R. H. Martin, *Tetrahedron Lett.*, **No. 21**, 1871 (1971).
(24) M. Weger, *Bell System Tech. J.*, **39**, 1013 (1960).
(25) P. C. Lauterbur, *J. Amer. Chem. Soc.*, **83**, 1838 (1961).
(26) A. Abragam, "Principles of Nuclear Magnetism," Oxford University Press, London, 1961, p 128.

reported,[27] plots of esr intensities expressed as free radicals/gram of coal and ^{13}C spectral line widths *vs.* carbon content (or other property) of the coals should show the same or quite similar functional dependence. That this is *not* the case is evident from the two lower plots of Figure 3. It should be noted that the initial exponential increase of free-radical concentration with carbon content of coals (Figure 3, middle) is based on esr measurements made on a large number of coals;[27] the ^{13}C line width data, however, are limited to the four samples of coal under discussion.

The inversion of the ^{13}C resonance in the meta-anthracite is tentatively attributed to passage effects of the type proposed above for the case of graphite. Both materials exhibit semiconductivity which probably leads to rapid rates of nuclear relaxation. A plot of the electrical resistivity of coals as a function of carbon content of the coals (Figure 3, top) illustrates the semiconductor properties of the high rank coal. The resisitivity plot is a composite one prepared from the experimental results of Schuyer and van Krevelen[28] and those of Ouchi.[29] It is interesting that each of the three plots of Figure 3 shows a pronounced inflection point near a carbon content value of 93%.

The ^{13}C results are best rationalized in terms of existing theories of coal constitution and coal metamorphosis; for background material, the reader is referred to three excellent reviews.[30-32] Coals, in general, are considered to be highly aromatic materials and a major feature of coal metamorphosis is the progressive increase in the size and number of condensed aromatic ring structures at the expense of nonaromatic material. In coals of very high rank, these aromatic structures become increasingly graphitic as evidence by the semiconductivity[28] and the graphite-like X-ray diffraction patterns[32,33] of anthracites and meta-anthracites.

The position of spectral maxima for the two bituminous coals and the anthracite sample confirms the relatively high carbon aromaticity of these materials. The much lower absorption in the spectral region attributed to saturated carbons in the anthracite spectrum indicates that aliphatic material is present in only small amounts if at all.

In the case of the coal of 83% carbon content, the resonance is broad and exhibits considerable intensity in the region of absorption by saturated carbons. This suggests that this material has the lowest aromaticity of the coals studied, a hypothesis in accord with other spectral studies of these coals.[34] Dipolar broadening, due to the presence of hydrogen in the lower rank coals, undoubtedly accounts for some of the observed line widths, however, paramagnetic contribution to the line widths, as considered above, appears negligible. Upon close inspection, the spectrum of the 83% carbon coal appears partially resolved into two components; the low-field one could be assigned to aromatic carbons, the high-field one to nonaromatic carbons. The signal/noise ratio in the spectrum, however, is quite low; the possibility of obtaining more highly resolved spectra, perhaps at higher magnetic fields, is an attractive one and should be explored. The present results do, however, provide strong evidence for an increase in carbon aromaticity of coals as the coalification process progresses. Another point of interest concerning the spectrum of the anthracitic coal is that the presence of large quantities of diamond-like structures can be ruled out strictly on the basis of spectral comparison. The spectrum of the meta-anthracite, because of its similarity to that of graphite, indicates qualitatively the presence of graphite-like structures in agreement with X-ray and electrical conductivity data.

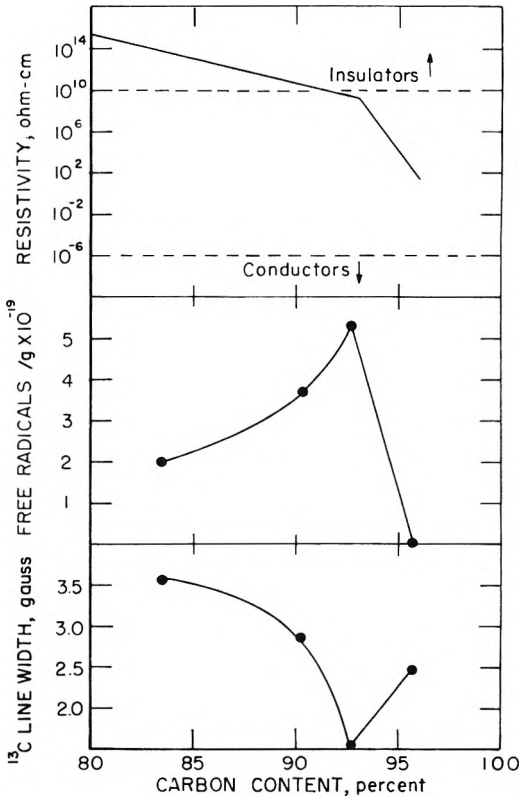

Figure 3. Some properties of coals.

(27) H. L. Retcofsky, J. M. Stark, and R. A. Friedel, *Anal. Chem.*, **40**, 1699 (1968).
(28) J. Schuyer and D. W. van Krevelen, *Fuel*, **34**, 213 (1955).
(29) K. Ouchi, *Fuel*, **46**, 71 (1967).
(30) H. Tschamler and E. DeRuiter, "Chemistry of Coal Utilization," Suppl. Vol., H. H. Lowry, Ed., Wiley, New York, N. Y., 1963, p 35.
(31) D. W. van Krevelen, "Coal," Elsevier, Amsterdam, 1961, p 431.
(32) J. G. Speight, *Appl. Spectrosc. Rev.*, **5**, 211 (1971).
(33) M. Mentser, H. J. O'Donnell, and S. Ergun, *Fuel*, **41**, 153 (1962).
(34) Reference 13, p 70.

Oxygen-17 and Nitrogen-14 $\sigma-\pi$ Polarization Parameters and Spin Density Distribution in the Nitroxyl Group

Haya Hayat and Brian L. Silver*

Department of Chemistry, Technion - Israel, Institute of Technology, Haifa, Israel *(Received May 16, 1972)*

Publication costs assisted by the U. S. National Bureau of Standards

The ^{17}O and ^{14}N $\sigma-\pi$ polarization parameters were calculated for the groups C_2N-O and H_2N-O using localized σ molecular orbitals. The isotropic ^{17}O and ^{14}N hyperfine splittings for 2,2,6,6-tetramethyl-4-piperdone 1-oxyl (TMPO) were measured in various solvents. The observed splittings and the calculated polarization parameters were used to calculate the $p\pi$ spin densities on the nitrogen and oxygen atoms, which were found to be essentially equal. A completely independent estimate of the spin densities was made on the basis of the esr spectrum of a frozen solution of TMPO, from which the anisotropic ^{17}O hyperfine tensor could be estimated. Taken together with the observed isotropic ^{17}O splitting in solution the results lead again to the conclusion that $\rho_O^{\pi} \simeq \rho_N^{\pi}$. The theoretical and experimental results are only compatible if the group is assumed to be bent with respect to the rest of the molecule.

Introduction

Free radicals containing one or more nitroxyl groups are currently the subject of intense theoretical and experimental interest. In the great majority of such radicals the unpaired spin is almost entirely concentrated in a $p\pi$ orbital built, to a first approximation, from 2p orbitals on the nitrogen and oxygen atoms of the >NO group. Despite the comparative simplicity of the π system as compared to that in most other π radicals, there is not a concensus of opinion as to the distribution of spin in the NO group, and the magnitudes of the relevant $\sigma-\pi$ polarization parameters. For example, the spin density on the nitrogen atom has been estimated to be as low as 0.23[1] and as high as 0.8 to 0.9.[2] Furthermore, a number of authors[3] have accepted the equation

$$a^N = Q_{NN}{}^N\rho_N \qquad (1)$$

as describing the relation between the spin density in the nitrogen $p\pi$ orbital and the observed nitrogen splitting constant. The implied independence of a^N on ρ_O (the spin density in the oxygen $p\pi$ orbital) seems improbable considering that $Q_{OO}{}^C$ for the carbonyl group, has been estimated to fall in the range from -16 to -27 G.[4] Furthermore $Q_{CC}{}^N$ has been calculated as -5 G in the amino radical fragment.[5]

In part I of the present paper we present the results of calculations of the $\sigma-\pi$ parameters of the planar π fragments

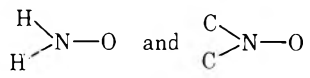

Experimentally observed values of a^N in nitroxide radicals are plentiful[6] and a few values for a^O, the ^{17}O isotropic hyperfine splitting, are also available.[7] In part II of this paper we report measurements of the isotropic ^{17}O splitting of 2,2,6,6-tetramethyl-4-piperidone 1-oxyl (TMPO) in various solvents and also the frozen solution esr spectrum of this radical, from which the anisotropic ^{17}O hyperfine interaction can be estimated.

In part III we use the experimental isotropic splitting constants and the calculated $\sigma-\pi$ parameters to estimate the spin density distribution in the >NO group of TMPO. In addition we have used the observed anisotropic ^{17}O interaction to independently estimate spin densities. In attempting to rationalize the observed splitting constants account was taken of the pyramidal conformation of the bonds around the nitrogen atom, as revealed by the results of X-ray structure analysis.[8]

I. Calculation of $\sigma-\pi$ Parameters

Method of Calculation. $\sigma-\pi$ parameters were calculated for the nitrogen (^{14}N) and oxygen (^{17}O) nuclei of the two fragments shown. We assume that both fragments are planar, the nuclei lying in the xy plane, which thus contains the interatomic σ bonds and lone pairs on the oxygen atom. Subsequently the effect of bending of the >NO group will be estimated. The unpaired electron is in a $p\pi$ orbital approximated as a linear combination of oxygen and nitrogen $2p_z$ orbitals, and having a nodal plane containing the nuclei. Interatomic distances (in Å) were taken as follows: C-N, 1.45; H-N, 1.03; N-O, 1.23.[9] The bonds around the nitrogen atom were assumed to be at 120° to each other. The σ bond system was built from Slater nodeless 1s, 2s, $2p_x$, and $2p_y$ atomic orbitals with exponents taken from Clementi and Raimondi.[10]

To obtain values for the $\sigma-\pi$ parameters of an atom A, it is necessary to evaluate the elements of the $\sigma-\pi$ polarization matrix which are given by the well-known expression

(1) O. Kikuchi, *Bull. Chem. Soc. Jap.*, **42**, 1187 (1969).
(2) C. L. Hamilton and H. M. McConnell, "Structural Chemistry and Molecular Biology," A. Rich and N. Davidson, Ed., W. H. Freeman, San Francisco, Calif., 1968, p 115.
(3) See, for example, A. Carrington and J. D. Santos-Veiga, *Mol. Phys.*, **5**, 21 (1962).
(4) R. Poupko, B. L. Silver, and M. Rubinstein, *J. Amer. Chem. Soc.*, **92**, 4512 (1970).
(5) R. Poupko and B. L. Silver, *J. Amer. Chem. Soc.*, **93**, 575 (1971).
(6) A. L. Buchachenko. "Stable Radicals," Consultants Bureau New York, 1965, p 111.
(7) (a) J. C. Baird, *J. Chem. Phys.*, **37**, 1879 (1962); (b) Z. Luz, B. L. Silver, and C. Eden, *ibid.*, **44**, 4421 (1966); (c) R. J. Faber, F. W. Markley, and J. A. Weil, *ibid.*, **46**, 1652 (1967).
(8) J. Lajzbrowicz-Bonneteau, *Acta Crystallogr., Sect. B.* **24**, 196 (1968).
(9) "Tables of Interatomic Distances and Configuration in Molecules and Ions," *Chem. Soc. Spec. Publ.*, **No. 11**, 241 (1958).
(10) E. Clementi and D. L. Raimondi, *J. Chem. Phys.*, **38**, 2686 (1963).

$$A = \frac{16}{3}\pi g_N \beta_n \sum_i \sum_p \frac{\langle \sigma_i(p_z)_r | e^2/r_{12} | (p_z)_s \sigma_p^* \rangle}{[E(0) - E(i \rightarrow p)]} \times \sigma_i(r_A)\sigma_p^*(r_A) \quad (2)$$

The symbols in this expression are defined in Henning's paper.[11]

The construction of the molecular orbitals was carried out using Melchior's[12] method which lays particular emphasis on the orthogonalization of the localized molecular orbitals of the basic σ set. The exchange integrals in eq 2 were computed using a program written by N. Epstein of this department. The estimation of the singlet-triplet (σ bonding → σ^* antibonding) excitation energies is discussed in the next section. Calculations on the carbonyl group[4] showed that the values obtained for the σ-π parameters are comparatively insensitive to the details of the σ bonding system. For example, a change from sp^2 to sp hybridization on oxygen, or the use of a polarity parameter of 0.7 for the carbonyl group caused only small changes in the calculated σ-π parameters. The elements of the Q matrix for ^{14}N and ^{17}O were, therefore, calculated only for a model using sp^2 hybridization on oxygen.

The elements of the Q matrices for ^{17}O and ^{14}N, calculated from eq 2, are listed below. The excitation energies have been left as parameters and are symbolized by the letters A to J. J and H are interbond excitation energies between similar bonds.

A = oxygen nonbonding → N-O σ^* antibonding
B = N-O σ bonding → N-O σ^* antibonding
C = N-H σ bonding → N-H σ^* antibonding
D = N-H σ bonding → N-O σ^* antibonding
E = C-N σ bonding → C-N σ^* antibonding
F = C-N σ bonding → N-O σ^* antibonding
G = N-O σ bonding → C-N σ^* antibonding
H = N-C σ bonding → N-C′ σ^* antibonding
I = N-O σ bonding → N-H σ^* antibonding
J = N-H σ bonding → N-H′ σ^* antibonding

In terms of these energies the values of the Q matrix for C_2NO are (in gauss)

$Q_{OO}^O = -4.48 + 37.53/A + 21.00/B$
$Q_{cross}^O = -0.32 - 3.05/A + 0.11/G + 0.07/B$
$Q_{NN}^O = -0.90 + 1.04/A - 18.26/B + 1.22/F + 0.27/G$
$Q_{NN}^N = -5.73 + 5.59/B + 5.08/H + 10.48/E + 4.45/G + 6.86/F$
$Q_{cross}^N = -0.15 + 0.91/E + 1.78/G + 0.14/F$
$Q_{OO}^N = -0.44 + 0.47/A - 6.42/B + 0.17/F$

and for H_2NO

$Q_{OO}^O = -4.52 + 37.93/A + 20.88/B$
$Q_{cross}^O = -0.31 - 2.92/A + 0.28/B + 0.11/I$
$Q_{NN}^O = -0.89 + 1.3/A - 17.8/B + 1.69/D + 0.26/I$
$Q_{NN}^N = -5.45 + 5.4/B + 9.42/C + 4.68/J + 6.93/D + 4.66/I$
$Q_{cross}^N = -0.15 + 0.82/C + 0.3/D + 2.06/I$
$Q_{OO}^N = -0.45 + 0.6/A - 6.33/B - 0.26/I$

In the above expressions a number of very small contributions have been neglected.

At this stage two problems arise: (1) the estimation of the excitation energies, and (2) the question of the planarity or nonplanarity of actual nitroxide radicals. Help is available in the theoretical and experimental results of previous workers, which we now discuss.

Estimation of Excitation Energies. The results of some calculations on the H_2NO and C_2NO fragments are summarized in Table I. In view of the similarity of the H_2NO and H_2CO fragments and the desirability of comparing the results of the present work with the results for the carbonyl group, we also include the orbital energies for H_2CO given by Newton and Palke[13] and Kikuchi.[14] Despite the widely different theoretical approaches of Kikuchi and Sallotto and Burnelle,[15] there is a remarkably good agreement between the calculated energies of almost all the orbitals of H_2NO. Not surprisingly, since the same method was used in both calculations, Kikuchi's results for H_2CO are very similar to his results for H_2NO. Newton and Palkes' results for H_2CO cover a wider energy range than those of Kikuchi's and therefore activation energies estimated from their results will tend to give lower values of the elements of the Q matrix. It should be noted that the values in the table taken from Newton and Palke do not include two very low lying a_1 levels which are essentially pure $1s_O$ and $1s_C$ orbitals.

TABLE I: Calculated Energies (eV) for the MOs of H_2NO, C_2NO, and H_2CO

		H_2NO^a	C_2NO^b	H_2NO^c	H_2CO^d	H_2CO^a
$1a_1$	σ	−41.24	−36.55	−39.84	−37.12	−39.96
$2a_1$	σ	−29.8	−22.01	−29.54	−22.76	−26.67
$1b_2$	π	−22.9	−16.10	−20.14	−18.29	−22.46
$3a_1$	σ	−19.2	−7.47	−17.83	−15.47	−18.48
$1b_1$	π	−18.53	−13.41	−18.48	−12.74	−16.97
$2b_2$	nb	−14.75	−7.44	−13.5	−10.43	−14.52
$2b_1$	π^*	−4.96	−2.39	−11.25	6.69	2.99
$4a_1$	σ	3.40	26.38		16.67	3.15
$3b_2$	σ	6.90	36.49		20.22	6.34
$5a_1$	σ^*	10.34	79.98		22.24	9.10

[a] Reference 14. [b] Reference 16. [c] Reference 15. [d] Reference 13.

It is obviously not possible to directly use the energies in Table I[16] in our calculations but they can be a guide to the range of energies which we can claim to be physically acceptable. Kikuchi's energy levels for H_2CO are bunched together closer than those he calculates for H_2NO. The only excitation energies of relevance are those between a_1 levels, and all pairs of a_1 levels in H_2NO are between 1 and 2 eV (~0.04–0.08 au) further apart than the corresponding levels in H_2CO. We conclude that the excitation energies chosen for H_2NO should be of the order of 0.05–0.10 au larger than the corresponding energies chosen for H_2CO in a comparable calculation.[4] The $\sigma \rightarrow \sigma^*$ intrabond excitation, P, will therefore be taken as 1.15 au. For purposes of comparison with the results for H_2CO the elements of the Q matrix are plotted as a function of P. As in the treatment of the carbonyl group, and for the same reasons, we will take the oxygen nonbonding → σ^*(N-O) energy as a fixed proportion (0.9–1.0) of the intrabond σ(N-O) → σ^*(N-O) excitation energy.

Melchior, in his original paper, using the present method of calculation,[12] calculated the elements of the Q matrix as functions of the ratio R of intrabond to interbond excitation energies. Values of R of less than unity were used, for reasons given by Melchior. The elements of the Q matrix are in general found not to be oversensitive to reasonable variations in the value taken for R. In the pres-

(11) J. C. M. Henning, *J. Chem. Phys.*, **44**, 2139 (1966).
(12) M. T. Melchior, *J. Chem. Phys.*, **50**, 511 (1969).
(13) M. D. Newton and W. E. Palke, *J. Chem. Phys.*, **45**, 2329 (1966).
(14) O. Kikuchi, *Bull. Chem. Soc. Jap.*, **42**, 47 (1969).
(15) A. W. Sallotto and L. Burnelle, *J. Chem. Phys.*, **53**, 333 (1970).
(16) G. Berthier, H. Lemaire, A. Rassat, and A. Veillard, *Theor. Chim. Acta*, **3**, 213 (1965).

TABLE II: Polarization Constants (in Gauss) for H_2NO

	P	Q_{OO}^{O}	Q_{cross}^{O}	Q_{NN}^{O}	Q_{OO}^{N}	Q_{cross}^{N}	Q_{NN}^{N}
	0.9	60.8	−3.1	−17.8	−6.8	2.7	23.9
$A = P$	1.0	54.3	−2.8	−16.1	−6.2	2.4	21.0
$B = P$	1.1	48.9	−2.6	−14.7	−5.7	2.2	18.6
$D = P/0.75$	1.2	44.5	−2.4	−13.7	−5.2	2.0	16.6
	1.3	40.7	−2.2	−12.6	−4.9	1.8	14.9
	0.9	60.5	−3.1	−18.2	−6.8	2.2	20.5
$A = P$	1.0	54.1	−2.8	−16.5	−6.2	2.0	17.9
$B = P$	1.1	48.7	−2.6	−15.1	−5.7	1.8	15.8
$D = P/0.55$	1.2	44.3	−2.4	−13.9	−5.2	1.6	14.0
	1.3	40.5	−2.2	−12.9	−4.9	1.5	12.5
	0.9	65.5	−3.4	−17.7	−6.8	2.7	23.9
$A = P$	1.0	58.5	−3.1	−16.0	−6.1	2.4	21.0
$B = 0.9P$	1.1	52.8	−2.8	−14.6	−5.6	2.2	18.6
$D = P/0.75$	1.2	48.0	−2.6	−13.5	−5.2	2.0	16.6
	1.3	43.9	−2.5	−12.5	−4.8	1.8	14.9
	0.9	65.5	−3.5	−18.1	−6.8	2.2	20.5
$A = P$	1.0	58.5	−3.1	−16.3	−6.1	2.0	17.9
$B = 0.9P$	1.1	52.8	−2.9	−14.9	−5.6	1.8	15.8
$D = P/0.55$	1.2	48.0	−2.7	−13.8	−5.2	1.6	14.0
	1.3	43.9	−2.5	−12.8	−4.8	1.5	12.5

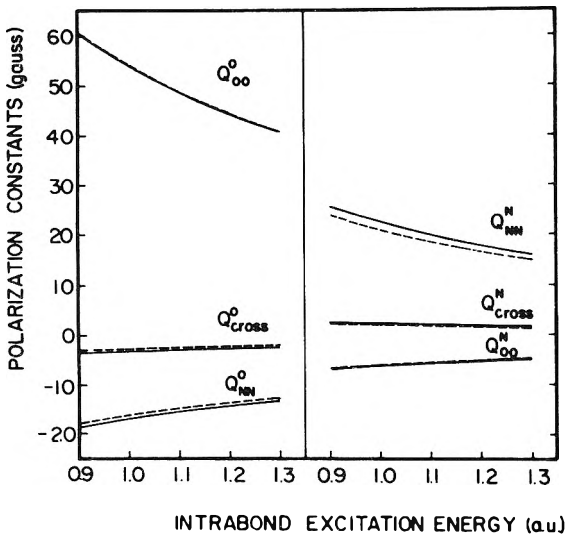

Figure 1. Polarization constants as a function of the intrabond excitation energy for the fragments C_2NO (——) and H_2NO (- - -). The n → σ^* excitation energy A and the σ(N–O) → σ^* (N–O) excitation energy B are both set equal to P. The σ(C–N) → σ^* (N–O) excitation energy F and the σ(H–N) → σ^* (N–O) energy D are given by $P/0.75$.

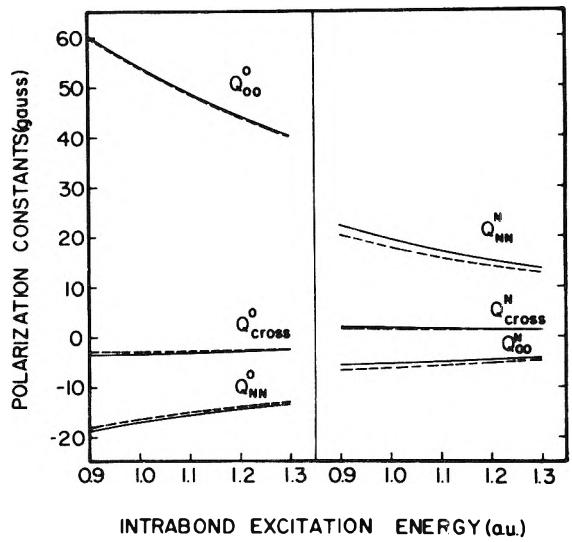

Figure 2. Same as Figure 1 except that $F = D = P/0.55$.

ent calculations R is defined as B/F and values of R = 0.55 and 0.75 were taken.

The excitation energies of the type $1s_O \rightarrow \sigma^*$(N–O) and $1s_N \rightarrow \sigma^*$ (N–O) can confidently be approximated by the 1s → 2s excitation energies of the relevant atoms, as determined from X-ray term values.[17]

The elements of the Q matrix for C_2NO were calculated as a function of the σ(N–O) → σ^*(N–O) excitation energy P, and with the following sets of conditions

1. $A = B = P$	$F = P/0.75$	
2. $A = B = P$	$F = P/0.55$	
3. $A = 0.9P$	$B = P$	$F = P/0.75$
4. $A = 0.9P$	$B = P$	$F = P/0.55$

where $E = B$ and $G = H = F$. Here we have equated several of the interbond excitation energies. This simplification is forced on us by lack of detailed information on the relevant energies, but they are certainly expected to be of comparable magnitude. Plots of these results are given in Figures 1–4 which also contain the corresponding plots for H_2NO. The detailed numerical results are in Tables II–IV.

σ–π Parameters Results. The σ–π parameters for ^{17}O are, not surprisingly, similar to those obtained using the same method of calculation for ^{17}O in the carbonyl group. Q_{OO}^{O} for the carbonyl group was estimated to fall in the range 53.9–64 G. A point of interest is the relatively large negative value of Q_{NN}^{O} (~ -15 G) which may be compared with the value of −21 G for Q_{CC}^{O}. On the other hand, the small value of Q_{OO}^{N} may be a source of comfort to those who have maintained that a^N depends only on ρ_N. The range of values for Q_{NN}^{N} falls slightly lower than

(17) "International Critical Tables of Numerical Data Physics, Chemistry, and Technology," Vol. 5, McGraw-Hill, N. Y., p 392.

TABLE III: Polarization Constants (in Gauss) for C_2NO

	P	Q_{OO}^{O}	Q_{cross}^{O}	Q_{NN}^{O}	Q_{CO}^{N}	Q_{cross}^{N}	Q_{NN}^{N}
	0.9	60.5	−3.6	−18.8	−6.9	2.4	25.8
$A = P$	1.0	54.1	−3.3	−17.0	−6.3	2.2	22.6
$B = P$	1.1	48.8	−3.1	−15.5	−5.8	2.0	20.0
$F = P/0.75$	1.2	44.3	−2.8	−14.3	−5.3	1.8	17.9
	1.3	40.6	−2.6	−13.3	−4.9	1.6	16.1
	0.9	60.5	−3.6	−19.1	−7.1	2.0	22.2
$A = P$	1.0	54.1	−3.3	−17.3	−6.4	1.8	19.4
$B = P$	1.1	48.8	−3.0	−15.8	−5.8	1.6	17.1
$F = P/0.55$	1.2	44.3	−2.8	−14.6	−5.4	1.5	15.2
	1.3	40.6	−2.6	−13.5	−5.0	1.3	13.6
	0.9	65.2	−4.0	−18.7	−6.8	2.4	25.8
$A = P$	1.0	58.2	−3.6	−16.9	−6.1	2.2	22.6
$B = 0.9P$	1.1	52.5	−3.3	−15.4	−5.6	2.0	20.0
$F = P/0.75$	1.2	47.8	−3.1	−14.2	−5.2	1.8	17.9
	1.3	43.8	−2.8	−13.2	−4.8	1.6	16.1
	0.9	65.2	−4.0	−19.0	−7.0	2.0	22.1
$A = P$	1.0	58.2	−3.6	−17.2	−6.3	1.8	19.4
$B = 0.9P$	1.1	52.5	−3.3	−15.7	−5.7	1.6	17.1
$F = P/0.55$	1.2	47.8	−3.1	−14.5	−5.3	1.5	15.2
	1.3	43.8	−2.8	−13.4	−4.9	1.3	13.6

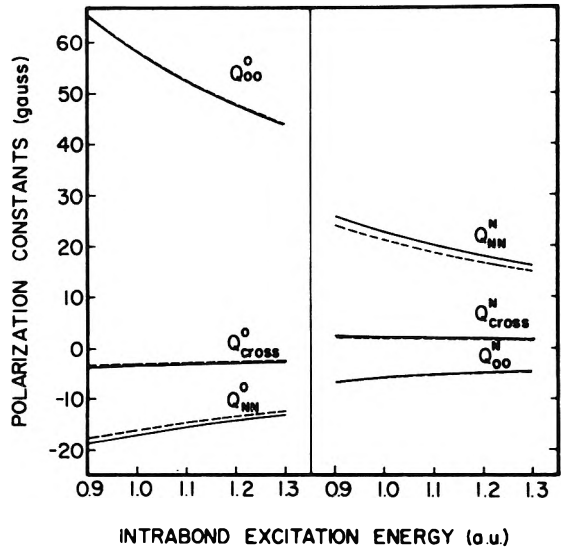

Figure 3. Same as Figure 1 except that $A = 0.9P$, $B = P$, $F = D = P/0.75$.

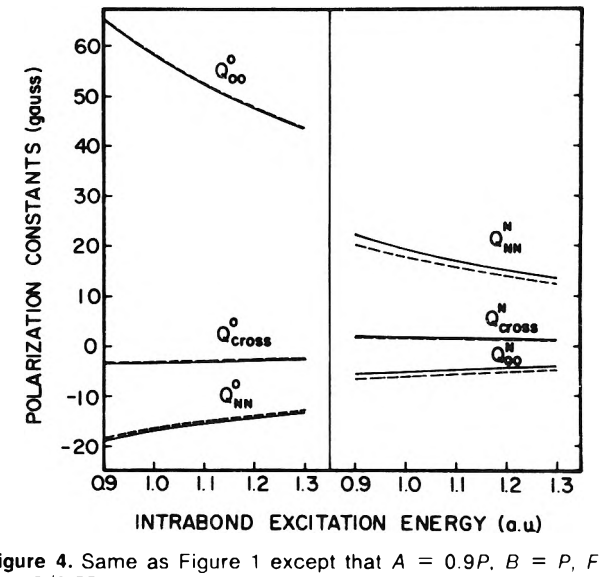

Figure 4. Same as Figure 1 except that $A = 0.9P$, $B = P$, $F = D = P/0.55$.

most semiempirical estimates in the literature,[18] the majority of which refer to the carbon bonded amine group.

In the above treatment the fragments H_2NO and C_2NO were assumed planar. There is very good evidence that this is not realistic. Experimentally, X-ray structure analysis[8] has shown that in TMPO the N-O bond is inclined at 21° to the plane defined by the C-N-C nuclei. On the theoretical side, Sallotto and Burnelle[15] have found that the planar conformation of H_2NO is unstable with respect to bending in agreement with the energetic predictions of the Walsh diagrams (they estimate an equilibrium out-of-plane bending angle of 26°).

Of course the Q matrices calculated above refer strictly only to planar fragments, but it is not very likely that the elements of Q^O will be significantly affected by bending. Using an SCF all-valence-electron method, Douady, *et al.*,[19] found that the energies of the orbitals calculated for H_2NO, and the magnitudes of the products $C_{2s}^{N}(\sigma)C_{2s}^{N}(\sigma^*)$ are hardly affected by bending up to 15°. The value of $C_{2s}^{O}(\sigma)C_{2s}^{O}(\sigma^*)$ should be even less sensitive to bending, and we feel that the previously estimated elements of the Q^O matrix should apply equally well to radicals bent at the nitrogen atom. From the results of Douady, *et al.*, we may conclude that the *σ-π polarization parameters* Q^N are not very sensitive to moderate bending. We will, therefore, take the calculated values of the Q matrix to apply to both planar and bent nitroxide radicals. In other words bending will be assumed not to affect the contribution of *polarization* to the isotropic hyperfine interaction. In the case of the amine $-NH_2$ group it was found necessary to assume bending in order to account for the ob-

(18) E. T. Kaizer and L. Kevan, "Radical Ions," Interscience, New York, N. Y., p 24.
(19) J. Douady, Y. Ellinger, A. Rassat, R. Suleva, and G. Berthier, *Mol. Phys.*, **17**, 217 (1969).

TABLE IV: Polarization Constants (in Gauss) Using P = 1.15 au

A	B	F	$Q_{OO}{}^{O}$	$Q_{cross}{}^{N}$	$Q_{NN}{}^{O}$	$Q_{OO}{}^{N}$	$Q_{cross}{}^{N}$	$Q_{NN}{}^{N}$
				H_2NO				
P	P	$P/0.75$	46.6	−2.5	−13.9	−5.6	2.1	18.1
P	P	$P/0.55$	46.6	−2.5	−14.3	−5.6	1.6	15.2
$0.9P$	P	$P/0.75$	48.6	−2.5	−13.8	−5.5	2.1	18.0
$0.9P$	P	$P/0.55$	48.6	−2.8	−14.1	−5.4	1.7	15.2
				C_2NO				
P	P	$P/0.75$	46.4	−2.9	−14.9	−5.5	1.8	18.9
P	P	$P/0.55$	46.4	−2.9	−15.1	−5.5	1.5	16.1
$0.9P$	P	$P/0.75$	48.4	−3.2	−14.8	−5.4	1.9	18.9
$0.9P$	P	$P/0.55$	48.4	−3.2	−15.0	−5.5	1.5	16.0

served nitrogen and proton coupling constants.[5] In the case of nitroxides it is known that bending occurs in TMPO, and presumable most other nonconjugated nitroxide radicals can be taken as being bent.

Bending affects the nitrogen hyperfine coupling by introducing some s character into the orbital containing the odd electron, which results in additional positive spin density at the nitrogen nucleus. The magnitude of this effect is not easy to predict. One approach is to estimate from the bending angle the degree of hybridation of the nitrogen 2s and 2p orbitals. The consequences for the isotropic nitrogen splitting are expressed in the equation[20]

$$a^N = a^N(O) + 550(2\tan^2\theta)\rho_N \qquad (3)$$

In part III we will use the calculated Q matrix, the observed ^{17}O and ^{14}N hyperfine splittings, and eq 3 to discuss spin density distribution in the nitroxyl group.

II. Experimental Measurements and Results

Synthesis of ^{17}O-Labeled TMPO. TMPO enriched in ^{17}O (in the nitroxyl group) was synthesized by the oxidation of triacetoneamine with $H_2{}^{17}O_2$. The ^{17}O-enriched hydrogen peroxide was obtained by hydrolyzing $Na_2{}^{17}O_2$ prepared from sodium metal and ^{17}O-enriched oxygen gas. The oxidation of the amine was carried out in the presence of phosphotungstic acid, following the prescription of Briere, *et al.*[21] TMPO enriched to 5% in ^{17}O was used for esr studies in solution. A sample enriched to 55% ^{17}O was used for the frozen solution spectra. Esr spectra were recorded on a Varian V-4503 X-band spectrometer. The field was calibrated with an aqueous solution of Fremy's salt taking a^N = 13.0 G and g = 2.0057.

Spectrum of ^{17}O-Labeled TMPO. The X-band esr spectrum of ^{17}O-labeled TMPO (~5 atom %) was observed in a variety of solvents. The results are tabulated in Table V and a typical spectrum is shown in Figure 5. All the hyperfine coupling constants observable, a^O, a^N, and a^C, are solvent dependent, as is the g value. The doubtful significance of the measured values of a^C will be discussed later. The esr spectrum of a frozen solution of ^{17}O-labeled TMPO in ethyl ether is shown in Figure 6. Satellites due to ^{17}O are clearly visible. The observed nitrogen hyperfine splitting, 32.1 G, is obviously equated to $A^N(\|)$. Using this value and the splitting of 406.6 G between the extreme ^{17}O satellites we obtain a value of 68.4 G for $A^O(\|)$. The value of $A_O(\perp)$ is probably too small to give observable satellites in frozen solution.

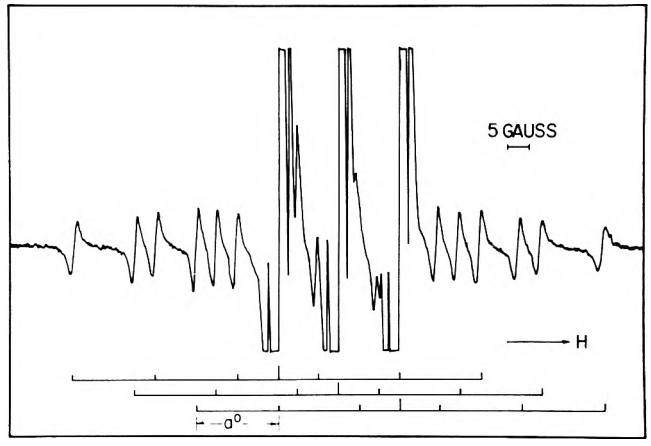

Figure 5. X-Band esr spectrum of ^{17}O-labeled TMPO in benzene at 21°.

TABLE V: Observed ^{13}C, ^{14}N, and ^{17}O Isotropic Hyperfine Splittings and g Values for 2,2,6,6-Tetramethyl-4-piperdone 1-Oxyl at 21 ± 1°

Solvent	a_C	a_N	a_O	g
Benzene		14.45	19.29	2.0062
Toluene	5.42	14.47	19.52	2.0063
N-*N*-Dimethylformamide	5.42	14.66	19.40	2.0062
Methylene chloride	5.45	14.77	19.36	2.0061
Dimethyl sulfoxide	5.92	14.90	19.74	2.0060
1-Butanol	5.66	15.01	19.11	2.0060
Formamide	5.75	15.28	18.88	2.0060
Ethylene glycol	5.81	15.40	18.72	2.0061
Ethyl ether		15.94	17.84	
Water	6.04	16.01	17.86	2.0058
10 *M* lithium chloride	6.12	16.11	17.57	2.0056

III. Spin Densities

The ^{14}N and ^{17}O splitting constants can be written as

$$a^N = f(\theta) + Q_{NN}{}^N\rho_N + Q_{OO}{}^N\rho_O + Q_{cross}{}^N(\rho_O\rho_N)^{1/2}$$

$$a^O = Q_{OO}{}^O\rho_O + Q_{NN}{}^O\rho_N + Q_{cross}{}^O(\rho_O\rho_N)^{1/2}$$

where $f(\theta)$ is given by eq 3. To solve these equations we choose (*cf.* Table IV) the values of the Q matrix for P = 1.15 au and the conditions $A = B = P$ and $F = P/0.55$. Taking the values of a^N and a^O observed in ethyl ether, *i.e.*, 15.94 and 17.84 G, respectively, we obtain ρ_O = 0.55, ρ_N = 0.45, and θ = 17. These values are slightly changed if the overlap between the pπ orbitals is taken into account, but such a correction is not felt to be justified in view of the uncertainties in the value of the Q matrix. Since we have decided to accept P = 1.15 au, the calcu-

(20) R. W. Fessenden, *J. Phys. Chem.*, 71, 74 (1967).
(21) R. Briere, H. Lemaire, and A. Rassat, *Bull. Soc. Chim. Fr.*, 3273 (1965).

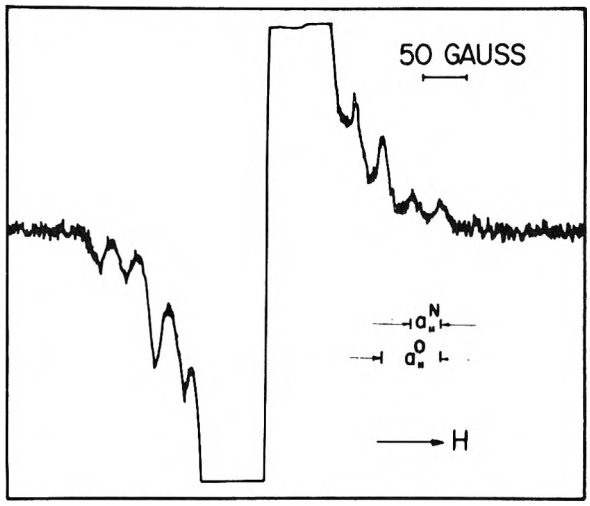

Figure 6. X-Band esr spectrum of a frozen solution of ^{17}O-labeled TMPO in ethyl ether. The main nitrogen hyperfine lines are off-scale.

lated spin densities and the bending angle are those that we will refer to as the "theoretically calculated" values. As a matter of interest, the values corresponding to two other, extreme choices for the elements of the Q matrix are given here. For Q_{OO}^{O} = 65.2(40.5), Q_{cross}^{O} = −2.9(−2.5), Q_{NN}^{O} = −19.1(−13.5), Q_{OO}^{N} = −6.9(−4.2), Q_{cross}^{N} = 2.4(1.3), and Q_{NN}^{N} = 25.8(13.6), we obtain respectively ρ_O = 0.46(0.6), ρ_N = 0.54(0.4), and θ = 10°(20°). We conclude that for any reasonable choice of excitation values the calculated spin densities on oxygen and nitrogen are roughly equal. The value of 0.55 for ρ_O is in sharp contrast to the results of Hamilton and McConnell[2] who find $\rho_N \sim 0.8$ to 0.9 on the basis of the observed isotropic and anisotropic ^{14}N splittings. Their discussion is partially based on the assumption that the C_2N-O group is planar. For TMPO this is certainly not true, and it seems probable that all nitroxides bonded to sp^3-hybridized carbon atoms are bent. Using a value of 27 G, calculated for the perpendicular one-electron anisotropic dipole–dipole interaction of ^{14}N, the observed ^{14}N splittings of 31 G (∥) and 5–6 G (⊥) are stated to be compatible with ρ_N = 0.8. In fact the splittings are far more compatible with ρ_N = 0.6 (using the observed isotropic ^{14}N splitting of ~15 G). Furthermore, there is much evidence that the anisotropic dipole–dipole parameters calculated from Slater orbitals are too low. Morton, Rowlands and Whiffen[22] calculate 2β to be 34 G for ^{14}N, using Hartree–Fock orbitals. Hurd and Coodin[23] put 2β at 39.6 G. Using these values we obtain ρ_N = 0.47 (MRW) or 0.40 (HC).

Newton and Palke[13] calculate $\rho_O \simeq \rho_C$ for the carbonyl group and Kikuchi[14] calculates $\rho_O \simeq \rho_N$ for the H_2NO radical. In general the fact that N is more electronegative than C should give a shift of the bonding electrons toward nitrogen and a corresponding shift away from nitrogen of the antibonding electrons as compared to the carbonyl group. Thus ρ_N for the nitroxide group can be expected to be smaller than ρ_C for the *isolated* carbonyl group. Such a group occurs in the hexamethyl acetone ketyl radical for which Broze and Luz[24] estimate ρ_C as 0.7–0.8. On this argument it seems likely that ρ_N does not exceed 0.7 in the >NO group. A similar conclusion has been reached by Hoffman and Eames[25] on the basis of protonation effects on the esr spectrum of TMPO.

Strong independent support for a relatively high spin density on oxygen comes from the value of 68.4 G for $A^O(\|)$ observed in the frozen ethyl ether solution spectrum of TMPO. In the same solvent at room temperature, a^O = 17.8 G, so that, assuming an axially symmetric dipolar tensor, we obtain $A_{dip}^{O}(\|)$ = 49.4 G and $A_{dip}^{O}(\perp)$ = −24.7 G. The value for $A_{dip}^{N}(\|)$ given by Griffith, *et al.*, is ~17 G.[26] Estimates of 2β for ^{17}O range from 83.4 G for $^{17}O^-$ ion[27] to 120 G given by Hurd and Coodin, which correspond here to ρ_O = 0.60 and ρ_O = 0.40. From studies of the ^{17}O hyperfine tensor in small radicals,[28] it appears that the value of 103 G given for 2β by Morton, Rowlands, and Whiffen[22] is the most consistent with experimental results. This corresponds to ρ_O = 0.49 in the present case. If we use these author's value of 34 G for 2β for ^{14}N we obtain a spin density of ρ_N = 0.49, *i.e.*, $\rho_O \simeq \rho_N$. Using Hurd and Coodin's value for 2β (^{14}N) of 39.6 G we obtain ρ_N = 0.42, and once again $\rho_O \simeq \rho_N$. Thus the spin densities estimated by this method agree well with those estimated theoretically in this work.

The H_2NO radical[29] has a very low nitrogen splitting (11.9 G) for a nitroxide radical with the unpaired electron confined to the >NO group. This could be due either to a low spin density on nitrogen, or to a small bending, or to both. It would be of interest to measure the ^{17}O splitting in this radical. If we take the σ-π parameters calculated here and assume that the spin density is distributed as estimated for TMPO, we obtain a bending angle of 13° using eq 3 compared to the calculated value of 26° given by Burnelle and Sallotto. It is of interest that if we take the nitroxide group in TMPO to be planar, we obtain a^N = 5.44. This can be compared with a^N = 7.68 calculated for planar H_2NO and a^N = 6.32 calculated for planar dimethyl nitroxide.[30] Thus widely different theoretical approaches applied to planar nitroxides all lead to a value of a^N which is far smaller than that observed experimentally. Although the values of θ derived in this work should not be taken too seriously, since it is doubtful if eq 2 is strictly applicable, there can be no doubt that bending is necessary to account for the observed values of a^N.

Solvent Effects. Solvent effects on the g value and on a^N have been observed and discussed by Kawamura, *et al.*,[31] who gave a detailed analysis of the various contributions to the g shift. The solvent effect on the g value of TMPO parallels that observed for diphenyl nitroxide and di-*tert*-butyl nitroxide.[31] In view of the smallness of the observed solvent effect on the g value and the numerous simplifying assumptions made by Kawamura, *et al.*, in their analysis, we feel that their conclusions are only qualitively significant.

Changes in the form and energies of π^* orbitals can di-

(22) J. R. Morton, J. R. Rowlands, and D. H. Whiffen, *Natl. Phys. Lab., Gr. Brit., Circ.*, **No. BPR 13.**
(23) C. M. Hurd and P. Coodin, *J. Phys. Chem. Solids*, **28**, 523 (1967).
(24) M. Broze and Z. Luz, *J. Chem. Phys.*, **51**, 749 (1969).
(25) B. M. Hoffman and T. B. Eames, *J. Amer. Chem. Soc.*, **97**, 2169 (1969).
(26) O. H. Griffith, D. W. Cornell, and H. M. McConnell, *J. Chem. Phys.*, **43**, 2909 (1965).
(27) E. Clementi and A. D. McLean, *Phys. Rev. A*, **133**, 419 (1964).
(28) (a) Z. Luz, A. Reuveni, R. W. Holmberg, and B. L. Silver, *J. Chem. Phys.*, **51**, 4017 (1969); (b) S. Schlick, B. L. Silver, and Z. Luz, *ibid.*, **52**, 1232 (1970); (c) *ibid.*, **54**, 867 (1971); (d) A. Reuveni, Z. Luz, and B. L. Silver, *ibid.*, **53**, 4619 (1970); (e) S. Schlick, *ibid.*, **56**, 654 (1972).
(29) J. Q. Adams, S. K. Nicksic, and J. R. Thomas, *J. Chem. Phys.*, **45**, 654 (1966).
(30) I. Morishima, K. Endo, and T. Yonezawa, *Chem. Phys. Lett.*, **9**, 143 (1971).
(31) (a) T. Kawamura, S. Matsunami, and T. Yonezawa, *Bull. Chem. Soc. Jap.*, **40**, 1111 (1967); (b) T. Kawamura, S. Matsunami, T. Yonezawa, and K. Fukui, *ibid.*, **38**, 1935 (1965).

rectly affect the g values and the spin distribution, but will not affect the elements of the Q matrix to first order, a fact which has been implicity assumed, and occasionally explicitly stated, in all previous treatments of solvent effects on hyperfine splitting constants. The possible effects of change of solvent include, among other things, (a) changes in the distribution of the unpaired electron, (b) changes in the energy of the lone pair electrons (c) changes in the energies of the π and π^* orbitals, and (d) changes in the energies of the σ and σ^* orbitals. We believe and assume that changes in solvent affect ρ_O and ρ_N but do not significantly alter the Q matrices, and that changes in a^O and a^N are mainly due to changes in spin density distribution. From Table V it can be seen that solvents which reduce a^N, increase a^O, which does not prove very much, but is at least consistent with our assumption and the conservation of total spin density.

Morishima, *et al.*,[30] have made INDO calculations on the hyperfine coupling constants in dimethyl nitroxide and on the expected effect of hydrogen bonding on the constants. Their calculated coupling constants are in poor agreement with experiment. They predict an increase in a^N in going from nonhydrogen bonding to hydrogen bonding solvents, and a decrease in a^O, as observed here. However, they predict the effect on a^O to be much larger than that on a^N, whereas, from Table V, it can be seen that the changes in a^O and a^N are very similar in going from benzene to water.

The esr spectrum of isotopically normal TMPO shows ^{13}C satellites on either side of the three main (^{14}N) lines. In ^{13}C-enriched (58.6%) di-*tert*-butyl nitroxide (DTBN), the observed ^{13}C satellites have been shown[32] to be due to a superposition of the satellites due to the tertiary carbon and the methyl (β) carbons, with splitting constants of 5.36 and 4.83 G, respectively, in 10 M aqueous LiCl solution. In isotopically normal DTBN the two sets of satellites could not be differentiated. In the case of the radical studied in this work only one set of ^{13}C satellites was observed. The measured splitting constant a^C for these lines is listed, for various solvents, in Table II. It can be seen that a^C decreases with decreasing a^N, as would be expected, since the spin density at the ^{13}C nuclei (either α or β) is probably proportional to the spin density at the nitrogen atom, and not significantly dependent on ρ_O. It is not possible to make a quantitive analysis of the ^{13}C splittings since the work on DTBN indicates that the satellites are probably due to a superposition of α and β ^{13}C satellites. The symbol a^C is thus merely a shorthand notation for the measured separation in gauss between the observed satellites.

Conclusion

Taken together, the theoretically calculated σ-π parameters for the nitroxyl group and the observed isotropic ^{14}N and ^{17}O splittings lead to an estimate of the spin density distribution which is in good agreement with that derived, completely independently, from the anisotropic hyperfine tensors. The unpaired electron is found to be shared almost equally between the nitrogen and oxygen atoms. The nitrogen and oxygen isotropic splitting constants of organic nitroxides are known to be relatively insensitive to substitution, a fact which suggests that the spin densities estimated in this work are applicable to most nitroxide radicals.[33]

Acknowledgment. This research was supported by Grant No. NBS (G)-141 from the National Bureau of Standards.

(32) R. Briere, H. Lemaire, and A. Rassat, *J. Chem. Phys.*, **48**, 1429 (1968).

(33) Note Added in Proof. An out of plane bending of 18.2° has been found by X-ray structure analysis for the nitroxyl group in di(2,2,6,6-tetramethyl-3-piperidinyl-1-oxyl suberate. (A. Capiomon, *Acta. Crystallogr., Sect. B*, **28**, 2298 (1972).

Unperturbed Polymer Chain Dimensions from Intrinsic Viscosities Determined in Good Solvents

Carl J. Stacy* and Raymond L. Arnett

Phillips Petroleum Company, Bartlesville, Oklahoma 74004 *(Received July 31, 1972)*

Publication costs assisted by the Phillips Petroleum Company

Experimental criteria are presented to determine the region of validity of the intrinsic viscosity-molecular weight relation proposed by Stockmayer and Fixman for use in good solvents. Use of these criteria in several good solvents yields the same value for unperturbed polymer dimensions as do measurements made at "θ" conditions. Intrinsic viscosity determinations conforming to these criteria, made in two good solvents, allow the determination of weight-average molecular weights of the polymer solute.

I. Introduction

The unperturbed conformation of a polymer chain determines a molecular weight independent constant, s_0^2/M, characteristic of the structure of the macromolecule; s_0^2 is the unperturbed mean-square distance of centers of mass from the center of gravity of a macromolecule having molecular weight M.[1,2] When the object of an experimental investigation is to gain knowledge about polymer

(1) P. J. Flory, "Statistical Mechanics of Chain Molecules," Interscience, New York, N. Y., 1969.

(2) T. M. Birshtein and O. B. Ptitsyn, "Conformations of Macromolecules," Interscience, New York, N. Y., 1966.

TABLE I: Molecular Weights of Polymers

Polymer	$M_n \times 10^{-3}$ [a]	$\sigma M_n \times 10^{-3}$	$M_w \times 10^{-3}$	$\sigma M_w \times 10^{-3}$	$M_\theta \times 10^{-3}$ [b]	M_w/M_n
1	2.2		2.98	0.06	2.76	1.36
3	3.9		5.12	0.05	4.78	1.31
10	10.0		13.34	0.16	12.41	1.33
30	34.7	0.3	41.7	0.6	39.9	1.20
44	50.2	0.4	53.3	0.9	52.4	1.06
100	87.5	3.5	109.9	1.1	103.9	1.26
58	100.7	3.2	122.8	0.9	117.0	1.22
64	139.0	4.6	188.0	3.2	174.0	1.35
67	182.0	8.2	244.0	5.0	227.0	1.34

[a] Polymers 1, 3, and 10 by ebullioscopy, all others by osmometry. [b] M_θ is that viscosity-average molecular weight appropriate for θ conditions; it's value is here taken as $M_n^{1/4}M_w^{3/4}$.

structure through observation of s_0^2/M, the experimenter frequently determines intrinsic viscosities, $[\eta]$, for members of a homologous series and interprets his results through the Flory-Fox relation

$$[\eta] = KM^{1/2},\ K = \Phi(6s_0^2/M)^{3/2} \qquad (1)$$

For example, linear polyethylene, the simplest structured polymer, has been investigated and the results interpreted[3,4] by eq 1 to give an observed value for s_0^2/M in good agreement with the theoretical values calculated by Hoeve[5] and by Abe, Jernigan, and Flory[6] using the rotational isomeric model. In eq 1, Φ is a universal constant.

In order to use relation 1 an experimental requirement is imposed that there be no perturbation of the polymer molecule by the solvent. The time and labor necessary to establish such conditions for each polymer structure of interest make it highly desirable to explore for means of determination of s_0^2/M by less onerous experimentation. Kurata and Stockmayer[7] have given a survey of the theoretical work aimed at extending relation 1 to include the effect of dimensional perturbation by good solvents. Among these works, a relation proposed by Stockmayer and Fixman[8] has appealing simplicity but suffers in its failure to handle adequately large polymer-solvent interactions.[9] Nevertheless, if the object of an investigation is to determine unperturbed polymer dimensions (as is our object here) rather than examine large polymer-solvent interactions, then certain experimental criteria for regions of validity of the Stockmayer-Fixman relation are suggested by the relation itself. This work presents these criteria and compares the values of s_0^2/M obtained by using them in good solvents with a value obtained by direct θ condition measurements.

II. Experimental Section

The polymers used in this investigation are nearly monodisperse hydrogenated polybutadienes prepared by polymerizing butadiene in cyclohexane using butyllithium as initiator[10,11] and subsequently hydrogenating the solution using Girdler prereduced nickel catalyst.[12] Infrared analyses monitored the unsaturation, oxidation, and solvent removal.

Analyses of the parent polybutadienes by infrared[13] yielded 19 vinyl groups per 1000 carbon atoms. Because of its high sensitivity, this determination was taken as the number of ethyl side chains in the hydrogenated product; spectra after hydrogenation were entirely consistent with this interpretation. Molecular weights were obtained by procedures described previously (weight-average from scattered light measurements,[14] number average by ebullioscopy[15] for the lower molecular weight samples, and osmometry[16] for the higher).

The intrinsic viscosities were determined using standard procedures[4] taking care to avoid oxidation of the solutions.

III. Results

The observed molecular weights, together with estimates of their standard deviations, σ, are listed in Table I. The ratio, M_w/M_r, given in the last column provides a measure of the degree of polydispersity.

The observed intrinsic viscosities and other pertinent quantities are listed in Table II. Relative viscosities, η_r, measured in several solvents and at two temperatures were related to polymer concentration, c, by the usual equations

$$\ln \eta_r = [\eta]c(1 + k''[\eta]c)$$

which in turn determined the intrinsic viscosity, $[\eta]$, and the molecular weight independent interaction constant, k''. The values of k'' listed in the table are seen to be correlated with solvent power; the values range from +0.22 for the θ solvent (1-dodecanol at 125°) to −0.11 for the best solvent.

IV. Interpretation

The relation suggested by Stockmayer and Fixman[8] to replace (1) for good solvents may be written

$$[\eta] = KM^{1/2} + JM$$

(3) R. Chiang, *J. Phys. Chem.*, **69**, 1645 (1965); **70**, 2348 (1966); A. Nakajima, *et al.*, *J. Polym. Sci., Part C*, **15**, 285 (1966).
(4) C. J. Stacy and R. L. Arnett, *J. Phys. Chem.*, **69**, 3109 (1965).
(5) C. A. J. Hoeve, *J. Chem. Phys.*, **35**, 1266 (1961).
(6) A. Abe, R. L. Jernigan, and P. J. Flory, *J. Amer. Chem. Soc.*, **88**, 631 (1966); P. J. Flory and R. L. Jernigan, *J. Chem. Phys.*, **42**, 3509 (1965).
(7) M. Kurata and W. H Stockmayer, *Fortschr. Hochpolym. Forsch.*, **3**, 196 (1963).
(8) W. H. Stockmayer and M. Fixman, *J. Polym. Sci., Part C*, **1**, 137 (1963).
(9) G. C. Berry, *J. Chem. Phys.*, **44**, 4550 (1966); **46**, 1338 (1967).
(10) R. P. Zelinski and C. F. Wofford, *J. Polym. Sci., Part A-3*, 93 (1965).
(11) H. L. Hsieh, *J. Polym. Sci., Part A-3*, 191 (1965); J. N. Short, R. P. Zelinski, and O. F. McKinney, IUPAC Symposium on Macromolecular Chemistry, Tokyo, Japan, 1966.
(12) C. W. Moberly, "Hydrogenation of Polymers," in "Encyclopedia of Polymer Science and Technology," Vol. VII, Wiley, New York, N. Y., 1967.
(13) R. S. Silas, J. Yates, and V. Thornton, *Anal. Chem.*, **31**, 529 (1959).
(14) C. J. Stacy and R. L. Arnett, *J. Polym. Sci., Part A-2*, 167 (1964).
(15) R. L. Arnett, M. E. Smith, and B. O. Buell, *J. Polym. Sci., Part A-1*, 2753 (1963).
(16) R. L. Arnett and R. Q. Gregg, *J. Phys. Chem.*, **74**, 1593 (1970).

TABLE II: Intrinsic Viscosity

Polymer	Solvent[a] 1	2	2	3	4	4	5	6
	Temp, °C 125	125	140	125	125	140	140	125
	$[\eta]$, dl/g × 10^2							
1	7.2				9.1			10.8
3	13.5				16.0			18.5
10	26.7				33.1			40.4
30	53.5	56.4	60.2	71.1	71.3	71.0	81.2	93.6
44	61.3	68.7	73.9	89.8	90.1	89.8	103.8	121.2
100	93.9	102.7	111.3		137.5	140.3	166.4	195.8
58	95.8	109.8	119.5	151.2	152.0	151.4	179.5	210.5
64	117.0	136.5	151.1	196.5	197.2	196.8	236.1	284.1
67	132.9	152.1	178.8	236.7	237.7	232.6	289.8	343.8
$\sigma[\eta]$, dl/g × 10^2	1.1	1.8	0.7	0.5	0.8	0.5	0.3	1.2
$k'' \times 10^2$	22.1	14.4	8.57	−2.63	−2.46	−2.67	−8.24	−11.4

[a] Key to solvents: (1) 1-dodecanol, (2) biphenyl, (3) hexadecane, (4) 1-chloronaphthalene, (5) tetrahydronaphthalene, (6) decahydronaphthalene.

for monodisperse polymer, which becomes

$$[\eta] = KM_\theta^{1/2} + JM_w \qquad (2)$$

for polydisperse polymer, where

$$M_\theta = [c^{-1}\sum c_i M_i^{1/2}]^2 = (M^{1/2})_w^2$$

The parameter J provides a measure of the perturbation of the polymer molecules by the solvent; its value is zero at θ conditions. A pleasing feature of relation 2 is that, although an operational definition of viscosity-average molecular weight is possible (the solution, M_v, of the quadratic $[\eta] = K(M_v)^{1/2} + JM_v$), it is neither desirable nor required in order that there be physical meaning for the molecular weight averages appearing in eq 2. The weight-average molecular weight, M_w, is a familiar quantity and M_θ is that viscosity-average molecular weight appropriate for θ conditions.

When eq 2 is rewritten in the form

$$[\eta]/M_\theta^{1/2} = K + JM_w/M_\theta^{1/2} \qquad (3)$$

certain experimental tests for the validity of the Stockmayer–Fixman formula suggest themselves. (i) Equation 3 being that of a straight line, the data, plotted according to (3), must be linear. Berry[9] has demonstrated that when the polymer–solvent interaction is sufficiently large, from either a high molecular weight or a strong solvent, the data are not linear; only the linear region may be used to determine K. (ii) Outside a possible small second-order specific solvent effect, K is constant, at constant temperature, for a fixed polymer structure;[1] therefore, not only must the data be linear for each solvent, they must also extrapolate to a common intercept in order for (3) to be valid. An experimental survey of several solvents serves as a test for these requirements.

We display, in Figures 1 and 2, the data of Tables I and II plotted in the form of relation 3. An independent, preliminary treatment of the data for each solvent determined straight lines with no significant difference in intercepts, except for decahydronaphthalene at 125°. The solid lines in both figures represent final, weighted least-squares fits of combined data at each temperature, with the constraint that there be a common intercept. Decahydronaphthalene data were not used in the final fitting. Data for the three lowest molecular weight polymers were used in neither fitting, since they are outside the range of validity of relations 1 and 2. In Figure 1, the hexadecane measurements, although used in the fitting, are not shown as they nearly coincide with those for 1-chloronaphthalene. Also from Figure 1, which contains measurements at θ conditions, we learn that with the restrictions noted above, relation 2 used with good solvents, yields the same value of K as do measurements made under θ conditions. Indeed the solvents, biphenyl, 1-chloronaphthalene, and hexadecane give the measured value $K = (2.80 \pm 0.09) \times 10^{-3}$ while the θ solvent, 1-dodecanol yields $K = (2.80 \pm 0.03) \times 10^{-3}$. Table III lists the results of the fitting shown in Figures 1 and 2. The last column of the table gives the values of s_0^2/M calculated according to relation 1 using $\Phi = 2.5 \times 10^{21}$.

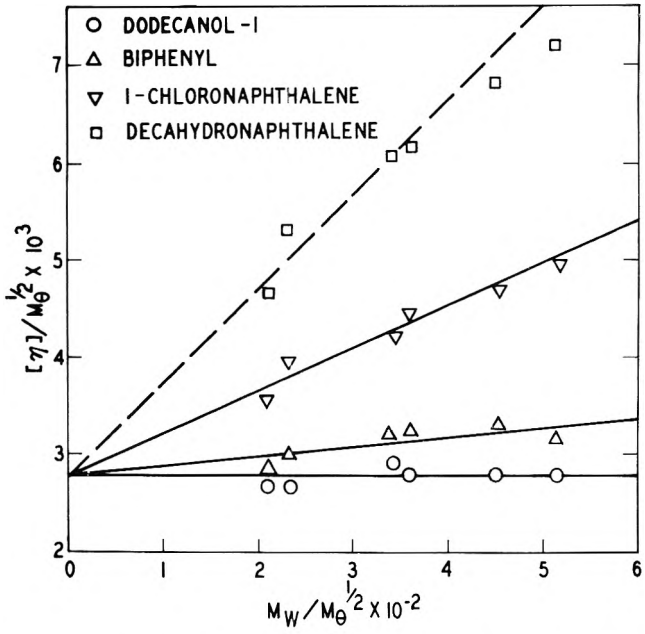

Figure 1. Intrinsic viscosity–molecular weight relations in several solvents at 125°.

We wish to point out another aspect of relation 2.

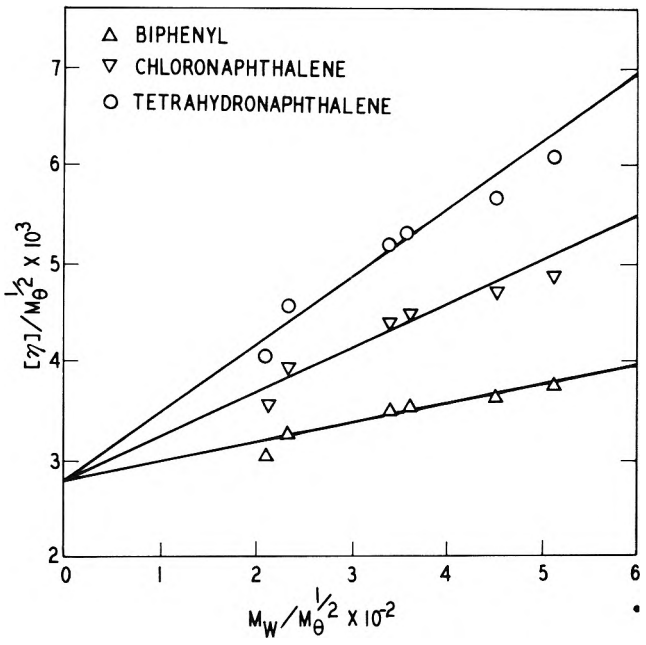

Figure 2. Intrinsic viscosity–molecular weight relations in several solvents at 140°.

Under the restrictive experimental conditions for validity, measurements of $[\eta]$ made in two solvents may be used to give each of the two average molecular weights appearing in (2). Since for a given polymer only $[\eta]$ and J change as the solvent changes, we obtain

$$M_w = ([\eta]_2 - [\eta]_1)/(J_2 - J_1) \quad (4)$$

and

$$M_\theta = [(J_2[\eta]_1 - J_1[\eta]_2)/K(J_2 - J_1)]^2 \quad (5)$$

where subscripts identify the quantities for the two solvents. Relation 4 should prove quite useful in that it provides a means of obtaining weight-average, rather than viscosity-average, molecular weights from intrinsic viscosity determinations made in good solvents. Figure 3 displays the data of two pairs of solvents plotted according to relation 4. It is noteworthy that data for the low molecular weight polymers are points on this line even though they are not part of the set described by eq 2.

Any specific solvent effect must be quite small for the systems we have explored here; the two quite dissimilar solvents, hexadecane and 1-chloronaphthalene, yield almost identical results.

Finally, we note that the unperturbed dimensions in

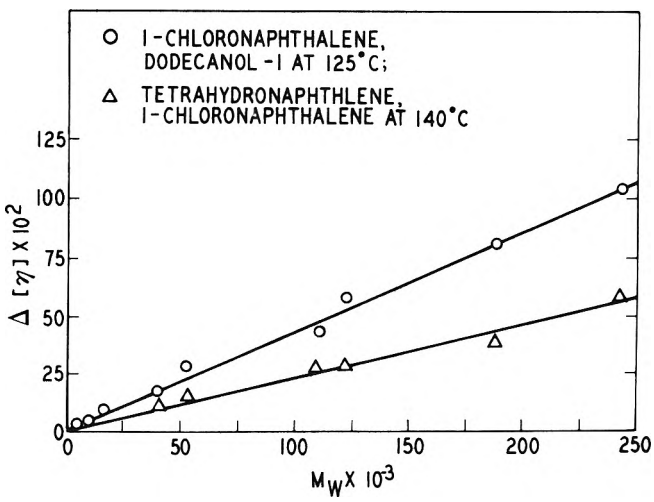

Figure 3. Intrinsic viscosity difference–molecular weight relation for solvent pairs.

TABLE III: Constants of Eq 2 for Ethyl-Branched Polymer[a] at Two Temperatures

Temp, °C	Solvent[b]	$K \times 10^3$	$\sigma_K \times 10^3$	$J \times 10^6$	$\sigma_J \times 10^6$	$(s_0^2/M) \times 10^{17}$
125	1	2.796	0.034	0.00		1.796
	2			0.95	0.16	
	3			4.38	0.14	
	4			4.39	0.14	
140	2	2.751	0.095	1.98	0.27	1.776
	4			4.55	0.30	
	5			6.89	0.32	

[a] Nineteen ethyl groups per 1000 carbon atoms. [b] Key to solvents given in Table II.

Table III are smaller than accepted values for linear polyethylene.[3,4] This trend has been confirmed with polymers of higher ethyl branch content, and will be the subject of a later contribution. A preliminary summary has recently appeared.[17]

Acknowledgment. We gratefully acknowledge the help of R. P. Zelinski, C. W. Moberly, A. O. Frenzel (deceased), and J. R. Donaldson, who, respectively, synthesized, hydrogenated, analyzed (by infrared), and characterized ($[\eta]$, M_n, and M_w) the above polymers.

(17) C. J. Stacy and R. L. Arnett, *Polym. Prepr., Amer. Chem. Soc., Div. Polym. Chem.*, **11**, (2), 1078 (1970).

An Equation of State for Medium-Density High-Temperature Conditions

D. R. Forshey, W. G. Courtney,*

Pittsburgh Mining and Safety Research Center, Bureau of Mines, U.S. Department of the Interior, Pittsburgh, Pennsylvania 15213

and J. B. Greenshields

Duquesne University, Pittsburgh, Pennsylvania 15219 *(Received July 3, 1972)*

Publication costs assisted by the U.S. Bureau of Mines

An equation of state for medium-density high-temperature conditions has been developed based upon an Abel-type covolume model. The formation of discrete clusters was examined using statistical thermodynamics but was found to be unimportant to the equation of state for most conditions considered here. Theoretical *PV* isotherms using this simple model agreed to within several per cent with experimental *PV* isotherms for Ar, N_2, and CO_2 for densities between about 0.001 and 1.5 g/cm^3 for temperatures about 100°K greater than the critical temperature. For these conditions the ideal gas, van der Waals, and Beattie-Bridgman models agreed only to within about 25%. Agreement for H_2O was less satisfactory and comparable to that obtained with the other models.

Introduction

The conversion of the chemical energy in a condensed explosive *via* a detonation to expansion work (rock shattering, plate pushing, etc.) involves expansion of the high-pressure, hot, gaseous detonation products to ambient pressure, cold, high-velocity gas. With a CHNO condensed explosive, for example, the gas pressure of the detonation products (typically CO, CO_2, H_2O, and N_2) decreases from 10^5 to 1 atm, the gas temperature decreases from 3000 to ~350°K, and the gas density decreases from 2 to ~0.001 g/cm^3.

Calculation of the actual degree of this conversion is dependent upon the coupling of the equation of state (EOS) of the expanding gas with gas dynamics and especially with reaction kinetics. For example, maintenance of shifting equilibrium in the expanding products continually liberates heat and thereby causes the expansion process to differ from a frozen-expansion process,[1] while slow secondary exothermic reactions in the expanding gas can significantly affect the gas dynamics and even lead to secondary shocks[2] which reheat and thus repressurize the expanding gas. Therefore, whether cold, low-pressure, high-velocity gas or warm, medium-pressure, medium-velocity gas is present at a certain time and place in the system depends upon the EOS, gas dynamics, and kinetics in the expanding products.

Numerous EOS for the high-density detonation region[3-6] and the low-density highly expanded gas[7] have been formulated, but no satisfactory model for medium-density conditions appears to be available.[8] In the medium-dense range, real gas effects such as molecular volume, intermolecule repulsion, long-range interaction, and perhaps cluster formation should occur and contribute to the EOS. Furthermore, since clusters seemingly are more reactive than the parent monomer molecules,[9] cluster formation would be especially important to the reactivity of the system.

In this paper we develop an EOS for a medium-dense system assuming (1) the formation of discrete clusters and (2) that the volume available for translational motion of monomer and clusters is the physical volume of the system minus the volume occupied by monomer and clusters. Cluster formation in compressed gases was mentioned by Boltzmann and has been intensively studied for low-density conditions in view of the importance of clusters in nucleation from the vapor phase.[10,11] The empirical virial coefficients also have been interpreted in terms of clusters.[7,12,13] Although a cluster model has been used for liquid-type conditions,[14] *i.e.*, a medium-dense, low-temperature system, such conditions are customarily analyzed in terms of a covolume cage model wherein a monomer molecule undergoes translational motion within a well-defined cage of lattice-type molecules.[6] Thus, previous models of a medium-dense system usually follow a liquid approach, while our model follows a gas approach using an Abel-type model.[6]

Approach

Background. Cluster formation has been described in terms of discrete clusters, long-range interaction,[7] molecular dynamics,[15] and other[16] models. The discrete-cluster approach has been formulated in terms of using the macroscopic surface energy for the cluster[10] and, by Reed[12] and others,[11,17] in terms of statistical thermodynamics based upon the translational, rotational, and vibrational

(1) D. L. Ornellas, J. H. Carpenter, and S. R. Gunn, *Rev. Sci. Instrum.*, **37**, 907 (1966).
(2) W. G. Courtney, "Condensation in a Rarefaction Wave," Thiokol Chemical Corp., Reaction Motors Division, Dec 1965.
(3) E. B. Gruneisen, *Handb. Phys.*, **10**, 22 (1926).
(4) S. J. Jacobs, *Amer. Rocket Soc.*, **30**, 151 (1960).
(5) M. J. Kamlet and S. J. Jacobs, *J. Chem. Phys.*, **48**, 23 (1968).
(6) J. O. Hirschfelder, C. F. Curtiss, and R. B. Bird, "Molecular Theory of Gases and Liquids," Wiley, New York, N. Y., 1954, Chapter 4.
(7) Reference 6, Chapter 3.
(8) J. J. Martin, *Ind. Eng. Chem.*, **59**, No. 12, 34 (1967).
(9) D. Golomb and R. D. Good, *J. Chem. Phys.*, **49**, 4176 (1968).
(10) J. Frenkel, "Kinetic Theory of Liquids," Dover Publications, New York, N. Y., 1955, Chapter 7.
(11) For example, W. G. Courtney, *J. Phys. Chem.*, **72**, 421 (1968).
(12) S. G. Reed, Jr., *J. Chem. Phys.*, **20**, 208 (1952).
(13) H. W. Woolley, *J. Chem. Phys.*, **21**, 236 (1953).
(14) G. Nemethy and H. A. Scheraga, *J. Chem. Phys.*, **36**, 3382 (1962); W. J. Dunning, Proceedings of the Case Institute of Technology Symposium on Nucleation, Cleveland, Ohio, 1965, p 1.
(15) B. F. Alder and T. E. Wainwright, *J. Chem. Phys.*, **33**, 1439 (1960).
(16) H. Reiss, J. L. Katz, and E. R. Cohen, *J. Chem. Phys.*, **48**, 5553 (1968).
(17) For example, J. Lothe and G. M. Pound, *J. Chem. Phys.*, **36**, 2080 (1962); **45**, 630 (1966).

partition functions of the monomer molecule and cluster. The surface-energy approach has become highly controversial[11] and indeed is of limited usefulness for present purposes where temperatures usually are well above the critical temperature of the gas. We will follow Reed's discrete-cluster statistical thermodynamic approach.

The concentration equilibrium constant K_g for the reaction of g molecules of monomer A to form an A_g cluster can be represented by

$$K_g = C_g/(C_1)g \tag{1}$$

where C_g and C_1 are the equilibrium concentrations of the A_g cluster and the A monomer in the system in molecules and clusters/cm^3. Assuming that intramolecular vibrations are conserved and free rotation of a molecule in the cluster occurs, the equilibrium constant is related to the cluster and monomer partition functions by

$$K_g = Q_t{}^0 Q_r Q_v \exp(-E_0/kT)/(q_t{}^0)^g \tag{2}$$

where $Q_t{}^0$, Q_r, and Q_v are the translational, rotational, and intermolecular vibrational partition functions of the cluster, $q_t{}^0$ is the translation partition function of the monomer, and E_0 is the cluster zero point energy. Partition functions can be written as

$$Q_t{}^0 = (2\pi g m k T/h^2)^{3/2}/V \tag{3}$$

$$Q_r = 8\pi^2(2\pi I_g kT)^{3/2}/\sigma_g h^3 \tag{4}$$

$$Q_v = \Pi_i \exp(-h\nu_i/2kT)/[1 - \exp(-h\nu_i/kT)] \tag{5}$$

$$q_t{}^0 = (2\pi m k T/h^2)^{3/2}/V \tag{6}$$

where the translational standard state is one molecule and cluster/cm^3, V is the standard-state volume in the system available for translation (here, V = 1 cm^3), m is the mass of the monomer gas molecule, k is Boltzmann's constant, T is absolute temperature, h is Planck's constant, $I_g = (2\pi mg/5)(3mg/4\pi\rho_g)^{2/3}$ and is the moment of inertia of the cluster which is assumed to be spherical for I_g calculations,[18] ρ_g is the density of the cluster and is assumed here to be equal to the bulk density of the solid at its freezing point, σ_g is the rotational symmetry numbers of the cluster, and ν_i is the vibrational frequency of the ith intermolecular vibrational mode in the A_g cluster. As formulated above, Q_v is the product of the vibrational partition functions of all intermolecular vibrational modes in the cluster and E_0 is the sum of the minimum values of the potential energy curves of each intermolecular vibrational mode relative to the infinitely separated monomer.

The main problems in predicting K_g then are to evaluate the vibrational partition function Q_v and the volume V available for translation. Reed's approach to cluster thermodynamics was (1) intramolecular vibrations were assumed to be conserved during cluster formation; (2) central-force intermolecular forces were assumed and represented by the Lennard-Jones 6–12 potential function; (3) the monomer–cluster mixture was assumed to behave as an ideal gas with no long-range interaction; (4) clusters containing two to eight molecules were considered; (5) only one configuration of a specific size cluster was calculated (all other configurations having the same number of nearest neighbor bonds were assumed to have the same K_g); (6) only nearest neighbor interactions between the molecules in a cluster were considered; (7) small classical harmonic vibrations around equilibrium positions by the molecules in the cluster were assumed; and (8) the volume occupied by monomer and clusters was assumed negligible.

TABLE I: Cluster Geometries

Molecules in cluster	Configuration	σ_g
2	Dimer	2
3	Triangle	6
4	Tetrahedron	12
5	Trigonal bipyramid	12
6	Octahedron	24
7	Octahedron + 1 on a face	1
8a	Octahedron + 2 on adjacent faces	2
8b	Octahedron + 2 on opposite faces joined by an apex	2
8c	Octahedron + 2 on symmetrically opposite faces	6
9a	Octahedron + 3 on adjacent faces	1
9b	Octahedron + 2 on adjacent faces + 1 on opposite face	1
9c	Octahedron + 3 on symmetrically opposite faces	3
10a	Octahedron + 4 on adjacent faces	4
10b	Octahedron + 3 on adjacent faces + 1 on face joined by an edge	3
10c	Octahedron + 3 on adjacent faces + 1 on face joined by an apex	1
10d	Octahedron + 3 on adjacent faces + 1 on opposite face	1
10e	Octahedron + 4 on linearly opposite faces	4
10f	Octahedron + 4 on symmetrically opposite faces	12
11a	Octahedron + 5 (same as 9a except extra 9a molecules are now vacancies)	1
11b	Octahedron + 5 (same as 9b except extra 9b molecules are now vacancies)	1
11c	Octahedron + 5 (same as 9c except extra 9c molecules are now vacancies)	3
12a	Octahedron + 6 (same as 8a except extra 8a molecules are now vacancies)	2
12b	Octahedron + 6 (same as 8b except extra 8b molecules are now vacancies)	2
12c	Octahedron + 6 (same as 8c except extra 8c molecules are now vacancies)	6
13	Octahedron + 7	1
14	Octahedron + 8 (2 complete shells)	24

Present Approach. In the present work, the following modifications were made to Reed's approach: (4′) clusters containing up to 14 molecules were evaluated; (5′) for clusters containing two to five molecules, all configurations that resulted in the minimization of cluster potential energy were examined (for larger clusters, configurations having inner-shell octahedral geometry were used. A total of 26 cluster geometries were examined (Table I)); (6′) nonnearest neighbor interactions were examined; (7′) anharmonicity for the dimer was examined; and (8′) a covolume term was included in the equation of state. Recently Burton[19] also used the 6–12 harmonic vibration approach to calculate C_g. He considered Ar and used cluster geometries based upon a central atom and successive shells of face-centered-cubic atoms. Vibration frequencies computed here for Ar are similar to those of Burton.

(18) The moment of inertia for the dimer using the exact formula $I_g = m/2\pi r^2$ differed by less than 5% from the value obtained by the text equation.

(19) J. J. Burton, *J. Chem. Phys.*, **52**, 345 (1970).

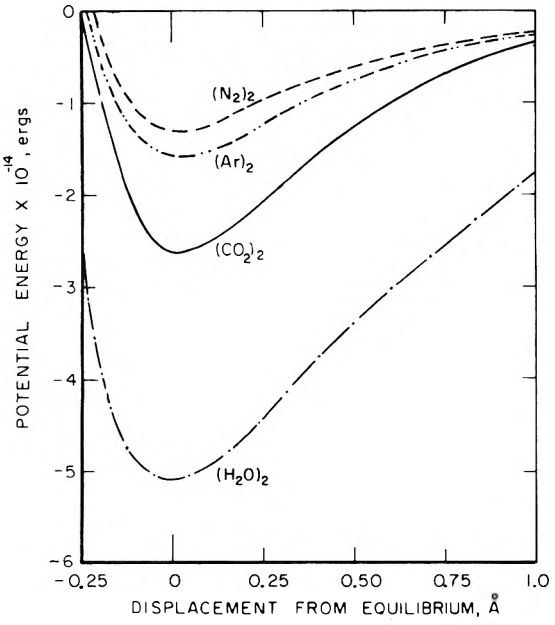

Figure 1. Potential energy curves for dimers.

TABLE II: Monomer Data

Monomer	ρ,[a] g/cm^3	V_0, cm^3	ϵ/k, °K	θ, Å
Argon	1.78	0.180	116.0[b]	3.465[b]
Nitrogen	1.026	0.120	95.05[c]	3.698[c]
Carbon dioxide	1.560	0.140	189.0[d]	4.486[d]
Water	1.000	0.150	373.0[e]	2.680[e]

[a] N. A. Lange, Ed., "Handbook of Chemistry," McGraw-Hill, New York, N. Y., 1961, p 214. [b] M. Trautz, A. Melster, and R. Zink, *Ann. Phys.*, **7**, 409 (1930). [c] A. Michels, H. Wouters, and J. deBoer, *Physica*, **1**, 587 (1934). [d] A. Michels and C. Michels, *Proc. Roy Soc., Sec. A*, **153**, 201 (1936). [e] F. G. Keyes, L. B. Smith, and H. T. Gerry, *Proc. Amer. Acad. Arts Sci.*, **70**, 320 (1936).

For each cluster configuration, the molecules were initially placed at face-centered solid-lattice positions. The total potential energy of the cluster, Φ_g, is the sum of all the Lennard-Jones potential energies due to the intermolecular distance r_{ij} between the ith and jth molecules

$$\Phi_g = \tfrac{1}{2}\Sigma_{ij} 4\epsilon[(\theta/r_{ij})^{12} - (\theta/r_{ij})^{6}] \quad (7)$$

where θ is the value of r_{ij} when $\Phi_g = 0$ and ϵ is the maximum attractive energy and occurs at $r_{ij} = 2^{1/6}\theta$ (Table II). The total potential energy Φ_g then was minimized with respect to the positions of all the molecules. For clusters containing two to five molecules, displacements of all molecules in all three coordinate directions were permitted. For larger clusters, the equilibrium positions were taken as those giving the minimum Φ_g while maintaining octahedral geometry.

The conventional $3g \times 3g$ force-constant matrix[20] then was generated. In calculations assuming only nearest neighbor interactions, the equilibrium positions of the molecules are such that all nearest neighbor intermolecular distances were equal to the molecular separation for the dimer. Since each first derivative of the potential function, $\partial\Phi_g/\partial r_{ij}$, is zero, the individual matrix elements are the coefficients of the second derivatives in terms of Cartesian coordinate displacements. When nonnearest neighbors are included, the summation over all

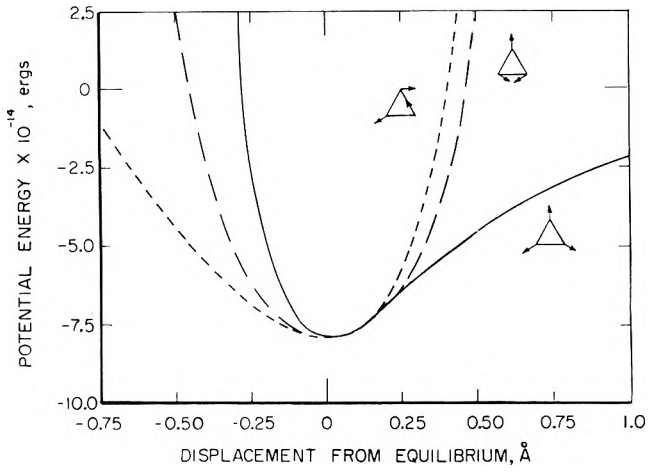

Figure 2. Potential energy curves for CO_2 trimer.

$\partial\Phi_g/\partial r_{ij}$ terms is equal to zero, but the individual terms are not zero. The longer range attraction terms with a positive value of $\partial\Phi_g/\partial r_{ij}$ cause the cluster to become somewhat smaller and hence shorten the nearest neighbor intermolecular distance to less than the dimer value. The $\partial\Phi_g/\partial r_{ij}$ terms for the shorter r_{ij} thus have negative values.

The resulting matrix was diagonalized by the Jacobi technique[21] to obtain eigenvectors associated with the motions of the $3g$–6 normal vibrational modes ($3g$–5 for dimer) and the eigenvalues associated with the energy levels of these normal modes. With the harmonic approximation, the eigenvalues can be used to calculate ν_i and then Q_v in eq 5. To examine the extent of anharmonicity, potential energy curves for various normal vibrational motions were calculated for several clusters. Figure 1 shows the energy curves for dimers and indicates definite anharmonicity. Figure 2 shows that two of the three normal modes of the CO_2 trimer also exhibit anharmonicity. Potential energy curves for larger clusters were much steeper and exhibited much less asymmetry. The vibrational partition function for a one-dimensional anharmonic oscillator[22] is

$$Q_v = \Sigma_n \exp\{-[(n + \tfrac{1}{2})(\omega_e/kT) - (n + \tfrac{1}{2})^2(\omega_e x_e/kT + \ldots]\} \quad (8)$$

where n is the vibrational level ($n = 0,1,2, \ldots$) and ω_e and $\omega_e x_e$ are related to the 2nd, 3rd, etc., derivatives of Φ_g.

Covolume Treatment. We assumed that the volume available for translational motion of the monomer and cluster is

$$V = V' - \Sigma_g n_g V_g \quad (9)$$

where V' is the physical volume of the system, n_g is the number of g-size clusters on the systems, and V_g is the volume of the A_g cluster. The cluster volume was taken to be $\pi D^3/6$ where D is the equilibrium distance between the centers of the farthest separated molecules in the cluster. The monomer volume V^0 (Table II) was computed using the dimer distance for D. This approach approximates a

(20) G. Herzberg, "Infrared and Raman Spectra," Van Nostrand, New York, N. Y., 1945, Chapter 2.
(21) D. K. Faddeeva and V. N. Faddeeva, "Computational Methods of Linear Algebra," W. H. Freeman, San Francisco, Calif., 1963, p 480.
(22) G. W. King, "Spectroscopy and Molecular Structure," Holt, Reinhart and Winston, New York, N. Y., 1964, p 164.

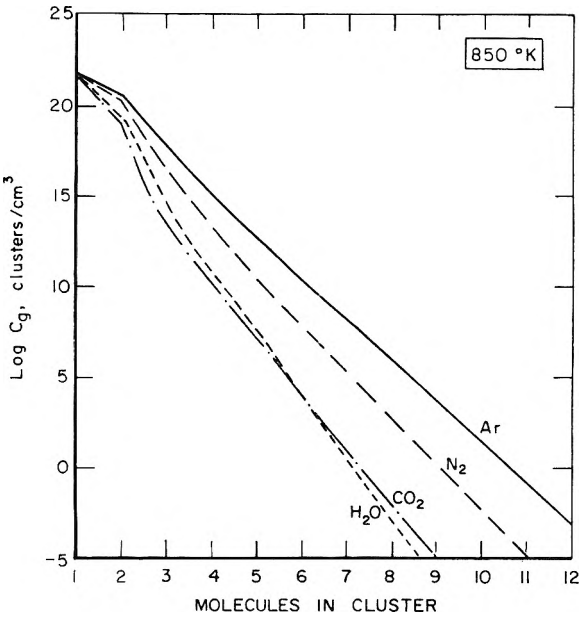

Figure 3. Cluster concentration *vs.* cluster size at 850°K and monomer concentration of 4.63 × 10^{21} molecules/cm^3.

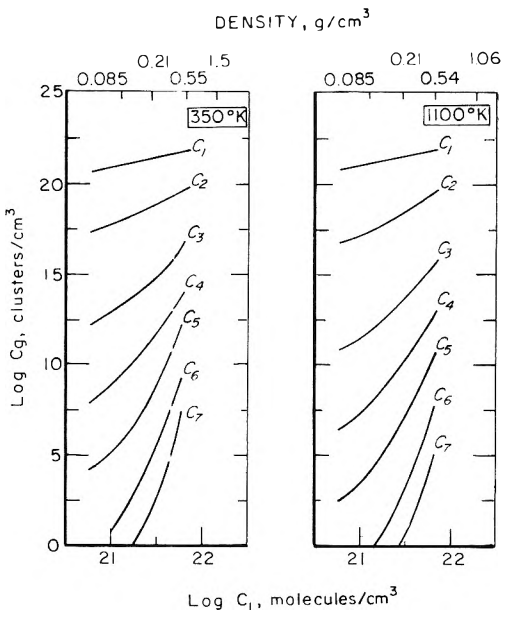

Figure 4. Cluster concentration *vs.* monomer concentrations for CO_2.

soft-sphere model that includes compressibility, *i.e.*, for a hard-sphere model[23]

$$V_g = 4(\pi D^3/6)$$

Equation of State. Rearrangement of the equilibrium constant in eq 1 gives

$$C_g/(C_1)^g = K_g/(1 - \Sigma_g C_g V_g)^{g-1} \qquad (10)$$

where C_1 and C_g are the monomer and cluster concentrations in number/cm^3. Assuming negligible interaction between monomer and clusters, an equation of state which incorporates clusters and covolume then can be written as

$$P = RT\Sigma_g C_g/[1 - \Sigma_g C_g V_g] \qquad (11)$$

and

$$\rho = mN\Sigma_g g C_g \qquad (12)$$

where P is the pressure in atmospheres, R is the gas constant, ρ is gas density in g/cm^3, and N is Avogadro's number.

In a typical calculation, T and C_1 were arbitrarily selected. C_g was computed by eq 10 assuming negligible covolume effect and then recomputed including covolume until successive C_g were unchanged. P and ρ were then calculated by eq 11 and 12. A CDC 3200 computer was used for all calculations.

Results

Cluster Thermodynamics. Cluster concentrations computed by considering only nearest neighbor interactions are within 0.1% of the values calculated by including nonnearest neighbor interactions, supporting Reed's assumption no. 6.

The anharmonic correction to the vibration partition function of the dimer increased the dimer concentration by less than 5% for Ar, N_2, and CO_2 and about 10% for H_2O. However, the influence of the dimer and other clusters on the EOS is small. Subsequent calculations used the nonnearest neighbor approach with the harmonic approximation.

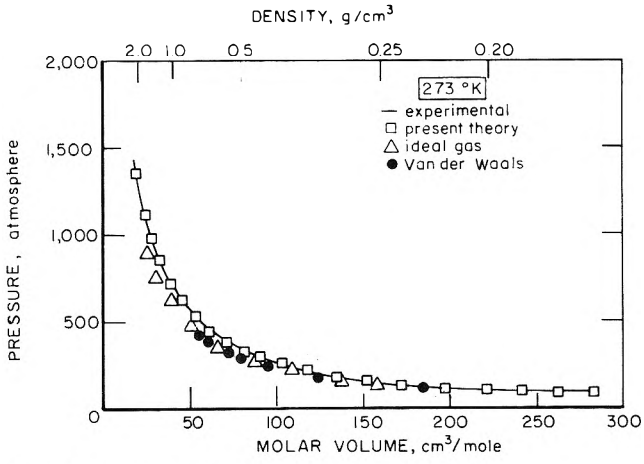

Figure 5. *PV* isotherms for Ar.

The computed concentrations for different configurations of a certain-size cluster were within one order of magnitude of each other. For example, the concentrations of the three configurations of the nine molecule CO_2 cluster were calculated to be 4.18 × 10^{-5}, 3.44 × 10^{-5}, and 2.83 × 10^{-5} clusters/cm^3 at 350°K and a monomer concentration of 4.63 × 10^{21} molecules/cm^3. Reed's assumption no. 5 therefore is also supported.

Inclusion of the covolume (eq 10) resulted in a significant increase in cluster concentration. For example, for CO_2 at 350°K, the increase was a factor of 2–3 for small clusters and several orders of magnitude for large clusters. The covolume effect was less pronounced at high temperature but was still significant to the EOS. This increase was largely due to the monomer volume because of the small concentrations of clusters, *i.e.*, omission of clusters caused a 5% decrease in the predicted pressure for CO_2 at 350°K and less than a 1% decrease for other conditions calculated at higher temperature.

In all cases considered here, cluster concentration monotonically decreased as the cluster size increased. Fig-

(23) W. J. Moore, "Physical Chemistry," 2nd ed, Prentice-Hall, Englewood Cliffs, N. J., 1955, p 170.

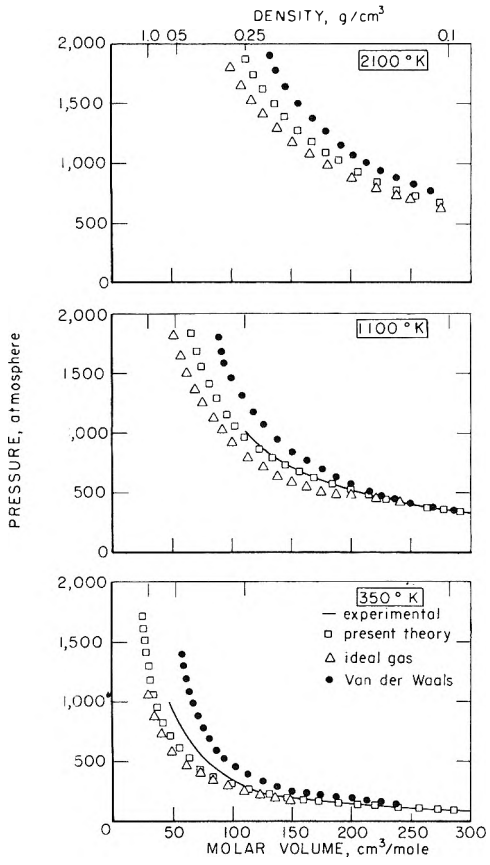

Figure 6. *PV* isctherms for N_2.

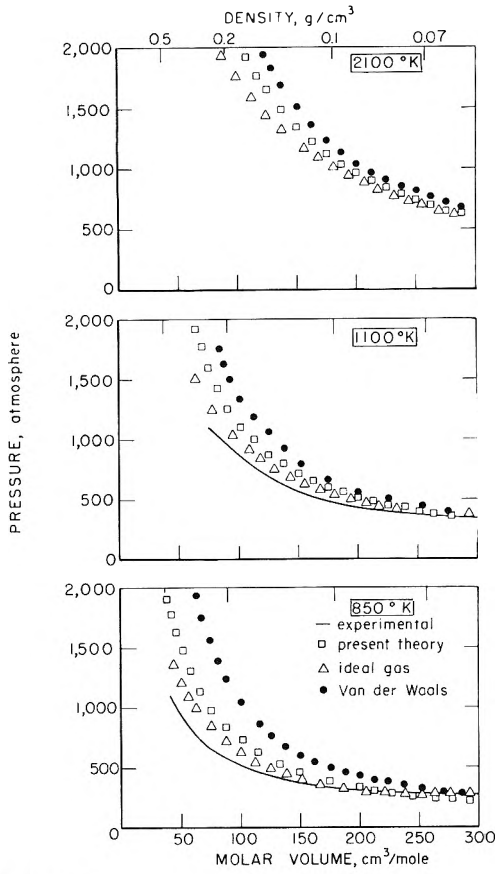

Figure 8. *PV* isotherms for H_2O.

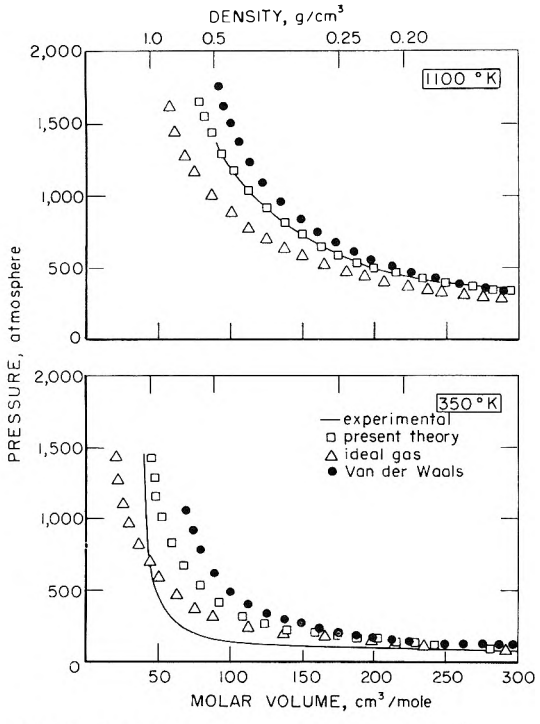

Figure 7. *PV* isotherms for CO_2.

ure 3 shows cluster concentration *vs.* size for Ar, N_2, CO_2, and H_2O at 850°K for a typical assumed monomer concentration of 4.63×10^{21} molecules/cm³. The differences in concentrations for different configurations of a particular size cluster are insignificant on the graph. Cluster concentrations increased significantly with increase in monomer concentration (Figure 4) but were still negligible compared to monomer concentration for conditions considered here.

Equation of State. The usefulness of the present approach to an EOS was tested by comparing theoretical *PV* isotherms of several gases with experimental *PV* data. Although fitting *PV* data is not a sensitive test of an EOS, this approach was used rather than matching theory and experiment at the critical point[6] since the partly expanded detonation products usually are at temperatures higher than the critical temperature. The present EOS described by eq 11 and 12 included all clusters and cluster configurations (to $g = 14$) and used the nonnearest neighbor approach with the harmonic approximation. However, as noted earlier, only the volume decrease due to monomer was significant in practice. *PV* isotherms using the ideal gas, van der Waals,[24] and Beattie–Bridgman[25] equations of state were also calculated for comparison purposes. The Beattie–Bridgman isotherms were essentially identical with the ideal gas isotherms for conditions examined here.

Figure 5 compares experimental *PV* data[26,27] for Ar at 273°K with the present covolume model and the other models. Agreement with the present model was within 1% to 1300 atm (the highest value computed here), while the other models predict a pressure which is 20% low above about 200 atm.

(24) Reference 22, p 14.
(25) Reference 6, p 254.
(26) A. Michels, R. J. Lunbeck, and G. J. Wolkers, *Appl. Sci. Res. Sect. A*, **2**, 345 (1951).
(27) A. Michels and H. Wijker, *Physica*, **15**, 627 (1949).

Figure 6 presents similar data[28-32] for N_2. For the 350°K isotherm, all models deviate about 30% above about 200 atm, although the present model gives a slightly smaller error. For the 1100°K isotherm, deviation occurs with all models above about 700 atm, but the error at 1000 atm is 5% with the present model and 25% with the other models.

Figure 7 presents similar data[29,33-35] for CO_2. At 350°K, agreement is very poor for all models, presumably because the temperature is near the critical temperature of 304°K. At 1100°K, the present model agrees to within 1% to 1300 atm while the other models predict a pressure 20–30% in error as the pressure increases.

For H_2O (Figure 8) all models deviate about 30% or more from the experimental pressure[36,37] above about 300 atm at 850°K and deviate about 10% at 1100°K. Inclusion of covolume does not significantly improve the present model.

Discussion

Pressures computed here agree to within several per cent with experimental PVT data for Ar, N_2, and CO_2 for densities between about 0.001 and 1.5 g/cm^3 at temperatures about 100°K or more above the critical temperatures. At temperatures nearer the critical temperature, the present covolume model breaks down. Comparison of this model with experimental PVT data indicates that deviation becomes appreciable when the volume available for translational motion is less than about 80% of the physical volume. This deviation may be due to the breakdown of the classical translational partition function, which assumes negligible volume of monomer and clusters, for such dense conditions. Also, at high densities, long-range interaction and repulsion energies may be important,[3-6] requiring an equation of state where $(\partial E/\partial V)_T \neq 0$.

In our computation of cluster concentration, the assumption of harmonic vibration is drastic at the elevated temperatures considered here. The assumption of conservation of intramolecular vibrations and the use of a simple 6-12 potential is similarly drastic for molecules such as CO_2 and H_2O, where an angle-dependent potential function such as the Stockmayer[38] potential would be much more appropriate.

(28) B. H. Sage and W. N. Lacey, "Thermodynamic Properties of the Lighter Paraffin Hydrocarbons and Nitrogen," Lord Baltimore Press, Baltimore, Md., 1950.
(29) E. W. Washburn, Ed., "International Critical Tables," McGraw-Hill, New York, N. Y., 1928, p 11.
(30) R. Wiebe and V. L. Gaddy, *J. Amer. Chem. Soc.*, **60**, 2300 (1938).
(31) E. P. Bartlett, H. L. Cupples, and T. H. Tremearne, *J. Amer. Chem. Soc.*, **50**, 1275 (1928).
(32) A. Michels, R. J. Lunbeck, and G. J. Wolkers, *Physica*, **17**, 801 (1951).
(33) G. C. Kennedy, *Amer. J. Sci.*, **252**, 225 (1954).
(34) K. E. MacCormack and W. G. Schneider, *J. Chem. Phys.*, **18**, 1269 (1950).
(35) R. L. Sweigert, P. Weber, and R. L. Allen, *Ind. Eng. Chem.*, **38**, 185 (1946).
(36) J. H. Keenan and F. G. Keyes, "Thermodynamic Properties of Steam," Wiley, New York, N. Y., 1953.
(37) C. A. Meyer, R. B. McClintock, G. J. Silvestri, and R. C. Spencer, Jr., "Thermodynamic and Transport Properties of Steam," American Society of Mechanical Engineers, New York, N. Y., 1967.
(38) W. H. Stockmayer, *J. Chem. Phys.*, **9**, 398 (1941).

Solubility of Mercuric Halides in Some Organic Solvents

I. Eliezer* and S. Adida

Institute of Chemistry, Tel-Aviv University, Tel-Aviv, Israel *(Received January 13, 1972)*

Publication costs assisted by the Tel-Aviv University

The solubilities of mercuric chloride and mercuric bromide in a series of paraffinic and aromatic solvents and in dioxane have been measured at several temperatures. The entropy of solution of these compounds has been calculated and compared with the entropy of fusion. The solubility parameters of these salts have been computed. In the case of nonaromatic solvents, the behavior of the solutions approaches that of regular solutions. In the case of aromatic solvents as well as dioxane, apparent solute-solvent interactions increase the solubility so that the values are larger than expected from regular solution theory and the entropy of solution is decreased.

Introduction

The degree of molecularity of the halides of zinc, cadmium, and mercury in nonaqueous solvents of low dielectric constants, such as, benzene, dioxane, etc., has been a controversial subject for many years. Much of the work on such solutions has been done with the mercuric halides but it is still not clear whether in benzene solution of mercuric chloride there are chemical effects or whether the solubility is due to induced dipoles and dispersion forces. Measurements of dipole moments,[1] X-ray diffraction,[2] and uv and ir spectra[3] have not really solved the problem as yet. It should be possible to contribute to its solution by adopting a thermodynamic approach and examining these solutions from the standpoint of the theory of regular solutions. This could be helpful since if

(1) (a) W. J. Curran and H. H. Wenzke, *J. Amer. Chem. Soc.*, **57**, 2162 (1935); (b) B. C. Curran, *ibid.*, **63**, 1470 (1941); **64**, 830 (1942); (c) A. R. Tourky, *et al.*, *J. Phys. Chem.*, **64**, 565 (1960); *Can. J. Chem.*, **35**, 630 (1957).
(2) C. L. Van Panthaleon Van Eck, Thesis, Leiden, 1957.
(3) I. Eliezer, *J. Chem. Phys.*, **42**, 3625 (1965).

there are no chemical and orientation effects, then the regular solution approximation would apply and therefore solubility measurements and calculations of solubility parameters should give results as expected for such solutions. If, on the other hand, there are chemical effects, these will cause deviations from the solubilities expected according to the theory and from the degree of deviation one should be able to draw conclusions about the degree of complexation.[4-7]

From another point of view, the theory of regular solutions is one of the better hypotheses brought forward to explain the behavior of nonelectrolytic solutions. While the number of systems to which it has been applied is not too large and these are often molecules of high symmetry, such as, I_2, P_4, SnI_4, and $Sn(C_6H_5)_4$, the usefulness of the regular solution concept is that it is a good zeroth approximation to a wide variety of systems and it is thus of interest to extend the studies to less "ideal" molecules such as the mercuric halides. The theory of regular solutions requires, of course, that the solute be largely undissociated and this makes the mercuric halides, which exhibit a high degree of covalency, particularly suitable.

Experimental Section

The solubility measurements were carried out by examining solutions saturated with the solute by shaking at constant temperature. The measurement method consisted of tagging the solute with a radioactive isotope, ^{203}Hg, and comparing the activity of aliquots of the saturated solution with standard solution of known solute content.

The ^{203}Hg isotope was obtained from the Amersham Radiochemical Centre as $HgCl_2$ aqueous solution. It has a half-life of 47 days with 0.279 MeV 100% γ activity. This was measured with a well-type scintillation counter with a Ge–Li crystal manufactured by Elscint.

Mercuric bromide was prepared by adding potassium hydroxide to the active chloride solution. The HgO precipitate was separated by centrifugation and washed, and concentrated hydrobromic acid was added.

Solutions for the activity measurements were prepared by taking aliquots ($\sim$100 μCi) of the original solution and diluting with alcoholic solution of nonactive salt, then repeatedly drying *in vacuo*.

Saturation of the solution necessitated shaking for 48 hr. The temperature was kept constant within 0.05°. In each case several samples were counted and the average value was taken. The error was estimated to be less than 1% for the more concentrated solutions increasing to 3% for the more dilute ones. The measurements were carried out at temperatures between 10 and 35°. Measurements at higher temperature proved to have large errors, possibly due to increased evaporation.

The solvents were of puriss grade and were used without further purification except for dioxane and chloroform. Dioxane was treated for peroxide removal while traces of ethanol (stabilizer) were removed from the chloroform by passing through an alumina column. However, the purified chloroform keeps for only 6–7 days and was renewed periodically. The same instability was found in carbon tetrachloride.

Results

The solubility results obtained were processed as follows. Curves were drawn representing the changes in solubility with temperature (in g per 100 g solution). Interpolation on the graphs permits verification of the points and more accurate determination of some points.

Using solubilities taken from the graphs, the molar fractions, X_2, of the solute at various temperatures were determined. The solubilities in the various solutions at different temperatures are given in Table I. Figures 1 and 2 show the dependence of the molar fraction of the solute on temperature in various solvents.

Solubility Parameters. The solubility parameters of the solutes are given by the expression

$$\delta_2 = (\Delta E/V_2^l)^{1/2} = [(\Delta H^v - RT)/V_2^l]^{1/2}$$

ΔH^v is determined from a curve which is assumed linear and gives ln p as a function of $1/T$ on solute evaporation. The error in ΔH^v is 1–2%. V_2^l is determined by extrapolation of the liquid properties to below the melting point. As the melting points of the chloride and bromide (238 and 277°) are relatively distant from 25°, the extrapolation involves an error of 3–4%.

The results of the calculations giving the thermodynamic properties of mercuric chloride and mercuric bromide are given in Table II.

The solubility parameters of the solutes were calculated from the expression correlating the solubility at 25° with the solubility parameters of the solvents

$$\ln a_2^S = \ln X_2 + (\Phi_1^2 V_2^l/RT)(\delta_2 - \delta_1)^2 \quad (1)$$

where Φ_1 is the volume fraction of the solvent, V_2^l is the molar volume of the liquid solute at 25°, and a_2^S is the activity of the solute at 25°, the standard state of the solute being the pure liquid. The second term in this equation is the activity coefficient in the regular solution model.

a_2^S is calculated from the expression

$$R \ln \alpha_2^S = \Delta H^f[(T_f - T)/T_f T] + \Delta C_p[(T_f - T)/T] - \Delta C_p \ln (T_f/T) \quad (2)$$

where ΔH^f and T_f are the heat and temperature of melting of the solute, $\Delta C_p = C_p^l - C_p^s$; and C_p^l and C_p^s are the molar heat capacities of the liquid and solid solute, which are assumed constant in the range $T_f - T$.

The values of δ_2 as calculated for various solvents from eq 1 are given in Table III. The uncertainty in δ_2, due to errors in X_2 and V_2^l, is within 0.2 units. However, it should be pointed out that this is not necessarily the actual uncertainty in the "thermodynamic" solubility parameter $\delta_2 = (\Delta E^v/V)^{1/2}$, since it is obtained on the assumption that eq 1 is exactly correct.

The various solvents were grouped in a manner allowing comparison of the values of δ_2 in solvents which could involve the same kind of interactions with the solute.

Entropy Changes. The partial molar entropy of solution at constant pressure is given by

$$\bar{S}_2 - S_2^s = R(\partial \ln X_2/\partial \ln T)_{sat}(\partial \ln a_2/\partial \ln X_2)_T \quad (3)$$

For an ideal solution the entropy charge equals ($-R \ln X_2 + \Delta S^F$) where ΔS^F is the molar entropy of melting at temperature T.

As a first approximation the factor $(\partial \ln a_2/\partial \ln X_2)_T$ remains almost unity. Assuming the solutions behave ac-

(4) J. H. Hildebrand and R. L. Scott, "Regular Solutions," Prentice-Hall, New York, N. Y., 1962, (a) p 119; (b) p 122; (c) p 125; (d) p 37; (e) p 171; (f) p 86; (g) p 102.
(5) K. Shinoda and J. H. Hildebrand, *J. Phys. Chem.*, **69**, 605 (1965).
(6) S. K. Suri and V. Ramakrishna, *Can. J. Chem.*, **47**, 3049 (1969).
(7) E. B. Smith and J. Walkley, *Trans. Faraday Soc.*, **56**, 220 (1960).

TABLE I: Solubilities of Mercuric Chloride and Bromide, $100X_2$ (mole%)

Solvent	No.	10°C	14°C	20°C	25°C	30°C	35°C	40°C
				$HgCl_2$				
Hexane	1	0.38×10^{-3}	0.41×10^{-3}	0.46×10^{-3}	0.55×10^{-3}	0.70×10^{-3}	0.92×10^{-3}	
Heptane	2	0.22×10^{-3}	0.23×10^{-3}	0.26×10^{-3}	0.32×10^{-3}	0.42×10^{-3}	0.59×10^{-3}	
Decane	3	0.31×10^{-3}	0.37×10^{-3}	0.45×10^{-3}	0.61×10^{-3}	0.84×10^{-3}	0.98×10^{-3}	
Isooctane	4	0.21×10^{-3}	0.21×10^{-3}	0.23×10^{-3}	0.27×10^{-3}	0.34×10^{-3}	0.44×10^{-3}	
Dimethyl-butane	5				0.19×10^{-3}			
Cyclopentane	6	0.72×10^{-3}	0.85×10^{-3}	0.11×10^{-2}	0.15×10^{-2}	0.22×10^{-2}		
Cyclohexane	7	0.39×10^{-3}	0.43×10^{-3}	0.57×10^{-3}	0.74×10^{-3}	0.98×10^{-3}	0.12×10^{-4}	
Methylcyclo-hexane	8	0.31×10^{-3}	0.36×10^{-3}	0.45×10^{-3}	0.61×10^{-3}	0.83×10^{-3}	0.12×10^{-2}	
CCl_4	9	0.14×10^{-2}	0.15×10^{-2}	0.16×10^{-2}	0.19×10^{-2}	0.27×10^{-2}	0.37×10^{-2}	
$CHCl_3$	10	0.012	0.015	0.018	0.022	0.026	0.031	
Benzene	11	0.104	0.118	0.134	0.156	0.188	0.224	
Toluene	12	0.162	0.170	0.184	0.211	0.247	0.304	
o-Xylene	13	0.256	0.274	0.304	0.349	0.403	0.467	
m-Xylene	14	0.187	0.197	0.221	0.250	0.288	0.345	
p-Xylene	15		0.290	0.304	0.325	0.363	0.431	
Mesitylene	16	0.169	0.180	0.195	0.222	0.260	0.322	
Dioxane	17	0.409	0.475	0.605	0.772	0.984	1.23	
				$HgBr_2$				
Hexane	1	0.91×10^{-3}	0.10×10^{-3}	0.15×10^{-3}	0.22×10^{-2}	0.33×10^{-2}	0.53×10^{-2}	
Heptane	2	0.92×10^{-3}	0.10×10^{-2}	0.13×10^{-2}	0.20×10^{-2}	0.31×10^{-2}	0.50×10^{-2}	0.63×10^{-2}
Decane	3	0.14×10^{-2}	0.16×10^{-2}	0.22×10^{-2}	0.32×10^{-2}	0.49×10^{-2}	0.73×10^{-2}	0.011
Isooctane	4	0.82×10^{-3}	0.92×10^{-3}	0.12×10^{-2}	0.16×10^{-2}	0.24×10^{-2}	0.34×10^{-2}	0.54×10^{-2}
Dimethyl-butane	5	0.48×10^{-3}	0.62×10^{-3}	0.98×10^{-3}	0.15×10^{-2}	0.22×10^{-2}	0.32×10^{-2}	
Cyclopentane	6	0.22×10^{-2}	0.27×10^{-2}	0.36×10^{-2}	0.52×10^{-2}	0.77×10^{-2}	0.12×10^{-2}	
Cyclohexane	7	0.16×10^{-2}	0.20×10^{-2}	0.28×10^{-2}	0.38×10^{-2}	0.53×10^{-2}	0.74×10^{-2}	0.010
Methylcyclo-hexane	8	0.18×10^{-2}	0.24×10^{-2}	0.32×10^{-2}	0.44×10^{-2}	0.58×10^{-2}	0.98×10^{-2}	
CCl_4	9	0.32×10^{-2}	0.39×10^{-2}	0.53×10^{-2}	0.75×10^{-2}	0.010	0.014	
$CHCl_3$	10	0.023	0.024	0.027	0.031	0.037	0.049	
Benzene	11	0.101	0.121	0.140	0.166	0.196	0.234	0.274
Toluene	12	0.157	0.172	0.195	0.227	0.237	0.312	0.363
o-Xylene	13	0.304	0.322	0.346	0.382	0.427	0.488	0.560
m-Xylene	14	0.181	0.201	0.230	0.265	0.302	0.349	0.403
p-Xylene	15		0.272	0.299	0.332	0.371	0.420	0.482
Mesitylene	16	0.162	0.182	0.208	0.238	0.277	0.325	0.390
Dioxane	17	0.623	0.794	1.12	1.42	1.50	1.63	1.83

TABLE II: Thermochemical Properties of Mercuric Chloride and Bromide

	T_f, °K	ΔC_p $(C_p^l - C_p^s)$, cal/deg/mol	ΔH at T_f, kcal/mol	ln a_2^s at 25°	ΔS^f at 25°, cal/mol/deg	V_2^l at 25°	ΔH^v at T_f, kcal/mol	δ_2
$HgCl_2$	550	8[a]	4.64[b]	−2.65[e]	3.4[e]	53.4[e,f]	15.50[d]	16.7[d]
$HgBr_2$	511	5[b,c]	4.28[b]	−2.54[e]	5.5[e]	62.0[e,f]	14.67[d]	15.5[d]

[a] L. E. Topol and L. D. Ransom, *J. Phys. Chem.*, **64**, 1339 (1960). [b] G. J. Janz, "Molten Salts Handbook," Academic Press, New York, N. Y., 1967. [c] International Critical Tables, McGraw-Hill, New York, N. Y. [d] Calculated from vapor pressure data from F. M. G. Johnson, *J. Amer. Chem. Soc.*, **24**, 777 (1911). [e] See text for the method of estimation. [f] The data for the liquid salts are taken from Janz (footnote *b*, above).

cording to eq 1, this factor can be calculated[5]

$$(\partial \ln a_2/\partial \ln X_2) = 1 - 2(\Phi_2/X_1) \ln (a_2/X_2) \qquad (4)$$

The correction introduced by this factor is of the order of 1–2%. This is small compared with the uncertainty of 5–6% in the factor $(\partial \ln X_2/\partial \ln T)_{sat}$ because of experimental error. The experimental results for entropy changes at 25° and the molar fractions of the solute in various solvents at this temperature are shown in Table IV. The entropy of solution as a function of $(-R \ln X_2)$ is given in Figures 3 and 4, which also show the linear relationship expected for ideal solutions so as to give an indication of the necessary corrections. The straight line for ideal solutions is of unit slope.

The entropy of melting at 25° (Table II) was calculated from the entropy of melting at T_f and the molar heat constants C_p^l and C_p^s which are assumed constant. For the liquid, an extrapolation was made below the melting point to 298°K. As the values of the thermodynamic parameters used in these calculations are not known with high precision, it is not possible to evaluate the entropy of fusion to within better than about 2 cal deg^{-1} mol^{-1}, which fact

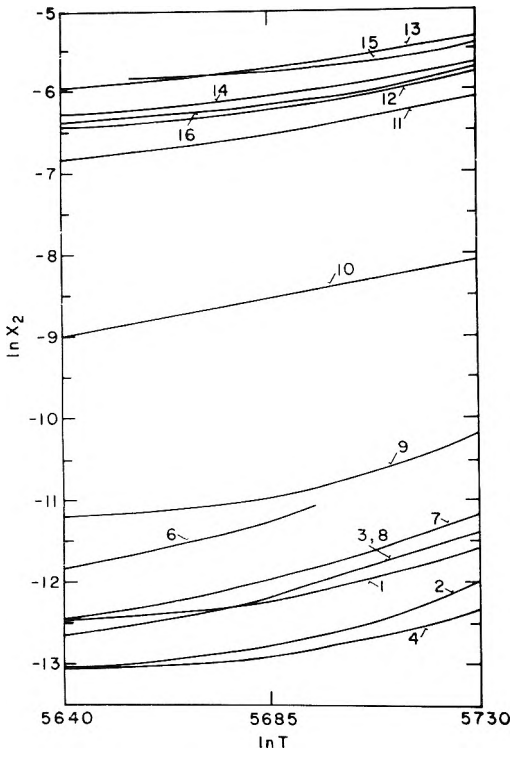

Figure 1. Solubility of $HgCl_2$. Numbers refer to solvents as given in Table 1.

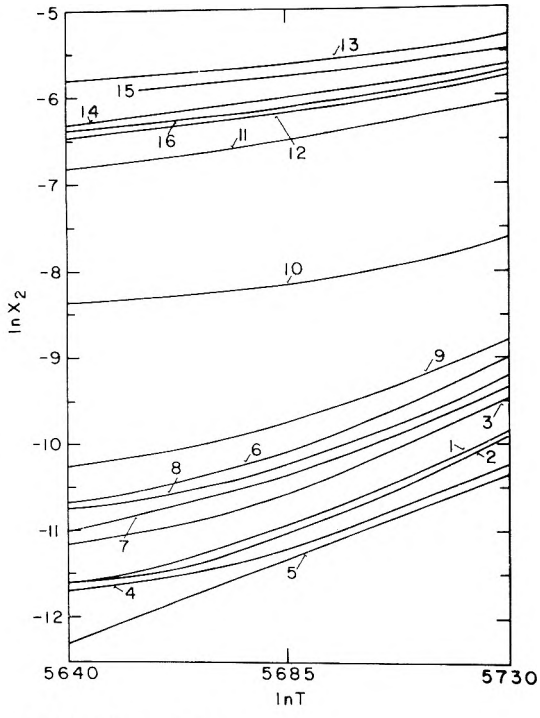

Figure 2. Solubility of $HgBr_2$.

introduces an approximation in the location of the ideal solution straight line in Figures 3 and 4.

Discussion

We shall discuss first the results for mercuric bromide as they were found to be the most accurate.

The solubility curves (Figure 2) fall in principle into two groups. The first includes nonaromatic solvents and in it the curves are arranged in the order of increasing solubility which corresponds to the order of the solubility parameters of the solvents. In the temperature range 20–35°, the curves approaching linearity are almost parallel and of large slope.

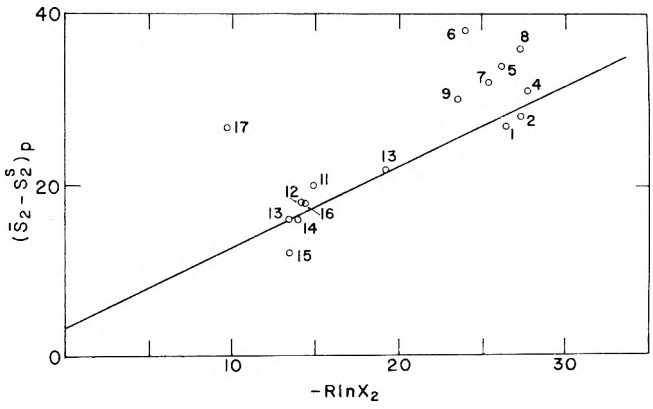

Figure 3. Entropy of solution of mercuric chloride at constant pressure *vs.* $-R \ln X_2$ at 25°.

TABLE III: Solubility Parameters of Mercuric Chloride and Bromide in Various Solvents

Solvent	No.	δ_1	δ_2 ($HgCl_2$)	δ_2 ($HgBr_2$)
Hexane	1	7.3	17.5	16.1
Heptane	2	7.4	17.9	16.3
Decane	3	7.7	17.9	16.3
Isooctane	4	6.9	17.5	15.9
Dimethylbutane	5	7.2	18.0	16.3
Cyclopentane	6	8.1	17.7	16.4
Cyclohexane	7	8.2	18.2	16.4
Methycyclohexane	8	7.8	17.9	16.3
CCl_4	9	8.6	18.1	16.7
$CHCl_3$	10	9.2	17.2	16.4
Benzene	11	9.2	15.6	15.3
Toluene	12	8.9	15.1	14.7
o-Xylene	13	9.0	14.8	14.4
m-Xylene	14	8.8	14.9	14.5
p-Xylene	15	8.8	14.6	14.3
Mesitylene	15	8.8	14.9	14.6
Dioxane	17	10.0	15.0	14.0

The second group includes the curves corresponding to aromatic solvents. The order of solubility parameters of the solvents is less well observed. The slopes are less steep and therefore the entropy of solution is smaller. This gives grounds to expect solute–solvent association which, on one hand, will increase the solubility beyond what is expected on the basis of the solubility parameter of the solvent and, on the other hand, will decrease the entropy of solution. Confirmation of this assumption comes from a comparison of the solubilities in benzene and chloroform. Although these solvents have the same solubility parameter, the solubility of mercuric bromide in benzene is much larger than in chloroform. Donor–acceptor interactions between the benzene and mercuric bromide[8] would explain this increase in solubility.

A comparison of the results of calculations of δ_2 in the various solvents also leads to a distinction between two types of solvents. The values of δ_2 remain clustered around 16.1–16.4 for saturated solvents while for aromatic solvents values smaller than 15.0 are obtained. This

(8) I. Eliezer and P. Avinur, *J. Chem. Phys.*, **55**, 2300 (1971).

TABLE IV: Entropy of Solution of Mercuric Chloride and Bromide and Solubility in Various Solvents at 25°

Solvent	No.	$HgCl_2$		$HgBr_2$	
		$(R\partial \ln X_2)/\partial \ln T$, cal/mol/°K	$-R \ln X_2$, cal/mol/°K	$(R\partial \ln X_2/\partial \ln T$, cal/mol/°K	$-R \ln X_2$, cal/mol/°K
Hexane	1	27	24.2	45	21.4
Heptane	2	27	25.3	45	21.6
Decane	3	35	24.0	47	20.7
Isooctane	4	31	25.7	40	22.0
Dimethylbutane	5			48	22.2
Cyclopentane	6	39	22.1	45	19.8
Cyclohexane	7	32	23.6	41	20.4
Methylcyclohexane	8	36	24.0	41	20.1
CCl_4	9	30	21.7	40	19.0
$CHCl_3$	10	22	16.8	20	16.2
Benzene	11	20	12.9	20	12.8
Toluene	12	18	12.3	19	12.2
o-Xylene	13	15	11.3	12	11.1
m-Xylene	14	15	12.0	15	11.9
p-Xylene	15	12	11.4	12	11.4
Mesitylene	16	18	12.1	18	12.1
Dioxane	17	27	9.8		8.5

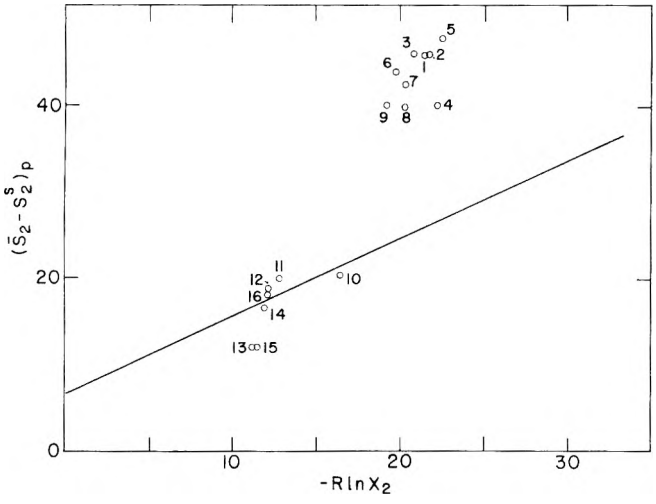

Figure 4. Entropy of solution of mercuric bromide at constant pressure *vs.* $-R \ln X_2$ at 25°.

agrees with the assumption of increase in solubility due to solvation in donor solvents such as benzene and dioxane.

It should be noted that the small variations in δ_2 which can be seen in Table III correspond to the variations found in systems such as SnI_4[7] and I_2.[4b,c] Aliphatic hydrocarbons and cyclic branched hydrocarbons give values somewhat smaller than the values for nonbranched cyclic hydrocarbons. This effect could be explained by assuming donor–acceptor interaction between the solvate and the lone pair electrons of the methyl groups of the solvent.[5] The somewhat high δ_2 value for carbon tetrachloride remains unexplained.

We shall take as a reasonable value for δ_2 the value obtained for cyclopentane, cyclohexane, and chloroform (16.4). In Figure 4 we again find two groups of points, those corresponding to inert solvents and those of the donor solvents. The following remarks are pertinent to this figure.

(a) The experimental points describe the entropy of solution at constant pressure. The straight line drawn gives the ideal entropy change at constant volume. A correction term

$$(\Delta \bar{S}_2)_v = (\Delta \bar{S}_2)_p - (\bar{V}_2 - V_2^0)(\partial p/\partial T)_v \qquad (5)$$

makes it possible to pass from one to the other. In order to calculate this term the excess volume of the solute in the solution must be known. Following the experiments carried out with $Sn(C_6H_5)_4$, SnI_4, Br_2, and I_2,[4d,9] it is known that the excess volume of the solute increases quickly when the solubility parameter of the solvent falls below 8–9. This explains the deviation of the experimental points for solvents such as the saturated hydrocarbons from the straight line.

In order to evaluate the correction term, the excess volume was calculated from [10]

$$\bar{V}_2 - V_2^0 = V_2^0(\delta_1 - \delta_2)^2/(\partial E/\partial V)_T \qquad (6)$$

where $(\partial E/\partial V)_T$ is the internal pressure of the solvent. This was done for the system CCl_4–$HgBr_2$ and the values taken for the isochore and the internal pressure were[10] 11.22 atm/°K and 81.0 cal/mol, respectively, at 25°. δ_2 was taken from the solubility data as 16.7. From this, 50 ml was obtained for the excess volume and 15 cal/mol/°K as the entropy correction term. According to the graph, the correction needed to place the point for this system on the straight line is 16 cal/mol/°K.

(b) Chloroform, usually considered a good solvent (δ_1 = 9.2) for which the entropy correction at constant volume should be negligible, is found on the "ideal" straight line in the entropy graph. It has already been noted that chloroform behaves like an inert solvent with respect to the theory of solubility parameters (δ_2 = 16.4).

(c) An interesting fact which is noteworthy concerning the solubility curves of mesitylene, *m*-xylene, and *p*-xylene is that all three solvents have the same solubility parameter. The solubility curves of *m*-xylene and mesitylene are very close. The *p*-xylene curve is much higher and the entropy of solution is considerably smaller than the other. This would indicate that the interactions in *p*-xylene are

(9) M. Vitoria and J. Walkley, *Trans. Faraday Soc.*, **65**, 62 (1969).
(10) J. H. Hildebrand, J. H. Prausnitz, and R. L. Scott, "Regular and Related Solutions," Van Nostrand-Reinhold, 1970, p 185.

TABLE V: Ionization Potentials of Some Aromatic Solvents

Solvent	I_v, eV	Ref
Benzene	9.22	*a*
Toluene	8.77	*a*
o-Xylene	8.58	*a*
m-Xylene	8.58	*a*
p-Xylene	8.48	*a*
Mesitylene	8.39	4f

[a] V. J. Hammond, W. C. Price, J. P. Teegan, and A. D. Walsh, *Discuss. Faraday Soc.*, **53**, 9 (1950).

stronger than in *m*-xylene and mesitylene.

If the ionization potentials of these solvents are compared (Table V), it is seen that I_v of mesitylene is lower (8.39) than those of *p*- and *m*-xylene (8.58 and 8.48). Solvation should have been stronger in mesitylene. It seems then that factors of molecular symmetry and stereometry determine the degree of solvation by the solvent.

The solubility of the chloride is much lower than that of the bromide, and the results for the chloride are thus less accurate. However, it appears that the conclusions drawn for the bromide hold also for the chloride.

(1) Figure 1 shows two groups of solubility curves, corresponding to inert saturated solvents and donor solvents such as benzene or dioxane. (2) According to the values of the solubility parameter δ_2 obtained for the various solvents the same difference is found in the behavior of δ_2 in the two groups of solvents. Its value is about 17–18 in the inert solvents and smaller than 15.6 in donor solvents. In this case, however, the values of δ_2 remain more scattered even in inert solvents and it is difficult to pinpoint the most probable value. (3) The chloroform solution apparently behaves like a regular solution. (4) The entropy graph also exhibits two groups of solvents. (5) The same remarks as above for mercuric bromide apply to the solvation in *p*-xylene.

Effective Fixed Charge Density Governing Membrane Phenomena. V. A Reduced Expression of Permselectivity

Naoki Kamo,* Masako Oikawa, and Yonosuke Kobatake

Faculty of Pharmaceutical Sciences, Hokkaido University, Sapporo, 060, Japan *(Received June 23, 1972)*

An equation representing the degree of permselectivity of membrane–electrolyte systems was derived by use of the empirical expressions of the activity coefficients and mobilities of small ions in charged membranes reported in previous parts of this series. The expression obtained for the permselectivity was shown to be applicable for various combinations of membranes and 1:1 type electrolytes. The systems examined here were collodion-based polystyrenesulfonic acid membranes, oxidized collodion membranes, and dextran sulfate and protamine-incorporated collodion membranes with LiCl, KCl, NaCl, KF, and KIO_3. Based on the permselectivity defined here a simple method for the determination of the effective fixed charge density which governs various transport processes in a charged membrane was proposed, and the implication of the permselectivity of a membrane–electrolyte system was discussed.

This series of papers is concerned with experimental study of the effective fixed charge density governing transport processes in charged membranes. In parts I[1] and IV,[2] the mobilities and activity coefficients of small ions in polystyrenesulfonic acid incorporated collodion membranes with various 1:1 type electrolytes were determined experimentally. It was shown that both activity coefficients and mobilities of small ions in charged membranes were represented by the same functional form with the "additivity rule," found empirically in the field of polyelectrolyte solutions study,[3] and they were expressed by the following equations.

$$\gamma_+ = \gamma_+^0(C_- + \phi X)/(C_- + X),\ \gamma_- = \gamma_-^0 \qquad (1)$$

$$u_+ = u_+^0(C_- + \phi X)/(C_- + X),\ u_- = u_-^0 \qquad (2)$$

Here γ_i, u_i, γ_i^0, and u_i^0 (i = +, −) stand for the activity coefficient and mobility of ion species i in the membrane and in the bulk solution, respectively, C_- and X are the concentration of anion adsorbed in the membrane (in moles per liter of the water in the membrane), and the stoichiometric concentration of charges fixed in the membrane. According to the convention suggested by Guggenheim,[4] γ_+^0 can be equated with γ_-^0 for a 1:1 type electrolyte, and they are replaced by the mean activity coeffi-

(1) N. Kamo, Y. Toyoshima, H. Nozaki, and Y. Kobatake, *Kolloid-Z. Z. Polym.*, **248**, 914 (1971).
(2) T. Ueda, N. Kamo, N. Ishida, and Y. Kobatake, *J. Phys. Chem.*, **76**, 2447 (1972).
(3) A. Katchalsky, Z. Alexadrowicz, and O. Kedem, "Chemical Physics of Ionic Solution," Wily, New York, N. Y., 1966, p 296.
(4) E. A. Guggenheim, *Phil. Mag.*, **19**, 588 (1935).

cient $\gamma_{\pm}^0$ of the electrolyte component. In eq 1 and 2, ϕ represents the fraction of counterions in the unbounded form, *i.e.*, excluding those tightly bound to the polymer skeletons constituting the membrane. ϕX may be referred to as the thermodynamically effective fixed charge density of the membrane. It must be noted that the concentration dependences of γ_+ and of u_+ have the same functional form with ϕX as a sole parameter, and that γ_- and u_- in the membrane are not affected appreciably by the presence of negative charges fixed in the membrane.

As was shown in a different series of papers,[5] various membrane phenomena are represented quantitatively in terms of the effective charge density ϕX of the membrane as a characteristic parameter for a given combination of membrane and electrolyte in question. However, each ion species has its own mobility in the bulk solution, and this leads to different values of observed membrane potential and of the other transport processes across the membrane depending on the species of electrolyte component used. Therefore, it may be worthy of developing a general method of characterization of membrane–electrolyte systems, which is applicable to any system irrespective of the ion species involved. This will be done by introducing a parameter representing the permselectivity ot the membrane as will be discussed in this article.

Consider a system in which a negatively charged membrane is immersed in an electrolyte solution of concentration C. Under this condition the Donnan equilibrium for small ions holds between the membrane phase and the solution. Then we have

$$(\gamma_{\pm}^0)^2C^2 = \gamma_+C_+\gamma_-C_- \tag{3}$$

The mass fixed transference number of anion in the membrane, τ_-, is defined by

$$\tau_- = u_-C_-/(u_+C_+ + u_-C_-) \tag{4}$$

Introducing eq 1, 2, and 3 into eq 4 together with the electrical neutrality condition, *i.e.*, $C_+ = C_- + X$, we obtain

$$\tau_- = 1 - \alpha\frac{(4\xi^2 + 1)^{1/2} + 1}{(4\xi^2 + 1)^{1/2} + (2\alpha - 1)} \tag{5}$$

where ξ and α stand for the relative concentration defined by $C/\phi X$, and $u_+^0/(u_+^0 + u_-^0)$, respectively. On the other hand, the apparent transference number of anion in the membrane, τ_{app}^-, is defined from the observed membrane potential $\Delta\varphi$ by the following Nernst equation.

$$\Delta\varphi = -(RT/F)(1 - 2\tau_{app}^-)\ln(C_2/C_1) \tag{6}$$

Here C_1 and C_2 are the concentrations of the external solutions on the two sides of the membrane, and R, T, and F have their usual thermodynamic meanings. In part II of this series,[6] the difference between τ_- and τ_{app}^- was shown to be less than 2% in wide range of salt concentration when the averaged concentration $(C_1 + C_2)/2$ was replaced by C. Therefore, if we replace τ_- by τ_{app}^-, and C by $(C_1 + C_2)/2$, eq 5 is applicable even when the concentrations on the two sides of the membrane are different. Rearrangement of eq 5 leads to

$$\frac{1}{(4\xi^2 + 1)^{1/2}} = \frac{1 - \tau_{app}^- - \alpha}{\alpha - (2\alpha - 1)(1 - \tau_{app}^-)} \equiv P_s \tag{7}$$

Here P_s is a measure of permselectivity of the membrane–electrolyte system as will be discussed in the subsequent paragraph.

When the external salt concentration C is high enough in comparison with ϕX, *i.e.*, $\xi = C/\phi X \gg 1$, the equation of membrane potential is reduced to

$$\Delta\varphi = -(RT/F)(2\alpha - 1)\ln(C_2/C_1) \tag{8}$$

This equation is nothing but a diffusion potential of an electrolyte in the bulk solution, and/or equal to the membrane potential for a system with a membrane having no fixed charges. In this case, τ_{app}^- becomes $(1 - \alpha)$, which in turn, P_s defined by eq 7 reduces to zero. On the other hand, when $C \ll \phi X$, the equation for the membrane potential is simplified to give

$$\Delta\varphi = -(RT/F)\ln(C_2/C_1) \tag{9}$$

which is the largest potential difference across a charged membrane with a given ratio of concentrations $\beta = C_2/C_1$. When the membrane potential is in line with eq 9, the membrane may be referred to as a perfectly permselective membrane, where τ_{app}^- becomes zero and hence P_s tends to unity. Therefore, one may consider that P_s defined by eq 7 takes a value between zero and unity depending on the external salt condition for a given system of a membrane and an electrolyte pair. P_s can be calculated only from the data of the membrane potential, while the left-hand side of eq 7 is a function of the relative concentration $\xi(= C/\phi X)$ or $(C_1 + C_2)/2\phi X$. Thus the value of the right-hand side of eq 7 must be independent of the mobilities of ion species involved. Equation 7 implies that P_s should give a straight line of slope unity when P_s is plotted against $(1 + 4\xi^2)^{-1/2}$.

Experimental Section

The procedures and apparatus for the measurements of the membrane potential were the same as those employed in previous studies.[1,5] The membrane used here were four different kinds of charged membranes. They were (1) three oxidized collodion membranes having different fixed charged densities (designated as M-1, M-2, and M-3); (2) two polystrenesulfonic acid collodion membranes used throughout in this series of papers (PS-1 and PS-3); (3) protamine collodion membrane which was prepared according to the method reported by Sollner[7] (PR membrane), and (4) dextran sulfate incorporated collodion membrane which was prepared by the method analogous to that of protamine collodion membranes (DS membrane). The salts used as electrolyte component were LiCl, KCl, NaCl, KF, and KIO_3. Each analytical grade reagent was used as received. The water used was prepared by passing distilled water through both cation and anion exchange resin column. The carbon dioxide desolved in water was not degassed and the pH of the water was 5.5. All measurements were carried out in an air oven whose temperature was regulated at 25°.

Results and Discussions

As an example, in Figure 1 the membrane potential data obtained with two PS membranes in various 1:1 electrolytes are plotted as functions of log $(C_1 + C_2)/2$ with the ratio of concentrations β $(= C_2/C_1)$ fixed at 2. The results at other values of β were essentially similar to

(5) Y. Toyoshima, M. Yuasa, Y. Kobatake, and H. Fujita, *Trans. Faraday Soc.*, **63**, 2803 (1967); Y. Toyoshima, Y. Kobatake, and H. Fujita, *ibid.*, **63**, 2814 (1967).
(6) N. Kamo, Y. Toyoshima, and Y. Kobatake, *Kolloid-Z. Z. Polym.*, **249**, 1061 (1971).
(7) M. Lewis and K. Sollner, *J. Electrochem. Soc.*, **106**, 347 (1959).

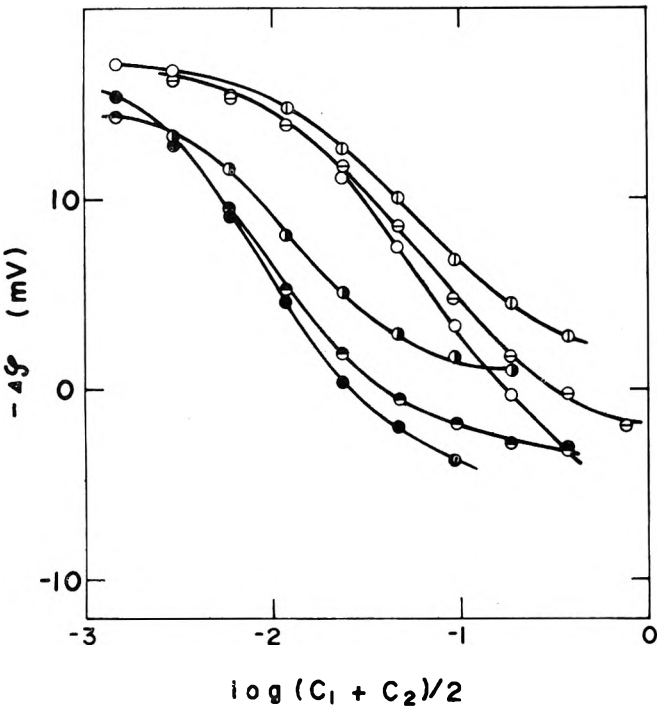

Figure 1. Plots of observed membrane potential, $\Delta\varphi$, against log $(C_1 + C_2)/2$ for combinations of SP-1 and SP-3 membrane and LiCl, NaCl, and KCl. The concentration ratio of two external solutions is kept at 2: O, LiCl for SP-1; Θ, NaCl for SP-1; Φ, KCl for SP-1; ●, LiCl for SP-3; ◒, NaCl for SP-3; ◑, KCl for SP-1.

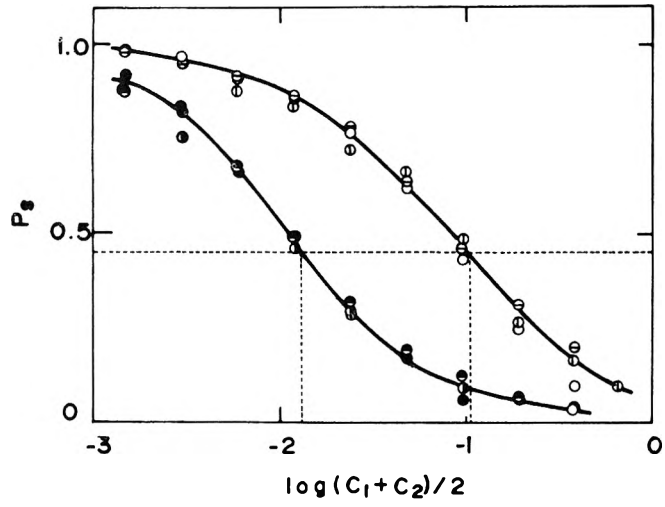

Figure 2. Plots of P_s defined by eq 7 against $\log(C_1 + C_2)/2$ for the same system as in Figure 1. Dotted horizontal line shows $P_s = 1/\sqrt{5}$, and the vertical line gives the value of ϕX for the corresponding membrane. Notations are the same as in Figure 1.

this graph. This figure illustrates that the membrane potential, $\Delta\varphi$, depends on the electrolyte species or on the mobilities of ions involved. As shown in Figure 2, this difference due to the mobilities of ions is eliminated when P_s defined by eq 7 is plotted against log $(C_1 + C_2)/2$, where the data points for various ion species are reduced in a single curve for the respective membrane unless the effective fixed charge density of the system depends strongly on the species of electrolyte component. When the average concentration $C = (C_1 + C_2)/2$ is equal to the effective fixed charge density ϕX, *i.e.*, $C/\phi X = \xi = 1$, the value of P_s must give $1/\sqrt{5} = 0.448$. In other words, from the data of P_s plotted as a function of C, we can determine the

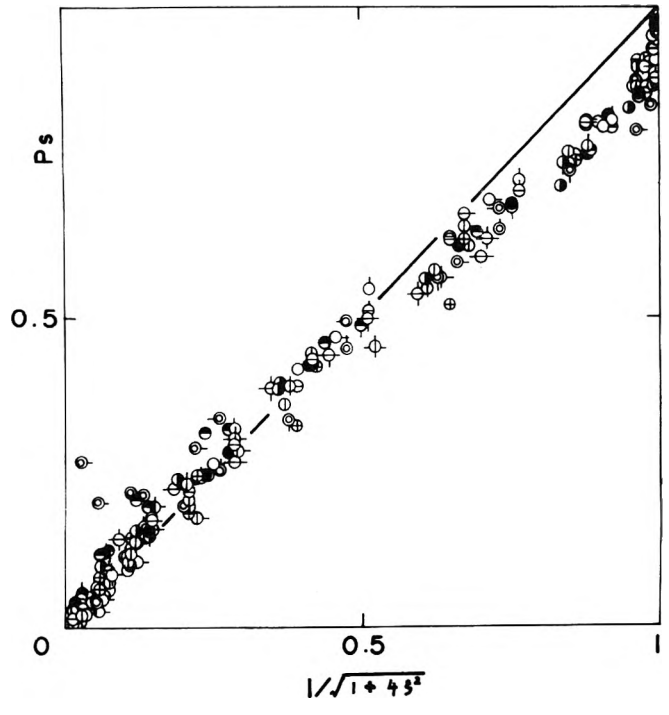

Figure 3. Plots of P_s against $1/(1 + 4\xi^2)^{1/2}$ for various combinations of membrane and electrolyte: oxidized collodion: Φ, KCl for M-1; O, LiCl for M-1; Θ, NaCl for M-1; ⊕, KIO_3 for M-1; Φ, KCl for M-2; Ó, LiCl for M-2; Θ, NaCl for M-2; ⊕, KIO_3 for M-2; Φ—, KCl for M-3; O—, LiCl for M-3; Θ—, NaCl for M-3; ⊕—, KIO_3 for M-3: PSSA collodion: ◑, KCl for PS-1; ●, LiCl for PS-1; ◒, NaCl for PS-1; ◑, KCl for PS-3; ●, LiCl for PS-3; ◒, NaCl for PS-3: dextran sulfate collodion: —Φ—, KCl for DS; —⊖—, NaCl for DS: protamine collodion: ⊙, KCl for PR; ⊙—, LiCl for PR; ⊛, NaCl for PR; —⊙, KF for PR.

value of the effective fixed charge density of a given pair of membrane and electrolyte (see dotted lines in Figure 2).

In a previous paper,[5] we suggested that the effective fixed charge density ϕX of a membrane-electrolyte system can be evaluated from the analysis of the membrane potential data in the concentrated region of the external salt solution. Thus the expansion of the apparent transference number τ_{app}^- in powers of $1/C_1$ with fixed ratio of concentrations $\beta = C_2/C_1$, and rearrangement lead to the following equation

$$\frac{1}{\tau_{app}^-} = \frac{1}{1-\alpha} + \frac{\alpha}{1-\alpha}\left[\frac{\beta - 1}{\beta \ln \beta}\right]\left(\frac{\phi X}{C_1}\right) + O(C_1^{-2}) \quad (10)$$

Equation 10 illustrates that the plots of $1/\tau_{app}^-$ against $1/C_1$ with fixed β gives a straight line, and the values of α and ϕX of the system can be evaluated from the ordinate intercept and the slope of the straight line. The values thus determined for various combinations of membranes and electrolytes were compared with those obtained from P_s *vs.* log C plots in Table I. The agreement between values of ϕX obtained by two different methods is satisfactory, although we have not evaluated the small variation of ϕX due to ion species in the present study.

Using values of ϕX predetermined by the method proposed above, the permselectivity P_s of all systems is replotted as a function of $(1 + 4\xi^2)^{-1/2}$ in Figure 3. Here the straight line of slope unity is the theoretical line with the assumption that the value of ϕX of each respective system is independent of the salt concentration. In the

TABLE I: Comparison of ϕX Determined from P_s and from Eq 10

Membrane		ϕX determined from P_s, M	ϕX determined[a] from eq 10, M
PSSA collodion	PS-1	0.091	0.082∼0.092
	PS-3	0.014	0.015∼0.009
Oxidized collodion	M-1	0.005	0.0044∼0.0058
	M-2	0.014	0.0158∼0.0168
	M-3	0.021	0.023∼0.027
Dextran sulfate collodion	DS	0.0029	0.0025∼0.0027
Protamine collodion	PR	0.038	0.018 for LiCl 0.024 for KF 0.034 for NaCl, KCl

[a] Deviation of ϕX values in this column depends on the electrolyte species used.[1,2,5]

case where a positively charged membrane is concerned, as in the protamine collodion membranes, P_s must be defined as $[\tau_{app}^{-} - (1 - \alpha)]/[1 - \alpha - (1 - 2\alpha)\tau_{app}^{-}]$ instead of eq 7. All the data studied here fall approximately on a curve which deviates systematically from the straight line of slope unity in a dilute salt solution. As discussed in previous papers,[1,2,8] the degree of unbounded counterions is slightly dependent upon the external salt concentration when the concentration decreases in comparison with ϕX. Thus the deviation of the data points from the straight line stems from the concentration dependence of ϕX. Figure 3 shows the dependence of ϕX on the external salt concentration is approximately equal for all combinations of membranes and electrolytes studied here. It is noted that for the system with protamine collodion membrane in LiCl the data deviate appreciably from the straight line in the concentrated region. This is also seen in Table I where the value of ϕX determined from P_s, *vs.* log C plots is much smaller than that obtained from the other method in a concentrated region of LiCl, and that the value of ϕX for LiCl is much larger than those for KCl or NaCl. Further study is necessary.

(8) M. Yuasa, Y. Kobatake, and H. Fujita, *J. Phys. Chem.*, **72**, 2871 (1968).

Hydrophobic Interaction in Light and Heavy Water

A. Ben-Naim,* J. Wilf, and M. Yaacobi

Department of Inorganic and Analytical Chemistry, The Hebrew University of Jerusalem, Jerusalem, Israel
(Received May 3, 1972)

The solubility, free energy, entropy, and enthalpy of solution of methane, ethane, *n*-butane, benzene, and biphenyl were determined in light and heavy water. The hydrophobic interaction between the pairs methane–methane, ethane–ethane, and benzene–benzene were computed in these two liquids. It was found that the strength of the hydrophobic interaction for the first two pairs is larger in H_2O than in D_2O. The order seems to be reversed for the pair benzene–benzene.

I. Introduction

Heavy water is known to have similar properties to light water. Yet there are some, usually small, differences between the two liquids. This makes them an ideal pair of liquids for testing various theories and conjectures made on the molecular origin of the outstanding properties of water. This paper is concerned with one aspect of these properties, namely, the strength of the solute–solute interaction between two simple solutes, which is referred to as hydrophobic interaction (HI).[1-5] A more detailed comparison of the properties of light and heavy water has been presented by Némethy and Scheraga.[6] In this paper we shall refer to HI as the indirect part of the work required to bring two solute particles from fixed positions at infinite separation to a small distance from each other. More specifically we define the HI between two simple solutes a and b at distance R by either of the following relations

$$\delta A_{ab}^{HI}(R) = \Delta A_{ab}(R) - U_{ab}(R) \qquad (1.1)$$

$$\delta G_{ab}^{HI}(R) = \Delta G_{ab}(R) - U_{ab}(R) \qquad (1.2)$$

where $U_{ab}(R)$ is the "direct" work required to bring the two solute particles, a and b, from infinity to a distance R in vacuum. $\Delta A_{ab}(R)$ is the Helmholtz free energy change for the same process, but carried out within the liquid at constant temperature and volume. $\Delta G_{ab}(R)$ is similarly the change in the Gibbs free energy for the same process carried out within the liquid but at constant temperature and pressure. The advantage of subtracting $U_{ab}(R)$ in (1.1) and (1.2) has been discussed in detail in previous articles.[4,5]

(1) W. Kauzmann, *Advan. Protein Chem.*, **14**, 1 (1959).
(2) G. Némethy and H. A. Scheraga, *J. Chem. Phys.*, **36**, 3382, 3401 (1962); *J. Phys. Chem.*, **66**, 1773 (1962).
(3) K. J. Kozak, W. S. Knight, and W. Kauzmann, *J. Chem. Phys.*, **46**, 675 (1968).
(4) A. Ben-Naim, *J. Chem. Phys.*, **54**, 1387, 3696 (1971).
(5) A. Ben-Naim, *J. Chem. Phys.*, in press.
(6) G. Némethy and H. A. Scheraga, *J. Chem. Phys.*, **41**, 680 (1964).

The process carried out at constant volume is usually slightly simpler for a statistical mechanical treatment than the one at constant pressure. The latter is, however, more directly related to the experimental quantities which are measured at constant pressure. Using the approximate relation, derived previously,[4,5] between HI and measurable quantities we write

$$\delta A_{ab}^{HI}(\sigma_1) = \Delta\mu_{a+b}^0 - \Delta\mu_a^0 - \Delta\mu_b^0 \quad (1.3)$$

$$\delta G_{ab}^{HI}(\sigma_1) = \Delta\mu_{a+b}^0 - \Delta\mu_a^0 - \Delta\mu_b^0 \quad (1.4)$$

where a + b stands for a single molecule produced by "fusing" together[7] the two particles a and b to a distance σ_1. $\Delta\mu_\alpha^0$ is the standard free energy of solution of the solute α. Since the temperature dependence of $\Delta\mu_\alpha^0$ is usually determined at constant pressure, it is appropriate to define the entropy and the enthalpy of HI by the relations

$$\delta S_{ab}^{HI}(R) = -(\partial\delta G^{HI}(R)/\partial T)_P \quad (1.5)$$

$$\delta H_{ab}^{HI}(R) = \delta G_{ab}^{HI}(R) + T\delta S_{ab}^{HI}(R) \quad (1.6)$$

These quantities are then estimated at a particular distance σ_1 by

$$\delta S_{ab}^{HI}(\sigma_1) = -\{\partial/\partial T[\Delta\mu_{a+b}^0 - \Delta\mu_a^0 - \Delta\mu_b^0]\}_P \quad (1.7)$$

$$\delta H_{ab}^{HI}(\sigma_1) = \delta G_{ab}^{HI}(\sigma_1) + T\delta S_{ab}^{HI}(\sigma_1) \quad (1.8)$$

In this paper we report the values of the HI and the corresponding entropy and enthalpy of HI for the pairs methane–methane, ethane–ethane, and benzene–benzene in light and heavy water. To the best of our knowledge, the only previous work with direct bearing to the present one has been published by Kresheck, Schneider, and Scheraga.[8]

In the next section, we summarize some of the experimental aspects of our work. Section III reports the results of the solubilities, free energies, entropies, and enthalpies of solution of some simple solutes in light and heavy water. Section IV presents the corresponding values for the hydrophobic interaction and its temperature dependence. Possible interpretations of these results are briefly discussed in section V.

II. Experimental Section

A. Solubilities of Methane, Ethane, and n-Butane. The solubilities of methane, ethane, and *n*-butane were determined according to the method developed by Ben-Naim and Baer.[9] All the gases were purchased from Matheson (with the following purity: methane 99.97%, ethane 99.9%, and *n*-butane 99.95%). D_2O, for this purpose, was from Darmstadt (99.75%) and was used as received.

Some modifications in the apparatus were introduced according to suggestions made by Wen and Hung.[10] These modifications have improved the accuracy of the measurements especially for the hydrocarbons. (It is worth noting that the solubilities of argon, determined in the new apparatus, were the same as in the older one.) We believe that the major improvement is in reducing the total amount of gas adsorbed on the surface of the vacuum grease, a phenomenon that seems to be more important as the chain length of the paraffin molecule increases. (This was checked directly by letting the gas in contact with the liquid for 24 hr before starting the dissolution process. In this way we could minimize the error due to adsorption.) Our values of the Ostwald absorption coefficient were systematically higher than those reported by Wen and Hung[10] (methane ~0.3%, ethane ~0.5%, and *n*-butane ~1.2%).

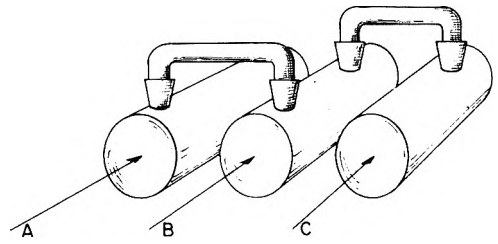

Figure 1. Three cells connected by bridges. The initial solution was placed in cell A whereas cell C contained the pure solvent. In cell B the concentration of the solute vapor was measured. Equilibrium is reached when the solute concentrations in A and C are equal.

The discrepancies, however, are quite small compared to the isotopic difference for the solubilities of these gases in H_2O and in D_2O.

B. Solubilities of Benzene and Biphenyl. The solubilities of benzene and biphenyl were determined spectroscopically. Benzene was purchased from Fluka (Puriss, 99.94%, used as received) as was biphenyl (Purum, recrystallized from ethanol, washed and dried at 65° until no effect on the spectrum of its solutions could be detected). Distilled water was purified by further distillation from alkaline $KMnO_4$ and acid $K_2Cr_2O_7$ solutions, the conductivity of the water finally used was 0.8×10^{-6} ohm^{-1} cm^{-1}. D_2O was also purchased from Fluka (99.75%) and used as received.

The absorbancies of the solutions and of their vapors were measured directly at λ_{max} with a Perkin-Elmer spectrophotometer (Model 450), operated with a slit width of 0.05 mm at 250 nm at low scanning speed, and fitted with a thermostat-controlled cell holder. The temperature was maintained within 0.05° in the range of 1–50°.

Saturated solutions of benzene were obtained in two ways: (1) by direct mixing of benzene and water (or D_2O) for about 48 hr and then measuring the absorbancy of the aqueous solution in equilibrium with the benzene (liquid) phase; (2) by dissolution of benzene through the vapor phase, in this case, there is no contact between the two liquids. Equilibrium is established between the aqueous solution and the gaseous phase.

The two methods gave identical solutions when the vapor pressure of benzene above the solution was equal to the vapor pressure of pure benzene. However, the latter method is superior for the purposes of the present study. Here, we are interested in the limiting value of the Ostwald absorption coefficient (see next section for more details) at a very low concentration of solute. A successive series of solutions with decreasing concentrations of benzene, obtained by the second procedure, showed no deviation from Beer's law. (There has been some controversy in the literature[11-15] regarding deviations from Beer's law of aqueous benzene solutions. At low concentrations of benzene, in which the Ostwald absorption coefficients have

(7) For more details of the process ascribed by "fusion," and the nature of the approximation involved in (1.3) and (1.4), the reader is referred to ref 4 and 5.
(8) G. C. Kresheck, H. Schneider, and H. A. Scheraga, *J. Phys. Chem.*, **69**, 3132 (1965).
(9) A. Ben-Naim and S. Baer, *Trans. Faraday Soc.*, **59**, 2735 (1963).
(10) Wen-Yang Wen and J. H. Hung, *J. Phys. Chem.*, **74**, 170 (1970).
(11) D. S. Arnold, C. A. Plank, E. E. Erickson, and F. P. Pike, *Ind. Eng. Chem., Chem. Eng. Data Ser.*, **3**, 253 (1958).
(12) L. J. Andrews and R. M. Keefer, *J. Amer. Chem. Soc.*, **71**, 3644 (1949).
(13) J. D. Worley, *Can. J. Chem.*, **45**, 2465 (1967).
(14) F. Franks, M. Gent, and H. H. Johnson, *J. Chem. Soc.*, 2716 (1963).
(15) D. G. Marketos, *Anal. Chem.*, **41**, 195 (1969).

been evaluated, we have found no curvatures in the plot of absorbancies *vs.* concentration.)

To ensure that the system has reached equilibrium with its vapor, we have connected a series of three quartz cells by means of two bridges as depicted in Figure 1. The first cell contained aqueous solutions of benzene (below saturation, and with different concentrations at different runs). The second cell contained only the vapor of the solution. The third cell was initially filled with *pure* water (or D_2O). The three cells formed a closed system so that the total amount of benzene was fixed. The absorbancies of the three cells were determined while stirring the solutions. The final reading was taken when the concentrations of benzene in the two liquid phases were identical. This indicates that the system has reached complete equilibrium, particularly between the solution and its vapor. (In a preliminary stage of this work we have tried to determine directly the concentration of benzene in the vapor in equilibrium with the solution. The ratio of these two concentrations approaches a constant value after about 24 hr. However it is difficult to be certain when the system has reached a complete equilibrium. In the three-cell method, we have quite a sharp indicator for the equilibrium point, since the third cell is being saturated through the gaseous phase. It is clear that once the two liquid cells have equal solute concentrations, the solute is also in equilibrium with its vapor.)

Saturated biphenyl solutions were obtained by stirring the solid biphenyl with water (or D_2O) for about 60 hr. The absorbancies of these solutions were determined at equilibrium with excess of the solid phase. Here, since the saturation concentrations are quite small, one may neglect solute–solute interaction at these concentrations. In order to determine the Ostwald absorption coefficient of these solutions, we have also measured the optical density of the vapor of pure biphenyl in a 10-cm quartz cell. From these measurements, we obtained the concentrations of biphenyl in the gaseous phase, which were used to compute the Ostwald absorption coefficients. The overall accuracy of the Ostwald absorption coefficient for benzene and biphenyl was lower than that for the gaseous solutes and the reliability is believed to be within ±5%.

C. Determination of the Molar Extinction Coefficients. The molar extinction coefficients, ϵ, of benzene in H_2O and in D_2O were determined by measuring the absorbancies of unsaturated solutions with known concentrations. The average value of ϵ at 254 nm in both H_2O and D_2O was found to be 180 at 20°, in satisfactory agreement with the reported value of Marketos.[15] Similarly, the value of ϵ for biphenyl in H_2O and D_2O has been determined. The average value of ϵ (in both H_2O and D_2O) at λ_{max} 247 nm was 1.05×10^4 and at λ_{max} 200 nm was 2.58×10^{-4}. (The latter was more convenient at very low concentrations of biphenyl.)

To determine the ϵ of benzene vapor we have adopted the following procedure. The absorbance of a sample of benzene vapor at low pressure (about 4.5 mm pressure in a 10-cm quartz cell at 20°) was determined at λ_{max} 252 nm. Then, the total quantity of benzene was solidified by introducing the cell into liquified air. At this state the cell was quickly filled with hexane and the temperature raised to 20°, so that the total quantity of benzene that had occupied the vapor is now dissolved in hexane. Next, the absorbance of the solution was measured, and using the value[16] of ϵ 250 at λ_{max} 254 we could determine the concentration of benzene in the solution and, hence, in the vapor phase as well.

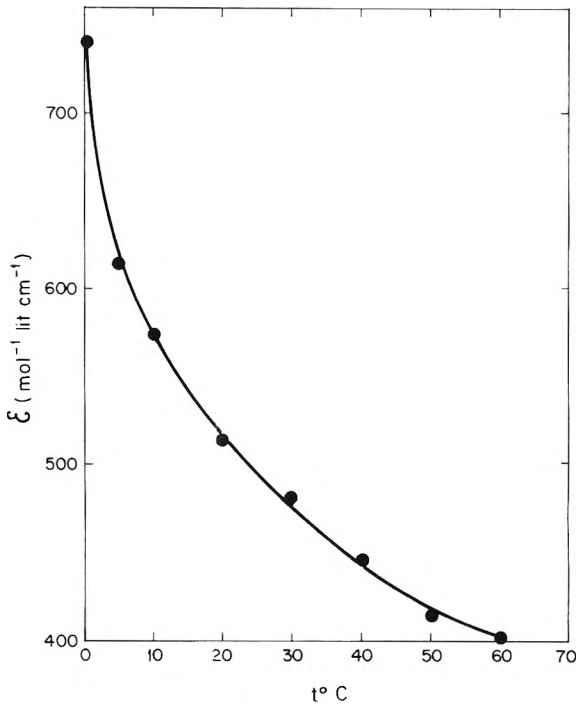

Figure 2. Temperature dependence of the molar extinction coefficient of benzene vapor at λ_{max} 252 nm (see section II for more details).

Repeating the same procedure with ten samples of benzene vapor (at low pressures) we obtained the average value $\bar{\epsilon}$ 515 (at λ_{max} 252 nm at 20°). Once we had determined the concentration of benzene vapor at one temperature, we could proceed to evaluate the temperature dependence of ϵ from 1 to 50°. These values are reported in Figure 2.

As a further check of consistency, we have determined the vapor pressure of benzene in equilibrium with the pure liquid (using the values of ϵ obtained by the above procedure). Assuming that the gas phase is ideal, the vapor pressures, computed by $p = DRT/\epsilon l$ (with D as the absorbance, l the optical way, and R the gas constant), were found to agree within 10% with the values reported in the literature.

The ϵ of biphenyl vapor (in a 10-cm quartz cell) was determined by measuring the ϵ of biphenyl in hexane, cyclohexane, ethanol, methanol, and methylcyclohexane. As no regular changes in ϵ at λ_{max} 247 nm in the various solvents were observed, we have assumed that the same value of ϵ is also valid for the vapor phase, namely, ϵ 17,000 at λ_{max} 236 nm. We have repeated the same measurements on samples of biphenyl at very low pressures (much lower than the equilibrium pressure in the presence of the pure solid) between 5 and 50°. No significant temperature effect was detected. By using this value of ϵ, we could also determine the vapor pressure of the pure biphenyl. A nice linear plot of ln P *vs.* T^{-1} was obtained (Figure 3), which coincides with the curve obtained from data from another source.[17]

III. Thermodynamic Quantities of Solution

The basic experimental ingredient that is employed in

(16) "U. V. Atlas of Organic Compounds," Vol. II, Butterworths, 1966.
(17) R. S. Bradley and T. G. Cleasby, *J. Chem. Soc.*, 1690 (1953).

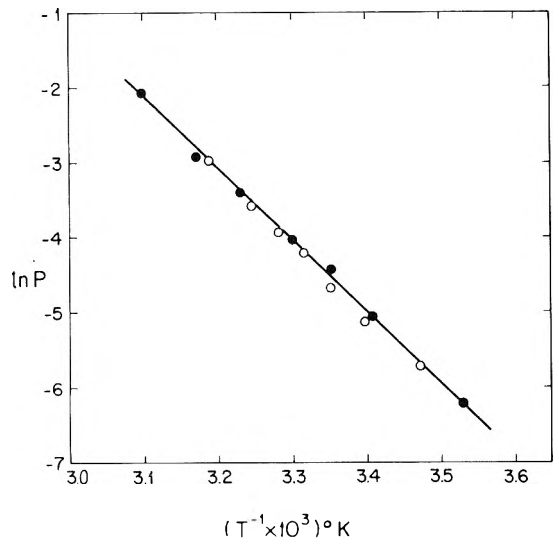

Figure 3. Vapor pressure (in mm) of biphenyl as a function of temperature. Open circles are values from ref 17 and full circles are values obtained spectroscopically (see section II).

computing the thermodynamic quantities of solution is the Ostwald absorption coefficient, defined for a solute s in a liquid l by

$$\gamma_s = (\rho_s^l/\rho_s^g)_{eq} \tag{3.1}$$

where ρ_s^l and ρ_s^g are the molar concentrations of the solute s in both the liquid and the gas at equilibrium, respectively.

It is important to realize that although γ_s is a well-defined quantity without any requirements on the absolute magnitude of the concentrations of s in the two phases, one must take the proper limiting value of γ_s for computation of the standard thermodynamic quantities. More specifically, the standard free energy of solution of s from the gas to the liquid is defined by

$$\Delta\mu_s^\circ = \lim_{\rho_s \to 0}[-RT \ln (\rho_s^l/\rho_s^g)_{eq}] \tag{3.2}$$

Note, that since the limit is taken along an equilibrium line, it is sufficient to let one concentration, ρ_s^l or ρ_s^g, tend to zero. In order to assure that we obtain the limiting value as in (3.2), we have made a series of measurements of γ_s at low concentrations. Figure 4 shows γ_s of benzene in water at various concentrations of ρ_s^l. It is clearly seen that the value of γ_s approaches a constant value. We have, in most of our work, determined γ_s at about half of the saturation concentration. As for the solubilities of the gases methane, ethane, and butane, we have found that the value of γ_s is almost constant when the total pressure is reduced to one-half or to one-third of the atmospheric pressure. Therefore, one may safely assume that the saturated solutions of these gases are, to a good approximation, dilute ideal solutions.

About ten values of $\Delta\mu_s^0$ were determined in the range of temperatures from 5 to 25° for the gases, and between 5 and 50° for the benzene and biphenyl. The temperature dependence of $\Delta\mu_s^0$ was fitted to a second-degree polynomial of the form

$$\Delta\mu_s^0 = a + bT + cT^2 \tag{3.3}$$

(T is the temperature in °C)

from which the entropy and the enthalpy of solution were

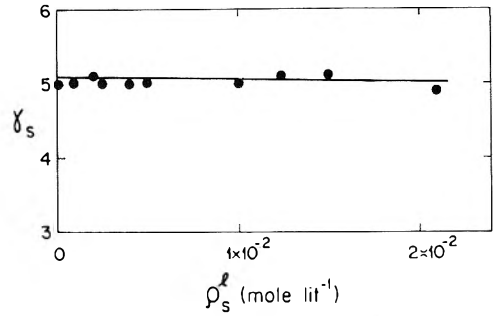

Figure 4. Dependence of the Ostwald absorption coefficient γ_s of benzene in water at various concentrations (at t = 20°). The least-squares fit of a straight line is also shown.

TABLE I: Polynomial Coefficients in (3.3) and the Standard Deviation for Each Set of Measurements

System	c	b	a	Standard deviation
Methane in H_2O	−0.09371	71.359	−10944.7	0.807
Methane in D_2O	−0.09185	71.233	−11102.5	1.36
Ethane in H_2O	−0.11611	89.432	−14509.6	2.039
Ethane in D_2O	−0.21988	149.86	−23335.8	2.041
n-Butane in H_2O	−0.15648	118.82	−19425.0	2.945
n-Butane in D_2O	−0.12702	104.26	−17694.0	4.124
Benzene in H_2O	−0.02666	37.122	−9536.2	8.788
Benzene in D_2O	−0.03864	44.618	−10657.5	15.103
Biphenyl in H_2O	−0.04126	52.057	−14740.4	22.794
Biphenyl in D_2O	−0.01945	39.059	−12827.6	27.015

computed. The values of the coefficients in (3.3) as well as the standard deviation in each case are reported in Table I.

The value of $\Delta\mu_s^0$ defined in (3.2) may be interpreted in two different ways.[18] (I) $\Delta\mu_s^0$ is the change of the Gibbs free energy[19] for transferring 1 mol of solute s from the gas to the liquid at constant P and T. In addition, we require that $\rho_s^l = \rho_s^g$ (provided that both ρ_s^l and ρ_s^g are small enough that the phases are dilute-ideal). (II) $\Delta\mu_s^0/N^0$ (with N^0 being the Avogadro number) is the change in the Gibbs free energy for transferring *one* solute particle from a *fixed* position in the gas phase to a *fixed* position[20] in the pure solvent at constant P and T.

The first interpretation is closer to an experimental procedure, and hence the more commonly used; the second one, on the other hand, has some advantages from a molecular point of view. It can be shown[18,19] that this quantity may be expressed as

$$\Delta\mu_s^\circ/N^\circ = \int_0^1 d\xi \int d\mathbf{X}_w U_{sw}(\mathbf{X}_s,\mathbf{X}_w)\rho(\mathbf{X}_w/\mathbf{X}_s,\xi) \tag{3.4}$$

where U_{sw} ($\mathbf{X}_s$,$\mathbf{X}_w$) is the solute-solvent pair potential at the specific configuration denoted by $\mathbf{X}_s$, $\mathbf{X}_w$. ρ ($\mathbf{X}_w/\mathbf{X}_s$, ξ) is the singlet conditional distribution function for solvent molecules around a given solute at a fixed configuration $\mathbf{X}_s$ and coupled to the extent ξ. Note that since U_{sw} has a range of a few molecular diameters and since $\rho(\mathbf{X}_w/\mathbf{X}_s,\xi)$

(18) A. Ben-Naim in "*Water and Aqueous Solutions*," R. A. Horne, Ed., Wiley-Interscience, New York, N. Y., 1972, Chapter 11.

(19) In ref 18, the treatment is confined to the *TVN* ensemble where the Helmholtz free energy changes are examined. In a similar fashion one may consider changes in the Gibbs free energy in the *TPN* ensemble.

(20) In the case of simple spherical particles, it is sufficient to require a *fixed* position only. For more complex solute molecules, one has to require a fixed orientation of the molecule and also a proper average over all internal rotations. For more details on this averaging procedure the reader is referred to ref 4 and 5.

TABLE II: Values of the Ostwald Absorption Coefficient γ_s, Standard Free Energy of Solution, and Standard Entropy and Enthalpy of Solution for Processes I and II (defined in Section III) for Methane in H_2O and in D_2O[a]

t, °C	γ_s	$\Delta\mu_s^0$	ΔS_s^0(I)	ΔS_s^0(II)	ΔH_s^0(I)	ΔH_s^0(II)
			H_2O			
5	0.0502	1654	−21	−19	−4200	−3700
10	0.0448	1747	−20	−18	−4000	−3400
15	0.0405	1836	−19	−17	−3700	−3200
20	0.0370	1921	−18	−16	−3400	−2900
25	0.0342	2001	−17	−15	−3100	−2600
			D_2O			
5	0.0549	1605	−22	−20	−4600	−4000
10	0.0485	1703	−21	−19	−4300	−3700
15	0.0434	1797	−20	−18	−4000	−3500
20	0.0393	1886	−19	−17	−3700	−3200
25	0.0360	1971	−18	−16	−3500	−2900

[a] The units for $\Delta\mu_s^0$ and ΔH_s^0 are cal/mol and for ΔS_s^0 are cal/mol deg.

TABLE III: Values of the Ostwald Absorption Coefficient γ_s, Standard Free Energy of Solution, and Standard Entropy and Enthalpy of Solution for Processes I and II (Defined in Section III) for Ethane in H_2O and in D_2O[a]

t, °C	γ_s^0	$\Delta\mu_s^0$	ΔS_s^0(I)	ΔS_s^0(II)	ΔH_s^0(I)	ΔS_s^0(II)
			H_2O			
5	0.0820	1383	−27	−25	−6100	−5500
10	0.0691	1504	−26	−24	−5700	−5200
15	0.0591	1620	−24	−23	−5400	−4900
20	0.0514	1730	−23	−21	−5100	−4500
25	0.0453	1834	−22	−20	−4700	−4200
			D_2O			
5	0.0889	1338	−30	−28	−6900	−6300
10	0.0733	1471	−27	−25	−6300	−5700
15	0.0621	1592	−25	−23	−5600	−5100
20	0.0539	1702	−23	−21	−5000	−4400
25	0.0479	1801	−20	−19	−4300	−3800

[a] Units as in Table I.

TABLE IV: Values of the Ostwald Absorption Coefficient γ_s, Standard Free Energy of Solution, and Standard Entropy and Enthalpy of Solution for Processes I and II (Defined in Section III) for *n*-Butane in H_2O and in D_2O[a]

t, °C	γ_s^0	$\Delta\mu_s^0$	ΔS_s^0(I)	ΔS_s^0(II)	ΔH_s^0(I)	ΔH_s^0(II)
			H_2O			
5	0.0641	1519	−34	−32	−7900	−7300
10	0.0511	1674	−32	−30	−7400	−6900
15	0.0416	1821	−31	−29	−7000	−6400
20	0.0346	1960	−29	−27	−6500	−6000
25	0.0293	2092	−27	−26	−6000	−5500
			D_2O			
5	0.0689	1479	−36	−34	−8500	−7900
10	0.0539	1644	−34	−32	−8100	−7500
15	0.0430	1802	−33	−31	−7700	−7100
20	0.0350	1954	−32	−30	−7300	−6800
25	0.0289	2100	−30	−29	−6900	−6400

[a] Units as in Table I.

TABLE V: Values of the Ostwald Absorption Coefficient γ_s, Standard Free Energy of Solution, and Standard Entropy and Enthalpy of Solution for Processes I and II (Defined in Section III) for Benzene in H_2O and in D_2O[a]

t, °C	γ_s	$\Delta\mu_s^0$	ΔS_s^0(I)	ΔS_s^0(II)	ΔH_s^0(I)	ΔH_s^0(II)
			H_2O			
10	7.9	−1163	−24	−22	−8000	−7400
20	5.1	−945	−23	−21	−7800	−7200
30	3.4	−734	−23	−21	−7600	−7100
40	2.3	−526	−22	−20	−7400	−6900
50	1.6	−324	−21	−20	−7300	−6800
			D_2O			
10	7.3	−1122	−25	−23	−8100	−7600
20	4.7	−898	−24	−22	−7900	−7300
30	3.1	−682	−23	−21	−7600	−7100
40	2.1	−474	−22	−20	−7400	−6900
50	1.5	−274	−21	−20	−7100	−6600

[a] Units as in Table I.

tends to a constant for large distances between the solvent and the solute, the integration over the location of the solvent molecule practically extends over a finite and small region about the location of the center of the solute. This "local character" of $\Delta\mu_s^0$ makes it a suitable quantity for studying solute-solvent interactions.

It is worth noting that although the two processes I and II produce the same value of $\Delta\mu_s^0$ (per one mole or per one particle), the situation is somewhat more complex for the corresponding changes of the entropy and the enthalpy, for which we have[18,19]

$$\Delta S_s^0(\mathrm{I}) = -\frac{\partial \Delta\mu_s^0}{\partial T} - RT\frac{\partial}{\partial T}(\ln(\rho^l/\rho^g)) \qquad (3.5)$$

$$\Delta S_s^0(\mathrm{II}) = -\partial\Delta\mu_s^0/\partial T \qquad (3.6)$$

$$\Delta H_s^0(\mathrm{I}) = \Delta\mu_s^0 + T\Delta S_s^0(\mathrm{I}) \qquad (3.7)$$

$$\Delta H_s^0(\mathrm{II}) = \Delta\mu_s^0 + T\Delta S_s^0(\mathrm{II}) \qquad (3.8)$$

where ρ^l and ρ^g are the densities of the two phases, respectively, and the derivatives are taken at constant pressure.

The second process (II) is more advantageous for the following reasons. (1) The thermodynamic quantities are simpler to obtain from measurable quantities. (Particularly, one does not need the coefficient of thermal expansion of the solvent for evaluating the entropy associated with process II.) (2) Because of the local character of $\Delta\mu_s^0/N^0$, the thermodynamic quantities associated with process II are more suitable for interpretation in terms of solute-solvent interaction. (3) The quantities associated with process II are naturally involved in the approximate expressions for the strength of the hydrophobic interaction[4,5] and its temperature dependence (see next section for more details).

In Tables II–VI we report the values of γ_s, $\Delta\mu_s^0$, ΔS_s^0, and ΔH_s^0 (for the two processes I and II as indicated) for methane, ethane, *n*-butane, benzene, and biphenyl in H_2O and in D_2O. There are a few points that are worth noting regarding these quantities. (1) The values of γ_s for methane and its temperature dependence for H_2O and D_2O are quite similar to the corresponding values for argon in these two solvents.[21] (2) The Ostwald absorption

(21) A. Ben-Naim, *J. Chem. Phys.*, **42**, 1512 (1965).

TABLE VI: Values of the Ostwald Absorption Coefficient γ_S, Standard Free Energy of Solution, and Standard Entropy and Enthalpy of Solution for Processes I and II (Defined in Section III) for Biphenyl in H_2O and in D_2O[a]

t, °C	γ_S	$\Delta\mu_S^0$	ΔS_S^0(I)	ΔS_S^0(II)	ΔH_S^0(I)	ΔH_S^0(II)
			H_2O			
10	357.4	−3309	−31	−29	−12,000	−11,400
20	180.0	−3026	−30	−28	−11,700	−11,200
30	96.2	−2752	−29	−27	−11,500	−10,900
40	54.2	−2485	−28	−26	−11,200	−10,700
50	32.0	−2227	−27	−25	−10,900	−10,400
			D_2O			
10	369.5	−3328	−30	−28	−11,800	−11,300
20	187.3	−3049	−30	−28	−11,700	−11,200
30	99.9	−2775	−29	−27	−11,600	−11,000
40	55.8	−2504	−29	−27	−11,400	−10,900
50	32.5	−2237	−28	−26	−11,300	−10,800

[a] Units as in Table I.

TABLE VII: Hydrophobic Interaction and the Corresponding Entropy and Enthalpy Values for the Reaction 2(Methane) → Ethane (eq 4.4) in H_2O and D_2O[a]

t, °C	δG^{HI}	δS^{HI}	δH^{HI}
	H_2O		
5	−1924	13	1900
10	−1990	12	1600
15	−2053	11	1500
20	−2112	11	1300
25	−2168	10	1000
	D_2O		
5	−1872	12	1700
10	−1936	13	1700
15	−2002	13	1900
20	−2071	13	2000
25	−2141	13	2000

[a] Units as in Table I.

coefficients of methane, ethane, and *n*-butane are smaller in H_2O than in D_2O (except for *n*-butane at 25°); the difference between the values in the two liquids tend to diminish as temperature increases. (3) The Ostwald absorption coefficient of benzene is larger in H_2O than in D_2O. In spite of the relatively low accuracy of these results, we believe that the sign of the isotope effect on γ_S is correct. The sign of the isotope effect on γ_S for biphenyl is estimated to be within the limits of our accuracy. (4) The standard entropy and enthalpy of solution are usually (but there are exceptions) more negative in D_2O than in H_2O. This result is in accordance with similar ones obtained for argon,[21] for which more accurate results could have been obtained.

IV. Hydrophobic Interaction

The hydrophobic interaction (HI) in this section refers to the indirect part of the Gibbs free energy change for bringing two solute particles from fixed positions at infinite separation to some close distance, the whole process being carried out within the liquid at constant pressure and temperature. For a particular close distance, say 1.53 Å for two methane molecules, an approximate measure of the strength of the HI has been suggested[4,5]

TABLE VIII: Hydrophobic Interaction and the Corresponding Entropy and Enthalpy Values for the Reaction 2(Ethane) → *n*-Butane (eq 4.5) in H_2O and D_2O[a]

t, °C	δG^{HI}	δS^{HI}	δH^{HI}
	H_2O		
5	−1248	18	3700
10	−1335	18	3500
15	−1419	17	3400
20	−1499	15	3000
25	−1576	14	2900
	D_2O		
5	−1198	22	4700
10	−1297	18	3900
15	−1381	15	3100
20	−1450	12	2000
25	−1502	9	1200

[a] Units as in Table I.

TABLE IX: Hydrophobic Interaction and the Corresponding Entropy and Enthalpy Values for the Reaction 4(Methane) → *n*-Butane (eq 4.6) in H_2O and in D_2O[a]

t, °C	δG^{HI}	δS^{HI}	δH^{HI}
	H_2O		
5	−5095	44	7500
10	−5316	42	6700
15	−5525	39	6400
20	−5724	37	5600
25	−5911	34	4900
	D_2O		
5	−4941	46	8700
10	−5170	44	7300
15	−5386	41	6900
20	−5591	38	6000
25	−5784	35	5200

[a] Units as in Table I.

$$\delta G^{HI} = \Delta\mu_{Et}^0 - 2\Delta\mu_{Me}^0 \quad (4.1)$$

The entropy and the enthalpy corresponding to this process are computed by

$$\delta S^{HI} = -(\partial\delta G^{HI}/\partial T)_P = \Delta S_{Et}^0(II) - 2\Delta S_{Me}^0(II) \quad (4.2)$$

$$\delta H^{HI} = \delta G^{HI} + T\delta S^{HI} \quad (4.3)$$

Note that for the purpose of computing the entropy and the enthalpy of the HI, only process II described in section III is of relevance.

The HI and the corresponding entropies and enthalpies were computed for the following "reactions"[4,5]

$$2(\text{methane}) \rightarrow \text{ethane} \quad (4.4)$$

$$2(\text{ethane}) \rightarrow n\text{-butane} \quad (4.5)$$

$$4(\text{methane}) \rightarrow n\text{-butane} \quad (4.6)$$

$$2(\text{benzene}) \rightarrow \text{biphenyl} \quad (4.7)$$

and are reported in Tables VII–X. The most conspicuous result is that the HI for the first three reactions, (4.4), (4.5), and (4.6), is stronger in H_2O compared to D_2O, in agreement with a conclusion reported in ref 8. The isotope

TABLE X: Hydrophobic Interaction and the Corresponding Entropy and Enthalpy Values for the Reaction 2(Benzene) → Biphenyl (eq 4.7) in H_2O and D_2O[a]

t, °C	δG^{HI}	δS^{HI}	δH^{HI}
	H_2O		
10	−983	15	3400
20	−1136	14	3200
30	−1284	15	3300
40	−1434	14	3100
50	−1579	15	3200
	D_2O		
10	−1085	18	3900
20	−1253	16	3400
30	−1410	15	3300
40	−1556	13	2900
50	−1689	14	2400

[a] Units as in Table I.

effect for the last reaction seems to have reversed its sign. The entropy and the enthalpy of the HI are all positive. This may well be attributed to the decrease of the "structure of the water" as the two solutes approach each other to a close distance.[22] The strength of the HI for reactions 4.4, 4.5, and 4.7 are in decreasing order. This effect was found earlier,[5] and was attributed to the relative extent of penetration of the two molecules compared to their molecular dimensions. We have estimated that the isotope effect on the entropy and the enthalpy of the HI are well within the limits of experimental error.

V. Discussion and Conclusion

The HI, being viewed as a property of the solvent, may be best investigated by using a pair of inert solutes. In fact, we have already argued[4] that the simplest solute for this purpose could be hard spheres.[23] Solutions of saturated paraffins may serve as a reasonable model for inert molecules for estimating the strength of HI. The case of benzene solution seems not to fall into this category probably because of the stronger interaction one expects between benzene and water. The results obtained for the HI between a pair of benzene molecules, though of some value in the context of the general solute–solute interaction problem, cannot convey faithful information on the properties of the solvent.

The question of interpreting the isotopic effect on the HI is a difficult one, since we have as yet no general relation between HI and molecular properties of the solvent. We should like to point out some possible sources for the isotopic effect, though it seems that no one points to the correct sign of this effect.

a. Density. The density of D_2O, in grams/ml, is about 10% higher than that of H_2O. However, expressing the densities in number of particles per unit volume, we get almost exactly the same value for the two liquids. In ref 5 we have studied the effect of the density of the solvent on the solute–solute interaction at short distances. That study was confined to a system of Lennard-Jones particles in two dimensions. It was found that the strength of the solute–solute interaction increases with the density of the solvent. Although it is difficult to infer from this result any sound conclusion for aqueous solutions, we may expect that, other things being equal, the small difference in the number density between H_2O and D_2O could not account for the observed isotopic effect on HI.

b. Cohesive Energy. In a simple solvent composed of, let us say, Lennard-Jones particles, the average cohesive energy may be represented by the depth of the pair potential function. Using again the simplified model in ref 5, we found that the solute–solute interaction *increases* with the cohesive energy of the solvent. In water it is difficult to point out a particular parameter that conveys the cohesive energy. As a rough measure of this, one may take the hydrogen bond energy which is estimated[6] to be larger in D_2O than in H_2O. Therefore, on the basis of hydrogen bond energy alone one would expect a stronger HI in D_2O, in contrast to the experimental findings.

c. Quantum Effects. Although it is extremely difficult to estimate the isotopic effect on the HI for such a complex fluid like water,[25] it is believed that the difference in mass of about 10% between the two liquids may be important in establishing the isotopic effect on HI. In the appendix we have shown that the first-order quantum correction to the HI even for simple fluids may not be estimated without a detailed knowledge of the intermolecular potential. This difficulty becomes even more acute for complex fluids, such as water.

All the above fractional information is strictly relevant to a simple solvent with pairwise additive potential. The fact that none of these points out the source of the isotopic effect on HI indicates that more complicated features of the solvent are involved. Using classical arguments only, it is possible that the peculiar mode of packing of the water molecules in the liquid state, a feature that is currently referred to as the structure of water, plays an important role in determining the strength of the HI. Thus far no general relation is available between HI and the structure of water. Therefore, it is impossible at present to explain the isotope effect on HI by classical arguments. Moreover, the fact that water has small moments of inertia, and having a strong orientational dependence interaction, may indicate that quantum correction to the rotational degrees of freedom may be very important in establishing the differences between the two liquids.

Acknowledgment. We are grateful to Professor Avner Treinin for discussions and suggestions concerning the spectroscopic aspects of the experimental work. We are also indebted to Dr. F. H. Stillinger for valuable comments on the manuscript.

This work was supported in part by the Central Research Fund of the Hebrew University of Jerusalem, for which the authors are very grateful.

Appendix

First-Order Quantum Correction to the Free Energy of Cavity Formation and Hydrophobic Interaction at Zero Separation. Consider a system of N simple molecules contained in a volume V and at temperature T. Assuming

(22) Here we use the undefined concept of the "structure of water." The statement made in the article is of course meaningless if one does not define this concept. For a reasonable definition of the structure of water, argument may be given to show that two methane molecules will enhance the structure more than a single ethane molecules. This point has been shown for a specific model by Némethy and Scheraga.[2] A more general argument, based on an exact mixture model approach to liquid water, will be published elsewhere.

(23) The HI between two hard-sphere solutes is the same as the cavity–cavity interaction.[4] For such a pair the HI at zero separation may be estimated using the scaled particle theory. It has been shown previously[4] that the HI between two cavities at zero separation is indeed stronger in water than in some nonaqueous solvents. This point has been further confirmed recently by Wilhelm and Battino.[24]

(24) E. Wilhelm and R. Battino, *J. Chem. Phys.*, **56**, 563 (1972).

(25) H. Friedmann, *Physica*, **30**, 921 (1964).

pairwise additivity of the total potential energy, the Helmholtz free energy may be expanded in power series of the Planck constant h. The first-order correction to the classical value of the free energy, A_{cl}, is[26]

$$A(T,V,N) = A_{cl}(T,V,N) + (h^2/24(2\pi kT)^2 m)\langle \Sigma_{i=1}^{N}(\nabla_i U)^2\rangle \quad (A.1)$$

Here, m is the mass of a single particle, $\nabla_i U$ is the gradient of the total potential function with respect to $\mathbf{R}_i$, and the average is taken over all the configurations of the system of the *classical* T,V,N ensemble, namely

$$\langle \Sigma_{i=1}^{N}(\nabla_i U)^2\rangle = \int \cdots \int d\mathbf{R}^N P(\mathbf{R}^N) \Sigma_{i=1}^{N}[\nabla_i U(\mathbf{R}^N)]^2 \quad (A.2)$$

with

$$P(\mathbf{R}^N) = \exp[-\beta U(\mathbf{R}^N)]/\int \cdots \int d\mathbf{R}^N \exp[-\beta U(\mathbf{R}^N)] \quad (A.3)$$

and $\beta = (kT)^{-1}$.

The free energy of cavity formation in the system, at constant TVN is the same as the standard free energy of solution of a hard sphere (HS) having a suitable radius[18]

$$\Delta\mu_{HS}^0 = A(T,V,N;\sigma) - A(T,V,N) \quad (A.4)$$

where $A(T,V,N;\sigma)$ denotes the Helmholtz free energy of the same system but having a cavity of radius σ at some fixed position. This is the same as imposing a restriction on all the centers of the particles, $\mathbf{R}_i$, to be excluded from the spherical region v_σ of radius σ about a fixed position.

Now compare two solvents, let us say α_H and α_D, which are identical except for having different molecular masses, m_H and m_D, respectively. The classical free energy contains the mass of the particles only in the momentum partition function, which is the same for the system with or without the cavity. Hence, the classical part of $\Delta\mu_{HS}^0$ is independent of the mass. The difference in the standard free energy of solution of an HS in the two fluids must be due to quantum effect, the first order of which is[27]

$$\Delta\mu_{HS}^0(\text{in } \alpha_D) - \Delta\mu_{HS}^0(\text{in } \alpha_H) = [h^2/24(2\pi kT)^2][(1/m_D)\langle \Sigma_i(\nabla_i U)^2\rangle_{cav} - (1/m_D)\langle \Sigma_i(\nabla_i U)^2\rangle - (1/m_H)\langle \Sigma_i(\nabla_i U)^2\rangle_{cav} + (1/m_H)\langle \Sigma_i(\nabla_i U)^2\rangle] \quad (A.5)$$

where $\langle\ \rangle_{cav}$ is the same average as in (A.2), but excluding the region v_σ over which the integrations carried out in (A.2) and in (A.3). Relation A.5 may be rearranged to

$$\Delta\mu_{HS}^0(\text{in } \alpha_D) - \Delta\mu_{HS}^0(\text{in } \alpha_H) = [h^2(m_D - (m_H)/24(2\pi kT)^2 m_D m_H] \times [\langle \Sigma_i(\nabla_i U)^2\rangle - \langle \Sigma_i(\nabla_i U)^2\rangle_{cav}] \quad (A.6)$$

In ref 4 we have shown that the HI between two cavities at zero separation is given by

$$\delta A_{HS}^{HI}(0) = -\Delta\mu_{HS}^0 \quad (A.7)$$

Hence

$$\delta A_{HS}^{HI}(0, \text{in } \alpha_D) - \delta A_{HS}^{HI}(0, \text{in } \alpha_H) = -[\Delta\mu_{HS}^0(\text{in } \alpha_D) - \Delta\mu_{HS}^0(\text{in } \alpha_H)] \quad (A.8)$$

Thus we see that the first-order quantum correction to the free energy of solution and to the HI of hard sphere will depend on the difference in masses, $m_D - m_H$, and on the type of the pair potential operating between the particles. The latter cannot be estimated without a detailed knowledge of the pair potential even for a simple fluid of spherical particles.

(26) See, for example, L. D. Landau and E. M. Lifshitz, "Statistical Physics," Pergamon Press, London, 1959, p 100.

(27) A strickt cavity produces a discontinous potential into the system, and therefore (A.2) may not be applicable. This difficulty may be overcome by considering a "soft cavity," in which the repulsive potential is built up continuously as the particles approach the region v_σ.

Quadrupole Interaction of Carbon Dioxide on Silica–Alumina Surface

Yun-yang Huang

Department of Chemistry, Texas A & M University, College Station, Texas 77843 *(Received August 11, 1972)*

The interaction between carbon dioxide and the specific adsorption sites on amorphous silica–alumina was studied by measurement of adsorption isotherms over a temperature range from 0 to 290°. These adsorption sites were found to be less than 1% of the surface and yielded a heat of adsorption of 14.5 kcal/mol. The major contribution of the adsorbate–adsorbent interaction was attributed to quadrupole energy, from which the electrostatic field gradient at the adsorption site of carbon dioxide was estimated to be -0.92 V/Å^2. Entropy calculation showed that adsorbed carbon dioxide was localized with almost no rotational degree of freedom. At surface coverages slightly above 1%, the heat decreased steeply to about 5 kcal/mol. On these sites, the presence of surface hydroxyl groups enhanced the adsorption of carbon dioxide.

Introduction

On the surface of metal oxides, hydroxyl groups are almost always present. When the material is subjected to extensive heat pretreatment under high vacuum, defect structures are formed on the surface due to the removal of hydroxyl groups. These surface sites, which could be exposed cations, oxygen vacancies, or cation vacancies, often show unusual catalytic activity and adsorption property. For example, when amorphous silica–alumina is evacuated at 800°, a small fraction of the surface sites is formed which adsorb nitrogen and carbon monoxide very specifically.[1] The heats of adsorption are unusually high, being 15 kcal/mol for carbon monoxide and 9 kcal/mol for nitrogen. These molecules have considerable quadrupole moments. On the other hand, for argon and krypton, which have about the same or greater polarizability than nitrogen or carbon monoxide but have zero quadrupole moment, the heats of adsorption are only 2.5 and 3.3 kcal/mol, respectively. The difference in adsorption behavior of the two groups of molecules suggests that the specific surface sites on the highly dehydrated silica–alumina are capable of quadrupole interaction. The effect of permanent electric quadrupole moments of molecules on the heat of adsorption has been discussed by Drain[2] and Hayakawa.[3] Detailed calculations of the quadrupole interaction of a nitrogen or a carbon dioxide molecule with the surface of ionic crystals show its significant contribution to the high heats of adsorption. It would be interesting to extend the investigation of silica–alumina to the adsorption of carbon dioxide. By determining the heat of adsorption, the nature of the quadrupole interaction can be better understood.

Peri[4] has investigated by infrared spectroscopy the adsorption of carbon dioxide on silica–alumina. Much information about the adsorbed state of carbon dioxide was obtained. From spectra and pressure measurements at three temperatures, he has also roughly estimated the heat of adsorption to be 15 kcal/mol. These specific adsorption sites, designated by Peri as "α sites," were suggested to be exposed aluminum cations. The possible role of quadrupole interaction with carbon dioxide was also pointed out. However, the results of the adsorption of nitrogen and carbon monoxide[1] indicate that the heat value for carbon dioxide might be greater, if the quadrupole interaction is predominant. By carefully measuring a number of adsorption isotherms over a wide temperature range, a more detailed information about the energetics of the adsorbate–adsorbent interaction, the state of adsorbed carbon dioxide, and the surface site distribution can be obtained. The effect of heat treatment of silica–alumina on the adsorption of carbon dioxide will also be studied.

Experimental Section

Carbon dioxide, Coleman instrument grade (99.99% purity) from Matheson Gas Products, was condensed in a liquid nitrogen cold trap, pumped for a few minutes, and then distilled into a gas storage bulb.

Silica–alumina, Davison 980 cracking catalyst, was obtained from W. R. Grace Co. It has a chemical composition of 13.2% Al_2O_3 and a surface area of 358 m^2/g when evacuated at temperatures below 450° and 326 m^2/g after evacuation at 800°. All the weight indicated throughout this paper is based on the sample prior to heat treatments. The amount used in the adsorption measurement was 6.74 g. Weight losses after the heat treatments have been reported[1] as 6.7% at 450° and 7.5% at 800°.

A volumetric adsorption apparatus in connection with a high-vacuum system was employed for the adsorption measurement. Pressures were measured between 1 and 500 Torr by a mercury manometer while temperatures between 0 and 300° for the adsorption runs by a chromel–alumel thermocouple. The sample was evacuated at 245° for 3 hr and an isotherm of CO_2 adsorption was taken at 25°. After further evacuation at 440° overnight, a series of adsorption isotherms between 0 and 241° were measured. The sample was again evacuated above 800° for 7 hr, the final temperature being 820°. Adsorption measurements were then taken for a temperature range between 0 and 292.5°. In all runs, the adsorption was rapid and reversible.

Results and Discussion

The adsorption isotherms at 25° of carbon dioxide on the silica–alumina sample evacuated at 245, 440, and 820°, respectively, are shown on Figure 1. Similar to those observed for the adsorption of nitrogen and carbon mon-

(1) Y. Y. Huang and P. H. Emmett, presented at the Second North American Meeting of the Catalysis Society, Houston, Tex., Feb 1971.
(2) L. E. Drain, *Trans. Faraday Soc.*, **49**, 650 (1953).
(3) T. Hayakawa, *Bull. Chem. Soc. Jap.*, **30**, 236 (1957).
(4) J. B. Peri, *J. Phys. Chem.*, **70**, 3168 (1966).

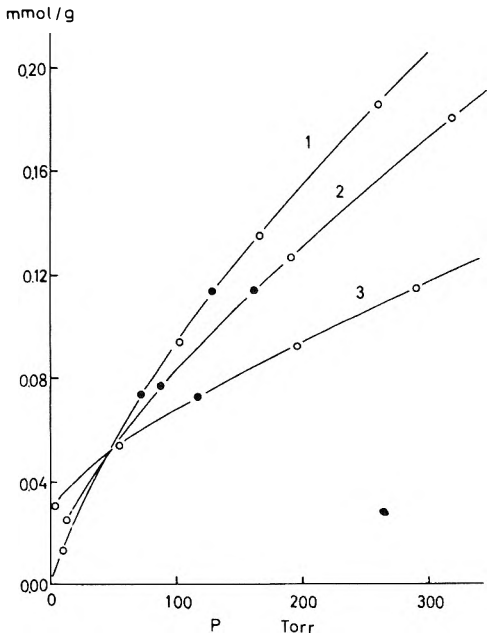

Figure 1. Adsorption isotherms at 25° of CO_2 on silica-alumina sample evacuated (1) at 245° for 3 hr, (2) at 440° for 8 hr, and (3) at 820° for 7 hr: open circles, adsorption; solid circles, desorption.

oxide,[1] the uptakes at very low pressures increased with the temperature of pretreatment. At a pressure of about 2 Torr, the amount of carbon dioxide adsorbed was 30 μmol/g for the sample evacuated at 820°. This corresponds to 5.6×10^{12} molecules/cm^2 as compared to 4.6×10^{12} molecules/cm^2 for carbon monoxide. Both are within the range of the surface concentration of α sites indicated by Peri,[4] namely, $3\text{-}9 \times 10^{12}$ molecules/cm^2.

In contrast to nitrogen and carbon monoxide, however, the adsorption of carbon dioxide at higher pressures was much greater on the sample evacuated at 245° than at 440 or 820°. Adsorption isotherms were not linear, but were concave toward the pressure axis. In this region, isotherms of both nitrogen and carbon monoxide were nearly parallel to the ones obtained on the least dehydrated sample.[1]

A series of isotherms between 142.5 and 292.5° for the sample evacuated at 820° is shown on Figure 2. Isosteric heats of adsorption q_{st} were determined from slopes of the Clausius-Clapeyron plots, *i.e.*,

$$q_{st} = -R[\partial \ln p/\partial(1/T)]_\theta \qquad (1)$$

Within the experimental region, these plots were linear. The variation of q_{st} with the surface coverage θ from θ = 0.001 to 0.05 is shown on Figure 3.

At $\theta > 0.01$, q_{st} is between 5 and 6 kcal/mol, the value which is approximately the same as that measured on graphitized carbon black.[5] Its magnitude indicates that the interaction between carbon dioxide and the majority of the surface sites of the amorphous silica-alumina is due to ordinary van der Waals force with negligibly small electrostatic contributions. The heat of adsorption is slightly greater on the sample evacuated at 440° than that evacuated at 820°. The presence of surface hydroxyl groups seems to enhance slightly the adsorption of carbon dioxide, as is also revealed from adsorption isotherms at 25° (Figure 1). In fact, strong interaction of adsorbed CO_2 and surface hydroxyl groups was observed on γ-alumina from the infrared study by Peri[4] and by Parkyns.[6] Bertsch and

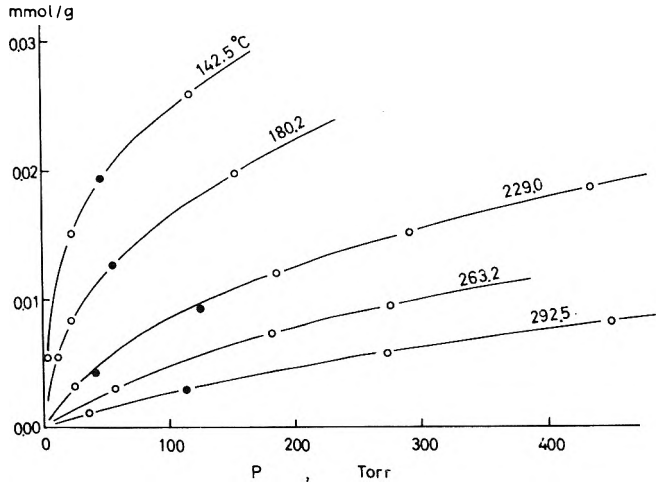

Figure 2. Adsorption isotherms of CO_2 on silica-alumina sample evacuated at 820°: open circles, adsorption; solid circles, desorption.

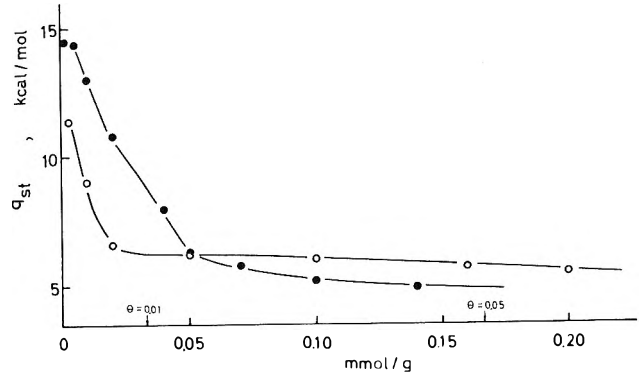

Figure 3. Heat of adsorption of CO_2 on silica-alumina as a function of surface coverage: open circles, sample evacuated at 440°; solid circles, sample evacuated at 820°.

Habgood[7] also pointed out that small amounts of preadsorbed water greatly accelerate the rate of carbon dioxide adsorption on NaX zeolite, although no evidence has been indicated from the infrared study on silica-alumina.

At $\theta < 0.001$, q_{st} is 11.5 kcal/mol for the sample evacuated at 440°, but increases to 14.5 kcal/mcl after evacuation at 820°. The latter confirms with the value roughly estimated by Peri. The high heat of adsorption shows that carbon dioxide is in strong interaction with the specific sites, which are present only in a very small fraction of the surface. Peri suggested that these adsorption sites were exposed aluminum cations, which were designated as α sites. They were formed on the surface of silica-alumina as a result of extensive dehydration. In electron spin resonance study, Lunsford[8] reported that the spectra of nitric oxide on γ-alumina and silica-alumina showed considerable hyperfine coupling with an ^{27}Al atom. The number of adsorption sites was a functuon of the degree of dehydration and that the maximum number was fcund to be 4×10^{12} sites/cm^2. He concluded that the adsorption sites for NO were the α sites, the same for carbon dioxide. It must be noted that NO has a quadrupole moment between

(5) C. H. Amberg, W. B. Spencer, and R. A. Beebe, *Can. J. Chem.*, **33**, 305 (1955).
(6) N. D. Parkyns, *J. Chem. Soc. A*, 410 (1969).
(7) L. Bertsch and H. W. Habgood, *J. Phys. Chem.*, **67**, 1621 (1963).
(8) J. H. Lunsford, *J. Catal.*, **14**, 379 (1969).

those of CO and N_2,[9] and its molecular properties are quite similar to CO. Therefore, its adsorption behavior would be similar to CO and N_2, especially in terms of quadrupole interaction.

In general, the electrostatic contribution of the adsorbate–adsorbent interaction consists mainly of polarization and quadrupole forces. The relative importance of these contributions depends on the nature of the adsorption sites as well as the nature of the probing molecule. Sufficient evidence has been displayed in a number of adsorption studies, for example, argon and nitrogen on X type zeolites,[10] carbon dioxide on X type zeolites,[11] and krypton on Y type zeolites.[12] The fact that α sites on silica–alumina are specific to CO, N_2, NO, and CO_2 but not to Ar and Kr clearly indicates that quadrupole interaction is the predominant contribution on these sites. In other words, the difference in heats of adsorption between the two groups of gas molecules must be mainly due to the quadrupole energy. We thus focus on the nature of this specific interaction between CO_2 and the α sites.

The quadrupole contribution to the energy of interaction U_Q of an axially symmetric charge system with an arbitrary electric field is given by the expression[13]

$$U_Q = -\tfrac{1}{2}QE' \tag{2}$$

where E' is the electrostatic field gradient along the axis of symmetry of the molecule, and Q is the quadrupole moment of the molecule and is defined by

$$Q = \tfrac{1}{2}\int \rho(r,\theta)(3\cos^2\theta - 1)r^2\,d\upsilon \tag{3}$$

where $\rho(r,\theta)$ is the volume charge density of the molecule at (r,θ) and the origin is the center of the molecule. Sometimes, Q is defined as twice the expression 3 so that the coefficient $\frac{1}{2}$ in (2) must be replaced by $\frac{1}{4}$. If Q is given in unit of 10^{26} (esu cm^2) and E' in unit of V/Å^2, then U_Q can be expressed in unit of kcal/mol with the proper conversion factor

$$U_Q = -2.40QE' \text{ kcal/mol} \tag{4}$$

According to Stogryn and Stogryn,[9] the recommended value of the quadrupole moment Q of carbon dioxide is -4.3×10^{-26} esu cm^2. Thus, the quadrupole energy of interaction U_Q can be determined if the electrostatic field gradient E' is known, or *vice versa*. If the difference in heat of adsorption of CO_2 on silica–alumina between $\theta \leq 0.001$ and $\theta \geq 0.05$ is attributed entirely to the quadrupole energy, then

$$-U_Q = q_{st}(\theta \leq 0.001) - q_{st}(\theta \geq 0.05) = 14.5 - 5.0 = 9.5 \text{ kcal/mol} \tag{5}$$

So that, from eq 4, $E' = -0.92$ V/Å^2.

Along the other two perpendicular axes of a CO_2 molecule, the principal quadrupole moments have the value $Q_{xx} = Q_{yy} = -\frac{1}{2}Q_{zz} = -\frac{1}{2}Q$. At an adsorption site above the surface, the field gradients along the three axes must satisfy Laplace's equation[13]

$$E_{xx}' + E_{yy}' + E_{zz}' = 0 \tag{6}$$

If we arbitrarily take the x and y axes to be parallel and the z axis to be perpendicular to the surface and if the field gradient at the adsorption site is the same along the x and y directions, then $E_{xx}' = E_{yy}' = -\frac{1}{2}E_{zz}'$. So that, when a CO_2 molecule is adsorbed with its axis of symmetry perpendicular to the surface, the quadrupole interaction is

$$U_{Q\perp} = -\tfrac{1}{2}QE_{zz}' \tag{7}$$

and if it is attached to the surface in lateral position

$$U_{Q\parallel} = -\tfrac{1}{2}Q\,E_{xx}' = \tfrac{1}{4}QE_{ZZ}' \tag{8}$$

In the vicinity of a positive charge like an exposed Al^{3+} ion, for instance, the field gradient should be negative in the z direction pointing outward from the surface so that $U_{Q\perp}$ is negative or attractive, but $U_{Q\parallel}$ is positive or repulsive. Therefore, if the adsorption site is an exposed Al^{3+} ion, the end-on approach of the CO_2 molecule would be a favorable position.

Some information concerning the adsorbed state of carbon dioxide may be obtained from entropy considerations. From the isosteric heat of adsorption, we can calculate the entropy of adsorption $\overline{\Delta S}$

$$\overline{\Delta S} = \bar{S}_a - \bar{S}_G = -q_{st}/T \tag{9}$$

where $\bar{S}_a$ is the differential molar entropy of the adsorbed molecule at pressure P and temperature T in equilibrium with the gas phase and $\bar{S}_G$ is the molar entropy in the gas phase at P and T. $\bar{S}_G$ can be calculated by means of statistical mechanics.[14] The evaluation of $\bar{S}_a$ depends on the model of the adsorbed state. For a heat of adsorption as high as 15 kcal/mol, it is very likely that the adsorption of carbon dioxide would be localized. In other words, three translational degrees of freedom in the gas phase will be transformed into three modes of surface vibration, and the rotation of CO_2 will be frozen or considerably hindered. Then

$$\bar{S}_a = \bar{S}_c + \bar{S}_{th} \tag{10}$$

where $\bar{S}_c$ is the configurational entropy and $\bar{S}_{th}$ is the thermal entropy. For adsorption on a uniform surface

$$\bar{S}_c = R \ln [(1-\theta)/\theta] \tag{11}$$

where θ is the surface coverage. On a heterogeneous surface, the evaluation of $\bar{S}_c$ is more complicated and often not feasible.[15] The thermal entropy $\bar{S}_{th}$ consists of surface vibration, internal vibration, and surface rotation. Assuming that the internal vibration remains the same in the adsorbed state as in the gas phase, we have

$$\overline{\Delta S} = \bar{S}_c + (\bar{S}_{vs} - \bar{S}_t) + (\bar{S}_{rs} - \bar{S}_r) \tag{12}$$

where $\bar{S}_{vs}$ is the entropy for surface vibration, $\bar{S}_{rs}$ the entropy for surface rotation, $\bar{S}_r$ is the rotational entropy, and $\bar{S}_t$ the translational entropy in the gas phase at the equilibrium pressure. By the use of eq 9, we have then

$$\bar{S}_{rs} + \bar{S}_c = -(q_{st}/T) - \bar{S}_{vs} + \bar{S}_t + \bar{S}_r \tag{13}$$

The rotational state of the adsorbed molecule may be understood if $\bar{S}_c$ and $\bar{S}_{vs}$ can be estimated. Since no information is available about the surface vibrational frequencies, only the mean value can be estimated by the relation

$$\nu(CO_2) = \nu(Ar)\sqrt{M(Ar)\Delta E(CO_2)/M(CO_2)\Delta E(Ar)} \tag{14}$$

(9) D. E. Stogryn and A. P. Stogryn, *Mol. Phys.*, **11**, 371 (1966).
(10) R. M. Barrer and W. I. Stuart, *Proc. Roy. Soc., Ser. A*, **249**, 464 (1959).
(11) R. M. Barrer and R. M. Gibbons, *Trans. Faraday Soc.*, **61**, 948 (1965).
(12) Y. Y. Huang, J. E. Benson, and M. Boudart, *Ind. Eng. Chem., Fundam.*, **8**, 346 (1969).
(13) A. D. Buckingham, *Quart. Rev., Chem. Soc.*, **13**, 183 (1959).
(14) T. L. Hill, "Introduction to Statistical Thermodynamics," Addison-Wesley, Reading, Mass., 1960, Chapter 9.
(15) D. H. Everett, *Trans. Faraday Soc.*, **46**, 942 (1950).

TABLE I: Entropy Calculations for Localized Adsorption of CO_2 on Silica–Alumina

T, °K	θ[b]	q_{st}, kcal/mol	$-\overline{\Delta S}$, eu	$\bar{S}_{vs}$, eu	$\bar{S}_t$,[a] eu	$\bar{S}_r$, eu	$\bar{S}_{rs} + \bar{S}_c$, eu	$\bar{S}_c$(hom), eu
273	0.0135	7.1	26.0	12.0	32.2	12.9	7.1	8.5
	0.0296	6.1	22.4	12.4	27.7	12.9	5.8	6.9
298	0.0108	8.3	27.8	12.1	32.7	13.1	5.9	9.0
	0.0200	6.2	20.8	12.9	28.1	13.1	7.5	7.7
373	~0.0075	9.8	26.3	12.9	33.8	13.5	8.1	9.7
	~0.012	8.0	21.4	13.5	29.2	13.5	7.8	8.8
500	0.0005	14.5	29.0	13.5	35.2	14.1	6.8	15.3
	0.0025	13.5	27.0	13.7	30.6	14.1	4.0	11.9
	~0.0075	11.7	23.4	14.1	26.6	14.1	3.2	9.7

[a] Standard state, gas phase at 1 atm. [b] $\theta = v/v_m$, where v_m = 3.34 mmol/g.

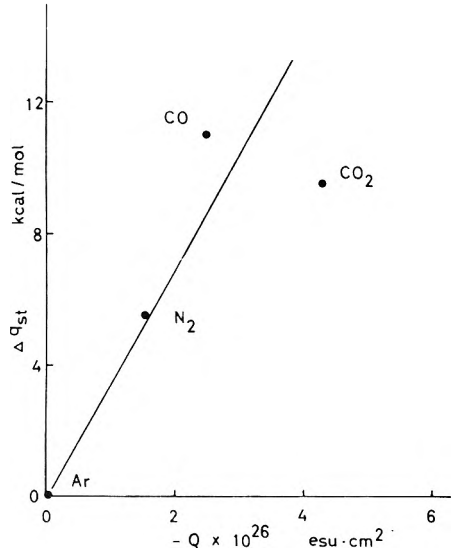

Figure 4. Quadrupole energy as a function of molecular quadrupole moment (from adsorption data on silica–alumina evacuated at 820°): Ar, N_2, and CO from Huang and Emmett;[1] CO_2, present work.

where ν(Ar), M(Ar), and ΔE(Ar) are the vibrational frequency, mass, and energy of adsorption, respectively, of argon on potassium chloride from the work of Orr.[16] This relation was used by Barrer and Gibbons[11] in their study of the adsorption of CO_2 on X type zeolites. The mean frequency $\nu(CO_2)$ is estimated to be between 1.9×10^{12} and 3.0×10^{12} sec^{-1}. The surface vibrational entropy is then calculated by the equation

$$\bar{S}_{vs} = 3R\{[x/(e^x - 1)] - \ln(1 - e^{-x})\} \quad (15)$$

where $x = h\nu(CO_2)/kT$. All terms on the right-hand side of eq 13 as well as their sum, $\bar{S}_{rs} + \bar{S}_c$, are listed in Table I as a function of temperature, surface coverage, and heat of adsorption. The last column is the configurational entropy calculated by eq 11, assuming that the surface is homogeneous. On a heterogeneous surface, the configurational entropy would be smaller, as has been indicated by Drain and Morrison[17] and also discussed by Everett.[18] From the last three columns of Table I, we see that the surface rotational entropy $\bar{S}_{rs}$ is considerably smaller than the gas-phase value. Moreover, the estimation of $\bar{S}_{vs}$ is only conservative because if part of the rotational degrees of freedom is transformed into surface vibration, the term $\bar{S}_{vs}$ would be greater and hence $\bar{S}_{rs}$ would become negligibly small. It can then be concluded that the adsorbed carbon dioxide is localized with almost no surface rotation.

According to eq 4 the quadrupole interaction energy is proportional to the quadrupole moment of the gas molecule. A plot is shown on Figure 4 for a series of gases adsorbed on silica–alumina. With the exception of CO_2, the correlation is quite good. Because CO_2 is larger than the other molecules, it is likely that the end-on approach to the surface site would not be as close. Hence, the field gradient at the adsorption site of carbon dioxide would be smaller than that of nitrogen or carbon monoxide. As a result, the quadrupole energy for carbon dioxide is not greater than that of carbon monoxide.

(16) W. J. C. Orr, *Trans. Faraday Soc.*, 35, 1247 (1939).
(17) L. E. Drain and J. A. Morrison, *Trans. Faraday Soc.*, **49**, 654 (1953).
(18) D. H. Everett, *Proc. Chem. Soc., London*, 38 (1957).

Theoretical Study of Singlet–Triplet and Triplet–Triplet Spectra. I. Selection of Parameters and the Basis of Configuration Interaction in Closed Shell and Restricted Open Shell Semiempirical Methods

J. Pancíř and R. Zahradník*

The J. Heyrovský Institute of Physical Chemistry and Electrochemistry, Czechoslovak Academy of Sciences, Prague, Czechoslovakia
(Received September 10, 1971)

The calculations of energies and oscillator strengths of singlet–triplet and triplet–triplet transitions were carried out by semiempirical closed shell as well as restricted open shell methods in the π-electron approximation. The investigation was concerned with the influence of semiempirical parameters and the configuration interaction basis set on the energies of triplet states. On the basis of this study, a procedure was developed, making it possible to interpret singlet–triplet and triplet–triplet spectra with approximately the same accuracy as attained by the standard Pariser–Parr–Pople method in the interpretation of singlet–singlet spectra.

Introduction

The semiempirical LCI–SCF method[1,2] has often been successfully employed for the interpretation of singlet–singlet spectra of conjugated compounds.[3] It is known, however, that the use of this method in its standard version for the study of singlet–triplet and especially triplet–triplet spectra may lead to results which are not even in qualitative agreement with experiment.[4] With the recent accumulation of experimental data on triplet states of conjugated molecules, it becomes desirable to modify the existing semiempirical method with a view to providing a satisfactory interpretation.

The failure of the conventional method is attributed by some authors[5,6] to the different correlation energy of singlet and triplet states. This "correlation error" can be reduced by a suitable choice of the semiempirical parameters or by expanding the basis in the configuration interaction. Only the letter procedure has been used to calculate triplet–triplet spectra. It was found that the energy of the lowest triplet state depends strongly on the number of configurations considered in the configuration interaction Pariser–Parr treatment.[5] Inclusion of further configurations, which are formally singly excited with respect to the lowest triplet configuration, leads to the correct ratio of the oscillator strengths of the two intense bands in the triplet–triplet spectrum of naphthalene.[4] By restriction of the configurational interaction to degenerate configurations of alternant hydrocarbons, it was possible to reproduce successfully the energies of intense[7] triplet–triplet bands,[6,8] but it was necessary to scale the results, arbitrarily by subtracting 0.4 eV. The energies and oscillator strengths of intense bands were also interpreted by a modified semiempirical method including a vibronic configuration interaction.[9]

In the present investigation, the influence of the basis set in the configuration interaction and of semiempirical parameters on the energies of triplet states and on the oscillator strengths of triplet–triplet transitions were examined for several typical molecules. The calculations were carried out by means of both the "closed shell" and the "restricted open shell" versions of the PPP method. On the basis of this study, a procedure was developed and applied to 15 systems, which provides an interpretation of all triplet–triplet bands, together with the singlet–triplet transition, with an accuracy of 0.2 eV. This is not possible by any earlier method known to the authors.

Calculations

If not otherwise specified, the standard method was used in the form employed in our laboratory for interpreting singlet–singlet spectra (see Appendix, ref 10). Semiempirical values of one-center integrals were taken from the paper by Miller, *et al.*,[11] and are summarized in Table I. The two-center repulsion integrals were approximated according to Mataga and Nishimoto,[12] and the resonance integrals $\beta_{\mu\nu}$ calculated according to the formula[10]

$$\beta_{\mu\gamma} = -2.318 \exp[0.335(p_{\mu\nu} - 2/3)] \quad (1)$$

where $p_{\mu\gamma}$ is the bond order from the preceding iteration. The same parameters and approximations were employed in the calculations by the restricted open shell method.[13] The electronic wave function was constructed[14] from the configurations of the lowest triplet state $^3\Psi_0$, formally singly excited $^3\Psi_I$ and $^3\Psi_T$ states, and doubly excited $^3\Psi_D$ states as described in the Discussion. Typical examples of these configurations are presented in Figure 1. The corresponding matrix elements and the contributions to the transition moment were not derived explicitly, but were

(1) R. Pariser and R. G. Parr, *J. Chem. Phys.*, **21**, 466, 767 (1953).
(2) J. A. Pople, *Trans. Faraday Soc.*, **49**, 1375 (1953).
(3) R. G. Parr, "Quantum Theory of Molecular Electronic Structure," W. A. Benjamin, New York, N. Y., 1963.
(4) R. L. de Groot and G. J. Hoytink, *J. Chem. Phys.*, **46**, 4523 (1967).
(5) K. Nishimoto and L. S. Forster, *J. Chem. Phys.*, **47**, 5451 (1967).
(6) M. K. Orloff, *J. Chem. Phys.*, **47**, 235 (1967).
(7) For qualitative determination of the intensities of spectral bands see, J. N. Murrell, "The Theory of the Electronic Spectra of Organic Molecules," Methuen, London, 1963, p 91.
(8) J. S. Brinen and M. K. Orloff, *J. Chem. Phys.*, **51**, 527 (1969).
(9) M. Bénard and A. Julg, *J. Chim. Phys.*, **67**, 1297 (1970).
(10) P. Hochmann, R. Zahradník, and V. Kvasnička, *Collect. Czech. Chem. Commun.*, **33**, 3478 (1968).
(11) R. L. Miller, P. G. Lykos, and H. N. Schmeising, *J. Amer. Chem. Soc.*, **84**, 4623 (1967).
(12) N. Mataga and K. Nishimoto, *Z. Phys. Chem. (Frankfurt am Main)*, **13**, 140 (1957).
(13) C. C. J. Roothaan, *Rev. Mod. Phys.*, **32**, 179 (1960).
(14) G. J. Hoijtnk, *Pure Appl. Chem.*, **11**, 393 (1965).

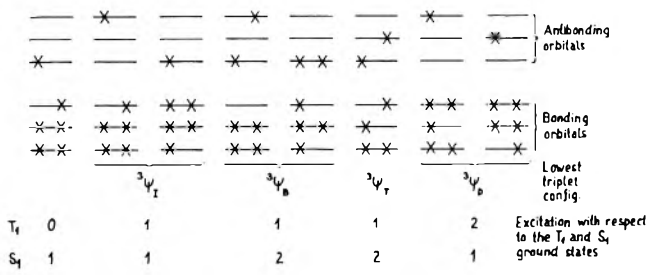

Figure 1. Typical examples of the configurations discussed in this work.

TABLE I: Semiempirical Values for the Ionization Potential (I_μ), the One-Center Repulsion Integral ($\gamma_{\mu\mu}$), and the Resonance Integral for a Bond Length of 1.397 Å ($\beta_\mu{}^0$), which Were Used in the Calculations by the Standard and the New Parameterization

	Standard parameters			New parameters		
Atom	I_μ	$\gamma_{\mu\mu}$	$\beta_{\mu\nu}{}^0$	I_μ	$\gamma_{\mu\mu}$	$\beta_{\mu\nu}{}^0$
Carbon	11.42	10.84	−2.318	8.6	8.2	−2.5
Nitrogen	14.1	12.30	−2.318[a]	11.66	9.45	−2.85[a]

[a] β_{CN} resonance integral.

TABLE II: Experimental Energies of Singlet–Triplet and Triplet–Triplet Transitions (eV)

Compound	$S \rightarrow T_1$	$T_1 \rightarrow T_x$[g]
Naphthalene	2.64[a]	2.32[b] (w)
		2.99[c] (s)
		4.77[c] (a)
Anthracene	1.84[a]	1.40[d] (w)
		2.91[c] (s)
		4.43[c] (a)
Phenanthrene	2.68[a]	2.54[c] (s)
Quinoline	2.71[e]	3.08[f] (s)

[a] D. F. Evans, *J. Chem. Soc.*, 1351 (1957). [b] D. Lavalette, *J. Chim. Phys.*, **66**, 1845, 1853, 1860 (1969). [c] G. Porter and M. W. Windsor, *Proc. Roy. Soc., Ser. A*, **245**, 238 (1958). [d] M. W. Windsor and J. R. Novak, The Triplet State Symposium, Beyrouth, 1967, p 229. [e] D. F. Evans, *J. Chem. Soc.*, 2753 (1953). [f] D. P. Craig and I. G. Ross, *ibid.*, 1589 (1954). [g] s denotes strong, w weak, and a allowed (ref 4).

directly generated by the program with the use of general formulas for the first- and second-order density matrix.[15]

The calculations were performed for three alternant hydrocarbons (naphthalene, anthracene, and phenanthrene) and one heterocyclic compound (quinoline). The experimental values of the energies and oscillator strengths for singlet–triplet and triplet–triplet transitions are presented in Table II. The calculations were performed by means of the IBM 7040 and the National Elliott 503 computers with the use of programs written in Fortran IV and Autocode Elliott by one of the authors of the present paper.

Results and Discussions

Before undertaking a more detailed analysis, it will be useful to discuss the possibilities of experimental verification of the calculations. With a few exceptions, it is not possible to determine experimentally the energy of a vertical transition in a singlet–triplet absorption spectrum, because this transition usually overlaps a singlet–singlet band of very much higher intensity. In common with other authors of theoretical papers we therefore compare the calculated energy of a singlet–triplet transition with

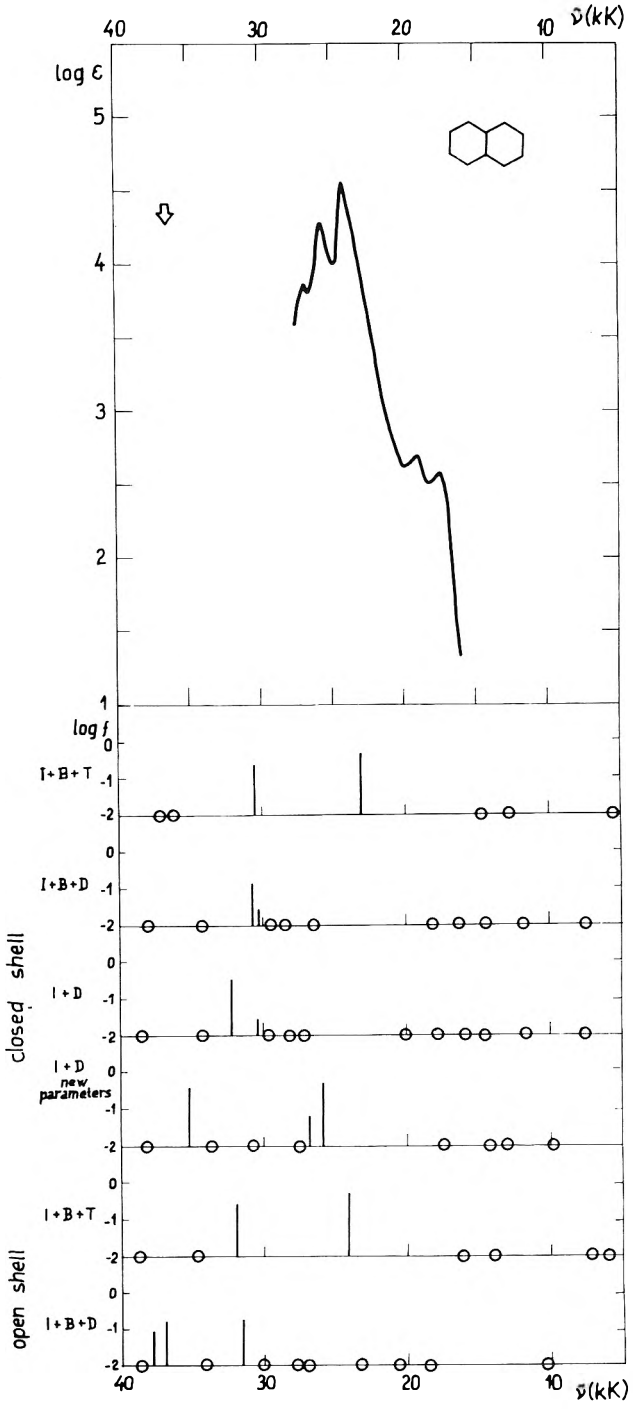

Figure 2. Experimental T–T spectrum of naphthalene together with theoretical values of energies and oscillator strengths. ⇩ is the position of the maximum of the experimental T–T band in the ultraviolet region the intensity of which was not specified;[16] letters I, B, T, and D denote the types of configurations included in the configuration interaction treatment (see Figure 1); *f* stands for oscillator strength; O denotes forbidden transitions.

the experimental energy of an 0–0 band. For a similar reason, the energies of symmetrically forbidden triplet–triplet bands can be measured only in the near-infrared and at the beginning of the visible region, *i.e.*, where intense triplet–triplet bands do not interfere. On the other hand, the measurement of triplet spectra is limited by the occurrence of singlet–singlet absorption at the end of the

(15) I. L. Cooper and R. McWeeny, *J. Chem. Phys.*, **45**, 236 (1966).

TABLE III: Closed Shell Calculation for Naphthalene[a]

Transitions	I + B + T				I + B + D				I + D			New parameters	
	E, eV	Log *f*	%B	%T	*E*, eV	Log *f*	%B	%D	*E*, eV	Log *f*	%D	*E*, eV	Log *f*
S → T	2.54		1.25	2.29	1.80		0.52	27.72	1.83		29.46	2.64	
1	0.72		0.02	0.78	0.99		0.38	14.53	1.01		14.30	1.23	
2	0.74		0.36	6.16	1.51		0.19	14.36	1.48		10.34	1.25	
3	1.62		0.04	0.15	1.8[illegible]		0.70	84.33	1.83		83.45	1.64	
4	1.85		0.00	14.89	2.04		0.00	34.10	2.00		34.10	1.78	
5	2.86	−0.37	6.06	2.91	2.26		0.00	2.21	2.22		2.21	2.18	
6	3.76	−0.64	0.00	13.86	3.28		3.95	84.95	3.37		89.01	3.20	−0.33
7	4.51		96.76	2.40	3.53		0.00	83.99	3.49		83.99	3.32	
8	4.62		94.13	5.86	3.64		3.88	27.11	3.67		31.99	3.32	−1.22
9	5.17		32.00	67.75	3.73	−0.87	9.11	2.39	3.75	−1.57	83.34	3.41	
10	5.23		0.00	87.40	3.78	−1.60	0.00	83.34	3.98	−0.47	0.86	3.80	
11	5.76		35.64	62.34	4.25		1.26	98.71	4.24		99.87	4.19	
12	5.80	0.04	87.12	8.55	4.72	−1.98	4.89	84.93	4.81		87.32	4.37	−0.44
13	5.87		95.56	4.41	5.01		81.77	14.82	5.11	−0.54	18.86	4.76	
14					5.15	−0.41	0.00	18.86	5.80	−1.58	99.33		
15					5.67	−1.33	9.86	84.13					
16					5.75	−0.60	95.24	4.71					

[a] The letters I, B, T, and D denote the types of configurations included in the configuration interaction (see Figure 1). The table presents transition energies in eV, the logarithms of the oscillator strengths log *f*, and the weighted contributions of the configurations of the given types to the total wave function.

TABLE IV: Closed Shell Calculation for Anthracene[a]

Transitions	I + E + T				I + B + D				I + D			New parameters	
	E, eV	Log *f*	%B	%T	*E*, eV	Log *f*	%B	%D	*E*, eV	Log *f*	%D	*E*, eV	Log *f*
S → T	1.83		0.00	1.30	1.37		0.90	12.95	1.43		14.15	1.84	
1	1.19		0.08	1.41	1.24		0.21	14.78	1.19		14.61	1.35	
2	1.63		0.47	0.22	1.82		0.38	27.98	1.79		26.72	1.77	
3	1.96		0.19	0.04	1.88		0.72	6.46	1.85		5.90	2.01	
4	2.09		0.00	4.89	2.30		0.03	3.14	2.25		3.21	2.10	
5	2.84	−0.24	7.26	1.39	2.43		0.69	44.93	2.39		45.37	2.56	
6	3.59		84.77	14.59	2.57		0.64	91.78	2.54		92.69	2.83	
7	3.60		0.00	96.89	3.24	−0.46	7.96	4.21	3.40	−0.14	4.54	2.88	−0.06
8	4.31		71.73	28.27	3.61	−1.11	0.15	69.78	3.56	−1.06	69.79	3.38	−0.85
9	4.55		99.29	0.66	3.63		9.60	86.48	3.70		98.32	3.72	
10	4.85		91.74	8.11	3.69		6.85	90.39	3.72		96.02	3.91	
11	5.17		2.91	97.09	4.12		2.05	0.00	4.11		55.47	3.97	
12	5.39		4.60	95.40	4.17		0.00	55.49	4.13		0.00	4.02	
13	5.44	0.32	89.53	4.37	4.47		0.88	74.53	4.43		74.82	4.19	
14	5.51	−2.58	63.47	36.53	4.63		7.49	92.24	4.64		99.77	4.39	−0.54
15	5.95		0.00	99.89	4.64		86.40	12.77					
16					4.80		9.33	80.37					
17					4.87	−0.57	0.06	30.21					
18					5.23		80.86	18.37					
19					5.36		87.27	12.65					
20					5.39		76.09	23.73					
21					5.58	−0.03	50.72	43.45					
22					5.79		65.63	33.67					

[a] The letters I, B, T, and D denote the types of configurations included in the configurational interaction (see Figure 1). The table presents transition energies in eV, the logarithms of the oscillator strengths log *f*, and the weighted contributions of the configurations of the given types to the total wave function.

visible and the beginning of the ultraviolet region. Where a high concentration of the triplet state makes it possible to find triplet bands in the short-wave region, the measurement is subject to a considerable error in both the energy of the spectral maximum and in the intensity.[16] For these experimental reasons, it is an adequate test of a calculation of a triplet–triplet spectrum that it interpret all bands up to the beginning of the visible and the near-infrared region and the intense bands in the ultraviolet region. It is known[17,18] that in calculations based on the Mataga–Nishimoto approximation[12] of the γ integrals, the SCF transition energies of the lowest triplet state provide a good estimate of the experimental energy of the singlet–triplet transition. Therefore, the first calculations were

(16) G. Porter and M. W. Windsor, *Proc. Roy. Soc., Sec. A*, **245**, 235 (1958).
(17) G. Wagnière, *Theor. Chim. Acta*, **9**, 312 (1968).
(18) R. Zahradník, I. Tesar-ová, and J. Pancíř, *Collect. Czech. Chem. Commun.*, **36**, 2867 (1971).

TABLE V: Closed Shell Calculation for Phenanthrene[a]

Transitions	I + B + T				I + B + D				I + D			New parameters	
	E, eV	Log *f*	%B	%T	*E*, eV	Log *f*	%B	%D	*E*, eV	Log *f*	%D	*E*, eV	Log *f*
S → T	2.95		1.67	0.72	2.13		0.20	31.18	2.14		32.29	2.78	
1	0.43		0.54	2.75	0.87		0.12	23.54	0.86		24.39	0.75	
2	0.76		0.01	0.44	1.03		0.45	64.98	1.04		63.58	0.95	
3	1.01	−2.55	0.18	0.80	1.29		0.78	10.04	1.32		9.63	1.19	−2.14
4	1.85		3.88	2.53	1.60		0.16	53.78	1.59		55.91	1.27	
5	2.29	−0.24	0.31	7.45	1.70	−2.60	0.09	5.53	1.70	−2.57	5.72	1.62	
6	2.53	−2.69	0.38	2.32	1.88		0.24	86.56	1.88		86.63	1.94	
7	4.01		5.41	93.52	1.89		0.30	52.01	1.89		53.35	2.00	
8	4.08		73.08	23.40	2.60	−2.54	0.49	68.62	2.61	−2.26	66.84	2.29	−2.20
9	4.51		81.61	17.12	3.29	−0.61	0.37	9.76	3.29	−0.60	10.57	2.70	−0.40
10	4.70	−1.02	2.48	97.43	3.42		11.67	31.54	3.59		94.74	3.12	
11	4.86	−0.92	79.92	20.07	3.58		0.81	94.17	3.65		34.45	3.25	−1.54
12	4.90				3.72	−2.08	5.76	19.33	3.85	−1.54	27.68	3.37	
13	5.00				3.79		17.21	61.02	3.92	−1.00	93.28	3.53	−1.29
14	5.10				3.92	−1.04	0.16	6.81	4.12		72.26	3.76	
15	5.24	−0.30			4.41		6.79	15.46				3.95	−0.28
16	5.39	−0.70			4.53	−0.70	3.38	11.03					
17	5.70	−0.08			4.55	−1.39	1.77	93.55					
18					4.87		4.65	94.61					

[a] The letters I, B, T, and D denote the types of configurations included in the configurational interaction (see Figure 1). The table presents transition energies in eV, the logarithms of the oscillator strengths log *f*, and the weighted contributions of the configurations of the given types to the total wave function.

TABLE VI: Closed Shell Calculation for Quinoline[a]

Transitions	I + B + T				I + B + D				I + D			New parameters	
	E, eV	Log *f*	%B	%T	*E*, eV	Log *f*	%B	%D	*E*, eV	Log *f*	%D	*E*, eV	Log *f*
S → T	2.49		1.24	2.36	1.78		0.50	26.18	1.81		27.94	2.77	
1	0.70	−3.21	0.28	4.53	0.98	−4.19	0.30	14.39	1.00	−4.11	14.24	1.02	−2.67
2	0.76	−5.02	0.07	1.24	1.43	−2.71	0.18	10.62	1.40	−2.67	8.83	1.32	−3.84
3	1.58	−3.32	0.11	2.02	1.82	−2.85	6.20	75.72	1.82	−2.74	79.90	1.60	−2.90
4	1.99	−2.03	0.33	13.49	1.97	−2.99	0.05	55.31	1.94	−2.99	29.03	1.68	−2.96
5	2.78	−0.44	6.54	4.58	2.35	−2.90	0.05	13.18	2.32	−2.84	13.55	2.24	−1.79
6	3.72	−0.67	1.27	15.28	3.26	−2.41	3.61	83.07	3.32	−2.32	87.03	3.11	−0.93
7	4.49	−2.53	92.92	6.42	3.47	−1.85	1.05	74.13	3.45	−2.33	81.57	3.18	−0.52
8	4.63	−1.19	88.33	10.15	3.56	−1.15	5.27	19.91	3.62	−1.55	31.37	3.27	−2.56
9	5.16	−1.56	27.16	67.99	3.67	−1.51	4.95	33.02	3.82	−0.67	24.53	3.65	−[illegible].27
10	5.25	−4.48	9.25	83.58	3.94	−1.46	0.91	77.60	3.92	−1.26	74.78	3.96	−[illegible].31
11	5.74	−0.38	62.20	34.94	4.38	−1.86	2.33	92.30	4.39	−1.63	91.57	4.42	−0.56
12	5.84	−0.35	50.43	46.02	4.90	−2.30	15.13	71.80	5.00	−1.25	77.66	4.53	−[illegible].26
13	5.96	−1.04	49.53	47.58	4.96	−1.35	45.69	25.45	5.18	−0.57	26.03	4.80	−[illegible].72
14					5.31	−0.64	27.81	22.47	5.85	−1.70	95.79	5.30	−2.63

[a] The letters I, B, T, and D denote the types of configurations included in the configuration interaction (see Figure 1). The table presents transition energies in eV, the logarithms of the oscillator strengths log *f*, and the weighted contributions of the configurations of the given types to the total wave function.

performed with a basis limited to singly excited configurations (here and later considered in relation to the lowest triplet configuration), which are denoted in the following part by $^3\Psi_I$, $^3\Psi_B$, and $^3\Psi_T$. A total of 40 configurations were employed, *i.e.*, all that can be formally derived by electron promotions among eight frontier orbitals. The results for the selected group of molecules are presented in the first column of Tables III–VI and in Figures 2 and 3. It is evident that this procedure successfully interprets the positions of the maxima of the singlet–triplet band and of the first intense triplet–triplet band (*cf.* Table II). In the region of the second intense triplet–triplet band observed for naphthalene and anthracene, however, there is no calculated allowed transition, and it is evidently not appropriate to assign this band to a transition forbidden[19] by symmetry or parity. For experimentally significant bands (see above), the contribution of the $^3\Psi_T$ configurations to the total wave function is not very high, and it seems possible to neglect these configurations. In order to verify this assumption, calculations were performed for a group of seven alternant hydrocarbons with all $^3\Psi_I$ and $^3\Psi_E$ configurations, which are not presented here. The experimental energies of singlet–triplet and strong and medium triplet–triplet bands were reproduced by this procedure with an accuracy of 0.1 eV, with one exception. This was an intense triplet–triplet band of polyacenes, located at 4.3 eV, which could not be assigned to any allowed transitions in this region. Orloff's assignment of these bands to transi-

(19) W. Moffitt, *J. Chem. Phys.*, **22**, 320 (1954).

TABLE VII: Restricted Open Shell Calculation for Naphthalene[a]

Transition	I + B + T				I + B + D			
	E, eV	Log *f*	%B	%T	*E*, eV	Log *f*	%B	%D
S → T	2.60		0.02	0.82	2.14		0.04	12.17
1	0.82		0.42	16.59	1.33		1.87	5.64
2	0.96		0.07	1.27	2.54		4.81	3.20
3	1.75		0.00	28.67	2.87		0.85	93.62
4	2.03		0.11	2.46	2.87		0.0	2.33
5	2.98	−0.35	5.46	6.09	3.35		0.0	100.00
6	3.96	−0.59	0.00	12.93	3.43		7.39	88.57
7	4.31		98.50	5.48	3.72		50.52	4.04
8	4.82		94.47	5.49	3.90	−0.77	8.43	1.16
9	5.29		9.74	89.84	4.23		0.0	91.96
10	5.47		0.00	78.17	4.58	−0.78	0.0	44.24
11	5.79	0.06	90.16	4.49	4.70	−[illegible].06	2.11	95.01
12					4.80		36.18	30.70
13					5.62		91.86	7.99
14					5.68	−1.40	12.18	84.36
15					5.69	0.01	0.0	57.17

[a] The letters I, B, T, and D denote the types of configurations included in the configuration interaction (see Figure 1). The table presents transition energies in eV, the logarithms of the oscillator strengths log *f*, and the weighted contributions of the configurations of the given types to the total wave function.

TABLE VIII: Restricted Open Shell Calculation for Anthracene[a]

Transition	I + B + T				I + B + D			
	E, eV	Log *f*	%B	%T	*E*, eV	Log *f*	%B	%D
S → T	1.53		0.00	0.08	1.46		0.02	1.93
1	3.14		34.97	57.81	2.69		0.48	40.19
2	3.36		30.60	69.40	2.96		0.74	43.09
3	3.68		3.10	6.83	3.49		2.11	20.78
4	3.87		2.51	4.72	3.73		0.01	11.96
5	3.89		0.00	10.03	3.93		5.94	39.53
6	3.93		0.90	0.12	4.31		4.22	87.81
7	4.23	−0.50	4.27	5.54	4.37	−0.29	0.39	1.50
8	4.76		0.00	7.15	4.41		20.94	74.05
9	4.78		59.80	34.68	4.74	−0.78	3.03	39.75
10	5.21	−0.02	60.83	30.29	4.96		0.82	0.00
11	5.23		2.79	97.21	5.15		25.99	53.48
12	5.46		72.66	26.41	5.37		0.64	57.30
13					5.60		53.86	41.69
14					5.64		9.90	59.15
15					5.84		18.23	70.00
16					5.93	−0.16	85.45	14.09

[a] The letters I, B, T, and D denote the types of configurations included in the configuration interaction (see Figure 1). The table presents transition energies in eV, the logarithms of the oscillator strengths log *f*, and the weighted contributions of the configurations of the given types to the total wave function.

tions forbidden by parity seems unsatisfactory to us in view of the high intensity.[4,16] This problem was solved by extending[14] the basis set of the configurational interaction by excited $^3\Psi_D$ configurations. The middle columns of Tables III–VI present the results obtained by configuration interaction with the basis of all $^3\Psi_I$, $^3\Psi_B$, and $^3\Psi_D$ configurations, corresponding to electron promotions among the five highest occupied and five lowest unoccupied molecular orbitals. This basis set was selected with regard to the internal memory of the computers employed. The effect is a strong depression of the lowest triplet state, sharply lowering the energy of the singlet–triplet transitions and increasing the energies of the triplet–triplet transitions, so that a comparison with experiment is not favorable. New forbidden bands in the infrared region are predominantly due to $^3\Psi_D$ configurations, while in the case of polyacenes a new allowed transition appears, and the difference between its energy and the energy of the first allowed transition suggests that this is an experimentally observed band in the ultraviolet region (*cf.* Table II). Whereas the wave functions of states participating in intense[7] triplet transitions are only slightly influenced by doubly excited configurations, the contrary applies to medium and weak bands. This is evidently one of the reasons why procedures[6,8] using first-order configuration interactions do not reproduce the energies of weaker triplet bands with satisfactory accuracy.

The circumstance that $^3\Psi_B$ configurations do not participate in experimentally interesting transitions (see above) induced us to perform a series of calculations

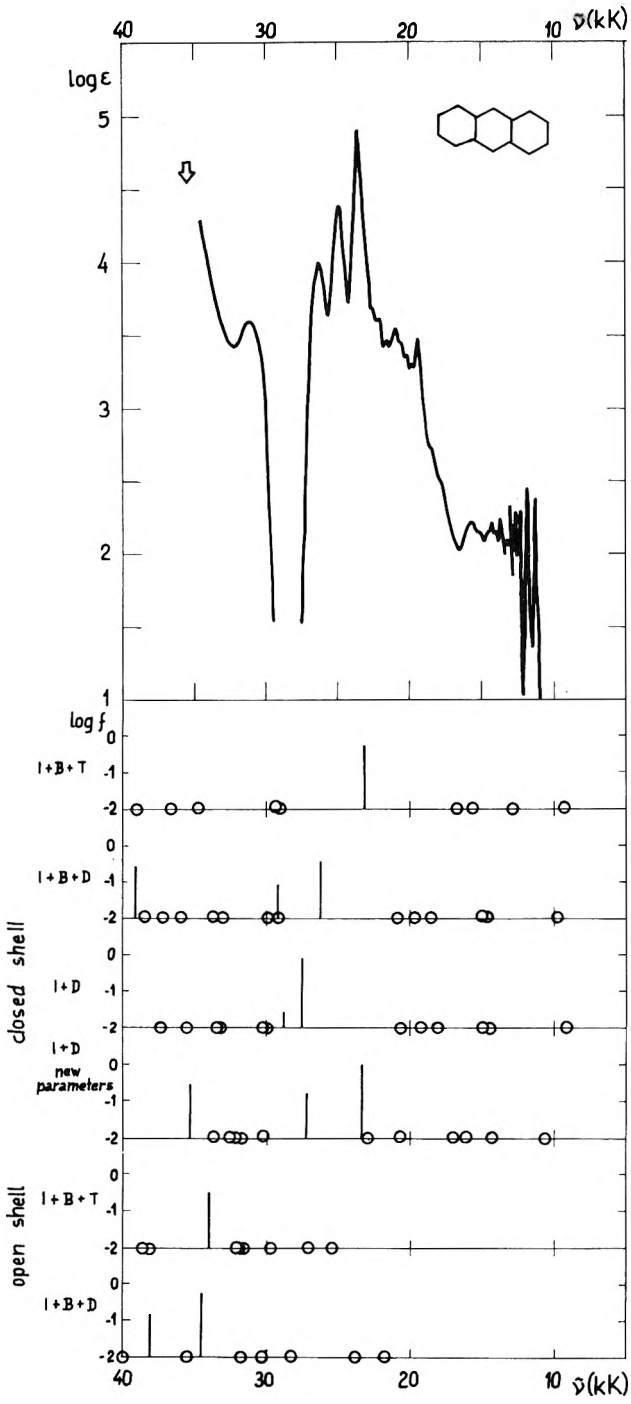

Figure 3. Experimental T–T spectrum of anthracene together with theoretical values of energy and oscillator strengths. For other details see caption to Figure 2.

based only on $^3\Psi_I$ and $^3\Psi_D$ configurations, which consequently corresponded to the standard Pariser–Parr CI basis. The selection of this basis was particularly advantageous in view of the fact that suitable programs are widely available. The results are listed in the third column of Tables III–VI. A comparison shows that the only major change was an increase of the oscillator strength of the transitions in the case of naphthalene and anthracene, which can be assigned to the intense bands in the visible region of the spectrum. The energies of the triplet states are almost unaffected. The absolute values of the triplet–triplet transition energies are thus still too high in comparison with experiment. Consequently it is evident that even with inclusion of the $^3\Psi_D$ configurations, which is necessary from the qualitative viewpoint, agreement with experiment can be obtained only by modification of the semiempirical parameters.

It was found[5] and confirmed by us that the selection of another semiempirical relationship for the two-center repulsion integrals results in a change of the energies of the singlet–triplet transitions, while the energies of the triplet–triplet transitions are influenced to a much lower extent. The only possibility, therefore, is to change the values of the one-center integrals or, possibly, of the resonance integrals. Such a method has been recently applied in our laboratory,[20] and the calculations with the use of the standard bases of configuration interaction are presented in the fourth column of Tables III–VI. The values of the one-center electronic repulsion integrals, $\gamma_{\mu\mu}$, and of the core resonance integral, β^c, were treated as parameters, the values of which were adjusted to the first and second experimental S–T transitions of benzene. The parameters found are given in the second part of Table I. A similar correction was made for hetero atoms; for details see ref 18. The method was applied to several dozen conjugated compounds, and the energies of the singlet–triplet and triplet–triplet transitions were reproduced with an error of 0.1–0.2 eV. A direct comparison of the transition moments was complicated by the circumstance that the experimental data are subject to a considerable error and also by the fact that the participation of several theoretical transitions in one observed band cannot be excluded. A comparison with the very exact data of Brinen[21] has shown that the calculated oscillator strengths are about two–three times as high, but they are at least in qualitative agreement with the experiment. Moreover, the use of the oscillator strength for quantitative calculations of band intensity has recently been questioned[22] for methods with a limited basis of configuration interaction.

The necessity to introduce a new parameter set seems to be rather unfortunate. However, one should keep in mind that until now in principle there exist only two fundamental parametrizations, those adequate for calculations of ground-state properties (Dewar) and those which are suitable for estimates of singlet–singlet excitation energies (Pariser, Parr, and Pople). The third parameter set, introduced in this paper, is suitable for calculation of triplet states. In fact, however, on the basis of an extensive, careful and critical analysis of all yet used approximations in semiempirical π-electronic calculations performed in our laboratory (during last 3 years) we have found that it is possible to interpret properties of *both* singlet *ground* (dipole moments, bond lengths, ionization potentials, and electron affinities) and *excited states* (excitation energies, transition moments, and dipole moments) by means of a *single* parameter set.[23] Therefore, it is possible to offer for calculations only two parameter sets, one adequate for singlet (ground and excited) states and the other one for triplet states. There is no reason to be astonished by this necessity because the correlation energy which is included implicitly in semiempirical parameters is different for singlet and triplet states.[5,6]

Thus it can be said that, at least for purposes of prediction and identification, it is fully satisfactory to employ a

(20) J. Pancíř and R. Zahradník, *Theor. Chim. Acta*, **14**, 426 (1969).
(21) J. S. Brinen, *J. Chem. Phys.*, **49**, 586 (1968).
(22) A. E. Hansen and E. N. Svendsen, *Theor. Chim. Acta*, **20**, 303 (1971).
(23) J. Pancíř, I. Matoušek, and R. Zahradník, *Collect. Czech. Chem. Commun.*, to be submitted for publication.

TABLE IX: Restricted Open Shell Calculation for Phenanthrene[a]

Transition	I + B + T				I + B + D			
	E, eV	Log *f*	%B	%T	*E*, eV	Log *f*	%B	%D
S → T	2.35		0.22	2.54	2.37		0.02	3.78
1	2.13		1.32	34.64	1.68		0.57	82.14
2	2.68		8.30	36.44	1.92		0.51	65.58
3	2.71		10.82	33.95	2.14		1.00	45.60
4	2.93	−0.93	0.01	17.21	2.49		0.95	68.88
5	3.75	−0.80	0.18	21.63	2.63	−2.12	0.23	36.01
6	3.92		5.86	77.65	2.71		1.41	80.67
7	3.96		28.70	63.35	2.86		0.57	92.00
8	3.97	−1.02	9.40	29.68	3.54	−2.52	0.91	77.79
9	4.69		26.00	61.51	4.07	−0.64	0.21	13.05
10	4.85		8.40	80.75	4.53		0.07	55.24
11	5.23	−0.27	34.64	41.30	4.64	−1.06	0.20	24.05
12	5.33	−0.16	0.49	43.02	4.66		0.56	43.41
					4.83		0.59	57.57
					4.88	−1.46	0.39	69.20
					5.11	−0.55	0.50	21.11
					5.25	−0.21	1.04	49.52

[a] The letters I, B, T, and D denote the types of configurations included in the configuration interaction (see Figure 1). The table presents transition energies in eV, the logarithms of the oscillator strengths log *f*, and the weighted contributions of the configurations of the given types to the total wave function.

method using $^3\Psi_I$ and $^3\Psi_D$ configurations and new parameters because it affords the same accuracy as the conventional procedure in the interpretation of singlet-singlet spectra. A further extension of the CI basis is thus obviously superfluous.

Tables VII-IX summarize the calculations for naphthalene, anthracene, and phenanthrene by means of the restricted open shell method. The first column contains the results obtained with the use of singly excited configurations of the types $^3\Psi_I$, $^3\Psi_B$, and $^3\Psi_T$, while the second column relates to configurations of the types $^3\Psi_I$, $^3\Psi_B$, and $^3\Psi_D$. The depression of the lowest triplet state caused by the variation principle itself leads to reduced energy of the singlet-triplet transition. An "improvement" of the wave function of the lowest triplet state by means of the open shell procedure manifests itself in the fact that this state interacts only very little with the other configurations. In the case of excited triplet states, however, a strong mixing of configurations takes place, and, therefore, even for transitions in the visible region it is not possible to neglect any of the mentioned types of configurations. The calculations of the energies of triplet-triplet transitions are subject to a larger error than the calculations by the closed shell method, and it is, therefore, obviously necessary to perform a special parametrization in this case. Consequently, the restricted open shell method does not appear promising for the study of triplet states. A more extensive comparison of the methods used is given in Figures 2 and 3 for naphthalene and anthracene.

Summary

The conventional PPP method does not afford satisfactory results for the energies of singlet-triplet and triplet-triplet transitions, even by a special selection of the basis set in configurational interaction, or by the restricted open shell procedure. The best results were obtained by a special parametrization, offering the possibility of reproducing the energies of triplet states with an accuracy of 0.1-0.2 eV.

Theoretical Study of Singlet–Triplet and Triplet–Triplet Spectra. II. Conjugated Hydrocarbons

J. Pancíř and R. Zahradník*

The J. Heyrovský Institute of Physical Chemistry and Electrochemistry, Czechoslovak Academy of Sciences, Prague, Czechoslovakia
(Received September 10, 1971)

The Pariser–Parr–Pople method with modified semiempirical parameters is used for calculating the energies and oscillator strengths of singlet–triplet and triplet–triplet transitions for 15 conjugated hydrocarbons. The triplet spectra of the individual molecules are discussed with reference to experimental data, and the spectral resemblances of significant bands are investigated. Additional bands, especially in the infrared and the visible regions, are predicted.

Introduction

In the preceding paper[1] it was shown that with suitably modified semiempirical parameters, the PPP method makes it possible to calculate the energies of singlet–triplet and triplet–triplet transitions as accurately as singlet–singlet transitions. By means of recent improvements in triplet–triplet spectral techniques, numerous new bands have been found,[2-13] and the polarization[10,14-18] as well as the extinction coefficients[9,10,18-23] measured for the most intense among them. We have now attempted to subject these data to a more thoroughgoing theoretical interpretation than that of Orloff,[24] which is limited to the assignment of intense triplet–triplet bands. The influence of molecular structure upon the energy of allowed transitions will be shown for a typical series of benzenoid hydrocarbons. The calculations were performed for three *trans*-polyenes, nine benzenoid, and three nonalternant hydrocarbons.

Calculations

Details on the computational method and parameters have been given.[1] As this method gives too low values for the S–T excitation energies in polyenes, we included, similarly as in the original PPP version, the "variable β approximation." The best fit was obtained by means of the following formula

$$\beta_{\mu\nu} = -2.5 \exp[0.2(p_{\mu\nu} - 2/3)] \qquad (1)$$

Figures 1–9 present the theoretical energies and the logarithms of the oscillator strengths drawn into the experimental triplet–triplet spectra of benzenoid hydrocarbons. The relation between the extinction coefficient ϵ and the oscillator strength f was given by the empirical formula

$$\log \epsilon = 4.5 + \log f \qquad (2)$$

which has proved satisfactory in the study of singlet–singlet spectra.

In the application of the Platt method[25] for classifying the individual spectral levels of benzenoid hydrocarbons, we have encountered numerous difficulties arising from the fact that the LCI–SCF and FE perimeter model wave functions are often different. With the aid of polarization diagrams[25] we have succeeded in classifying some but not all of the triplet levels of naphthalene. For other benzenoid hydrocarbons, we modified the procedure. We arranged the calculated orbital wave functions into groups according to the number of nodal planes, and within each group according to the energy. The individual spectral states were then compared with the corresponding states of naphthalene on the basis of the contributions of the individual configurations to the total wave function. This procedure proved suitable for assigning the majority of the bands found experimentally, and permitted a similar classification even for pericondensed hydrocarbons. We should like to point out, however, the somewhat different classification of triplet states,[13] suggested by the similarity between them and singlet–singlet spectra.

Polyenes. The lowest triplet state in the case of fully conjugated *trans*-polyenes exhibits, according to our calculations, a $^3B_u^+$ symmetry (here and later we employ the nomenclature of Pariser[26]), whereas in Platt's nomenclature the symbol ^3B is used. A singlet–triplet transition is spin forbidden and is polarized approximately in the direction of the polyene chain. Its energy decreases strongly with increasing chain length. The lowest triplet–triplet transition $^3B_u^+ \rightarrow {}^3A_g^+$ is forbidden by parity.[26] Its energy has been calculated as 14.18 kK for butadiene and 11.90 kK for hexatriene. From these values, as well as

(1) J. Pancíř and R. Zahradník, *J. Phys. Chem.*, 77, 107 (1973).
(2) H. Labhart, *Helv. Chim. Acta*, **47**, 2279 (1964).
(3) B. R. Henry and M. Kasha, *J. Chem. Phys.*, **47**, 33-9 (1967).
(4) M. W. Windsor and J. R. Novak, "The Triplet State," Cambridge University Press, New York, N. Y., 1967, p 229.
(5) R. Astier and Y. H. Meyer, ref 4, p 447.
(6) K. Kimura, S. Azimitan, N. Yamamoto, and H. Tsumobura, *Bull. Chem. Soc. Jap.*, **41**, 1274 (1968).
(7) E. J. Land and A. J. Swallow, *J. Chem. Phys.*, **49**, 5552 (1968).
(8) R. Astier and Y. H. Meyer, *Chem. Phys. Lett.*, **3**, 389 (1969).
(9) W. Heinzelmann and H. Labhart, *Chem. Phys. Lett.*, **4**, 20 (1969).
(10) D. Lavalette, *J. Chim. Phys.*, **66**, 1845, 1853, 1860 (1969).
(11) T. M. Naumova and V. I. Glabkovskii, *Opt. Spektrosk.*, **27**, 228 (1969).
(12) M. A. Slifkin and R. H. Walmsley, *Photochem. Photobiol.*, **13**, 57 (1971).
(13) G. Nouchi, *J. Chim. Phys.*, **66**, 548, 554 (1969).
(14) M. A. El-Sayed and T. Paulopoulos, *J. Chem. Phys.*, **39**, 834 (1963).
(15) K. B. Eisenthal, *J. Chem. Phys.*, **46**, 3268 (1967).
(16) K. B. Eisenthal, *J. Chem. Phys.*, **50**, 3120 (1969).
(17) D. Lavalette, *Chem. Phys. Lett.*, **3**, 67 (1969).
(18) J. B. Gallivan and J. S. Brinen, *J. Chem. Phys.*, **50**, 1590 (1969).
(19) R. A. Keller and S. G. Hadley, *J. Chem. Phys.*, **42**, 2382 (1965).
(20) E. J. Land, *Proc. Roy. Soc., Sec. A*, **305**, 457 (1968).
(21) J. S. Brinen, *J. Chem. Phys.*, **49**, 586 (1968).
(22) J. S. Brinen and M. K. Orloff, *J. Chem. Phys.*, **51**, 527 (1969).
(23) S. G. Hadley and R. A. Keller, *J. Phys. Chem.*, **73**, 4351 (1969).
(24) M. K. Orloff, *J. Chem Phys.*, **47**, 235 (1967).
(25) J. R. Platt, *J. Chem. Phys.*, **17**, 484 (1949).
(26) R. Pariser, *J. Chem. Phys.*, **24**, 250 (1956).

from the known energies of S–T transitions, it follows that the second triplet state lies below the first excited singlet state and should consequently participate in the intersystem crossing. Experimental proof of this assertion is lacking.

The first allowed triplet-triplet transition $^3B_u^+ \rightarrow {}^3A_g^-$ ($^3B \rightarrow {}^3C$ according to Platt) should be located in the ultraviolet region. For butadiene, theory predicts an energy of 34.8 kK and for hexatriene 30.2 kK. The calculated oscillator strength f = 0.5–1 is in agreement with Platt's[25,27] selection rules, because it relates to a transition where the total quantum number changes by a unit. These calculations can not at present be compared with experimental data, which are lacking. The 31.25-kK band, measured by a giant pulse laser photolysis of benzene,[28] can be tentatively assigned to the triplet-triplet transition of hexatriene arising by photoreduction; a definitive assignment, however, will require more experimental evidence. Direct comparison of experiment with theory in this region is likely to be hampered by the photochemical sensitivity of the polyenes and by major changes in the geometry of the excited states.

Benzenoid Hydrocarbons. Among all the substances studied, the best triplet-triplet spectral data are available for the benzenoid hydrocarbons, which we therefore discuss in some detail. Our calculations have confirmed Kearns'[29] general assignment of the lowest triplet state as ^3L_a. Although the experimental verification of the symmetry of the lowest triplet state is complicated by the fact that the phosphorescence is predominantly polarized out-of-plane by the influence of the spin-orbit coupling with the $\sigma\pi^*$ and $\pi\sigma^*$ singlet states, the in-plane components of the polarization confirm the theoretical assignment (see, *e.g.*, ref 18 and 30). For centrally symmetric molecules, the lowest allowed triplet-triplet bands will then be formed by the transition $^3L_a \rightarrow {}^3K_a$, polarized approximately longitudinally, and by the transitions $^3L_a \rightarrow {}^3K_b$ and $^3L_a \rightarrow {}^3C_b$, polarized transversely. According to Platt's rules,[25] the transition $^3L_a \rightarrow {}^3C_b$ will be less intense than transitions of the type $^3L_a \rightarrow {}^3K_{a,b}$. From a study of the polarization diagrams constructed on the basis of the LCI–SCF functions, it follows that for molecules without a center of symmetry there appears an additional allowed, though not intense, transition $^3L_a \rightarrow {}^3B_a$, polarized longitudinally. These conclusions will now be verified by a more detailed analysis of the singlet-triplet and triplet-triplet spectra of the individual molecules.

Benzene. The first two experimental energies of triplet states obtained by optical methods[31,32] were used for the adjustment of the parameters of our procedure.[33] The symmetry $^3B_{1u}^+$ corresponds to the first triplet state ^3L_a, and the symmetry $^3E_{1u}^+$ to the second $^3B_{a,b}$ state.[29] To the excitation of the electron into the third triplet state ^3L_b of the theoretical symmetry $^3B_{2u}^-$ and the energy 41.2 kK we can assign a band at 43 kK found by the method of electron impact.[34,35] The weak triplet-triplet band of the energy of 23.3 kK and the extinction coefficient ϵ 100 can be assigned to the symmetrically forbidden transition from the first into the fourth triplet state (calculated energy 22.7 kK) of the symmetry $^3B_{1u}^+ \rightarrow {}^3E_{2g}^-$ or $^3L_a \rightarrow {}^3C_{a,b}$ according to Platt. The energy of the $^1A \rightarrow {}^3C_{a,b}$ transition is very near the energy of the singlet $^1A \rightarrow {}^1L_a$ transition, casting some doubt on the assignment of the corresponding absorption band in the electron impact spectrum.[34] The fifth triplet state $^3K_{a,b}$ of symmetry $^3E_{2g}^-$ has, according to our calculations, energy of 52.3 kK (relative to the singlet ground state) and thus is close to the ionization potential of the molecule. The transition $^3L_a \rightarrow {}^3K_{a,b}$, of energy 39.2 kK, is the first allowed transition of the triplet-triplet spectrum and corresponds to the measured band[11] at 39.22 kK.

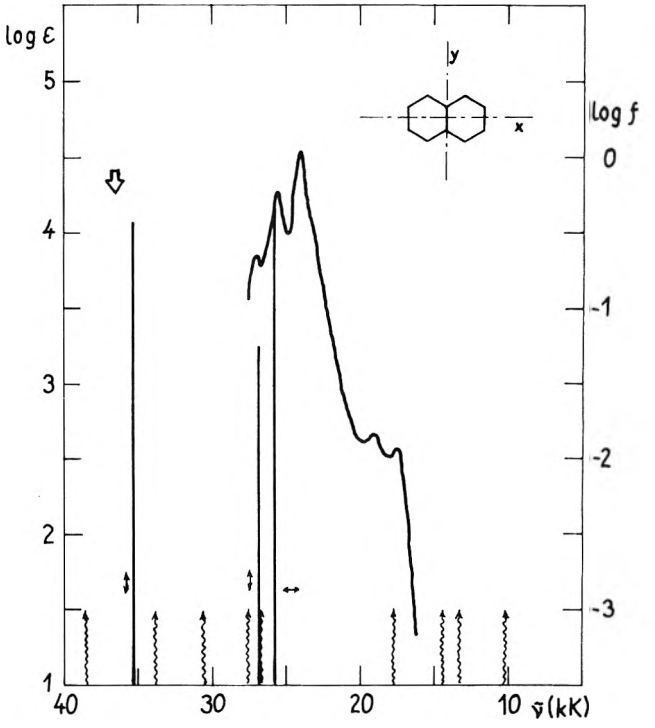

Figure 1. Triplet-triplet spectrum of naphthalene[36] drawn with the use of the extinction coefficient from ref 21 together with theoretical data. ⇨ denotes position of the maximum of the experimental T–T band in the ultraviolet region intensity of which was not specified;[11] —— shows allowed transitions; ⇝ shows forbidden transitions; ↔ shows direction of polarization relative to the drawn orientation of the molecule.

Naphthalene. For the first singlet-triplet transition $^1A_g^- \rightarrow {}^3B_{2u}^+$ ($A \rightarrow {}^3L_a$ according to Platt), the calculated energy of 21.3 kK is in good agreement with the experimental value of 21.2 kK.[31] The second singlet-triplet transition $^1A_g^- \rightarrow {}^3B_{1g}^+$ is according to theory at 31.2 kK, *i.e.*, very near the singlet-singlet absorption band.

The triplet-triplet spectrum determined by Melhuish[36] was drawn with the use of Brinen's[21] value of the extinction coefficient of the most intense maximum, only relative absorption being measured. This is given, together with theoretical values, in Figure 1.

The first triplet-triplet band, which lies theoretically at 9.9 kK, is allowed by symmetry but forbidden by parity (transition $^3B_{2u}^+ \rightarrow {}^3B_{1g}^+$); it is polarized along the longer axis of the molecule. As the parity determination of allowed and forbidden transition is due to approximations involved in the theoretical method, the bands forbidden by parity should be more intense than those forbidden by symmetry.[10] Unfortunately, no measurement has as yet been made in the infrared region to confirm this result. The next band forbidden by parity is given by theory at 17.6 kK (the transition $^3B_{2u}^+ \rightarrow {}^3A_g^+$). This region contains a very weak band (ϵ 200–300) observed by Melhuish[36] and Lavalette.[10] The intense band at 24.1 kK (see Figure 1) is undoubtedly produced by the transition $^3B_{2u}^+ \rightarrow {}^3B_{1g}^-$ ($^3L_a \rightarrow {}^3K_\epsilon$ according to Platt), and according to theory[24,26] and experiment[10] is polarized parallel to the

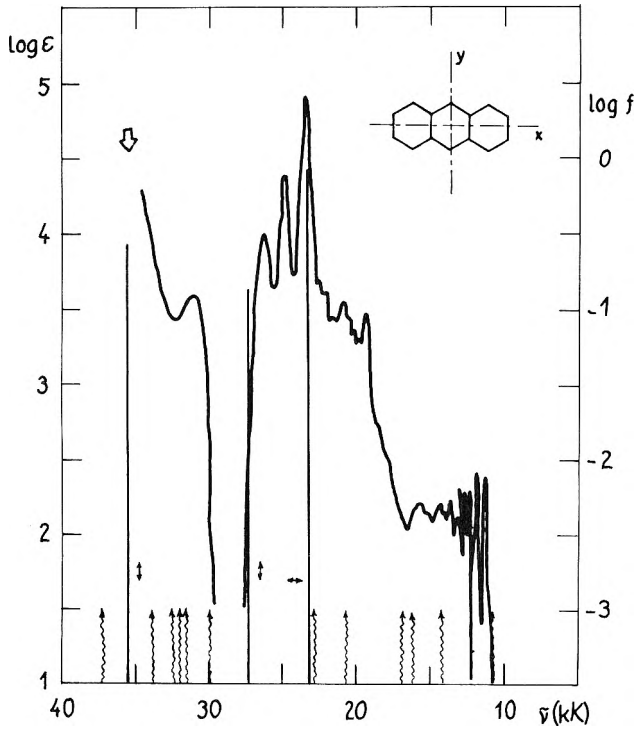

Figure 2. Triplet–triplet spectrum of anthracene[5] together with theoretical data. ⇨ denotes the position of the maximum of the experimental T–T band in the ultraviolet region, intensity of which was not specified.[38] For further explanation see caption to Figure 1.

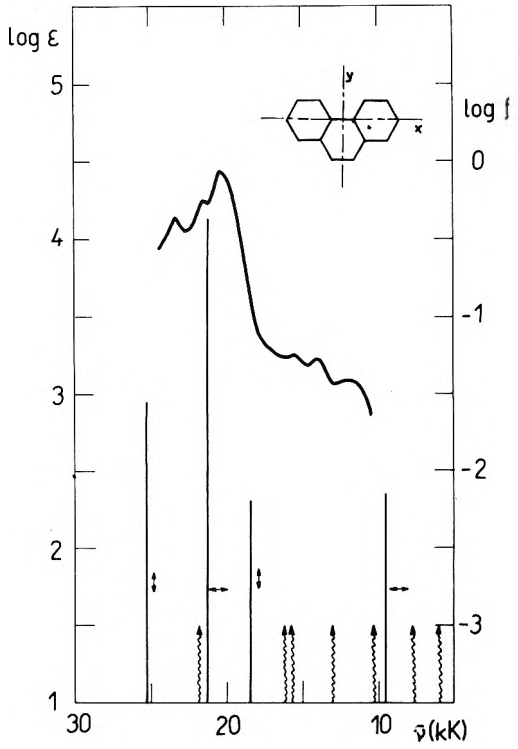

Figure 3. Triplet–triplet spectrum of phenanthrene[4] together with theoretical data. For explanation of symbols, see caption to Figure 1.

longer axis of the molecule. Our calculation shows a weaker band nearby, $^3B_{2u}^+ \rightarrow {}^3A_g^-$ ($^3L_a \rightarrow {}^3C_b$), which can be assigned to the band at 29 kK found by the method of pulse radiolysis.[37] It is possible that the weak maxima found at 17.5 and 19.0 kK[10,36] (see Figure 1) are the beginning of this band; calculation gives only the position of the Franck–Condon maximum. This assumption seems to be supported by the formal similarity of this spectrum and that of phenanthrene (Figure 3), but is in disagreement with the shift of this band on going from naphthalene to anthracene, which will be dealt with later. The solution of this problem probably would require careful vibrational analysis of a spectrum better resolved than is now available.

The intense transition $^3B_{2u}^+ \rightarrow {}^3A_g^-$ ($^3L_a \rightarrow {}^3K_b$) can be assigned to Porter's band[38] at 38.5 kK or to the band at 37 kK as determined in ref 11. Since this region is already subject to strong singlet–singlet absorption, it is hardly possible to measure its relative intensity accurately enough. It seems, however, that in view of the similarity of the spectra of the polyacenes,[38] and the similarity between the triplet–triplet spectra and the spectra of the corresponding dianions,[39] we have here an actually allowed transition. We take this in support of our assignment, contrary to Orloff's classification[24] of this band as $^3B_{2u}^+ \rightarrow {}^3B_{1g}^+$.

Anthracene. Anthracene belongs to the substances with the best-measured triplet–triplet spectra[4,5] (Figure 2). The experimental energies of the two lowest triplet levels (14.87[31] and 26.1 kK[40]) are comparable with the theoretical energies of 14.9 and 25.7 kK of the states of the symmetries $^3B_{2u}^+$ and $^3B_{1g}^+$. Both these states are theoretically below the lowest excited singlet and should consequently participate in the intersystem crossing. The participation of the second triplet state of anthracene in this process has been proven photochemically.[41,42]

A comparison of the triplet–triplet spectrum of anthracene with the spectrum of naphthalene reveals that the band $^3L_a \rightarrow {}^3K_a$ is strongly bathochromically shifted, while the positions of the bands $^3L_a \rightarrow {}^3C_b$ and $^3L_a \rightarrow {}^3K_b$ are not much changed. The $^3B_{2u}^+ \rightarrow {}^3A_g^+$ transition forbidden by parity, which we are not able to classify according to Platt, is shifted strongly hypsochromically. For this reason, we assume that the transition $^3B_{2u}^+ \rightarrow {}^3A_g^+$ participates in the case of both substances in the absorption in the region about 20 kK (*cf.* Figures 1 and 2). As with naphthalene, the intensity of the band in the ultraviolet region has not been published (its position is indicated in Figure 2 by an arrow), but it can again be assumed to be allowed by parity as well as by symmetry. The theoretical transition $^3L_a \rightarrow {}^3K_b$, which matches this assumption, is very near the experimental maximum.

Phenanthrene. According to our calculations, the two

(27) J. R. Platt, *J. Chem. Phys.*, **18**, 1168 (1950).
(28) R. Bonneau and J. Joussot-Dubien, *Chem. Phys. Lett.*, **3**, 353 (1969).
(29) D. R. Kearns, *J. Chem. Phys.*, **36**, 1608 (1962).
(30) M. A. El-Sayed, *Accounts Chem. Res.*, **1**, 8 (1968).
(31) D. F. Evans, *J. Chem. Soc.*, 1351 (1957).
(32) S. D. Colson and E. R. Bernstein, *J. Chem. Phys.*, **43**, 2661 (1965).
(33) J. Pancíř and R. Zahradník, Theor. Chim. Acta, **14**, 426 (1969).
(34) R. N. Compton, R. H. Huebner, P. W. Reinhardt, and L. G. Christophorou, *J. Chem. Phys.*, **48**, 901 (1968).
(35) J. P. Doering, *J. Chem. Phys.*, **51**, 2866 (1969).
(36) W. H. Melhuish, *J. Chem. Phys.*, **50**, 2779 (1969).
(37) G. R. A. Johnson and M. C. Sauer, Jr., *J. Chem. Phys.*, **51**, 496 (1969).
(38) G. Porter and M. W. Windsor, Proc. Roy. Soc., *Ser. A*, **245**, 238 (1958).
(39) G. J. Hoijtink, *Pure Appl. Chem.*, **11**, 393 (1965).
(40) R. E. Kellog, *J. Chem. Phys.*, **44**, 411 (1966).
(41) R. S. H. Liu and J. R. Edman, *J. Amer. Chem. Soc.*, **90**, 213 (1968).
(42) R. S. H. Liu and R. E. Kellog, *J. Amer. Chem. Soc.*, **91**, 250 (1969).

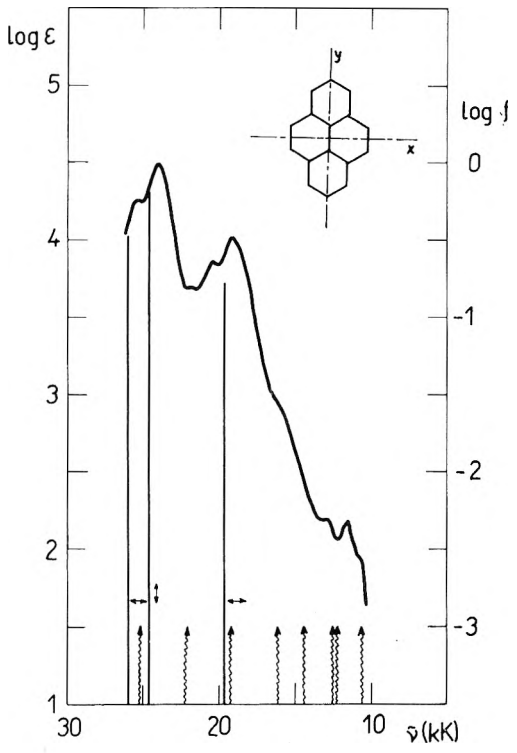

Figure 4. Triplet-triplet spectrum of pyrene[4] together with theoretical data. For explanation of symbols, see caption to Figure 1.

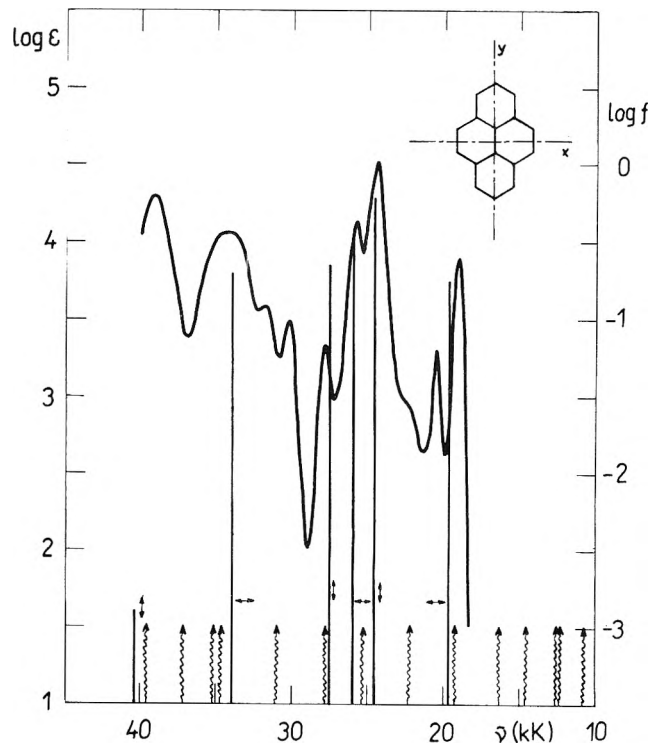

Figure 5. Triplet-triplet spectrum of pyrene[9] together with theoretical data. For explanation of symbols, see caption to Figure 1.

lowest triplet states $^3B_2^+$ and $^3A_1^+$ have energies of 22.4 and 28.4 kK. The first energy is comparable with the experimental value of 21.6 kK.[31] The triplet-triplet spectrum measured by Windsor and Novak[4] and the theoretical values are given in Figure 3. Besides the intense band with a maximum at 20.5 kK, which we assigned, in agreement with the measurement of the intensity[21] and the polarization,[10,18] to the transition $^3B_2^+ \rightarrow {}^3A_1^-$ (according to Platt $^3L_a \rightarrow {}^3K_a$), there appears a weaker very broad band, which has so far been assigned to a band forbidden by parity or to the transition $^3L_a \rightarrow {}^3C_a$.[13] According to our results (*cf.* Figure 3) it can be concluded that we have here the beginning of the band $^3B_2^+ \rightarrow {}^3B_2^-$ ($^3L_a \rightarrow {}^3C_b$), whose Franck-Condon maximum is given by theory at 18.4 kK, and which is polarized along the molecular axis. In the infrared region at 9.6 kK, the theory predicts a further allowed, though very weak, transition $^3B_2^+ \rightarrow {}^3A_1^-$ ($^3L_a \rightarrow {}^3B_a$), polarized perpendicularly to the molecular axis. No triplet-triplet spectrum has so far been measured in this region. The participation of the latter transition in the weak band in the visible region should be decided on the basis of the polarization measurement.

Pyrene. The lowest triplet state theoretically has the symmetry $^3B_{3u}^+$; its energy is theoretically equal to 17.2 kK and experimentally to 16.5 kK.[31] The triplet-triplet spectrum (Figure 4) begins at 11 kK with a band to which, according to our calculations, the symmetry $^3B_{3u}^+ \rightarrow {}^3B_{2u}^+$ was assigned. The second triplet state consequently has an energy somewhat higher than that of the lowest excited singlet and should thus no longer participate significantly in intersystem crossing unless the singlet state were thermally activated. This result was experimentally verified by the study of the thermal dependence of the half-life of the fluorescence.[4,43]

Two parity forbidden but symmetry allowed transitions of energies of 12.3 and 14.5 kK, and symmetries $^3B_{3u}^+ \rightarrow {}^3B_{1g}^+$ and $^3B_{3u}^+ \rightarrow {}^3A_g^+$, are probably the cause of the weak absorption maxima measured at 11.5 and 12.9 kK.[4] The transition $^3B_{3u}^+ \rightarrow {}^3B_{1g}^-$ ($^3L_a \rightarrow {}^3C_b$) obviously gives rise to the band at 19.2 kK (*cf.* Figures 4 and 5). In the intense band on the boundary between the visible and the ultraviolet region, three allowed transitions participate according to our calculations: $^3B_{3u}^+ \rightarrow {}^3A_g^-$ ($^3L_a \rightarrow {}^3K_a$), $^3B_{3u}^+ \rightarrow {}^3B_{1g}^-$ ($^3L_a \rightarrow {}^3K_b$), and $^3B_{3u}^+ \rightarrow {}^3A_g^-$.

For pyrene, the triplet-triplet spectrum has been measured far into the ultraviolet region, where it is to be expected that our configuration interaction basis set will be inadequate. Nevertheless all but the shortest wavelength band at 39 kK can be interpreted by the method used (Figure 5).

Naphthacene. The theoretical difference in energy between the first two triplet states is almost equal to the energy of the lowest singlet-triplet transition. A phosphorescence from the second excited state is therefore possible, and would explain the emission band[44] at 19.5 kK, which was formerly ascribed to the normal phosphorescence of naphthacene. (It is also possible, however, that this band was emitted by an impurity of the sample under study.) The calculated energy of the singlet-triplet transition, 10.8 kK, is comparable with the experimental value of 10.3 kK.[45]

The first triplet-triplet transition was measured experimentally[46] in the infrared region with a maximum at 10.4 kK. This value is also in agreement with the energy of the

(43) B. Stevens, M. F. Thomas, and J. Jones, *J. Chem. Phys.*, **46**, 405 (1967).
(44) S. P. McGlynn, M. R. Padhye, and M. Kasha, *J. Chem. Phys.*, **23**, 593 (1955).
(45) A. A. Lamola, W. G. Herkstroeter, J. C. Dalton, and G. S. Hammond, *J. Chem. Phys.*, **42**, 1715 (1965).
(46) R. Astier, A. Bokobza, and Y. H. Meyer, *J. Chem. Phys.*, **51**, 5174 (1969).

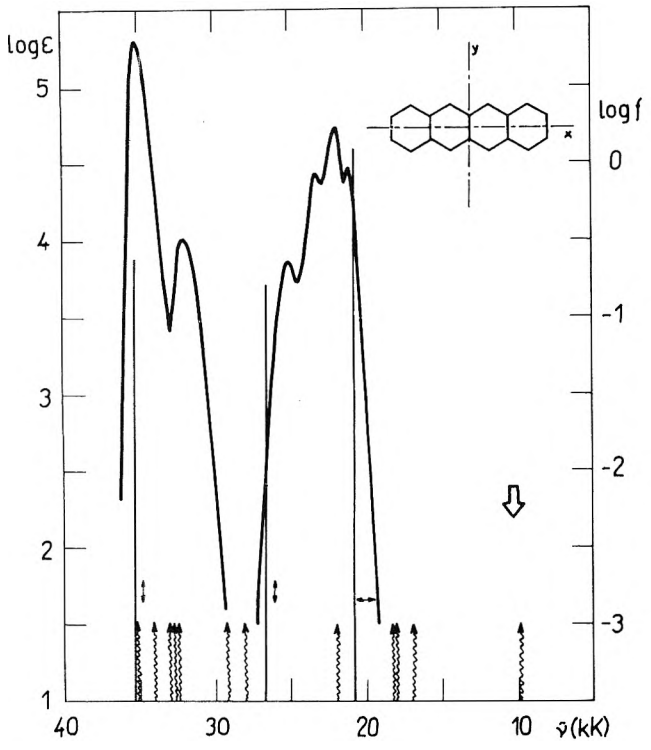

Figure 6. Triplet–triplet spectrum of naphthacene[38] together with theoretical data. ⇨ denotes the position of the maximum of the band of the greatest wavelength found experimentally.[8] For explanation of further symbols, see caption to Figure 1.

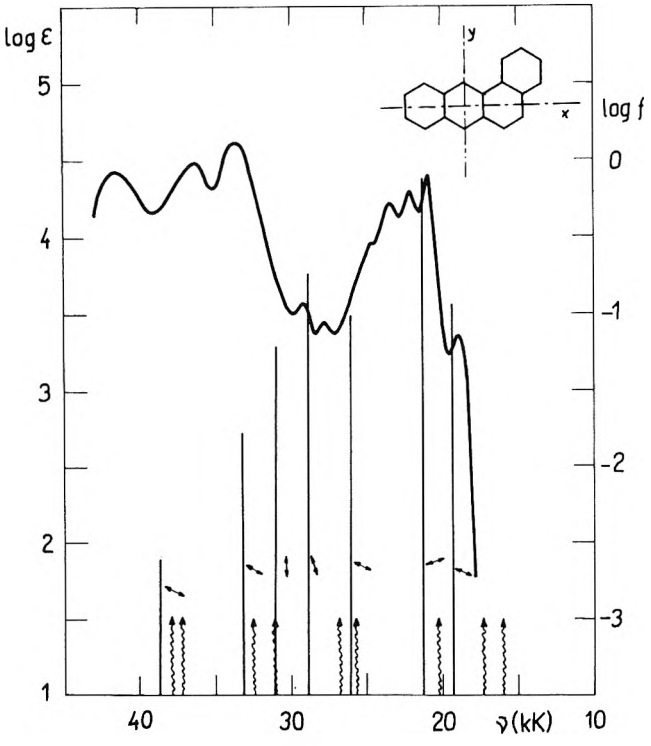

Figure 7. Triplet–triplet spectrum of benz[a]anthracene[9] together with theoretical data. For explanation of symbols, see caption to Figure 1.

$^3B_{2u}^+ \rightarrow {}^3B_{1g}^+$ transition, 9.9 kK. The measured triplet–triplet spectrum given in ref 38 is presented in Figure 6. The bands $^3B_{2u}^+ \rightarrow {}^3B_{1g}^-$ ($^3L_a \rightarrow {}^3K_a$) and $^3B_{2u}^+ \rightarrow {}^3A_g^-$ ($^3L_a \rightarrow {}^3K_b$) are relatively easy to identify; the assignment of the band $^3L_a \rightarrow {}^3C_b$ will possible only after a careful measurement of the spectrum in the region of 25–30 kK.

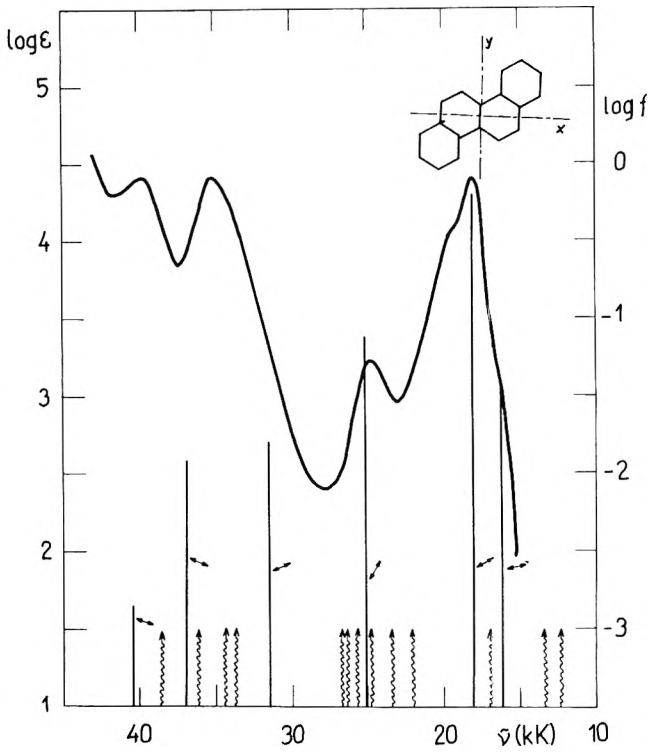

Figure 8. Triplet–triplet spectrum of chrysene[9] together with theoretical data. For explanation of symbols, see caption tc Figure 1.

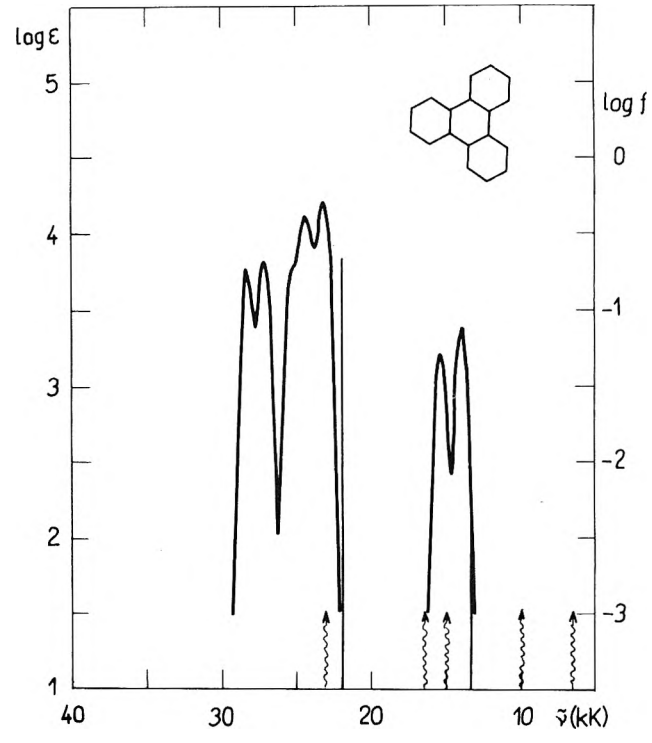

Figure 9. Triplet–triplet spectrum of triphenylene[13] drawn with the use of the extinction coefficient from ref 21, together with theoretical data. For explanation of symbols, see caption to Figure 1.

Other Benzenoid Hydrocarbons. The energies of the singlet–triplet transitions of hydrocarbons with four rings

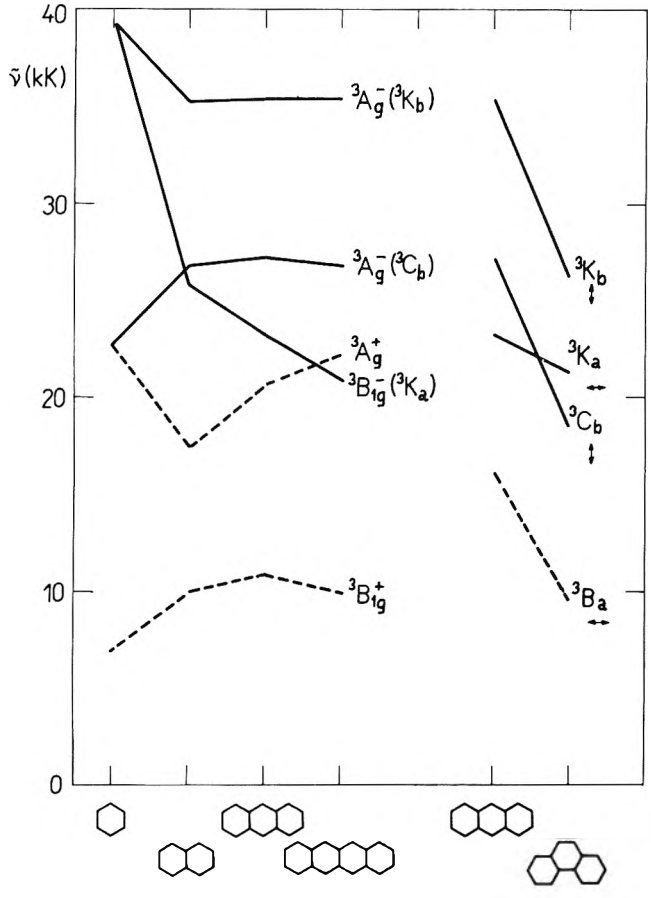

Figure 10. Spectral resemblance of benzenoid hydrocarbons: polyacenes and three-ring hydrocarbons.

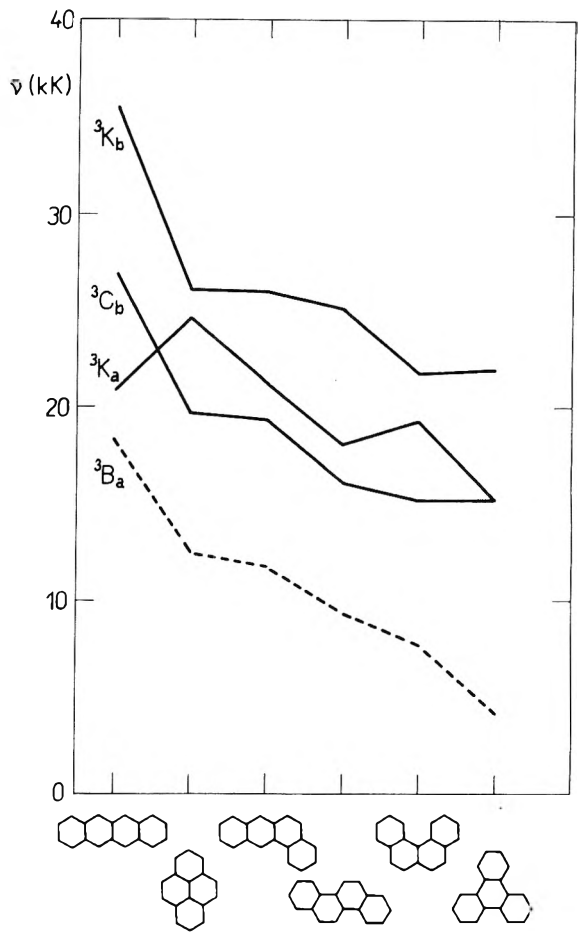

Figure 11. Spectral resemblance of benzenoid hydrocarbons: four-ring hydrocarbons.

were interpreted by this method with the same accuracy as those with a lower number of atoms. From the theoretical viewpoint, no new findings result from the study of the triplet–triplet spectra of benz[*a*]anthracene and chrysene (Figures 7 and 8). The sequence of the individual bands is the same as for phenanthrene. It is obvious that for energies higher than 30 kK, a significant role is played by configurations not included in our basis set.

For triphenylene (Figure 9), two triplet–triplet bands have been identified, a weaker band $^3B_{2u}^+ \rightarrow {}^2E_{2g}^-$ ($^3L_a \rightarrow {}^3C_{a,b}$) at 15 kK and a stronger one $^3B_{2u}^+ \rightarrow {}^3E_{2g}^-$ ($^3L_a \rightarrow {}^3K_{a,b}$) at 23 kK.

For benzo[c]phenanthrene, a triplet–triplet spectrum was published in the classical paper by Porter and Windsor.[38] Since the extinction coefficients were measured with only limited accuracy, this spectrum is not given here. However, both measured bands are easy to interpret. The intense band with a maximum at 19.34 kK can be compared with the calculated transition $^3B_2^+ \rightarrow {}^3A_g^-$ ($^3L_a \rightarrow {}^3K_a$, $\tilde{\nu}_{th}$ = 19.27 kK); a broad band of medium intensity with maximum at 25 kK is probably formed by superposition of three allowed transitions, lying theoretically at 23.4, 25.2, and 27.0 kK. The theory predicts two further weak, but allowed bands in the infrared and visible regions; this relates to the transition $^3L_a \rightarrow {}^3C_b$, polarized along the axis of the molecule, with a maximum at 15.2 kK, and to the transition $^3L_a \rightarrow {}^3B_a$, polarized perpendicularly with a maximum at 7.7 kK. In the case of this molecule it is interesting to point out the theoretical extremely low energy of the first triplet-triplet transition ($\tilde{\nu}_{th}$ = 3.6 kK).

Spectral Resemblances of Benzenoid Hydrocarbons. On the basis of theoretical and experimental results, it is possible to characterize several typical bands in the triplet–triplet spectra. The very intense band $^3L_a \rightarrow {}^3K_a$ (log ϵ_{max} = 4–5), which is polarized longitudinally, has a rich vibrational structure, and the 0–0 transition is usually at the same time a vertical transition. The band $^3L_a \rightarrow {}^3K_b$, polarized perpendicularly to the band $^3L_a \rightarrow {}^3K_a$, is usually very intense for polyacenes and somewhat weaker for other hydrocarbons, mostly without a resolved vibrational structure. The band $^3L_a \rightarrow {}^3C_a$, parallel to it, is overlapped in the polyacene case by the band $^3L_a \rightarrow {}^3K_a$; it is of medium intensity (log ϵ_{max} = 3–4) and usually has a vibrational structure. The transition $^3L_a \rightarrow {}^3B_a$, which should be allowed for molecules without central symmetry, lies theoretically in the infrared region.

Figures 10 and 11 present the changes in the energies of triplet–triplet transitions as a function of structure. Linear annelation (Figure 10) is characterized by a strong bathochromic shift of the $^3B_{2u}^- \rightarrow {}^3B_{1g}^-$ band ($^3L_a \rightarrow {}^3K_a$); the energies of the allowed bands $^3L_a \rightarrow {}^3K_b$ and $^3L_a \rightarrow {}^3C_b$, beginning with naphthalene, are not essentially changed by additional annelation. The band $^3B_{2u}^+ \rightarrow {}^3A_g^+$, forbidden by parity, which probably is the cause of the weak absorption of naphthalene and anthracene in the visible region, shifts hypsochromically with rising number of atoms, and already for naphthacene its maximum is, according to theoretical results, overlapped by the band $^3B_{2u}^- \rightarrow {}^3B_{1g}^-$. The energy of the lowest triplet–triplet transition attains its maximum for anthracene and then

TABLE I: Spectral Characteristics of Azulene

Singlet–triplet transitions		Triplet–triplet transitions			
No.	*E*, kK	No.	*E*, kK	Log *f*	Polarization in relation to axis of molecule
1	14.64	1	2.93	−3.140	⊥
2	17.57	2	6.98	−2.326	⊥
		3	15.46	−1.756	∥
		4	19.33	−0.908	∥
		5	24.00	−1.978	⊥
		6	24.75	−0.928	⊥
		7	25.05	−0.616	∥
		8	30.47	−4.186	∥
		9	33.49	−1.789	⊥
		10	34.70	−2.112	⊥
		11	38.29	−0.833	

TABLE II: Spectral Characteristics of Acenaphthylene

Singlet–triplet transitions		Triplet–triplet transitions			
No.	*E*, kK	No.	*E*, kK	Log *f*	Polarization in relation to axis of molecule
1	17.11	1	2.77	−2.629	⊥
2	19.88	2	9.53	−3.086	∥
		3	17.48	−3.476	∥
		4	17.53	−1.769	⊥
		5	18.72	−2.846	⊥
		6	19.69	−2.522	∥
		7	23.94	−1.091	⊥
		8	27.61	−0.582	∥
		9	28.38	−0.866	⊥
		10	30.16	−1.100	∥
		11	32.17	−1.704	⊥
		12	32.55	−0.437	∥
		13	35.10	−1.895	⊥
		14	38.52	−1.775	∥

again slowly decreases with further annelation.

Annelation of the phenanthrene type (Figures 10 and 11) leads to an interchange of the bands $^3L_a \rightarrow {}^3K_a$ and $^3L_a \rightarrow {}^3C_b$; the latter transition probably participates in the medium absorption band in the visible region of phenanthrene and related compounds.

With our relatively small configuration interaction basis set, we cannot expect to obtain correct values of the transition moment. (For more details see ref 1.) Nevertheless, after a comparison of our calculations with available experimental data[10,19-21] we have concluded that our modified procedure can give at least qualitative information on the relative intensity of the individual bands as a function of the structure of the molecule. An increase of the number of atoms in polyacenes is accompanied by a roughly parallel increase in the intensity of the transitions $^3L_a \rightarrow {}^3K_b$ and $^3L_a \rightarrow {}^3C_b$; beginning with naphthalene, the intensity of the band $^3L_a \rightarrow {}^3K_a$ gradually decreases. The study of isomers of equal numbers of atoms reveals that a deviation from the linear arrangement of the rings leads to a decrease in the intensity of all studied allowed bands. Weakening is least for the band $^3L_a \rightarrow {}^3K_b$. The transition $^3L_a \rightarrow {}^3C_b$ is most sensitive to the change, the intensity falling by as much as two orders of magnitude.

Nonalternant Hydrocarbons. Three molecules of this group have been studied, namely, acenaphthylene, fluoranthene, and azulene. For all three molecules we know the singlet–triplet spectrum,[31,47,48] which in the case of acenaphthylene and fluoranthene is in agreement with the calculated data. For azulene[48] there is rather large difference between the calculated and the experimental energy (about 4 kK). For the time being we are not able to explain such a disagreement. The low half-life of the emission of the observed singlet–triplet seems noteworthy.[49] Theoretical data on the triplet spectra of these three substances are given in Tables I–III. For triplet–triplet spectra, experimental data are very scarce. For azulene, a band is known at 20 kK, which can be assigned to the theoretical transition $^3B_2 \rightarrow {}^3B_2$ ($^3L_a \rightarrow {}^3K_a$) with an energy of 19.3 kK, polarized parallel to the axis of the molecule. For fluoranthene we have found a strong absorption band, beginning at 23 kK and with its first maximum at about 25 kK. This band could not be measured further, because its wavelength is at the end of the spectral range of the spectrograph employed. Theoretically it can be assigned to the transition $^3A_1 \rightarrow {}^3A_1$ ($^3L_a \rightarrow {}^3K_a$ according to Platt) of energy 24.9 kK, polarized in the direction of the axis of the molecule.

TABLE III: Spectral Characteristics of Fluoranthene

Singlet–triplet transitions		Triplet–triplet transitions			
No.	*E*, kK	No.	*E*, kK	Log *f*	Polarization in relation to axis of molecule
1	19.79	1	3.21	−2.481	⊥
2	23.00	2	9.32	−2.872	⊥
		3	11.88	−1.760	⊥
		4	13.20	−1.371	∥
		5	15.41	−2.086	⊥
		6	15.44	−1.964	∥
		7	16.19	−2.504	⊥
		8	17.93	−2.270	∥
		9	19.60	−1.392	∥
		10	24.67	−0.651	⊥
		11	24.92	−0.205	∥
		12	27.29	−1.770	∥
		13	28.58	−0.737	⊥
		14	30.32	−1.516	∥
		15	30.99	−1.221	⊥

On the basis of these data, it seems that this method is also suitable for the study of triplet states of nonalternant hydrocarbons. A complete analysis of triplet–triplet spectra, however, requires far more detailed experimental data than at present available.

Conclusion

It was the aim of this work to examine the suitability of the modified PPP method[1,33] for the study of triplet states of molecules, as well as to discuss the known singlet–triplet and triplet–triplet spectra of conjugated hydrocarbons. Spectral similarities have been studied in particular for benzenoid hydrocarbons, where a wealth of experimental data are available. In the present paper we have not published all calculations. Pertinent tables will be sent on request.

(47) C. Dijgraaf, Ph.D. Thesis, University of Amsterdam, 1962.
(48) P. M. Rentzepis, *Chem. Phys. Lett.*, **3**, 717 (1969).
(49) G. W. Robinson and R. P. Frosch, *J. Chem. Phys.*, **38**, 1187 (1963).

Theoretical Study of Transitions from the First to Higher Excited Singlet States

J. Pancíř and R. Zahradník*

The J. Heyrovský Institute of Physical Chemistry and Electrochemistry, Czechoslovak Academy of Sciences, Prague, Czechoslovakia
(Received September 10, 1971)

The energies and oscillator strengths of electronic transitions from the first excited singlet state were calculated for eight conjugated hydrocarbons by the semiempirical Pariser-Parr-Pople method. The calculations are compared with available experimental data.

Introduction

The spectroscopy of molecules in electronically excited states belongs undoubtedly among the significant recent advances of electronic spectroscopy. Whereas triplet-triplet transitions have been known for years,[1-6] the measurement of absorption bands from the first excited state[7-15] has been made possible only by the development of nanosecond flash photolysis.[16] The theoretical interpretation of the measured spectra must be based, as in the case of triplet-triplet spectra,[17] upon a comparison of the relative intensities and thus on the oscillator strengths of the individual bands. It is the aim of this investigation to show that the semiempirical Pariser-Parr-Pople (PPP) method is suitable for such an interpretation.

Calculations

The calculations were performed by means of a slightly modified version of the PPP method, used in our laboratory[18,19] for the study of singlet-singlet spectra. In the present paper we have employed a different expression to calculate the resonance integral $\beta_{\mu\nu}$

$$\beta_{\mu\nu} = -9.44S_{\mu\nu} \qquad (1)$$

where $S_{\mu\nu}$ is the overlap integral between the $2p_z$ Slater atomic orbitals on those centers μ and ν which are connected by a chemical bond. The bond lengths were corrected in each SCF iteration[20] by means of the relation

$$r_{\mu\nu} = -0.19p_{\mu\nu} + 1.523 \qquad (2)$$

where $p_{\mu\nu}$ is the bond order of the bond between the atoms μ and ν. These relationships appear to be more exact than those given in ref 19, but their introduction exerts little influence on the calculated positions and intensities of the bands. The calculations were performed on an Elliott 503 computer by means of a program formulated in the Autocode Elliott language for the purposes of the present study.

Results and Discussion

The question of the selection of the basis set for the configuration interaction was thoroughly examined for triplet-triplet transitions in ref 17. It was found[17] that the basis set of the singly excited configurations (with regard to the ground state) is sufficient for electronic transitions up to 30-35 kK. We have taken this result in the present work for calculations of the spectra from the first excited singlet state, which are formally similar to the triplet-triplet spectra. The configuration interaction matrix was based on all configurations of singly excited states (with regard to the ground state), and corresponding to transitions among ten frontier orbitals, while for benzene all singly excited configurations were employed. In the present paper we consider more thoroughly the influence of the geometry of excited states on the singlet-singlet transition energies. On the assumption that eq 2 can be applied to molecules in excited states, it was possible to modify the semiempirical method so as to calculate the resonance and the repulsion integrals by using the theoretical bond lengths in the electronic state $^1\psi_{12}{}^+ = 2^{-1/2}[V_{12'} + V_{21'}]$ (nomenclature taken from ref 21), which participates to a considerable extent in the excited singlet state of lowest energy in the case of the molecules under investigation.

The calculation was carried out for naphthalene. In view of the geometry of the virtual singlet state, the wave number of the $S_0 \rightarrow S_1$ transition fell to 31.2 kK and corresponds exactly to the wave number of the maximum of the fluorescence band.[22] The absorption transitions from the first excited singlet state were very insensitive to a change of geometry, and the energies of the individual bands differed on an average by 0.08 eV. For this reason, we calculated the transition moment directly from the wave functions obtained by the standard method.

The theoretical energies, the logarithms of the oscillator strengths, and the directions of the transition moments

(1) D. C. McClure, *J. Chem. Phys.*, **17**, 905 (1949).
(2) D. P. Craig and I. G. Foss, *J. Chem. Soc.*, 1589 (1954).
(3) G. Porter and M. W. Windsor, *Proc. Roy. Soc., Ser. A*, **245**, 235 (1958).
(4) G. Nouchi, *J. Chim. Phys.*, **66**, 548, 554 (1969).
(5) W. Heinzelmann and H. Labhart, *Chem. Phys. Lett.*, **4**, 20 (1969).
(6) D. Lavalette, *J. Chim. Phys.*, **66**, 1845, 1853, 1860 (1969).
(7) Y. Nakato, N. Yamamoto, and H. Tsumobura, *Chem. Phys. Lett.*, **2**, 57 (1968).
(8) R. Bonneau, J. Faure, and J. Joussot-Dubien, *Chem. Phys. Lett.*, **2**, 65 (1968).
(9) J. R. Novak and M. W. Windsor, *Science*, **161**, 1342 (1968).
(10) G. Porter and M. R. Topp, *Nature (London)*, **220**, 1228 (1968).
(11) R. Bonneau and J. Joussot-Dubien, *Chem. Phys. Lett.*, **3**, 353 (1969).
(12) J. B. Birks, *Chem. Phys. Lett.*, **3**, 567 (1969).
(13) D. S. Klinger and A. C. Albrecht, *J. Chem. Phys.*, **50**, 4109 (1969).
(14) L. M. Theard, F. C. Peterson, and R. A. Holroyd, *J. Chem. Phys.*, **51**, 4126 (1969).
(15) P. M. Rentzepis, personal communication.
(16) L. Patterson and G. Porter, *Chem. Brit.*, **6**, 246 (1970).
(17) J. Pancíř and R. Zahradník, *J. Phys. Chem.*, **77**, 107 (1973).
(18) J. Koutecký, P. Hochmann, and J. Michl, *J. Chem. Phys.*, **40**, 2439 (1964).
(19) P. Hochmann, R. Zahradník, and V. Kvasnička, *Collect. Czech. Chem. Commun.*, **33**, 3478 (1968).
(20) A. Julg and M. Benard, *Tetrahedron*, **24**, 5575 (1968).
(21) R. Pariser, *J. Chem. Phys.*, **24**, 250 (1956).
(22) I. B. Berlman, "Handbook of Fluorescence Spectra of Aromatic Molecules," Academic Press, New York, N. Y., 1965.

TABLE I: LCI-SCF Spectral Characteristics of the Transitions from the First Excited Singlet State

Compound	E, 10^{-3} cm^{-1}	Angle,[a] deg	Log f[b]	E_{expt}
Benzene	9.97			
	16.66			
	16.66			20.4[c]
	28.36			
	28.36			
Naphthalene	3.83			
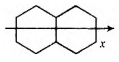	12.48			
	12.61			
	14.14			
	16.42			
	16.66			
	23.36			
	24.60	0	−0.177	23.3,[d] 21.5[e]
	29.07			
	29.08	270	−0.546	
	29.46	180	−1.015	
	29.76			
Phenanthrene	4.18	90	−2.821	
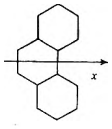	7.50			
	10.11	270	−1.747	
	10.79	0	−1.368	
	12.95			
	14.90			
	17.49			
	18.13			
	18.66	90	−3.628	
	19.81	90	−0.124	19.8[f]
	23.43			
	23.45			
	23.96	180	−2.559	
	24.64	90	−2.390	
	27.13	270	−0.928	
	27.51	0	−0.474	
	28.89			
	30.53	0	−1.982	
Pyrene	1.59			
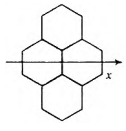	8.01			
	8.14	90	−2.021	
	10.81			
	12.62			
	13.63			
	14.75			
	15.45			
	15.60	180	−2.692	
	21.33	0	−0.430	21.3[f]
	21.96	270	0.010	
	22.13			
	22.22			
	25.01			
	25.12	270	−1.932	
	26.98			
	27.32	180	−0.971	
	28.39			
	30.62			
	30.95			
Benz[*a*]anthracene	1.45	338	−2.747	
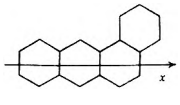	6.65			
	6.82	39	−1.474	
	9.91	1	−1.820	
	10.56			
	12.05	312	−1.157	
	14.92			
	16.97	25	−0.334	

Compound	E, 10^{-3} cm^{-1}	Angle,[a] deg	Log f[b]	E_{expt}
	17.09			
	17.98	192	−0.501	17.9,[e] 18.2[f]
	18.88			
	20.06	198	−0.775	
	21.40	195	−1.250	
	22.00			
	23.67	168	−0.864	
	26.39	293	−0.986	
	26.92			
	28.73	131	−1.636	
	29.34	224	−2.333	
	31.49	18	−1.709	
Benzo[a]pyrene	7.51			
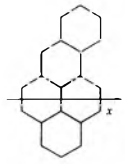	8.10	204	−1.814	
	9.27	122	−1.545	
	10.21			
	10.92	175	−2.756	
	11.32			
	13.51	182	−1.427	
	15.78			
	18.14	198	−0.113	18.7[f]
	18.99			
	20.49	47	−0.372	
	22.44	152	−0.621	
	23.28			
	23.89	137	−1.229	
	24.57	26	−1.703	
	26.05	124	−2.290	
	26.13			
	27.25			
	27.61	262	−2.406	
	30.19			
	31.44	315	−3.489	
	31.66	323	−2.751	
Triphenylene	2.83			
	6.37			
	6.37			
	7.68		−3.376	
	7.68		−3.376	
	11.82		−0.841	
	11.82		−0.841	
	15.59			
	15.59			
	15.81			
	16.44			
	17.59			
	18.07		−0.472	
	18.07		−0.472	
	19.39			
	24.00		−2.729	25.0[f]
	24.00		−2.729	
	24.22			
	24.22			
	24.91			
	28.51			
	30.02			
	31.94		−2.831	
	31.94		−2.831	
Azulene	11.62	270	−2.748	
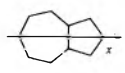	18.56	360	−1.319	
	21.52	90	−1.506	
	28.54	180	−1.357	
	31.31	270	−0.836	

[a] Polarization angle with regard to the x axis. [b] Logarithm of the oscillator strength. [c] Reference 11. [d] Reference 8. [e] Reference 14. [f] Reference 10.

are listed for eight conjugated hydrocarbons in Table I, together with the experimental data. As far as the latter are concerned, it must be borne in mind that the experimental arrangements permitted only very intense bands to be measured, that the determination of the wave numbers of absorption maxima is not very exact and, finally, that the measurement is possible only for bands in regions where neither singlet–singlet transitions from the ground state nor intense triplet–triplet transitions take place. As a consequence, few bands have been measured. By an improvement of experimental technique, however, it should be possible to measure medium bands as well, particularly in the visible and near-infrared regions.

The structure of the wave functions of the states participating in the allowed transitions is very complex, and it has not been possible, therefore, to classify the individual bands as was done for triplet–triplet transitions.[17] On the basis of a comparison of the wave functions of singlet states with the functions corresponding to triplet states, and the calculated directions of the transition moments, it was possible to assign the most intense band to the $^1L_b \rightarrow {}^1K_b$ transition of Platt,[23] however, this assignment cannot be supported by polarization diagrams.[23] It is interesting that in the case of all benzenoid hydrocarbons, this band follows the triplet band, $^3L_a \rightarrow {}^3K_a$, and is bathochromically shifted in relation to it. The experimental shift for all benzenoid hydrocarbons, except phenanthrene, is constant and amounts to about 2.6 kK.

Apart from benzene, the difference between the measured and the calculated energies of intense spectral maxima does not exceed 0.2 eV and corresponds to the inaccuracy of the experimental method. For benzene, the difference is larger (about 0.5 eV), and we have not been able to find a satisfactory explanation. The possibility of the formation of an excimer was excluded by ref 11, however, the participation of σ–π^* transitions or a change in the solvation energy due to loss of the high symmetry of the molecule in the excited state, cannot be excluded.

In the case of benzo[*a*]pyrene it is possible to specify[23] the lowest calculated excited singlet state as ^1L_a, which is in disagreement with experiment.[24] For this reason, the oscillator strengths were also calculated from the second excited singlet state, which can be classified as ^1L_b. The agreement of the experimental and the theoretical results (see Table I) confirms that the further excitation takes place from the ^1L_b state. Since the difference between theoretical and experimental energies of the ^1L_a and the ^1L_b states is very small (theoretically 0.05 eV), it is clear that the theory is not at fault. In addition, this error can be explained at least partly by the energy differences of the 0–0 and the Franck–Condon transitions (*cf.* the published absorption spectrum[24]).

Conclusion

By means of the semiempirical PPP method, it was found that the measured bands of the absorption spectra from the excited singlet state correspond to the electronic transitions with the highest oscillator strength. The most intense transition $^1L_b \rightarrow {}^1K_b$ is very near the $^1L_a \rightarrow {}^3K_a$ transition of the triplet spectrum. It has been shown that the changes in the bond lengths accompanying the excitation of the molecule exert only a very small influence upon the energies of the absorption bands under investigation. The spectral characteristics given in Table I may be of use for experimenters studying properties of excited states of molecules.

(23) J. R. Platt, *J. Chem. Phys.*, **17**, 484 (1949).
(24) "UV Atlas of Organic Compounds," Verlag Chemie, Weinheim Bergstr., Germany, 1966.

Observations on the Argon and Xenon Metastable Atom Energy Transfer Reactions with Carbon Disulfide, Carbonyl Sulfide, and Thiophosgene

Gene W. Taylor[1]

Department of Chemistry, Kansas State University, Manhattan, Kansas 66502 *(Received August 16, 1971)*

Publication costs assisted by the U.S. Army Research Office—Durham

The energy transfer reactions of metastable Ar atoms with carbon disulfide, carbonyl sulfide, and thiophosgene have been investigated in a fast flow system by spectroscopic observation of the resulting chemiluminescence. The reactions of metastable Xe atoms with SCS and SCO also were studied. Diagnostic tests for the presence of the resonance and metastable states of Xe and Ar are summarized and applied. The energy transfer reactions principally resulted in observations of the $CS(A^1\Pi, v' \rightarrow X^1\Sigma^+, v'')$ and the $CS(a^3\Pi, v' \rightarrow X^1\Sigma^+, v'')$ transitions; however, electronic excitation of the CO*, Cl_2*, and S* fragments also were observed. The Ar* + $SCCl_2$ and SCS reactions also appear to give some new carbon monosulfide emissions, which probably are from higher triplet states. Relative intensities of the observed spectra from each reaction are reported and discussed. The reaction, $Ar(^1P_1)$ + SCO → $CS(A^1\Pi; v' \lesssim 6)$ + $O(^3P)$ + $Ar(^1S_0)$ yields $D_0°$ (SC–O) ≤ 144.6 kcal/mol and $\Delta H_{f0}°$ (CS) ≤ 52.5 kcal/mol.

Introduction

Recently, considerable interest has been focused on the energy transfer reactions of rare gas metastable ($^3P_{0,2}$) atoms[2] as a source of electronic excitation for the spectroscopic, thermodynamic, and kinetic study of a variety of molecules. These energy transfer reactions, which have been studied in flow systems, cover a large energy range and, for some cases, provide a relatively "clean" source of radicals, electronically excited diatomics, and other transient species, the study of which is important to astrophysics, environmental pollution, and the understanding of elementary reactions. The same energy range can be reached by direct photolysis, which excites to the singlet electronic manifold, while the rare gas metastable reactions initially yield the triplet electronic state of the reagent. For molecules with ionization potentials less than 11.7 eV, the reactions with Ar* provide a potential method for the determination of the importance of Penning ionization relative to other available reaction paths, and further study is needed in this area. This paper presents some results for the general reaction, Ar* + R–CS → CS* + R + Ar (R–CS = SCS, OCS, and $SCCl_2$) and Xe* + R–CS → R + CS* + Xe (R–CS = CS_2 and OCS). An asterisk will be used to denote electronic excitation. For situations in which this can lead to confusion, the electronic states will be explicitly noted. As will become evident later, the discharge flow technique predominately yields the $Ar(^3P_{0,2})$ and $Xe(^3P_2)$ states; however, small concentrations of resonance states are present under some experimental conditions of operation.

The utility of rare gas metastable atom energy transfer reactions with polyatomic molecules leading to dissociative excitation for placing upper limits on bond energies has been successfully demonstrated.[3] The highest observed level of the excited fragment gives the upper limit to the bond energy; *e.g.*, for Ar* + RCS → R + Ar + CS* the relation is $D°(R–CS) \leq E_{Ar}* - E_{CS}*$. The usefulness of the metastable atom reactions in obtaining reliable upper limits for bond energies and heats of formation for transient species depends greatly on the reaction being studied and on a complete knowledge of the energy carriers present. The latter limitation depends upon the experimental configuration[2,3b,4] and can be alleviated by the consistent application of diagnostic tests for the known energy carriers. Some important diagnostic tests in the Ar* and Xe* reaction systems will be summarized. In the present study values of $D°$(SC–O) and $\Delta H_{f0}°$(CS) were obtained which support the lower range of values reported by the JANAF Tables.[5a]

Experimental Section

Two flow tubes were employed in these studies. (1) The 28-mm i.d. flow tube pictured in Figure 1 was used to view the spectra under diffuse flame conditions (low reagent concentrations). Most observations were taken at the second quartz window ~5 cm downstream from the initial mixing zone. (2) A flow tube identical with that described by Stedman and Setser[4] was employed for viewing the initial mixing zone under tight flame conditions (high reagent concentrations). Limited control over the type and quantity of metastable and resonance states produced by the hollow cathode discharge was achieved by the use of light traps and extended delay times (greater distances) between the discharge and initial mixing zone. Consequently, several configurations of the discharge tube were employed and these are described later.

The argon flow was held constant (~650 μmol sec^{-1}) in all experiments and typical reagent flows were from 0.1 to 10.0 μmol sec^{-1}. The method of production of Xe* metastables was identical with that previously described.[4] Both flow tubes were mechanically pumped with an Edward's 1000 l. min^{-1} single-stage pump resulting in a flow

(1) Present address: University of California, Los Alamos Scientific Laboratory, Los Alamos, N. M. 87544.
(2) D. H. Stedman and D. W. Setser, *Prog. React. Kinet.*, **6**, 4, (1971).
(3) (a) D. W. Setser and D. H. Stedman, *J. Chem. Phys.*, **49**, 467 (1968); (b) D. H. Stedman, *ibid.*, **52**, 3966 (1970) (c) J. A. Meyer and D. W. Setser, *J. Phys. Chem.*, **74**, 3452 (1970). The $\Delta H_f°$-(C_3N) was incorrectly calculated; the correct value for the quoted data should read $\Delta H_f°$ (C_3N) ≤ 149 kcal/mol.
(4) D. H. Stedman and D. W. Setser, *J. Chem. Phys.*, **52**, 3957 (1970), and references therein.
(5) (a) "JANAF Thermochemical Tables," Dow Chemical Co., Midland, Mich., 1965, and references therein; (b) "Bond Dissociation Energies in Simple Molecules," U. S. Department of Commerce, NSRDS-NBS-31, 1970, and references therein; (c) E. Gallegos and R. W. Kiser, *J. Phys. Chem.*, **65**, 1177 (1961); (d) C. L. Beckel, M. Shafi, and R. Engelke, *J. Mol. Spectrosc.*, **40**, 519 (1972), and references therein.

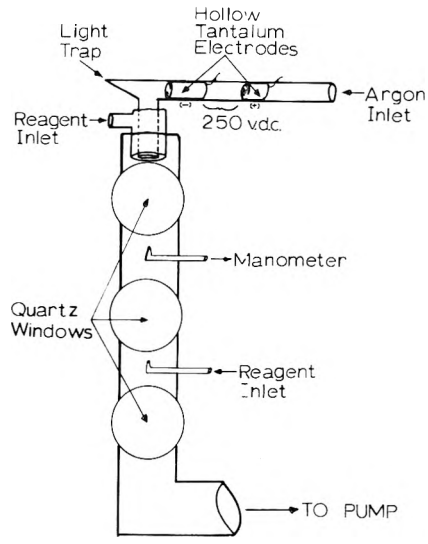

Figure 1. Diagram of flow tube, 28 mm (i.d.) and hollow tantalum cathode discharge in configuration C-1. The quartz windows were spaced 50 mm apart. The upper and lower entry ports were separated 80 and 30 mm from the center of the third quartz window, respectively.

velocity of $\sim 2 \times 10^3$ cm sec^{-1} at a total pressure of 2 Torr.

Argon (N.R.C.) was used directly from the tank after passing, at low pressures, through a cold trap (77°K) packed with 5A molecular sieve and metered into the tantalum hollow cathode discharge.[3a,b,4] Xenon was Matheson research grade. The carbonyl sulfide was Matheson C.P. grade, thiophosgene was Aldrich reagent grade, and carbon disulfide was Baker reagent grade. Dilute mixtures of these reagents with Ar(1:10) were prepared and stored in 12-l. Pyrex vessels from which they were used.

The spectra were obtained on a 0.75-m Jarrell-Ash, Czerny-Turner scanning monochromator equipped with a S.S.R. photon counter and E.M.I. 9558QA photomultiplier tube.

Results and Discussion

Ar + CS_2.* The argon metastable energy transfer reaction with carbon disulfide was investigated under both tight and diffuse flame conditions, *i.e.*, with CS_2 flows of $\sim$10.0 and $\sim$0.10 μmol sec^{-1}, respectively. Under tight flame conditions (the flame was a pale yellow-green) the only banded emission was the strong CS($A^1\Pi$; $v' \leq 7 \rightarrow X^1\Sigma^+$; v'') system. A weak pair of S atom emissions at 1900.3 and 1914.7 Å were assigned to the ($^5S_2^\circ \rightarrow {}^3P_2$) and ($^5S_2^\circ \rightarrow {}^3P_1$) transitions. The atomic S($^5S_2^\circ$) state at $\sim$6.53 eV is energetically accessible only for CS($X^1\Sigma^+$) formation; S($^3S^\circ$) is also energetically feasible, but the S($^3S^\circ \rightarrow {}^3P$) transitions occur outside of our range of detection. The S($^1S \rightarrow {}^1D$) transition at 7726 Å would have been masked by an overlapping argon line from the discharge; however, even if S(^1S) is produced from Ar* + CS_2 it would be difficult to detect because removal by collisions with Ar[6] and CS_2 is fast. The S(^1S) quenching rate constants[6] for Ar and SCO have been reported to be $\lesssim 5 \times 10^{-15}$ and 1.0×10^{-11} cc molecules^{-1} sec^{-1}, respectively. The rate constant for S(^1S) quenching by CS_2 has not yet been reported, but is probably slightly larger than that for SCO. The mean radiative lifetime of the S(^1S) is $\sim$500 msec.[6] For diffuse flame conditions and 2 Torr, [Ar] $\sim 10^{17}$ molecules cc^{-1} and [CS_2] $\sim 10^{12}$ molecules cc^{-1},

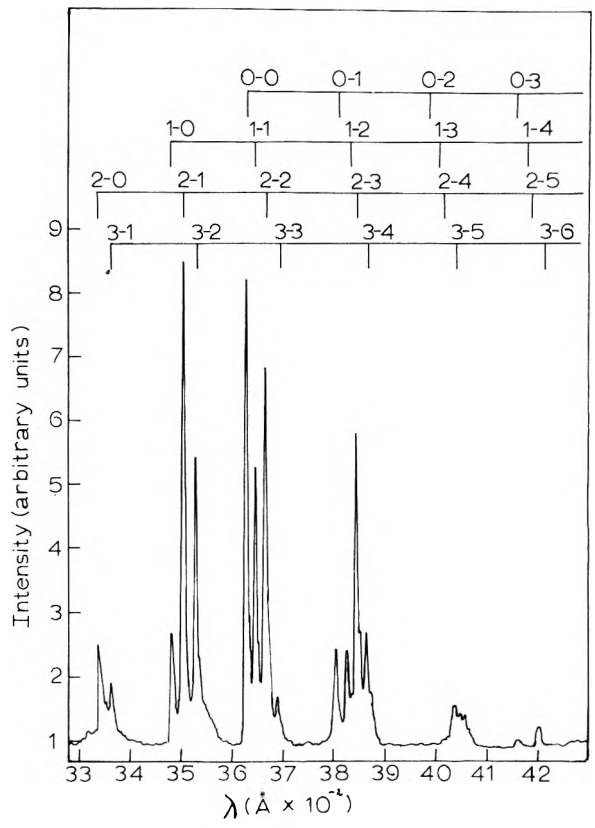

Figure 2. CS($a^3\Pi$; $v' \leq 3 \rightarrow X^1\Sigma^+$) spectrum from Ar($^3P_{0,2}$) + SCS reaction. Total pressure was 2 Torr. The CS_2 flow was $\sim$0.1 μmol/sec.

the ratio of quenching to radiative loss would be 50–100 and observation of the S($^1S \rightarrow {}^1D$) transition would not be expected. Under diffuse flame conditions the CS(A $\rightarrow$ X) and the S atom ($^5S^\circ \rightarrow {}^3P$) transition intensities decreased, as expected, for lower [CS_2], and a relatively strong CS($a^3\Pi$; $v' \leq 3 \rightarrow X^1\Sigma^+$; v'') Cameron emission Å. The suppression of the CS(a $\rightarrow$ X) emission with increasing [CS_2] indicated a fast electronic quenching reaction between the relatively long lived CS(a) and CS_2.[7a,b] The relative vibrational populations of CS($a^3\Pi$) were estimated from the ratios of the integrated band areas for a given progression to the total integrated area of the CS(a $\rightarrow$ X) emission; *i.e.*, $\Sigma_i A_{ij}/\Sigma_{ij} A_{ij}$, where A is the band area and i and j indicate the upper and lower vibrational states, respectively. For the data of Figure 2, 2-Torr total pressure, the populations are v' = 0(1.00), 1(0.86), 2(1.62), and 3(0.81). Data[7b] taken at 0.3 Torr gave relative vibrational populations of v' = 0(1.00), 1(1.31), 2(2.75), and 3(1.19); these must be close to the initial relative vibrational populations and evidently some relaxation has oc-

(6) R. J. Donovan and D. Husain, *Chem. Rev.*, **70**, 489 (1970), and references therein.

(7) (a) G. W. Taylor, unpublished results. The CS($a^3\Pi$) diatomic was generated from Ar* + $SCCl_2$, which gave the most intense downstream emission from this molecule. Experiments were done in which sufficient $SCCl_2$ was added to remove Ar*, then SCS, OCS, and additional $SCCl_2$ were added downstream of the Ar* + $SCCl_2$ flame. Using the fixed-point observation technique, quenching rate constants, k(SCS) $\geq 6.9 \times 10^{-11}$, k(OCS) $\geq 8.5 \times 10^{-11}$, and $k(SCCl_2) \geq 3.5 \times 10^{-11}$ cc molecules^{-1} sec^{-1}, were calculated from log $(I/I_0) = k_q[Q]t$. The reliability of these measurements is probably no better than a factor of 5. (b) L. G. Piper, W. C. Richardson, G. W. Taylor, and D. W. Setser, *Discuss. Faraday Soc.*, **53**, 100 (1972); (c) A. Tewarson and H. B. Palmer, *J. Mole. Spectrosc.*, **27**, 246 (1368); (d) H. B. Palmer, *J. Chem. Phys.*, **54**, 3245 (1971).

TABLE I: Frank-Condon Factors[a] for CS($a^3\Pi \rightarrow X^1\Sigma^+$)

	v'					
v''	0	1	2	3	4	5
0	3622[b]	3481	3353	3235	3128	3029
	0.774	0.192	0.029	0.004	0.000	0.000
1	3797	3642	3502	3374	3258	3151
	0.201	0.410	0.294	0.078	0.015	0.002
2	3988	3818	3664	3524	3397	3281
	0.023	0.322	0.165	0.315	0.132	0.034
3	4197	4008	3839	3685	3547	3421
	0.002	0.067	0.364	0.035	0.272	0.177
4	4426	4217	4030	3861	3709	3571
	0.000	0.008	0.123	0.339	0.000	0.192
5	4678	4445	4238	4052	3885	3734
	0.000	0.001	0.021	0.181	0.266	0.031

[a] Calculated on an IBM-360 computer by the "asymptotic expansion method" of Chang and Karplus.[8] [b] The upper value in table is the vacuum wavelength (A) of the bandhead calculated from the molecular constants[9b] and the lower number is the F-C factor.[8]

curred at 2-Torr pressure. The band strengths of CS(a → X) are not known, but the Franck-Condon (F-C) factors (Table I) were calculated by the "asymptotic expansion method" of Chang and Karplus,[8] using recent molecular constants.[9] The calculated F-C factors and integrated band intensities from the $\Delta v = -1$ sequence in Figure 2 yield relative vibrational populations of $v' = 0(1.00)$, $1(0.67)$, $2(1.13)$, and $3(0.65)$. The agreement with the populations from the integrated intensity method is satisfactory. Even under the most sensitive conditions, no $v' = 4$ level was ever detected. This may indicate a strong perturbation[9] at the $v' = 4$ level similar to that existing in the CO(a) state.[10a]

In the 4200-7200-Å region approximately 18 new bands were observed (see Figure 4 in ref 9b). The energy spacings and multiheaded character of these bands indicates that, at least, three band systems are involved and similarities between these bands and the known triplet-triplet emissions of CO[10] suggest that they should be assigned to higher CS triplet states. Unfortunately, these bands are weak and complex; thus a definitive analysis was not attempted.

Ar + SCO.* In earlier work[11a] (also see ref 4, Figure 2) we reported the very weak CS($a^3\Pi$; $v' \leq 2 \rightarrow X^1\Sigma^+$; v'') transition and the much stronger fourth positive CS($A^1\Pi$, $v' \leq 6 \rightarrow X^1\Sigma^+$, v'') from the "golden" Ar* + SCO flame. The intensity of the CS fourth positive from SCO was only slightly less than that from Ar* + SCS. The S($^5S^\circ \rightarrow {}^3P$) transitions were also present, being much stronger than those from Ar + SCS; S($^1S \rightarrow {}^1D$) and S($^3S^\circ \rightarrow {}^3P$) were not detectable for the reasons previously discussed. For tight flame conditions the CS(a → X) was insignificant relative to the CS(A → X) emission intensity; however, upon decreasing [SCO] (diffuse flame), the CS(a → X) intensity increased more than a factor of 100 relative to the total emission intensity and a fast electronic quenching[7a] of CS(a) by SCO must occur. For the same experimental conditions, the CS(a) vibrational populations were similar to those just discussed for Ar + CS_2 (Figure 2); emission from $v' > 3$ was never observed.

In addition to the CS* emission, strong CO* emissions, which are responsible for the golden color of the flame, were observed (Figure 3). The following transitions were assigned:[9,10] CO($a^3\Pi$; $v' \leq 3 \rightarrow X^1\Sigma^+$; v''), Cameron

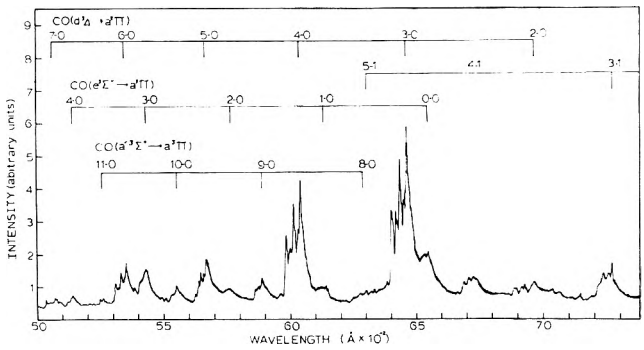

Figure 3. CO triplet-triplet band systems. The figure shows assignments to the triplet, Asundi, and Herman bands resulting from Ar($^3P_{0,2}$) + OCS reaction. Argon lines scattered from the discharge have been omitted from the figure.

bands (not included in Figure 3); CO($d^3\Delta$; $v' \leq 7 \rightarrow a^3\Pi$; v''), triplet bands; CO($e^3\Sigma^-$; $v' \leq 4 \rightarrow a^3\Pi$; v''), Herman system; and CO($a^3\Sigma^+$; $v' \leq 10 \rightarrow a^3\Pi$; v''), Asundi bands.

Ar + $SCCl_2$.* Only a limited number of experiments were conducted with thiophosgene because of its toxicity and the related inconvenience of handling. However, several interesting results were extracted from a brief examination. Emissions from CS(A; $v' \leq 7 \rightarrow X$; v'') and CS(a; $v' \leq 3 \rightarrow X$; v'') were present. The CS(a → X) intensity decreased by a factor of ~3-5 in changing from diffuse to tight flame conditions; indicating that $SCCl_2$ has a smaller rate constant for electronic quenching of CS(a) than either SCO or SCS (see ref 7a). Consequently, Ar* + $SCCl_2$ was investigated by mostly viewing the tight Ar* + $SCCl_2$ flame (pale yellow-green). The bands tentatively attributed to CS triplet-triplet emissions from Ar* + SCS also were observed from Ar* + $SCCl_2$ in the 4200-7000-Å region. In addition to the emissions just described, an apparent continuum maximum at 2050 Å was observed. This continuum could not be observed below 1850 Å on our instrument because of the $O_2(B^3\Sigma_u^- \rightarrow X^3\Sigma_g^-)$ Schumann-Runge absorption; however, vacuum-ultraviolet spectroscopic studies[11b] show a cut-off of the continuum between 1600 and 1700 Å. The observed continuum is probably from Cl_2*; however, unambiguous assignment has not yet been made. In the Ar* + $OCCl_2$ reaction the 3075- and 2580-Å Cl_2 continua were present,[11a] but in Ar* + $SCCl_2$ this region is overlapped by intense CS(A → X) emission.

Xe + SCO.* The reaction of Xe* with carbonyl sulfide gave no detectable chemiluminescence from either OCS or fragments. Emission from fragments was not expected since Xe* (~9.4 eV) only has sufficient energy to dissociate OCS *without* electronic excitation of the fragments.

Xe + SCS.* Four experimental configurations of the apparatus were tested and are designated as C-1 through C-4. (C-1) The hollow cathode discharge was separated from the initial mixing zone by a single light trap and 90° bend. The delay time, calculated from the reciprocal of the flow velocity times the linear distance between the discharge and mixing zone, was 1-2 msec. (C-2) This configuration was identical with C-1 except the distance be-

(8) T. Y. Chang and M. Karplus, *J. Chem. Phys.*, **52**, 783 (1970).
(9) (a) R. W. Field and T. H. Bergeman, *J. Chem. Phys.*, **54**, 2936 (1971); (b) G. W. Taylor, D. W. Setser, and J. A. Coxon, *J. Mole. Spectrosc.*, **44**, 108 (1972).
(10) (a) P. H. Krupenie, *Nat. Stand. Ref. Data Ser.*, **No. 5**, (1966); (b) R. W. B. Pearse and A. G. Gaydon, "The Identification of Molecular Spectra," 3rd ed, Wiley, New York, N. Y., 1963.
(11) (a) G. W. Taylor and D. W. Setser, *Chem. Phys. Lett.*, **8**, 51 (1971); (b) W. H. Duewer, Kansas State University, private communication.

TABLE II: Observations of the Xe* + SCS Reaction as a Function of the Experimental Configuration

Energy carries present	Configuration[b]	Observed spectrum
Ar*, Xe($^3P_{0,1,2}$)	C-1[c]	CS(A; $v' \sim 3 \rightarrow X$)[c] and (a; $v' \leq 2 \rightarrow X$)
Ar*, Xe($^3P_{0,1,2}$)	C-2[c]	CS(A; $v' \sim 3 \rightarrow X$)[c] and (a; $v' \leq 2 \rightarrow X$)
Xe($^3P_{1,2}$)	C-3	CS(a; $v' \leq 2 \rightarrow X$)
Xe($^3P_{0,1,2}$)	C-4	CS(a; $v' \leq 2 \rightarrow X$)

[a] The presence of the CS(A → X) emission in this system indicates the presence of Ar* formed as a consequence of resonance radiation trapping by the argon carrier gas. The argon state cannot be definitely assigned but probably is $^3P_1$ or $^3P_2$. [b] See text for a description of the configurations. [c] The CS(A → X) spectrum in this system is very weak, and $v' \sim 3$ is the highest detectable level; however, the CS(A → X) resulting from Ar* + CS_2 is excited to the $v' = 6$ level.

tween discharge and mixing zone was lengthened so that the delay time was 6–8 msec. (C-3) The discharge and initial mixing zone were separated by two light traps and two 90° bends. The delay time was 6–8 msec. (C-4) This configuration was identical with C-3 except the delay time was shortened to 2–3 msec.

A diagnostic test for Ar^+ now is available;[12] namely, adding HBr and observing emission from HBr^+ ($A^2\Sigma^+ \rightarrow X^2\Pi$;). This test was applied to C-1 of the present system, but no evidence for HBr^+ (A → X) emission was found. As far as is known, metastable argon atoms ($^3P_{0,2}$) in an approximate ratio of 1:5 and trace quantities of atoms in the resonance states ($^3P_1$, $^1P_1$) are the only significant energy carriers from this hollow cathode flow apparatus.

The results of the Xe* + SCS reaction for various experimental configurations are summarized in Table II. For short delay times (1–2 msec) between the discharge and mixing zone and for a tight flame Xe* + SCS gave CS(A; $v' \sim 3 \rightarrow X$, v'') and (a; $v' \sim 2 \rightarrow X$; v''). These emissions were quite weak and the highest vibrational levels assigned are uncertain. Upon extending the delay time to 6–8 msec (C-2), the CS(A), and (a) were *still* evident. The addition of a second light trap and 90° bend (C-3) at the long delay time (6–8 msec) caused the CS(A) emission to disappear, but the CS (a; $v' \leq 2 \rightarrow X$; v'') remained. The delay time was then decreased to 2–3 msec (C-4), and the CS(a) was still evident, but the CS(A) did not return.

The disappearance of the CS(A → X) from the C-3 and 4 configurations is clear evidence that this emission does not arise from the Xe($^3P_0$) reaction because $^3P_0$ was present in C-4. Apparently CS(A) emission arises from Ar* + SCS with Ar* (the excited state was not identified, but could be $^3P_1$ or $^3P_2$) being formed by resonance radiation trapping outside of the discharge.[2] The CS(A → X) emission was not found from Xe($^3P_0$) even though the 9.4 eV of energy is sufficient to dissociate SC–S and to excite the CS(A; $v' \leq 6$)! The Xe($^3P_{1,2}$) + SCS dissociative excitation must give only CS(a; $v' \leq 2 \rightarrow X$; v'') since this emission was found from C-3, with no Xe ($^3P_0$) present. It is worth noting that the CS(a → X) spectrum from Xe ($^3P_{1,2}$) appears unchanged with respect to vibrational excitation in the presence of Xe($^3P_0$). It was earlier reported[13] that CS(A) was excited from Xe($^3P_1$) + SCS, but the present result shows this is not the case.

Relative Intensities. The relative integrated band intensities taken from diffuse flame conditions for each Ar* + R–CS reaction are given in Table III. The reported values are the ratios of the integrated peak areas for a given band system to the total integrated areas of all observable emissions between 1900 and 8000 Å, corrected for the monochromator response as a function of wavelength. The relative intensities of the CS(a → X) and CO(a → X) were obtained under diffuse flame conditions, where losses due to electronic quenching by the parent molecule should be minimized, and are noted in Table III as being lower limit values to account for any remaining collisional losses. The most significant source of error in the relative intensities arises from the necessary extrapolation of the monochromator response curve below ~2200 Å. This is most significant to the S lines at ~1900 Å and to a few of the CS(A → X) bands; however, the extrapolation is not believed to introduce a serious error.

Wauchop and Broida[14] have recently shown that CO($d^3\Delta$, $a'^3\Sigma^+$ and $a^3\Pi$) come from $CO_2^+ + e^-$ recombination in the He(2^3S) + CO_2 reaction. The possibility that the CS triplet states from Ar($^3P_{0,2}$) + R–CS arise from ion–electron recombination was tested in the present study by adding SF_6 as an electron scavenger to the Ar* + R–CS reaction and observing the relative integrated band intensities. The addition of SF_6 did not affect the relative band intensities in any way; therefore, all of the observed emissions from Ar* + R–CS are assigned to dissociative excitation reactions.

Table III is a first step toward partitioning the rate constants[7b] for quenching of metastable argon atoms into the individual reaction channels. The ionization potentials of SCS (10.08 eV), OCS (11.24 eV), and $SCCl_2$ (~10 eV) all lie just below the metastable Ar atom energy (11.7 eV); therefore, Penning and associative ionization reaction channels are possible and prevent assignment of absolute cross sections to the known channels. Additionally, some reaction channels probably exist that are beyond the detectability of the present experiments; *e.g.*, the S($^3S^\circ$ → ^3P) transitions already suggested.

The rate constants and reactive cross sections (in parentheses) for quenching Ar($^3P_2$) by OCS and SCS have recently been reported as 5.0×10^{-10} (98 Å^2) and 5.6×10^{-10} cc molecule^{-1} sec^{-1} (115 Å^2), respectively.[7b] The Ar($^3P_2$) quenching rate constant with $SCCl_2$ has not yet been determined. Approximately 70% of the dissociative excitation from Ar($^3P_{0,2}$) + OCS results in excited carbon monoxide and ground state (^3P) sulfur atoms. The ratio of CO-to-CS emissions is ~20:1. Of the available channels leading to CO, two of these constitute 92% of the total CO production.

$$Ar(^3P_{0,2}) + OCS \rightarrow CO(d^3\Delta) + S(^3P) + Ar(^1S_0) \quad (1)$$

$$Ar(^3P_{0,2}) + OCS \rightarrow CO(X^1\Sigma^+) + S(^5S^\circ) + Ar(^1S_0) \quad (2)$$

Reaction 2 accounts for 30% of the total reaction and is one of the few examples in these energy transfer reactions where spin is not conserved. This same reaction was observed, but very weakly ~1.0%, in the Ar* + SCS reaction.

$$Ar(^3P_{0,2}) + SCS \rightarrow CS(X^1\Sigma^+) + S(^5S^\circ) + Ar(^1S_0) \quad (3)$$

The energy of the $S(^5S^\circ)$ is 6.53 eV; therefore, reaction 2 and 3 will be 2.1 and 1.1 eV exothermic, respectively (see discussion of ΔH_{f0}° (CS) that follows). The exothermicity

(12) M. J. Haugh and K. D. Bayes, *J. Chem. Phys.*, **54**, 1472 (1971).
(13) G. W. Taylor and D. W. Setser, 162nd National Meeting of the American Chemical Society, Washington, D. C., Sept 1971.
(14) T. W. Wauchop and H. P. Broida, *J. Quant. Spectrosc. Radiat. Transfer*, **12**, 371 (1972).

TABLE III: Relative Intensities[a] of Observed Spectra

Reaction[b]	Observed spectra							
	CS(a → X)[c]	CS(A → X)	CS(triplets → a)	CO(a → X)[c]	CO(d → a)	CO(a′ → a)	CO(e → a)	S($^5S^0$ → ^3P)
Ar* + SCS	≥0.01	0.97	0.02					≤0.01
Ar* + OCS	≥0.01	0.03		≥0.04	0.58	0.03	0.01	0.30
Ar* + $SCCl_2$[d]	≥0.09	0.88	0.03					

[a] The relative intensities were taken as the ratio of the total band area of the observed spectrum to the total area of all observed emiss ons (1950–8000 Å), adjusted for response of the monochromator as a function of wavelength. Reaction channels (Penning ionization, etc.) which do not result in emission, of course, are not included. [b] The ratios reported here were taken from spectra obtained solely from the C-4 experimental configuration. [c] The relative intensities of the CS(a → X) and CO(a → X) have been indicated as being somewhat larger than the number given to allow for possible electronic quenching by the parent molecule. [d] Does not include the vacuum-ultraviolet continuum.

TABLE IV: Summary of Diagnostic Tests for Ar* and Xe* $^1P_1$, $^3P_0$, $^3P_1$, and $^3P_2$ States[a]

System	Level	Reagent	Reaction	Diagnostic test
Ar*	$^1P_1$	N_2	$Ar(^1P_1) + N_2 \rightarrow N_2(C^3\Pi_u; v' \leq 3) + Ar(^1S_0)$	Presence of $v' = 3$ in N_2(C → B)
Ar*	$^3P_0$	N_2	$Ar(^3P_0) + N_2 \rightarrow N_2(C^3\Pi_u; v' \leq 2) + Ar(^1S_0)$	$N_2(C^3\Pi)\mu$ with $v' \leq 2$
Xe*[b]	$^3P_0$	C_2N_2	$Xe(^3P_0) + C_2N_2 \rightarrow CN(B^2\Sigma; v' \leq 2) + Xe(^1S_0)$	Presence of CN(B; $v' \leq 2$ → A)
Ar*[c]	$^3P_1$			None
Xe*[c,d]	$^3P_1$	N_2	$Xe(^3P_1) + N_2(B^3\Pi_g; v' \leq 5) + Xe(^1S_0)$	Presence of $v' = 5$ in N_2(B → A)

[a] Most of these diagnostic tests were taken from ref 2–4. [b] An additional test was discovered for $Xe(^3P_0)$ using Xe* + N_2; it is the presence of the $N_2(B'^3\Sigma_u^-; v' \leq 2 \rightarrow X^1\Sigma_g^+; v'')$ spectrum. [c] Ar* and Xe*($^3P_1$) concentrations are maintained by a collisional excitation–deexcitation process of the $^3P_0$ and $^3P_2$ states leading to a ($^3P_1$) steady-state concentration (see R. Turner, *et al.*, *Phys. Rev. B*, **15**, 121 (1967); **140**, A426 (1955); *Can J. Phys.*, **41**, 1949 (1963)). [d] The presence of $Xe(^3P_2)$ is implied by the presence of N_2(B; $v' \leq 4$).

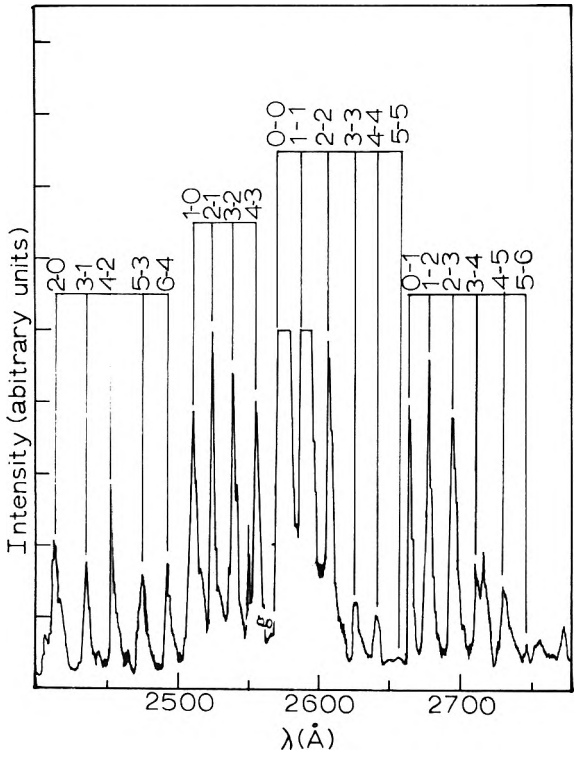

Figure 4. Expanded view of the 2–0, 1–0, 0–0, and 0–1 sequences of the CS forth positive bands. The highest observed level of vibrational excitation is to the $v' = 6$ level. The 7–5 transition *may* be present, but it is badly overlapped by the 1–0 transition.

of neither reaction is sufficient to give an electronically excited diatomic fragment, but the S($^3S°$) state may be formed rather than S($^5S°$).

$D_0°(SC-O)$ and $\Delta H_{f0}°$ (CS) from Ar($^1P_1$) + SCO. The reaction, $Xe(^3P_{1,2})$ + SCS → CS (a; $v' \leq 2$) + S(^3P) + $Xe(^1S_0)$, did not give a useful upper limit for $D_0°$ (SC–S), since the high levels of CS(a) were not found. For the Ar* reactions a sharp cut off in the vibrational populations at $v' = 4$ was observed. Thus the CS($a^3\Pi \rightarrow X^1\Sigma^+$) emission system was not useful as a means for determining limits to the bond energies.

The reaction Ar* + SCO was studied using the experimental configuration C-1. The test for $Ar(^1P_1)$ (see Table IV) was carried out and the presence of $N_2(C^3\Pi_u, v' = 3)$ confirmed that Ar ($^1P_1$) was present. The resonance state may be removed by using configurations C-3 or C-4 containing double light traps; however, the intensity of the CS(A → X) was so diminished in these configurations that assignment of the highest vibrational level was difficult. Therefore, we chose to use the data having $Ar(^1P_1)$ as the highest energy carrier. The reaction, $Ar(^1P_1)$ + SCO → CS(A; $v' \leq 6$) + O(^3P) + $Ar(^1S_0)$ may be used to calculate a reliable upper limit for $D_0°$ (SC–O) and $\Delta H_{f0}°$-(CS), since the lifetime of CS(A) (2×10^{-7} sec)[15] is short and collisional relaxation does not occur. The energy of the highest observed level (Figure 4), CS($A^1\Pi$; $v' = 6$), is 44,811.8 cm^{-1} above CS($X^1\Sigma^+$; $v'' = 0$)[16] and the energy of $Ar(^1P_1)$ is 95,400 cm^{-1} above $Ar(^1S_0)$.[2] The 0°K enthalpies of formation for OCS (11,577.1 cm^{-1}) and O($^3P_2$) (20,635.8 cm^{-1}) were taken from JANAF Tables.[5a] Combining these terms according to eq I, results in

$$\Delta H_{f0}°(CS) \leq E[Ar(^1P_1)] - E[CS(A; v' \leq 6)] - \Delta H_{f0}°[O(^3P_2)] + \Delta H_{f0}°(OCS) \quad (I)$$

$\Delta H_{f0}°(CS) \leq 52.5$ kcal/mol and from this value $D_0°$(SC–O) ≤ 144.6 kcal/mol is calculated. From the $\Delta v = +2$ sequence in Figure 4 it seems likely that $v' = 7$ is present, but the 7–5 band badly overlapped by the $\Delta v = +1$ sequence. Every attempt to unambiguously detect $v' = 7$ failed and the upper limit value of $\Delta H_{f0}°$(CS) was calcu-

(15) S. J. Silvers, T. H. Bergeman, and W. Klemperer, *J. Chem. Phys.*, **52**, 4385 (1970).
(16) A. Lagerqvist, H. Westerlund, C. V. Wright, and R. F. Barrow, *Ark. Fys.*, **14**, 387 (1958); **18**, 543 (1960).

lated using $v' = 6$. The calculated values compare favorably but are substantially lower (~2 kcal) than the presently accepted values for $\Delta H_{f0}°$(CS), 54.2 + 5 kcal/mol,[5a] and $D_0°$(SC-O), 150 ± 5 kcal/mol.[5b-d] The most uncertain quantity in eq I is E[CS(A)], since the presence of emission from $v' = 7$ could not be definitely ascertained. Inclusion of the $v' = 7$ level would lower $\Delta H_{f0}°$(CS) by ~2.5 kcal/mol. The possibility of dissociation from OCS molecules with excitation in the bending modes (~1.5 kcal/quantum)[17] was neglected; this could raise the upper limit of $\Delta H_{f0}°$(CS). However, excitation of the OCS bending modes would be expected to result in rotational rather than vibrational excitation of CS($A^1\Pi$). Since the translational and rotational energy of the products have been neglected, and since higher CS(A) vibrational levels may be populated, $\Delta H_{f0}°$(CS) ≤ 52.5 kcal/mol and $D_0°$(SC-O) ≤ 144.6 kcal/mol are upper limit values.

Okabe[18] has recently reported values of $\Delta H_{f0}°$(CS) = 64.96 ± 0.4 kcal/mol and $D_0°$(SC-S) = 102.92 ± 0.32 kcal/mol from the threshold measurement of the vacuum-ultraviolet photodissociation of SCS to CS($A^1\Pi$) + S(^3P). These values critically disagree with both our derived $D_0°$(SC-S) ≤ 90.4 kcal/mol and the accepted values.[5] Okabe[18] observed the total fluoresence (2300-4200 Å) from CS_2 as a function of the incident wavelength; the onset of fluorescence was assigned to an incident photon energy of 9.27 eV (1337 Å). The total fluorescence was not resolved into vibrational components, but experiments with the 1236-Å Kr line were done in which the CS($A^1\Pi$; $v' \leq 5 \rightarrow X^1\Sigma^+$) emission was resolved. The value of $D_0°$(CS-S) ≤ 4.46 eV is the threshold energy, 9.27 eV, less T_0[CS($A^1\Pi$; $v' = 0$)], 4.81 eV.[16] Okabe's value of $D_0°$(SC-S)[18] also is an upper limit measurement, since the onset of the dissociation must be selected for the correct dissociative mechanism and the initial translational, rotational, and vibrational energies of the products have been neglected.

A significant uncertainty in Okabe's value[18] could be from the assumption that CS($A^1\Pi$) is produced in $v' = 0$ at the threshold energy. The inclusion of initial vibrational excitation in CS($A^1\Pi$) would lower Okabe's $D_0°$(SCS) by ~2.7 kcal/vibrational level. Okabe[18] has argued that S($^1D_2$) is not produced in the photolysis of CS_2 at 1200–2000 Å on the basis of photolysis studies[19] at 1850–2300 and 1900–2100 Å. However, both of these studies were done at high pressures of inert bath gases and recent evidence shows that S($^1D_2$) quenching rates are reasonably fast.[6] In our opinion the production of S($^1D_2$) in the photolysis region 1200–2000 Å cannot yet be eliminated from consideration.[20]

Acknowledgments. The author gratefully acknowledges the financial support of this work by the U. S. Army Research Office—Durham under Grant No. DA-AROD-31-124-71-G127. The advice and support of Dr. D. W. Setser is thankfully acknowledged. The author also thanks Dr. W. H. Duewer for his unpublished vacuum-ultraviolet data and R. L. Johnson for his computer programming of the F-C factor calculations. The author also is grateful for the referee's very helpful suggestions for improvement of the first version of this paper.

(17) G. Herzberg, "Molecular Spectra and Molecular Structure. III. Electronic Spectra and Electronic Structure of Polyatomic Molecules," Van Nostrand, Princeton, N. J., 1966.
(18) H. Okabe, *J. Chem. Phys.*, **55**, 4381 (1972).
(19) (a) A. B. Callear, *Proc. Roy. Soc., Ser. A*, **276**, 401 (1963); (b) M. de Sorgo, A. J. Yarwood, O. P. Strausz, and H. E. Gunning, *Can. J. Chem.*, **43**, 1886 (1965).
(20) Note Added in Proof. Recently, several studies[21] in support of the higher value of $\Delta H_{f0}°$(CS) have appeared in the literature. The most recent values of $\Delta H_{f0}°$(CS) range from ~63[21a] to ~ 70 kcal/mol;[21b] approximately 10–17 kcal/mol above the accepted value[5a] and the present study. Nearly all of these recent studies[21] are based on CS_2 as the CS diatomic source, while this study was based on OCS as the diatomic precursor. The discrepancy in the value of $\Delta H_{f0}°$(CS) suggests that our determination might be improved by an adjustment in the value of $\Delta H_{f0}°$(OCS).
(21) (a) G. Hancock, C. Morley, and I. W. M. Smith, *Chem. Phys. Lett.*, **12**, 193 (1971); (b) D. L. Hildenbrand, *ibid.*, **15**, 379 (1972); (c) S. Bell, T. L. Ng, and C. Suggitt, *J. Mol. Spectrosc.*, **44**, 267 (1972).

Pressure-Jump Relaxation Kinetics of the Complexation of Nickel(II) Thiocyanate in Methanol[1]

Joseph Williams and Sergio Petrucci*

Department of Chemistry, Polytechnic Institute of Brooklyn, Brooklyn, New York 11201 *(Received May 3, 1972)*

Pressure-jump relaxation spectra of the complexation of $Ni(NCS)^+$ and NCS^- in methanol in the concentration range 10^{-3}–10^{-1} M and at the temperatures 19.7, 25, 30, and 33.5° are reported as the averaged relaxation times. The data are interpreted by a two-step dissociative interchange mechanism. In terms of this mechanism the activation parameters suggest an increase of the activation entropy for solvent exchange of $Ni(MeOH)_5NCS^+$ with respect to $Ni(MeOH)_6^{2+}$. Calculations of the outer-sphere parameters ΔS_0 and ΔH_0 are done in a corrected way by means of the Fuoss theory of association. Alternate calculations of ΔS_0 and ΔH_0 by means of the Bjerrum theory are reported.

Introduction

After the development of the techniques of relaxation kinetics and their application to aqueous solutions,[2a] activity in recent years has shifted to the investigation of the mechanism of complexation of transition metals in nonaqueous solvents. The general Eigen multistep mechanism,[2a] reclassified by Langford[2b] as dissociative interchange, has found support in the work by Ellgen and Pearson[3] for Ni^{2+} in methanol with various nucleophilic ligands.

More recently, however, Bennetto and Caldin[4] have questioned the general validity of the relation $k_f = K_0k_1$ (where K_0 is the outer-sphere ion-pair pre-equilibration constant and k_1 is the rate constant for solvent exchange). Bennetto and Caldin[4] argue that values of k_f(expt) as low as 1/100 of the required product K_0k_1 have been found. It is true that the k_{exch} should be multiplied by a statistical factor $1/S$, with S a parameter corresponding to the solvation number of the cation in the second coordination shell. However, S has been found in water[2b] to be equal to 5–10 (by comparing k_f(expt) with K_0k_{exch}), about one order of magnitude too small in order to rationalize the above differences.

The doubt that some of the observed discrepancies[5] were due to the theoretically calculated K_0 was clarified when an investigation[6] of the outer-sphere ion-pair formation proved that the calculated K_0's correspond in order of magnitude to the experimental ones.

The problem of determining the mechanism of complexation becomes even more challenging when the entrance of the second ligand is considered. Hammes and Steinfeld[7] were the first to notice changes in the rate constants of substitution with respect to the entrance of the first ligand in the case of aqueous Ni^{2+} and Co^{2+} with amino acids. A qualitative rationalization in terms of a releasing effect on the rate of the exchange of the solvent by the first ligand was proposed. Later, similar results were found by Hunt, *et al.*, in a series of papers.[8]

Recently the pressure jump kinetics of $NiNCS^+$ with NCS^- in MeOH at 25° have been investigated by Hoffmann, *et al.*[9] The same rate constant, within experimental error, that Ellgen and Pearson[3] determined for the process $Ni(MeOH)_6^{2+} + NCS^- \rightarrow Ni(MeOH)_5NCS^+$, namely, $k_f = 1.5 \times 10^5$ M^{-1} sec^{-1}, has been found. However, whereas $K_0 = 150$ M^{-1} for a 2:1 electrolyte, K_0 is only 10 M^{-1} for a 1:1 electrolyte. Therefore, for the reaction studied by Ellgen and Pearson (assuming the interchange mechanism) $k_1 = 1 \times 10^3$ sec^{-1} which is in excellent accord with the rate constant for solvent exchange. On the contrary, for the reaction studies by Hoffmann, *et al.*,[9] $k_1 = 15 \times 10^3$ sec^{-1}, that is, 15 times as high. The doubt that a circular argument had been used, namely, that the differences were due to the assumption of the mechanism rather than to differences in rates of exchange of NiS_6^{2+} with respect to NiS_5NCS^+ (S = MeOH), was present.

One way to try to ascertain the reality of a difference between the two reactions was to determine the parameters of activation for the second reaction. For this reason it was decided to reinvestigate $Ni(NCS)_2$ in methanol by the available pressure-jump relaxation technique extending the work to various temperatures.

Experimental Section

The pressure-jump instrumentation has been described elsewhere.[5,10] For the present work the 3C-66 Tektronix carrier amplifier connected to the 564 oscilloscope was used. The temperature of the solution was maintained within ±0.05° by a Forma Junior circulating bath. The temperature of the solutions in the pressure-jump cell was measured by a Pt—Pt-10% Rh thermocouple assembly within ±0.1°.

(1) This work is part of the thesis of J. Williams in partial fulfillment to the requirements of the Ph.D. degree, Polytechnic Institute of Brooklyn. Support by the IBM Corporation in the form of a graduate fellowship to J.W. is acknowledged.

(2) (a) M. Eigen and L. DeMaeyer, "Techniques of Organic Chemistry," Vol. VIII, Part II, 2nd ed, S. L. Friess, E. S. Lewis, and A. Weissberger, Ed., Interscience, New York, N. Y., 1963, p 895; (b) C. H. Langford and H. Gray, "Ligand Substitution Reactions," W. A. Benjamin, New York, N. Y., 1965; C. H. Langford and T. Stengle, *Annu. Rev. Phys. Chem.*, **19**, 193 (1968); C. H. Langford, "Ionic Interaction," Vol. II, S. Petrucci, Ed., Academic Press, New York, N. Y., 1971 Chapter I.

(3) R. G. Pearson and P. Ellgen, *Inorg. Chem.*, **6**, 1379 (1967).

(4) H. P. Bennetto and E. F. Caldin, *J. Chem. Soc.*, 2191, 2198 (1971).

(5) G. Macri and S. Petrucci, *Inorg. Chem.*, **9**, 1009 (1970).

(6) A. Fanelli and S. Petrucci, *J. Phys. Chem.*, **75**, 2649 (1971).

(7) G. G. Hammes and J. G. Steinfeld, *J. Amer. Chem. Soc.*, **84**, 4639 (1962).

(8) M. Grant, H. W. Dodgen, and J. P. Hunt, *J. Amer. Chem. Soc.*, **92**, 2321 (1970); A. G. Desai, H. W. Dodgen, and J. P. Hunt *ibid.*, **91**, 5001 (1969); **92**, 798 (1970).

(9) F. Dickert, H. Hoffmann, and W. Jaenicke, *Ber. Bunsenges. Phys. Chem.*, **74**, 500 (1970).

(10) D. Saar, G. Macri, and S. Petrucci, *J. Inorg. Nucl. Chem.*, **33**, 4227 (1971).

$Ni(NCS)_2$ (K & K Labs.) was dried at 105° and used without further purification. Methanol (Matheson Coleman) (ACS) was distilled over aluminum amalgam in a 5-ft all-Pyrex Vigreux column collecting only the central portion (about 1/3). The boiling point was 64.5°. Solutions were prepared by weighing $Ni(NCS)_2$ on an analytical balance (Mettler 6 H) and dissolving the salt into a volumetric flask. Dilutions from this stock solution were prepared by pipetting a desired amount into a volumetric flask and diluting to mark with distilled methanol. The comparison solution for the pressure-jump cell was prepared by matching the impedance of the $Ni(NCS)_2$ solution to be examined with a methanolic solution of Bu_4NBr.

Two stock solutions were prepared during the present work. Dilutions from both solutions gave the same results within experimental error.

Filling of the pressure-jump cell took less than 60 sec. Longer period exposure to atmosphere gave no apparent deviations in pressure-jump relaxation spectra.

After having filled the cell, the system was left to reach temperature equilibrium; generally, 1 hr was sufficient. This was checked by the pressure-jump recording which was repeated at 15-min intervals until constancy of relaxation times within experimental error was reached. About five–seven photographs of the relaxation spectra were recorded for each solution.

Results

Table I reports the concentrations and averaged relaxation times with their standard deviations at the various temperatures investigated. The relaxation times were calculated from the oscillograph recordings as $1/e$ of the ordinate corresponding to the maximum displacements of the bridge potential.

Calculations

In the concentration range investigated (10^{-1}–10^{-3} M) the concentration of Ni^{2+} is negligible (Table II). Hoffmann, *et al.*,[9] have shown that the average ligand number $\bar{n}$ determined through potentiometric titrations can be quantitatively reproduced by considering only the species $NiNCS^+$ and $Ni(NCS)_2$ without the necessity of accounting for higher aggregates such as $Ni(NCS)_3^-$ and $Ni(NCS)_4^{2-}$. The two thermodynamic formation constants for the two former species are[9] $K_1 = 4.9 \times 10^5\ M^{-1}$ and $K_2 = 2000\ M^{-1}$ at 25°.

TABLE I: Concentrations of $Ni(NCS)_2$, Averaged Relaxation Times, and Their Standard Deviations at the Various Temperatures Investigated

C, M	τ, msec	C, M	τ, msec
	t = 19.7°		t = 25°
		0.001	4.08 ± 0.05
0.002	6.65 ± 1.33	0.002	3.74 ± 0.10
0.005	4.70 ± 0.50	0.005	2.63 ± 0.17
0.010	3.76 ± 0.39	0.010	1.84 ± 0.24
0.025	2.37 ± 0.11	0.025	1.31 ± 0.10
0.05	1.56 ± 0.10	0.05	0.88 ± 0.03
0.10	1.21 ± 0.15	0.10	0.67 ± 0.04
	t = 30°		t = 33.5°
0.001	3.41 ± 0.21	0.001	2.70 ± 0.11
0.002	2.82 ± 0.10	0.002	2.09 ± 0.12
0.005	2.17 ± 0.06	0.005	1.50 ± 0.20
0.010	1.45 ± 0.07	0.010	1.20 ± 0.09
0.015	0.93 ± 0.09	0.025	0.77_5 ± 0.039
0.05	0.72 ± 0.03	0.05	0.57_1 ± 0.03_6
0.10	0.50 ± 0.04	0.10	0.38_6 ± 0.01_0

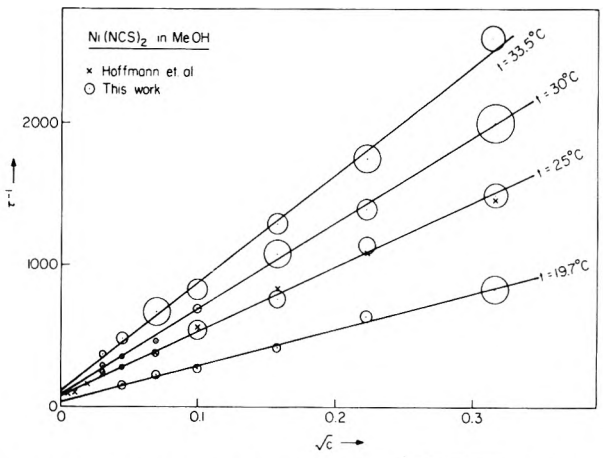

Figure 1. Plot of τ^{-1} (sec^{-1}) *vs.* $\sqrt{[Ni(NCS)_2]}$ ($M^{1/2}$) for $Ni(NCS)_2$ at the temperatures investigated.

Because of the above, at 25° the system $Ni(NCS)_2$ in MeOH in the concentration range in question (Table II) is in effect a 1:1 electrolyte, that is, $NiNCS^+$ and NCS^- partially associated to $Ni(NCS)_2$, all the other species being negligible.

This being the case, a plot of τ^{-1} *vs.* $\sqrt{C}$, with C the total concentration of electrolyte, should be approximatively a straight line. Indeed, according to Eigen[2a] for a symmetrical electrolyte one may write

$$\tau^{-1} = k_f\theta + k_R \qquad (1)$$

where

$$\theta \cong 2\alpha C\gamma_\pm^2$$

and

$$K = k_f/k_R$$

for large K one has $\alpha = 1/\sqrt{Kc}$ and taking $\gamma_\pm^2 \approx 1$ as a first approximation

$$\tau^{-1} \cong \frac{2k_f}{\sqrt{K}}\sqrt{C} + k_R \qquad (2)$$

Plots of τ^{-1} *vs.* $\sqrt{C}$ for $Ni(NCS)_2$ in MeOH at 19.7, 25, 30, and 33.5° are shown in Figure 1. The solid straight lines have been calculated by least-squares analysis. This analysis gives at 25° a slope = 4523.9 $M^{-1/2}$ sec^{-1} and an intercept = 78.80 sec^{-1}. Ratio of slope over intercept gives K = 824 M^{-1} which is of the same order of magnitude as the thermodynamic[9] K_2 = 2000 M^{-1}. Then $k_f = 6.49 \times 10^4\ M^{-1}\ sec^{-1}$ and $k_R = 78.8\ sec^{-1}$.

In the same figure the crosses represent the average data of Hoffmann, *et al.*,[9] at 25°. The agreement with the present data is excellent. The straight lines reproduce the trend of the data without systematic deviations within experimental error.

At 25° it would be enough to use the value of K_2 = 2000 M^{-1} to compute θ. Since, however, no association data are available at the other temperatures, a successive approximation method has been tested to see whether kinetic data would suffice to provide K_2 and therefore θ. With the value of K_2 determined from the τ^{-1} *vs.* $\sqrt{C}$ plot, a

TABLE II: Concentration of Various Species Present for $Ni(NCS)_2$ in MeOH in the Concentration Range 10^{-3}–10^{-1} M[a]

$[Ni(NCS)_2]$, M[b]	$[Ni^{2+}]$, M	$[NiNCS^+]$, M	$[NCS^-]$, M	$[Ni(NCS)_2]$, M
0.001	3.00×10^{-6}	5.72×10^{-4}	5.80×10^{-4}	4.30×10^{-4}
0.005	4.00×10^{-6}	1.55×10^{-3}	1.57×10^{-3}	3.45×10^{-3}
0.010	4.60×10^{-6}	2.48×10^{-3}	2.50×10^{-3}	7.50×10^{-3}
0.050	7.06×10^{-6}	7.52×10^{-3}	7.53×10^{-3}	4.25×10^{-2}
0.10	8.9×10^{-6}	1.15×10^{-2}	1.15×10^{-2}	8.85×10^{-2}

[a] Calculations based on $K_1 = 490{,}000\ M^{-1}$ and $K_2 = 2000\ M^{-1}$. [b] Stoichiometric concentration of the salt.

TABLE III: Results of k_f (M^{-1} sec^{-1}), k_R (sec^{-1}), Their Standard Deviation, and Average Ratio $\bar{K}$ (M^{-1}) for $Ni(NCS)_2$ in MeOH at the Temperatures Investigated

t, °C	k_f, $(M^{-1}\ sec^{-1})10^{-5}$	k_R, sec^{-1}	$\bar{K}_2$, $(M^{-1})\ 10^{-3}$
19.7	0.66 ± 0.04	27 ± 27	
25	1.40 ± 0.05	73 ± 25	1.9
30	2.21 ± 0.08	72 ± 33	3.1
33.5	3.32 ± 0.14	91 ± 54	3.7

first set of values of θ has been computed as follows. A two equation system has been solved

$$K_2 = \frac{1-\alpha}{\alpha^2 C \gamma_{\pm}^2}$$
$$-\log \gamma_{\pm}^2 = \frac{2S\sqrt{C\alpha}}{1 + Aa\sqrt{C\alpha}} \qquad (3)$$

where S and A are the Debye–Hückel values. The parameter a has been set $a = 6 \times 10^{-8}$ cm, as done by Ellgen and Pearson.[3] Starting with the above value, within two cycles of approximations, one obtains $k_f = 1.40 \times 10^5$ M^{-1} sec^{-1} and $k_R = 73.17$ sec^{-1}, their ratio being $K_2 = 1915$ M^{-1} in good accord with the thermodynamic $K_2 = 2000$ M^{-1}. The above figures have been calculated by least-squares analysis. Considering the last figures approximate enough to be taken as final, statistical analysis of standard error on slope and intercept[11] give $k_f = (1.40 \pm 0.05)\ 10^5$ M^{-1} sec^{-1}, $k_R = (73 \pm 25)$ sec^{-1} and average $K_2 = 1.9 \times 10^3$ M^{-1}.

Similar calculations at 30 and 33.5° are reported in Figure 2 and Table III together with the data at 25°. For the data at 19.7°, since k_R is practically zero, the value of K_2 has been obtained as extrapolation of a plot of log K_2 *vs.* $1/T$ giving $K_2 = 1.2 \times 10^3$ M^{-1}.

In order to correlate the data of k_f at various temperatures, the Eyring expression has been used

$$k_f = \frac{kT}{h} e^{\Delta S_f^{\neq}/R}\, e^{-\Delta H_f^{\neq}/RT} \qquad (4)$$

a plot of log (k_f/T) *vs.* $1/T$ gives an intercept = 17.46 ± 0.90 and a slope = −4422 ± 269, both being calculated by least-squares analysis (Figure 2, insert). Then because

$$\text{intercept} = \log \frac{k}{h} + 0.43 \frac{\Delta S_f^{\neq}}{R}$$
$$\text{slope} = -\frac{\Delta H_f^{\neq}}{2.30\,R}$$

one obtains $\Delta S_f^{\neq} = 32.6 \pm 4.1$ eu and $\Delta H_f^{\neq} = 20.2 \pm 1.2$ kcal/mol.

Discussion

By retaining the interchange mechanism[2b] for the present reaction

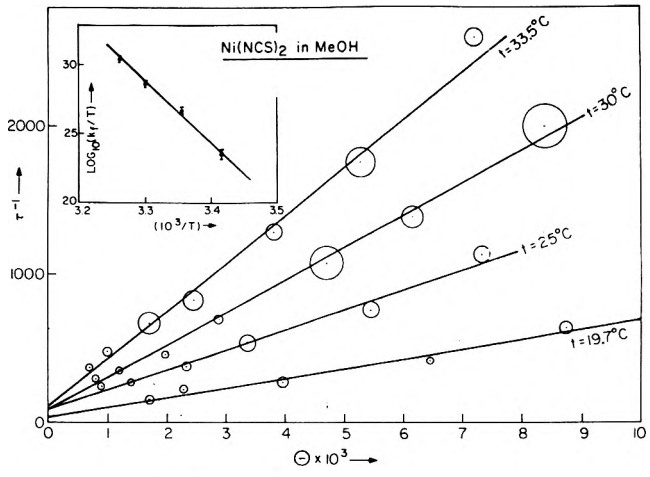

Figure 2. Plot of τ^{-1} (sec^{-1}) *vs.* $\theta = 2\alpha c \gamma_{\pm}^2$ *(M)* for $Ni(NCS)_2$ at the temperatures investigated. Insert shows plot of log (k_f/T) $(M^{-1}\ sec^{-1})$ vs. $(1/T)$ (deg^{-1}) for $Ni(NCS)_2$ in MeOH.

$$(SCN)S_4NiS^{2+} + NCS^- \underset{}{\overset{K_0}{\rightleftharpoons}} (SCN)S_4Ni^{2+}S, NCS^- \underset{k_-}{\overset{k_1}{\rightleftharpoons}} S_4Ni(NCS)_2 \qquad (5)$$

with S a solvent molecule, the rate constants for the overall process

$$(SCN)S_4Ni^{2+} + NCS^- \underset{k_R}{\overset{k_f}{\rightleftharpoons}} S_4Ni(NCS)_2 \qquad (6)$$

are related to the above ones by the expressions $k_f = K_0 k_1$ and $k_R = k_{-1}$. One may retain the Fuoss[12] association constant for K_0 and for a 1:1 electrolyte in methanol one has

$$K_0 = \frac{4\pi N a^3}{3000} \exp\left(\frac{|Z_A Z_B| e^2}{aDkT}\right) = 9.48\ M^{-1} \qquad (7)$$

for $a = 6 \times 10^{-8}$ cm. Then at 25° $k_1 = 14.7 \times 10^3$ sec^{-1}, about 15 times the rate of solvent exchange from the first coordination shell of NiS_6^{2+}, as already observed.[9]

Using the same mechanism, the two relations between enthalpies and entropies, respectively, may be derived

$$\Delta H_f^{\neq} = \Delta H_0 + \Delta H_1^{\neq} \qquad (8)$$
$$\Delta S_f^{\neq} = \Delta S_0 + \Delta S_1^{\neq}$$

By retaining the values of ΔH_0 and ΔS_0 calculated through the Fuoss theory (see Appendix), the calculated activation parameters for the second step of the mechanism of association of $NiNCS^+$ and NCS^- in methanol are

(11) Y. Beer, "Introduction to the Theory of Error," 2nd ed, Addison-Wesley, Reading, Mass., 1962, Chapter VI.

$$\Delta H_1^{\neq} = (20.2 - 1.4) \pm 1.2 = 18.8 \pm 1.2 \text{ kcal/mol}$$
$$\Delta S_1^{\neq} = (32.6 - 9.1) \pm 4.1 = 23.5 \pm 4.1 \text{ eu}$$

It may be seen that although the reported inconsistencies (see Appendix) for ΔS_0 and ΔH_0 are theoretically significant, they are numerically small and contained within the standard errors of $\Delta H_f^{\neq}$ and $\Delta S_f^{\neq}$.

Comparison of Activation Parameters for Solvent Substitution and Exchange. The activation parameters for solvent exchange from the first coordination shell of $Ni(MeOH)_6^{2+}$ are $\Delta H_{exch}^{\neq} = 15.8$ kcal/mol and $\Delta S_{exch}^{\neq} = 8.0$ eu.[13] It may be seen that the enthalpy of activation for the entrance of the second ligand NCS^- is comparable with one for solvent exchange. The difference in the rates of solvent substitution from NiS_6^{2+} and NiS_5NCS^+ seems due mainly to an increase in the entropy of activation for solvent substitution of the second species. In other words, the obtained results suggest that[2b] the "dissociative event" of ejecting one solvent molecule from the activated complex is entropically easier for NiS_5NCS^+ than for NiS_6^{2+}.

A parallel effect of a slight increase in the enthalpy of activation and strong increase in the entropy of activation for solvent exchange has been found by Hunt, *et al.*,[8] for $Ni(H_2O)_6^{2+}$, $Ni(H_2O)_4$ $bipy^{2+}$, and $Ni(H_2O)_2$ $bipy_2^{2+}$ the values being $\Delta H_{exch}^{\neq} = 12.1 \pm 0.5$, 12.6 ± 0.5, and 13.7 ± 0.5 kcal/mol and $\Delta S_{exch}^{\neq} = 2.6 \pm 2$, 5.1 ± 2, and 9.2 ± 4 eu, respectively. Clearly, extensive data are needed for any generalization to be drawn.

In substance, the present data and the previous ones by Ellgen[3] are consistent with the Eigen dissociative interchange mechanism if one accepts the hypothesis that the rate of solvent *exchange* from $Ni(MeOH)_5$ NCS^+ is larger than for $Ni(MeOH)_6^{2+}$.

Comparison of Second-Order Activation Parameters. The objection could be advanced that the conclusion just reached for the activation parameters is based on the assumption of the interchange mechanism, namely, it is vitiated by the same circularity in argumentation[9] that gives $k_1 = 15 \times 10^3$ sec^{-1} from the experimental $k_f = 1.5 \times 10^5 M^{-1}$ sec^{-1}.

It is important therefore to be able to compare the experimental $\Delta H_f^{\neq}$ and $\Delta S_f^{\neq}$ with the activation parameters for solvent exchange *without* the drawback of the assumption of a particular mechanism.

This may be done, according to Caldin and Bennetto,[4] by transforming the activation parameters for the first-order rate constant of solvent exchange, k_{exch}^{I}, to the parameters for the second-order rate constant, k_{exch}^{II}, called total exchange rate.[4] The relation between the two constants is[4]

$$k_{exch}^{II} = k_{exch}^{I} \frac{N_c}{[S]} \tag{9}$$

where N_c is the coordination number of the cation in the first coordination sphere taken as 6 and [S] is the concentration of solvent. At 25° for methanol $\rho = 0.7866$ g/cc, [S] $= (1000 \times 0.7866/32.04) = 24.551$ and $k_{exch}^{II} = 0.25 \times 10^3$ sec^{-1}.[4] Assumption of Eyring expressions for k_{exch}^{II} and k_{exch}^{I} with elimination of the frequency factors kT/h, taking the derivative with respect to T of the logarithmic expressions for k_{exch}^{II} and k_{exch}^{I}, and neglecting the dependence of [S] on temperature give the identity

$$\Delta H_{exch}^{\neq II} = \Delta H_{exch}^{\neq I}$$

Then from the expression

$$0.25 \times 10^3 = \frac{kT}{h} \exp\left(-\frac{15{,}800}{RT}\right) \exp\left(\frac{\Delta S_{exch}^{\neq II}}{R}\right)$$

one may calculate $\Delta S_{exch}^{\neq II} = +5.6$ eu in accord with Bennetto and Caldin.[4] The same result could be obtained from the relation

$$\Delta S_{exch}^{\neq II} = \Delta S_{exch}^{\neq I} + R \ln \frac{N_c}{[S]}$$

It may then be seen that the second-order entropy of activation for *solvent exchange* from NiS_6^{2+} is only 5.6 eu compared to the determined $\Delta S_f^{\neq} = 32.6 \pm 4.1$ eu for *solvent substitution* from $(NiNCS)^+S_5$. This seems to prove that there is a substantial increase for the entropic parameter of activation for solvent ejection from NiS_6^{2+} to $NiNCS^+S_5$ (unless one invokes the unlikely possibility of a ligand participation in the free energy of the activated rate, namely a S_N2 or associative activation mode of substitution[2b] for $NiNCS^+S_5$).

One should point out, however, in evaluating the above result, that criticism has appeared[14] concerning formula 9 and the conversion of k_{exch}^{I} to k_{exch}^{II} using the bulk solvent concentration.

Appendix

Calculation of ΔH_0 and ΔS_0 for the Outer-Sphere Pre-Equilibration Process. The usual procedure reported in textbooks[15] is to calculate ΔG^0 from a model (so called double-sphere model) visualizing two charged spheres Z_+e and Z_-e, brought from infinity to the contact distance a. This result extended to one mole of ions is

$$\Delta G_0 = -N \frac{|Z_+ Z_-| e^2}{Da} \tag{10}$$

which may be rewritten, multiplying and dividing by T and recalling that $N = R/k$, with R the gas constant

$$\Delta G_0 = -RTb \tag{11}$$

with b the Bjerrum parameter $b = |Z_+ Z_-| e^2/aDkT$. Notice that since $\Delta G_0 = -RT \ln K_0$, this implies $K_0 = e_b$, namely, the Denison-Ramsey[16] association constant calculated from a Born cycle.

The calculation of ΔS_0 then proceeds as usual[15]

$$\Delta S_0 = -\left(\frac{\partial \Delta G_0}{\partial T}\right)_p = Rb + RT \frac{db}{dT}$$

and since

$$\frac{db}{dT} = -b\left(\frac{1}{T} + \frac{d \ln D}{dT}\right)$$
$$\Delta S_0 = -RTb\left(\frac{d \ln D}{dT}\right)_p \tag{12}$$

which is identical with the usual formula reported in text books.[15]

$$\Delta S_0 = -N \frac{|Z_+ Z_-| e^2}{Da} \left(\frac{d \ln D}{dT}\right)_p$$

once the transformations indicated between eq 10 and 11

(12) R. M. Fuoss, *J. Amer. Chem. Soc.*, **80**, 5059 (1958).
(13) Z. Luz and S. Meiboom, *J. Chem. Phys.*, **40**, 2688 (1964).
(14) C. H. Langford, *J. Chem. Educ.*, **46**, 557 (1969).
(15) K. J. Laidler, "Chemical Kinetics," McGraw-Hill, New York, N. Y., 1965 Chapter 5, p 212; A. A. Frost and R. G. Pearson, "Kinetics and Mechanism," J. Wiley, New York, N. Y., 2nd ed, 1961, Chapter 7, p 135.
(16) J. T. Denison and J. B. Ramsey, *J. Amer. Chem. Soc.*, **77**, 2615, (1955).

are performed. If one writes

$$\Delta H_0 = \Delta G_0 + T\Delta S_0$$

one obtains

$$\Delta H_0 = -RTb\left(1 + \frac{\mathrm{d}\ln D}{\mathrm{d}\ln T}\right) \tag{13}$$

The above is consistent with the use of the Denison–Ramsey[16] equation for K_0, namely, $K_{DR} = e^b$. If, however, the Fuoss association constant[12] $K_F = K_0 e^b$ is retained as is usually the case for K_0, an inconsistency occurs in the above calculations of ΔG_0, ΔS_0, and ΔH_0 and consequently in $\Delta H_1^{\neq}$ and $\Delta S_1^{\neq}$ in eq 8. In fact if $K_0 = K_0^0 e^b$

$$\begin{aligned}\Delta G_0 &= -RT\ln K_0^0 - RTb\\ \Delta S_0 &= R\ln K_0^0 - RTb\frac{\mathrm{d}\ln D}{\mathrm{d}T}\end{aligned} \tag{14}$$

Comparing eq 14 with 11 and 12 we may notice that the terms $-RT\ln K_0^0$ and $R\ln K_0^0$, respectively, are missing in the latter equations.

In the Fuoss equation the terms $K_0^0 = 4\pi Na^3/3000$ represent, approximately, the volume fraction due to 1 mol of ions or, in other words, the excluded volume from the solution due to the presence of ions.[17] It is natural then that, because of the entropic nature of K_0^0 in the association constant K_0 (representing the probability of collision between neutral particles increasing with the cross section πa^2),[17] K_0^0 had to appear in the ΔS_0 expression. Combination of eq 14 to calculate ΔH_0 gives the same expression as eq 13 since the terms $RT\ln K_0^0$ cancel out. Hence, the two theories, the Denison–Ramsey and the Fuoss, give the same result for ΔH_0, but not for ΔS_0 and ΔG_0. Unfortunately, many authors have used eq 12 for calculating ΔS_0, and in calculating ΔH_0 have used the Fuoss expression for ΔG_0

$$\Delta H_0 = RT\ln K_F - RTb\frac{\mathrm{d}\ln D}{\mathrm{d}\ln T}$$

$$\Delta H_0 = -RT\ln K_0^0 - RTb\left(1 + \frac{\mathrm{d}\ln D}{\mathrm{d}\ln T}\right)$$

mixing up the two theories and introducing inconsistencies such as omitting the $R\ln K_0^0$ terms for ΔS_0 and improperly introducing $-RT\ln K_0^0$ into ΔH_0.

At 25°, for methanol $(\mathrm{d}\log D/\mathrm{d}t) = -0.264 \times 10^{-2}$, $D = 32.63$, $a = 6 \times 10^{-8}$ cm, and $|Z_+Z_-| = 1$ giving $K_0^0 = 0.545$ and $\Delta S_0 = -1.20 + 10.3 = 9.1$ eu.

Notice that by retention of the Denison–Ramsey theory for K_0, $\Delta S_0 = 10.3$ eu.

Similarly, for ΔH_0 from eq 13 $RTb = 1688$ cal, $RT^2b\,(\mathrm{d}\ln D/\mathrm{d}T) = -3071$ cal, and $\Delta H_0 = 1.38$ kcal/mol. The term $-RT\ln K_0^0 = 358$ cal/mol if improperly introduced in the ΔH_0 expression would make $\Delta H_0 = 1.74$ kcal/mol.

Exceptions could be raised for having used the Fuoss or the Denison–Ramsey theory instead of the more accurate Bjerrum theory to evaluate the thermodynamic parameters ΔS_0 and ΔH_0. The Fuoss statistical theory is superior to the thermodynamic theory by Denison and Ramsey because it contains the preexponential term K_0^0 which accounts for the excluded volume due to the presence of 1 mol of ions per liter of solution. However, it has been experimentally shown[18] that the exponential term e^b of the Fuoss theory is an approximation to the Bjerrum term $b^3Q(b)$ in the expression

$$K_{Bj} = \frac{4\pi Na^3}{1000}b^3Q(b) = \frac{4\pi Na^3}{1000}b^3\int_2^b e^Y Y^{-4}\mathrm{d}Y \tag{15}$$

with

$$Y = \frac{|Z_1Z_2|e^2}{rDkT}$$

(In fact, only for low D where b is large $b^3Q(b) \approx e^b/b \approx e^b$ and the two theories give similar numerical values of association constants.) Therefore given

$$\ln K_{Bj} = \ln 3K_0^0 + 3\ln b + \ln Q(b)$$

$$\frac{\mathrm{d}\ln K_{Bj}}{\mathrm{d}T} = \left(\frac{3}{b} + \frac{1}{Q(b)}\frac{\mathrm{d}Q(b)}{\mathrm{d}b}\right)\frac{\mathrm{d}b}{\mathrm{d}T} =$$

$$-b\left(\frac{3}{b} + \frac{1}{Q(b)}\frac{\mathrm{d}Q(b)}{\mathrm{d}b}\right)\left(\frac{1}{T} + \frac{\mathrm{d}\ln D}{\mathrm{d}T}\right)$$

then

$$\Delta S_0 = R\ln K_{Bj} - RT\left(3 + \frac{b}{Q(b)}\frac{\mathrm{d}Q(b)}{\mathrm{d}b}\right)\left(\frac{1}{T} + \frac{\mathrm{d}\ln D}{\mathrm{d}T}\right)$$

but[19]

$$\frac{\mathrm{d}Q(b)}{\mathrm{d}b} = b^{-4}e^b$$

and

$$\Delta S_0 = R\left[\ln K_{Bj} - \left(3 + \frac{e^b}{b^3Q(b)}\right)\left(1 + \frac{\mathrm{d}\ln D}{\mathrm{d}\ln T}\right)\right] \tag{16}$$

also

$$\Delta H_0 = -RT\ln K_{Bj} + T\Delta S_0$$

$$\Delta H_0 = -RT\left(3 + \frac{e^b}{b^3Q(b)}\right)\left(1 + \frac{\mathrm{d}\ln D}{\mathrm{d}\ln T}\right) \tag{17}$$

At 25° in methanol $a = 6 \times 10^{-8}$ cm, $b = 2.858$, $Q(b) = 0.305$, $K_{Bj} = 11.63\ M^{-1}$, $\Delta S_0 = 13.63$ eu, and $\Delta H_0 = 2.6$ kcal/mol. It may be seen that although these last two figures are significantly different from the ones calculated by the Fuoss theory, namely, $\Delta S_0 = 9.1$ eu and $\Delta H_0 = 1.4$ kcal/mol, the differences are of the orders of the standard errors of $\Delta S_f^{\neq}$ and $\Delta H_f^{\neq}$. In any case the conclusions of the present work remain unaltered regardless of the theory chosen for calculating the outer-sphere association parameters.[20]

(17) S. Petrucci, "Ionic Interactions," Academic Press, New York, N. Y., Vol I, 1971, p 136.
(18) C. DeRossi, B. Sesta, M. Battistini, and S. Petrucci, *J. Amer. Chem. Soc.*, **94**, 2961 (1972).
(19) A. Bronwell, "Advanced Mathematics in Physics and Engineering," McGraw-Hill, New York, N. Y., 1953, p 110.
(20) Note Added in Proof. In the above calculations of ΔG_0, ΔH_0 and ΔS_0 the concentration scale used was the molarity. For thermodynamic calculations it may be useful to modify the derivation to the molality concentration scale. Given $m\rho \cong c$, with m, ρ, and c the molality, solvent density, and molarity, respectively, K_m and K_c the equilibrium constants in the two units, it follows that $K_m = K_c\rho$ (neglecting differences in the activity coefficients). Then

$$\mathrm{d}\ln K_m/\mathrm{d}T = \mathrm{d}\ln K_c/\mathrm{d}T - \alpha$$

with α (the expansion coeeficient of the solution) $= -(\mathrm{d}\ln\rho/\mathrm{d}T)$. If one identifies K_c with one of the theoretically calculable association constants, say K_{Fuoss}, then eq 14 and 13 from above become

$$\Delta G_0 = RT\ln K_0^0 - RTb - RT\ln\rho$$

$$\Delta S_0 = R\ln K_0^0 - RTb\,\mathrm{d}\ln D/\mathrm{d}T + R\ln\rho - RT\alpha$$

$$\Delta H_0 = -RTb(1 + \mathrm{d}\ln D/\mathrm{d}\ln T) - RT^2\alpha$$

The additional contribution to ΔG_0, ΔS_0, and ΔH_0 in methanol at 25° ($\rho = 0.7866$ g/cm^3, $\alpha = 1.16 \times 10^{-3}$ deg^{-1}) are $\delta\Delta G_0 = 0.14$ kcal/mol, $\delta\Delta S_0 = -1.2$ eu, and $\delta\Delta H_0 = -0.21$ kcal/mol, bringing the thermodynamic parameters in the molality scale to $\Delta S_0 = 7.9$ eu and $\Delta H_0 = 1.2$ kcal/mol.

COMMUNICATIONS TO THE EDITOR

On the Isotope Effect in the Decomposition of Ammonia on Tungsten Surfaces

Sir: It was recently suggested by Sheets and Blyholder[1] that the observed isotope effect in the decomposition of ammonia on tungsten surfaces could be understood as a β-secondary isotope effect, allowing nitrogen desorption to be rate limiting. Their conclusion that this interpretation brings harmony to isotope[2,3] and kinetic[4,5] measurements is optimistic and it is based on a very selective and incorrect use of the available data. In the kinetic measurements referred to[4,5] the authors use the term nitrogen desorption rate limiting in the sense that nitrogen desorption *alone* occurs in the rate-limiting step. The prime evidence for this conclusion is that the surface intermediate *contains no hydrogen.* It is assumed that the surface is saturated with nitrogen and that hydrogen desorption is extremely fast at temperatures below those required for nitrogen desorption. These conclusions, far from being resolved with the isotope effect by the model of Sheets and Blyholder are completely at variance with it. No such secondary isotope effect is possible in a surface devoid of hydrogen (in the absence of a carbon skeleton the term β secondary is confusing and will not be adopted). Furthermore, this conflict no longer exists. Thermal desorption mass spectrometry studies[6,7] of the interaction of ammonia with tungsten surfaces have shown that at steady state during catalytic decomposition, except at very low reactant pressure, the surface is saturated with a species (η species) which *does* contain hydrogen. Possible reasons for a misinterpretation of Tamaru's experiments[4] have been presented.[8] Matsushita and Hansen's experiments[5] were carried out at too low a temperature and reactant pressure to permit formation of the hydrogen-containing η species.

Sheets and Blyholder have been selective in their use of the thermal desorption mass spectrometric data. These experiments are rather more than desorbed gas analysis and contain more information than overall surface stoichiometry. Let us summarise this information. In 1966, it was pointed out[9] that the desorption rate of β nitrogen (at the time, the only known surface species of nitrogen on tungsten stable at catalytic temperatures) was more than 10^7 times slower than nitrogen production during ammonia decomposition on tungsten surfaces. Clearly a process, or processes, must be identified which allows this faster desorption of nitrogen. Since that time two additional surface species have been identified, δ nitrogen[5,7] and the η species.[6,7] The formation and decomposition reactions which can occur can be summarized in the following way (where W^s denotes a surface tungsten atom)

β

$$2W^s + NH_3(g) \rightarrow W_2{}^sN(\beta) + \tfrac{3}{2}H_2(g) \quad (1)$$

$$W_2{}^sN(\beta) \rightarrow 2W^s + \tfrac{1}{2}N_2(g) \quad (2)$$

δ

$$W_2{}^sN(\beta) + NH_3(g) \rightarrow 2W^sN(\delta) + \tfrac{3}{2}H_2(g) \quad (3)$$

$$2W^sN(\delta) \rightarrow 2W^s + N_2(g) \quad (4)$$

η

$$2W^sN(\delta) + NH_3(g) \rightarrow W_2{}^sN_3H(\eta) + H_2(g) \quad (5)$$

$$W_2{}^sN_3H(\eta) \rightarrow W_2{}^sN(\beta) + N_2(g) + H(g) \quad (6)$$

While the kinetic parameters for these reactions are known, for the present purposes the relative rates will be adequate and these are (1) > (3) >> (5) and (2) <<< (4) < (6). It can be seen that as the surface density of nitrogen increases the rate of nitrogen desorption increases, reactions 2, 4, and 6, but also the rate of formation of the adlayer decreases, reactions 1, 3, and 5. For any given reaction conditions, *viz.*, reactant pressure and catalyst temperature, a steady state will be attained in which the rate of formation and removal of the surface intermediates will be equal. This determines the nature of the surface intermediate. Reaction 2 is too slow to be part of the decomposition mechanism. Since the rate of reaction 5 is dependent on the reactant pressure, we anticipate two regimes for the decomposition mechanism determined by competition between reactions 4 and 5. At high reactant pressure reaction 6 should be rate limiting and we anticipate a hydrogen isotope effect, whereas at very low reactant pressure reaction 4 should be rate limiting and the isotope effect should disappear. The observed kinetic parameters for reactions 3–6 suggest that the transition pressure should be in the vicinity of 10^{-1} Torr at 1000°K; this is currently under investigation.

Reaction 6 is unlikely to be an elementary step. The desorption of N_2 and H are closely related at the molecular level since the desorption peaks are simultaneous and first order. However, the critical question of whether on the time scale of molecular vibrations hydrogen desorption precedes or follows nitrogen desorption is clearly not answered by such experiments. An answer must await, at least, an unambiguous determination of the structure of the η adlayer. Two structures have been proposed,[7] (a) $WN_2H{\cdot}WN$ and (b) $WN_2{\cdot}WNH$, both of which preserve the N–H bond of the reactant. Sheets and Blyholder[1] question this assumption, which is surprising since it is a requirement of their model. It is known that N–H bond breaking becomes increasingly difficult as the density of the adlayer increases.[7] Structures a and b imply the following pairs of elementary steps for reaction 6

$$WN_2H{\cdot}WN \rightarrow WN_2{\cdot}WN + H(g) \quad (6a)$$

(1) R. Sheets and G. Blyholder, *J. Phys. Chem.*, **76**, 970 (1972).
(2) J. C. Jungers and H. S. Taylor, *J. Amer. Chem. Soc.*, **57**, 679 (1935).
(3) R. M. Barrer, *Trans. Faraday Soc.*, **32**, 490 (1936).
(4) K. Tamaru, *Trans. Faraday Soc.*, **57**, 1410 (1961).
(5) K. Matsushita and R. S. Hansen, *J. Chem. Phys.*, **52**, 4877 (1970).
(6) P. T. Dawson and Y. K. Peng, *J. Chem. Phys.*, **52**, 1014 (1970).
(7) Y. K. Peng and P. T. Dawson, *J. Chem. Phys.*, **54**, 950 (1971).
(8) P. T. Dawson and R. S. Hansen, *J. Chem. Phys.*, **48**, 623 (1968).
(9) P. T. Dawson and R. S. Hansen, *J. Chem. Phys.*, **45**, 3148 (1966).

$$WN_2 \cdot WN \rightarrow W_2N + N_2(g)$$
$$WN_2 \cdot WNH \rightarrow W \cdot WHN + N_2(g) \qquad (6b)$$
$$W \cdot WNH \rightarrow W_2N + H(g)$$

and a primary or secondary nature, respectively, for the isotope effect. Both possibilities adequately account for the thermal desorption results. Molecular nitrogen, α nitrogen,[10] is weakly chemisorbed, desorbing at much lower temperatures than the η species, *viz.*, 400°K compared with 900°K. Thus in (6a) its desorption would immediately follow that of H. In (6b), desorption of N_2 would free adjacent surface tungsten atoms for formation of transition states in breaking the N–H bond of the imide group and H desorption would follow immediately. However, the relative instability of adsorbed N_2 suggests that its desorption would not be rate limiting and it seems unlikely that an inductive effect from an adjacent NH (or ND) group would lead to a stabilization of the required magnitude. In the alternative model (6a) the presence of an N–H bond in the N_2 species, *i.e.*, N–NH, forces a lower bond order for the N–N bond, stronger bonding to the surface and a species desorbing at higher temperature as observed.

The behavior of coadsorbed films of CO and NH_3 on iron and nickel films reported by Sheets and Blyholder has little in common with the adlayer during ammonia decomposition on tungsten. NH_3 and ND_3 contain a lone electron pair and one would anticipate that chemisorbed NH_3 would bond to a transition metal surface with accompanying electron donation to the metal. This would result in a dipole array which would lower the work function of the surface. This was confirmed in 1968 in field emission experiments of Dawson and Hansen;[8] chemisorbed NH_3 changes the work function of a tungsten surface by amounts varying from −1.0 to −1.6 eV depending on crystallographic orientation. At catalytic temperatures undissociated ammonia adsorption does not occur. Hydrogen desorption accompanies ammonia adsorption in the formation of both δ nitrogen (3) and the η species (5). The work functions of the δ and η adlayers have recently been measured in this laboratory and are found to be 4.70 and 5.00 eV, respectively. Since the emitting regions in both cases correspond to those emitting for the clean surface (work function 4.50 eV), we can conclude that the δ and η species change the work function by +0.20 and +0.50 eV, respectively. Thus, whatever the structure of the η adlayer, whether it contains NH groups, N–NH groups, or neither, the incorporation of hydrogen into the surface *via* reaction 5 has the effect of *withdrawing* electrons from the tungsten. The electron donation picture of Sheets and Blyholder is unsatisfactory.

Finally we are concerned as to the magnitude anticipated for a secondary isotope effect for this reaction. By implication,[1] an observed isotope effect of 1.6[2,3] compared with a quoted maximum of 1.5 for β-secondary isotope effects[11] lends credence to the secondary isotope mechanism. It should be pointed out that secondary isotope effects are generally much smaller than this and there is no evidence to suggest that such a large value would be appropriate for the effect under discussion, *e.g.*, reaction 6b. More important still the maximum β-secondary isotope effect of 1.5 is for *room temperature* whereas that observed in the decomposition of NH_3 and ND_3 on tungsten surfaces is for a temperature of 1000°K. The exact temperature dependence of secondary isotope effects is impossible to predict but one would anticipate that, depending on the relative magnitudes of the vibrational frequencies and temperature, the magnitude of the isotope effect varies exponentially as either $1/T$ or $1/T^2$, or both if the reacting system contains high- and low-frequency vibrations.[12,13] In the latter case anomalous temperature dependencies (maxima, minima, and crossovers) are possible if the high- and low-frequency contributions to the isotope effect are opposite in sign.[13] In this case, however, the overall effect is expected to be smaller and in any case over a large temperature range the magnitude of the isotope effect will still diminish. It has been pointed out[13] that such anomalies are expected to be even less frequent in kinetic isotope effects than in the equilibrium isotope effects considered. The existing evidence suggests that secondary isotope effects would not have sufficient magnitude at 1000°K to account for the observed effect. No such problems arise with the primary isotope effect interpretation. The differences in the zero point energy for the six normal vibrational modes of NH_3 and ND_3 vary from 575 to 2600 cal mol^{-1}. Without a detailed knowledge of the reaction trajectory and potential surface it is uncertain what magnitude a primary isotope effect would attain but it would be expected to lie between these limits. In order to account for NH_3 decomposition occurring 1.6 times faster than ND_3 at 1000°K a difference in activation energy of 940 cal mol^{-1} is required. This does indeed fall within the limits expected for a full primary isotope effect and provides strong evidence for this mechanism.

In conclusion, the identification of a hydrogen-containing η species during the catalytic decomposition of NH_3 on tungsten surfaces has removed any problems created by the existence of a hydrogen isotope effect. However, there is still considerable speculation as to the nature of the isotope effect. Nevertheless, its magnitude suggests that it is a primary isotope effect. Conversely, this strengthens those structural models which imply a primary isotope effect.

(10) G. Ehrlich, *J. Chem. Phys.*, **34**, 29 (1961).
(11) J. March, *Advan. Org. Chem.*, **6**, 216 (1968).
(12) M. Wolfsberg and M. J. Stern, *Pure Appl. Chem.*, **8**, 225 (1964).
(13) M. J. Stern, W. Spindel, and E. U. Monse, *J. Chem. Phys.*, **48**, 2908 (1968).

Department of Chemistry and Institute for Materials Research
McMaster University
Hamilton, Ontario, Canada
P. T. Dawson*
Y. K. Peng

Received May 15, 1972

Mass Spectrometric Determination of the Dissociation Energies of AlC_2, Al_2C_2, and $AlAuC_2$[1]

Publication costs assisted by the National Aeronautics and Space Administration

Sir: As part of a study of the thermodynamics of aluminum-containing molecules[2a] and as a continuation of our studies on the vaporization of metal carbides,[2b] we have

(1) Presented in part at the Twentieth Annual Conference on Mass Spectrometry and Allied Topics, ASMS-ASTM E-14, Dallas, Tex., June 4–9, 1972.
(2) (a) C. A. Stearns and F. J. Kohl, *High Temp. Sci.*, in press; (b) C. A. Stearns and F. J. Kohl, *J. Chem. Phys.*, **54**, 5180 (1971); **54**, 1414 (1971); *J. Phys. Chem.*, **74**, 2714 (1970); *High Temp. Sci.*, **2**, 274 (1970); *J. Chem. Phys.*, **52**, 6310 (1970).

TABLE I: Ions Observed in the Al-Au-C System

Ion	Relative intensity (2147 K, 30 eV)	Appearance potential, eV		Parent species
		Present work	Literature	
Al^+	1.00	Standard	5.984[b]	Al
AlC^+	1.7×10^{-6}	14.0 ± 1.0		AlC_2, (AlC?)
AlC_2^+	2.4×10^{-5}	9.3 ± 1.0		AlC_2
Al_2^+	2.5×10^{-5}	5.4 ± 1.0		Al_2
Al_2C^+	1.3×10^{-6}	a		Al_2C?, Al_2C_2
$Al_2C_2^+$	6.4×10^{-5}	8.0 ± 0.5		Al_2C_2
Au^+	$\sim 7 \times 10^{-2}$	Standard	9.22[b]	Au
$AlAu^+$	3.4×10^{-1}	7.6 ± 0.3		AlAu
$AlAuC^+$	$\sim 10^{-6}$	a		AlAuC?, $AlAuC_2$
$AlAuC_2^+$	2.0×10^{-6}	a		$AlAuC_2$
Au_2^+	a	9.5 ± 0.3	9.2,[c] 9.7[d]	Au_2

[a] Not measured. [b] Reference 5. [c] Reference 6. [d] References 7 and 8.

TABLE II: Third-Law Enthalpies for Reactions Involving $AlC_2(g)$, $Al_2C_2(g)$, and $AlAuC_2(g)$

Temp, K	Log K_p	$-\Delta[(G_T^\circ - H_0^\circ)/T]$, JK^{-1} mol^{-1}	ΔH_0° (III), kJ mol^{-1}
	$Al(g) + 2C(s) = AlC_2(g)$		
2082	−4.858[a]	56.65	311.6
2113	−4.505	56.58	301.8
2147	−4.818	56.51	319.4
2171	−4.784	56.46	321.4
2162	−4.818	56.48	321.5
		Av	315.1 ± 7.6(±21)[b]
	$Al_2(g) + 2C(s) = Al_2C_2(g)$		
2051	0.218[a,c]	35.38	64.0
2074	0.386	35.41	58.1
2085	0.423	35.43	57.0
2059	0.537	35.39	51.7
2082	0.333	35.42	60.5
2113	0.492	35.47	55.1
2147	0.346	35.52	62.1
2171	0.106	35.55	72.8
2162	0.126	35.54	71.6
		Av	61.4 ± 6.7(±20)[b]
	$AlAu(g) + 2C(s) = AlAuC_2(g)$		
2113	−5.325[a,d]	49.50	320.0
2147	−5.332	49.57	325.6
2171	−5.191	49.61	323.5
2162	−5.247	49.60	324.4
		Av	323.4 ± 2.1(±20)[b]

[a] $K_p = (I(AlC_2^+)/I(Al^+))(\sigma(Al)/\sigma(AlC_2))_{30eV}(\gamma(Al^+)/\gamma(AlC_2^+))(1/a(C))^2$. The cross sections for Al and C were taken from Mann (ref 9). $(\sigma(Al)/\sigma(AlC_2)) = 0.6246$. The γ terms were assumed to cancel and the activity of graphite was assumed to be 1. [b] Overall estimated uncertainty. [c] $K_p = (I(Al_2C_2^+)/I(Al_2^+))(\sigma(Al_2)/\sigma(Al_2C_2))_{30eV}(\gamma(Al_2^+)/\gamma(Al_2C_2^+))(1/a(C))^2$; $(\sigma(Al_2)/\sigma(Al_2C_2)) = 0.7755$. [d] $K_p = (I(AlAuC_2^+)/I(AlAu^+))(\sigma(AlAu)/\sigma(AlAuC_2))_{30eV}(\gamma(AlAu^+)/\gamma(AlAuC_2^+))(1/a(C))^2$; $(\sigma(AlAu)/\sigma(AlAuC_2)) = 0.7921$.

identified and measured the dissociation energies of the molecules AlC_2, Al_2C_2, and $AlAuC_2$. Chupka, *et al.*,[3] have previously identified Al_2C_2 but were uncertain with regard to the existence of other aluminum-carbon molecules.

The mass spectrometer and experimental procedure used in the present study have been described adequately elsewhere.[2,4] The aluminum-carbon-containing molecules were observed with the mass spectrometer by vaporizing a mixture of Al and Au from a graphite liner in a tantalum Knudsen cell. The ions reported in Table I[5-8] were observed when the sample was heated to temperatures above 2000 K. The appearance potentials (AP) measured for AlC_2^+, Al_2^+, $Al_2C_2^+$, $AlAu^+$, and Au_2^+ indicated that these were parent molecular ions whose neutral precursors originated in the Knudsen cell. AlC^+ is probably a fragment ion from AlC_2 because of its high AP of 14 eV. We assume that $AlAuC_2^+$ is a parent molecular ion while the origin of the low-intensity Al_2C^+ and $AlAuC^+$ are uncertain.

Ion intensity measurements were made for the ions of interest over the temperature range of 2051 to 2171 K. The pressure calibration independent reactions involving AlC_2, Al_2C_2, and $AlAuC_2$ are listed in Table II[9] along with the logarithms of the equilibrium constants, free-energy function changes, and third-law heats of reaction at each experimental temperature.

The values of the thermodynamic functions for Al(g) and C(s) were taken from the JANAF tables;[10] for $Al_2(g)$ and AlAu(g) other recently reported[2a] values were used. For $AlC_2(g)$ a linear asymmetric Al-C-C structure and for $Al_2C_2(g)$ a linear symmetric Al-C-C-Al structure were chosen by analogy to other metal dicarbides.[2b] The Al-C interatomic distance was estimated as 1.61 Å, consistent with the choice of Chupka, *et al.*,[3] while the C-C distance of 1.31 Å was taken from $C_2(g)$.[11] The fundamental vibrational frequencies were calculated according to the valence force formulation.[12] The stretching force constant for the Al-C was assumed to be 5.0×10^2 N/m[3] and the C-C force constant of 9.25×10^2 N/m was taken from $C_2(g)$.[11] The calculated frequencies in cm^{-1} for AlC_2 are 755, 503(2), and 1751 and for Al_2C_2, 1842, 492, 1011, 321(2), and 109(2). For $AlAuC_2(g)$ a linear Al-C-C-Au

(3) W. A. Chupka, J. Berkowitz, C. F. Giese, and M. G. Inghram, *J. Phys. Chem.*, **62**, 611 (1958).
(4) C. A. Stearns and F. J. Kohl, *NASA Tech. Note*, No. D-5027 (1969); No. D-5646 (1970).
(5) R. W. Kiser, "Introduction to Mass Spectrometry," Prentice-Hall, Englewood Cliffs, N. J., 1965, Appendix IV.
(6) K. A. Gingerich, *J. Chem. Phys.*, **50**, 5426 (1969).
(7) K. A. Gingerich, *J. Chem. Phys.*, **54**, 2646 (1971).
(8) K. A. Gingerich and H. C. Finkbeiner, *J. Chem. Phys.*, **52**, 2956 (1970).
(9) J. B. Mann, *J. Chem. Phys.*, **46**, 1646 (1967).
(10) D. R. Stull, Ed., "JANAF Thermochemical Tables," Dow Chemical Company, Midland, Mich.
(11) G. Herzberg, "Molecular Spectra and Molecular Structure. Vol. I. Spectra of Diatomic Molecules," 2nd ed, Van Nostrand, New York, N. Y., 1950, Appendix.
(12) G. Herzberg, "Molecular Spectra and Molecular Structure. Vol. II. Infrared and Raman Spectra of Polyatomic Molecules," Van Nostrand, New York, N. Y., 1945.

structure was assumed and the Au-C stretching force constant was taken as equal to the Al-C force constant. The Au-C interatomic distance of 1.86 Å was obtained by comparison of the values from AuSi and AuB with the Pt, Rh, Ru, and Ir carbides, silicides, and borides.[13-15] The negative of the free-energy functions in JK^{-1} mol^{-1} at 2000, 2100, and 2200 K are 284.79, 287.40, and 289.90 for $AlC_2(g)$; 347.19, 350.93, and 354.52 for $Al_2C_2(g)$; and 379.55, 383.32, and 386.94 for $AlAuC_2(g)$.

The atomization energies for the molecules were calculated by combining the third-law heats of the reactions listed in Table II with the heat of formation of C(g), $\Delta H_{0,f}^\circ$ = 709.5 ± 1.9 kJ mol^{-1},[10] the dissociation energy of $Al_2(g)$, D_0° = 149.8 ± 14 kJ mol^{-1},[2a] and the dissociation energy of AlAu(g), D_0° = 322.2 ± 6 kJ mol^{-1}:[16] $D_{0,atoms}^\circ(AlC_2)$ = 1104 ± 21 kJ mol^{-1}, $D_{0,atoms}^\circ(Al_2C_2)$ = 1507 ± 25 kJ mol^{-1}, and $D_{0,atoms}^\circ(AlAuC_2)$ = 1418 ± 21 kJ mol^{-1}. The atomization energy of $Al_2C_2(g)$ is in good agreement with the value calculated from the experimental results of Chupka, *et al.*,[3] of 1556 ± 42 kJ mol^{-1}.

The measurement of the dissociation energies of AlC_2 and Al_2C_2 is an extension of previous work in this laboratory on the determination of the stabilities of the transition metal dicarbides and comparison of metal-carbide and -oxide bond energies.[2b] Again we see that dicarbide molecules are formed which are analogous to the stable monoxides AlO and Al_2O. For most metal dicarbide molecules it is found that the dissociation energy of the $M-C_2$ bond is 40-130 kJ mol^{-1} less than that of the corresponding M-O bond. The Al-C bond in AlC_2 is an apparent exception to this empirical rule because $\bar{E}(Al-C_2)$ of 514.2 ± 21 is slightly higher than $D_0^\circ(AlO)$ of 502 ± 15 kJ mol^{-1}.[17] On the other hand, each Al-C bond in Al_2C_2 of 459 kJ mol^{-1} is 63 kJ mol^{-1} lower in energy than the Al-O bonds in $Al_2O(g)$ and follows the trend for most metal dicarbides.

For the $AlAuC_2$ molecule we have assumed the structure Al-C-C-Au. If the energies of the Al-C and C-C bonds are subtracted from the experimentally determined atomization energy, the balance (365 kJ mol^{-1}) may represent the energy for an Au-C bond. This value is consistent with an upper limit (375 kJ mol^{-1}) determined[14] for D_0° of the unobserved AuC molecule.

(13) A. VanderAuwera-Mahieu, R. Peeters, N. S. McIntyre, and J. Drowart, *Trans. Faraday Soc.*, **66**, 809 (1970).
(14) A. VanderAuwera-Mahieu and J. Drowart, *Chem. Phys. Lett.*, **1**, 311 (1967).
(15) N. S. McIntyre, A. VanderAuwera-Mahieu, and J. Drowart, *Trans. Faraday Soc.*, **64**, 3006 (1968).
(16) K. A. Gingerich, *J. Crystal Growth*, **9**, 31 (1971).
(17) M. Farber, R. D. Srivastava, and O. M. Uy, *J. Chem. Soc., Faraday Trans. 1*, **68**, 249 (1972).

National Aeronautics and Space Administration
Lewis Research Center
Cleveland, Ohio 44135

Carl A. Stearns
Fred J. Kohl*

Received September 18, 1972

A Crystallographic Study of the Structure of a Partially Filled Ammonia Sorption Complex of Zeolite 4A

Publication costs assisted by The National Institute of Health

Sir: In the crystal structure of the nearly filled 32 ammonia complex[1] of zeolite 4A, four sorption sites containing 8, 4, 8, and 12 NH_3 molecules, respectively, were found. The most favorable site at lesser loadings, or the site selected by the first molecules to enter each unit cell, was not determined. Accordingly, the heat of sorption which might be calculated from the initial slope of the sorption isotherm[1] cannot be associated with a particular site. To resolve this issue, the eight ammonia (per $Pm3m$ unit cell) complex was prepared and studied by crystallographic procedures similar to those previously employed.[1]

A single crystal of zeolite 4A, a cube 0.070 mm on an edge, was dehydrated at 350° and 10^{-6} Torr for 24 hr, and was then exposed to zeolitically dried ammonia gas at 28° and at a pressure of 12 Torr for 30 hr. The crystal in its glass capillary was then sealed off from the vacuum system and studied without exposure to the atmosphere. The cell constant based on a least-squares treatment of 15 intense reflections is 12.289(5) Å. Of the intensities observed, 137 unique reflections were significant at the 3σ level and these were used throughout.

The initial structural parameters used in least-squares refinement were those previously found[1] for Na, Si, Al, and O atoms in the 32 ammonia zeolite 4A complex. The twelfth sodium ion, found in the structure of dehydrated 4A[2] was included and refined well. The error indices at convergence with this model were R_1 = 0.067 and R_2 = 0.076, and the goodness of fit was 0.92. The final parameters are given in Table I, and a tabulation of structure factors is available.[3]

A difference Fourier synthesis was prepared and refinements were attempted at the positions of several small peaks found there, even though this function appeared to be particularly featureless. The positions for nitrogen atoms as determined in the filled ammonia complex[1] were subjected to least-squares refinement at occupancies corresponding to four nitrogen atoms per equipoint. Positions off threefold axes were also considered and their refinement was attempted. In no case was a site located which satisfied the elementary crystallographic criteria of statistically significant occupancy and lowered error functions.

It appears that even at a loading of as few as eight ammonia molecules per unit cell the sorbed molecules are not predominantly found at one kind of sorption site. Perhaps all three kinds of Na^+ compete favorably at room temperature for NH_3 association, all at sites where further hydrogen bonding can occur to framework oxygen atoms. This result is consistent with the complete absence of any indication of plateauing or unevenness in the sorption isotherm;[1] even the first derivative decreases entirely regularly as a function of ammonia content.

The zeolite framework and cation positions have altered slightly upon the introduction of eight ammonia molecules, confirming that sorption has indeed occurred (see Table II). The geometries of the fully ammoniated and fully hydrated 4A structures are very similar,[1,4] and may be referred to as the relaxed conformation, the conformation of zeolite 4A at its synthesis. Eight ammonia mole-

(1) R. Y. Yanagida and K. Seff, *J. Phys. Chem.*, **76**, 2597 (1972).
(2) R. Y. Yanagida and K. Seff, *J. Phys. Chem.*, in press.
(3) Listings of the observed and calculated structure factors for both structures will appear following these pages in the microfilm edition of this volume of the journal. Single copies may be obtained from the Business Operations Office, Books and Journals Division, American Chemical Society, 1155 Sixteenth St., N.W., Washington, D. C. 20036. Remit check or money order for $3.00 for photocopy or $2.00 for microfiche, referring to code number JPC-73-138.
(4) V. Gramlich and W. M. Meier, *Z. Kristallogr.*, **133**, 134 (1971).

TABLE I: Positional, Thermal, and Occupancy Parameters[a]

	Wyckoff position	x	y	z	B, Å² or b_{11} and b_{12}	Occupancy factor
(Si,Al)	24(*k*)	0	0.1831(5)	0.3721(4)	1.70(8)	1
O(1)	12(*h*)	0	0.2251(15)	1/2	2.1(4)	1
O(2)	12(*i*)	0	0.2917(11)	0.2917(11)	2.9(4)	1
O(3)	24(*m*)	0.1124(8)	0.1124(8)	0.3433(11)	2.8(3)	1
Na(1)	8(*g*)	0.2016(9)	0.2016(9)	0.2016(9)	0.0064(8)[b]	1
					0.0052(16)	
Na(2)	24(*m*)	0.027(5)	0.431(3)	0.431(3)	3.3(15)	1/8
Na(3)	12(*j*)	0.23(2)	0.23(2)	1/2	10(8)	1/12

[a] Standard deviations are in the units of the least significant digit given for the corresponding parameter. See ref 1 for the identities of the atoms. [b] For Na(1), the anisotropic temperature factor = $\exp[-b_{11}(h^2 + k^2 + l^2) - b_{12}(hk + hl + kl)]$.

TABLE II: Selected Structural Parameters

	Dehydrated 4A[a]	4A·8NH_3	4A·32NH_3[b]
Cell constant	12.263(2)	12.289(5)	12.29(1)
Distance of Na(1) from O(3) plane	0.20(1)	0.26(1)	0.59(1)
Framework angle at O(1)	145(1)	143(1)	145(1)
Framework angle at O(2)	166(1)	163(1)	159(1)
Framework angle at O(3)	146(1)	144(1)	142(1)
Na(1)-O(3)	2.32(1)	2.33(1)	2.35(2)
Na(1)-O(2)	2.90(1)	2.92(1)	2.98(1)
Na(2)-O(2)	2.40(6)	2.43(6)	2.70(14)
Na(2)-O(1)	2.64(3)	2.68(3)	2.90(14)
Na(3)-O(3)	2.47(7)	2.75(25)	*C*
Na(3)-O(1)	2.51(7)	2.77(25)	*C*

[a] Reference 2. [b] Reference 1. [c] Na(3) was not located in this structure.

cules, then, suffice to return the dehydrated 4A structure part of the way to its relaxed state. Qualitatively similar effects are observed in a trimethylamine sorption complex[5] of zeolite 4A prepared in a similar way.

Acknowledgment. This work was supported by the U. S. Army Research Office—Durham. We are also indebted to the NSF for their assistance (Grant No. GP-18213) in the purchase of the diffractometer, and to the University of Hawaii Computation Center.

(5) R. Y. Yanagida, M. S. Thesis, University of Hawaii, 1973.

Department of Chemistry
University of Hawaii
Honolulu, Hawaii 96822

Russell Y. Yanagida
Karl Seff*

Received August 28, 1972

Detection of Fluoroalkyl and Acyl Radicals in the Gas-Phase Photolysis of Ketones and Aldehydes by Electron Spin Resonance Gas-Phase Spin Trapping Techniques[1]

Publication costs assisted by the Environmental Protection Agency

Sir: In recent communications[2] a technique for the detection and identification of gas-phase free radicals at relatively low pressures (~0.1 Torr) has been described. Thus when azomethane is photolyzed at 0.10–0.20 Torr in a flow experiment upstream from powdered phenyl *N-tert*-butyl nitrone (PBN), the methyl radical addition product, α-methylbenzyl *tert*-butyl nitroxide, can be collected in a liquid nitrogen trap downstream.[3] The contents of the trap are analyzed by esr after the addition of benzene and warming to room temperature. The apparatus used and typical results have been shown.[2] Methyl radicals were also detected from the photolysis of acetone and ethyl radicals from the photolysis of 3-pentanone, tetraethyllead, and diethylmercury.

$$CH_3N{=}NCH_3 \xrightarrow{h\nu} 2CH_3\cdot + N_2$$

$$CH_3\cdot + C_6H_5CH{=}NC(CH_3)_3 \longrightarrow C_6H_5\overset{\cdot O}{\underset{|}{C}}H(CH_3)NC(CH_3)_3$$

In a continuation of this study, the results summarized in Table I have been obtained. Trifluoromethyl and pentafluoroethyl radicals are readily detected by PBN in the photolysis of the iodides in the gas phase. The spectrum obtained from 1,3-dichlorotetrafluoroacetone is almost identical with that obtained from photolysis of pentafluoroethyl iodide and is assigned on this basis to the chlorodifluoromethyl spin adduct.[5] Although methyl or trifluo-

(1) This work is supported by the Environmental Protection Agency Air Pollution Control Office, Public Health Service, Grant No. AP 01096.
(2) E. G. Janzen and I. G. Lopp, *J. Phys. Chem.*, **76**, 2056 (1972); see also E. G. Janzen and J. L. Gerlock, *Nature (London)*, **222**, 867 (1969).
(3) This method of detecting radicals has wide application in liquid solution and has been named spin trapping.[4] The nitroxide produced is called a spin adduct. For reviews see E. G. Janzen, *Accounts Chem. Res.*, **4**, 31 (1971); C. Lagercrantz, *J. Phys. Chem.*, **75**, 3466 (1971); M. J. Perkins, *Chem. Soc., Spec. Publ.*, **No. 24**, 97 (1970).
(4) E. G. Janzen and B. J. Blackburn, *J. Amer. Chem. Soc.*, **91**, 4481 (1969).
(5) Presumably the radical could also be produced from the loss of chlorine atom[6] but no evidence for chlorine atom chemistry was found.

TABLE I: Conditions for the Detection of Radicals by Phenyl *tert*-Butyl Nitrone in the Photolysis of Ketones and Aldehydes

Compounds	Lamp[a]	Pressure,[b] Torr	Time,[c] hr	Radicals detected[d]
CF_3I	LP	0.1–0.5	1–3	CF_3
CF_3CF_2I	LP	0.1	2.5	CF_3CF_2
$(ClC{=}F_2)_2CO$	HP	0.07–0.10	3.5[e]	$ClCF_2$
$(ClCF_2)_2CO$	LP	0.10–0.15	3[e]	$ClCF_2$
CF_3COCH_3	HP	0.025–0.10	2–5[e]	CF_3
CF_3COCH_3	HP	0.025 + 0.3N_2	4[e]	CF_3
CF_3COCH_3	HP	0.07 + 0.7N_2	4[e]	CF_3
CF_3COCH_3	LP	0.025–0.4	2.5–6.5[e]	CH_3
CF_3COCH_3	LP	0.025 + 0.25–2.5N_2	4[e]	CH_3
CF_3COCH_3	LP/Hg*	0.05–0.25	2–4[e]	CF_3
CF_3COCH_3	LP/Hg*	0.015–0.05 + 0.5N_2	4–5[e]	CF_3
CF_3COCF_3	HP	0.1	3–4[e]	CF_3
HCHO	HP/F	0.06	4	HC=O (HC=O)[f]
CH_3CHO	HP	0.05–0.06	4	CH_3 (CH_3, CH_3C=O)[f]
CF_3CHO	HP	0.1	4	CF_3
CH_3CH_2CHO	HP	0.1	4	CH_3CH_2 (CH_3CH_2)[f]
$CH_3CH_2CH_2CHO$	HP	0.2	4	$CH_3CH_2CH_2$ ($CH_3CH_2CH_2$, HC=O)[f]

[a] LP = low-pressure Hg lamp; HP = high pressure Hg lamp with Pyrex filter; LP/Hg* with Hg vapor sensitization; HP/F = with Corning CS 7-54 filter to cut out visible region 450–660 nm; we gratefully acknowledge Professor K. Kuwata for this suggestion. [b] Total pressure in photolysis cell of ketone or aldehyde; in some cases total pressure is increased by addition of N_2. Pressure ranges indicated give range of pressures studied in different experiments. [c] Total time of photolysis and collection of spin adducts. [d] Hyperfine splittings of PBN spin adducts in gauss for $C_6H_5CH(R)\,N(O\cdot)\,C(CH_3)_3$: R = CH_3, a_N = 14.82, a_β^H = 3.47 (ref 2); R = CF_3, a_N = 13.30, $a_\beta^H = a_\gamma^F$ = 1.54 (E. G. Janzen and B. J. Blackburn, *J. Amer. Chem. Soc.*, **90**, 5909 (1968)); R = CF_3CF_2, a_N = 14.05, a_β^H < 1.2, a_γ^F = 1.46; R = $ClCF_2$, a_N = 14.06, a_β^H < 1.3, a_γ^F = 2.14; R = CH_3CH_2, a_N = 13.99, a_β^H = 3.08 (ref 4); R = $CH_3CH_2CH_2$, a_N = 13,8, a_β^H = 3.2; R = HCO, a_N = 14.02, a_β^H = 3.17, a_γ^H = 1.36. [e] The PBN chamber was warmed to 40–50° to increase the number of radicals detected. [f] The radicals indicated were detected by *tert*-nitrosobutane produced *in situ* by photolysis of PBN in the gas phase. Hyperfine splittings in gauss for $RN(O\cdot)C(CH_3)_3$ (see Table II for R = acyl): R = CH_3, a_N = 15.5, a_β^H = 11.3 (G. Chapelet-Letourneux, H. Lemaire, and A. Rassat, *Bull. Soc. Chim. Fr.*, 3283 (1965)); R = CH_3CH_2, a_N = 15.9, a_β^H = 13.8, (G. Chapelet-Letourneux, H. Lemaire, R. Lenk, M. A. Marechal, and A. Rassat, *Bull. Soc. Chim. Fr.*, 3963 (1968)); R = $CH_3CH_2CH_2$, a_N = 13.8, a^H = 3.2; see E. G. Janzen, *Top. Stereochem.*, **6**, 177 (1971), for tables of nitroxide coupling constants.

romethyl radicals are readily detected in the photolysis of acetone,[2] 1,1,1-trifluoroacetone or hexafluoroacetone (see Table I for wavelength dependence on the structure of radical produced in the photolysis of trifluoroacetone), no acetyl radicals could be detected by this method. In a solution experiment in benzene at room temperature the acetyl spin adduct can be obtained by allowing *tert*-butoxy radicals (from di-*tert*-butylperoxalate, a thermal source of *tert*-butoxy radicals (BuO·) at room temperature) to react with acetaldehyde in the presence of PBN

$$BuOOCCOOBu \longrightarrow 2BuO\cdot + 2CO_2$$

$$CH_3CHO \xrightarrow{BuO\cdot} CH_3\dot{C}{=}O \xrightarrow{PBN} C_6H_5CH(COCH_3)N(O\cdot)C(CH_3)_3$$

$$a_N = 14.16,\ a_\beta^H = 3.1\ G$$

This approach was unsuccessful with trifluoroacetaldehyde and the following reaction sequence was used to make the trifluoroacetyl spin adduct of PBN in solution

$$C_6H_5CH_2COCF_3 \xrightarrow{BuO\cdot} C_6H_5\dot{C}HCOCF_3 \xrightarrow{t\text{-}BuN=O} C_6H_5CH(COCF_3)N(O\cdot)C(CH_3)_3$$

$$a_N = 14.0,\ a_\beta^H = 5.4\ G$$

It is clear from the difference in splitting constants that the spectra of the acetyl spin adducts could be recognized in the presence of the methyl or trifluoromethyl spin adducts if present in significant quantities. Formyl radicals were detected by PBN in the photolysis of formaldehyde in the gas phase. In benzene solution spectra of the formyl PBN spin adduct could be obtained by reacting *tert*-butoxy radicals with formaldehyde in the presence of PBN

$$HCHO \xrightarrow{BuO\cdot} H{-}\dot{C}{=}O \xrightarrow{PBN} C_6H_5CH(CHO)N(O\cdot)C(CH_3)_3$$

$$a_N = 14.02,\ a_\beta^H = 3.17,\ a_\beta^H = 1.36\ G$$

We are forced to conclude that acetyl radicals do not add

TABLE II: Conditions for the Detection of Radicals by *tert*-Nitrosobutane in the Photolysis of Ketones and Aldehydes[a]

Compound	Lamp	Pressure, Torr	Time, hr	Radicals detected[b]
$CH_3N_2CH_3$	HP/F	0.2	3	CH_3
CH_3COCH_3	LP	0.18–0.20	3	CH_3C=O
CH_3COCH_3	LP/Hg*	0.15–0.20	3	CH_3C=O
CF_3COCH_3	LP	0.20–5.0	4	CF_3, CH_3C=O
CF_3COCH_3	LP	0.5–2.75	1	CF_3, CH_3C=O
CF_3COCH_3	LP/Hg*	0.20–0.25	2	CF_3, CH_3C=O
CF_3COCH_3	HP/F	0.20	2.5	CH_3, CH_3C=O
HCHO	HP/F	0.10	3.5	HC=O
CH_3CHO	HP/F	0.25	2	CH_3C=O
CH_3CHO	HP/F	0.5 + 0.5N_2	2	CH_3C=O
CF_3CHO	HP/F	0.25	2	CF_3

[a] The column titles and symbols have the same meaning as in Table I; *tert*-nitrosobutane was 0.01–0.025 Torr pressure. [b] Hyperfine splittings of *tert*-NB spin adducts in gauss for $RN(O\cdot)C(CH_3)_3$: R = CF_3, $a_N = a_\beta^F$ = 12.28 (K. J. Klabunde, *J. Amer. Chem. Soc.*, **92**, 2427 (1970)); R = CH_3CO, a_N = 7.86 (A. Mackor, Th. A. J. W. Wajer, and Th. J. DeBoer, *Tetrahedron*, **24**, 1623 (1968)); R = HCO, a_N = 6.93, a_β^H = 1.4 (J. W. Hartgerink, J. B. F. N. Engberts, and Th. J. de Boer, *Tetrahedron Lett.*, 2709 (1971)).

We are forced to conclude that acetyl radicals do not add

(6) R. Bowles, J. R. Majer, and J. C. Robb, *Trans. Faraday Soc.*, **58**, 1541 (1962).

to PBN in a gas-phase experiment under the conditions described, or if addition occurs the spin adduct is not collected where it can be detected by our method.

In the photolysis of aldehydes, extra lines in the spectra obtained could be assigned to acyl and alkyl spin adducts of *tert*-nitrosobutane (see footnote *f* of Table I). Apparently PBN sublimed to some extent into the photolysis chamber and was photolyzed in the gas phase to *tert*-nitrosobutane (*t*-NB). This compound is an excellent spin trap in solution[3] and also apparently in the gas phase (as further experiments have shown, see below). Also some di-*tert*-butyl nitroxide is produced from the photolysis of *t*-NB.[7] It should be noted that the usefulness of *t*-NB as a spin trap may be limited because relatively large amounts of di-*tert*-butyl nitroxide are produced during the photolysis and collected along with the spin adducts. The di-*tert*-butyl nitroxide triplet often dominates certain portions of the observed spectrum.

In an effort to find a spin trap suitable for detecting both acetyl and alkyl radicals, *tert*-nitrosobutane vapor was used instead of PBN under similar conditions. Preliminary results are shown in Table II. For some reason, unknown to us at this time, methyl radicals are difficult to detect by this method in the photolysis of acetone or acetaldehyde but not azomethane. Trifluoromethyl, formyl, and acetyl radicals are readily detected. No trifluoroacetyl radicals are detected in the photolysis of trifluoroacetone or hexafluoroacetone although in benzene solution at room temperature the spectrum of the trifluoroacetyl *tert*-butyl nitroxide could be obtained

$$CF_3CHO \xrightarrow{BuO\cdot} CF_3\dot{C}{=}O \xrightarrow{t\text{-NB}} CF_3CON(O\cdot)C(CH_3)_3$$
$$a_N = 5.92, a_\delta^F = 0.88$$

Although the data obtained by the two spin traps are not entirely consistent, the following conclusions can be made. In the low-pressure gas-phase photolysis of ketones and aldehydes at room temperature (1) acetone dissociates to methyl and acetyl radicals. (2) Hexafluoroacetone dissociates to trifluoromethyl radicals and CO. Trifluoroacetyl radicals, if produced at all in the photolysis, apparently dissociate more readily than if produced chemically in benzene at room temperature. (3) Trifluoroacetone dissociates to trifluoromethyl and acetyl radicals at longer wavelengths but at shorter wavelengths methyl and trifluoroacetyl radicals are produced (although the latter has not been detected). The latter result may be reversed to the former in the presence of mercury vapor or *tert*-nitrosobutane (or the products of its photolysis). (4) Formaldehyde dissociates to formyl radical and hydrogen atom (the latter has not been detected to date). (5) Acetaldehyde, propionaldehyde, and butyraldehyde dissociate into methyl, ethyl, and propyl radicals, respectively, and formyl radical (although to date the latter has been detected only from the last named compound). The detection of acetyl radicals by *t*-NB in the photolysis of acetaldehyde is the only exception but the significance of this result is not understood at this time. (6) Trifluoroacetaldehyde dissociates into trifluoromethyl and formyl radicals (although the latter has not been detected to date).

Some of the above conclusions have been reached by others on the basis of different studies.[8] Thus the existence of acetyl radicals in the photolysis of acetone[9] or trifluoroacetone[10] is verified by the isolation of biacetyl under certain conditions. Most reports agree that trifluoroacetyl is very unstable[11] and only a trace of hexafluorobiacetyl has been observed in the flash photolysis of hexafluoroacetone at 195°K.[12] The production of alkyl and formyl radicals from the photolysis of aldehydes (hydrogen atoms and formyl radicals from formaldehyde) has been shown to occur by radical scavenging with I_2 or NO,[8] but usually these studies have been carried out at higher temperatures than used in this work.

Formaldehyde was handled by the method of Spence and Wild.[13] Trifluoroacetaldehyde was generated by dropwise addition of polyphosphoric acid to the ethyl hemiacetal of trifluoroacetaldehyde (commercially available from PCR) at 150–180°. 1,1,1-Trifluoro-3-phenylacetone was made by the method of Sykes, Tatlow, and Thomas.[14]

(7) The "unknown triplet" in ref 2 is probably di-*tert*-butyl nitroxide produced in this manner.
(8) See R. B. Cundall and A. S. Davies, *Progr. React. Kinet.* **4**, 149 (1967).
(9) M. Barak and D. W. G. Style, *Nature (London)*, **135**, 307 (1935).
(10) E. A. Dawidowicz and C. R. Patrick, *J. Chem. Soc.*, 4250 (1964).
(11) P. B. Ayscough and J. C. Polanyi, *Trans. Faraday Soc.*, **52**, 960 (1956); B. G. Tucker and E. Whittle, *ibid.*, **61**, 484 (1965); J. J. Magenheimer and R. B. Timmons, *J. Chem. Phys.*, **52**, 2790 (1970).
(12) J. S. E. McIntosh and G. B. Porter, *Trans. Faraday Soc.*, **64**, 119 (1968).
(13) R. Spence and W. Wild, *J. Chem. Soc.*, 338 (1935).
(14) A. Sykes, J. C. Tatlow, and C. R. Thomas, *J. Chem. Soc.*, 835 (1956).

Department of Chemistry
University of Georgia
Athens, Georgia 30601

Edward G. Janzen*
Irene G. Lopp
T. Vance Morgan

Received October 10, 1972

Interaction of Oxygen with Acetone and 2-Propanol Adsorbed on Magnesium Oxide

Sir: As an extension of the work on the formation of olefin–oxygen adsorption complexes on oxide catalysts,[1] the infrared study of the interaction of oxygen with acetone and 2-propanol adsorbed on MgO was carried out. A series of spectra was obtained by admission of oxygen at room temperature on MgO containing previously adsorbed acetone-d_6 and then raising the temperature of the catalyst. The spectra are shown in Figure 1. It is seen that new bands appear at 1602, 1576, and 1408 cm^{-1} on admission of oxygen. On raising the temperature to 190° the band at 1602 cm^{-1} disappears while the bands at 1576 and 1408 cm^{-1} increase in intensity. The bands at 1576 and 1408 cm^{-1} appear as a pair and occur in the carboxylate frequency range. Furthermore, no shift in frequency was observed with both bands when adsorbing undeuterated acetone in place of acetone-d_6. Thus, both bands can be attributed to the surface carboxylate groups. It was found that adsorption of oxygen was induced already at room temperature by acetone previously adsorbed, its induced amount being nearly 0.6 times the amount of acetone adsorbed. Such behavior together with the appearance of a transient band at 1602 cm^{-1} suggest that the formation of acetone–oxygen adsorption complex takes place, which is converted to the surface compound containing the carboxylate groups. The band at 1602 cm^{-1} appears to be attributable to such an adsorption complex.

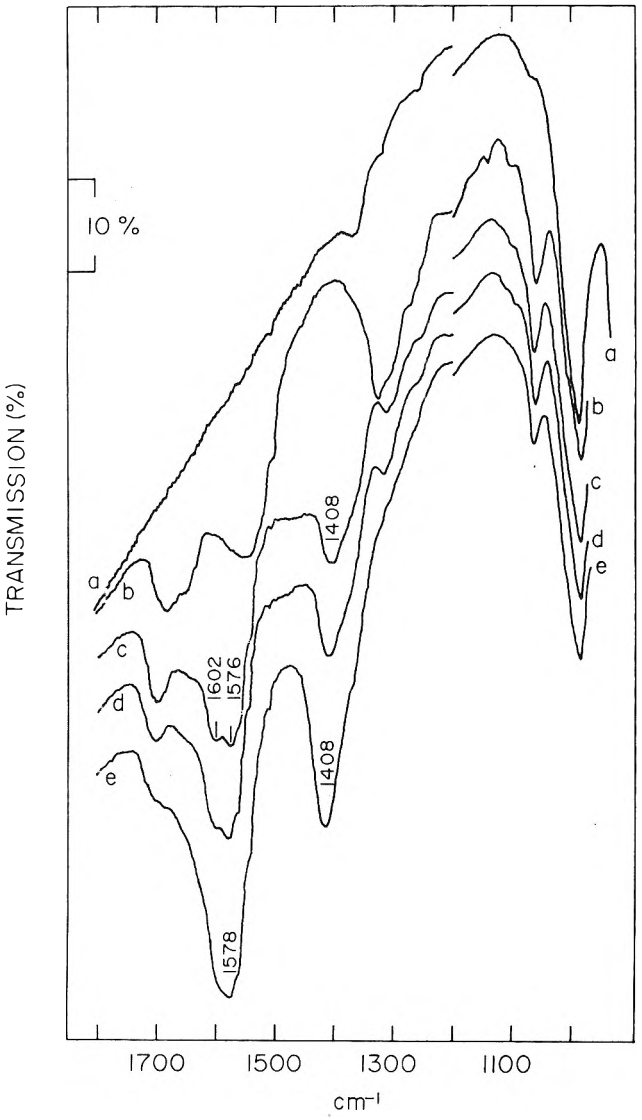

Figure 1. Infrared spectra of acetone-d_6 adsorbed on MgO: (a) MgO (129 mg) outgassed at 500°; (b) after 2-hr adsorption of acetone-d_6 followed by 2-min evacuation at 25°; (c) 20 hr after admission of 17 mm of oxygen at 25°; (d) after 2 hr at 80°; (e) after 2 hr at 190°. (The ordinates are displaced to avoid overlapping of traces.)

Similar experiments were carried out with 2-propanol-d_7 adsorbed on MgO. After admission of oxygen no change in the spectra was observed at room temperature, but on raising the temperature to 160° new bands appeared at 1600 and 1418 cm^{-1} while the band at 1179 cm^{-1} due to the alkoxide group began to disappear.[2] The bands at 1600 and 1418 cm^{-1} are attributed to the carboxylate groups by analogy with acetone described above. The adsorption of oxygen induced by 2-propanol previously adsorbed was found to occur around 120–140°. Simultaneously with the oxygen adsorption acetone was found to desorb from the surface. Such behavior suggests that, during the interaction of oxygen with 2-propanol on MgO, 2-propanol is dehydrogenated to acetone, which is desorbed from the surface or converted to the acetone–oxygen complex and then to the surface compound containing the carboxylate groups. Since the formation of the carboxylate group from acetone takes place even at room temperature as described above, dehydrogenation of 2-propanol to acetone appears to proceed at a slower rate compared to the subsequent step, *i.e.*, the formation of the carboxylate groups. It was found in a separate experiment that in the absence of oxygen dehydrogenation of 2-propanol adsorbed on MgO takes place around 400°. This suggests that the dehydrogenation of 2-propanol is accelerated by the presence of oxygen although the nature of such acceleration is not yet clear.

(1) Y. Kubokawa, T. Ono, T. Tomino, and N. Yano, *Bull. Chem. Soc. Jap.*, **43**, 291 (1970).
(2) Although the appearance of the transient band was uncertain, it appeared that the band at 1600 cm^{-1} was composed of two overlapping bands in contrast with the band at 1418 cm^{-1}

Department of Applied Chemistry
University of Osaka Prefecture
Mozu-Umemachi, Sakai, Osaka, Japan

Yutaka Kubokawa*
Hisashi Miyata
Masayuki Wakamiya

Received June 27, 1972

Here is the ideal way to obtain the ***most reliable reference data available today!*** *All you need is a subscription to the new*

JOURNAL OF PHYSICAL AND CHEMICAL REFERENCE DATA

published by the American Chemical Society and the American Institute of Physics for the National Bureau of Standards.

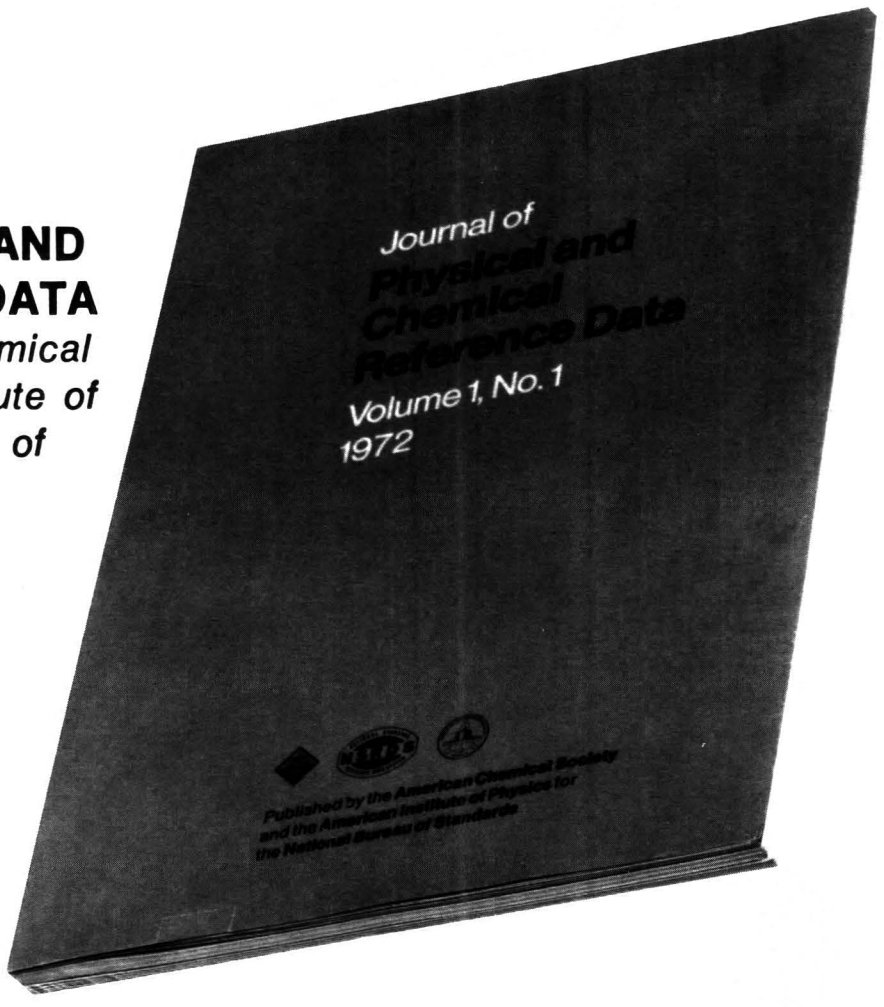

The *Journal of Physical and Chemical Reference Data* fills an important gap in the literature of the physical sciences. Its subject matter is the quantitative numerical data of physics and chemistry. As the new publication vehicle of the National Standard Reference Data System, the *Journal* will contain carefully evaluated data, with recommended values and uncertainty limits chosen by experts in each field. Critical commentary on methods of measurement and sources of error, as well as full references to the original literature, will be an integral part of each compilation.

Examples of some of the critical compilations scheduled for publication in the four issues of Volume I (1972) include:

- Tables of Molecular Vibrational Frequencies, Part 5, T. Shimanouchi
- Gaseous Diffusion Coefficients, by T. R. Marrero and E. A. Mason
- The Spectrum of Molecular Oxygen, by P. Krupenie
- Thermal Conductivity of the Elements, by C. Y. Ho, R. W. Powell and P. E. Liley
- Selected Values of Critical Supersaturation for Nucleation of Liquids from the Vapor, by G. M. Pound
- Gas Phase Reaction Kinetics of the Hydroxyl Radical, by W. E. Wilson, Jr.
- Selected Values of Heats of Combustion and Heats of Formation of Organic Compounds Containing the Elements CHNOPS, by E. S. Domalski
- Microwave Spectra of Molecules of Astrophysical Interest: Formaldehyde, Formamide, Thio-Formaldehyde, by D. R. Johnson, F. J. Lovas and W. H. Kirchhoff

Future compilations are expected to cover areas such as the following:

Band gaps in semiconductors
Nuclear moments
Atomic energy levels and transition probabilities
Diffusion in metals
Electron swarm data
Elastic constants of metals
Surface tension of liquids
Properties of molten salts
Activity coefficients of electrolytes
Equation of state of atmospheric gases
Ionization and appearance potentials

The *Journal of Physical and Chemical Reference Data* is intended to be a definitive source of reliable data on physical and chemical properties. Just fill in the order form at the bottom of this page to receive this invaluable reference source.

JOURNAL OF PHYSICAL AND CHEMICAL REFERENCE DATA
AMERICAN CHEMICAL SOCIETY
1155 Sixteenth Street, N.W.
Washington, D.C. 20036

Yes, I would like to receive the JOURNAL OF PHYSICAL AND CHEMICAL REFERENCE DATA at the one-year rate checked below:

	U.S.	Canada	PUAS	Other Countries
AIP and ACS members	$20.00	$20.00	$23.00	$23.00
Nonmembers	$60.00	$60.00	$63.00	$63.00

Bill me ☐ Bill company ☐ Payment enclosed ☐

Name _____

Street _____ Home ☐ Business ☐

City _____ State _____ Zip _____

JP 72

what's happening on the frontiers of chemical research?

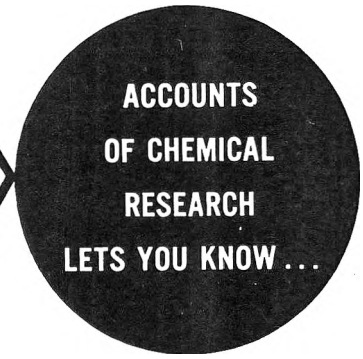

in short, critical articles that cover all areas *of chemical research.*

Whether you are a practicing chemist, professor or student, you want to keep up with the latest developments. Yet few of you have the time to read thoroughly all the journals of primary publications. ACCOUNTS fills the gap.

Written by investigators active in the fields reviewed, ACCOUNTS' concise, brief articles place recent developments in perspective—and relate them to earlier work and their probable future significance.

Once you start relying on ACCOUNTS to keep you informed, you'll wonder how you got along without its monthly arrival.

Complete and mail back the form below. We'll prove how valuable this publication can be to you.

American Chemical Society / 1155 Sixteenth Street, N.W., Washington, D.C. 20036

Please send me ACCOUNTS OF CHEMICAL RESEARCH at the following subscription rates:

ACS members:	☐ U.S. $ 5.00	☐ Canada, PUAS $ 9.00	☐ Other Nations $10.00
Nonmembers:	☐ U.S. $15.00	☐ Canada, PUAS $19.00	☐ Other Nations $20.00

Name _____ Title _____

Employer _____

Address: ☐ Home ☐ Business _____

City _____ State/Country _____ Zip _____

Nature of employer's business? ☐ Manufacturing or processing ☐ Academic ☐ Government
☐ Other _____
(Please indicate)

Note: Subscriptions at ACS Member Rates are for personal use only.

☐ I am an ACS member ☐ I am not an ACS member

Payment must be made in U.S. currency, by international money order, UNESCO coupons, U.S. bank draft; or order through your book dealer.

323